Wide-Area Monitoring based Smart Frequency Control in Future Low-Variable Inertia Systems with CCGT/Wind/PV/BES/Load

A Thesis submitted to the University of Manchester for the degree of

Doctor of Philosophy

in the Faculty of Science & Engineering

2018

Rasoul Azizipanah-Abarghooee

School of Electrical and Electronic Engineering

Table of Contents

List of Figures

List of Tables

List of Abbreviation

AFE	Active Front-End
AVR	Automatic Voltage Regulator
BES	Battery Energy Storage
CCGT	Combined Cycle Gas Turbine
CCL	Constant Current Load
CIL	Constant Impedance Load
COI	Centre Of Inertia
CPL	Constant Power Load
CS	Central Supervisor
DFIG	Doubly-Fed Induction Generator
DOL	Direct On Line
DPL	DigSILENT Programming Language
DSL	DIgSILENT Simulation language
DSR	Demand Side Response
EFCC	Enhanced Frequency Control Capability
GB	Great Britain
GOV	Governor
GT	Gas Turbine
HRSG	Heat-Recovery Steam Generator
IE	Inertia Emulator
IGV	Inlet-Guide-Vane
IM	Induction Motor
IR	Inertial Response
LC	Local Controller
LoG	Loss of Generation

MCS	Monitoring and Control System
MPPT	Maximum Power Point Tracking
NG	National Grid
OCGT	Open Cycle Gas Turbine
PCO	Primary Controller
PDC	Phasor Data Concentrator
PFE	Passive Front-End
PFR	Primary frequency response
PMU	Phasor Measurement Unit
PSS	Power System Stabilizer
PV	Photovoltaic
RA	Regional Aggregator
RoCoF	Rate of Change of Frequency
SFC	Smart Frequency Control
SG	Synchronous Generator
SIM	Smart Induction Motor
ST	Steam Turbine
TSO	Transmission System Operator
VCO	Voltage Controller
VFD	Variable Frequency Drive
VRB	Vanadium-Redox Battery
VSWT	Variable Speed Wind Turbine
WA	Wide-Area
WAMS	Wide-Area Monitoring System
WT	Wind Turbine
WECS	Wind Energy Conversion System

Abstract

The University of Manchester

Faculty of Faculty of Science & Engineering

Rasoul Azizipanah-Abarghooee

Doctor of Philosophy

Wide-Area Monitoring based Smart Frequency Control in Future Low-Variable Inertia Systems with CCGT/Wind/PV/BES/Load

29/09/2018

Renewable energy sources have been extensively developed in many countries like United Kingdom and academia like enhanced frequency control capability (EFCC) project in the last decades due to environmental and energy security risks, however, the system inertia is decreased and frequency response imposes a new challenge for power system operators to maintain power quality. Additionally, restricting RoCoF within satisfactory restrictions is so critical to prevent triggering protection relays that can result in cascaded problems and violate system security. The inertial response (IR) and droop based primary frequency response (PFR) using available spinning reserve power are inherently deployed in conventional power plants (CPPs) to restore sudden frequency deviations. However, power converter interfaces decouple the network frequency from the rotational part of wind energy conversion systems (WECS). In addition, the photovoltaic (PV) units have static dc generators. Thus, these generating units, by themselves, neither obtain the IR nor participate in PFR mechanism. A faster and smarter frequency response is required in order to compensate this phenomenon.

The objective of the research presented in this thesis is to derive the local and wide-area smart frequency control based wide-area monitoring system (WAMS) supported by PMU-based local and wide-area monitoring systems, which is able of releasing fast, smart and robust primary frequency response from fast service providers like combined cycle gas turbine (CCGT), WECS, PV, battery energy storage (BES) and smart induction motors (SIMs). The research proposed in this thesis includes the creation of a novel robust process for the on-line estimation of loss of generation considering load damping impact, PMU latency and implausible spike in frequency data. Furthermore, the CCGT dynamic behaviour is accurately modelled and their unique fast frequency response following the frequency excursions is investigated. This research study also proposes a new wind unit control architecture based on inertial emulator and pitch controller to enhance its frequency response for its high integration in large-scale power systems. The novelty lies in the technique to defining the reference injection power from a control structure based on the novel maximum power point tracking (MPPT) surface deploying rotor speed and pitch angle which doesn't rely on wind speed information. Additionally, the accurate drive train aerodynamic equations of wind turbine are also implemented beside the double-mass mechanical dynamics to investigate the oscillation frequency of electromechanical eigenvalues. Furthermore, a PV and vanadium redox BES enhanced with the control framework to provide primary frequency control, suitable for large scale frequency studies are provided. In case of PV, a primary controller is introduced which permits droop-control operation at deloaded MPPT based on available reserve power and emulated inertial power capturing from dc link capacitor by adjusting the dc link reference voltage. A frequency controller deploying a traditional droop based controller as well as inertial emulator regulates the vanadium redox battery's active power transfer following the disturbance. It is notable that the inertial power is taken from dc link capacitor by adjusting the dc link reference voltage. In addition, a new speed controller is derived enabling the smart induction motor variable frequency drive systems to alter their consumption power in proportion to the grid frequency changes. With this

aim, the reserve rotor speed of primary frequency controller is quantified accordingly and multiplied in a droop gain in order to create fast and controllable reserve power through power electronic interface. A rate limiter is also deployed to pose the rate of change of reserve rotor speed. The motor active power and load inertia are utilized to determine this rate for the first time. The motor inertial power is also suitably emulated. In order to evaluate the effectiveness of the proposed techniques and modelling, a large-scale 36-Zone Great Britain (GB) transmission system network reduction from National Grid (NG) and further data and developed modelling of all service providers is presented to support research into future power networks. The model is intended to be purely indicative of the topology, impedance characteristics driving inter-area and other phenomena across a network of such scale within which a variety of control approaches and dynamic performance characteristics of connected sources may be explored. Flexible architecture of test network permits a broad range of sensitivity studies and physical phenomena critical for design of future power networks.

Declaration

No portion of the work referred to in the thesis has been submitted in support of an application for another degree or qualification of this or any other university or other institute of learning.

Copyright Statement

Acknowledgments

I would like to show my foremost and sincere gratitude to Prof. Vladimir Terzija. He has been an excellent supervisor, constantly pushing me when required and always available to support and secure my research activities, despite his already commitments with many research projects. It was his comprehensive and insightful comments and deep knowledge of power systems that inspired me to study this thesis' subject in depth.

I would like to thank all my past and current friends and colleagues in The University of Manchester for their kind assistances and times in all aspects. In particular, I also would like to express my appreciation to Mostafa Malekpour for his kind help through the several interesting talks, discussions and collaborations as such I learned power system dynamics and simulations.

I would also like to thank the EFCC industrial partners and NationalGrid. I would like to particularly thank Benjamin Marshal from NationalGrid for his kind assistance and discussions from the view of industry throughout a lot of joint and steering group meetings of the EFCC project.

Very special thanks to my family particularly my great parents for their support, unconditional love and encouragement over the past few years.

1. Introduction

During the last decade, there have been some variations in power industry. The usual conventional generators based fossil fuel type as the primary energy resources for about a century is gradually substituted with more efficient and environmental friendly technologies like renewable energy sources. This motivation has arisen from the predicted international growth in power demand and the mitigation of fossil fuels [1]. In addition, the concerns regarding the ecological influence of fossil fuels are putting further pressure on the power industry to eradicate them [2]. As a matter of fact, the Great Britain (GB) electricity industry along with many other countries' power industry from Europe and other continents are trying to adjust their power division to the forthcoming changes. For instance, three main issues which are related to the GB network are as follows [3]:

i) Ageing power plants: Estimation shows that 25 GW of current power equipment are due to be closed by 2020.
ii) Greenhouse gas pollutions: Targets were set to 80% in GB [4] – by 2050, from 1990, in order to ensure considerable emission depletions.
iii) Imports of fossil fuels: Withdrawal of oil and natural gas from the UK Continental Shelf is unceasingly declining which leads to import them from other regions and to reduce security of fossil fuel type resources.

Therefore, the GB electricity system is undergoing huge change, with de-carbonisation process resulting in massive investments in new power plants, renewables and control measures. The GB is expected to deliver 30 % of its electricity from renewable sources by 2020 [5], Germany has a more ambitious goal: 50 % by 2030, 65 % by 2040 and 80 % by 2050 [6] and Denmark aims to reach a 100 % of renewables integration by 2050 (already predicted 70 % share by 2020) [7].

Traditionally, an important natural aid in achieving frequency stability has been system inertia. This is provided largely by thermal power plants, which use rotating synchronous generators. Renewable units, notably converter-connected wind turbines and solar PV, do not provide inertia. As a result of this, as the level of renewable generation and interconnection connected to the system increases there will be a corresponding decrease in the level of system inertia and therefore frequency behaviour following system events will be more dynamic than is presently the case. System inertia will become increasingly variable over time, and will not be uniform across the grid. This thesis will address overall inertia change and geographic variations. The key impact of reduced/variable inertia will be that frequency will change more quickly following an event. A greater volume of response will required to arrest frequency decline which brings a significant increase in costs. An alternative approach proposed in this thesis under the new primary frequency support of new service provers as well as new monitoring and control scheme provides a smaller volume of rapid response which can act very quickly after a system event. This offers significant cost savings and environmental benefits. To reflect the reality of the modern GB electricity system, this thesis will trial a method of monitoring and instructing response from a range of resources: demand side response (DSR), combined cycle gas turbine (CCGT), PV power plants (solar), battery energy storage (BES), and wind power. In this respect, a simple and reliable technique based on the inertial response is deployed to obtain the power mismatch. This research study aims to investigate the dynamic performance of all service providers and improve their controlling structure to help frequency restoration process quickly and sustainably. A new monitoring and control system (MCS) will be developed and used, alongside existing and additional phasor measurement units (PMUs), to monitor the electricity system and instruct response from these resources as required. This response will use local and wide-area frequency and RoCoF to initiate the appropriate frequency response. The methods being trialled will enable the development of new balancing services and additional response capability in the grid. These will mitigate the reduction of system inertia and allow effective management of system frequency. There are three streams of development and demonstration being undertaken which are shown in Figure 1-1.

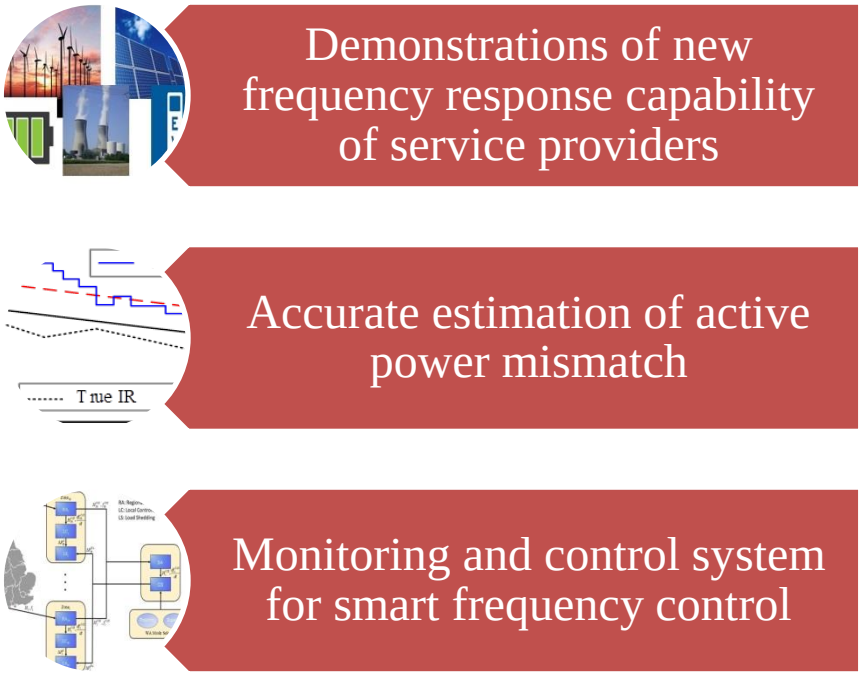

Figure 1-1: Outline of thesis's streams

This chapter provides the basic aims, background and motivation, as well as the specific targets and contributions of the research introduced in this thesis.

1.1 Motivations

One of the key challenges resulting from the renewable energy penetration growth is their impact on the system frequency control capability [8]. The frequency stability of the system depends on the kinetic energy of rotating machines connected to the power system (generators and motors). Elements connected to the power system through power electronics do not contribute to the kinetic energy of the system, therefore decreasing its overall inertia. Wind turbines can provide little or no inertia to the system, because in both of the two newer doubly-fed induction generator (DFIG) and full converter designs, the wind turbine (WT) with its rotating mass is effectively de-coupled from the transmission system by the AC/DC converter. Thus, they cannot be used as sources of natural inertia for the purpose of frequency response. Albeit they can give synthetic inertia by varying their power output, there are technical challenges related to this approach. Solar PV installations do not comprise of any rotating parts, thus have no natural inertia.

One effect of integrating large amounts of renewables is the system inertia reduction. System inertia is forecast to decrease from the level of 130 GVAs down to 50 GVAs by 2025 under National Grid's Slow Progression scenario and 2022 under Gone Green. The rate of change of frequency (RoCoF) following a system disturbance (unbalance between supply and demand) correspondingly goes up from a current level of 0.125Hz/s to 0.3Hz/s (similar size of loss). Furthermore, the system inertia will become increasingly variable over time depending on the level of the penetration of converter-connected generation. Moreover, the inertia mitigation is not uniform across the grid. Areas with high renewable energy penetration show greater frequency deviations within the first few seconds of disturbance compared to the areas where rotating plants are concentrated. The increase in RoCoF makes the system much more vulnerable to sudden changes and therefore, more accelerated frequency response services are

needed to maintain the frequency within its threshold values. There are so many other challenges relating to the inertia reduction of the network such as RoCoF relay, transient stability, cascading the loss of generators, generator withstand capability, power oscillations and recovery post-fault. This work have been and will be addressed the overall inertia change.

Accordingly, a new smart control technology that injects additional power into the power system more quickly than conventional service providers should be created. However, the quicker release of extra active power can put higher stress on the power system network, especially the angular-stability in the initial moments following the incident. In addition, power injection far from the event, can possibly lead to the unreasonable power flows through the transmission lines and rise the cascading outages' risk. On the other hand, injecting power in the proximity to the event can minimise the effect on the normal power system operating circumstance and keeps power flows more intact. Moreover, the provided local response can mitigate the voltage instability risk as it prevents a large amount of power transferred over the long distances [9]-[11].

In order to address the above mentioned issues, once the event is detected the additional active power should be deployed in proportion to the severity of disturbance size and the vicinity to the event location. These fast frequency service providers are enabled by the novel strategies in real time like wide-area monitoring system (WAMS) and fast and new technologies like CCGT, WT, PV, BES, and demand side response. Due to the requirement to adapt this fast frequency response to the synchronous generators (SGs) and the event size, different approaches for bringing new inertial and droop based controllers to WT, PV, BES and smart loads as well as estimation of disturbance size based on time synchronised measurements gathered via Phasor measurement units (PMU) have gained a lot of interests over the last decade [12].

1.2 Aims and objectives

It is worth to notice that this work aims at providing a smaller volume of rapid response than conventional larger volume of slow response after a system event. This study looks to provide a method to enable the development of new balancing services and additional response capability in the grid. The key aspect of deployment of this method in GB network is to mitigate the reduction of system inertia and consent effective supervision of the overall system frequency. In addition, the response will be proportional to the RoCoF than system frequency change.

1.2.1 Demonstrations of frequency response capability

The system frequency response is and will be examined frequency control capability of the resources in terms of response speed and sustainability. Additionally, the effects of different parameters like reheat time constant, inertia constant, damping factor, fraction of total power generated by the turbine, governor regulation, and mechanical power gain factor on system frequency are investigated. After which, the local and wide area SFC based MCS which is explained in the next subsection will be deployed to instruct response from service providers. The characteristics of different forms of response provided by disparate sources are and will be investigated and demonstrated. It means that one of the key aspects of the work is to test and understand the capabilities of different providers. This can be accomplished through a complete system study based on diverse types of scenarios and dynamic performances of service providers.

- Combined cycle gas turbine (CCGT): The purpose of implementing CCGT units is to demonstrate that they can respond to RoCoF in proportion of their dead band and/or a wide-area unblocking signal. The CCGT primary frequency response cannot be as fast as converter-connected units, but the target response should start to deploy by 0.5s from the trigger, and provide a significant volume of response by 2-3s [13].
- Wind turbines (WTs): The potentials of WTs in terms of speed and sustainability are and will be tested and demonstrated with local RoCoF and/or external control signal. The synthetic inertia approach is tested to measure the capability of DFIG based WT to help control the frequency. A target of 10% additional power, fully deployed in 0.2-0.5s from the trigger, and sustained for 5s is feasible in favourable wind conditions without reaching stall [14].
- PV: PV power plants only have a limited capacity to provide reserve power, since for economic reasons, they usually operates at maximum power point (MPP) and their reserve provision is restricted to times when they create considerable amount of power. However, in these cases, they might be implemented for negative response, i.e. whenever frequency is so high. The frequency response of PV power plant will be also investigated to demonstrate an output power curtailment in accordance with frequency, validate a positive frequency response by operating at a power less than MPP. As the PV technology is connected via static converters, the response can be fast. A response within 0.5s is expected [15].
- Battery: Albeit renewable power stations do not save fuel, lose yield revenue whenever they deliver below their maximum power output. Thus, they usually work at full power. Due to this fact, they aren't usually preferred to attain frequency response. This opens the door for the storage units to compensate for that and obtain the positive and negative reserve power from a zero power operating point. Therefore, the renewable power plants can be combined with storage units which are equivalent to combine the no-loss-operation of renewable power plants with the reserve power provision of conventional power plants. Furthermore, this combination allows for considerably higher reaction speeds than conventional power plants may provide, up to the simulation of grid inertia at very high reaction speeds. The principle operability of a frequency control battery on the network will be demonstrated. In today's applications of storage devices, the full response is achieved within 0.5s, and trials of accelerating the response to a target of 0.1s will be carried out. The procedures of practically measuring and combining it with PV power plants need to be investigated as well [16].
- Demand side resources (DSR): DSR will be investigated with local and global control to test the frequency response capability in terms of RoCoF control, Synthetic inertia and real inertia. Demand side response is expected to be longer-term response, and not required to respond within the first second of the event [17].

1.2.2 Accurate estimation of active power mismatch

Following an unintended disconnection of a synchronous generator (SG) from the power system, known as a loss of generation (LoG), it is not trivial to precisely estimate the post-event power system's inertia and LoG size. One of reasons for that is that both of them are a function of the unknown inertia reduction. To solve this challenging problem, this thesis presents an analytical method based on the rate-of-change-of-frequency (RoCoF). The method relies on a modified swing equation, allowing a simultaneous estimation of both unknowns. To this end, the values of mechanical starting time, apparent power and loading of lost generator are formulated for the power system under study. In a practical application, the method can use RoCoF measured by phasor measurement units (PMUs). This thesis discusses the impact of various frequency estimation approaches to the proposed LoG estimation. Furthermore, a method for LoG size estimation, based on the interpolated estimated inertial response, is proposed.

1.2.3 Monitoring and control system

Development of the local and wide-area SFC based monitoring and control system (MCS) is the essential to monitor the transmission networks at a regional and national levels and instruct response from a range of resources. This MCS will use available and additional phasor measurement units (PMUs) to monitor the system in order for providing the response from the frequency service providers. Now, most response is on the basis of the absolute value of frequency. Corrective responses are initiated automatically when this value violates the predefined thresholds. However, the traditional techniques have inherent delays to prevent spurious triggering and over-response. The MCS will deploy the local and global frequency and RoCoF to trigger a response as soon as an event occurs, without spurious triggering. It will focus on the response near to the area of the event so that the disturbance extension is minimised. The frequency response will be proportional to the event size by employing frequency and RoCoF to define the extent of the required response.

1.3 Research Background

The frequency control of power system is inevitable for their stable and reliable operation. The frequency of the system is a measure of balance between supply and demand. Its variation has to be small, almost insignificant and usually it has to be between certain thresholds in order to avoid unwanted events such as the loss of supply or a total blackout. Thus, the frequency stability is the capability of a power system to maintain its frequency within a predefined tolerance band.

The conventional power plants such as thermoelectric and hydroelectric stations are traditionally and still typically deployed to control system frequency. They are as the instantaneous power reserves are used to balance the possible mismatch between generation power and load. The larger the inertia of the system is, the slower the RoCoF is [10]. The conventional generating units are wisely substituted with wind and photovoltaic power plants and this phenomenon will considerably affect the system frequency response. The power network loses the active power reserves of conventional plants as well as instantaneous power reserve since the renewable energy sources are connected to the grid via fast controlled power electronics [18], [19].

Regarding to the WTs, as an example, the Hydro-Québec distribution (HQD) equips all wind power plants with the installed capacity of more than 10 MW to provide inertial response [20]. After that the independent electricity system operator (IESO) in the Canadian province of Ontario did the same for wind power plants greater than 50 MW connected to their transmission system. It is to be noticed that frequency regulation is considered in the market rules [21] and the associated market manual for performance validation [22]. The transmission system operators (TSOs) EirGrid in Ireland has recommended the implementation of an ancillary service market for various technical features like fast frequency response with the aim of mitigating RoCoF [23]. The British TSO National Grid Electricity Transmission (NGET) is working on the results of decreasing inherent inertia of the power system due to integration growth of inverter based equipment [24]. The EFCC project has been started as part of the annual network innovation competition by NGET to find solutions for the RoCoF and frequency challenges [25].

1.4 Configuration of the whole process

The 36-zone GB power network contains of number of zones separated by constraining boundaries, each of which comprises of some PMUs and different frequency response capabilities like fast-acting short-term response as well as longer-term. The ambition is to treat each zone as a block in which the frequency turbulences are detected

and measured and the appropriate response is utilized. This response is controlled through a central system including regional aggregators (RAs) and central application processor. The phase angles, frequency and RoCoF will be measured by the PMUs of each zone. These signals will be sent to the RAs to form zonal frequency and RoCoF signals which are less sensitive to the local variations observed by individual PMUs. The output signals will be received by central application processor to derive a control response. Additionally, the RAs get communicate with the service providers to update the record of available resources. The resiliency and reliability of the system will be improved by deploying these RAs. The data of each zone will be passed to the central application processor to coordinate the mandatory actions. A data list of time/volume capability and availability will be preserved in the controller. This capability can help controller to properly select the available resources, generate the optimal level of response and finalise the frequency response. The action will be consequently sent to the appropriate providers through the control initiation block. Detection of event, computing the required response, optimizing the response and employing the service providers are the functions of central controller.

The central controller must directly communicate with the service providers using an appropriate interface that transform the control signal of the controller into an actuating signal for the service provider. Following the initial action of the central controller, the control process will be delivered to the local controllers considered for each individual resource level which will respond to local measurements. This characteristic allows the scheme to be self-limiting. It should be mentioned that the fast frequency response provided by PVs, wind units and BESs will be still used while the RoCoF reduces to zero at frequency nadir (maximum frequency excursion). Additionally, the CCGT power plants need to be smoothly transferred from fast-acting response to the traditional primary and secondary response. Furthermore, some provisions will be considered to prevent improper operation in oscillatory instability mode.

The whole process of EFCC project is depicted in Figure 1-2.

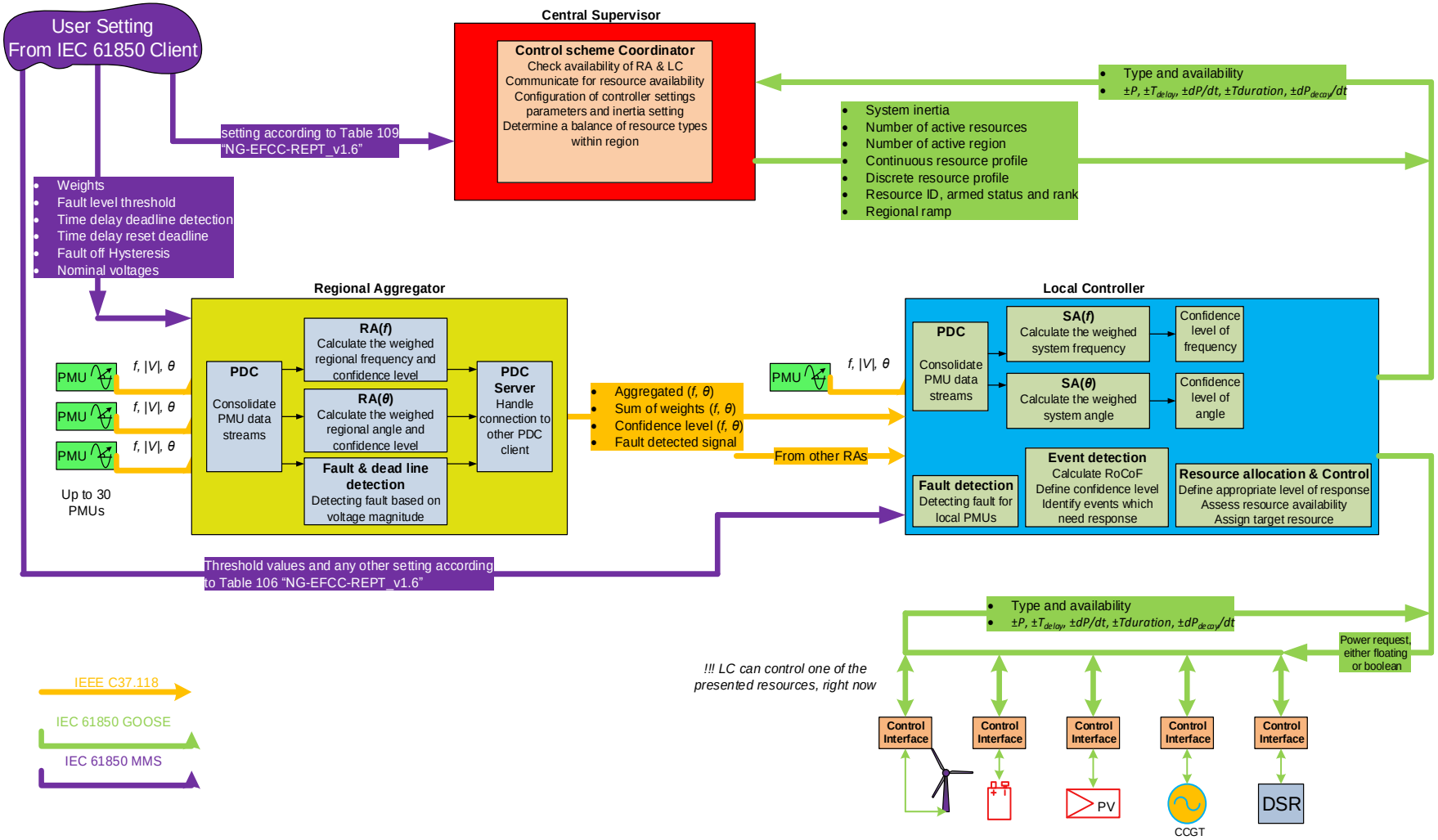

Figure 1-2 : SFC based monitoring and control sche

The first phase of the MCS is to capture data from the zones and send them to the RAs. On the RA, there are a number of functions as follows:

1. *Time Synchronisation:* Providing time configuration characteristic of the individual PMU streams so that it would be equivalent to the phasor data concentrator (PDC) with a suitably low wait time for delayed packets to arrive. The wait time for control should be lower than monitoring applications.
2. *Regional aggregation of frequency and angle:* The inertia weights will be used in the weighted averaging method to obtain a frequency and angle which are represented the center of inertia of the region.
3. *Fault detection:* As can be seen from Figure 1, if a fault is identified by the PMUs, the RA will send a signal as the fault flag. This can be done by measuring the voltage magnitude and comparing it with a threshold.
4. *Dead line detection:* If a contingency is occurred in a line (e.g. disconnected), the voltage level might be less than threshold. In order to prevent a situation that dead line is detected as fault, an algorithm will be used to determine it. If the PMU send a signal from a dead line, the data of angle and frequency will be neglected from the aggregation process.

The frequency and angle of centre of inertia of the region (aggregated frequency and angle) will be calculated in RA and sent as a single IEEE C37.118 frame beside the fault detected and quality information signals to the local controllers (LCs). As the PDC in RA mimics the behaviour of PMU, it can send data through IEEE C37.118 hioghlighted by amber colour. In a power system with *n* zones, each LC will receive *n* aggregated frequency and angle values. On the LC, there are a number of functions related to the different applications. The data from the wide-area must firstly be consolidated, plus the additional PMU stream from the local PMU must be captured. The data is then sent to the event detection application function block for processing. The functions on the LC from the monitoring point of view are as follows:

1) *Confidence level check for frequency and angle:* In this process, the LC will determine this matter that the corresponding data sufficiently represents the behavior of that region or not.
2) *Fault detection:* Apart from the RA, the fault detection is also employed for each local PMU signal.
3) *System aggregation frequency and angle:* The frequency and angle of center of system inertia will be calculated here.
4) *Selection of local/regional aggregated frequency/angle:* The quality of the local signals received by regional PMUs and wide-area signals received by RA will be compared and the better one will be selected. In this case, the LC will utilize this signal and provide an appropriate response, accordingly.
5) *Event detection:*

- The event detection block takes either the system or local frequency as an input, including the fault detected flags. If a fault is detected, the detection is suppressed until the fault is cleared
- By analyzing the slope on the frequency signal, the block will determine if a frequency event has occurred in the system or not. It will also calculate a RoCoF value which is used later for resource deployment in order to characterize the event magnitude.
- The block will also select a pre-event set of angles for the system (from each region and the system)

The resource allocation function is mainly confined to the LC. Parts of the resource allocation occur on the CS in terms of the portfolio management which is communicated to the LC at either periodic intervals or upon report of a change. If an event is detected, the update from the central supervisor (CS) is held at the most recent update. The real time control is all performed on the LC itself autonomously. The interaction here is between the LC and the resource (or resource customer-side controller). The following functions make up the LC control elements:

1) *Define response:* Using the RoCoF output from the event detection, the size of the event is approximated based on the RoCoF and the system inertia estimate. The size of the event is used to create a target response value from the system. This system target response is then spread between the regions according to the post event angular trajectory with more response assigned to regions which see the largest angular movement in relation to the event. This local target response required from each LC is then determined from the regional target response based on a priority ranking function.

2) *Initiate response:* When each LC has determined an appropriate response from its connected resource, it will initiate that response by sending an appropriate signal to the partner resource. Due to the number of potential resources, there are a variety of protocols potentially required which will be investigated and tested throughout the project.

When the signal is received by the resource, or the resource customer-side controller, it will convert this request into physical action on the hardware to deliver the fast frequency response.

1.5 Contributions

The main contributions made during this research are as follows:

- A 36-Zone Great Britain (GB) transmission system network reduction from National Grid (NG) and further data and modelling developed by the authors is presented to support research into future power networks. The model as presented is not intended to be roughly reflective of actual GB network dynamics rather is intended to be purely indicative of the topology, impedance characteristics driving inter-area and other phenomena across a network of such scale within which a variety of control approaches and dynamic performance characteristics of connected sources may be explored. The dynamic performance of this test network is investigated following these modifications against the condition of loss of generation. Illustrative dynamic models of generator, governor, power system stabilizer, voltage controller and static voltage controller for the purpose of frequency control dynamic studies are selected. Impact of system inertia on electromechanical modes is examined using the modal analysis approach. Mode shape concept is employed to determine dominant units and contribution of different zones in network frequency oscillations. Time domain simulation studies are undertaken to validate the modal analysis results. The condition of different regions from the viewpoint of frequency nadir and maximum rate of change of frequency for contingency cases and extreme cases are examined. Flexible architecture of test network permits a broad range of sensitivity studies and physical phenomena critical for design of future power networks. (Chapter 2)
- Whilst combined cycle gas turbines (CCGT) have become more popular in power systems due to their economically efficient and environment friendly characteristics, their frequency responses are substantively diverse from other conventional units. Therefore, this study develops and provides researchers a four-area based Klein-Rogers-Kundur (KRK) and 36-zone Great Britain (GB) networks with high integration of CCGTs based on UK National Grid data. The suitable dynamic modelling of CCGT, generator, governor, power system stabilizer, voltage controller and static voltage controller for the purpose of frequency control dynamic studies are chosen. Dynamic impact of CCGTs on small signal stability and electromechanical modes is investigated using the modal analysis. Time domain dynamic studies are utilized to validate the CCGT integration effects. The condition of different areas from the frequency nadir and maximum rate of change of frequency point of view for N-1 contingency and worst cases are evaluated. The prodigious design of test system documents a broad series of sensitivity analysis to be prearranged (Chapter 3).
- There is an upward trend of integrating wind energy conversion systems throughout modern power networks; therefore their grid codes seem to be revised so that they should be able to assist in frequency regulation currently carried out by conventional units. Thus, a new validate and average wind energy conversion system is derived and its associated novel droop and inertial based frequency controllers is investigated. In this approach, wind turbine aerodynamic is perfectly formulated and the maximum power point tracking surface is obtained in terms of pitch angles and rotor speed. The reference pitch angles are also determined by droop based primary frequency controller in proportion of required

reserve power. Not only does this unique strategy make a trade-off between fast injection power and small rotor speed change, it also doesn't require measured wind speed data. (Chapter 4)

- Flexible induction motors are tested to analyse the potential of industrial demand response to handle the system frequency in smart grids at the demand side, which can mitigate the network reliance on expensive generation side controllers. A new speed controller is derived enabling the smart induction motor variable frequency drive systems to alter their consumption power in proportion to the grid frequency changes. With this aim, the reserve rotor speed of primary frequency controller is quantified accordingly and multiplied in a droop gain in order to create fast and controllable reserve power through power electronic interface. A rate limiter is also deployed to pose the rate of change of reserve rotor speed. The motor active power and load inertia are utilized to determine this rate for the first time. This is due to the fact that amplitude of electromagnetic torque variation and motor stator's current variation would be largely underestimated neglecting motor's load inertia. Additionally, the motor inertial power is suitably emulated and the grid frequency variation is directly integrated into motor inverter reference frequency instead of rate of change of frequency (Chapter 7).
- Following an unintended disconnection of a synchronous generator (SG) from the power system, known as loss of generation (LoG), it is quite difficult for power systems operators to correctly estimate the post-event power system's inertia and LoG size as they are both functions of the unknown inertia reduction. To solve this problem, the chapter presents a novel analytical method based on the rate-of-change-of-frequency (RoCoF). The method relies on a modified swing equation that allows to directly take into account the inertia reduction and the consequent LoG estimation. To this end, the averaged values of mechanical starting time, apparent power and loading are introduced for the power system under study. Since the method may be implemented by RoCoF measurements provided by phasor measurement units (PMUs), the impact of various frequency estimations on the proposed LoG estimation is discussed. Furthermore, a method to get a reliable estimation of the LoG size based on the interpolated estimated inertial response is also proposed. (Chapter 8).
- The local and wide-area SFC based monitoring and control schemes are derived. The local SFC algorithm would, based on knowing the max delta P deployment for the system prior to the disturbance and from the RoCoF (df/dt) as calculated for the centre of inertial mass in the region, deploy this scale of response in sufficient time, assuming (to make it easy) this is being achieved purely from demand reduction action. This to objective then to be delivered based on an "event trigger" based on regional RoCoF (df/dt) and absolute frequency measured in a defined period which can be up to as long as there is a respond, the volume of response deployed by zone being dependent on the observed RoCoF (df/dt). The objective to see if this "simple" system, which would be less reliant on wide area coms and real-time calculation but which will see a regionally different RoCoF (df/dt) across the system during the event, whether it deploys enough response fast enough in practice or not (Chapter 9).

1.6 Outline of the Thesis

Chapter 2-System studies of an appropriate GB network without Monitoring and Control Scheme (MCS)

To study the dynamics of power system frequency, a simplified and equivalent GB dynamic network model is developed and evaluated against the traditional disturbances. The GB system, the frequency event and its containment are dynamically modelled. The key factors contributing to differences in frequency change across the system are identified and understood. The differences between the regional and national frequency across the period of fast response is investigated. The mode shape and participation factor concepts are deployed to analyse the oscillation of the signals and determine the dominant units. Additionally, the minimum post-contingency frequency (frequency nadir), rate of change of frequency and settling frequency are evaluated to determine their importance.

Chapter 3-Development and Investigation of Fast Frequency Response of CCGT

This chapter firstly concentrates on describing the main components models of combined cycle gas turbines (CCGTs). Then the control loops of the combined-cycle plant which either directly affect the response of the power plant to power system disturbances or have an effect on the design or operation of the plant are addressed. The model incorporates gas turbine, heat recovery steam generator and steam turbine and includes speed control, temperature control and inlet guide vane control. Then, an appropriate model of CCGTs for short-term dynamic study following the frequency excursion is simulated in DIgSILENT PowerFactory. The performance of the combined cycle plant is investigated following system disturbances.

Chapter 4-New Wind Energy Conversion System Architecture for Power System Primary Frequency Regulation

This chapter proposes a new wind unit control architecture based on inertial emulator and pitch controller to enhance its frequency response for high wind-integrated large-scale power systems. The novelty lies in the technique to defining the reference injection power from a control structure based on the novel maximum power point tracking surface deploying rotor speed and pitch angle. The pitch angle reference regulation made by a governing function identical to conventional units. This pitch-angle based control model employs a trade-off of two essential objective functions in selecting the wind turbine operating point those are small rotor speed change and fast injection power. Moreover, this novel structure doesn't rely on wind speed information. The accurate drive train aerodynamic equations of wind turbine are also implemented beside the double-mass mechanical dynamics to investigate the oscillation frequency of electromechanical eigenvalues.

Chapter 5-Reserve Power and Inertial Emulator Based PV System: Development and Formulation

A suitable model of PV system for studying its short-term dynamic response to a system frequency deviation is developed. The developed primary frequency controllers permit the droop-control operation at deloaded MPPT based on available reserve power and emulated inertial power capturing from dc link capacitor by adjusting the dc link reference voltage. The main benefit of the deployed PV model is that it has almost no influence on generated power of PV system. It has also this ability to greatly track the solar irradiance and module temperature variation and scavenge maximum possible energy.

Chapter 6-Assessment of the Fast Frequency Support of BES

A suitable model of battery energy storage system (BESS) system for studying its short-term dynamic response to a system frequency deviation is developed. In the chpater, the concentration is on describing the main component of the BESS system and its relevant equations. Available inertia and droop responses from the BESS system to help supporting the primary frequency control in power system networks are also analytically investigated. Then the model is utilised in conjunction with a simple but practical two-area Klein-Rogers-Kundur (KRK) power systems as well as 36-zone GB system to study the impact of increasing levels of wind energy conversion system (WECS) and photovoltaic (PV) generations on frequency control. The modal analysis and dynamic time-domain simulation tools are utilised to study the power system frequency response and investigate how the BESS can impact this response on a test power system with high penetration of the wind turbines (WTs) and PV systems.

Chapter 7-Smart Induction Motor Variable Frequency Drive Systems for Frequency Regulation

Flexible induction motors are tested to analyze the potential of industrial demand response to handle the system frequency in smart grids at the demand side, which can mitigate the network reliance on expensive generation

side controllers. A new speed controller is derived enabling the smart induction motor variable frequency drive systems to alter their consumption power in proportion to the grid frequency changes. With this aim, the reserve rotor speed of primary frequency controller is quantified accordingly and multiplied in a droop gain in order to create fast and controllable reserve power through power electronic interface. A rate limiter is also deployed to pose the rate of change of reserve rotor speed. The motor active power and load inertia are utilized to determine this rate for the first time. This is due to the fact that amplitude of electromagnetic torque variation and motor stator's current variation would be largely underestimated neglecting motor's load inertia. Additionally, the motor inertial power is suitably emulated and the grid frequency variation is directly integrated into motor inverter reference frequency instead of rate of change of frequency.

Chapter 8-Assessment of the Value of Wide-Area and Local SFC in GB Power Systems

Development of the wide-area and local SFC schemes as the MCS are the central to the fast frequency response which monitor the transmission networks at the national and regional levels and instruct response from a range of resources, respectively. This MCS use available and additional data from PMUs to monitor the system and a central control unit to provide the flexible response from the frequency service providers. The SFC is modelled deploying purely static load response, however, the algorithms developed are flexible to look at more complex deployments of response as needed. In traditional frequency controllers, most response is on the basis of the absolute value of frequency. Corrective responses are initiated automatically when this value violates the predefined thresholds. However, the traditional techniques have inherent delays to prevent spurious triggering and over-response. The wide-area and local SFC respectively deploy the global and local RoCoF to trigger a response as soon as an event occurs, without spurious triggering. They can focus on the response near to the area of the event so that the disturbance extension is minimised. The frequency response is proportional to the event size by employing frequency and RoCoF to define the extent of the required response. This methodology is characterised to be self-limiting and not over-respond.

Chapter 9-A New Approach to the On-line Estimation of the Loss of Generation Size in Power Systems

A novel analytical approach based on the rate of change of frequency (RoCoF) for estimating the size of such a LoG is presented. It is based on modifying swing equation to consider inertia reduction in LoG size estimation, as much as possible. To this end, the averaged values of mechanical starting time, apparent power and loading are defined for the power system. Moreover, how different load models and characteristics of frequency measured by phasor measurement units (PMUs) effect on LoG size estimation is well addressed. Furthermore, a method to get a reliable estimation of LoG size based on the interpolated estimated inertial response is proposed.

Chapter 10-Thesis Summary

This chapter summarises the research presented in this thesis and its contribution plus some possible opportunities for further development of this research.

1.7 List of Publications

Journal Papers

1. R. Azizipanah-Abarghooee, M. Malekpour, M. Paolone, and V. Terzija, A new approach to the on-line estimation of the loss of generation size in power systems, *IEEE Trans. Power Syst. 2018, Accepted.*
2. R. Azizipanah-Abarghooee, M. Malekpour, Y. Feng, and V. Terzija, Modeling DFIG based system frequency response for frequency trajectory sensitivity analysis, *Int. Trans. Electr. Energy Syst., 2018, Accepted.*

3. M. Malekpour, R. Azizipanah-Abarghooee, M. Zare, A. Kiyoumarsi, and V. Terzija, Synchronous machine modeling based on transient time constants and reactances, *Int. J. Electr. Power Energy Syst. 2018, Accepted.*
4. R. Azizipanah-Abarghooee, M. Malekpour, F. Teng, G. Strbac, and V. Terzija, Smart frequency response of induction motor variable frequency drive system, *IEEE Trans. Power Syst., 2018. Submitted.*
5. R. Azizipanah-Abarghooee and V. Terzija, 36-zone network based on reduced GB transmission network data: development and frequency response application, *IET Gener. Transm. Distrib. 2018, To be Submitted.*

Conference Papers

1. R. Azizipanah-Abarghooee, M. Malekpour, M. Zare, and V. Terzija, A new inertia emulator and fuzzy-based LFC to support inertial and governor responses using Jaya algorithm, *IEEE PES General Meeting, Boston, USA, 2016.*
2. R. Azizipanah-Abarghooee, M. Malekpour, N. Shams, M. Karimi, and V. Terzija, Trajectory sensitivity analysis of rate of change of frequency using system frequency response model, *IEEE PES Innov. Smart grid. Tech., ISGT Europe, 2018.*
3. R. Azizipanah-Abarghooee, M. Malekpour, M. S. Ayaz, M. Karimi, and V. Terzija, Small Signal Based Frequency Response Analysis for Power Systems, *IEEE PES Innov. Smart grid. Tech., ISGT Europe, 2018.*

Technical Reports

1. R. Azizipanah-Abarghooee, M. Karimi, and V. Terzija, Frequency response of a system without supervisory control, *WP3.1.1, NIC based EFCC Project.*
2. R. Azizipanah-Abarghooee, M. Karimi, and V. Terzija, System studies of selected and known test networks without Monitoring and Control Scheme (MCS) in PowerFactory, *WP1.4.1, NIC based EFCC Project.*
3. R. Azizipanah-Abarghooee, M. Karimi, and V. Terzija, System studies of an appropriate GB network without Monitoring and Control Scheme (MCS) in PowerFactory, *WP1.4.2, NIC based EFCC Project.*
4. R. Azizipanah-Abarghooee, M. Karimi, and V. Terzija, Integration of wind turbine based DFIG intro the representative 2-area test power networks; assessment of the frequency, *WP1.4.1, NIC based EFCC Project.*
5. R. Azizipanah-Abarghooee, M. Karimi, and V. Terzija, Integration of wind turbine based DFIG intro the representative GB test power networks; assessment of the frequency, *WP1.4.2, NIC based EFCC Project.*
6. R. Azizipanah-Abarghooee, M. Karimi, and V. Terzija, Integration of CCGT intro the representative 2-area test power networks; assessment of the frequency, *WP1.4.1, NIC based EFCC Project.*
7. R. Azizipanah-Abarghooee, M. Karimi, and V. Terzija, Integration of CCGT intro the representative GB test power networks; assessment of the frequency, *WP1.4.2, NIC based EFCC Project.*
8. R. Azizipanah-Abarghooee, M. Karimi, and V. Terzija, Integration of PV intro the representative 2-area test power networks; assessment of the frequency, *WP1.4.1, NIC based EFCC Project.*
9. R. Azizipanah-Abarghooee, M. Karimi, and V. Terzija, Integration of PV intro the representative GB test power networks; assessment of the frequency, *WP1.4.2, NIC based EFCC Project.*
10. R. Azizipanah-Abarghooee, M. Karimi, and V. Terzija, Integration of BESS intro the representative 2-area test power networks; assessment of the frequency, *WP1.4.1, NIC based EFCC Project.*
11. R. Azizipanah-Abarghooee, M. Karimi, and V. Terzija, Integration of BESS intro the representative GB test power networks; assessment of the frequency, *WP1.4.2, NIC based EFCC Project.*
12. R. Azizipanah-Abarghooee, M. Mingyu, H. Pan, Y. Liu, M. Karimi, and V. Terzija, Modelling and Study of Interim, Equality and Proximity based Wide-Area Monitoring and Control Scheme (MCS) using 36-Zone GB Model in PowerFactory, *WP3, NIC based EFCC Project.*

1.8 References

[1] Projecting Electricity Demand in 2050 No. PNNL-23491, *Pacific Northwest National Laboratory* (PNNL), Richland, WA (US), 2014.

[2] M. R. Islam, S. Mekhilef, and R. Saidur, "*Progress and recent trends of wind energy technology*, " *Renew Sustain Energy Rev.*, vol. 21, pp. 456-468, 2013.

[3] Meeting the Energy Challenge "*A white paper on energy*", May 2007.

[4] Climate Change Act, November 2008.

[5] The UK Renewable Energy Strategy, Department of Energy and Climate Change, July 2009.

[6] Energy Concept for an Environmentally Sound, Reliable and Affordable Energy Supply, September 2009.

[7] Energy Policy in Denmark, Danish Energy Agency, December 2012.

[8] System Operability Framework (SOF) – National Grid – July 2016.

[9] A. Ghaleh, M. Sanaye-Pasand, and A. Saffarian, "Power system stability enhancement using a new combinational load-shedding algorithm," *IET generation, transmission & distribution*, vol. 5, pp. 551-560, 2011.

[10] V. Terzija, G. Valverde, D. Cai, P. Regulski, V. Madani, J. Fitch, et al., "Wide-area monitoring, protection, and control of future electric power networks," *Proceedings of the IEEE*, vol. 99, pp. 80-93, 2011.

[11] A. G. Phadke and J. S. Thorp, "Synchronized Phasor Measurements and Their Applications," Synchronized Phasor Measurements and Their Applications, pp. 1-247, 2008.

[12] V. Terzija, "Adaptive underfrequency load shedding based on the magnitude of the disturbance estimation," *IEEE Transactions on Power Systems*, vol. 21, pp. 1260-1266, Aug 2006.

[13] G. Lalor, J. Ritchie, D. Flynn, and M. O'Malley, "The impact of combined-cycle gas turbine short-term dynamics on frequency control," *IEEE Trans. Power Syst*., vol. 20, no. 3, pp. 1456-1464, Aug. 2005.

[14] Wilches-Bernal F, Chow JH, Sanchez-Gasca JJ. A Fundamental Study of Applying Wind Turbines for Power System Frequency Control. *IEEE Transactions on Power Systems*. 2016 Mar;31(2):1496-505.

[15] V.A.K. Pappu, B. Chowdhury, and R. Bhatt, "Implementing frequency regulation capability in a solar photovoltaic power plant," *In Proc. North American Power Symp. (NAPS)*, Sep. 26-28, Arlington, TX, 2010, pp. 1-6.

[16] S. Chen, T. Zhang, H. B. Gooi, R. D. Masiello, and W. Katzenstein, "Penetration rate and effectiveness studies of aggregated BESS for frequency regulation," IEEE Trans. Smart Grid, vol. 7, no. 1, pp. 167-177, Jan. 2016.

[17] V. Trovato, I. M. Sanz, B. Chaudhuri, and G. Strbac, "Advanced control of thermostatic loads for rapid frequency response in Great Britain," IEEE Trans. Power Syst., vol. 32, no. 3, pp. 2106-2117, May 2017.

[18] Smart Frequency Control Project, http://www.nationalgridconnecting.com/The_balance_of_power/

[19] P. Kundur, N. Balu, and M. Lauby, "Power system stability and control," New York: McGraw-Hill; 1994.

[20] X. Yingcheng and T. Nengling, "Review of contribution to frequency control through variable speed wind turbine," Renew Energy, pp. 11, pp. 1671-1677, 2011.

[21] G. Lalor, A. Mullane, and M. O'Malley, "Frequency control and wind turbine technologies," IEEE Trans Power Syst., vol. 20, pp. 1905-1913, 2005.

[22] Requirements for the interconnection of distributed generation to the hydro-québec medium-voltage distribution system, February 2009', http://www.hydroquebec.com/transenergie/fr/commerce/pdf/e1201_fev09_en.pdf, accessed 01 April 2015

[23] 'Market Rules for the Ontario Electricity Market, March 4 2015', http://www.ieso.ca/Pages/Participate/Market-Rules-and-Manuals-Library.aspx, accessed 01 April 2015

[24] ‘Market Manual 2: Market Administration, Performance Validation, Issue 1.1’, http://www.ieso.ca/Documents/imowebpub/201406/IESO_REQ_0208_v1.1.pdf, accessed 01 April 2015

[25] ‘DS3 System Services, Procurement Design, SEM Committee Consultation, SEM-14-059, 09 July 2014’, http://www.eirgrid.com/media/DS3_System_Services_Procurement_Consultation_SEM-14-059.pdf, accessed 01 April 2015

[26] System Operability Framework 2014, September 2014’, http://www2.nationalgrid.com/mwg-internal/de5fs23hu73ds/progress?id=oTf7dd-c2QkY4LQbBoR1nvWuggyz1mbqyOZQlnJ_SVE, accessed 01 April 2015

[27] Enhanced Frequency Control Capability (EFCC), October 2014’ //www.smarternetworks.org/Files/Enhanced_Frequency_Control_Capability_141125 101940.pdf, accessed 01 April 2015

2. System studies of an appropriate GB network without Monitoring and Control Scheme (MCS)

To study the dynamics of power system frequency, a simplified and equivalent GB dynamic network model is developed and evaluated against the traditional disturbances for its appropriateness to carry out studies of the EFCC project to be demonstrated. Using the simplified model, case studies are undertaken to exhibit system frequency response in the GB systems against the generator trip. Based on the simulation results, discussions are made on the performance of the 36-zone GB network to arbitrate the suitability of applying different frequency-based scenarios in GB power network. All the nonlinearities of the system and devices including governor (GOV), generator, power system stabiliser (PSS), voltage controller (VCO) and static voltage controller (SVC) have been considered in the simulation studies and neglected from the modal analysis in the model. In this study, the small signal analysis is investigated and its pertinent to the frequency response of the system is analysed. Then, the effects of disparate devices like VCO, PSS, GOV and SVC as well as some controlling parameters are investigated by small-signal analysis and time-domain simulation studies. Additionally, the mode shape and participation factor concepts are deployed to analyse the oscillation of the signals and determine the dominant units. Additionally, the minimum post-contingency frequency (frequency nadir), rate of change of frequency and settling frequency are evaluated to determine their importance. The summary would be useful for system operators to know the local and entire frequency response of the system using the modal analysis, mode shape, participation factor and time domain analysis.

2.1.1 Literature Review

Power system frequency expresses the electrical active power balance between generation and consumption sides second-by-second. A power network can be subjected to large excursions of system frequency with lengthy settling times and unsatisfactorily large steady-state bias in a power system with low inertia level and/or a system without sufficient governor controlling action. Balancing generation and demand in the Great Britain (GB) power system will become more challenging as the generation mix changes towards higher levels of non-synchronous generation, the illustration used for this chapter being the 2011 Gone Green 2020 scenario [1]. This rate against which the trend in this scenario is realized is principally driven by increasing penetration of inertia-less converter-connected renewable energy sources, alongside traditional thermal power plant reduced availability and increased levels of HVDC based interconnection with external networks. Traditional analysis of frequency tends to be done at a purely national level, however, it is to be noticed that the point of frequency loss is localised and can vary in a physical power network. Moreover, the delivery of response occurs in discrete localised actions across the system. Therefore, in addition to any frequency response resulting in oscillations following the infeed loss in a low inertia system at the point of frequency recovery, the low frequency oscillations can be also observed during that recovery period, and differently across the physical power network as the power transfers supporting an energy balance excite inter-area modes [2]. Within a low inertia system environment, it can be examined that what extent the loss of the fast power responses provided by system inertia may be mitigated by the fast response from different frequency ancillary service providers. These services have the potential to excite the inter-area modes within a transmission system and their control and effects of deployment need to be understood against the network impacted [3].

During a frequency event, there is the potential for further instability to develop and for particular control approaches to develop towards instability while the inter-area modes with insufficient damping are excited [4]. It is also possible for nodal frequency nadir and rate of change of frequency (RoCoF) to substantively differ from the equivalent national level. To avoid such scenarios, the small signal stability, modal analysis, mode shape concept, time-domain simulation, frequency Nadir and RoCoF evaluation should be examined offline through multiple scenarios. This analysis which is commonly employed by the system operators in the control center room improves the situational awareness by providing a visualization of the damping of slowest

electromechanical modes, their mode shapes, frequency response, RoCoF, and worse case time-domain analysis in terms of minimum frequency Nadir and maximum RoCoF.
Generally speaking, for running practical dynamic analysis, both the parameters and types of the dynamic modeling should be accessible for all power system components. On one hand, each electric company has its own dynamic types and parameters for its power system devices. On the other hand, it is noteworthy that several IEEE power test systems which are available for steady state analysis suffer from lack of dynamic models. In this regard, a few IEEE standards note that practical test systems are proposed in [5], [6]. There are several cases where researchers are enforced to select their own dynamic models which lead to inconsistency between them [7].
This study develops a further modification of a 36-zone model as provided by National Grid (NG) to the researchers for the sake of improving inter-area, frequency nadir, and RoCoF evaluations using this reduced model of the GB system [8]. The dynamic parameters for a sixth-order and fifth order cylindrical round and salient pole rotors synchronous machine models, voltage controllers (VCOs), power system stabilizer (PSSs) and governors (GOVs) are defined. The provided system is configured using illustrative structural characteristics and data applied in DIgSILENT PowerFactory and can also be modeled in other software packages like RSCAD/RTDS. Therefore, the test system users can readily adjust its characteristics to satisfy their preferences, or to study other problems like power system dynamic voltage stability that have not yet investigated on this network.
The 36-zone network differs in purpose and scale from previously developed test systems. This is a reduced model which has sought to preserve in its reduction known aspects of the inter-area dynamics of the GB system this representing a reduction of publically available network topology data as found within National Grids Electricity Ten Year Statement [9]. This network is currently being utilized for EFCC project [3] and is proposed to be used in forthcoming work packages of MIGRATE project [10] in collaboration with industry and university partners. The proposed 36-Zone GB test network can be an optimal candidate for development and testing of novel solutions in the areas of power system monitoring, protection, control, optimal exploitation and in general testing of smart grid methods, tools and solutions, a number of which are discussed below. The exhibition of a combination of local, inter-area and electromechanical modes, deployment of all VCO-PSS-GOV-SVC damping controllers, evaluation of the small signal and modal analysis results are achieved by comparing the eigenvalues and time-domain responses.

2.1.2 UK Map: How the UK Generates its Electricity by 36-Zone GB Network?

All simulations regarding locational aspect of frequency response are done on 36-zone GB network in DIgSILENT PowerFactory. The single line diagram of GB network is depicted in Figure 2-1 in which the numerous generation and consummation sites are concentrated on the southern part rather than the northern one. As a matter of this fact, the zones are numbered from the bottom to top. As mentioned before, the total load demand of this grid is approximately 40 GW. In this case it is supposed that this load is supplied by 41 power stations consisting of 22 gas power plants, 6 nuclear power stations, 8 biomass plants, 4 hydroelectric generations and one pumped storage unit. It is notable that total power generated by these units is 48 GW. Moreover, 4 western HVDC stations can transfer 3 GW electric powers to the UK. The electric power difference between the power output of 41 power plants plus 4 western HVDC links and grid power consumptions and losses (about 10 GW) can be transferred to the neighbourhoods using 8 eastern and southern HVDC links. Table 2-1 tabulates complete information about the generating units' types and their equipment like voltage controllers (VCOs), power system stabiliser (PSSs) and governors (GOVs). Data of this equipment and relevant parameters are detailed hereinafter. The geographical distribution of loads and their values are portrayed in Figure 2-2. It is to be noted that demand of each zone is modelled by a complex load. The lowest and highest amounts of loads i.e. 60 MW and 3,670 MW are located in zones 31 (Northern area) and 8 (south-eastern area near to London), respectively. The 36-zone GB network can be divided by three parts of bottom, middle and top where 58%, 32% and 10% are respectively assigned to them. Thus, the load demand is increased significantly from the northern area to southern one.

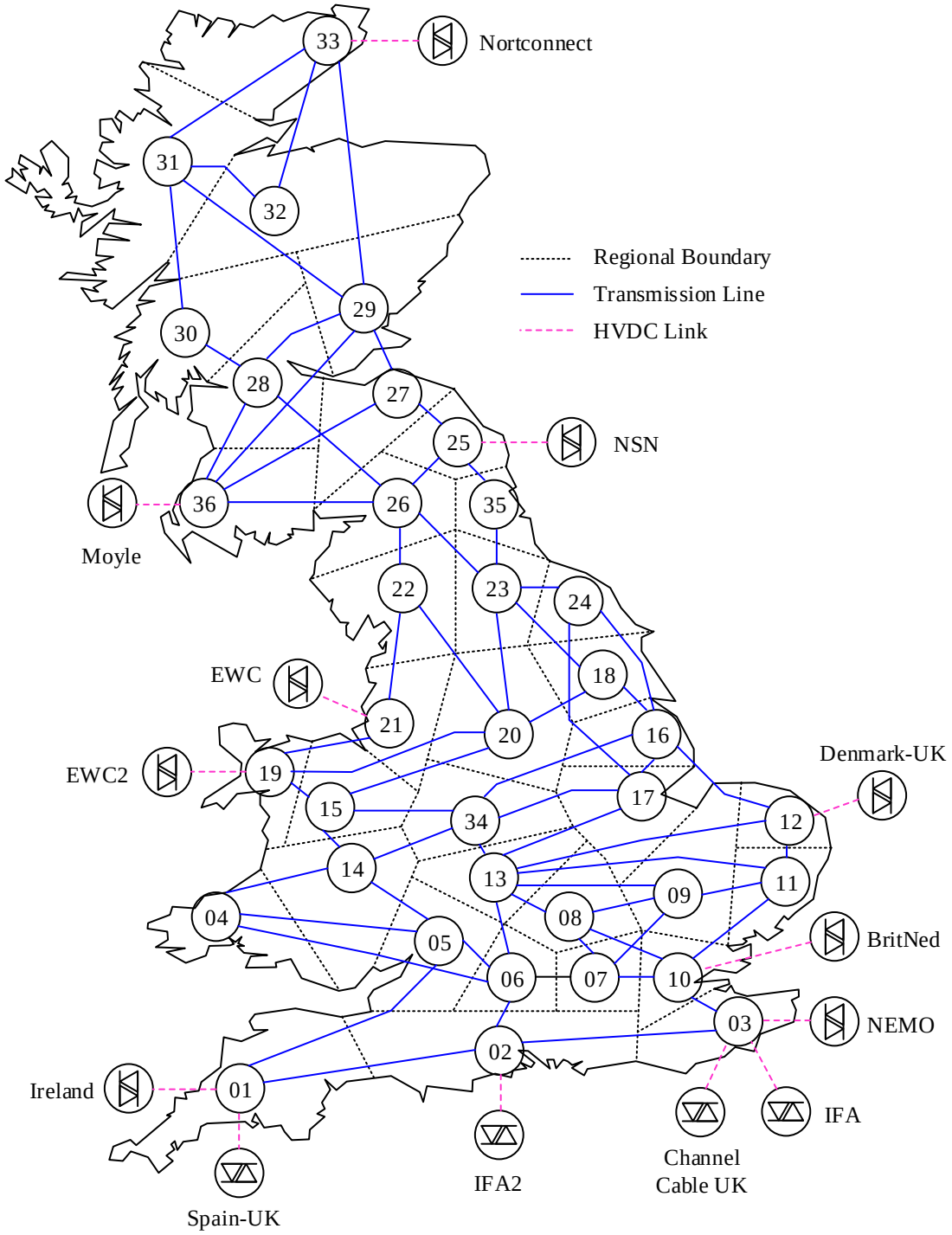

Figure 2-1 : Single line diagram of 36-zone GB network.

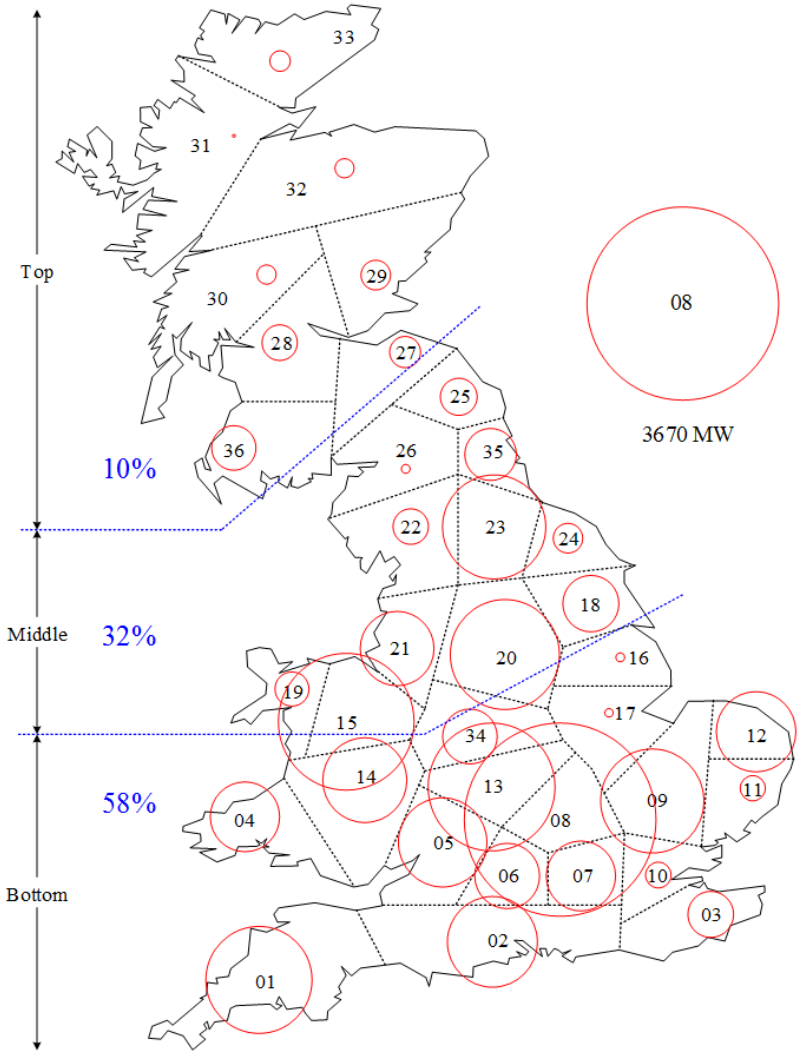

Figure 2-2: Geographic distribution of active power demand.

The geographical distribution of the UK's power stations in an interactive map is plotted in Figure 2-3 to illustrate the diversity of the UK's electricity supply. As can be seen, they are not shared evenly. The maps show how the UK's hydroelectric power plants are limited to Scotland, where plentiful rainfall, mountains and thinly populated valleys make the dams construction easier. As shown in this figure, 4 hydro-electric are in zones 30, 31, 32 and 36. The largest hydro-electric power plants are in zone 32 with the capacity of 500 MWW. Additionally, the UK's pumped storage reservoir that performs like network's battery is in zone 32 with the capacity of 600 MW. The UK's gas and nuclear power sites are more steadily dispersed which is revealed by the UK's map. For example, all the nuclear sites are located near to the coast since they require guaranteed access to cooling water suppliers. The smallest and largest power stations with the amounts of 11 MW and 4.7 GW are gas-based ones which are placed in zones 32 and 10, respectively. The largest gas power plants are in zones 10, 4, 24, 16 and 20. The largest and smallest nuclear power sites are 4.5 GW and 1.2 GW which are located in zones 12 and 22, respectively. The UK's biomass power plants are more evenly distributed and their location correlates with their input sources. The smallest and largest biomass stations are 45 MW and 1.7 GW which are placed in zones 36 and 23, respectively. Based on Figure 2-2 and Figure 2-3, it is clear-cut that high-consumption zones 8 and 13 are supplied by their neighbouring zones.

Table 2-1: Zonal equipment distribution of 36-zone GB network

Zone	**G**	VCO	PSS	GOV	**B**	VCO	PSS	GOV
1		×	×	×				
2		×		×				
3								
4		×	×	×				
5		×	×	×		×	×	×
6		×	×	×				
7								
8		×	×	×				
9								
10		×	×			×	×	
11		×	×	×				
12		×	×	×				
13								
14								
15		×	×	×				
16		×	×	×				
17		×	×	×				
18								
19		×	×	×				
20		×	×	×				
21		×	×	×				
22								
23		×	×	×		×	×	×
24		×	×	×				
25						×	×	×
26								
27		×	×	×		×	×	×
28		×	×	×				
29		×	×	×		×	×	×
30								
31								
32		×	×	×				
33								
34								
35		×	×					
36						×	×	×

Note: G: Gas, B: Biomass

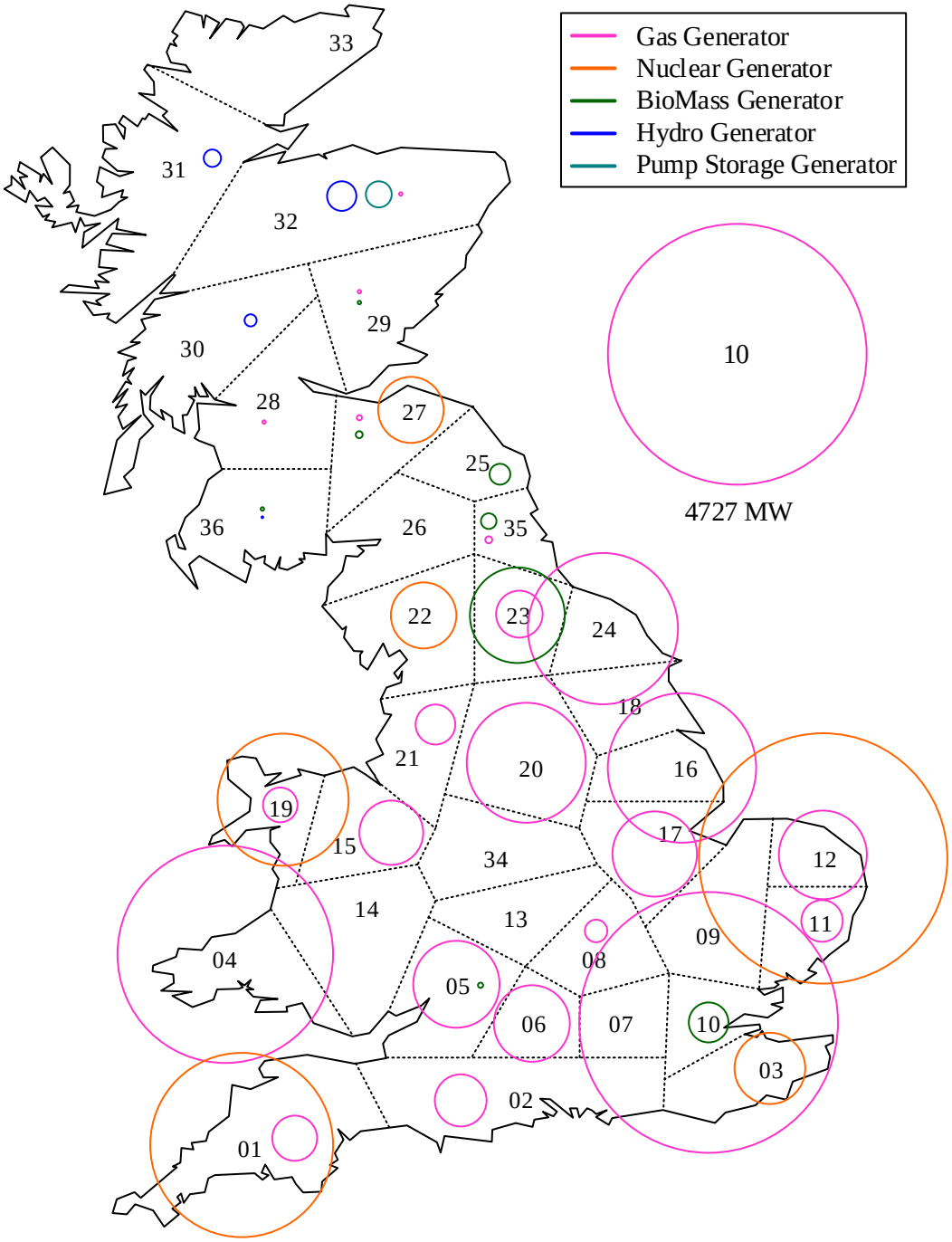

Figure 2-3: Geographic distribution and capacity of power plants.

2.1.3 Dynamic Modelling

The turbines' mechanical power of 41 power stations is transferred to electrical power using synchronous generators (SGs). The first step in power system dynamics studies to investigate the dynamic characteristics of the grid following a loss of generation disturbance and etc. is to model the SGs. The conventional SG model is achieved from the relations of the coupled stator and rotor electric circuit by transforming the variables of the

SG into *qd* axes based on Park transformation matrix [11]. The main advantage of *dq* representation compared to *abc* model is that the mutual reactance between the stator and rotor becomes time free. The SG is modelled based on the equivalent circuits shown in Figure 2-4 with one damper winding in *q*-axis, three windings in *d*-axis including one field and two rotor dampers (subscripts *q*, *Q* and *x* stand for these windings, respectively). Note that damping windings in *q*-axis of salient pole rotor are characterised with only one parallel branch, as shown in Figure 2-4.d. All the below mentioned formulations are written under the balanced and symmetrical three-phase system with motor convention. The saturation of magnetic parts of the SG is neglected. All the parameters and variables of SG are referred to the stator side and are in p.u., while second and electrical radian are taken as time and angle units, respectively.

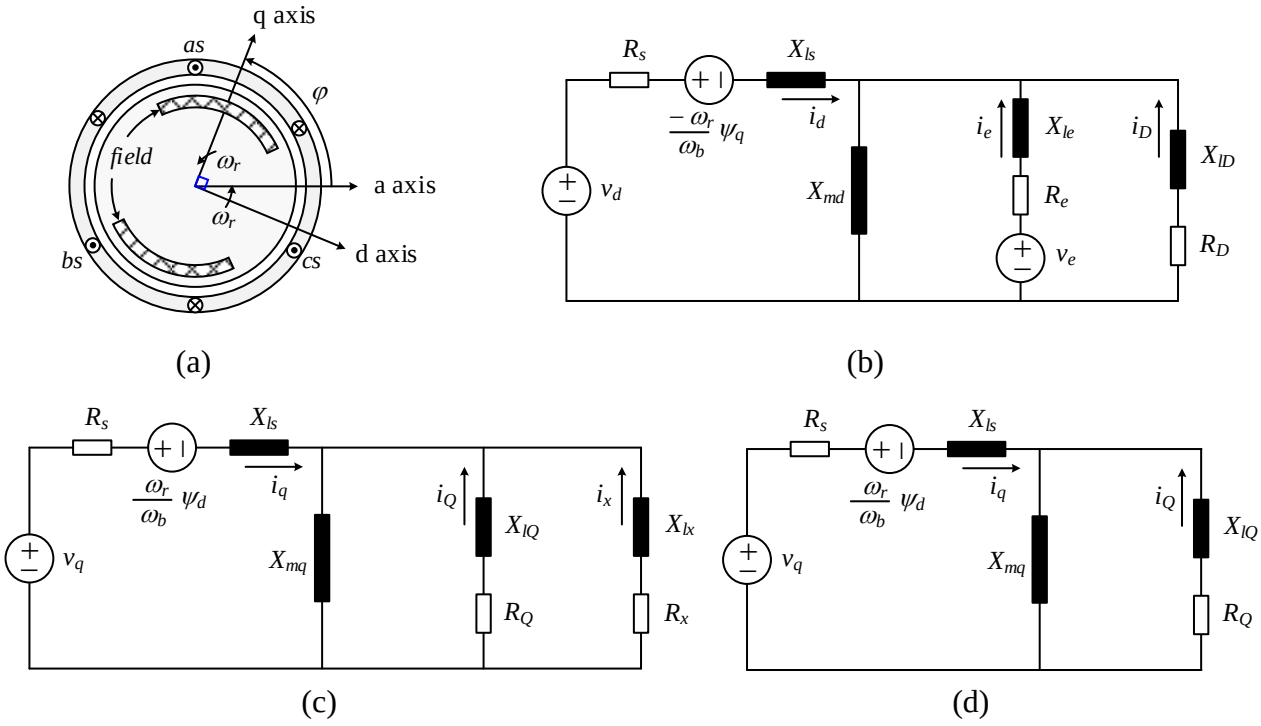

Figure 2-4: Synchronous machine representation: a) Park's coordination, b) d-axis equivalent circuit, c) q-axis equivalent circuit, d) d-axis equivalent circuit (salient pole rotor).

- *Stator voltage equations:*

$$v_d = R_s i_d - \frac{\omega_r}{\omega_b}\psi_q + \frac{1}{\omega_b}\frac{d\psi_d}{dt}$$
$$v_q = R_s i_q + \frac{\omega_r}{\omega_b}\psi_d + \frac{1}{\omega_b}\frac{d\psi_q}{dt} \quad (2.1)$$

- *Rotor voltage equations (d-axis):*

$$v_e = R_e i_e + \frac{1}{\omega_b}\frac{d\psi_e}{dt}$$
$$0 = R_D i_D + \frac{1}{\omega_b}\frac{d\psi_D}{dt} \quad (2.2)$$

- *Rotor voltage equations (q-axis):*

$$0 = R_x i_x + \frac{1}{\omega_b}\frac{d\psi_x}{dt}$$
$$0 = R_Q i_Q + \frac{1}{\omega_b}\frac{d\psi_Q}{dt} \quad (2.3)$$

- *Equations of SG's motions:*

$$2H\frac{d\omega_r}{dt} = T_m - T_e$$
$$\frac{d\theta_r}{dt} = \omega_r \quad (2.4)$$

Where, ψ_d and ψ_q are the *d*- and *q*-axis flux linkages of stator, ψ_e is the flux linkage of rotor, ψ_D is flux linkage of *d*-axis damper winding of rotor, ψ_x, ψ_Q are the flux linkages of *q*-axis rotor's windings. ω_b is the base generator speed. T_m, T_e are the mechanical and electromagnetic torques, respectively. The above-written equations consist of 6 electrical state variables (flux linkages) and 2 mechanical state variables (speed and angle). In this chapter, the SG is modelled based on voltage behind reactance (VBR) theory to make a direct interface between the network and the machine at the stator terminal [12]. The voltage equations of rotor are expressed in the state space model so that the state variables are the rotor flux linkages. The outputs of the state space model are sub-transient voltages as the dependent sources. In this VBR model, the time derivative of the stator flux is neglected. Therefore, the state variables of SG for cylindrical round and salient pole rotors are equal to 6 and 5, respectively. The SGs' parameters of 36-zone GB network are listed in Table 2-2.

Table 2-2: Zonal power plants distribution of GB 36 Zone Network

Parameters	***Round Rotor***	***Salient Pole***	***Unit***
H	5.6	7.5	s
Rs	0.003	0.0019	p.u.
Xls	0.19	0.12	p.u.
Xd	1.8	0.85	p.u.
Xq	1.8	0.48	p.u.
Xd′	0.32	0.28	p.u.
Xq′	0.73	0	p.u.
Xd″	0.24	0.2	p.u.
Xq″	0.27	0.2	p.u.
Tdo′	5	6.048	p.u.
Tqo′	3.61	0	p.u.
Tdo″	0.042	0.06	p.u.
Tqo″	0.2	0.09	p.u.

The controlling strategy structure of SG is plotted in Figure 2-5. In this scheme, the voltage controller (VCO) tunes the exciting voltage of SG according to the terminal voltage. The PSS sends auxiliary signal to VCO using SG's speed. The turbine dynamics is modelled by means of PMU. The primary controller (PCO) controls the turbine output power using the SG's speed variations. In this chapter, the PMU and PCO are called governor (GOV). The above controllers are explained in detail hereinafter.

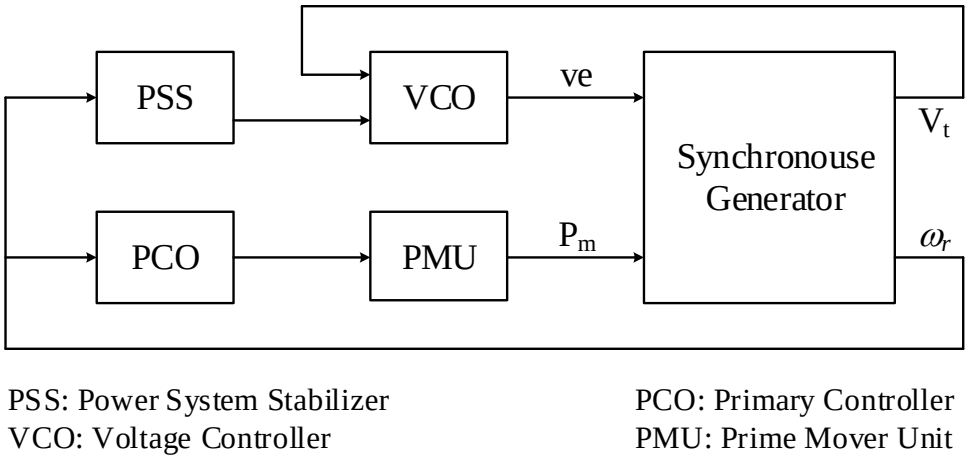

Figure 2-5: Control structure of power plants.

The VCO's control block is shown in Figure 2-6 [13]. This is a thyristor exciter with a transient gain reduction. The PSS produces an electrical torque with the same phase with the rotor speed change which leads to rotor oscillation damping increment. This in turn improves the small signal stability of the whole system. The PSS block diagram which is utilised in this chapter is shown in Figure 2-7. At first, the speed change with respect to reference one is multiplied in a gain and passed through a washout block to remove the slow variation of speed. As shown, two blocks of lead and lag are deployed to compensate the phase difference between the input signal of VCO and electromagnetic torque of SG. Finally, the output signal of PSS is restricted to a predefined value using a limiter.

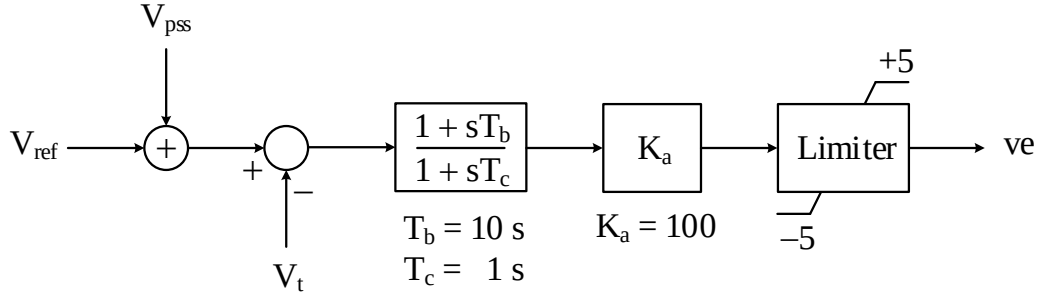

Figure 2-6: Block diagram of voltage controller (VCO).

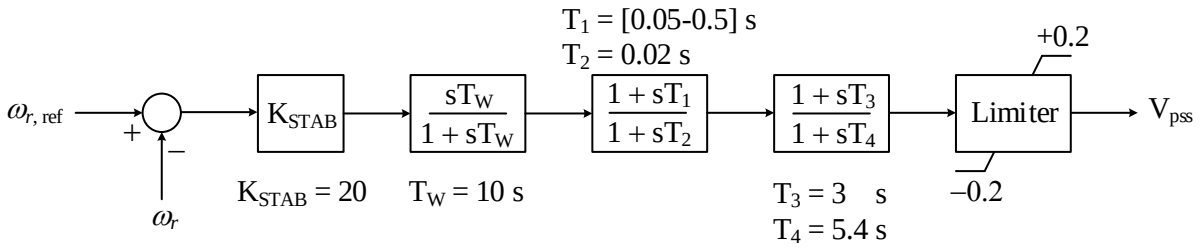

Figure 2-7: Block diagram of power system stabilizer (PSS).

The heat turbine transfers the energy of high pressure steam with great temperature to mechanical energy. The heat source can be a nuclear reactor or a gas or biomass furnace. The block diagram of a heat turbine is illustrated in Figure 2-8 [13]. The time constants of T_g and T_{ch} are pertinent to governor (GOV) and steam chest,

respectively. The most biggest and important time constant in this turbine model is T_r which shows the re-heater time delay. The parameter F_h determines the high pressure turbine contribution to generate power.

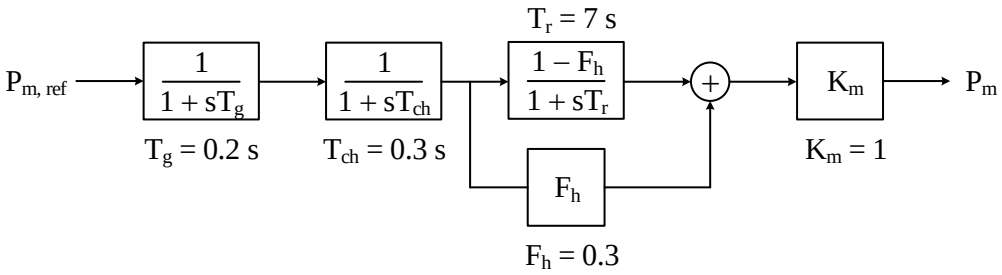

Figure 2-8: Block diagram of round rotor synchronous generator prime mover unit (PCO).

The block diagram of primary controller (PCO) related to the heat turbine is shown in Figure 2-9. In this structure, a value is added to the mechanical reference power based on the speed variation with respect to rated speed [13]. The hydro-electric dynamic model can be illustrated by Figure 2-10 which represents the its non-linear model. The parameter T_w is called water starting time indicating the required time for water to accelerate in penstock from zero speed to U_0 for a head equals to H_0.

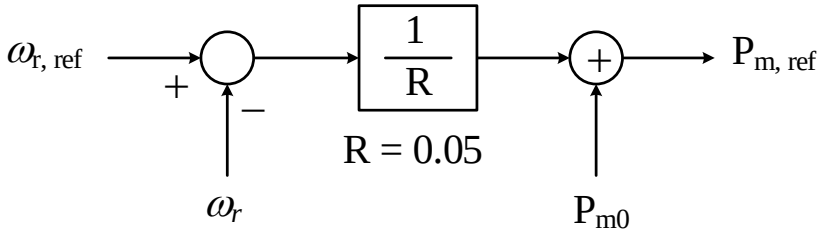

Figure 2-9: Block diagram of round rotor synchronous generator turbine primary controller.

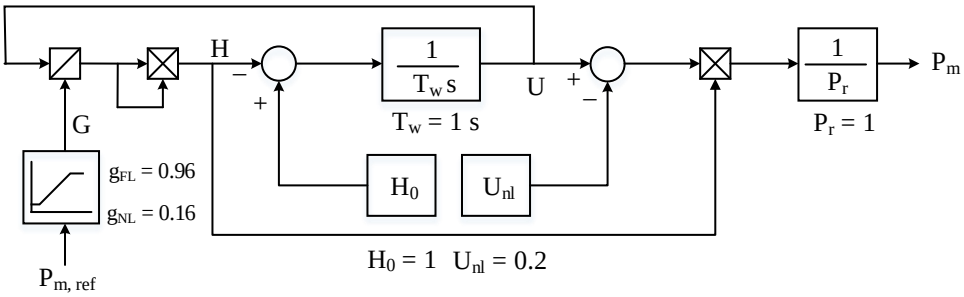

Figure 2-10: Block diagram of hydro turbine prime mover unit (PCO).

The PCO block diagram related to hydro-turbine is depicted in Figure 2-11. In this structure, to overcome the water inertia and stabilise the system, one transient droop equal to R_T is appended into PCO. It is to be noted that the resetting time related to this droop in isolated network is almost 5 s and in interconnected grids is around 0.5 s.

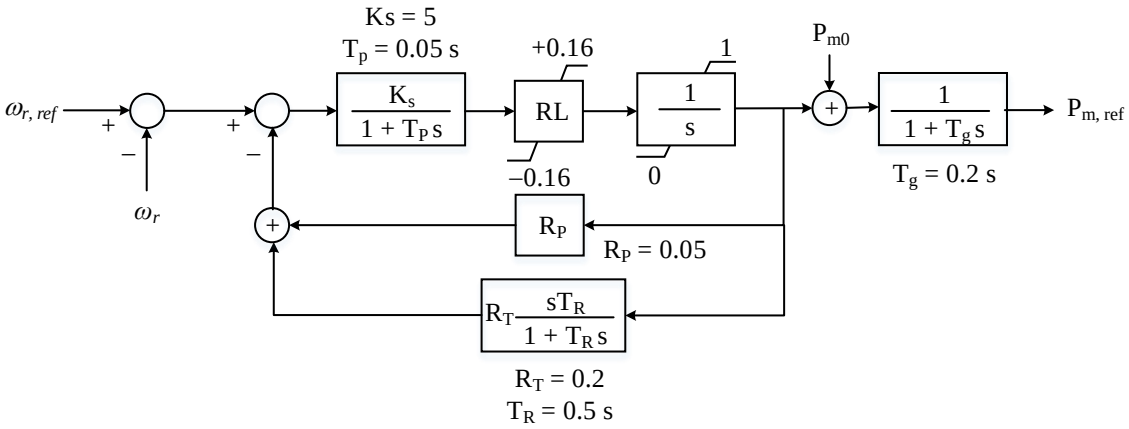

Figure 2-11: Block diagram of hydro turbine primary controller.

2.1.4 Modal Analysis of 36-Zone GB Network

2.1.4.1 Modal Analysis of 36-Zone GB Network without Any Controlling Equipment like VCO and etc

According to the above discussions, the power grid under the study consists of 41 power plants. The SGs of 4 hydro-turbines are salient pole rotor and other 37 SGs are wounded rotor. As a result, the system includes 242 state variables which are equal to the number of eigenvalues. These eigenvalues are plotted in Figure 2-12. It should be pointed out that the horizontal axis of all relevant graphs is titled "Negative Damping" to show that the damping factor is in the stable region i.e. left hand side of real axis. It is assumed that VCO, PSS and etc. are deactivated and the SGs' dynamic characteristic are considered. In this figure, the dominant state variables related to different eigenvalues are determined. Note, the eigenvalues of flux linkages have all real values. Additionally, the eigenvalues corresponding to the damping windings have the higher damping compared to the field's windings ones. It is noteworthy that eigenvalues related to the rotor speed and angle is complex with pretty lower damping as compared to eigenvalues of rotor damping windings. These eigenvalues which are so important in modal analysis are called electromechanical modes. In this network, there are 41 SGs with two mechanical modes. Consequently, the electromechanical modes of the system are 82. Furthermore, their number will be decreased to 80 with removing two modes of slack SG i.e. nuclear unit in zone 1. The detail information about these eigenvalues is listed in Table 2-1. Note, the dominant units of each mode are specified based on their participation factors. To do this, it is supposed that participation factors of dominant units are greater than 0.5.

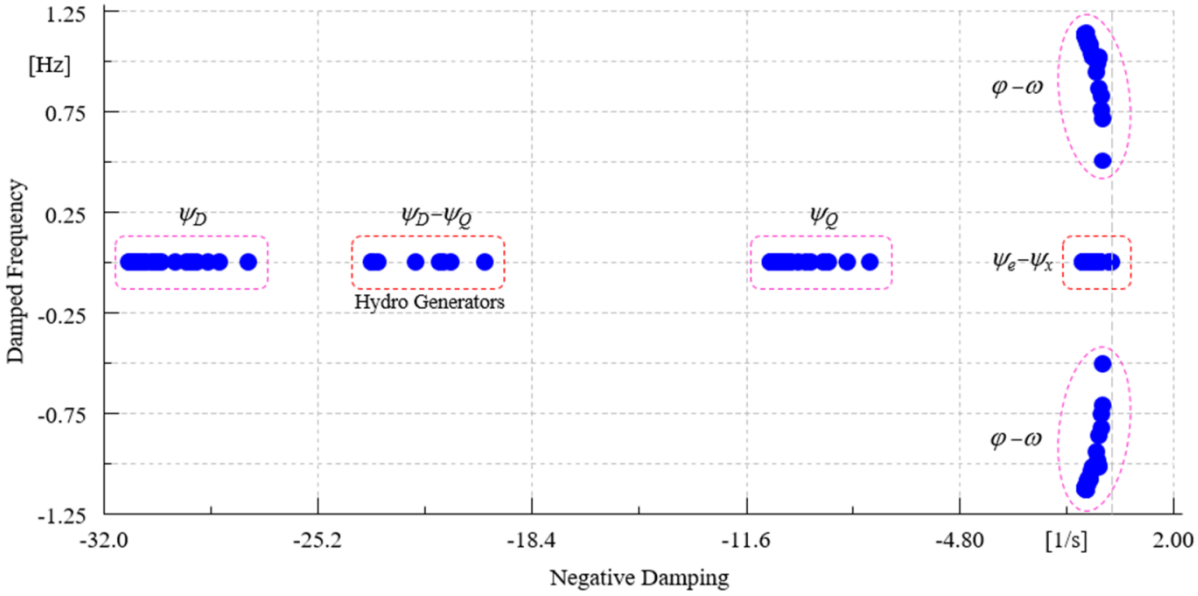

Figure 2-12: Eigenvalues of network: only generator model is included, no VCO, PSS, etc.

In order to precisely investigate the electromechanical modes, these modes as well as dominant units are portrayed in Figure 2-13. As mentioned above, the modes related to the angle and speed of SG slack's rotor is not complex. In this context, the following parameters are defined for the investigation procedure [13]:

For each complex eigenvalue which is formed as follows:

$$\lambda = \sigma \pm j\omega_d \tag{2.5}$$

The oscillation frequency can be defined as follows:

$$f_d = \frac{\omega_d}{2\pi} \tag{2.6}$$

This is called as damped frequency. The damping ratio can be defined as follows:

$$\zeta = \frac{-\sigma}{\sqrt{\sigma^2 + \omega_d^2}} \tag{2.7}$$

In addition, the damping time constant of oscillation amplitude is as follows:

$$T_d = \frac{1}{|\sigma|} \tag{2.8}$$

In other words, the oscillation amplitude is reduced to (1-1/e = 0.63) after T_d s and will be around zero after $3T_d$. As can be seen from Figure 2-13, the electromechanical modes can be divided into four groups. According to relation (2.8), the time constant of these modes are reduced by moving from right hand side of this figure to left hand side. It means that last left hand side group has a time constant of 1 s, while this is 1.5 and 1.7 for the second and third left hand side groups. In other word, the damping process of these modes takes less than 2 s to be damped, while this is 2.3 to 4 s for the right hand side group. This type of modes is most vital compared to others due to their less damping which will be investigated more than others hereinafter. It is observable that dominant power plants for this mode group are 3 units of largest nuclear units, 4 stations from the largest gas units and all 4 hydro-electric units. Albeit the capacity of these four hydro turbines except one in zone 32 is negligible with respect to other 7 gas and nuclear power plant, the salient rotor nature of these hydro-electric

power stations makes their contribution in these modes more considerable. It has been investigated that if these hydro-electric SGs convert to wounded rotor ones, the hydro-turbines of zone 30, 31 and 36 are not most dominant any more.

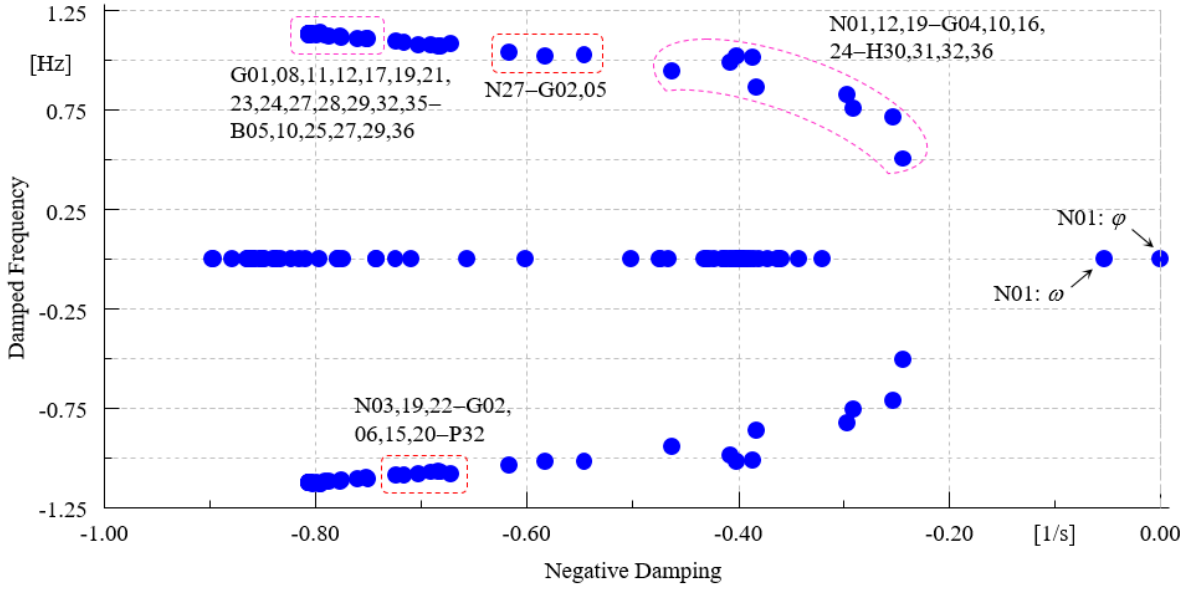

Figure 2-13: Dominant power plants in electromechanical modes: only generator model is included, no VCO, etc.

The geographical distribution and dominant power plants number of each electromechanical mode group are plotted in Figure 2-14 using the UK's map. It is to be observed that those 7 dominant nuclear and gas power stations of first group are located beside the coasts.

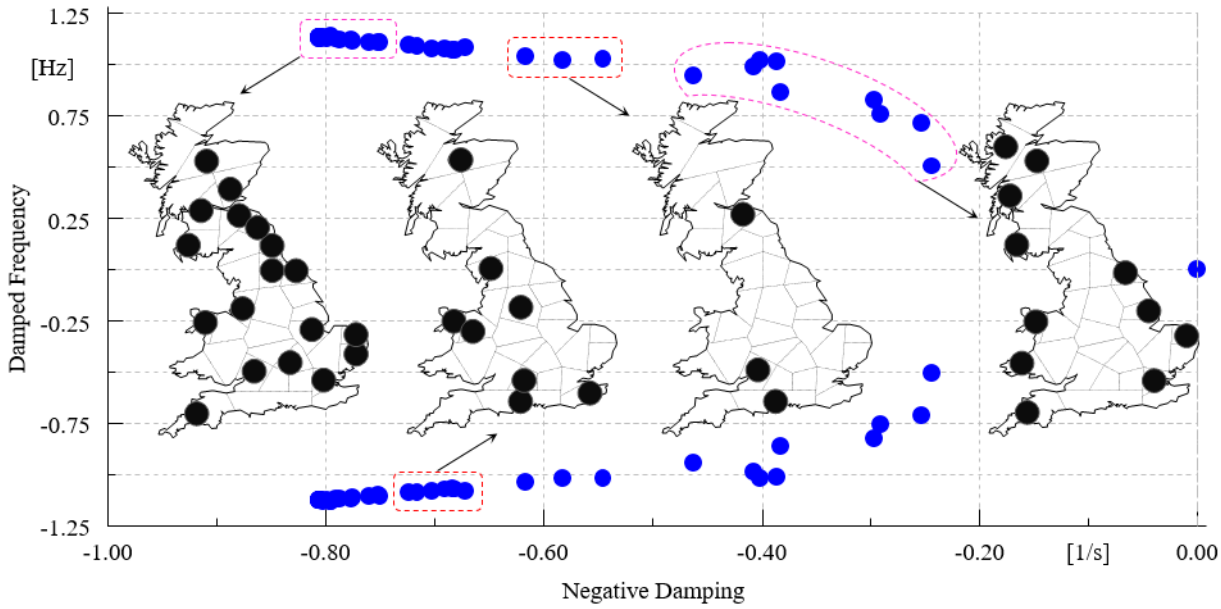

Figure 2-14: Geographic distribution of dominant power plants in electromechanical modes: only generator model is included, no VCO, etc.

2.1.4.2 Modal Analysis of 36-Zone GB Network Considering Effects of Load Models

In this step, the load demand effects on electromechanical modes' damping are explored. These modes are plotted in Figure 2-15 for three scenarios of considering constant impedance, constant current and constant power loads. It should be mentioned that all the previous discussions was related to constant impedance loads. As can be seen from this figure, the load demand models don't have considerable impact on electromechanical modes' damping. However, the modes' damping in case of constant current loads is a bit bigger than constant impedance case. Moreover, it is a bit greater in case of constant power loads compared to constant current loads.

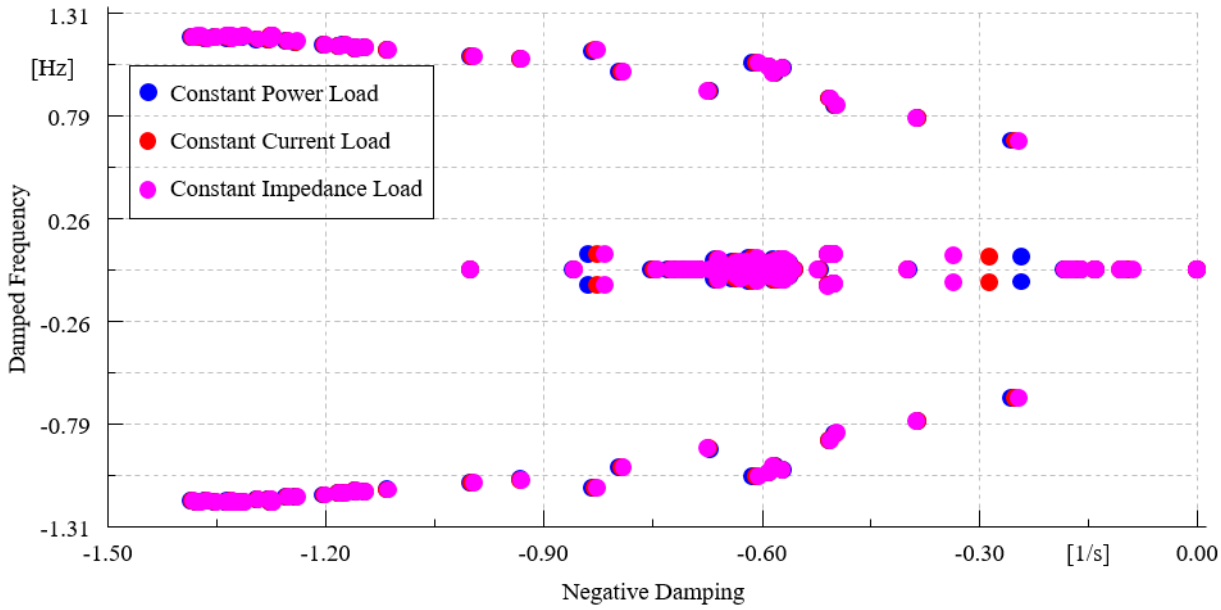

Figure 2-15: Electromechanical modes with different load types.

The effect of load models on the slowest modes is depicted in Figure 2-16. It is clear-cut that damping of the mode is increased from the constant impedance scenario to constant current and from constant current to constant power one. Similar to the case of adding VCOs to the network, the voltage derivative for different types of load including constant power, constant current and constant power can be equalised by the coefficient value of zero, one and two, respectively. It is to be noticed that whereas the constant impedance load is proportional to the square of voltage, the voltage derivative coefficient is equal to zero using the voltage differential equation in small signal studies. Thus, the damping of electromechanical modes in constant impedance load is lower than constant current and for the constant current is lower than constant power.

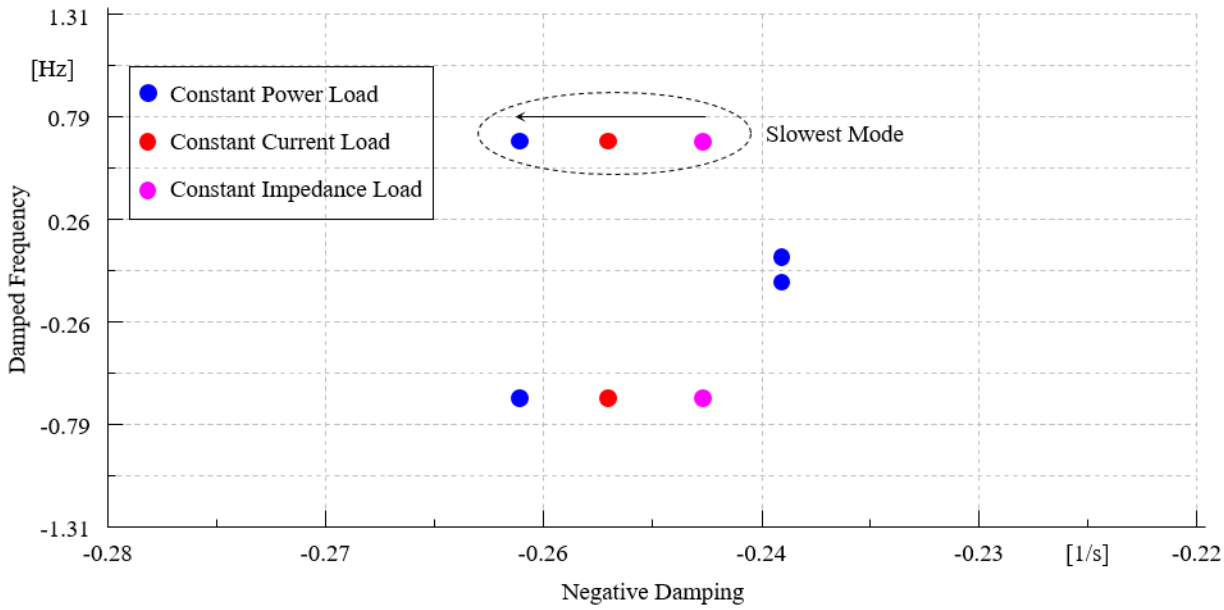

Figure 2-16: Effect of different load types in damping of slowest electromechanical mode.

2.1.4.3 Modal Analysis of 36-Zone GB Network Considering Frequency Dependent Loads

In this subsection, the frequency dependency impact of active load on electromechanical modes is studied. It is considered that 20%, 35% and 45% of loads are constant power, constant current and constant impedance, respectively. These modes are shown in Figure 2-17 for three frequency dependency coefficients of 0, 1 and 2. The one value means that if the frequency decreases 1% with respect to the rated one, the active part of load will be also reduced 1%. It is quite observable that frequency dependencies of the load don't have great impact on electromechanical modes. However, it can increase slightly the modes' damping.

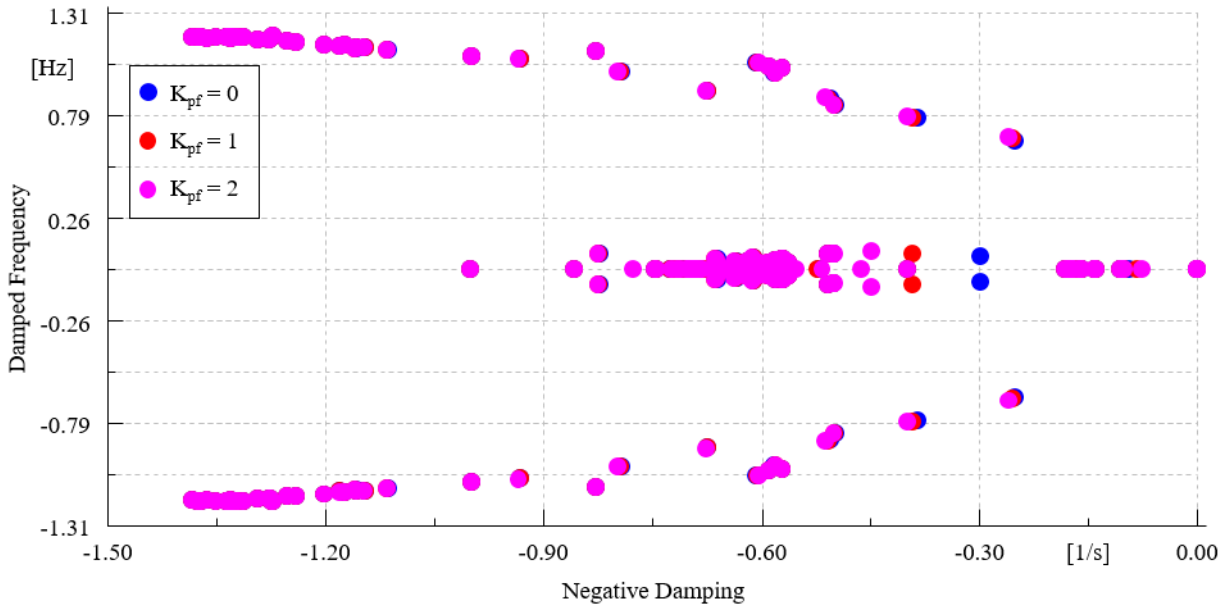

Figure 2-17: Electromechanical modes with different frequency dependency coefficients of loads.

Figure 2-18 illustrates the effect of load frequency dependency on slowest mode. It is observable that increasing of this coefficient from zero to two can increase the mode's damping. It can be justified in this way that increasing the dependency to frequency change is like PSS operation and can lead to damping increment of these modes. In the rest of this chapter, this value is set to one.

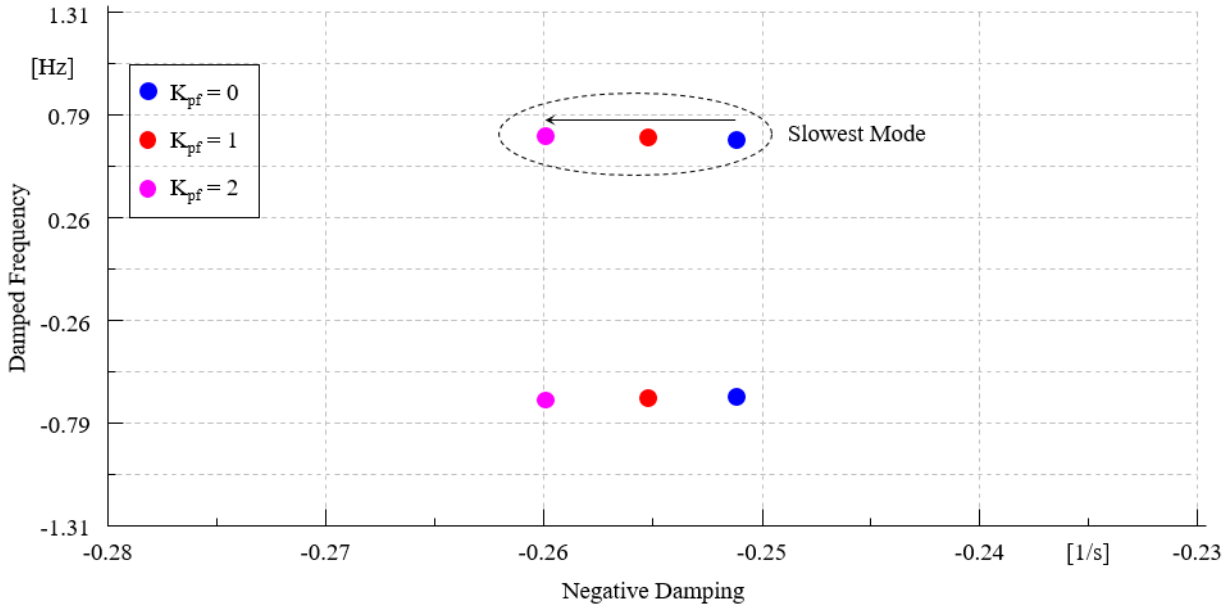

Figure 2-18: Effect of frequency dependency coefficients of loads in damping of slowest electromechanical mode.

2.1.4.4 Modal Analysis of 36-Zone GB Network Considering System Inertia Effect

It is to be notified that damping frequency and damping ratio of a SG connected to an infinite bus can be calculated as follows [13]:

$$\zeta = \frac{1}{2}\frac{K_d}{\sqrt{2K_s\omega_b H}} \tag{2.9}$$

$$\omega_d = \sqrt{\frac{K_s\omega_b}{2H}} \tag{2.10}$$

Where, K_d and K_s are damping torque coefficient and synchronising coefficient, respectively. Figure 2-18 shows the electromechanical modes in two more scenarios of increasing and decreasing the inertia of all 41 SGs with the amount of 25%. It is visible that damping and its frequency for all modes are significantly decrease by increasing the system inertia. This can be also justified based on equations 10 and 11.

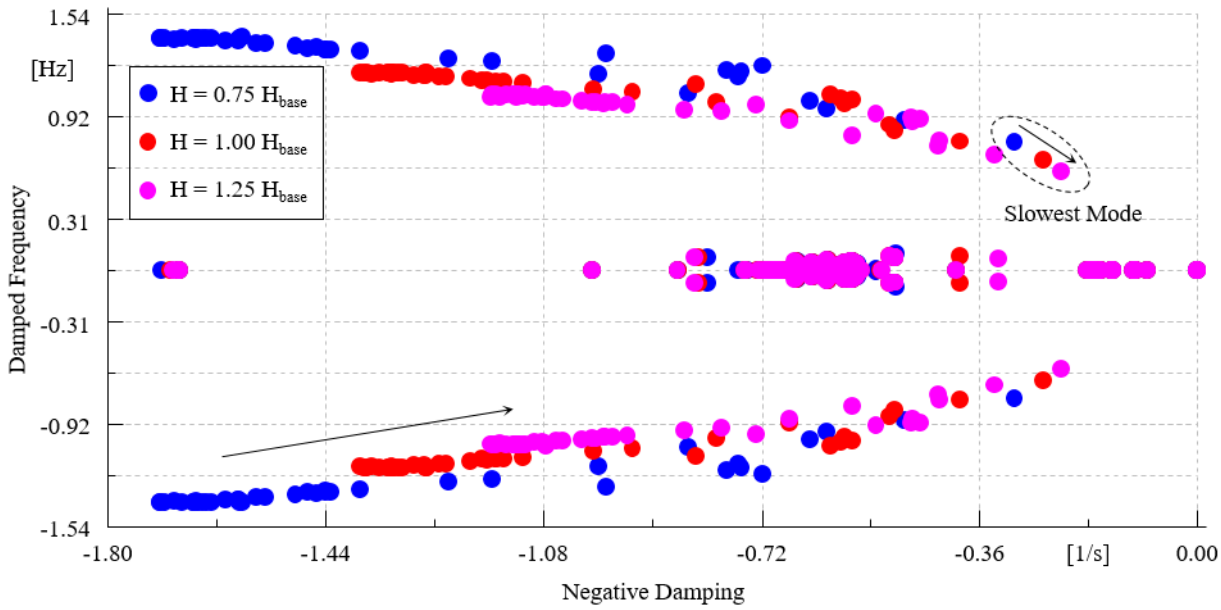

Figure 2-19: Electromechanical modes with different inertia time constants of all power plants.

To precisely evaluate this matter (inertia variation effect on modes), the dominant power plants discussion is deployed. Figure 2-20 shows how the dominant units are changed for the slowest modes before and after adding the dynamics of controlling devices. It is observable that damping and its frequency are respectively dropped down and grown for slowest mode, while the dominant unit in both case is the nuclear power of zone 1. In contrast, the damping of other three modes where the gas turbines of zone 4 and hydroelectric of zone 32 are dominant units increases after considering the dynamics of control devices. It is to be noted that the damping of fifth mode where the gas turbine of zone 10 is dominant grows slightly. As a result, it can be inferred that the nuclear power plant of zone 1, the gas turbines of zones 4 and 10 as well as hydro-turbine unit of zone 32 have significant impact on damping of slowest electromechanical modes.

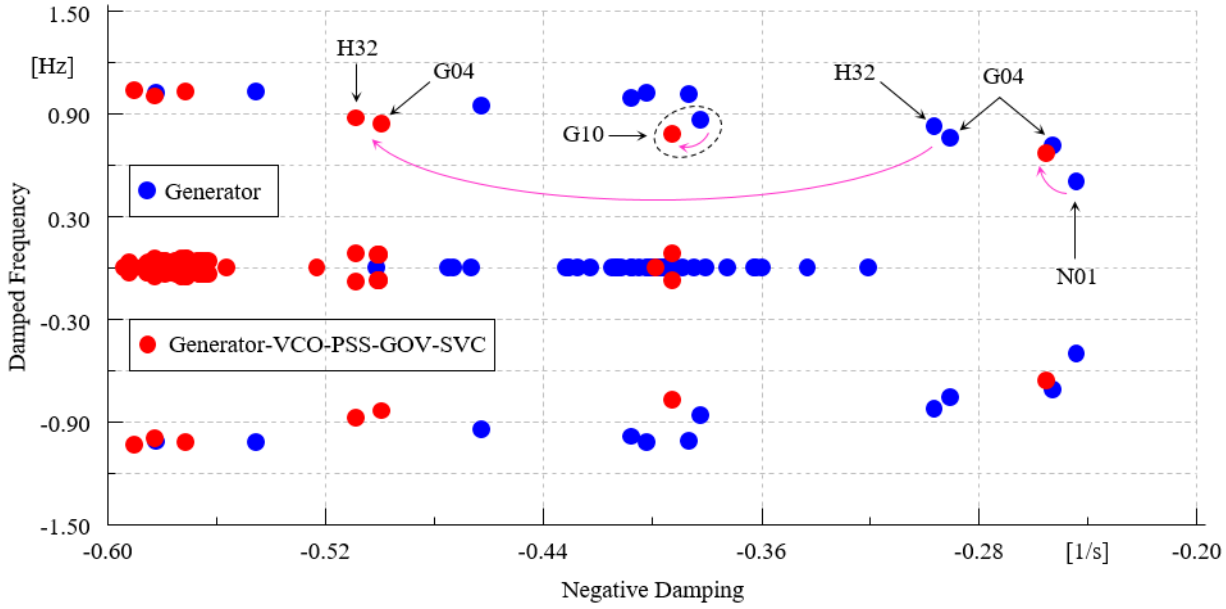

Figure 2-20: Dominant power plants in slow electromechanical modes.

According to the result presented in Figure 2-20, the system electromechanical slowest modes in just the dominant units are plotted for the abovementioned scenarios of inertia. For the sake of comparison, these scenarios are also plotted for all existing 41 power plants in Figure 2-21. As highlighted in the ellipsoid, the damping and its frequency of faster modes don't have considerable change in case of inertia change.

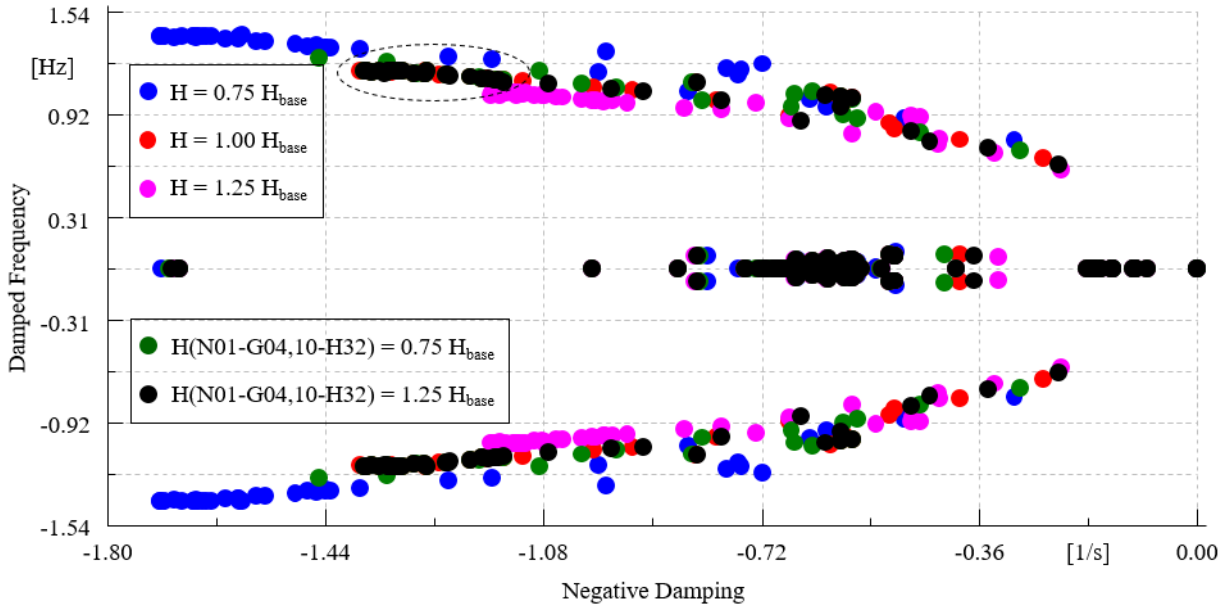

Figure 2-21: Electromechanical modes with different inertia time constants of dominant power plants.

Figure 2-22 shows the slowest mode location change in case of increasing and decreasing the inertia of dominant units. The first and second slowest modes are highlighted by two big ellipsoids. The locations of these two modes in case of base inertia are bolded by two squares. It is clear that the locations of these two modes when the inertia of 4 dominant units vary are almost equal to the case in which the inertia of all 41 SGs changes.

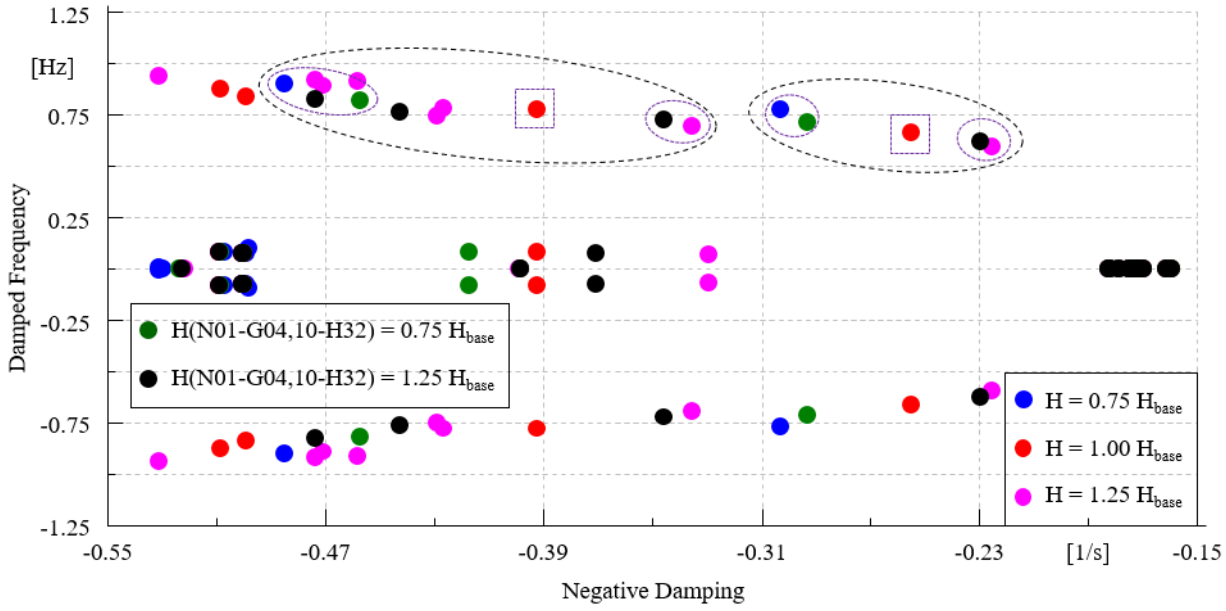

Figure 2-22: Slow electromechanical modes with different inertia time constants of dominant power plants.

2.1.4.5 Obtaining and Investigating the Eigenvalues of 36-Zone GB Network following the loss of generator Using Modal Analysis and Mode Shape

In this subsection, the system's eigenvalues is obtained using the modal analysis and the impact of different equipment and parameters like the load models and SGs' inertia on these eigenvalues are examined. Furthermore, the dominant power plants in electromechanical modes are determined and explored using the participation factor of state variables in these modes. In order to precisely investigate the frequency oscillation of SGs following the event of loss of generator, the mode shape concept is deployed [13]. The mode shape is the observability or the normalised right eigenvector of a predefined state variable for a determinate eigenvalue. The mode shape parameters related to the state variable of speed of SGs for the first, second and fifth slowest electromechanical modes are listed in Table 2-3. It is clear that the amplitude of 37 power plants in the first two modes is bigger than 0.1, so that these two modes are inter-area modes. In contrast, the amplitude of all SGs except 4 hydroelectric units in fifth mode shape is less than 0.1. Therefore, this mode is a local one in the northern area or an inter-area mode amongst the northern areas.

Table 2-3: Mode shapes of the first, second and fifth slowest electromechanical modes.

Mode = 0.25 ± j 4.18			***Mode = 0.40 ± j 4.88***			***Mode = 0.57 ± j 6.44***		
Unit	*Amplitude*	*Angle (deg)*	***Unit***	*Amplitude*	*Angle (deg)*	***Unit***	*Amplitude*	*Angle (deg)*
G 01	1	0	H 32	1	0	H 30	1	0
N 01	1	-0.0004	H 31	0.7379	-0.2447	H 31	0.8748	-181.5712
H 32	0.7271	-176.2057	P 32	0.6844	-10.4882	H 36	0.1793	-14.6986
H 31	0.6257	-176.1159	G 32	0.6841	-10.5226	H 32	0.1401	1.4750
P 32	0.5685	-183.6414	H 30	0.5922	-1.1209	G 28	0.0339	-23.1245
G 32	0.5683	-183.6673	G 01	0.5629	-11.6053	B 35	0.0129	-62.1770
H 30	0.5669	-176.3774	N 01	0.5629	-11.6059	B 36	0.0122	-33.4008
H 36	0.5210	-177.0367	H 36	0.4735	-2.8063	B 29	0.0082	-190.7025
B 29	0.4515	-183.8227	B 29	0.4147	-11.9301	G 29	0.0082	-190.9810
G 29	0.4509	-183.9298	G 29	0.4140	-12.0738	G 35	0.0073	-80.4841
N 27	0.4386	-184.3689	G 10	0.3746	-197.9738	B 25	0.0072	-66.0300
G 27	0.4380	-184.4666	B 10	0.3745	-197.9892	G 19	0.0068	-225.7784
B 27	0.4377	-184.5286	N 27	0.3699	-13.2128	N 19	0.0068	-225.8808
G 28	0.4278	-184.2861	G 27	0.3694	-13.3439	P 32	0.0065	22.1082
B 35	0.4205	-179.2361	B 27	0.3690	-13.4271	G 32	0.0065	22.0476
B 36	0.4146	-184.2816	G 28	0.3679	-12.7850	G 24	0.0065	-127.5316
B 25	0.3877	-184.6075	N 03	0.3541	-195.0313	B 23	0.0061	-94.4208
G 35	0.3716	-185.9111	G 12	0.3509	-200.6684	G 23	0.0061	-94.4416
N 22	0.3567	-186.1807	N 12	0.3509	-200.6739	G 16	0.0056	-136.5083
G 21	0.3540	-186.4345	B 36	0.3330	-13.2080	G 17	0.0055	-135.4958
G 19	0.3434	-187.1940	G 11	0.3316	-196.0029	G 21	0.0048	-223.4282
N 19	0.3432	-187.2362	G 04	0.3059	-186.5770	N 27	0.0046	-87.5921
B 23	0.3247	-185.9156	G 08	0.2998	-195.9881	G 27	0.0045	-87.8622
G 23	0.3247	-185.9235	B 25	0.2636	-14.0805	B 27	0.0045	-88.0316
G 20	0.3176	-186.0656	B 35	0.2532	-7.1018	G 20	0.0042	-199.8467
G 02	0.3029	8.8347	G 06	0.2287	-192.8149	G 15	0.0038	-185.8263
G 24	0.2647	-187.3919	G 35	0.2141	-16.4274	G 12	0.0030	79.0744
G 16	0.2364	-187.9597	N 22	0.1997	-21.8420	N 12	0.0030	79.0626
G 17	0.2205	-187.6710	G 02	0.1964	-184.1441	N 22	0.0028	-217.6977
G 05	0.2198	2.0730	G 21	0.1958	-23.1777	G 02	0.0026	80.8622
B 05	0.2194	1.8955	G 19	0.1762	-25.1646	N 03	0.0015	29.0865
G 04	0.1879	3.0021	N 19	0.1761	-25.2207	G 04	0.0010	12.3287
G 12	0.1765	-192.1707	G 20	0.1431	-23.5029	G 10	0.0009	20.7350
N 12	0.1765	-192.1746	G 05	0.1260	-186.4784	B 10	0.0009	20.7068

G 15	0.1752	-187.6244	B 05	0.1257	-186.7102	G 05	0.0007	-215.8171
G 06	0.1092	5.2256	B 23	0.1219	-17.0116	B 05	0.0007	-216.3045
N 03	0.1010	4.5764	G 23	0.1219	-17.0221	G 11	0.0006	53.0071

*G: gas, N: nuclear, B: biomass, H: hydro and P: pump storage

In order to better evaluate the mode shape related to SGs' speeds in the slowest modes, data of Table 2-1 is shown in Figure 2-23, Figure 2-24 and Figure 2-25. The mode shape corresponding to the slowest mode is shown in Figure 2-23. It is observable that the network is divided into two regions once the SG's speed oscillation is around 0.7 Hz and the zones 1 to 10 swings against the others.

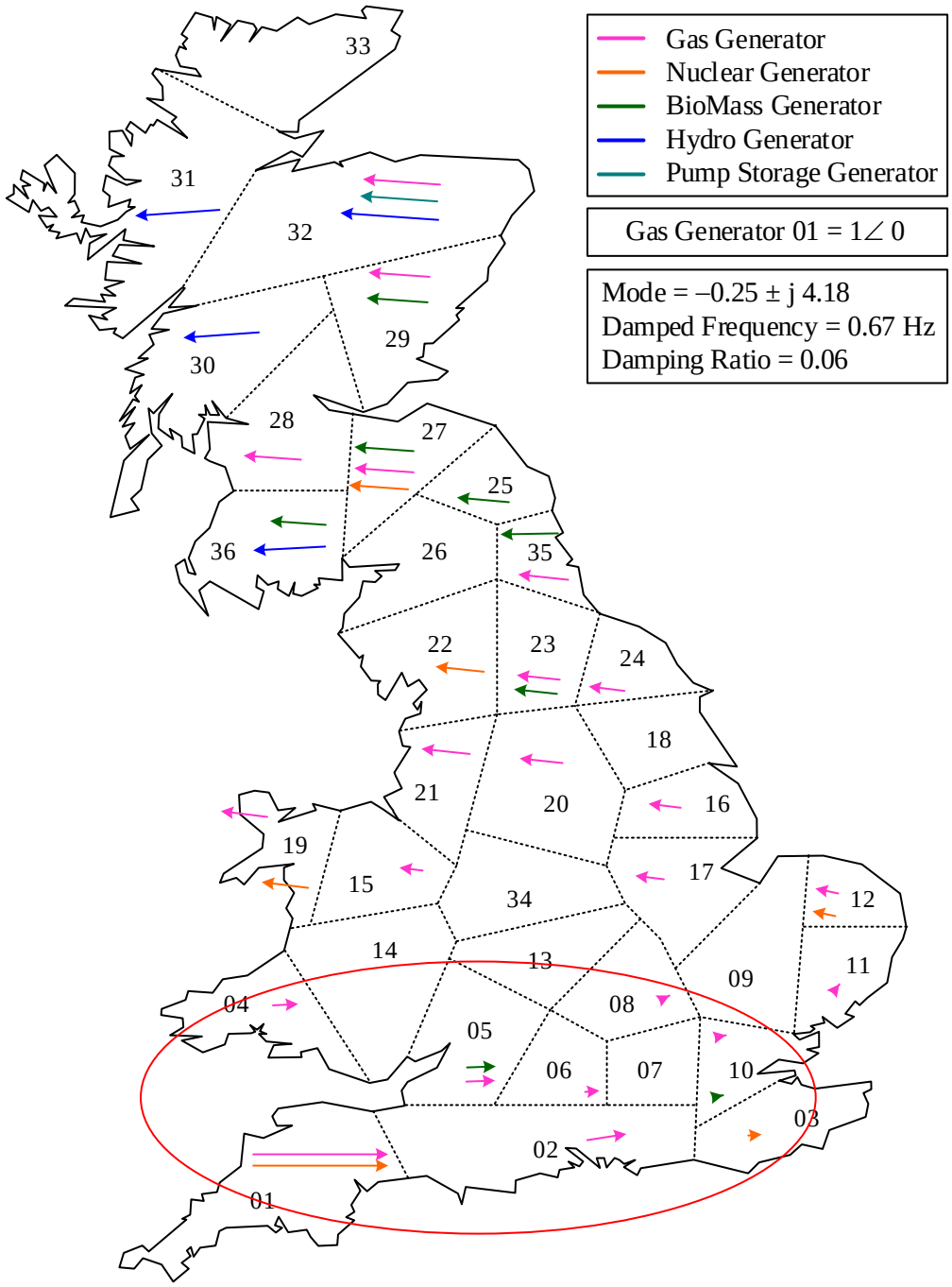

Figure 2-23: Mode shape of the first slowest electromechanical mode.

Figure 2-24 shows the mode shape of second slowest mode. It is clear-cut that the network is divided into two regions once the SG's speed oscillation is around 0.8 Hz with this difference with Figure 2-23 that the SGs of zone 1 swings with the similar direction to the northern areas' SGs.

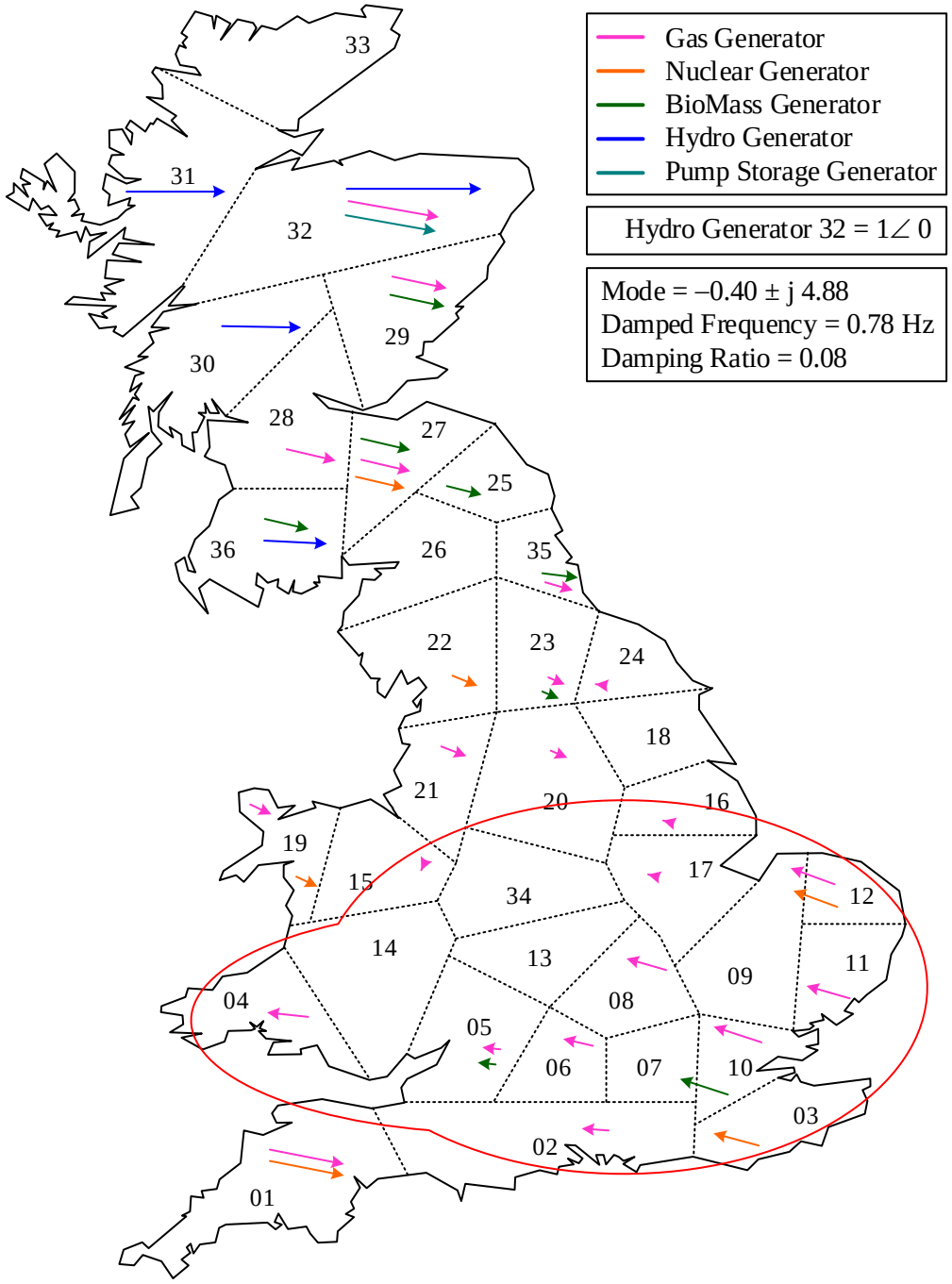

Figure 2-24: Mode shape of the second slowest electromechanical mode.

Finally, Figure 2-25 illustrates the mode shape related to fifth slowest mode. As discussed above, four hydro-electric power plants have a considerable contribution to this mode. It is observable that the network is divided into two regions once the SG's speed oscillation is around 1 Hz and the hydroelectric unit of zone 31 swings against the other hydroelectric plants.

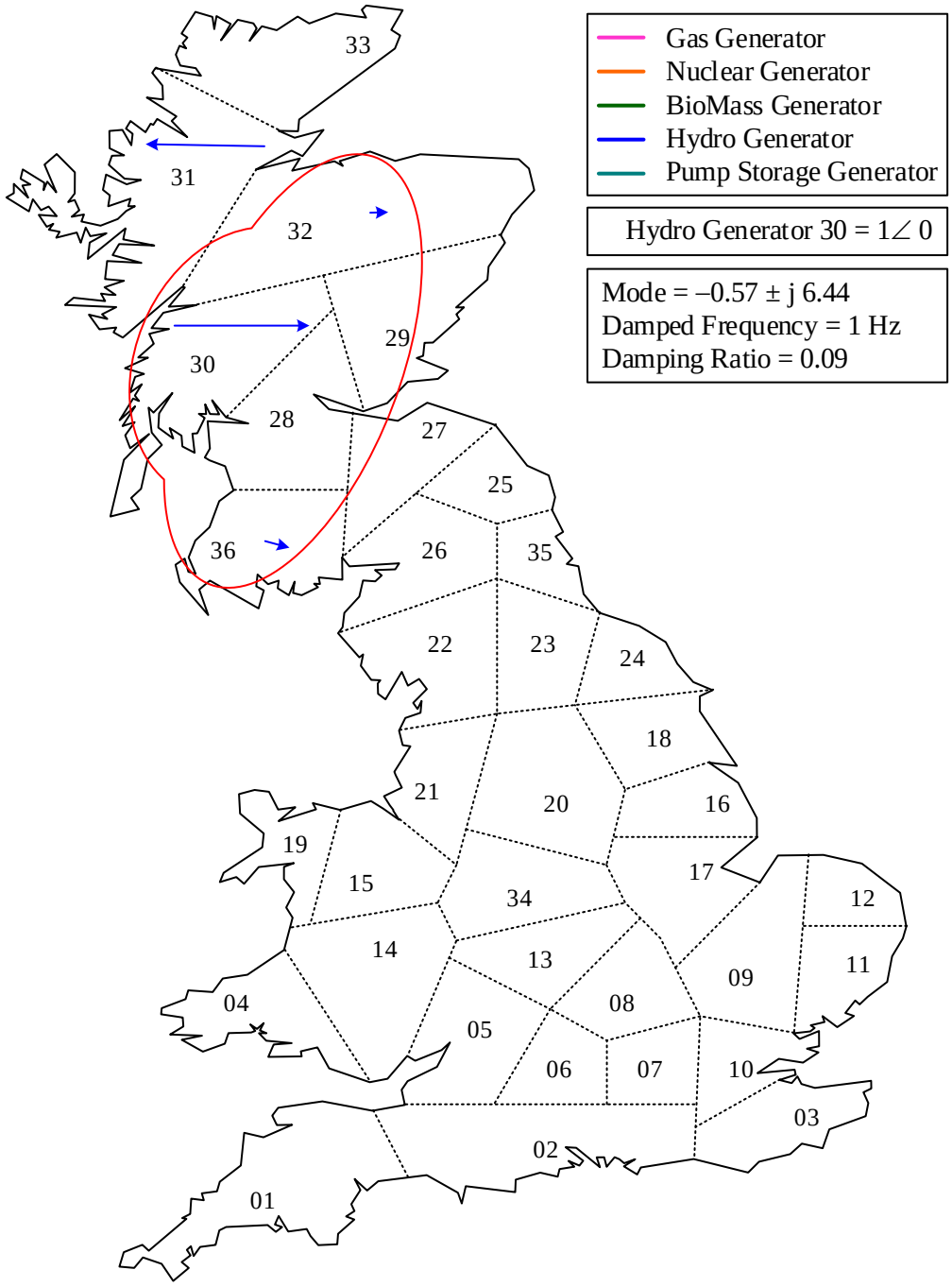

Figure 2-25: Mode shape of the fifth slowest electromechanical mode.

2.1.5 Time Domain Analysis of 36-Zone GB Network

In this subsection, the time domain simulation results for network primary frequency control are provided to confirm the modal analysis outputs. In this context, 8 power plants from different regions of the network are selected and the network dynamic performance is investigated for 20 s following the loss of each of them, as shown in Figure 2-26. The capacity of these generating units change from 600 MW to 4700 MW which are

equivalent to 1.5% to 12% of total demand of the network. In these figures, the COI frequency is illustrated beside the SGs' frequencies based on the following relation:

$$\omega_{COI} = \frac{\sum_{i=1}^{N} H_i S_i \omega_i}{\sum_{i=1}^{N} H_i S_i} \tag{2.11}$$

Where, H_i, S_i and ω_i are the inertia, apparent power and frequency of the ith SG, respectively.

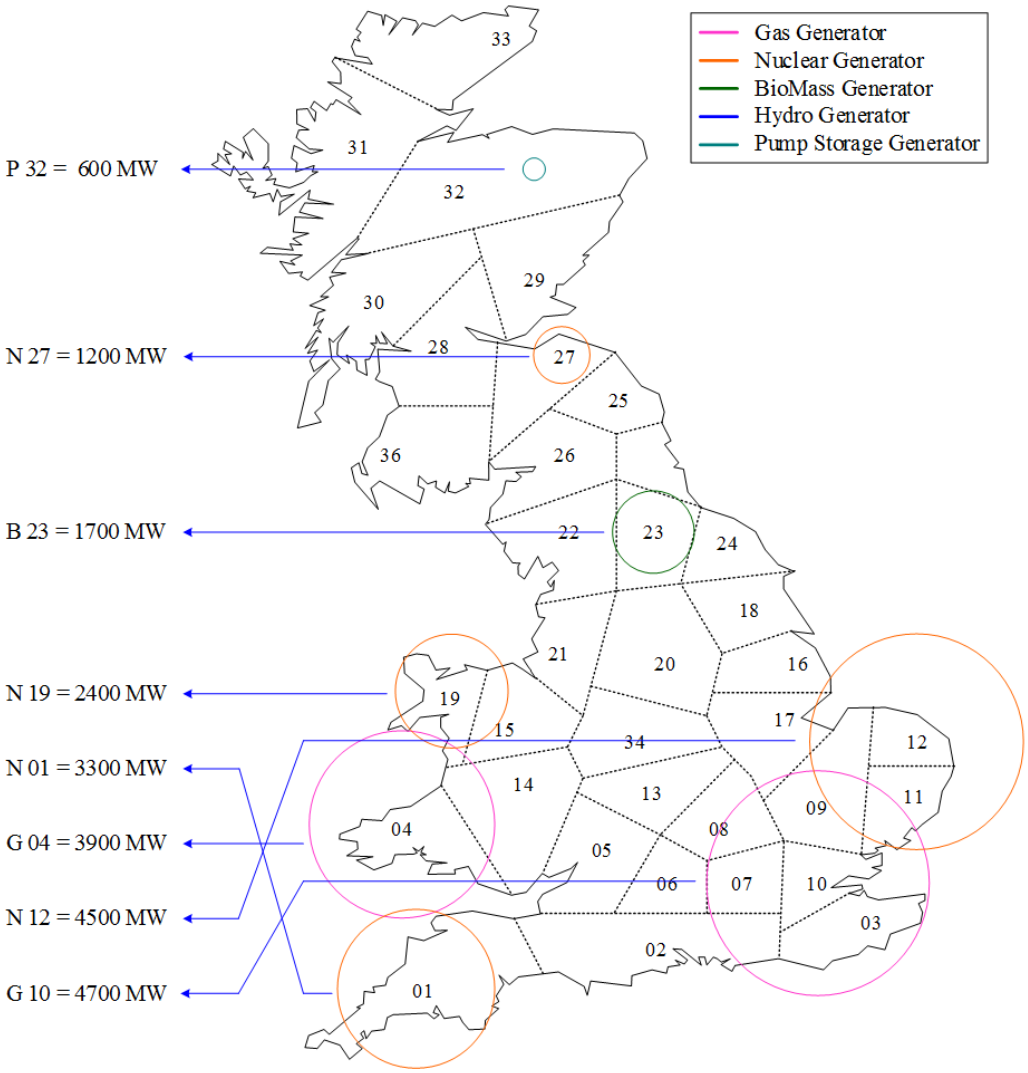

Figure 2-26: Geographic distribution of selected loss of generation.

2.1.5.1 Loss of 1,700 MW Generation in Zone 23

In this event, the biomass of zone 23 with the capacity of 1,700 MW is disconnected from the grid. The frequencies of gas turbine in zone 23, nuclear in zone 1, gas turbine in zone 35 and hydroelectric in zone 32 are portrayed in Figure 2-27 and Figure 2-28. Moreover, their RoCoFs are plotted in Figure 2-29. It can be seen that the gas power plants in zone 23 and 35 as well as hydroelectric unit in zone 32 oscillate more than nuclear power in zone 1 which is due to their short distance to the faulty zone and their smaller capacities. However, the

oscillation amplitude of nuclear unit in zone 1 is increased over the time following the damping of fast electromechanical modes. The maximum RoCoF is corresponded to gas generating unit in zone 23 with the amount of 0.5 Hz/s. Also, the maximum Nadir is around 49.8 Hz which is more than previous events. The steady-state frequency drop should be almost 0.1 Hz since the loss of generation is 1.4 times bigger than the previous event. This value is quite matched with Figure 2-27.

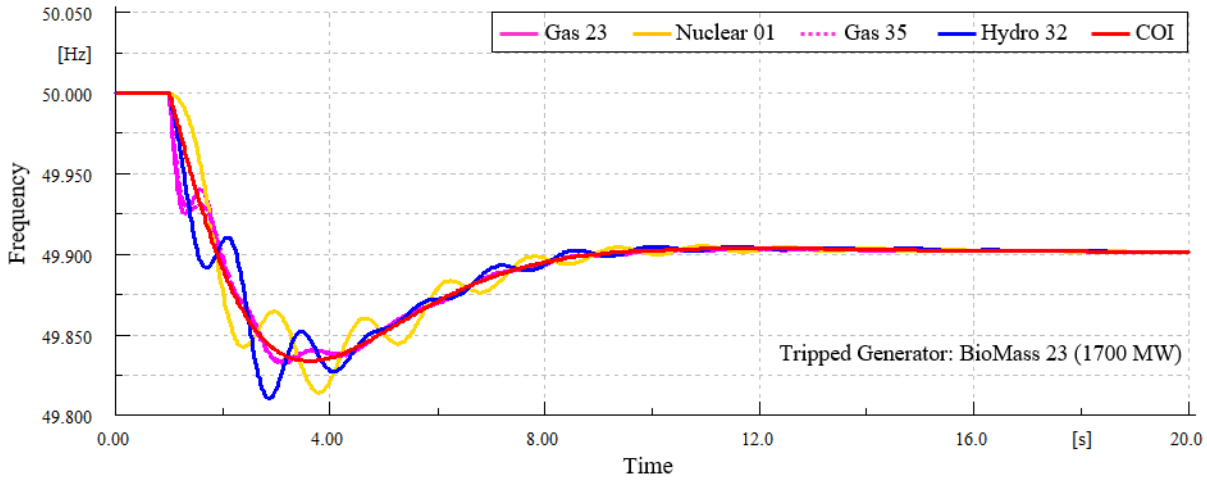

Figure 2-27: Frequency response with loss of 1700 MW generation in middle of network.

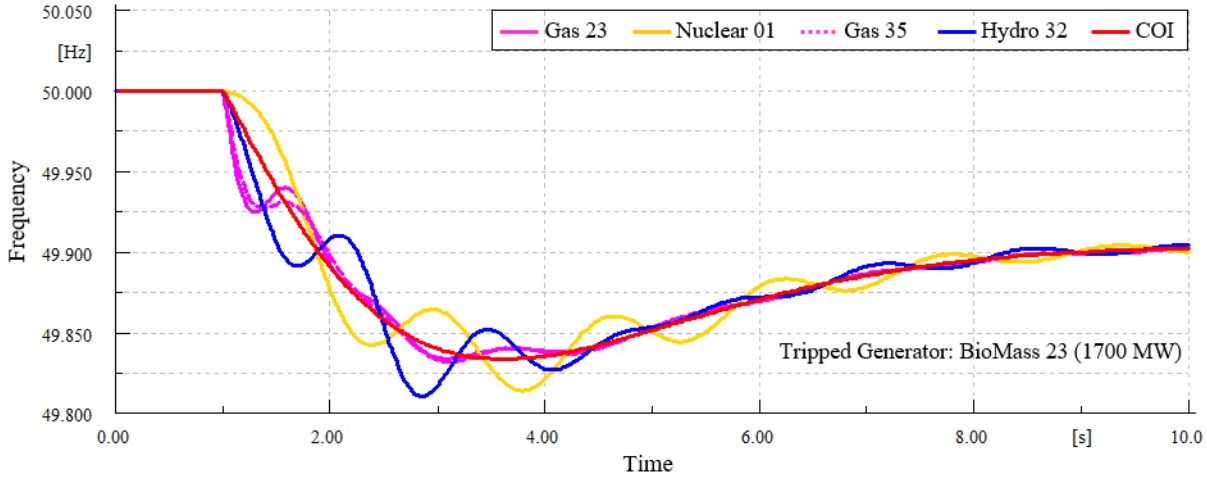

Figure 2-28: Frequency oscillations with loss of 1700 MW generation in middle of network.

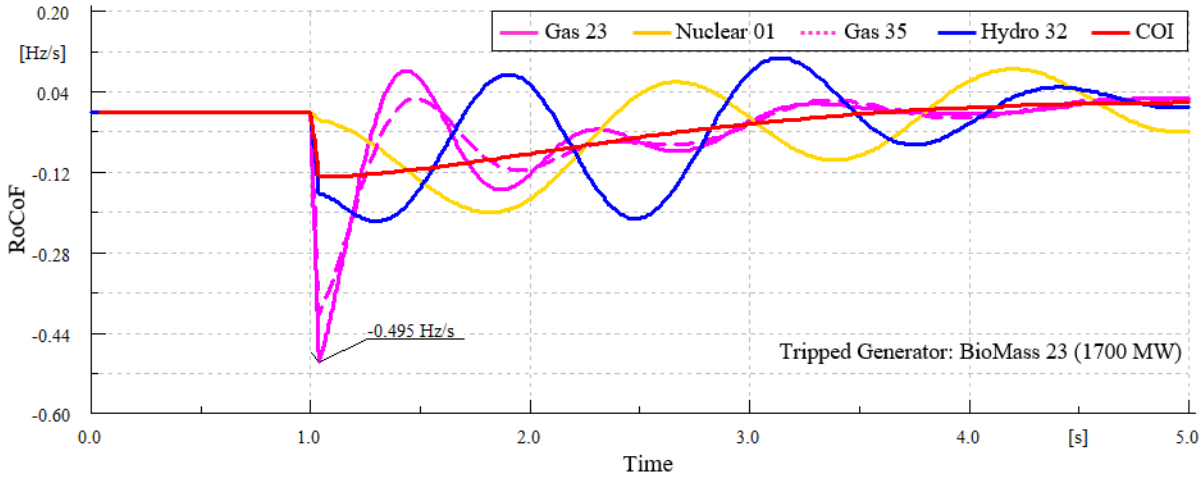

Figure 2-29: RoCoF deviations with loss of 1700 MW generation in middle of network.

2.1.5.2 Loss of 3,300 MW Generation in Zone 1

In this event, the nuclear unit of zone 1 with the capacity of 3,300 MW is disconnected from the grid. The frequencies of gas turbine in zone 1, biomass unit in zone 10, gas turbine in zone 27 and hydroelectric in zone 32 are plotted in Figure 2-30 and Figure 2-30. Additionally, their RoCoFs are shown in Figure 2-31. It can be observable that the gas power plants in zone 1 oscillate more than other units due to its short distance to the faulty zone and the loss of generation size (8% of grid nominal power). The circles 1 and 2 in Figure 2-31 are corresponded to Figure 2-23 and Figure 2-24, respectively. It is clear-cut that gas unit 1 and hydroelectric 32 swings firstly across each other (Circle 1) and then against each one (Circle 2). The maximum amount of RoCoF is pertinent to gas turbine in zone 1 which is equal to huge value of 4.2 Hz/s. The steady state frequency drop should be almost 0.2 Hz since the loss of generation is 1.4 times bigger than the previous event. This value is quite matched with Figure 2-30.

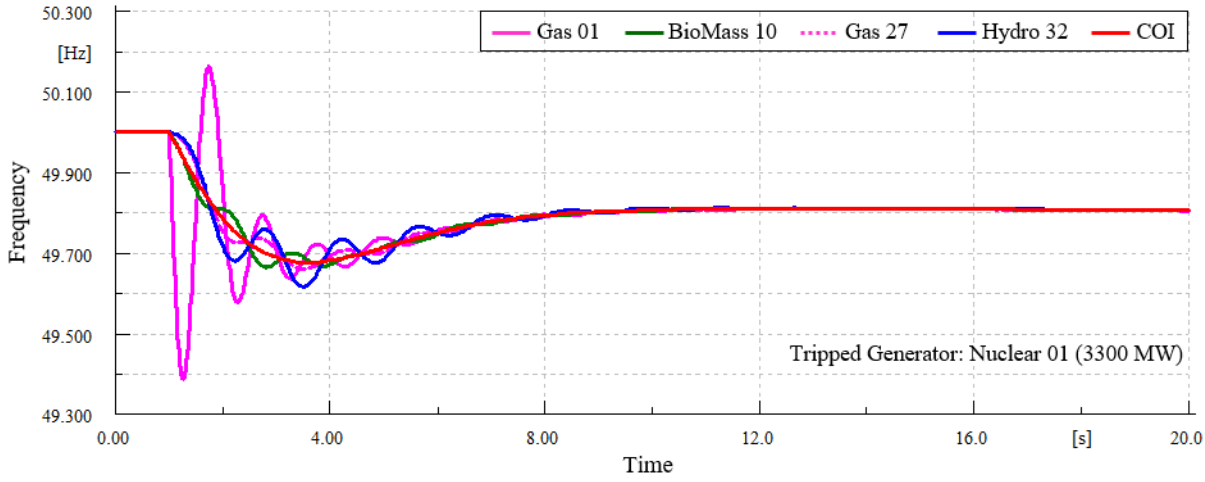

Figure 2-30: Frequency response with loss of 3300 MW generation in left bottom of network.

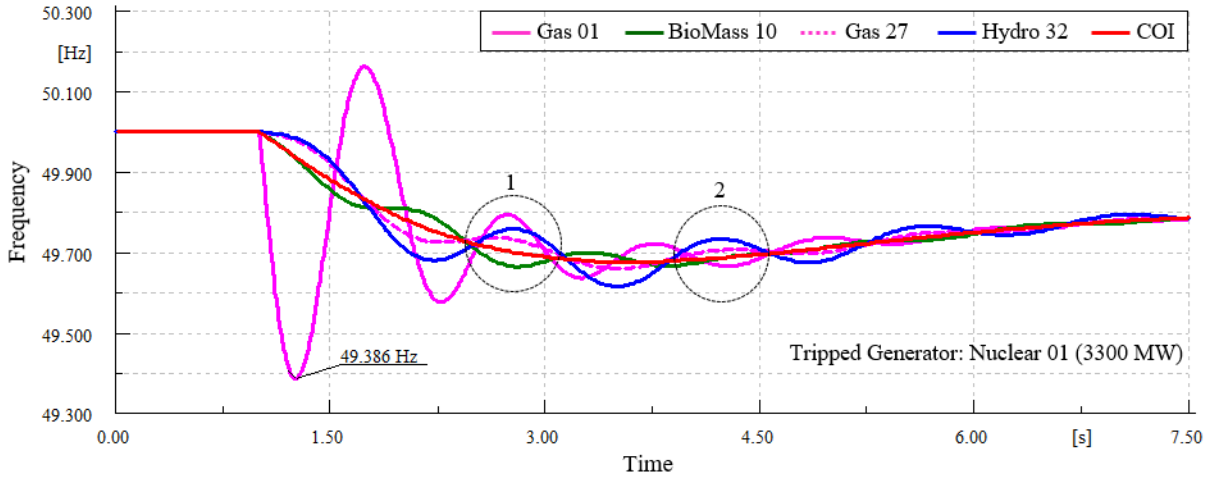

Figure 2-31: Frequency oscillations with loss of 3300 MW generation in left bottom of network.

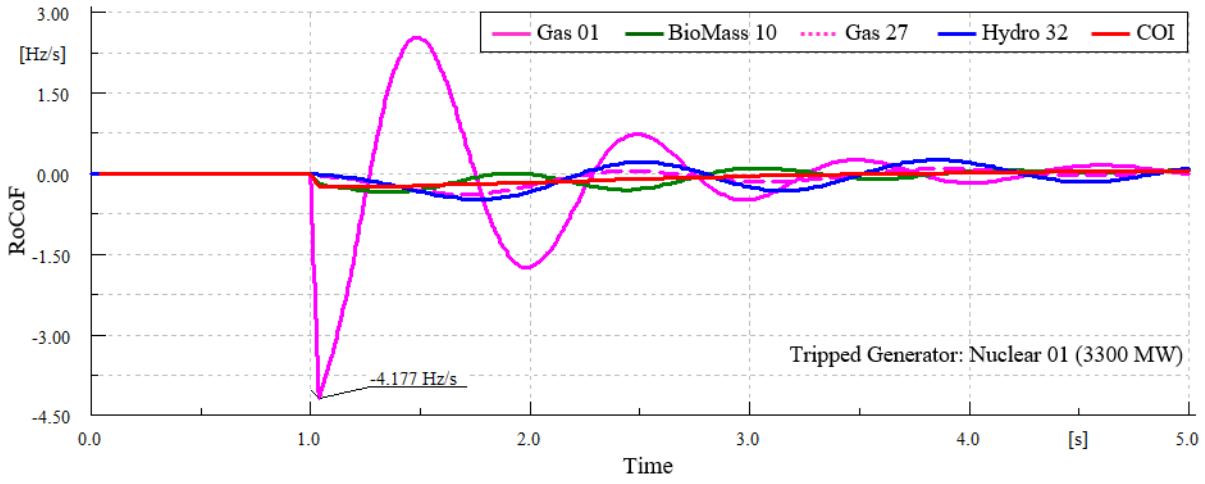

Figure 2-32: RoCoF deviations with loss of 3300 MW generation in left bottom of network.

2.1.5.3 Worse Case Time Domain Analysis for 36-Zone GB Network

In previous subsection, the frequency response performance of the grid in case of disconnecting all the power plants is explored for most 8 critical and susceptible areas and the maximum value of frequency Nadir and RoCoF are measured and portrayed in bar diagrams. Whereas these 8 candidate SGs could show the most critical frequency scenarios of the grid, it can't be said that they are the worse frequency cases since other 33 out of 41 SGs weren't investigated. Furthermore, the simulation results provided aren't appropriate for finding the relationship of the measured parameters like maximum RoCoF and the disturbance size. To this end, the worse contingency in terms of frequency Nadir as well as maximum RoCoF for loss of 41 SGs are calculated and shown in Figure 2-33 to Figure 2-38. The horizontal axis shows the disconnected SGs with an ascending order from the smallest SG to biggest one. The amount of disturbance is mentioned in parenthesis. In these figures, each bar is pertinent to a power plant having the worse situations from the viewpoint of frequency Nadir and RoCoF once the SG specified in the vertical axis is disconnected. The value inside the parenthesis of the bar's label determines the power generated by the corresponding unit. As can be seen from Figure 2-33 to Figure 2-35, the frequency Nadir is mitigated in proportion of disturbance size growth. However, this has some exceptions. For instance, albeit the power capacity of G10 is almost 1,400 MW greater than N01 in Figure 2-35,

the minimum value of frequency Nadir following the loss of N01 is less than G10 case. It's due to the enormous oscillations of the SGs in zone 1 with respect to zone 10. In the other hand, as can be seen from Figure 2-36 to Figure 2-38, the frequency Nadir is increased in proportion of disturbance size increment. However, this has some exceptions. This is case similar to the frequency Nadir discussion which its reason is high oscillation of some zones with respect to others. For instance, albeit the power capacity of G10 is almost 1,400 MW bigger than N01 in Figure 2-38, the maximum value of RoCoF following the loss of N01 is almost two times of the loss of G10. Another reason for these exceptions is the power network structure from the point of view of power plants locations. For example, the maximum value of RoCoF in case of N19 disconnection is approximately two times more than loss of G16, as shown in Figure 2-37. However, the capacity of N19 is almost 300 MW less than G16. This is due to this fact that there are three big units i.e. G17, G20 and G24 near to G16 which are bigger than G19 in the zone of N19. As a result, the lower value of G19 with respect to other three nearby units to G16 can effect on the maximum RoCoF of the grid more than the case in which the G16 is 300 MW bigger with respect to N19.

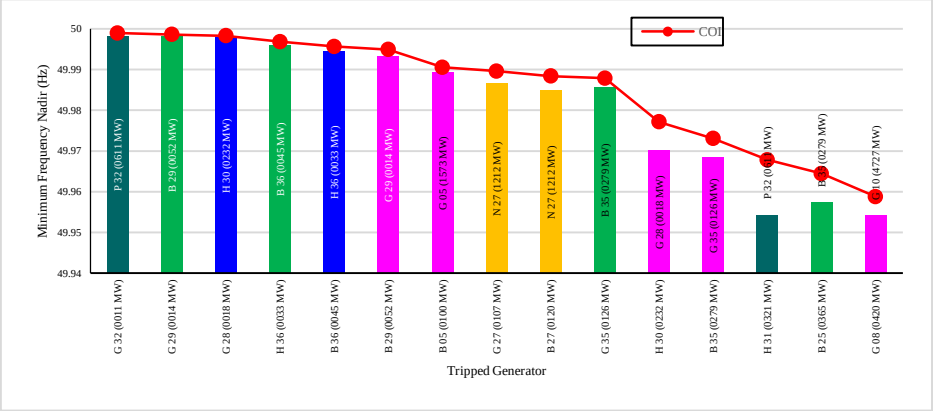

Figure 2-33: Minimum frequency Nadir of network with loss of generations from 11 MW to 420 MW.

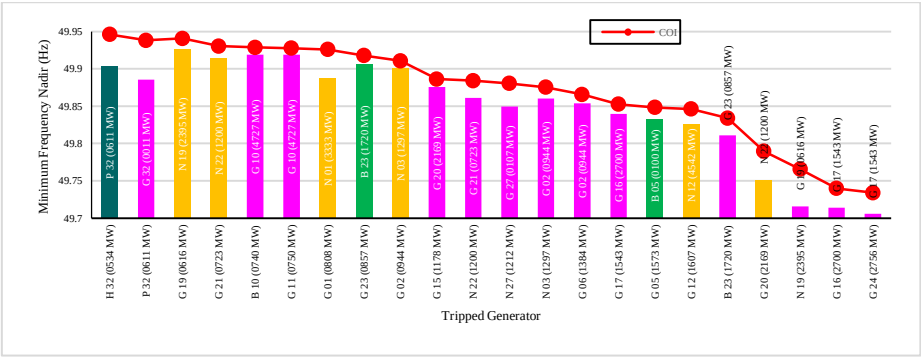

Figure 2-34: Minimum frequency Nadir of network with loss of generations from 534 MW to 2756 MW.

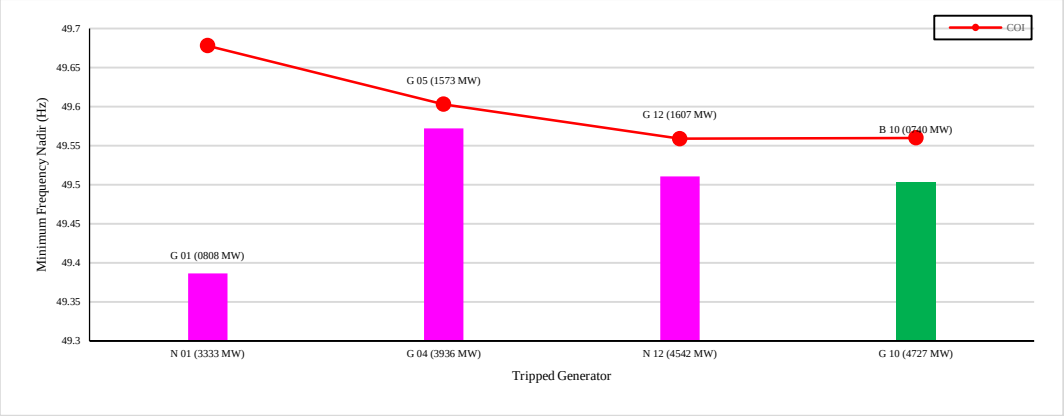

Figure 2-35: Minimum frequency Nadir of network with loss of generations from 3333 MW to 4727 MW.

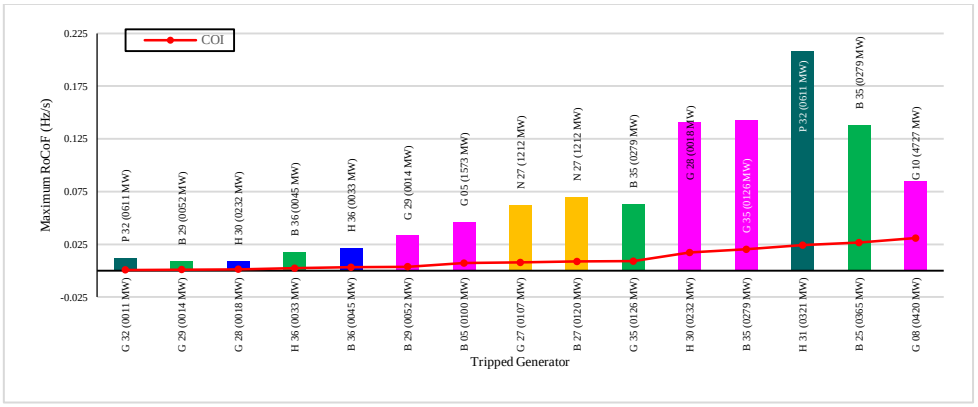

Figure 2-36: Maximum RoCoF of network with loss of generations from 11 MW to 420 MW.

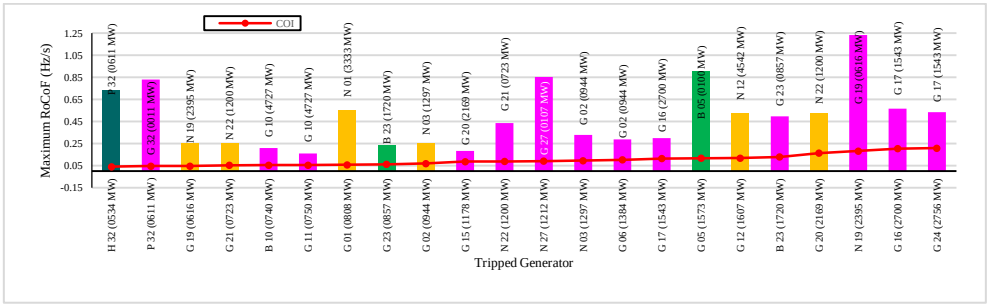

Figure 2-37: Maximum RoCoF of network with loss of generations from 534 MW to 2756 MW.

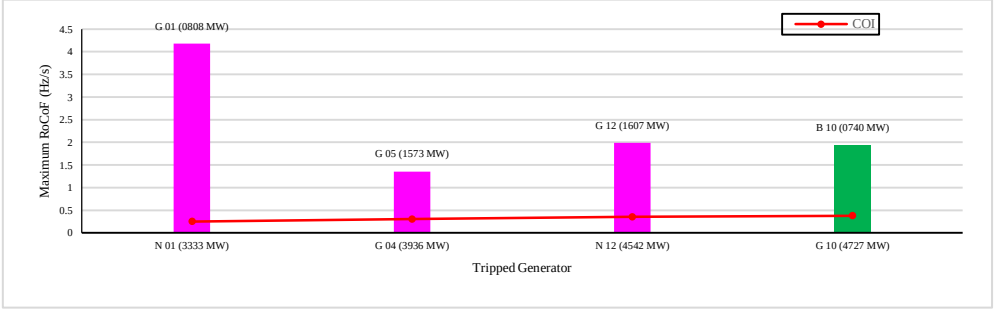

Figure 2-38: Maximum RoCoF of network with loss of generations from 3333 MW to 4727 MW.

2.1.6 Summary of system studies of an appropriate GB network

The dynamics of power system frequency are studied in this project study. In addition, a simplified and equivalent GB dynamic network model is developed and evaluated against the traditional disturbances for its appropriateness to carry out studies of the EFCC project to be demonstrated. The results of both test networks are similar confirming that the new test system is acceptable. Using the simplified model, case studies are undertaken to exhibit system frequency response in the GB systems against the abrupt load step, generator trip and short-circuit events. According to the simulation results, the discussions are made on the performance of new and old structures of 36-zone GB network to arbitrate the suitability of applying different frequency-based scenarios in the GB power network.

In this chapter, the dynamic performance of 36-zone GB network is investigated following the loss of generation. In the first phase of the chapter, the appropriate dynamic models of exciter system, thermal and hydroelectric units and SVCs for the purpose of frequency control dynamic studies are selected. After which, the dynamic impact of these devices on small signal stability and electromechanical modes in the frequency interval of 0.5-1.25 Hz is exmained using the modal analysis. Then, it is observed that gas and nuclear power plants located in the south eastern and south western parts of the GB network as well as the hydroelectric units in the northern ereas have the most influence on the slowest electromechanical modes and determine their damping ratios. Furthermore, it is shown that the 36-zone GB network has the similar dynamic behaviour with a single machnie infinte bus system while the inertia of the whole SGs is increased. This can lead to the reduction of damping and its frequency related to electromechanical modes. Moreoevr, it can be deduced that change of the inertia by increasing the penetration of converter-connected units in zones where nuclear unit 1, gas turbines 4 and 10 and hydroelectric unit 32 are located would be sufficient to control the damping of the slowest electromechanical modes. It meanhs it is not necessary to vary the inertia of all 41 SGs. Afterward, the mode shape concept is employed and it is observed that the first and second slowest modes of electromechanical mode group are the inter-area modes and devides the network into two major parts which swings against each other. From the mode shape concept, it is deduced that coast area in the southern part like zones 1, 3, 4, and 9 to 12 as well as the northern areas have the utmost contribution in network frequency oscillation following the loss of SGs. However, the middle parts of the network have the least effect on the oscillations so that the frequency oscillation of these areas are damped quickly. In the next phase of the chapter, time domain simulation studies are deployed to investigate the dynamic response of the network following the loss of SGs and validate the modal analysis results. In the time-domain studies, the condition of different regions from the viewpoint of frequency Nadir and maximum RoCoF for all N-1 criteria is examined. The results of this phase confirm the modal analysis process and determine the most critical zones of 1, 10 and 12 at the bottom, 19 in the middle and 32 at the top area. Additionally, it is to be noted that the maximum RoCoF for the COI is less than 0.15 Hz/s once the loss of generation is less than 5% of total load demand that is 2 GW.

2.2 References

[1] National Grid plc, “Operating the Electricity Transmission Networks in 2020,” Jun. 2011 [Online]. Available: http://www.nationalgrid.com/uk/Electricity/Operating+in+2020/

[2] F. J. DeMarco; N. Martins, and J. C. R. Ferraz, “An automatic method for power system stabilizers phase compensation design,” *IEEE Trans. Power Syst.*, vol. 28, no. 2, pp. 997-1007, May 2013.

[3] Smart Frequency Control Project, Available: http://www.nationalgridconnecting.com/The_balance_of_power/

[4] C. Canizares, T. Fernandes, E. Geraldi, L. Gerin-Lajoie, M. Gibbard, I. Hiskens, J. Kersulis, R. Kuiava, L. Lima, F. DeMarco, and N. Martins, B. C. Pal, A. Piardi, R. Ramos, J. dos Santos, D. Silva, A. K. Singh, B. Tamimi, and D. Vowles “Benchmark models for the analysis and control of small-signal

oscillatory dynamics in power systems," *IEEE Trans. Power Syst.*, vol. 32, no. 1, pp. 715-722, Jan. 2017.
[5] IEEE Committee Rep., "Transient stability test systems for direct stability methods," *IEEE Trans. Power Syst.*, vol. 7, no. 1, pp. 37-44, Feb. 1992.
[6] G. Rogers, *Power System Oscillations*. New York, NY, USA: Springer-Verlag, 2000.
[7] P. Demetriou, M. Asprou, J. Quiros-Tortos, and E. Kyriakides, "Dynamic IEEE test systems for transient analysis, *IEEE Syst. J.*, Jul. 2015.
[8] National Grid, Innovation, Enhanced Frequency Control Capability, Available: http://www2.nationalgrid.com/UK/Our-company/Innovation/NIC/EFCC/
[9] National Grid, Electricity Ten Year Statement, Available: https://www.nationalgrid.com/uk/publications/electricity-ten-year-statement-etys
[10] MIGRATE Project, Available: https://www.h2020-migrate.eu/
[11] R. H. Park, "Two-reaction theory of synchronous machines, generalized method of analysis—Part I," Trans. AIEE, vol. 48, no. 3, pp. 716-727, Jul. 1929.
[12] S. D. Pekarek, O. Wasynczuk and H. J. Hegner, "An efficient and accurate model for the simulation and analysis of synchronous machine/converter systems" IEEE Trans. Energy Convers., vol. 13, no. 1, pp. 42-48, Mar 1998.
[13] Kundur P. Power system stability and control. Balu NJ, Lauby MG, editors. New York: McGraw-hill; 1994 Jan 1.

3. Development and Investigation of Fast Frequency Response of CCGT

This chapter firstly concentrates on describing the main components models of combined cycle gas turbines (CCGTs). Then the control loops of the combined-cycle plant which either directly affect the response of the power plant to power system disturbances or have an effect on the design or operation of the plant are addressed. The model incorporates gas turbine, heat recovery steam generator and steam turbine and includes speed control, temperature control and inlet guide vane control. Then, an appropriate model of CCGTs for short-term dynamic study following the frequency excursion is simulated in DIgSILENT PowerFactory. The designed combined cycle power plant model and its controllers are tested on a simple but practical two-area Klein-Rogers-Kundur (KRK) power system. Moreover, the impact of high penetrations of CCGT on frequency response of two-area network is evaluated. The performance of the combined cycle plant is investigated following system disturbances in DIgSILENT PowerFactory software. The results illustrate that frequency control might become more challenging as a result of increasing the penetration and number of CCGTs working on their base load. It means that the system frequency excursions will be more likely with additional CCGTs working on full-load operation mode.

3.1 Literature Review

Combined-cycle gas turbines (CCGTs) have received significant attentions during the last decades due to their high overall efficiency, low green-house gas emission as well as flexibility. Therefore, a lot of power industries like UK (EFCC project) especially the ones operating with significant penetration of renewable power generation have deployed OCGTs. Although, the renewable energy sources like wind and solar power plants have extensively been incorporated into the power grids, their high variability and intermittency have resulted in several challengeable matters during the power system operation. Thus, the gas turbines (GTs) and its modified version i.e. CCGTs became a practical fast-start power generating unit to deal with the wind/solar power generation variability.

The combined-cycle power plant (CCPP) or CCGT contains of a GT, a steam turbine (ST), a heat-recovery steam generator (HRSG), and an electric generator. A variety of combinations exist, employing multiple GTs, HRSGs, and generators in several possible configurations.

The main pros of CCGT are its improved overall efficiency. The total thermal efficiency of the CCGT is considerably higher than that of the traditional fossil fuel type power plant. The matter of this fact is that the total enthalpy produced by the combustion process in the GT is utilised greatly through the combination of the GT Brayton cycle and the ST Rankine cycle. Therefore, the term combined-cycle is originated from the combination of these two cycles. It is to be noted that a typical simple-cycle conventional fossil fuel power plant (Open cycle gas turbine (OCGT)) has an efficiency of 30-35%, while the CCGT has an efficiency of more than 55%. As a result, the CCGT characterizes the integration of above mentioned two cycles, one being the high temperature cycle or "topping" (the GT Brayton cycle) and the other one being the low temperature cycle or "bottoming" (the ST Rankine cycle). These two cycles are coupled using a heat exchanger which transfers the exhaust low-energy of the high temperature cycle to the low temperature one so that it can produce additional work. In the CCGT, the output heat of the exhaust of GT is recovered in the HRSG to generate steam for the high temperature steam cycle as shown in the thermodynamic cycle of Figure 3-1.

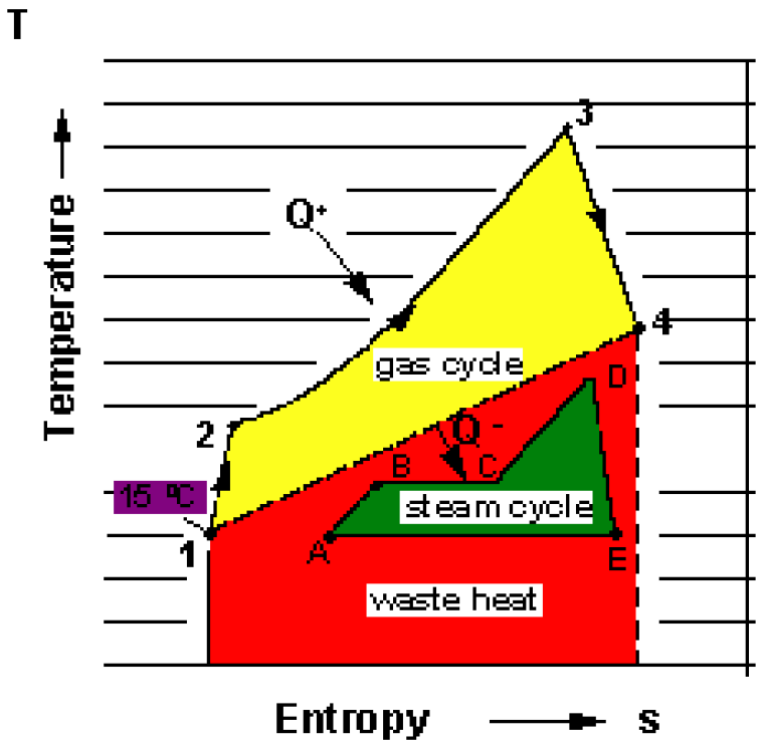

Figure 3-1: Combined-cycle diagram in temperature (T)/entropy (S) coordinates.

As can be seen from this figure, the line between point 1 and 2 is corresponded to the process in which air is brought into the compressor and the compressor raises the pressure and temperature on the incoming gas to point 2. Point 2 to 3 denotes the addition of heat by fuel injection and combustion in order to raise the gas temperature. The expansion of the hot gas through the turbine, transferring energy to the turbine blades and to the shaft for conversion to electric power by the generator is represented by path between point 3 and 4. The benefit of the CCGT is its ability to deploy the heat remaining in the exhaust of GT. The HRSG is supplied by GT exhaust where its heat energy is transferred to the working fluid of the ST, as indicated by the path from points 4 to 1 and the heat transfer Qc.

The Rankine cycle is used in the ST procedure. The heat extracted from the exhaust of GT is transferred to the water in the economizer tubes which leads to the water temperature increment (points A to B). The drum boiler creates steam (B to C) and extra heat energy is transported to the extracted steam in the super-heater (C to D) so that the pressure and temperature of heat will be increased. The steam is then expanded through the steam turbine (D to E), transferring energy to the steam turbine blades and thus the shaft and electric generator. The steam is then condensed (E to A) and pressurized in a pump (A to B) to start the cycle again.

In recent decade, the CCGT utilisation following the deregulation of the electricity market has went up quickly. As it is discussed above, the reasons are high efficiency, low unit cost, quick construction and low emission. Nevertheless, the dynamic performance of CCGT differs significantly from those of conventional power plants [1]. Therefore, the modelling of CCGTs as one of the EFCC's service providers and their controllers is vital to understand its dynamic characteristics and impacts on power system frequency response and performance following system disturbances.

There are several studies on the GT modelling of CCGT which are presented for dynamic and stability cases [1]-[5]. A pioneering model is proposed by Rowen in [2] and improved by authors to integrate variable inlet-guide-vanes (IGVs) to control air-flow injected to the combustion chamber. Another dynamic model of GT is derived by the IEEE working group in [1] for a single-shaft, constant-speed GT with IGVs with the physical thermodynamic characteristics and rules. The special studies on GTs modelling for system frequency events are presented in [3] and [4] in which a physical model to precisely determine the power output of GT is developed.

A GT model for dynamic studies of power networks on the basis of the Rowen's model is developed by CIGRE working group in [5], however, the turbine dynamics are characterized by a second-order block compared to the function in the Rowen's model for the calculation of torque. Additionally, the dynamic model comparisons of GT, estimation and validation processes of parameters are introduced in [6]-[8].

It is to be noted that power systems are influenced by their unique frequency response with respect to other conventional power plants following the frequency excursions in the network. The CCGTs' output power particularly decreases in their full operation mode due to reduced compressor airflow following the in-feed and control activities triggered by their temperature controller. This is detrimental for system frequency stability and needed to be investigated especially in Great Britain (GB) power network.

In this regard, the small signal stability, modal analysis, time-domain simulation, frequency nadir and rate of change of frequency (RoCoF) evaluation should be implemented offline by multiple case studies. These breakdowns enhance the situational awareness for system operators of CCGT integrated power network by providing a damping visualization of slowest electromechanical modes, frequency response, RoCoF and worse case time domain simulations in terms of minimum frequency nadir and maximum RoCoF. It is also noticeable that when the proportion of CCGTs on power systems especially large scale ones increases, their influence on frequency deviations will become more considerable and sizeable.

This chapter tries to discuss and illustrate the CCGT model adopted from that developed by Rowen [2], by making reference to more recent CCGT models based on CIGRE working group [5] and [9] as well as [10], [11] in DIgSILENT PowerFactory. Developing the mathematical model of the CCGT and its modelling derived in DIgSILENT simulation language (DSL) and DigSILENT programming language (DPL) for power system frequency studies are the main aims of this chapter.

3.2 CCGT Configuration

CCGT can be configured into the following two arrangements:

3.2.1 Single-shaft (SS) CCGT or CCPP

GT, ST and electrical generator are all in tandem on a single rotating mechanical shaft. This configuration can be divided into two designs:

i) The first one has the generator at one end, driven by both turbines (GT and ST) from the same side. The ST is rigidly coupled to the GT on one side and the generator on the other. To understand the structure of this SS CCGT, it is shown in Figure 3-2.

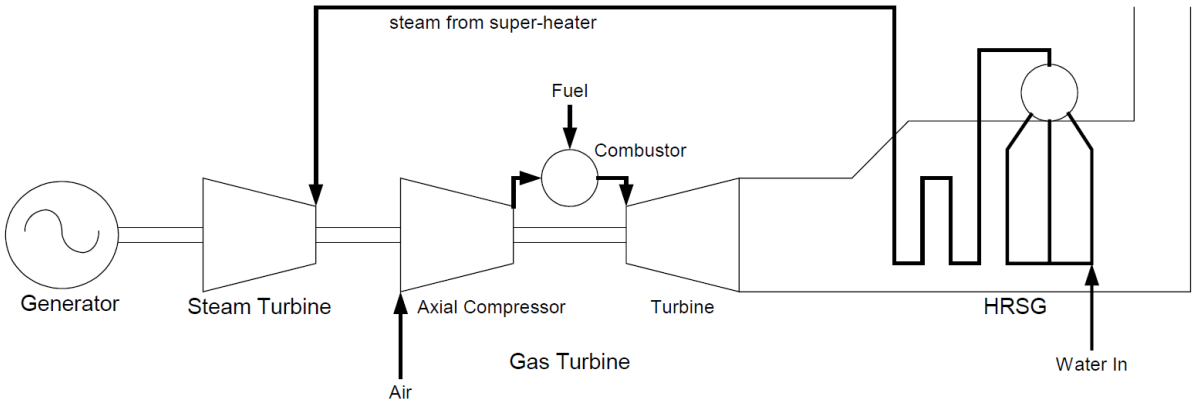

Figure 3-2: SS CCGT (generator on end).

ii) The second one has the generator between the GT and ST, each turbine driving one end of the generator. Note, the ST engages and disengages with a clutch. To understand its structure, it has been portrayed in Figure 3-3.

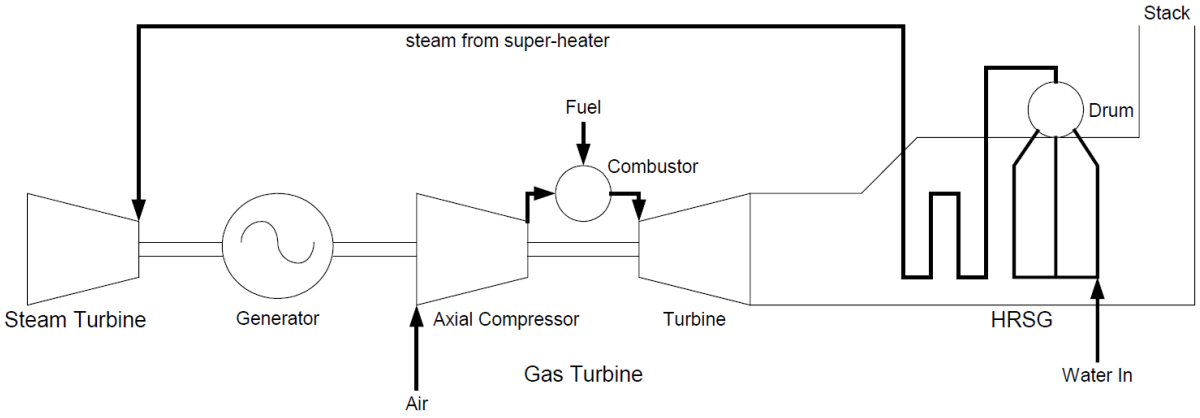

Figure 3-3: SS CCGT (generator between GT and ST).

3.2.2 Multi-shaft (MS) CCGT or CCPP

One or more GT each with its own HRSG which provide the single ST steam, all on separate shafts with separate generators. Different configurations of MS CCGTs are depicted in Figure 3-4 and Figure 3-5, for a single GT plant and two GT plant, respectively. The procedure is basically the same, except for the two GT plant, the steam outputs of the two HRSGs are combined in order to supply a single ST.

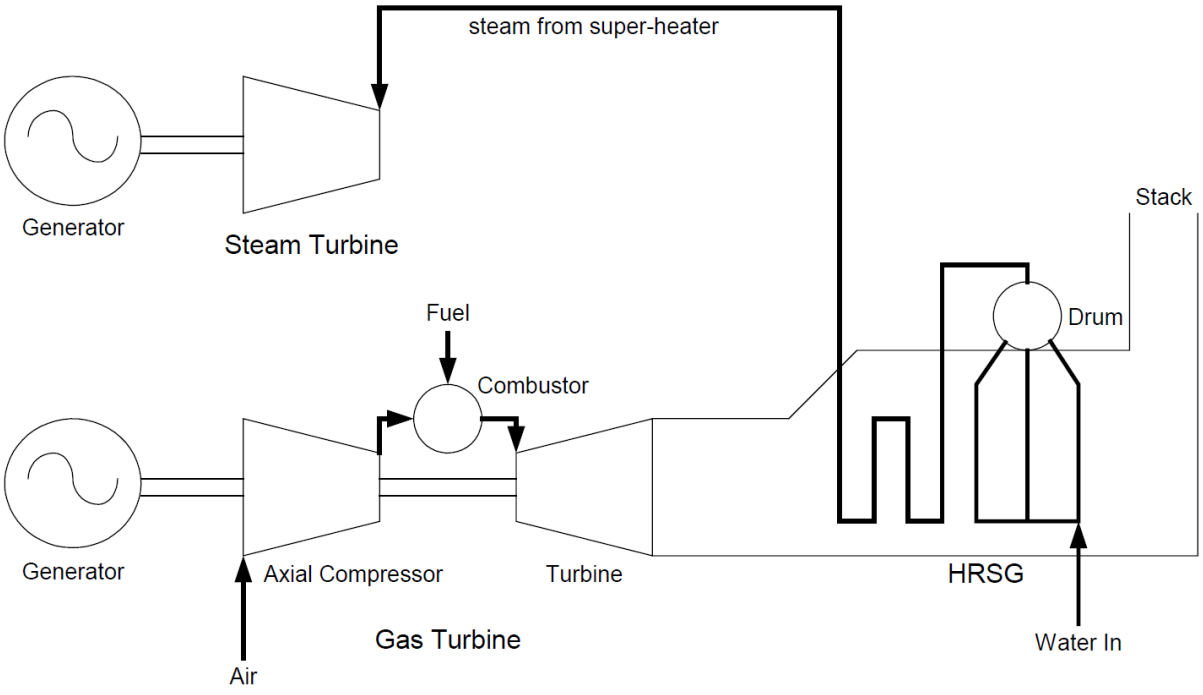

Figure 3-4: MS CCGT configuration with a single GT.

3.2.3 Cogeneration/Supplementary Firing

Cogeneration is the consecutive creation of the heat needed for industrial procedure (mostly in the form of steam) and production of power using energy recovery from this production. Note that power can be cogenerated in either the high temperature cycle or low temperature one. The steam necessities of the procedure (pressure, temperature and volume of steam) control the optimal system configuration. Although, the steam from the steam turbine is basically condensed in the abovementioned combined-cycle process, it could apparently be deployed in industrial mechanism. It is to be noted that if the steam requirements are significantly increased, supplemental firing of the HRSG which is also known as post combustion in Europe can be incorporated. Therefore, the supplementary firing system is mostly applied in combined-cycle cogeneration power plants where the amounts of process steam needs to be changed independently of the generated electrical power.

3.3 Main Components of CCGTs

3.3.1 Gas Turbines (GTs)

GTs usually contain of a turbine working based on the Brayton cycle, an axial compressor, and a combustion chamber. These three thermal elements complement by the auxiliaries, the exhaust system, controls and air intake system. Air is drawn into the axial compressor by compressor inlet and compressed through multiple stages of stator and rotor blades. It is worth to note that the rotor blades add kinetic energy to the air at each stage, while the kinetic energy is converted to potential energy by raising the static pressure of the air through the stator blades. The net pressure ratio of the whole axial compressor is normally located between 15 and 20. After which, the compressed air is combined with the fuel in the combustion chamber to make the combustion process happened. The resulted hot gas is expanded by a multi-stage turbine to drive the generator and compressor.

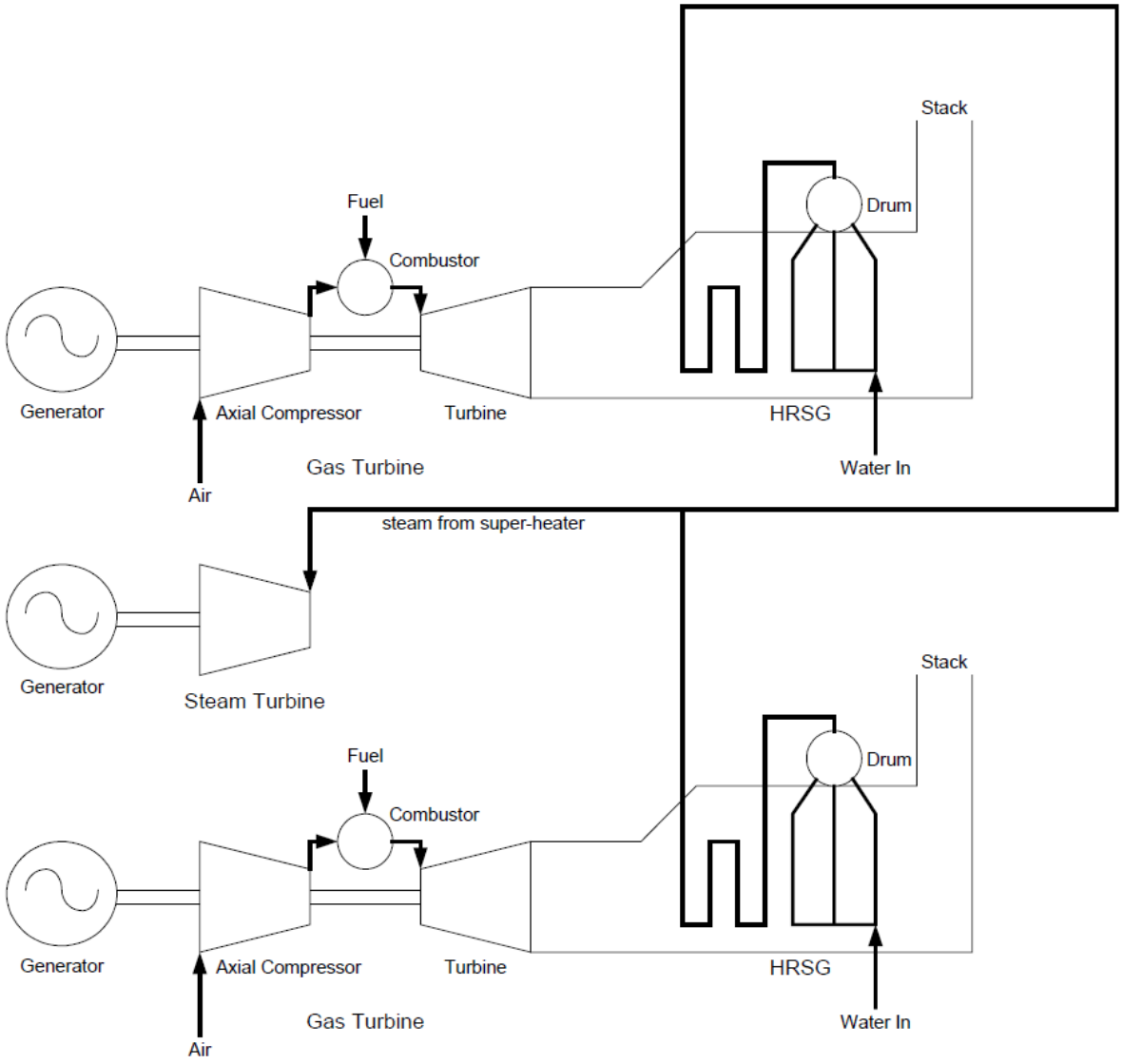

Figure 3-5: MS CCGT configuration with two GTs.

The power input to the HRSG is determined by the temperature of the exhaust gas and exhaust gas flow. Moreover, the power output of a GT is specified by the fuel flow. The firing temperature that is the temperature of gas at the combustion chamber exit point is determined by both the fuel flow and airflow. The measurement of the exhaust temperature and the compressor pressure ratio adjust the fuel flow and airflow to keep the firing temperature below a predefined limit. The measurements of the inlet and compressor discharge air pressures determine the compressor pressure ratio.

The airflow can be tuned by varying the angular position of the IGVs. The IGVs are basically the first few stages of stator blades within the axial-compressor assembly. By decreasing the airflow, the temperature exhaust gas is reserved high at reduced loading levels in order to preserve the desired amount of heat transfer into the HRSG and provide overall higher power plant efficiency. While the GT is loaded close to the base load, the IGVs are wide open. Thus, the airflow is a functioned by the atmospheric pressure, the IGV angle, the shaft speed as well as ambient temperature at compressor inlet.

There are disparate kinds of combustion chambers. Moreover, it is to be noted that the GTs utilised for generating power can be classified into two groups: i) the heavy duty GTs and ii) the aero-derivative GTs. The main differences between these two types of GTs are as follows:

- The combined moment of inertia of the turbine and generator (H) is considerably higher for the heavy-duty GT than a typical aero-derivative one. This is due to the fact that the power turbine and generator are typically on a separate mechanical shaft for the aero-derivative GT than the high-pressure turbine and axial compressor. As a result, the combined moment of inertia of the multi-stage axial compressor and turbine for heavy-duty turbines is much larger than the relatively light low pressure turbine that drives the generator load on a typical aero-derivative unit [9].
- For the cases where all compressor stages of the aero-derivative GT are on a separate shaft than the generator and power turbine, the unit may not be as susceptible to operations restrictions due to severe changes in electrical frequency. The first limit on the prolonged off-nominal frequency operation of heavy-duty GTs is the characteristic of compressor. The operation constraints of the GT through mechanically decoupling the compressor from the generator become dominated by the operational characteristics of the high-speed shaft and differ from the behaviour of a heavy-duty GT [9].

3.3.2 Heat Recovery Steam Generator (HRSG)

The HRSG is deployed to make a link between GT and ST procedure. It can be divided into three main categories as follows:

- **HRSG without supplementary firing:** The HRSG without supplementary firing is basically an entirely convective heat exchanger. It means that no additional fuel will be burned in the exhaust gases. The mainstream of the large CCGTs built and operated today utilise unfired HRSGs.
- **HRSG with supplementary firing:** Extra fuel is burned in the exhaust duct to grow the generation of steam. Supplementary firing system is most often implemented in the combined-cycle cogeneration plants where the steam levels should be changed individualistically of the generated electric power generated. In this situation, supplementary firing system controls the generated process steam value. For such a cogeneration application, the exhaust gases may be diverted at low loads and the steam is created by means of independent firing [9].
- **Steam generators with maximum supplementary firing:** In fact, the GT is replacing the forced draught air blower, feeding hot combustion air into the boiler. This application is basically for repowering of the existing power plant.

The main functionality of the HRSG is to convert the exhaust energy of the gas turbine into the steam. After the heating procedure in the economizer, water enters the drum and slightly sub-cooled. From the drum, it is circulated to the evaporator and returns as a water/steam mixture to the drum where water and steam are separated. The saturated steam leaves the drum for the super-heater where it reaches the maximum heat exchange temperature with the hottest exhaust gas leaving the gas turbine.

3.3.3 Steam Turbine (ST)

The ST comprises of the stationary blades which are a rotor with the spinning blades reinforced based on journal bearings, and main stop and control valves. The ST can be built with a single casing or have multiple casings which is dependent to its capacity. Typically, the ST has a low pressure (LP) turbine, a combined intermediate pressure (IP) as well as a high pressure (HP) turbine. In the reheat system, steam of high pressure turbine will be turned back to the HRSG to reenergise receiving additional heat before going to the IP and LP turbine stages.

In the CCPPs, the ST can be worked in two operation modes of fixed pressure or sliding pressure control. The combination of these modes is practically usual for CCPPs, depending on the output power level. During sliding pressure control, the throttling or control valves are fully open. The steam pressure is a function of the steam

mass flow entering the steam turbine. The load (power output) of the steam turbine depends on the mass flow and is not directly controlled. Consequently, the ST load can only be gone up by raising the steam flow which involves generating more steam in the HRSG and needs the heat grow from the GTs or supplemental firing system. Accordingly, the STs operating in the sliding pressure mode will not answer considerably to control action in the first few seconds after the disturbance and may take at least a minute to numerous minutes to respond with a noteworthy grow in electrical power. Once they operate close to full power, most CCPPs operate with the sliding pressure control of the ST.

Once the operating mode changes to the fixed pressure one, the control valve position (valve opening) is varied in order to throttle the flow of steam in such a way keeping pressure at the preferred level. A better part-load efficiency of the ST can be obtained through partly throttling the flow of the steam.

3.3.4 Generator

Generators for CCPPs or CCGTs are basically similar to other high speed generators. The electrical controls and protection devices and structures are the same as the deployed one in the traditional fossil fuel plant.

3.4 CCGT Modeling

In this section, the modelling of CCGT is described for implementing in dynamic simulations. After which, all the models are provided and derived using the dynamic simulation language (DSL) part of DIgSILENT PowerFactory software.

3.4.1 GT Modelling and Controls

CCGT incorporates the GT and ST technologies together. The output gases from the GT are fed into the HRSG that can produce steam for ST driving. The GT elements of CCGT are pretty similar to that of the OCGT. Although both the OCGT and CCGT systems have a maximum acceptable temperature restricted by the materials used in the structure of GT's blades, any change in the exhaust gases' temperature in going to the HRSG can definitely affect its efficiency and, therefore, the ST's efficiency. As a result, the temperature of exhaust gas needs to be conserved at the maximum acceptable level (the rate value) in order to reach the optimal efficiency in CCGTs. It will be accomplished by two main control loops on the GT, those are, temperature and speed controllers by means of fuel flow as well as airflow controls, respectively.

The outline of CCGT prime mover unit model is shown in Figure 3-6. The required input signals to the CCGT dynamic model are turbine shaft speed (ω_r) as well as reference mechanical power ($P_{m,ref}$). The output of the model is the mechanical power of CCGT (summation of GT and ST output powers). As shown in Figure 3-6, the dynamic model of CCGT consists of the following three controllers: 1) Gas Fuel Controller; 2) Temperature Controller; and 3) Inlet Guide Vanes (IGV) Controller.

3.4.1.1 IGV Controller

The airflow is controlled by using the IGV controller. The rated exhaust temperature is compared with the calculated one so that if there is a difference value, the IGVs regulate the airflow to get exhaust temperature back to the nominal amount. However, as the airflow is also subjected to the compressor speed, the expected

airflow, due to the IGV position, is modulated by the actual value of speed (ω_r) in order to yield the computed flow. It is to be noted that the IGV controller model is also armed with an over-firing box that permits the exhaust temperature restrictions to be amplified for a short time interval during the transient of the plant frequency response.

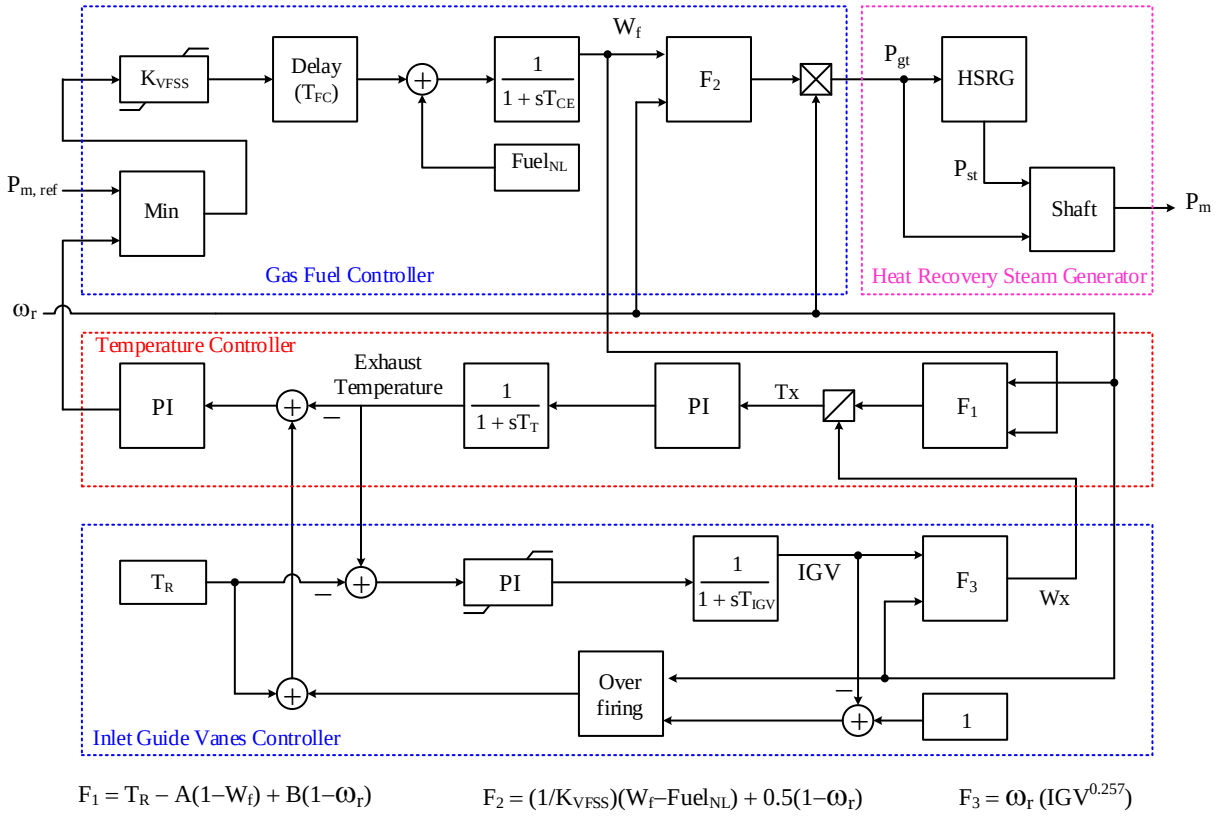

Figure 3-6: Outline of CCGT prime mover unit model.

3.4.1.2 Temperature Controller

As can be seen from Figure 3-6, a scaling strategy is integrated into the system speed input to the exhaust temperature computation process of F1 block in order to control the CCGT frequency sensitivity. Afterwards, the temperature of exhaust extracted from the computation procedure of F1 is modulated using the designed airflow through the compressor (IGV), since the actual temperature relates to the compressor airflow. Then, the temperature of the exhaust gases is measured by radiation shield and thermocouple time lags. Finally, this measured temperature is compared with the reference signal received from IGV controller and then passed through a proportional-integral (PI) controller to achieve the fuel flow input to the combustion chamber of GT. Under normal operations of CCGT, the measured temperature is less than reference value leading to the situation in which the temperature controller is at the maximum limit. Therefore, the speed controller controls the fuel supply in 'Gas Fuel Controller' and takes the form of an ordinary droop governor. If the measured temperature exceeds the reference one, the temperature controller will come off the maximum restriction and integrate down to the point where its output takes over as fuel request signal in the minimum value selector box of 'Gas Fuel Controller'.

3.4.1.3 Gas Flow Controller

The output signals of both the temperature and speed controllers are sent to the low value select block so that the lesser the value of these two inputs can obtain the fuel flow into the GT within permissible restrictions. The unobtainable fuel flow demand is cut off using the upper fuel limit. The lower bound is considered to ensure that the gas fuel fed to the combustor is not mitigated below the self-sustaining combustion point. It is to be noted that the amount of 0.23 as an offset considers the minimum fuel limitation at no-load which is important to keep the compressor in operation mode. Accordingly, the fuel control signal interval of the governor can be from 23% to 100%. In order to permit the utilization of the parameters of the GT governor comparable to those of ST, the governor of GT needs to operate from 0 to 100% of actual load interval. After which, this range should be corrected to 23% to 100% fuel flow interval to be consistent with the GT thermodynamics. There is a time lag named (T_{CE}) in the model which is corresponded to the discharge volume of compressor. Block F2 deployed in Figure 3-6 corresponds to GT torque calculation.

3.4.2 HRSG Modelling and Controls

In the HRSG section, the output power of ST (P_{st}) is determined based on GT output power (P_{gt}) and finally the mechanical output power of CCGT is specified according to the shaft. This block determines the contributions of GT and ST in overall power output of CCGT plant. For instance, the GT and ST generate 70% and 30% of total power of CCGT, respectively. The HRSG block diagram is shown in Figure 3-7.

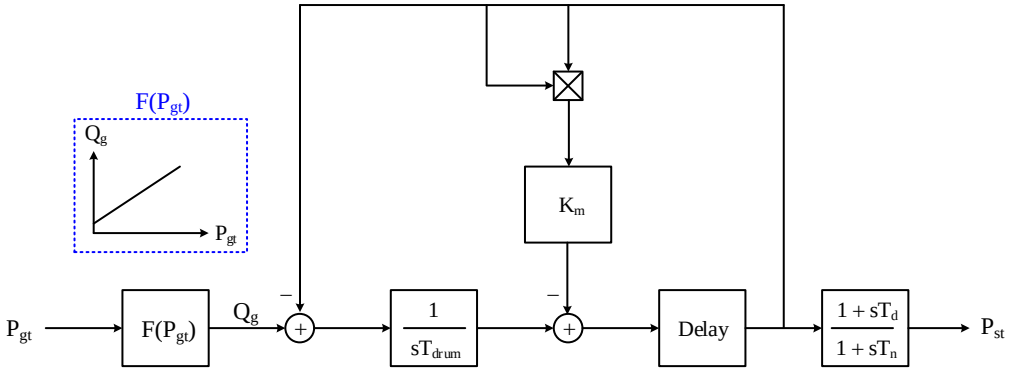

Figure 3-7: Outline of HRSG model.

3.4.3 DSL Based Model of CCGT

Hereinafter, a CCGT plant using the DSL part of DIgSILENT PowerFactory is simulated. The DSL models shown in Figure 3-8 and Figure 3-9 are corresponded to those of Figure 3-6 and Figure 3-7, respectively. The nominal apparent and active powers of CCGT are 500 MVA and 400 MW, respectively. GT and ST can generate 270 MW and 130 MW, respectively.

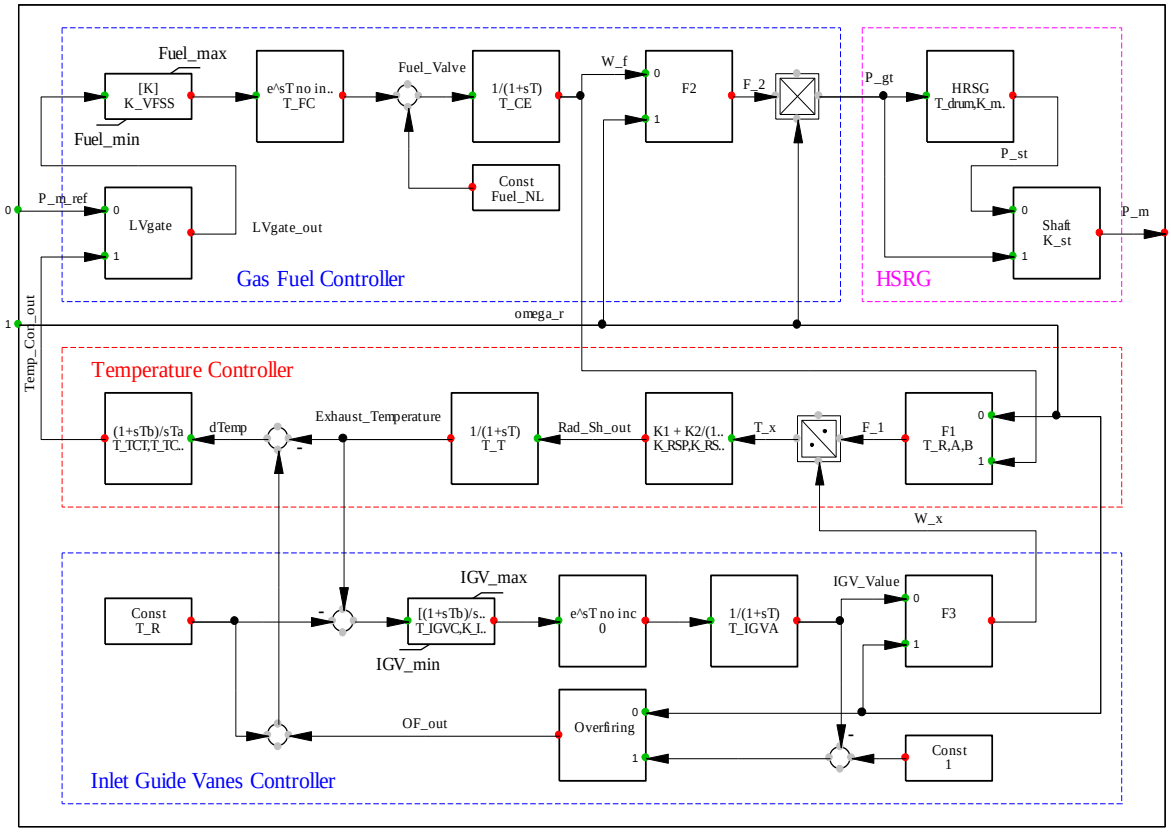

Figure 3-8: Outline of CCGT prime mover unit DSL model.

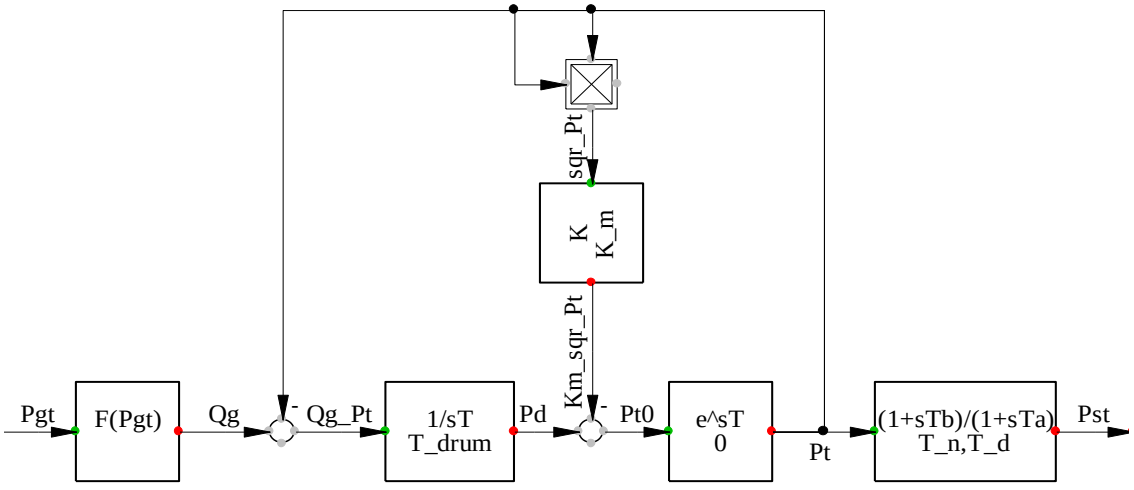

Figure 3-9: Outline of HRSG DSL model.

The controlling strategy structure of CCGT and other two plants is plotted in Figure 3-10. In this scheme, the voltage controller (VCO) tunes the exciting voltage of synchronous generator (SG) according to the terminal voltage. The PSS sends auxiliary signal to VCO using SG's speed. The turbine dynamics is modelled by means of prime mover unit (PMU). The primary controller (PCO) controls the turbine output power using the SG's speed variations. In this chapter, the PMU and PCO are called governor (GOV). The above controllers are explained in detail hereinafter.

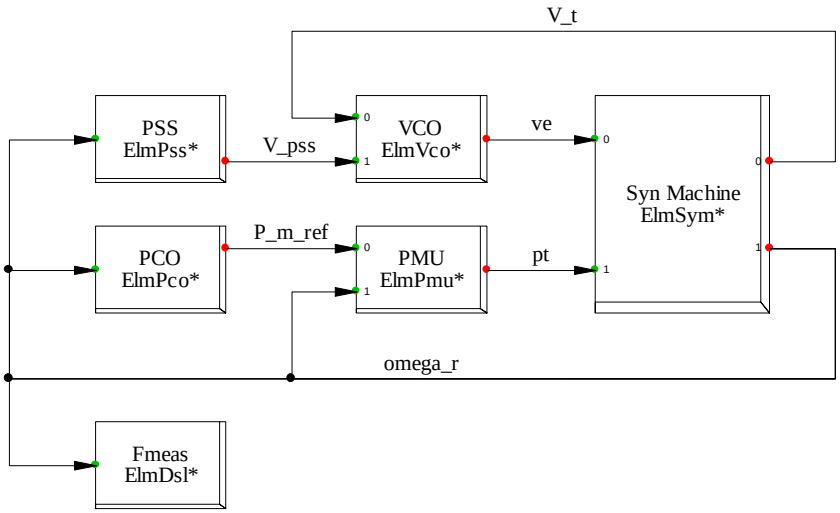

Figure 3-10: Control structure of power plants.

The VCO's control block is shown in Figure 3-11 [12]. This is a thyristor exciter with a transient gain reduction. The PSS produces an electrical torque with the same phase with the rotor speed change which leads to rotor oscillation damping increment. This in turn improves the small signal stability of the whole system. The PSS block diagram which is utilised in this chapter is shown in Figure 3-12. At first, the speed change with respect to reference one is multiplied in a gain and passed through a washout block to remove the slow variation of speed. As shown, two blocks of lead and lag are deployed to compensate the phase difference between the input signal of VCO and electromagnetic torque of SG. Finally, the output signal of PSS is restricted to a predefined value using a limiter.

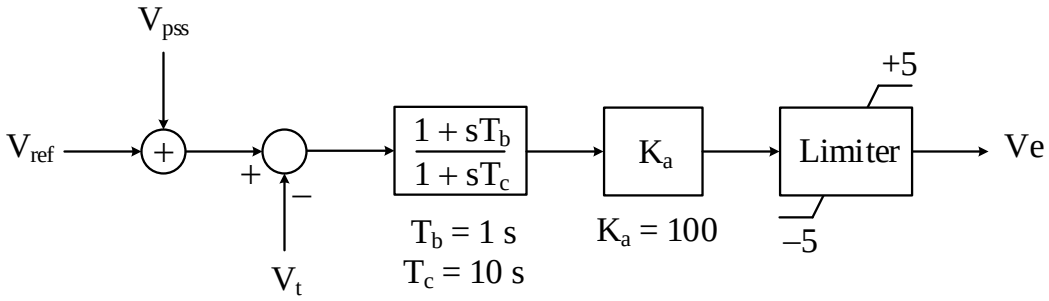

Figure 3-11: Block diagram of voltage controller (VCO).

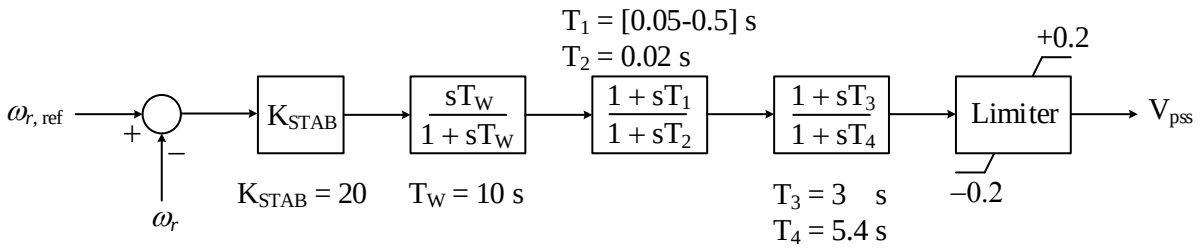

Figure 3-12: Block diagram of power system stabilizer (PSS).

The ST transfers the energy of high pressure steam with great temperature to mechanical energy. The block diagram of a ST is illustrated in Figure 3-13 [12]. The time constants of T_g and T_{ch} are pertinent to governor (GOV) and steam chest, respectively. The largest and important time constant in this turbine model is T_r which shows the re-heater time delay. The parameter F_h determines the high pressure turbine contribution to generate power.

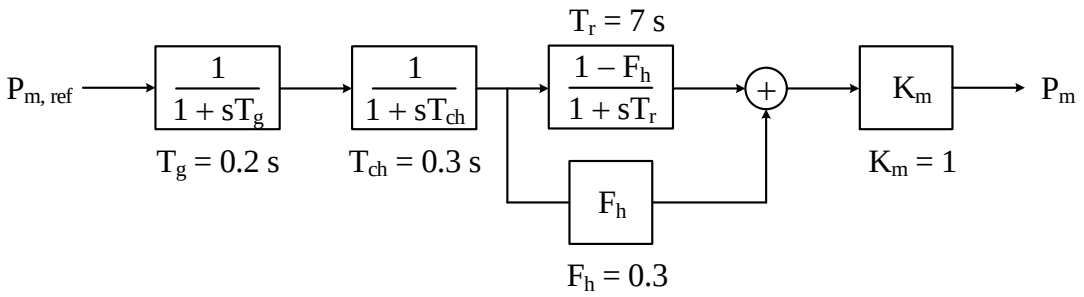

Figure 3-13: Block diagram of ST power plants prime mover unit (PCO).

The block diagram of primary controller (PCO) related to the ST is shown in Figure 3-14. In this structure, a value is added to the mechanical reference power based on the speed variation with respect to rated speed [12].

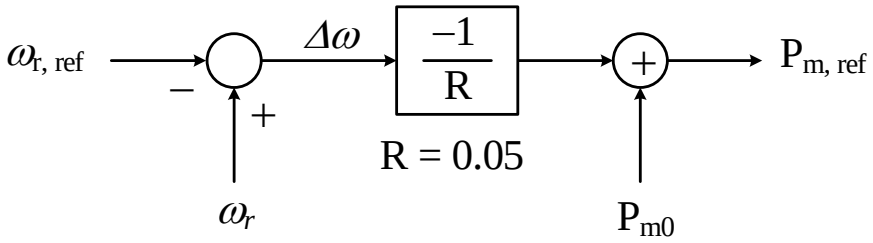

Figure 3-14: Block diagram of primary controller.

The CCGT power plant parameters are depicted in Table 3-1.

Table 3-1: Parameters of CCGT model

T_{drum}	300	T_{FC}	0.06	T_{CE}	0.45	T_{RST}	15	K_{st}	0.325
K_m	0.15	T_R	950	A	700	T_{TCT}	450	$Fuel_{min}$	0.15
T_n	3	$Fuel_{NL}$	0.23	B	550	T_{TCG}	3.3	$Fuel_{max}$	0.77
T_d	10	T_T	0.5	K_{RSP}	0.8	T_{IGVC}	20	IGV_{min}	0.095
K_{VFSS}	0.77	T_{IGVA}	3	K_{RSI}	0.2	K_{IGVC}	4	IGV_{max}	1

3.5 Dynamic Response of CCGT in Simple Test System

The proposed CCGT power plant beside two others supply a load demand equal to 1,200 MW as shown in Figure 3-15.

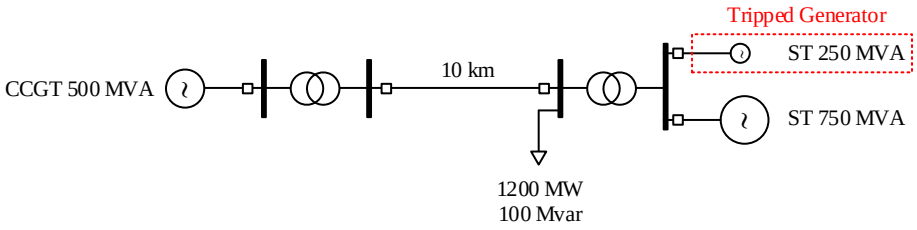

Figure 3-15: Single line diagram of studied network.

The dynamic performance of CCGT following the loss of ST generator 250 MVA shown in Figure 3-15 in two different scenarios of full load and partial load are investigated. Before the event occurrence, the CCGT plant produces 400 MW and 350 MW for full load and partial load cases, respectively. The results related to these scenarios are illustrated in Figure 3-16 to Figure 3-27. The frequency response and RoCoF of CCGT for the aforementioned scenarios are shown in Figure 3-16 and Figure 3-17, respectively. As can be seen, the RoCoF in these two scenarios are similar. This is due to the fact that the CCGT model is identical in these two cases. In other word, the inertial response of this power generating unit is independent of turbine type and just relevant to the inertia of generator's shaft. However, the frequency Nadir as well as the steady state values of frequency at full load scenario are less than partial load one.

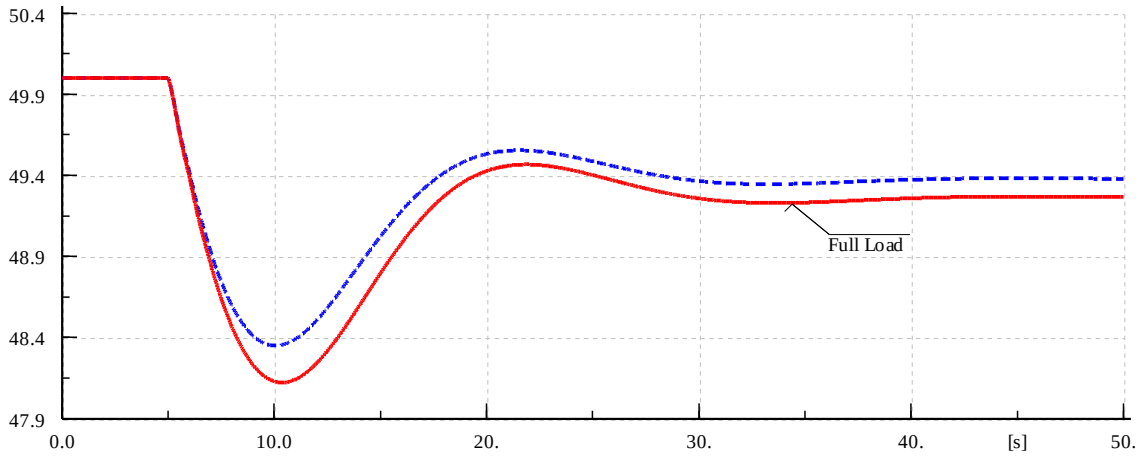

Figure 3-16: Frequency of CCGT power plant: full load (solid) and partial load (dashed) scenarios.

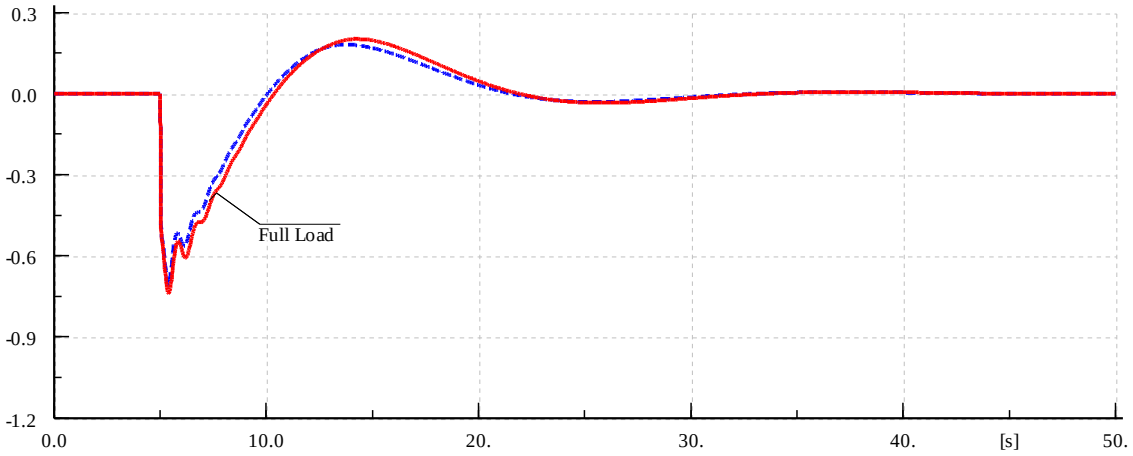

Figure 3-17: RoCoF of CCGT power plant: full load (solid) and partial load (dashed) scenarios.

The mechanical power obtained by CCGT for full load case is depicted in Figure 3-18. It is clear-cut that albeit some portion of power produced in network is lost and the frequency is dropped down, the power generated by CCGT is unexpectedly decreased and the governor droop can't help any more. It is to be noted that generation power of CCGT isn't imposed by 1 p.u. and the reason behind of this power reduction is turbine characteristic. In contrast, the power generated by CCGT for partial load is increased in response of network frequency mitigation as shown in Figure 3-19.

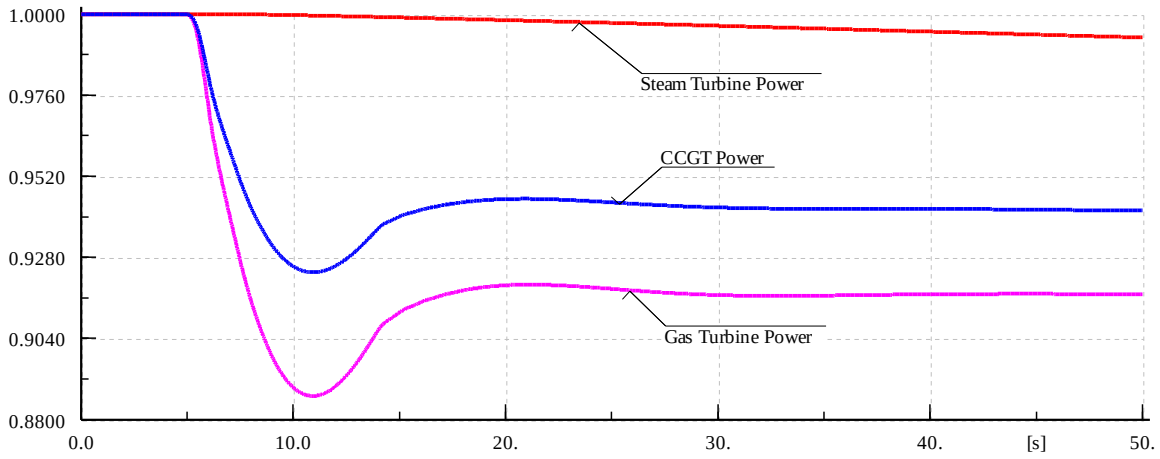

Figure 3-18: Mechanical power of CCGT power plant at full load scenario.

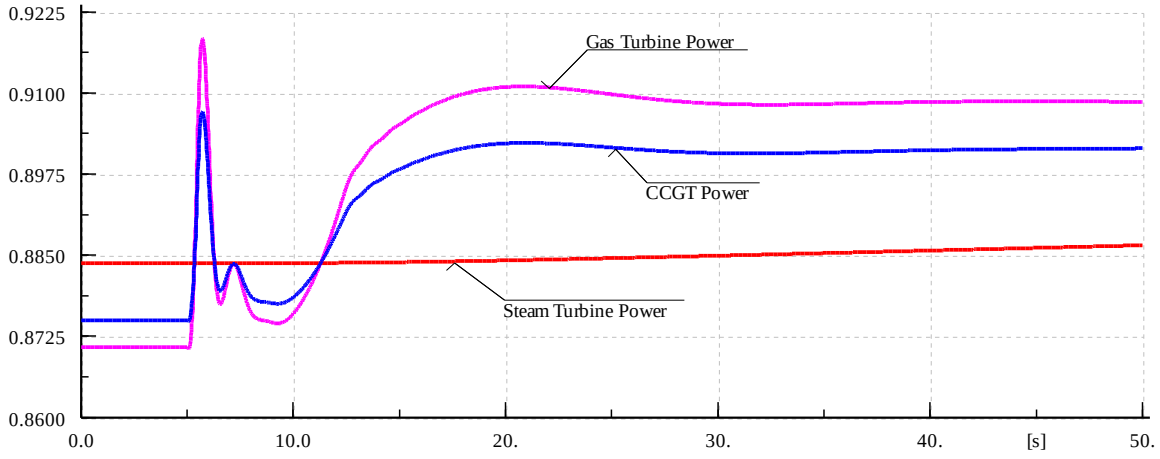

Figure 3-19: Mechanical power of CCGT power plant at partial load scenario.

To explain this, it is noteworthy that in the full load operation mode of CCGT, the IGVs and fuel valve are fully open and the airflow can't be gone up further (See Figure 3-20 and Figure 3-21). As the network frequency drops, the compressor slows down since the GT of CCGT is synchronized to the network. The compressor speed reduction leads to the pressure ratio mitigation across the compressor, and therefore, the airflow into the combustion chamber is reduced (Figure 3-22). The airflow reduction in the compressor leads to an increase in the fuel-to-air ratio (See Figure 3-23) so that it can directly specify the GT inlet temperature and the exhaust temperature in consequent. Thus, any increase of fuel-to-air ratio results in a rise in the temperature of exhaust (See Figure 3-24). In the full load scenario, as the exhaust temperature rises, the temperature controller overrides other inputs rapidly and decreases the fuel flow (See Figure 3-25) in order to restore the correct fuel-

to-air ratio. Additionally, this can lead to exhaust temperature reduction. In order to keep constant and optimal outlet temperature (950°F), it is mandatory to adjust the airflow as the fuel flow varies.

The operation of low value (minimum) select block is shown in Figure 3-26. According to the fully loaded CCGT, the input signal to this block sent by PCO (Speed Controller) i.e. $P_{m,ref}$ is 1 p.u. In addition, the output signal of temperature controller is independent of base- or partial-load of CCGT which is 1 p.u. In response to falling frequency, the PCO increases $P_{m,ref}$ to compensate the loss of power generation and avoid further dropping down of frequency. In contrast, the temperature controller reduces 'Temp_Con_Out' in order to decrease temperature. As a result, the min block selects the second signal as the input to the gas fuel controller and thus, the power output of CCGT is unexpectedly decreased due to the fuel reduction and remains below rated one as long as the frequency is less than nominal one [13].

When operating at partial load, the fuel flow and IGV value are less than 1 p.u and similar to the base load case, once the system frequency falls very fast, the compressor speed and consequently airflow into the combustion chamber are reduced (See Figure 3-22). Accordingly, this causes an increase in the fuel-to-air ratio (See Figure 3-23), which directly increases the exhaust temperature (Figure 3-24). In contrast to full-load scenario, the output signal of speed controller i.e. $P_{m,ref}$ is less than 1 p.u (See Figure 3-27). As a result, this controller responds within a very short time to falling frequency and results in more fuel to be injected into the combustor and to increase the power output of CCGT. This can increase significantly the exhaust temperature as shown in Figure 3-24. In other hand, the IGV signal is gone up based on simultaneous increment of gas fuel and exhaust temperature in order to control the fuel-to-air ratio as shown in Figure 3-23. As can be seen from Figure 3-27, the output signal of temperature controller i.e. 'Temp_Con_Out' becomes less than 1 p.u. Therefore, the fuel valve is controlled by this signal from 5.5 s and the increased value of exhaust temperature is reduced back to the nominal one as shown in Figure 3-24. Finally, since the IGV is less than 1 p.u., the fuel flow can be increased based on an IGV increment and fuel-to-air ratio. This can increase the CCGT output power as depicted in Figure 3-19. Thus, the frequency Nadir and its steady-state value of partial load scenario are less than full load ones (See Figure 3-16).

What should be underscored is that ST power output variation is pretty slower than GT power output following the abrupt frequency change. This can be found from Figure 3-18 and Figure 3-19.

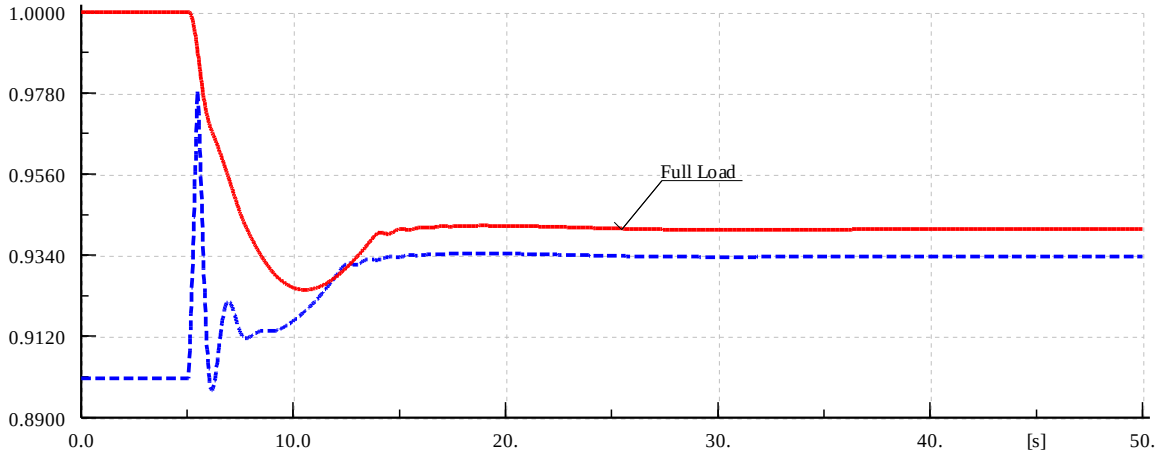

Figure 3-20: Fuel valve position of CCGT power plant: full load (solid) and partial load (dashed) scenarios.

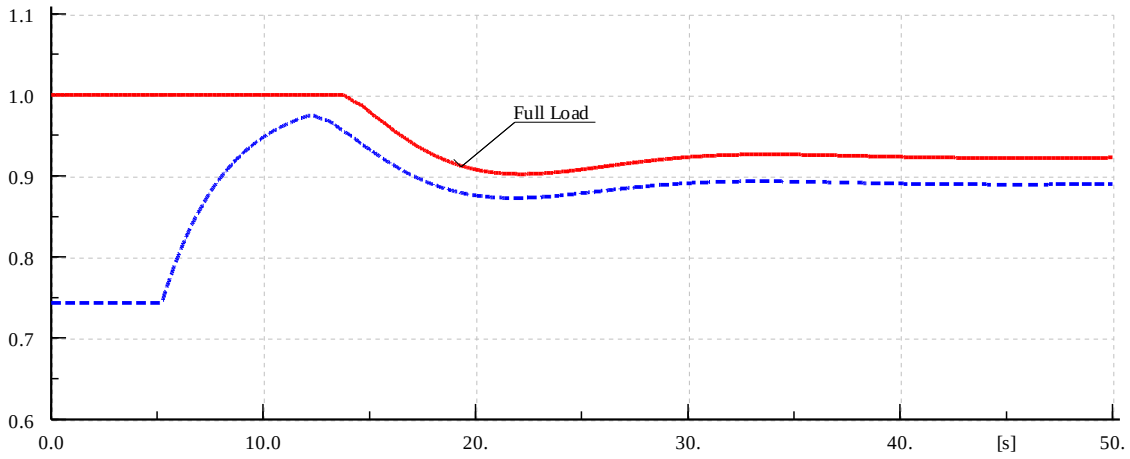

Figure 3-21: IGV value of CCGT power plant: full load (solid) and partial load (dashed) scenarios.

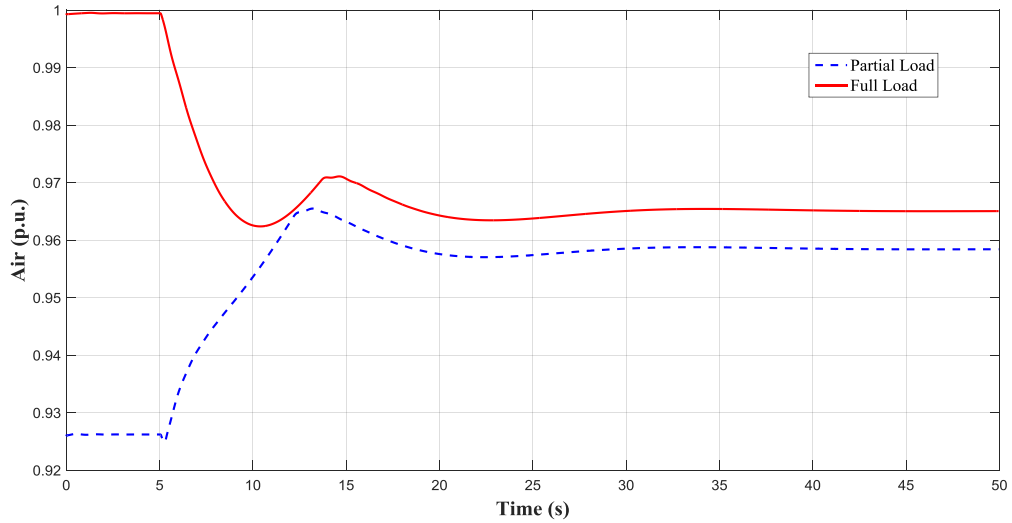

Figure 3-22: Air flow of CCGT power plant: full load (solid) and partial load (dashed) scenarios.

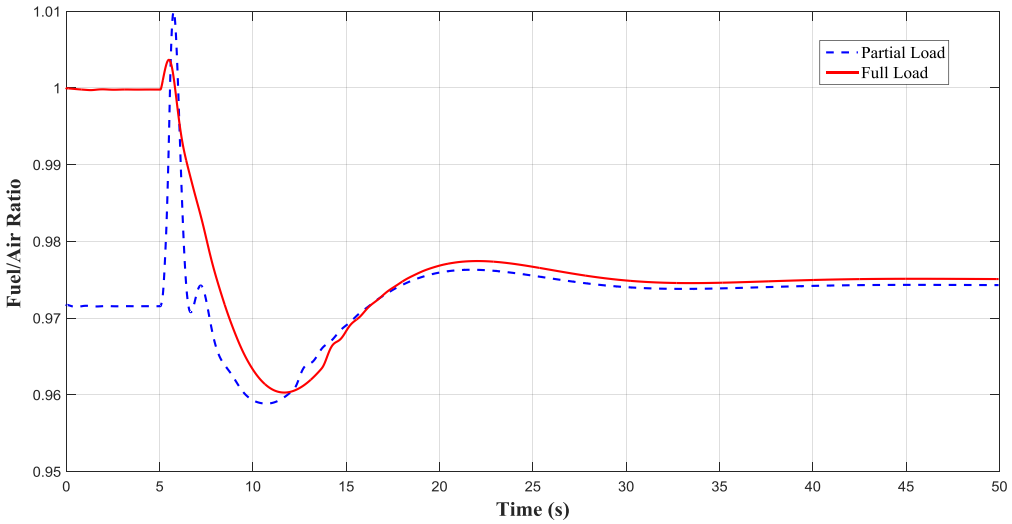

Figure 3-23: Fuel-to-Air Ratio of CCGT power plant: full load (solid) and partial load (dashed) scenarios.

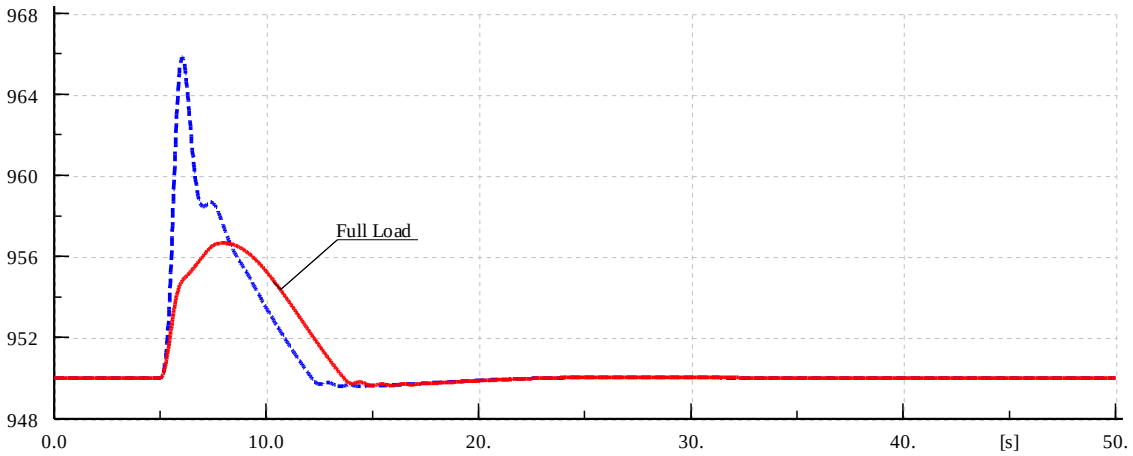

Figure 3-24: Exhaust temperature of CCGT power plant: full load (solid) and partial load (dashed) scenarios.

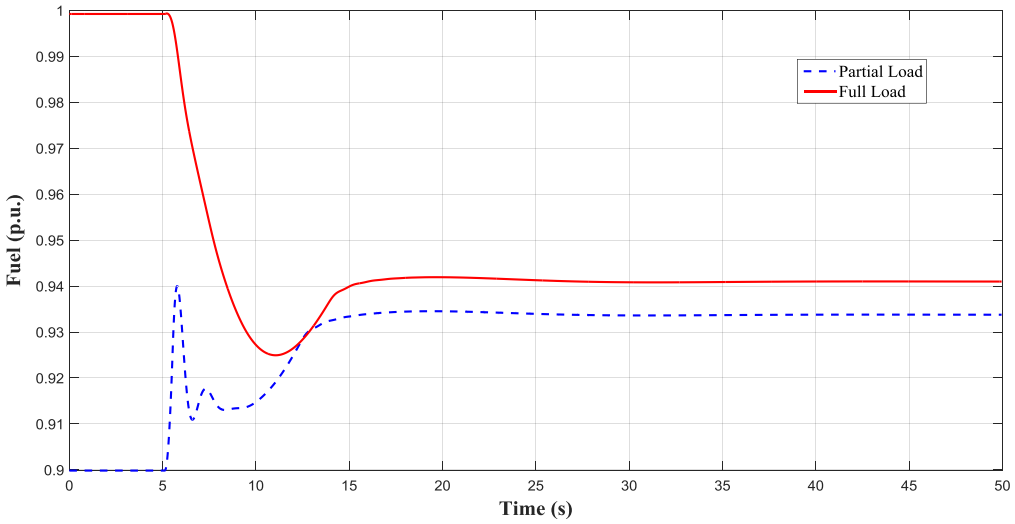

Figure 3-25: Fuel flow of CCGT power plant: full load (solid) and partial load (dashed) scenarios.

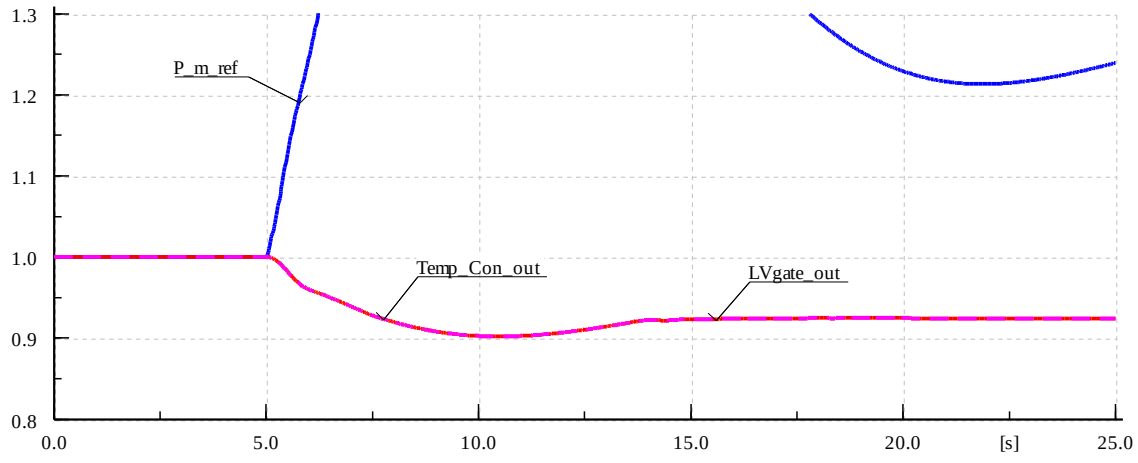

Figure 3-26: LVgate signals of CCGT power plant at full load scenario.

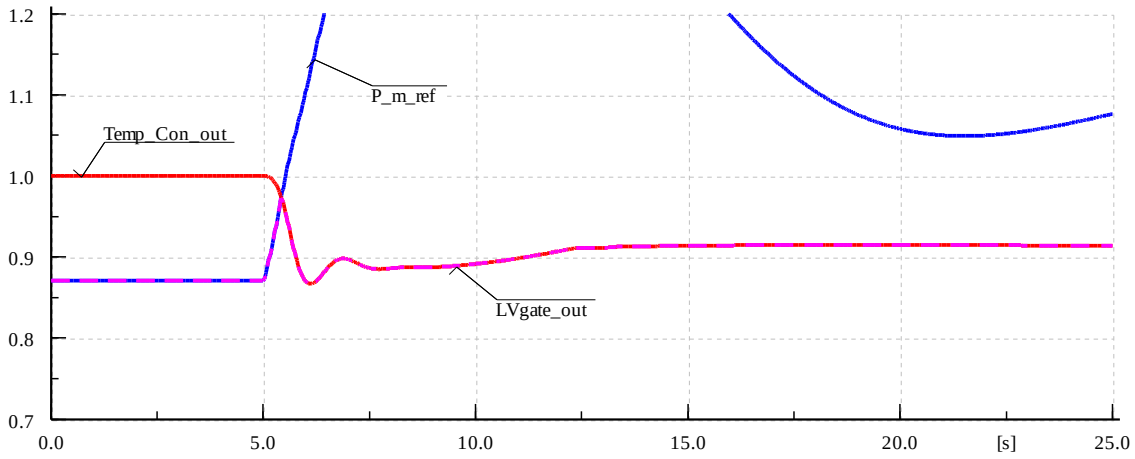

Figure 3-27: LVgate signals of CCGT power plant at partial load scenario.

3.6 Integration of CCGT unit in 2-Area Klein-Rogers-Kundur (KRK) Test System

The CCGT unit is integrated into two-area Klein-Rogers-Kundur (KRK) test system and its influence on network frequency is investigated using modal and time domain analysis. To do this, 2-area test system is changed as shown in Figure 3-28. This is exactly the two-area KRK test system so that each generator is equivalently split into 4 similar generators. Therefore, this test system is converted to 4-area test network. All generating units except 44 are cylindrical wounded rotor and power plant 44 is salient pole rotor. Data of this test system is detailed in Table 3-2.

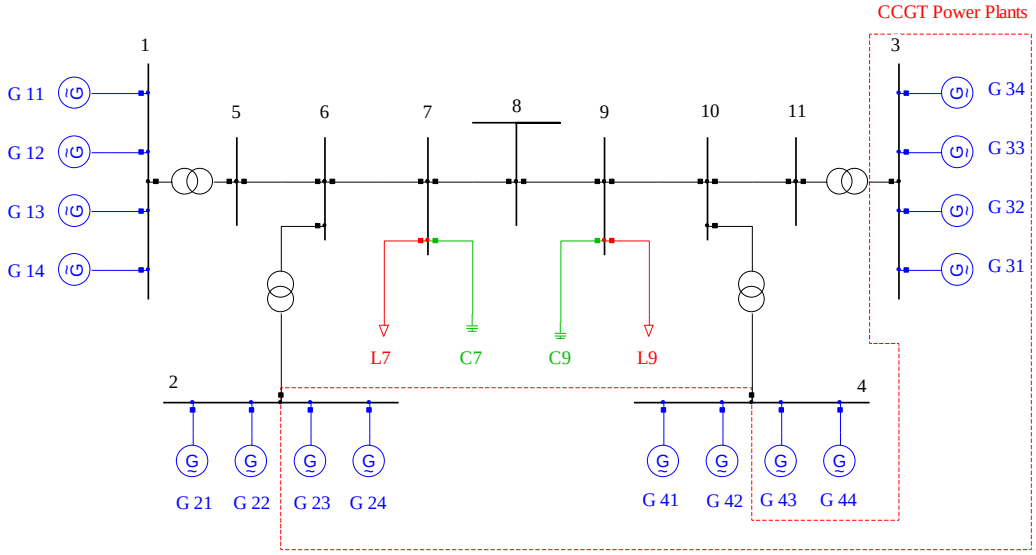

Figure 3-28: Single line diagram of studied four-area network (based on two-area KRK system).

Table 3-2: Generator data

Unit	Nominal apparent power (MVA)	Nominal power factor	H (s)
G11:G24	225	0.8	6.5
G31:G43	225	0.8	6.175
G44	225	0.8	7.5

All the units except 44 are supposed to have reheat steam turbine (RST). The PMU and PCO of these units are shown in Figure 3-29 and Figure 3-30, respectively. The unit numbered 44 is hydro-turbine power plant.

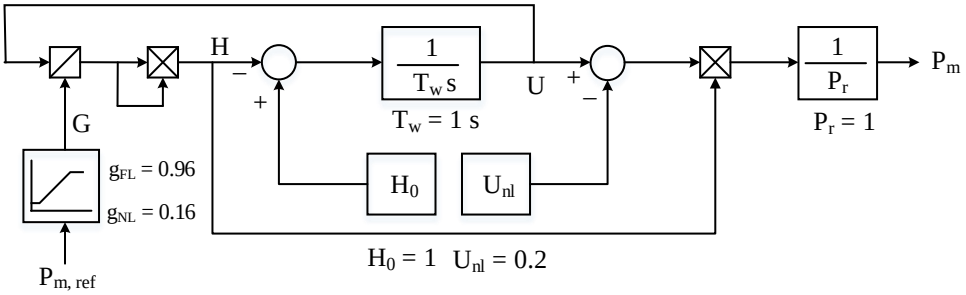

Figure 3-29: Block diagram of hydro turbine prime mover unit (PMU).

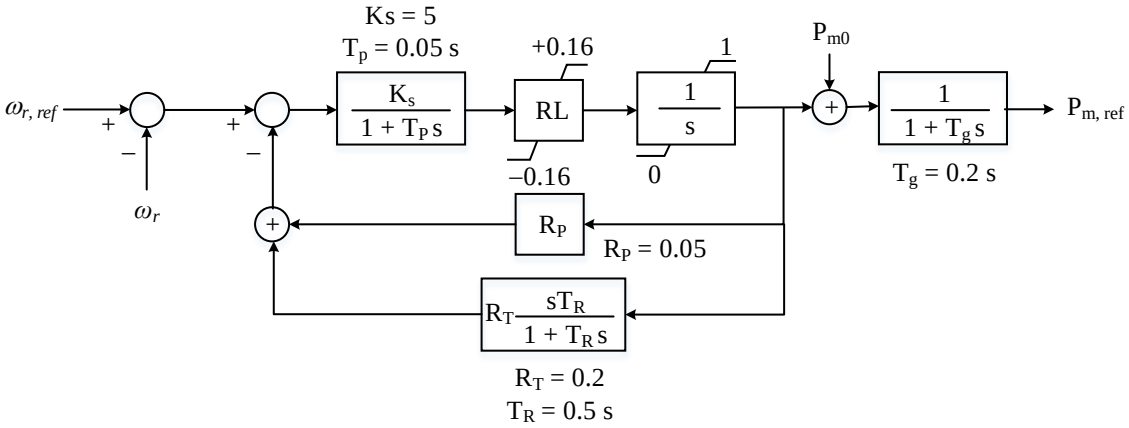

Figure 3-30: Block diagram of hydro turbine primary controller (PCO).

The exciter system of all units is static in which Ka is set to 200. All generating units are equipped with the PSS.

In order to evaluate the effects of CCGT, 4 different scenarios are defined hereinafter:

- All generating units except 44 are RST for the first two scenarios 1 and 2.
- 6 generating units are substituted with CCGT units for scenarios 3 and 4 as shown in Figure 3-28. They generate 90% and 100% of their nominal active power in partial- and full-load operation modes. The rest produce their nominal active power.

The operational information related to the above scenarios is tabulated in Figure 3-28.

Table 3-3: Operational data of four scenarios.

No.	Scenario	Active power loading of G23, G24, G31:G34, G41, G42 (%)	Act. Power of L7 (MW)	Act. Power of L9 (MW)
01	RST Partial Load	90	950	1700
02	RST Full Load	100	1100	1700
03	CCGT Partial Load	90	950	1700
04	CCGT Full Load	100	1100	1700

3.7 Modal Analysis of 2-Area Network Considering CCGT Integration

In power system networks, the small signal stability problems may be either local or global which are pertinent to the local and inter-area modes' locations of the system. The local problems involve a small portion of the system and they may be associated with rotor angle oscillation of a generator in an area against others. The global small-signal stability problems are caused by interactions of a group of generators in one area swing against a group in other area. To identify the local and inter-area modes of the two area test system depicted in Figure 3-28, the electromechanical modes (angle and speed of rotor) of first scenario with frequencies in the range of 0 and 2 Hz are shown in Figure 3-31 using modal analysis. The network has three inter-area modes and 5 batches of local area modes. Generally, the frequencies of inter-area modes are less than local ones. The expression 1-2 shows the inert-area modes associated to 4 generators located in area one opposed to all 4 units in area 2. Furthermore, the expression of 21:4 illustrates represents the local mode associated to area 2. It is to be noticed that three modes of this network are equivalent to local area and inter-area modes of original 2-area KRK test system. For instance, two inter-area modes of two areas place in left hand side of this figure are equivalent to local modes of original two-area system. Two sets of local modes located in right hand side of modal graph are pertinent to area 4. Unlike local modes of areas 1 to 3, the local modes of fourth area are depicted with 2 groups associated with different values of damping. This is due to the fact that there is a hydro-turbine unit in this region.

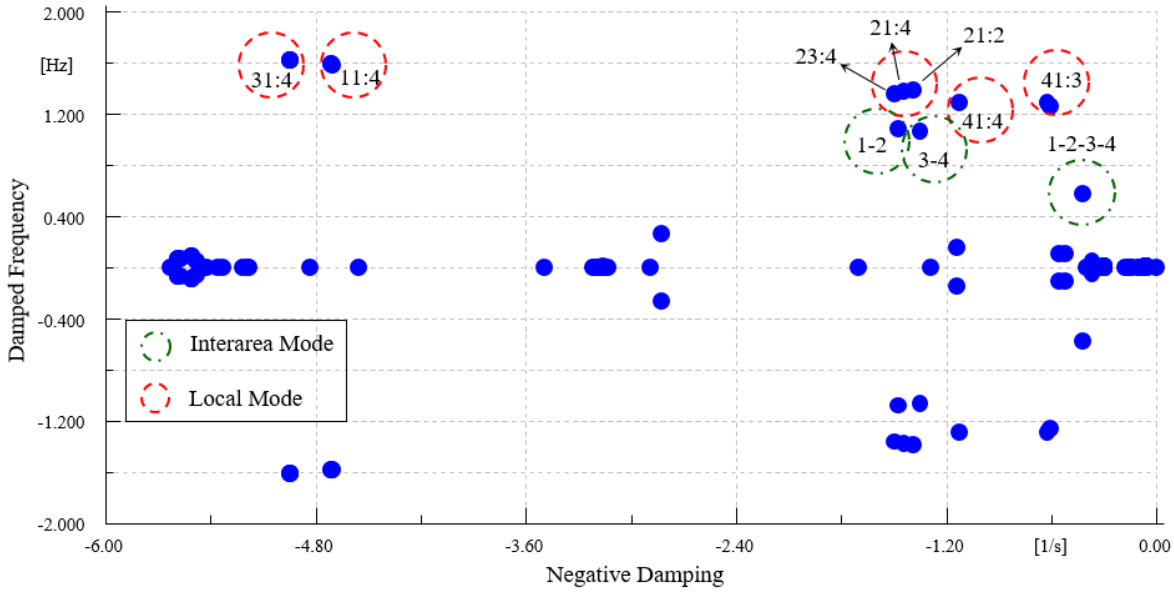

Figure 3-31: Electromechanical modes of four-area network at RST partial load scenario.

The electromechanical modes related to four discrepant scenarios are portrayed in Figure 3-32. The electromechanical modes locations for these four scenarios are almost similar since only their loadings and the dynamic types of units are different.

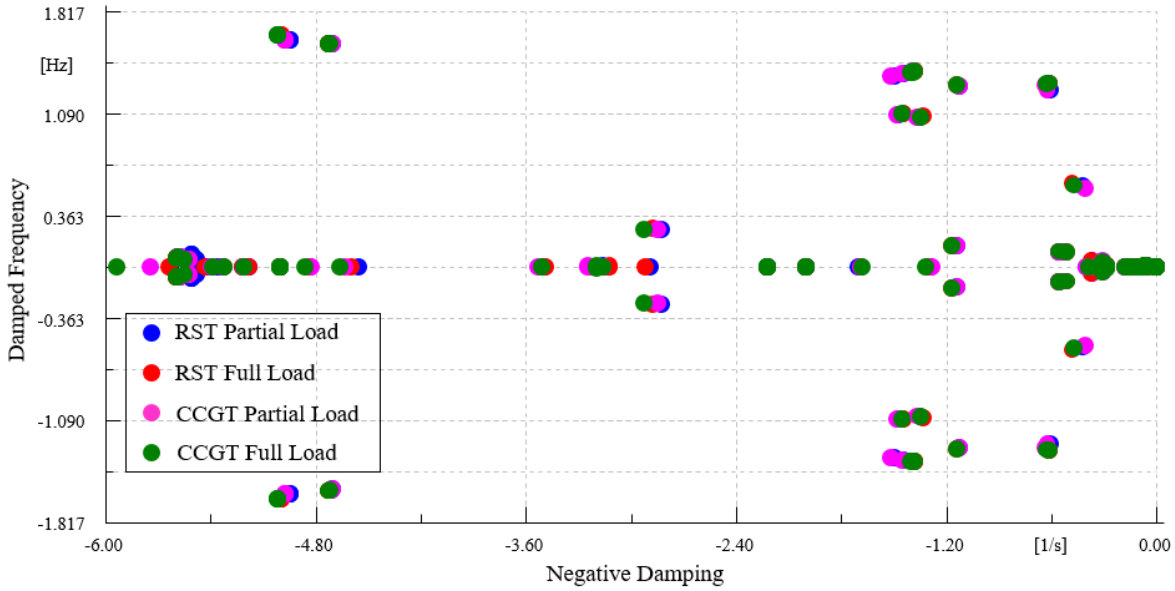

Figure 3-32: Electromechanical modes of four-area network at all scenarios.

To precisely evaluate the electromechanical modes of these scenarios, the slowest mode are shown in Figure 3-33. It is observable that loading increment of generating units leads to damping growth. In other hand, converting 6 units from RTS into CCGT can reduce the electromechanical damping value.

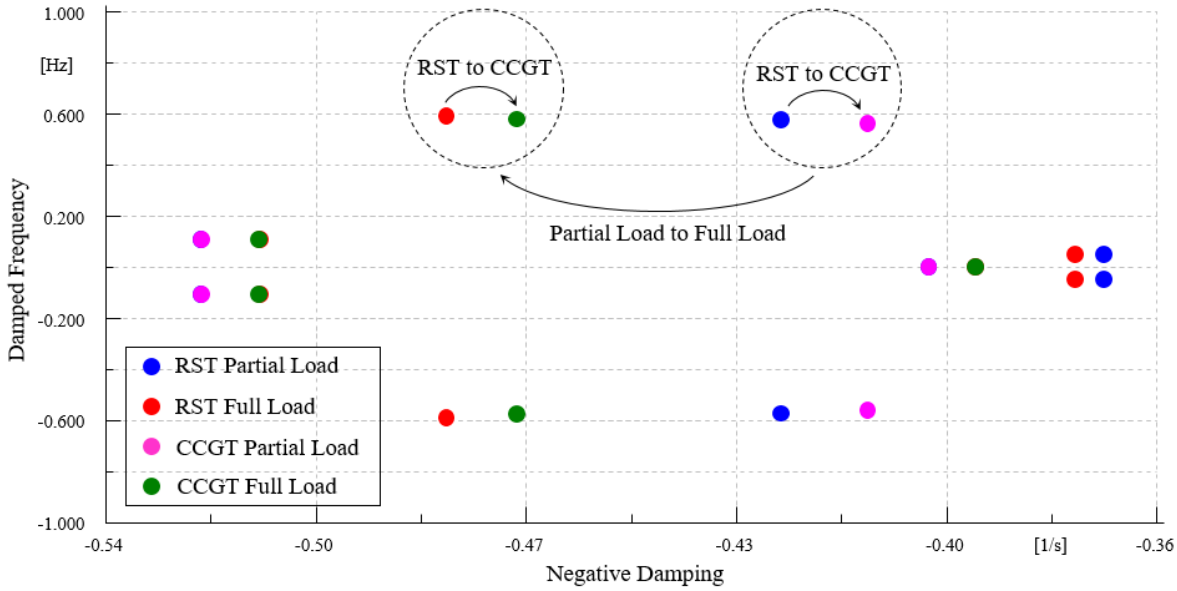

Figure 3-33: Slowest electromechanical mode of four-area network at all scenarios.

3.8 Time-Domain Analysis of 2-Area Network Considering CCGT Integration

In this case study, it is assumed that generator 21 is disconnected from network at time 2.5 *s*. It is worth mentioning that only the PSS of G1 and G3 are activated. The loss of generation in two operation modes of full- and partial-load is equal to 180 MW. However, the generation lost amounts are 6.6% and 6.25% of the whole

network generation for full- and partial-load modes since the load demands of these two operation modes are different. It is worth mentioning that the droop values of all PCO are set to 0.05. Figure 3-34 to Figure 3-38 illustrate different results following the disturbance of generation trip. The COI frequencies related to above mentioned 4 scenarios are plotted in Figure 3-34. The full-load RST and full-load CCGT scenarios have the maximum and minimum steady-state frequency deviation, respectively. The main reason that this value for full-load RST scenario is less than partial-load RST is the lower amount of loss of generation percentage in first scenario opposed to second one. Albeit the frequency deviation in partial-load CCGT is almost identical to two scenarios of RST, the frequency deviation in full-load CCGT scenario has a huge difference with other three scenarios so that it is far less than them.

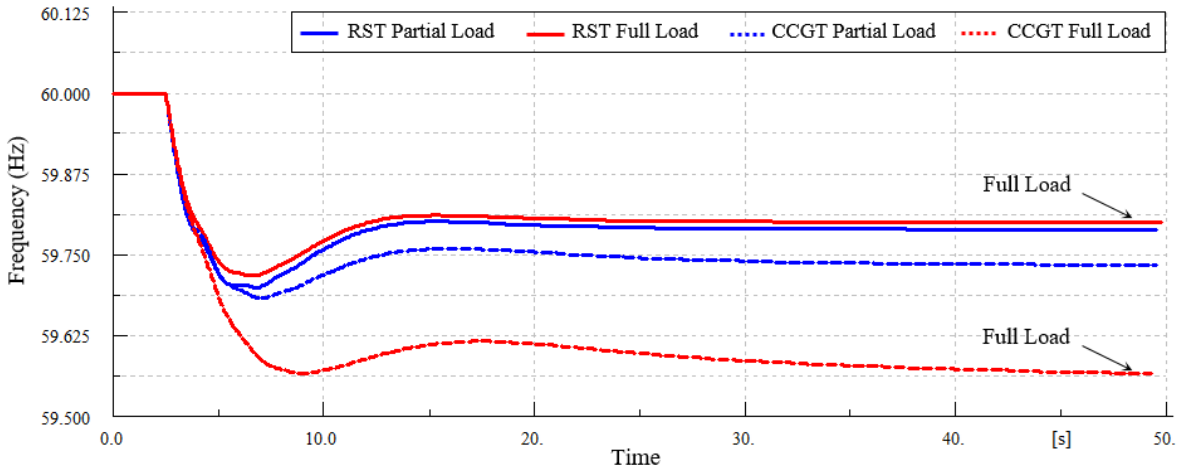

Figure 3-34: COI frequency of four-area network at all scenarios.

The RoCoF change related to these four scenarios are shown in Figure 3-35. It is clear-cut that its amount is similar in all four scenarios in first 0.5 s following the incident. This is because the inertia constants of generating units have the same values in all scenarios.

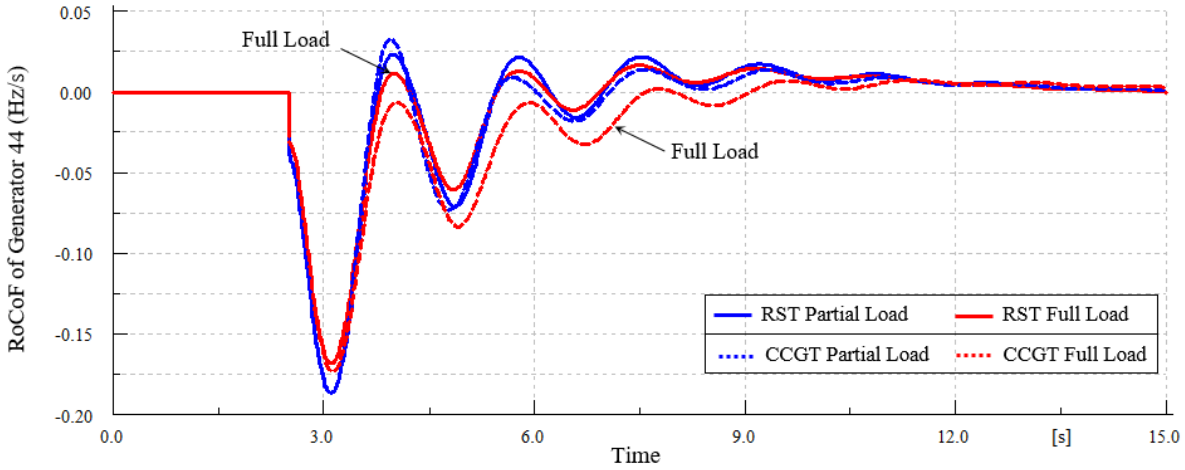

Figure 3-35: RoCoF of Generator 44 at all scenarios.

The turbine power changes of units 12 and 44 related to these four scenarios are plotted in Figure 3-36 and Figure 3-37, respectively. Their extra generations in partial- and full-load operation modes of RST scenarios are approximately similar. However, these units generate more power in other two scenarios. The amount of this variation in full-load CCGT scenario is significantly higher than the rests.

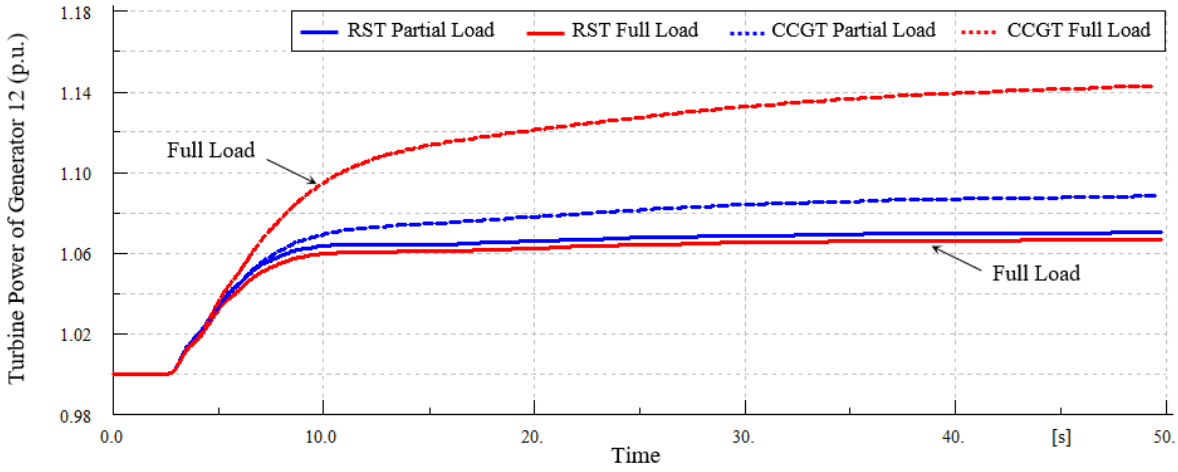

Figure 3-36: Turbine power of Generator 12 at all scenarios.

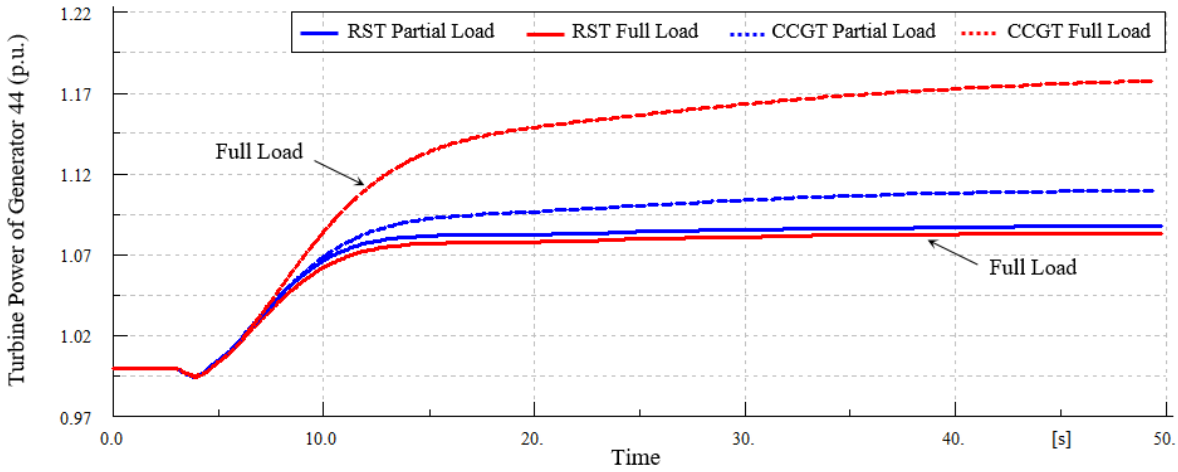

Figure 3-37: Turbine power of Generator 44 at all scenarios.

The output power changes of unit 31 associated with four scenarios is shown in Figure 3-38. The output power of this power plant in two scenarios of full- and partial-load RST following the in-feed is increased. Furthermore, this quantity is grown in partial-load CCGT scenario. However, this increment is less than two scenarios of RST. It can be observed that the output power of this unit in full-load operation mode of CCGT scenario is dropped down. This lack of generation for supporting frequency control leads to power increment of others. This will considerably mitigate frequency nadir and steady-ate value of frequency in full-load CCGT scenario with respect to others.

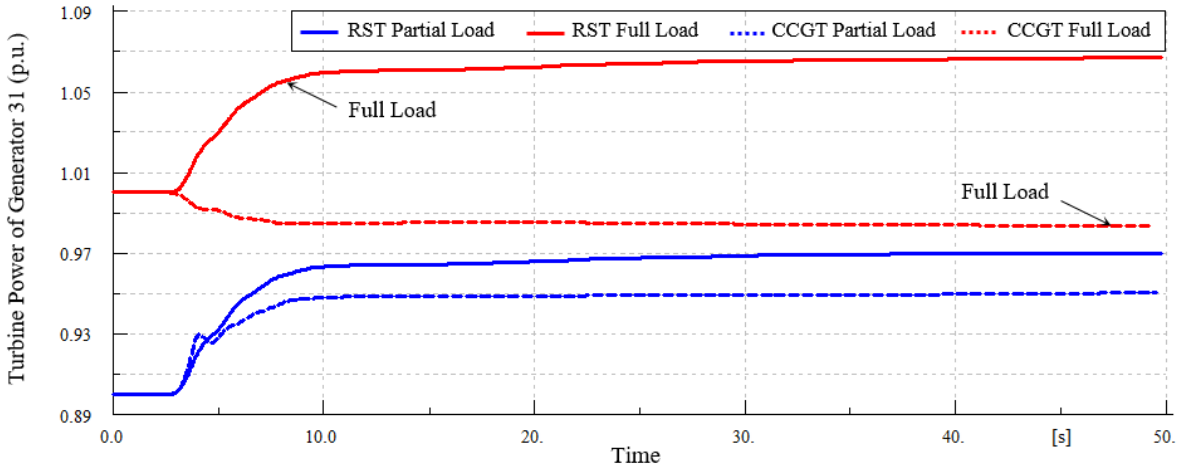

Figure 3-38: Turbine power of Generator 31 at all scenarios.

3.9 Executive summary of deploying CCGT in two-area System

The dynamics of power system frequency are studied in this project study. A valid dynamic model of a CCGT is developed in DIgSILENT PowerFactory that incorporates three controllers of IGV, temperature and fuel flow as well as a mechanism for varying the frequency dependency of the GT. The dynamic performance of CCGT in two modes of full- and partial-load is validated using a simple test network and 2-area KRK power system. Although the RoCoF of the whole system is identical in these two scenarios, the frequency nadir and steady state frequency of CCGT in full load are less than partial-load mode. This CCGT model is incorporated to the two-area KRK network in order to study the influence of high penetration CCGTs on frequency control following the loss of generation. The appropriate dynamic models of exciter system, thermal and hydroelectric units and SVCs for the purpose of frequency control dynamic studies are selected. After which, the modal analysis is selected to provide the small signal results. It is clear-cut that the change of turbine dynamic form GT to CCGT does not have considerable effect on electromechanical modes. However, converting the GT units to CCGTs can increase the damping of the electromechanical modes. Furthermore, time domain simulation studies are deployed to investigate the dynamic response of the network in four different scenarios of full-load RST, partial-load RST, full-load CCGT and partial-load CCGT following the loss of SGs. In the time-domain studies, the condition of different areas from the viewpoint of frequency Nadir, RoCoF, and power output of different generating units is examined. As large scale CCGTs substitute with current conventional power plant in future, frequency control might become more challenging. The results depict that with supplementary CCGTs on the power system, large frequency decay in Nadir and steady state conditions will be more probable, and the system operators need to review their frequency control approaches in future to prevent enormous load shedding.

3.10 Modal Analysis of 36-Zone GB Network Considering CCGT Integration

The power grid under the study consists of 41 power plants. The SGs of 4 hydro-turbines are salient pole rotor and other 37 SGs are wounded rotor. As a result, the system includes 242 state variables which are equal to the number of eigenvalues. It is noteworthy that eigenvalues related to the rotor speed and angle is complex with pretty lower damping as compared to eigenvalues of rotor damping windings. These eigenvalues which are so important in modal analysis are called electromechanical modes. In this network, there are 41 SGs with two mechanical modes. Consequently, the electromechanical modes of the system are 82. Furthermore, their number will be decreased to 80 with removing two modes of slack SG i.e. nuclear unit in zone 1.

The 36-zone GB network has 22 GTs, which generate their nominal power. Some of these generating units can be substituted with the CCGT power plants. The results illustrated in previous scenario indicate that the power output of CCGT decreases following the sudden change of frequency, while it generates rated power. Therefore, the worst case is to increase the penetration of CCGTs in the network. In this regard, two different operating scenarios have been examined in this chapter, those are: i) none of the GT power plants is replaced with CCGT; and ii) All the 22 GTs are replaced with CCGTs. The influence of replacing all 22 GTs with CCGTs on damping ratio and frequency of GB network is shown in Figure 3-39. It is clear-cut that the change of turbine dynamic form (GT) to CCGT does not have considerable effect on electromechanical modes. However, converting the GT units to CCGTs can increase the damping of the electromechanical modes. This can be clearly inferred form Figure 3-40.

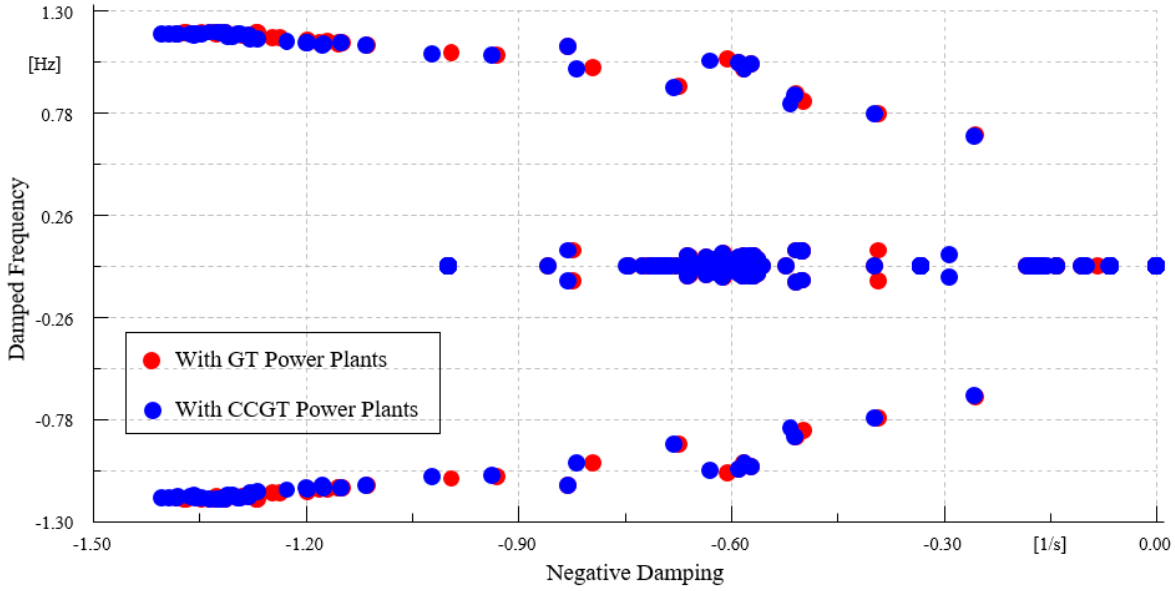

Figure 3-39: Effect of CCGT power plants in electromechanical modes.

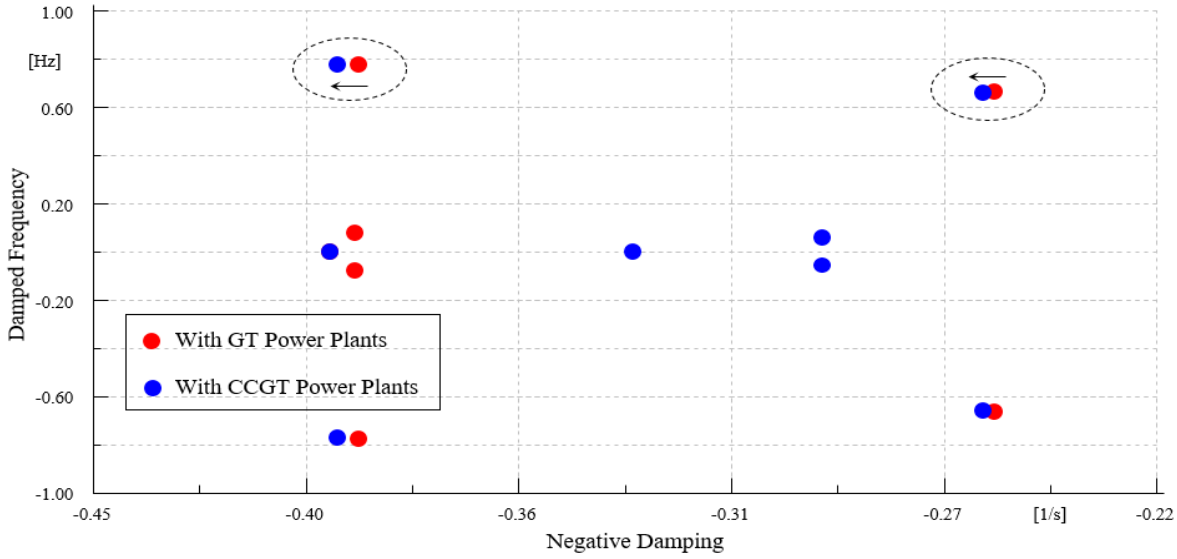

Figure 3-40: Effect of CCGT power plants in two slowest electromechanical modes.

3.11 Time Domain Analysis of 36-Zone GB Network Considering CCGT Integration

In this subsection, the time domain simulation results for network primary frequency control are provided to confirm the modal analysis outputs and to consider special dynamic behaviour of full loaded CCGT power plants following the generation disconnection events. The aforementioned two scenarios of 36-zone GB with 100% penetration of GT power plants and 36-zone GB with 100% integration of CCGTs are deployed. In the first scenario, the PMUs of all GTs are of the ordinary thermal prime mover types. In the second scenario, it is presumed that all the CCGTs utilises the same PMUs. To do this, 6 candidate power plants from different zones of the network are chosen as the tripped ones and the dynamic performance of the network is investigated for an interval of 75 s after the loss of each of them, as shown in Figure 3-41. The capacity of these generating units change from 600 MW to 3900 MW which are equivalent to about 1.5% to 10% of total demand of the network. In the following results, the centre of inertia (COI) frequency is illustrated beside the SGs' frequencies based on the following relation:

$$\omega_{COI} = \frac{\sum_{i=1}^{N} H_i S_i \omega_i}{\sum_{i=1}^{N} H_i S_i} \tag{3.1}$$

Where, H_i, S_i and ω_i are the inertia, apparent power and frequency of the ith SG, respectively.

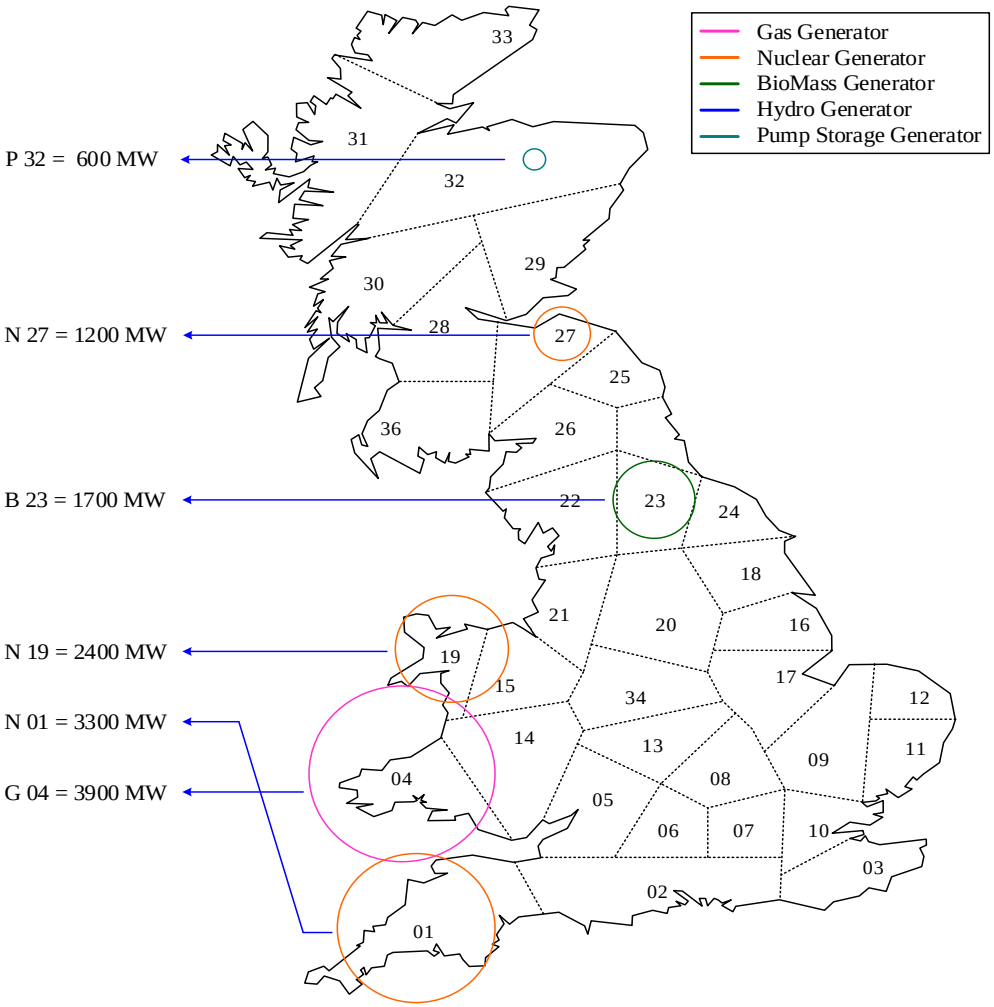

Figure 3-41: Geographic distribution of selected loss of generation.

3.11.1 Loss of 1,700 MW Generation in Zone 23

In this event, the biomass of zone 23 with the capacity of 1,700 MW is disconnected. The frequencies of GT in zone 23, nuclear in zone 1, GT in zone 35 and hydroelectric in zone 32 are shown in Figure 3-42 and Figure 3-43 for the abovementioned two scenarios. Furthermore, their RoCoFs are plotted in Figure 3-44. Also, turbine output powers of the mentioned power plants are shown in Figure 3-45. The deviations in mechanical power of turbines after event are depicted in Figure 3-46 by three traces for each scenario.

It can be seen that the frequency nadir and steady-state value of frequency in second scenario is lower than first one. The maximum amount of RoCoF i.e. 0.5 Hz/s is corresponded to the GT of zone 23 which is quite near to the event.

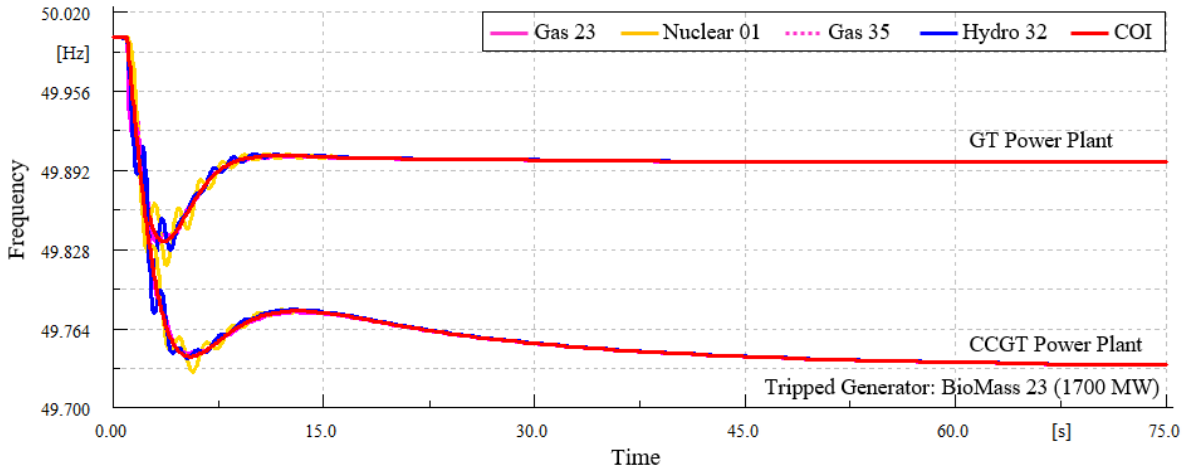

Figure 3-42: Frequency response with loss of 1700 MW generation in middle of network.

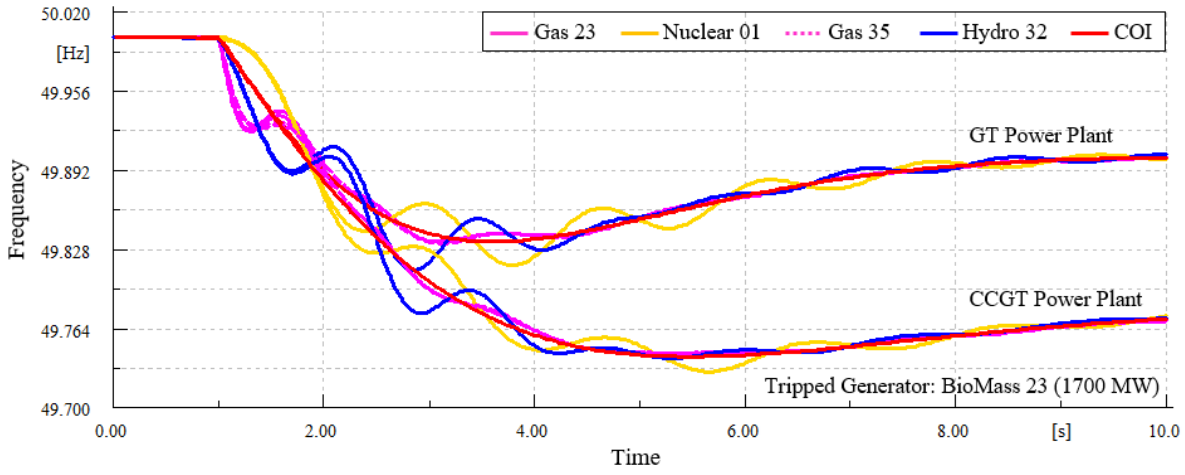

Figure 3-43: Frequency oscillations with loss of 1700 MW generation in middle of network.

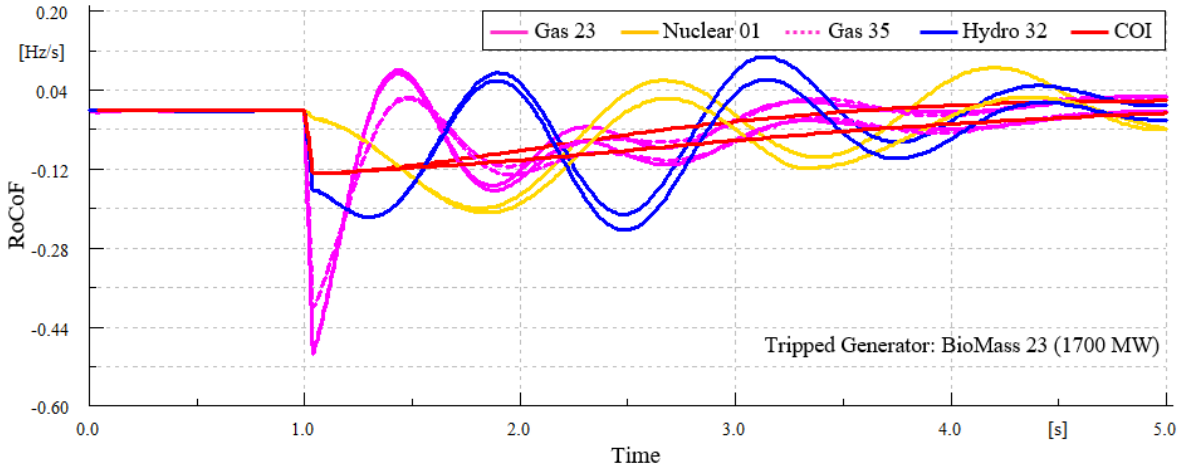

Figure 3-44: RoCoF deviations with loss of 1700 MW generation in middle of network.

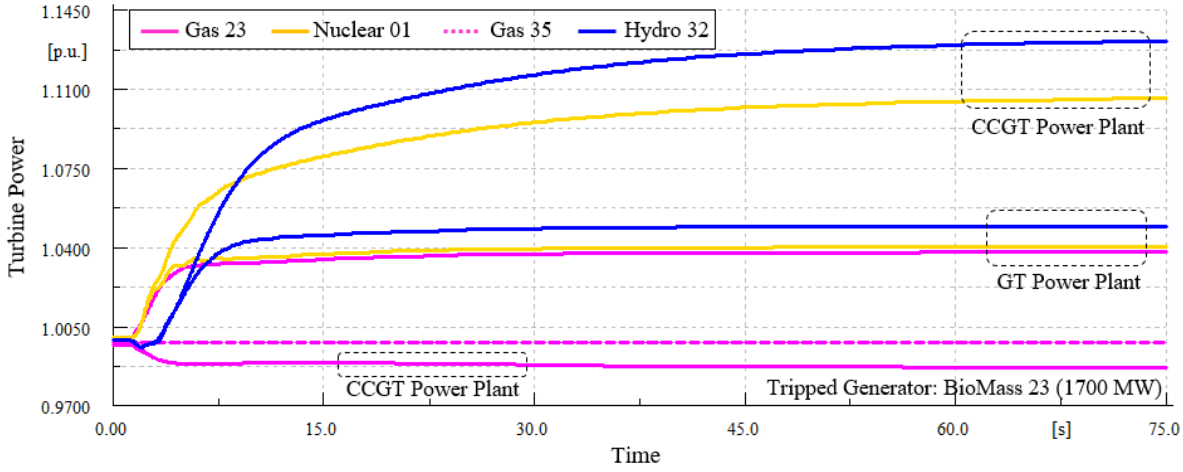

Figure 3-45: Turbine power changes with loss of 1700 MW generation in middle of network.

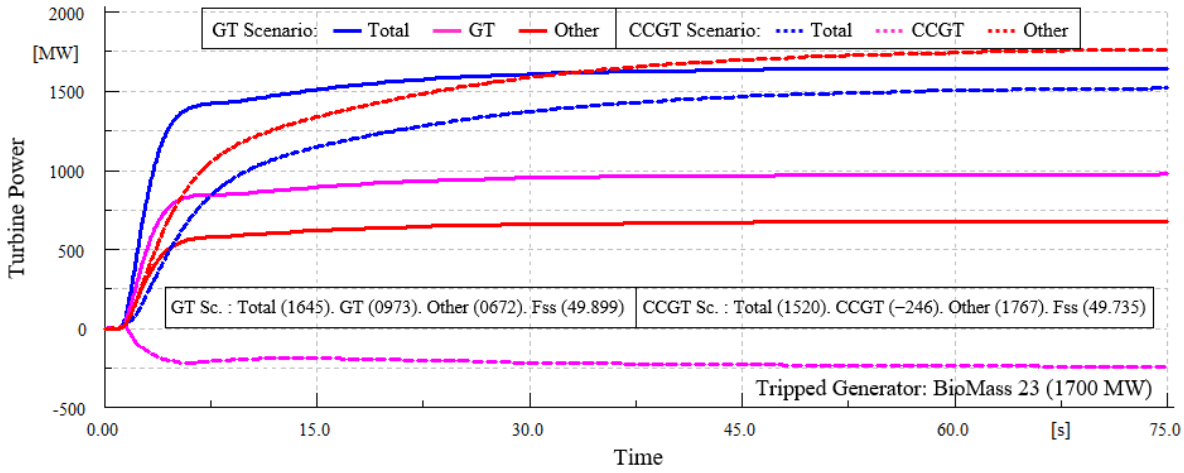

Figure 3-46: Turbine power deviations with loss of 1700 MW generation in middle of network.

3.11.2 Loss of 3,300 MW Generation in Zone 1

In this event, the nuclear unit of zone 1 with the capacity of 3,300 MW is disconnected. The frequencies of GT in zone 1, biomass in zone 10, GT in zone 27 and hydroelectric in zone 32 are shown in Figure 3-47 and Figure 3-48 for the abovementioned two scenarios. Furthermore, their RoCoFs are plotted in Figure 3-49. Also, turbine output powers of the mentioned power plants are shown in Figure 3-50. The deviations in mechanical power of turbines after event are depicted in Figure 3-51 by three traces for each scenario.

It can be seen that the frequency nadir and steady-state value of frequency in second scenario is lower than first one. The maximum amount of RoCoF i.e. 4.2 Hz/s is corresponded to the GT of zone 19 which is quite near to the event.

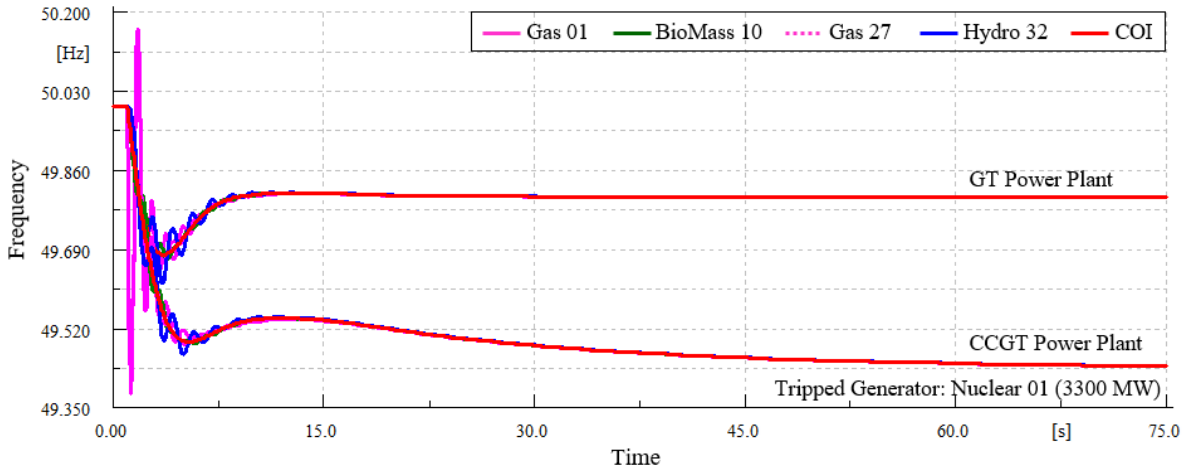

Figure 3-47: Frequency response with loss of 3300 MW generation in left bottom of network.

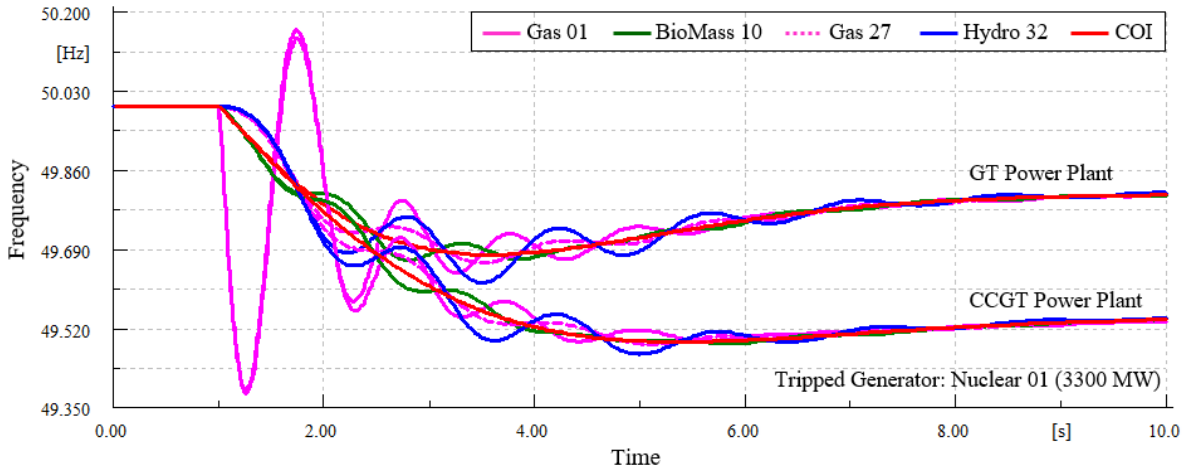

Figure 3-48: Frequency oscillations with loss of 3300 MW generation in left bottom of network.

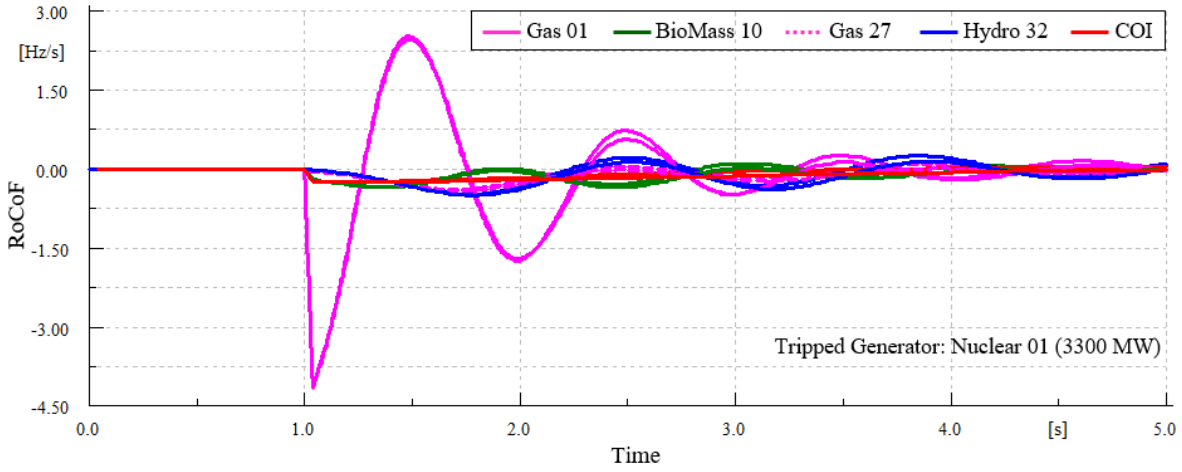

Figure 3-49: RoCoF deviations with loss of 3300 MW generation in left bottom of network.

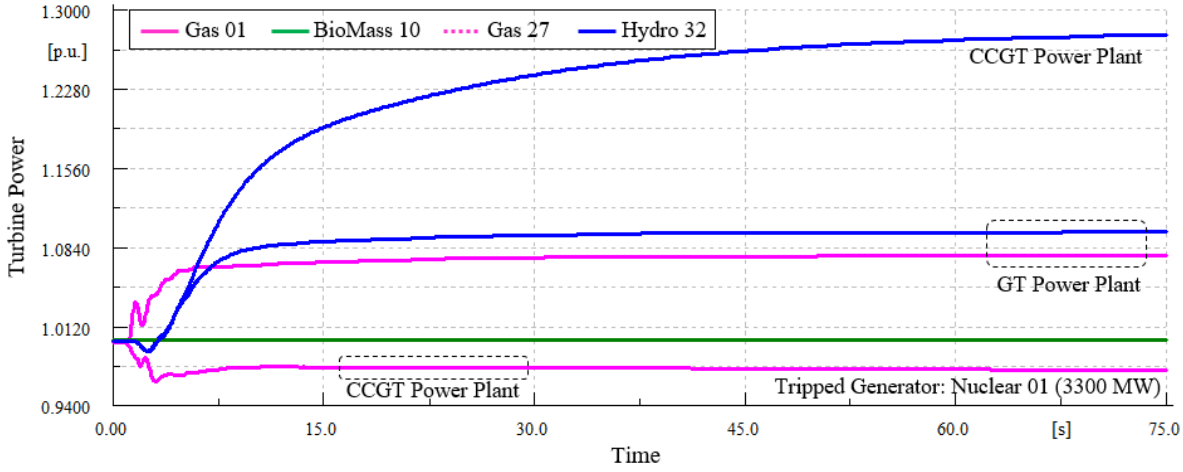

Figure 3-50: Turbine power changes with loss of 3300 MW generation in left bottom of network.

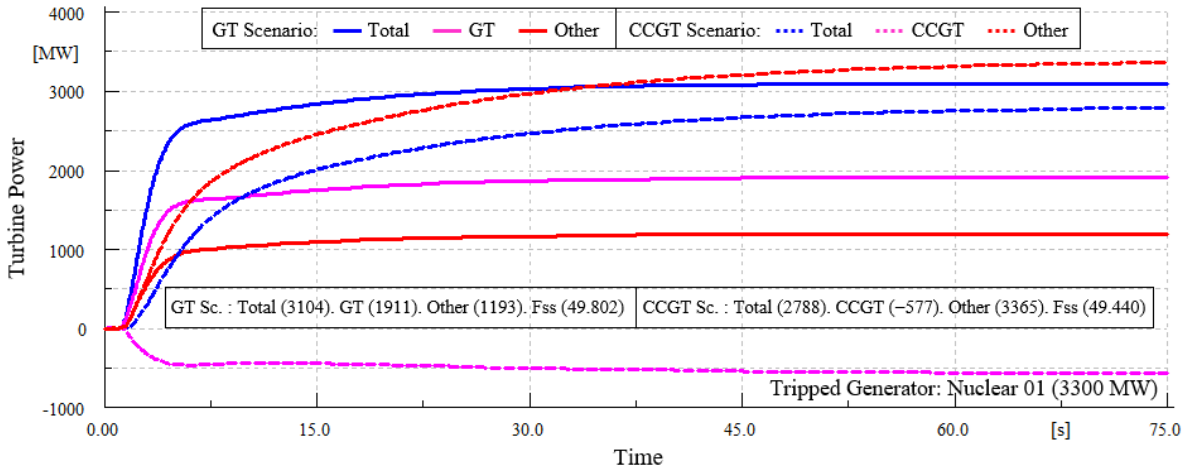

Figure 3-51: Turbine power deviations with loss of 3300 MW generation in left bottom of network.

3.12 Worse Case Time Domain Analysis for 36-Zone GB Network Considering CCGT Integration

In previous subsection, the frequency response performance of the grid in case of disconnecting all the power plants is explored for most 6 critical and susceptible areas and the maximum value of frequency Nadir and RoCoF are measured and portrayed in bar diagrams for two different scenarios of CCGT and GT. Whereas these 6 candidate SGs could show the most critical frequency scenarios of the grid, it can't be said that they are the worse frequency cases since other 35 out of 41 SGs weren't investigated. Furthermore, the simulation results provided aren't appropriate for finding the relationship of the measured parameters like maximum RoCoF and the disturbance size. To this end, the worse contingency in terms of frequency Nadir as well as maximum RoCoF for loss of 41 SGs are calculated and shown in Figure 3-52 and Figure 3-53. The horizontal axis shows the disconnected SGs with an ascending order from the smallest SG to biggest one. The amount of disturbance is mentioned in parenthesis. In these figures, each bar is pertinent to a power plant having the worse situations from the viewpoint of frequency Nadir and RoCoF once the SG specified in the vertical axis is disconnected. The value inside the parenthesis of the bar's label determines the power generated by the corresponding unit. As can be seen from Figure 3-52, the frequency Nadir is mitigated in proportion of disturbance size growth. However, this has some exceptions. In the other word, as can be seen the frequency Nadir is increased in proportion of disturbance size increment. However, this has some exceptions. This is case similar to the frequency Nadir discussion which its reason is high oscillation of some zones with respect to others. Another reason for these exceptions is the power network structure from the point of view of power plants locations. Form Figure 3-53, it can be deduced that maximum RoCoF in both scenarios CCGT and GT and in COI and unit cases are identical. The maximum RoCoF is related to the disconnection of nuclear power 19 in which the RoCoF of GT or CCGT located near to the incident in zone 19 has the highest value of RoCoF. This works for COI as well.

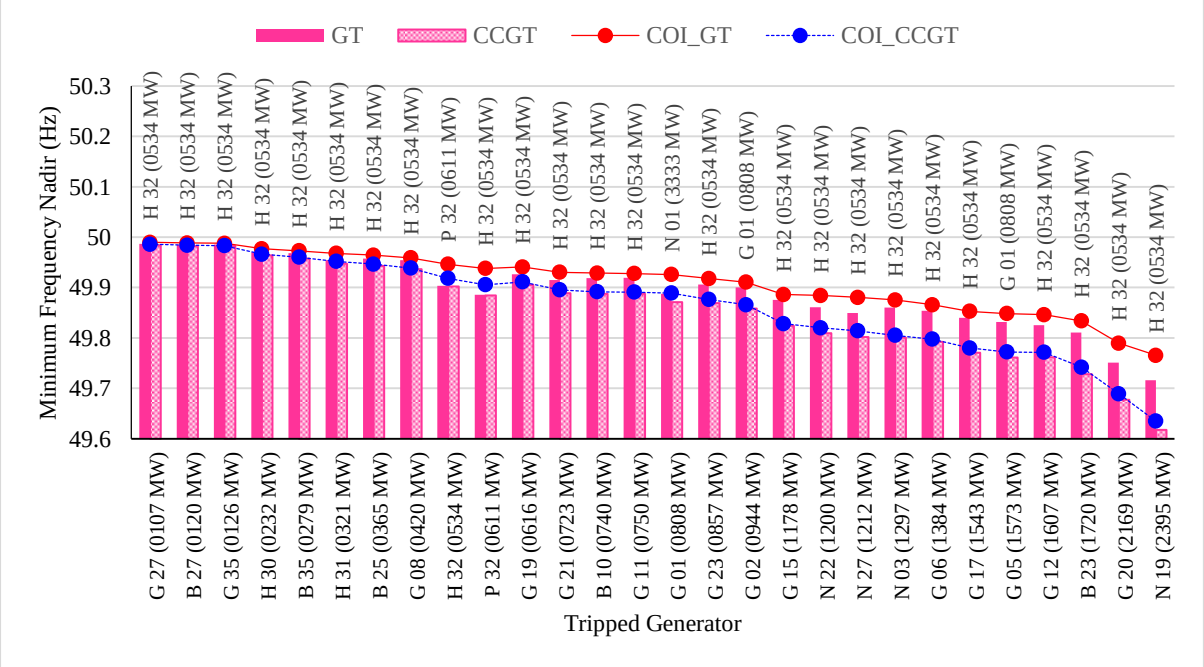

Figure 3-52: Minimum frequency Nadir of network with loss of generations from 100 MW to 2400 MW.

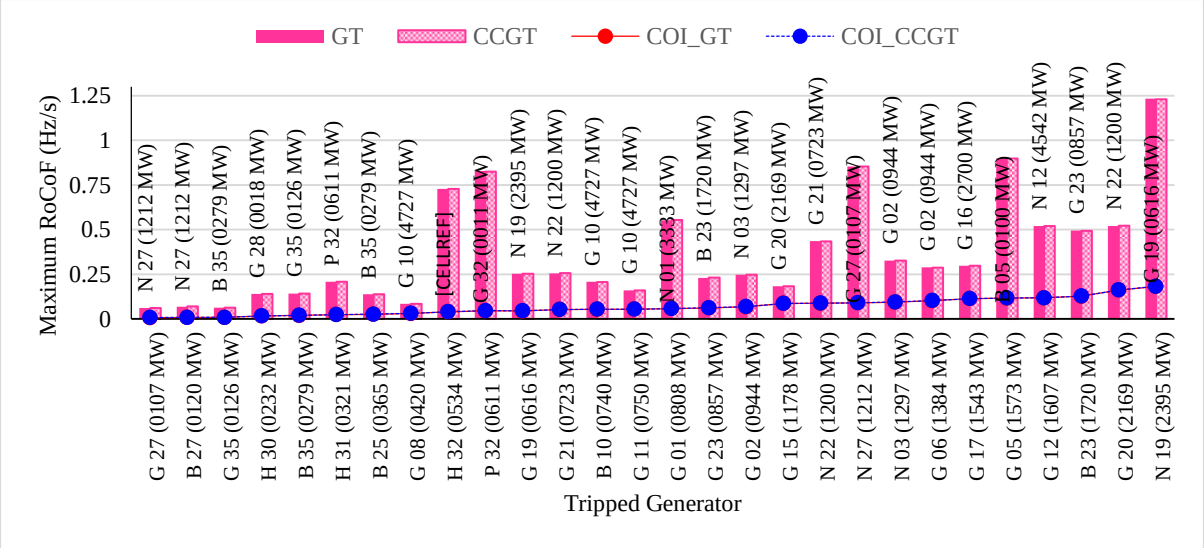

Figure 3-53: Maximum RoCoF of network with loss of generations from 100 MW to 2400 MW.

3.13 Executive Summary of Deploying CCGT in 36-Zone GB System

The dynamics of power system frequency are studied in this project study. A valid dynamic model of a CCGT is developed in DIgSILENT PowerFactory This CCGT model is incorporated to the 36-zone GB network in order to study the influence of high penetration CCGTs on frequency control following the loss of generation. It means that 22 GTs are substituted by 22 CCGTs and the simulation results are analysed for these two scenarios (i.e. CCGT and GT scenarios). The appropriate dynamic models of exciter system, thermal and hydroelectric units and SVCs for the purpose of frequency control dynamic studies are selected. After which, the modal analysis is selected to provide the small signal results. It is clear-cut that the change of turbine dynamic form GT to CCGT does not have considerable effect on electromechanical modes. However, converting the GT units to CCGTs can increase the damping of the electromechanical modes. Furthermore, time domain simulation studies are deployed to investigate the dynamic response of the network in two different scenarios of CCGT and GT following the loss of SGs. In the time-domain studies, the condition of different regions from the viewpoint of frequency Nadir and maximum RoCoF for all N-1 criteria is examined. The results of this phase determine the most critical zones. Additionally, the worst case time domain analysis is also deployed.

As large scale CCGTs substitute with current conventional power plant in future, frequency control might become more challenging. The results depict that with supplementary CCGTs on the power system, large frequency decay in Nadir and steady state conditions will be more probable, and the system operators of GB network need to review their frequency control approaches in future to prevent enormous load shedding.

3.14 References

[14] R. H. Park, “Two-reaction theory of synchronous machines, generalized method of analysis—Part I,” Trans. AIEE, vol. 48, no. 3, pp. 716-727, Jul. 1929.

[15] S. D. Pekarek, O. Wasynczuk and H. J. Hegner, “An efficient and accurate model for the simulation and analysis of synchronous machine/converter systems” IEEE Trans. Energy Convers., vol. 13, no. 1, pp. 42-48, Mar 1998.

[16] Kundur P. Power system stability and control. Balu NJ, Lauby MG, editors. New York: McGraw-hill; 1994 Jan 1.

[17] G. Lalor, J. Ritchie, D. Flynn, M. J. O'Malley, "The impact of combined-cycle gas turbine short-term dynamics on frequency control," IEEE Trans. Power Syst., vol. 20, no. 2, pp. 1456-1464, Aug. 2005.
[18] Rowen, W.I.: 'Simplified mathematical representations of heavy-duty gas turbines', J. Eng. Power, 1983, 105, (1), pp. 865–869.
[19] Kunitomi, K., Kurita, A., Okamoto, H., Tada, Y., Ihara, S., Pourbeik, P., Price, W.W., Leirbukt, A.B., Sanchez-Gasca, J.J.: 'Modeling frequency dependency of gas turbine output', In Proc: IEEE Power Eng. Soc. Winter Meeting, Columbus, USA, 2001.
[20] Kunitomi, K., Kurita, A., Tada, Y., Ihara, S., Price, W.W., Richardson, L.M., Smith, G.: 'Modeling combined-cycle power plant for simulation of frequency excursions', IEEE Trans. Power Syst., 2003, 18, (2), pp. 724- 729.
[21] CIGRE Task Force: 'Modeling of gas turbines and steam turbines in combined cycle power plants', 2003.
[22] Pourbeik, Pouyan. "Modeling of combined-cycle power plants for power system studies." IEEE Power Eng. Soc. General Meeting. Vol. 3. 2003.

4. New Wind Energy Conversion System Architecture for Power System Primary Frequency Regulation

Wind power generation has reached extensive interest and penetration in more power systems over the last decade. Therefore, a lot of power industries like UK (EFCC project) have deployed variable speed wind turbine (VSWT) based doubly-fed induction generator (DFIG). On the other hand, todays, unavoidable development of WSWTs as a sustainable and cheap source of energy adds more difficulty and challenges to the power system frequency stability by importing another source of fluctuations, in addition to load. More importantly, this type of asynchronous generation does not contribute to the entire system inertia leading to the faster and larger frequency decay. In addition, the conventional types of VSWTs operate in their maximum power point tracking (MPPT) curve so that reserve power is unavailable. Thus, DFIGs naturally can provide small or even no contributions to the frequency control of power networks [1].

The reduction of synchronous inertia results in faster and more considerable changes in system frequency response (SFR), rate of change of frequency (RoCoF) and the frequency deviation following the incidents. Whereas VSWTs based DFIGs do not essentially contribute in ancillary services like conventional power plant, they can provide a wide variety of services comprising of ramping control, frequency responsiveness and reactive power support. In the EFCC project, the main focus is on fast system frequency control support immediately after a power mismatch. These controllers can be divided into two major parts those are emulated inertial response (EIR) and de-loading operation. The former one deploys the rotational kinetic energy stored in the turbine to obtain a temporary injection of power [2], while the later one makes VSWTs to operate over a de-loaded MPPT curve to provide reserve power. In this context, it is to be noted that for VSWTs operated underneath rated wind speed and not dispatched down before the disturbance, their injection power is followed by the energy recovery phase as VSWTs track back to their MPPT. While the VSWT's blades are pitched out of the wind before the in-feed, those are, curtailed or operating beyond rated wind speed, the energy recovery phase can be reduced or avoided by means of pitching the VSWT's blades back into the wind to handle earlier unused energy. It is to be mentioned that VSWTs operating near to their lowest operation speed cannot deliver frequency response without stalling [3].

With high integrations of VSWTs into power systems especially Great Britain (GB) transmission network, frequency instability is a prominent challenge, and therefore the expectation of transmission system operator (TSO) i.e. National Grid (NG) in U.K. is also that the wind farms could take part in the frequency response [4], [5].

This chapter tries to discuss and illustrate the DFIG model adopted from that developed by Klark et. al [6] in DIgSILENT PowerFactory. Developing the mathematical model of the CCGT and its modelling derived in DIgSILENT simulation language (DSL) and DigSILENT programming language (DPL) for power system frequency studies are the main aims of this chapter.

4.1 Literature Review

Variable Speed Wind Turbines (VSWTs) employing power converter offer significantly lower inertia amount to the power systems compared to similar sized conventional power plants [7]. Moreover, the upward trend in VSWT installation around the world has aggravated this challenge and resulted in increased rate of change of frequency (RoCoF) following every system disturbance. In the UK, the total operational capacity of wind turbines by the first quarter of 2017 was over 14.6 GW with more wind units under construction to meet 2020 EU renewable energy commitments [8]. Under such penetrations, the system frequency oscillations may influence on power system stability situations. In order to facilitate this issue, the system operators need to enforce grid code that forces VSWTs to contribute to system frequency regulation [9].

The current technologies implemented in WECSs do not provide system frequency response so that the effective droop is infinite. As a result, the system effective stiffness mitigates as the droop grows by high penetration of

WECSs. Therefore, a closed-form solution approach to control the RoCoF and frequency deviation is essential. Various techniques are presented in literature to enable frequency regulation in WECSs. They can be categorized as: 1) Inertial emulator by extracting extra power from the VSWT rotor inertia to alleviate the frequency nadir and RoCoF [10]-[24] and 2) Deloaded maximum power point tracking curve for VSWT to provide headroom for primary frequency control and steady-state frequency enhancement [18]-[24]. The later approach can be done by pitching the rotor blade angle [17], [18], and [21] and operating the WECSs at a suboptimal rotor speed [19]-[24]. The response speed of former approach is not fast due to the pitch angle mechanical regulation [14]. In the later one, the frequent and large variation of rotor speed for system frequency support will grow the VSWT mechanical stress and fatigue [22]. Moreover, both previously developed deloaded operations for WECS relies on the measured wind speed which is their main drawback. Furthermore, the measurements exactness affects the available reserve power estimation, thus, due to possible measurement errors, some WECSs may become unstable due to lack of sufficient reserve margin while providing primary frequency support. Additionally, in most of previous studies, the turbine generator mechanical dynamics is characterized by using a single mass model. In the current literature, the relations between the two-mass dynamic behaviors and the frequency regulation techniques in VSWT based WECS are not carefully addressed. To get rid of all these issues, the whole structure of WECS is changed and a new one is derived in this study.

Motivated by the above-noticed difficulties, an analytical model of the VSWT rotational speed control-based de-loading operating mode is derived, which makes it suitable to formulate energy captured from the WECS on the basis of blade element momentum theory and modified functional representations of power coefficient. In the proposed primary frequency control, an inertial power injection takes places followed by an active power determined by a novel pitch control when the network frequency excursion happens. This electrical power injection is defined from a control structure with a power reference adjustment obtained from rotor speed and pitch angle using a novel maximum power point tracking (MPPT) surface and the pitch angle reference regulation made by a governing function identical to conventional units. The control scheme and designed WECS is on the basis of the available reserve power margin and frequency regulation mode which is adjusted to resemble the Great Britain (GB) power grid frequency response. Not only does this strategy make a trade-off between fast injection power and small rotor speed change, it also doesn't require measured wind speed data. Furthermore, the accurate drive train aerodynamic equations of VSWT are implemented beside the double-mass mechanical dynamics to find and investigate the oscillation frequency of electromechanical eigenvalues.

4.2 DFIG based WT structure

According to the literature and manufacture manual, the common technique for representing the power performance of WT is the C_p-λ curve. A typical curve is illustrated in Figure 4-1. In order to clearly show this relationship, the following equation is written for the tip velocity ratio which depends to the R and Ω as follows:

$$\lambda = \frac{R\Omega}{U_\infty} \tag{4.1}$$

To start the definition and description of the DFIG, the relationship between the C_p and turbine speed/λ are firstly illustrated in Figure 4-1 and Figure 4-2, respectively.

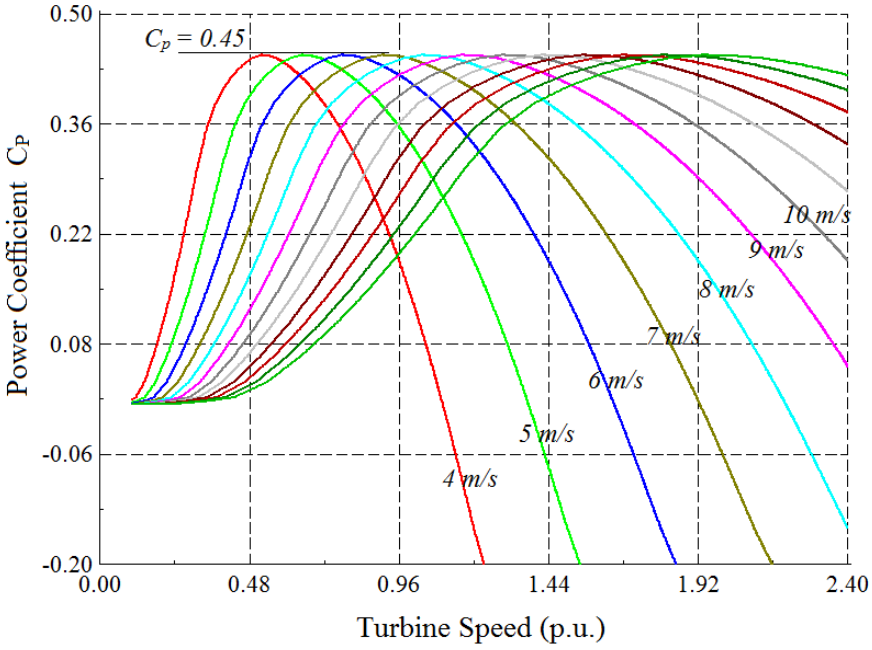

Figure 4-1: Power coefficient-turbine speed curves for different amounts of wind speeds.

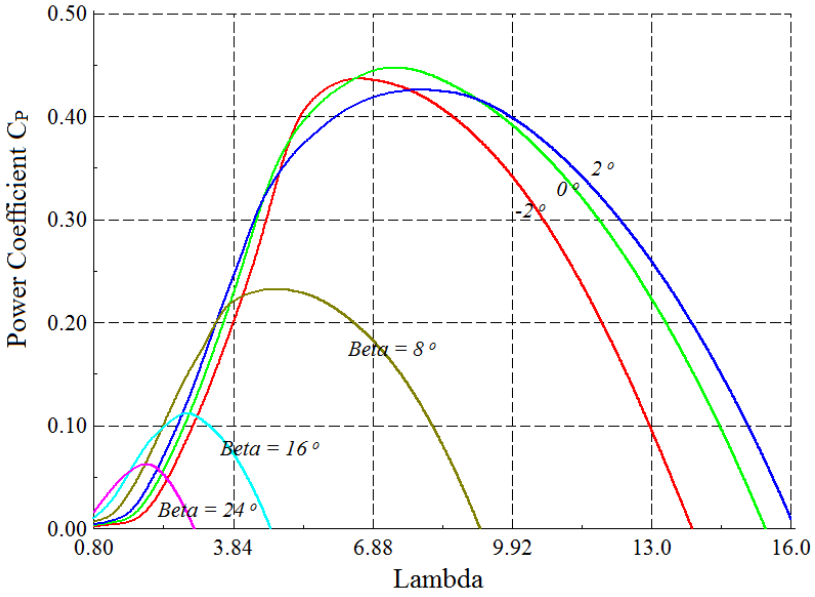

Figure 4-2: Power coefficient-tip velocity curves for different amounts of β .

Additionally, the WT mechanical torque is formulated as follows:

$$T_{mech} = \frac{P_{mech}}{\Omega_{tur}} = C_p \frac{1}{2\Omega_{tur}} \rho A U_\infty^3 = C_p \frac{R}{2\lambda} \rho A U_\infty^2 = C_t \frac{R}{2} \rho A U_\infty^2 \tag{4.2}$$

with C_t as the torque coefficient which has the following relation with the power coefficient C_p:

$$C_p(\lambda,\beta) = \lambda C_t(\lambda,\beta) \tag{4.3}$$

It is to be noted that the torque coefficient C_t is dependant to the pitch angle as well as tip velocity. Figure 4-3 shows this relationship.

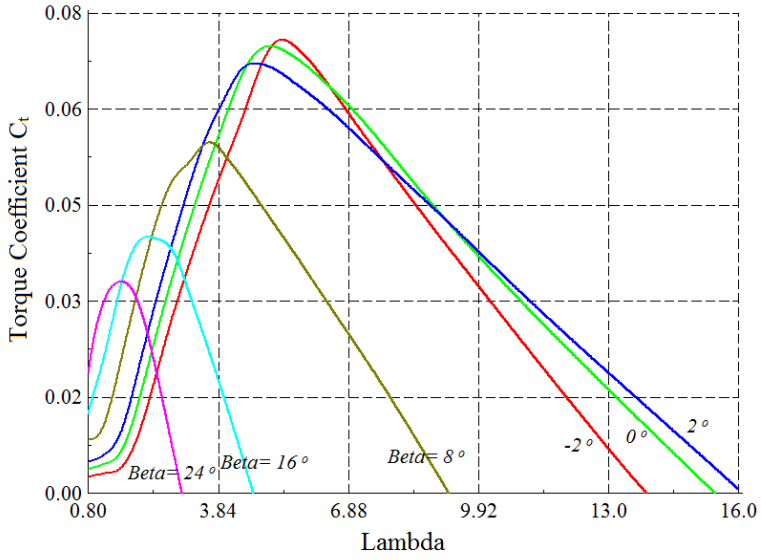

Figure 4-3: Torque coefficient-tip velocity curves for different amounts of β.

The control strategy of DFIG based WT is on the basis of two static optimal curves, shown in Figure 4-4 and Figure 4-5 which are relevant to the following curves: i) Mechanical power of turbine versus wind speed, and ii) Electrical power versus generator speed.

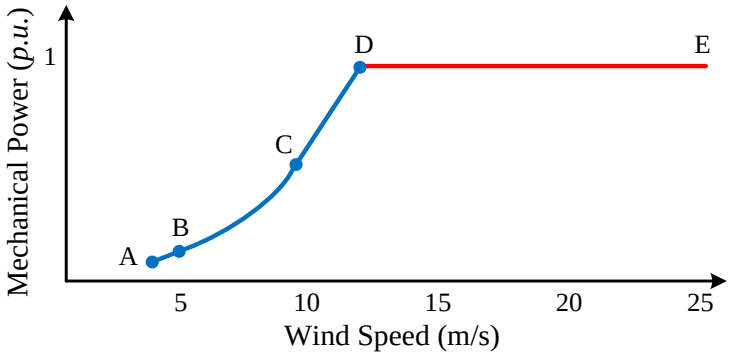

Figure 4-4: Mechanical power versus wind speed.

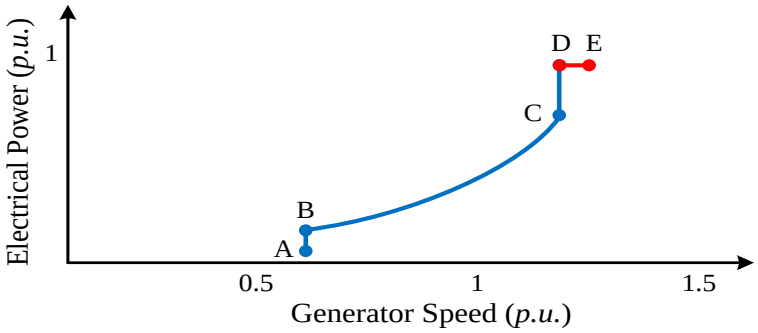

Figure 4-5: Electrical power versus generator speed.

These characteristics are determined based on predefined aerodynamically data of the turbine. In general, two control mechanisms for the variable speed wind turbine like DFIG are depicted in the aforementioned Figures which are as follows:

i) Power optimisation mechanism: This strategy is utilised for the wind speed below the nominal wind speed where the energy capture is optimised. It is indicated by the range A-B-C-D in Figure 4-4 and Figure 4-5.

ii) Power limitation mechanism: This strategy is implemented for the wind speed above the rated wind speed where the aim of the controller is to track the nominal power of the WT. It is indicated by the range D-E in abovementioned Figures. It uses pitch servo motor to keep the WT output power to its rated value.

To control the variable speed WT, four different control approaches are highlighted in these figures which are explained hereinafter.

1) Power optimisation mechanism for zone A-B:

This region relates to the condition once the wind speeds are so small that the rotational speed Ω_{tur} is less than the lower limit $\Omega_{tur}^{\min}$ i.e. $\Omega_{tur} \le \Omega_{tur}^{\min}$. Therefore, the WT's reference speed is set to the minimal value i.e. $\Omega_{tur}^{ref} = \Omega_{tur}^{\min}$ and the tip speed ratio $\lambda(U_\infty)$ is computed as follows:

$$\lambda(U_\infty) = \frac{R\Omega_{tur}^{\min}}{U_\infty} \tag{4.4}$$

It is to be notified that for each amount of tip speed ratio λ , the optimal power coefficient $C_p^{opt}(\lambda,\beta)$ and then the corresponding pitch angle β is found from the look-up table. The optimum mechanical power can be thus obtained by maintaining the turbine speed at the lower limit as follows:

$$P_{mech}^{opt}(U_\infty) = \frac{1}{2}\rho\pi R^5 \frac{C_p^{opt}(\lambda,\beta)}{\lambda^3(U_\infty)}\left(\Omega_{tur}^{\min}\right)^3 \tag{4.5}$$

2) Power optimisation mechanism for zone B-C:

This strategy corresponds to the condition when the value of the rotational speed Ω_{tur} is higher than the lower restriction $\Omega_{tur}^{\min}$ and less than the rated rotational speed $\Omega_{tur}^{\max}$ i.e. $\Omega_{tur}^{\min} < \Omega_{tur}^{ref} \le \Omega_{tur}^{\max}$. The main aim of this strategy is to maximise the captured power by tracking the maximum power coefficient $C_p^{\max}$ curve. This corresponds to a pitch angle β and a tip speed ratio λ_{opt} . It is to be noticed that the pitch angle is thus kept constant, while the tip speed ratio is tuned to the optimal value λ_{opt} over different wind speeds by adjusting Ω_{tur} with respect to its reference one, which is expressed as follows:

$$\Omega_{tur}^{ref}(U_\infty) = \frac{\lambda_{opt}U_\infty}{R} \tag{4.6}$$

Finally, the maximum mechanical power can be calculated as follows:

$$P_{mech}^{\max}(U_\infty) = \frac{1}{2}\rho\pi R^5 \frac{C_p^{\max}(\lambda,\beta)}{\lambda^3(U_\infty)}\left(\Omega_{tur}^{tur}\right)^3 \tag{4.7}$$

3) Power optimisation mechanism for zone C-D:

This strategy relates to the circumstance when the WT speed is limited by the rated value $\Omega_{tur}^{ref} = \Omega_{tur}^{nom}$ and once the generated power is less than the nominal one i.e. $P_{mech} < P_{mech}^{rated}$. The control approach is similar to the first region A-B, with the only modification that the controlling parameters are determined based on Ω_{tur}^{nom} instead of $\Omega_{tur}^{\min}$. In this strategy, the highest efficiency is achieved by operating the WT at Ω_{tur}^{nom} .

4) Power limitation mechanism for zone D-E:

This strategy corresponds to the condition of wind speeds higher than the nominal one. The reference output power is the rated mechanical power i.e. $P_{mech}^{ref} = P_{mech}^{rated}$ while the reference rotor speed is the rated rotor speed as $\Omega_{tur}^{ref} = \Omega_{tur}^{nom}$. Therefore, the tip speed ratio and power coefficient can be written as follows:

$$\lambda(U_\infty) = \frac{R\Omega_{tur}^{nom}}{U_\infty} \tag{4.8}$$

$$C_p(\lambda) = \frac{2P_{mech}^{rated}\lambda^3(U_\infty)}{\rho\pi R^5\left(\Omega_{tur}^{nom}\right)^3} \tag{4.9}$$

Once the power coefficient value is calculated and the tip speed ratio is provided, the pitch angle β can be determined by interpolation in the power coefficient table.

4.3 Variable speed WT controllers

The WT control strategy comprises of two essential controllers, which are cross-coupled together:

a) Speed controller

b) Power limitation controller

Their architecture is on the basis of the previous mentioned control mechanisms. The main controller in the power optimisation mechanism is the former one, while both controllers are active and cross-coupled to each other in the power limitation mechanism.

4.3.1. Speed controller

This controller has the following tasks:

1. Achieving the optimum output power by maintaining the speed of the generator at the lower restriction $Speed_{\min}$ in zone A-B of the power optimisation strategy with fixed low reference speed limitation.

2. Keeping the optimal tip speed ratio λ_{opt} over different wind speeds U_∞, by adapting the steady-state speed of the generator to its reference $Speed_{ref}$ in the B-C zone of the power optimisation strategy with variable reference speed.

3. Controlling the generator speed to its nominal value

Figure 4-6 illustrates the speed control loop. As can be seen, it has difference between the reference generator speed $Speed_{ref}$ and the measured generator speed $Speed_{gen}$ i.e. $Speed_{ref} - Speed_{gen}$ as the input. It is notable that $Speed_{ref}$ is achieved from the predetermined static characteristic, and it corresponds to the generator speed at which the measured active power P_{meas} on the grid is optimal. The error is sent to the PI controller and the output of the speed controller is the reference power value of the DFIG. It is to be noticed that the difference between the fixed speed and variable speed WTs in capturing maximum power in different wind speeds can be illustrated by Figure 4-7. For instance, the fixed speed WT can extract the maximum power in the wind speed of 9 m/s. However, the variable speed WT can adaptively change the tips speed ration to extract maximum power.

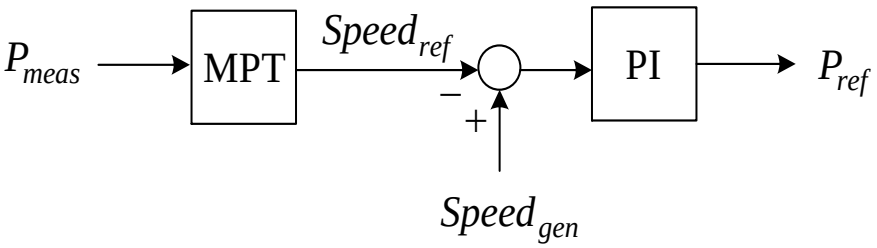

Figure 4-6: Speed controller.

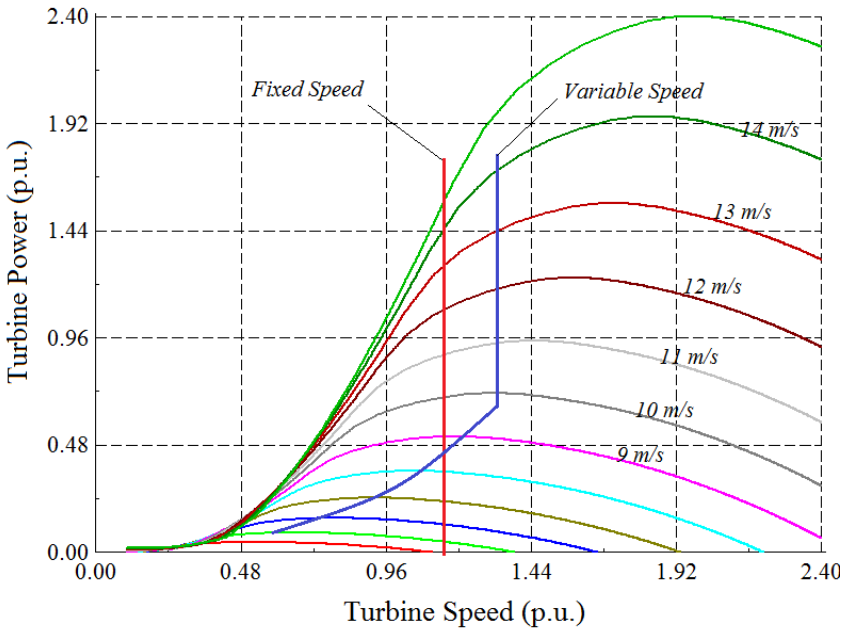

Figure 4-7: Wind turbine power versus speed for different wind speeds.

4.3.2. Power limitation controller

The power limitation controller has a task to increase/decrease the pitch angle to limit the generated power to the rated power. Figure 4-8 illustrates the control loop of this controller. The error signal $P_{meas} - P_{rated}$ is sent to the PI controller to produce the reference pitch angle β_{ref}. It is further compared to the actual pitch angle β and then the error is corrected by the servomechanism. In order to get a realistic response in the pitch angle control system, the servomechanism model accounts for a servo time constant T (delay of servo motors) and the

limitation of both the pitch angle and its gradient. The output of the power limitation controller is the pitch angle of the blades.

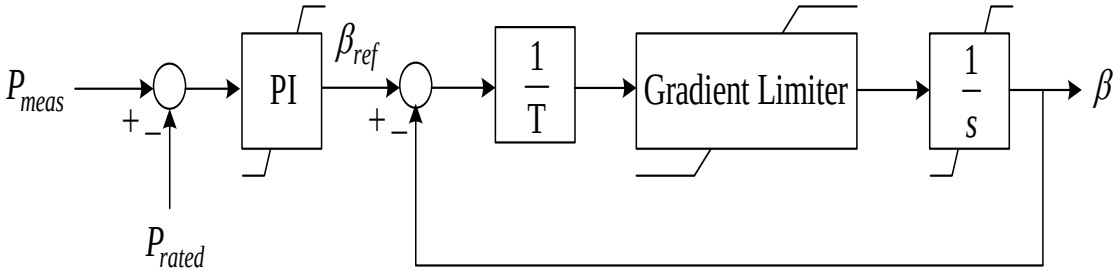

Figure 4-8: Power limitation controller of the WT control, which controls the pitch angle.

To better understand the performance of the aforementioned controllers, the generator speed and pitch angle versus wind speed for four different controlling zones are shown in Figure 4-9. It is to be noticed that once the generated power of WT becomes bigger than the rated power, the pitch angle of blades will be increased by the power limitation controller. It means that the pitch angles is fixed to zero in the first three zones A-B-C-D.

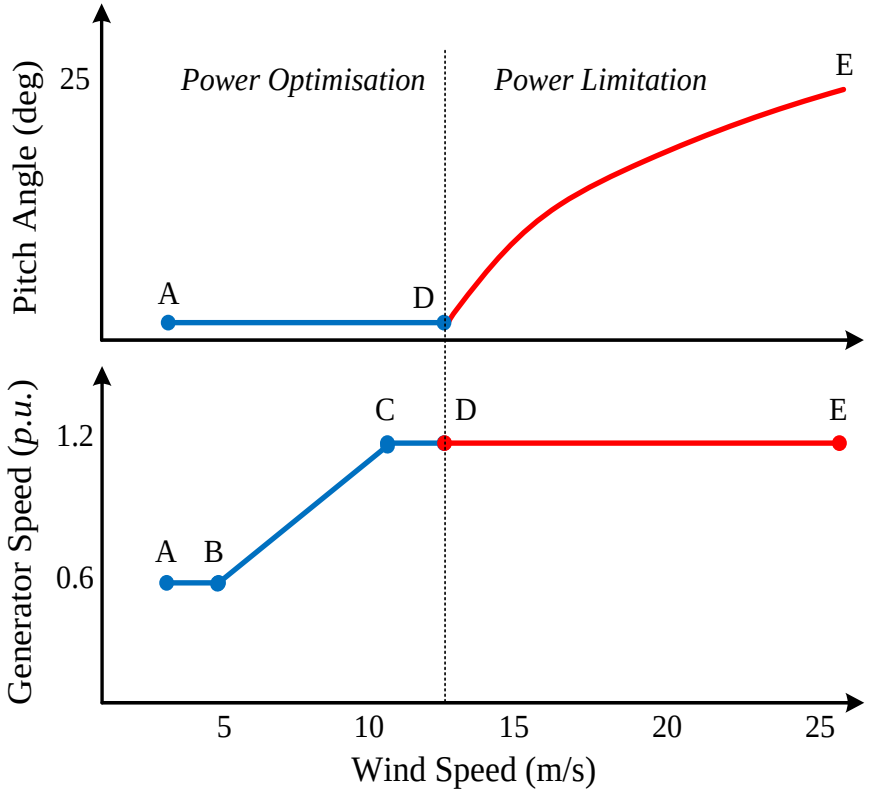

Figure 4-9: Generator speed and pitch angle versus wind speed.

4.4 Energy Captured from the Wind Based on Blade Element Momentum (BEM) theory

Wind turbine (WT) can be explained as an energy conversion system which is capable of harnessing the wind energy and converting it to the electrical energy. There are different types of WTs which

horizontal axis triaxle shafts is the famous and popular one. The analysis of the aerodynamic behaviour of WTs can be explained by considering the general device that carries out the task called the actuator disc (Figure 4-10). The stream-tube has a smaller cross-sectional area in upstream side of the disk compared to downstream one. The matter of this fact is that the mass flow rate should have the similar value everywhere. In order to calculate the extracted power by WT, three stations (1: free-stream region, 2: just on the blades, and 3: far wake region) need to be considered. The wind speed behind the WT is less than the front side since some part of wind kinetic energy is captured by WT. Wind kinetic energy (E_{wind}) for one unit volume can be written as follows:

$$E_{wind} = \frac{1}{2} M_{wind} V_{wind}^2 \tag{4.10}$$

With M_{wind} and V_{wind} as the air mass in a unit length of volume and wind speed, respectively. The following formula describes the amount of power that can be attained from the wind speed blowing from the area swept by blades, i.e. A:

$$P_{wind} = \dot{E}_{wind} = \frac{1}{2} \dot{M}_{wind} V_{wind}^2 = \frac{1}{2} (\rho A V_{wind}) V_{wind}^2 = \frac{1}{2} \rho A V_{wind}^3 \tag{4.11}$$

Where, ρ is the air density. The relation of the mass of the air which flows through the given cross-section of the stream-tube in a unit length of time is equal to ρAU , with U as the flow speed. According to the equality of the mass flow rate ($\dot{M}_{wind}$) in different parts of stream-tube, the following equation can be written:

$$\rho A_1 V_{wind1} = \rho A_2 V_{wind2} = \rho A_3 V_{wind3} \tag{4.12}$$

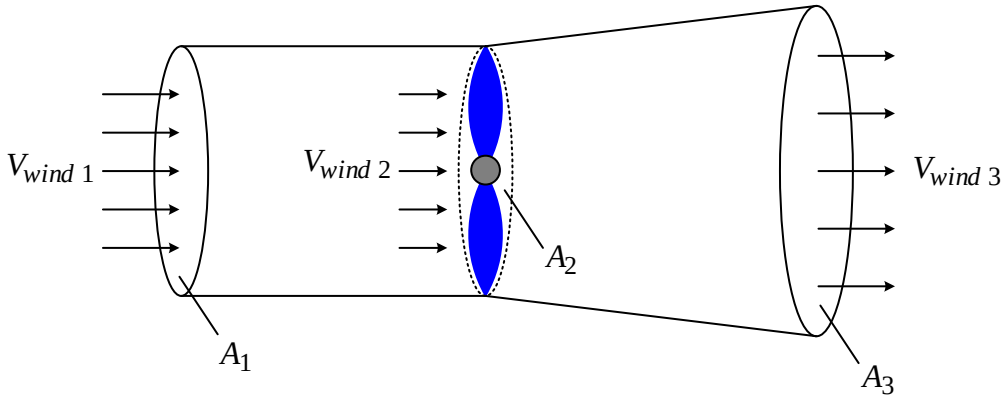

Figure 4-10: Schematic diagram of the connection of a WECS

The captured wind power by WT can be computed by subtracting wind power in the far wake region from free-stream one. Combining this point with (4.12) yields:

$$P_{extracted} = P_{wind1} - P_{wind3} = \frac{1}{2} \dot{M}_{wind} V_{wind1}^2 - \frac{1}{2} \dot{M}_{wind} V_{wind3}^2 = \frac{1}{2} \dot{M}_{wind} \left(V_{wind1}^2 - V_{wind3}^2 \right) = \frac{1}{2} \rho A V_{wind2} \left(V_{wind1}^2 - V_{wind3}^2 \right) \tag{4.13}$$

According to the Froud-Rankine theorem, velocity through the disk can be obtained as follows [25]:

$$V_{wind2} = \frac{V_{wind1} + V_{wind3}}{2} \tag{4.14}$$

By inserting (4.14) in (4.13), the extracted power can be rewritten as follows:

$$P_{extracted} = \frac{1}{2}\rho\pi R_{blade}^2 \left(\frac{V_{wind1}+V_{wind3}}{2}\right)\left(V_{wind1}^2 - V_{wind3}^2\right)$$
$$= \frac{1}{2}\rho\pi R_{blade}^2 V_{wind1}^3 \left(\frac{1}{2}\left(1+\frac{V_{wind3}}{V_{wind1}}\right)\left(1-\left(\frac{V_{wind3}}{V_{wind1}}\right)^2\right)\right) \quad (4.15)$$

The last term in (4.15) defines as the power coefficient as follows:

$$C_p = \frac{1}{2}\left(1+\frac{V_{wind3}}{V_{wind1}}\right)\left(1-\left(\frac{V_{wind3}}{V_{wind1}}\right)^2\right) \quad (4.16)$$

The C_p has the sub unity figure and shows the ratio of the extracted mechanical power to the available power. Therefore, equation (4.15) can be rewritten as follows:

$$P_{extracted} = \frac{1}{2}\rho\pi R_{blade}^2 V_{wind1}^3 C_P \quad (4.17)$$

Based on Betz's law, the maximum amount of C_p is attained once the outgoing wind speed is one out of three of incoming one. The maximum value of the C_p is 0.593, which is known as the Betz limit. In order to justify this matter, it's sufficient to calculate the derivation of C_p in relation (4.16) in term of V_{wind3}/V_{wind1} and set it equal to zero [26]. As a result, the WT can capture 60% of power available in the air. However, in practice, this considers as 50% due to non-ideal criteria. The C_p can be written as follows:

$$\frac{V_{wind3}}{V_{wind1}} = \frac{1}{3}, \qquad C_P = C_P^{Betz} = \frac{16}{27} \approx 0.593 \quad (4.18)$$

It is expected that the forces on the blade equipment can be calculated by means of two dimensional aerofoil features implementing the pitch angle (θ) and attack angle (α) determined from the incident resultant speed in the cross-sectional flat of the equipment. The velocity elements at the radial situation on the blade expressed in terms of the wind velocity, the flow factors and the rotational velocity of the rotor determine the attack angle. The blade linear speed and resultant relative velocity are indicated with V_{linear} and V_{wind}^{net}, respectively. The lift (L) and drag (D) forces as well as their relationship are depicted in Figure 4-11. In some turbine's types, each blade can be rotated around its axis by multiple servo motors in order to change pitch angle θ. The pitch angle θ increment can increase friction blades with the wind and decrease the wind power, consequently.

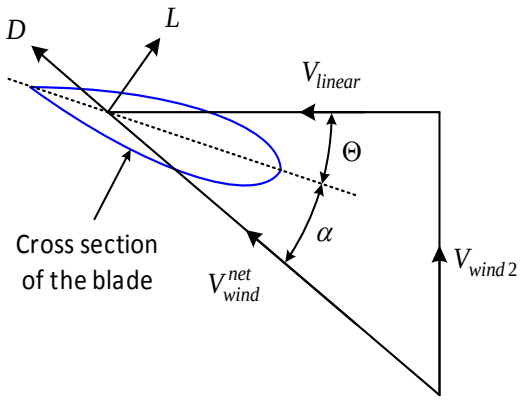

Figure 4-11: The blade element velocities and angles

The ratio of linear speed of the blade's tip to wind speed is called tip speed ratio and can be expressed in dimensionless as follows:

$$\lambda = \frac{R_{blade}\omega_{turbine}}{V_{wind}} \tag{4.19}$$

The R_{blade} defines as K1 in equation (4.20) in which $C_P^{\max}$ is 0.5.

$$K_1 = \frac{\left(\lambda\big|_{C_P=C_P^{\max}}\right)\left(V_{wind}\big|_{C_P=C_P^{\max}}\right)}{\omega_{turbine}\Big|_{C_P=C_P^{\max}}} \tag{4.20}$$

The $\left(V_{wind}\big|_{C_P=C_P^{\max}}\right)$ and $\left(\omega_{turbine}\big|_{C_P=C_P^{\max}}\right)$ are nominal wind speed and WT speed, respectively. $\left(\lambda\big|_{C_P=C_P^{\max}}\right)$ is the optimal amount of tip speed ratio. Thus, (4.19) can be rewritten in the following form:

$$\lambda = \frac{K_1\ \omega_{turbine}}{V_{wind}} \tag{4.21}$$

In other hand, K_2 can be defined as follows:

$$K_2 = \frac{P_{turbine}\Big|_{C_P=C_P^{\max}}}{\left(V_{wind}^3\Big|_{C_P=C_P^{\max}}\right)C_P^{\max}} \tag{4.22}$$

Where, $\left(P_{turbine}\big|_{C_P=C_P^{\max}}\right)$ is nominal WT power. In this context, (4.17) can be rewritten as follows:

$$P_{turbine} = K_2 V_{wind}^3 C_P \tag{4.23}$$

4.4.1. Functional Representations for C_P-λ Tables

Some researchers worked in this matter to drop down the parameters number required to present the C_P-λ tables. It is to be noticed that C_p is generally a function of tip speed ratio and the blade pitch angle, as depicted in the following form [27]:

$$C_P = c_1\left(\frac{c_2}{\lambda_i} - c_3\Theta - c_4\Theta^{c_5} - c_6\right)e^{\frac{c_7}{\lambda_i}} \tag{4.24}$$

Where,

$$\lambda_i = \left(\frac{1}{c_8\Theta + \lambda} - \frac{c_9}{\Theta^3 + 1}\right)^{-1} \tag{4.25}$$

4.4.2. Modified Functional Representations for C_P-λ Tables

The comparison based blade data studies used in modern WTs shows that the accuracy of (4.24) is not reasonable for modern WTs. The parameter sets given by the authors does not fit with modern blades good enough. Based on the research activities done by Jens Forthmann, a rescaling of pitch angle allows an improved representation [28]. This can be obtained by:

$$\Theta' = c_{10}\Theta \tag{4.26}$$

By substituting Θ by Θ′ in (4.24) and (4.25), a significantly improved correlation of the C_P-λ data generated by (4.24) with real WTs can be achieved [28]. The following parameters are considered in this chapter:

$$c_{1-10} = \begin{bmatrix} 0.279 & 118 & -0.5 & 0.922 & 1.12 & 3.33 & 15.6 & 0.102 & 0.017 & 0.751 \end{bmatrix} \tag{4.27}$$

According to the above discussion, it can be concluded that the WT power output is not only function of wind speed, but also C_P. In other hand, the WT power output can be controlled by adjusting this valuable parameter which is function of pitch angle and tip speed ratio. The WT's parameters which is utilised in this chapter are tabulated in Table 4-1.

Table 4-1: Parameters of the wind turbine

Parameter	Value	Unit	Parameter	Value	Unit	Parameter	Value	Unit
$\lambda\big\vert_{C_P=C_P^{\max}}$	9.147	-	$\omega_{turbine}\big\vert_{C_P=C_P^{\max}}$	1	p.u.	$C_P^{\max}$	0.5	-
$V_{wind}\big\vert_{C_P=C_P^{\max}}$	11.8	m/s	$P_{turbine}\big\vert_{C_P=C_P^{\max}}$	1	p.u.	P_{rated}	2	MW

Based on data provided in Table 4-1 and relation (4.27), C_P is portrayed in left hand side Figure 4-12 in terms of tip speed ratio for different values of wind speed and pitch angle. As can be seen, C_P is dropped down by increasing pitch angle. Therefore, the pitch angle is usually set to zero in order to extract maximum power point. The right hand side of Figure 4-12 shows the WT power in term of its speed for discrepant wind speeds and settling pitch angle at zero. It is quite obvious that for a constant value of the blade pitch angle and a given speed of rotation, there is a single wind speed value (equal to nominal one) that gives the most efficient operation. The reverse also applies, meaning that for the same value of the blade pitch angle and a given wind speed value, there is a single speed of rotation that ensures the most efficient operation. It is to be noticed that for a constant wind velocity, there is a single speed point at which the generators' rotor have to rotate to achieve the maximum mechanical power or power coefficient available. Depending on the wind velocity, the speed of the rotor can be regulated in variable speed wind turbines (VSWTs) so that the generator could track only its maximum power point (MPP), as highlighted by blue line in this figure.

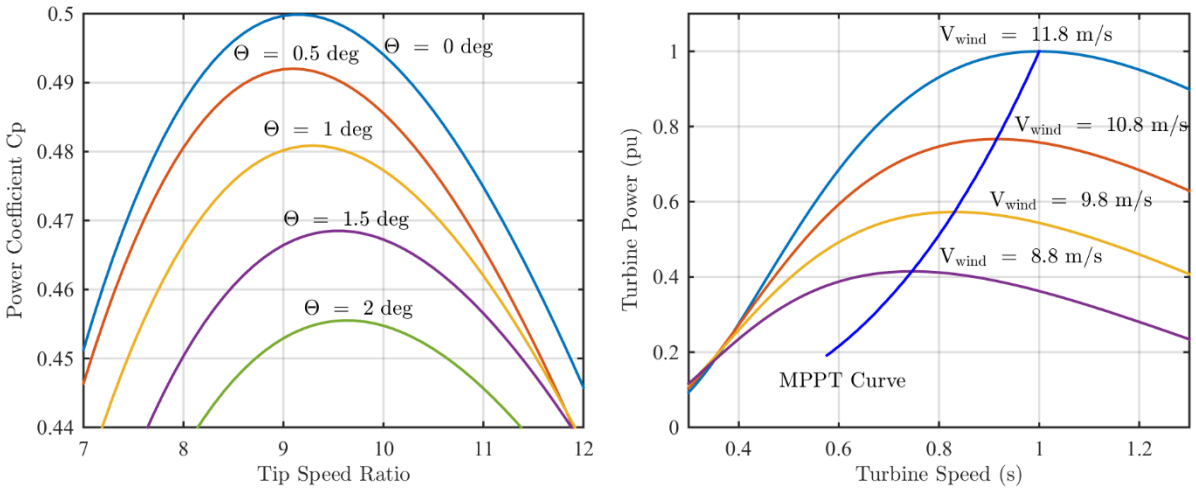

Figure 4-12: Power coefficient versus tip speed ratio for different pitch angle (Left), Turbine power versus turbine speed with zero pitch angle for different wind speed (Right).

4.5 Wind Energy Conversion System (WECS)

WECS can be explained as an energy conversion system which is capable of harnessing the VSWT is shown in Figure 4-13. The whole controlling procedures of energy conversion includes mechanical and electrical parts are depicted in Figure 4-13. The mechanical parts comprises of blades, turbine shaft, and drive train. Generator, power electronic converters and transformers constitute the electrical part. The mechanical power generated in mechanical part is transferred to the generator via drive train. The main focus of maximum power point tracker (MPPT) is to control the operating point of WT. In VSWT, the injected power to the grid is controlled by power electronic converters using Pref. The refrence power Pref is determined by MPPT. The MPPT utilises the MPPT curve shown in right hand side of Figure 4-12 and determines Pref based on WT speed. One of the most significant advantages of this approach is that it can operate without measuring wind speed.

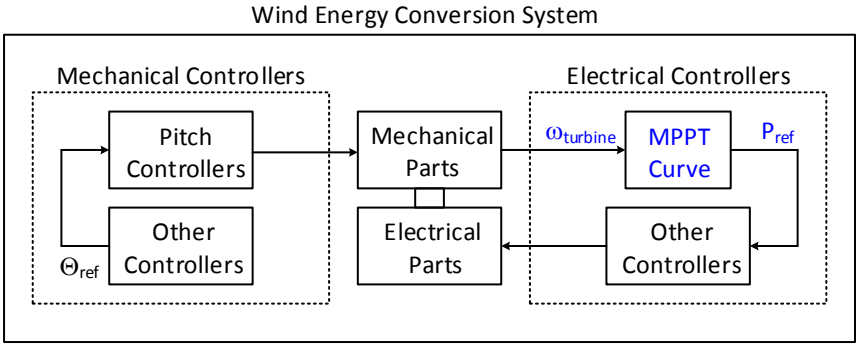

Figure 4-13: Operating point selection by MPPT curve in WECS.

4.6 Proposed Frequency Control for WT

In order for any unit to be deployed for primary frequency control, the sufficient reserve availability is a vital requirement to be injected to the grid following the incident and regulate frequency. A precondition for taking primary frequency support from WTs is to create a controllable reserve power. The suggested technique to address this issue is by changing the WT operating point from its MPPT to a reduced power level. For instance, in order to reserve wind power, the de-loaded MPPT curves are deployed [23]. For example, the left hand side of Figure 4-14 illustrates a 10% de-loading in the right side of the MPPT curve. The WT might be similarly de-

loaded by shifting the operating point to the left side of MPPT curve. For instance, due to the huge reduction of WT speed in this case, the operating points determined for the left side deloaded MPPT curve are not applicable and the right side is preferred [23]. However, the deloading percent is to be applied considering the acceptable maximum restriction of WT speed. It is observed that WT speed variation required for wind power reserve is considerably huge. For the sake of clarity, the WT speed deviation versus deloading percent is illustrated in right side of Figure 4-14. If the WT is 10% deloaded, during nominal frequency conditions, the WT speed should rise 30% with respect to the WT speed on original MPPT curve. This is one of the main drawbacks of this deloading strategy in practical cases.

As discussed earlier and depicted in left hand side of Figure 4-12, increasing pitch angles can drop WT output power down. As a result, another technique for WT deloading is to pitch the WT blade angle. For the sake of better explanation, C_P is portrayed in Figure 4-15 in terms of tip speed ratio and pitch angle. The operating points for 10% to 2% deloading with pitch length of 2% are highlighted with grey horizontal curves. It is observed that blade pitch angles are zero juts only two points on each of these curves. These points are the right and left sides deloaded MPPT curves. However, as discussed above, WT speed variations in these operating points are big; thus, the operating points need to be selected in a way that WT speed changes are small. In this chapter, the operating points for delaoding WT output power are chosen based on MPPT curve plotted in Figure 4-14. This curve is illustrated with blue curve in Figure 4-15. As can be seen from the curves presented at the bottom of Figure 4-15, the tip speed ratio and WT speed change are pretty low while the loading amount is varied from 0% to 10%. Moreover, it can be possible to define another curve so that its pitch angle is changed proportionally to deloading amount and its pitch angle is set to the optimal amount listed in Table 4-1. In this circumstance, WT speed change for discrepant amounts of deloading is zero and of course the operating point is not MPPT.

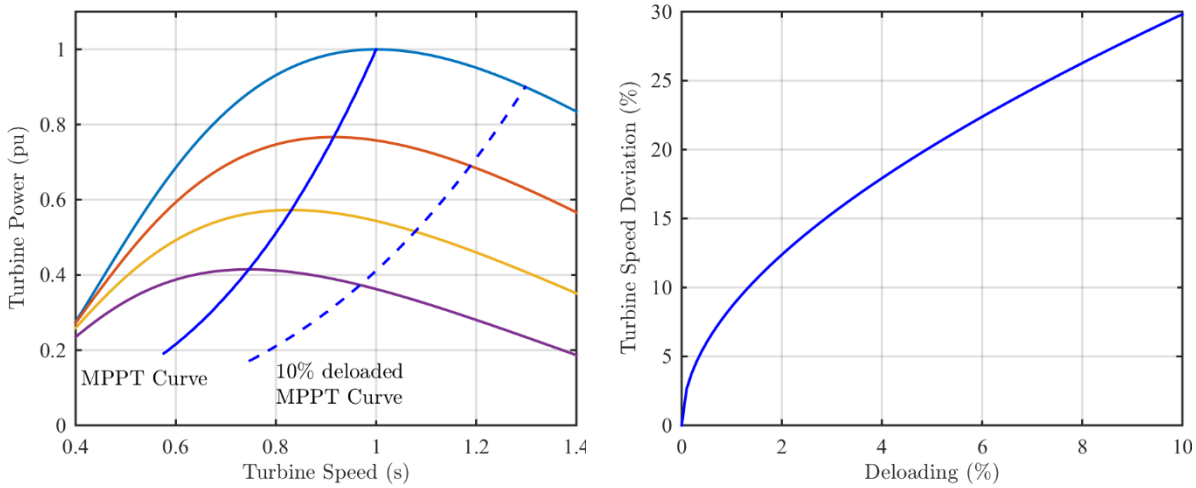

Figure 4-14: MPPT and deloaded MPPT curves (Left), Turbine speed deviation versus deloading (Right).

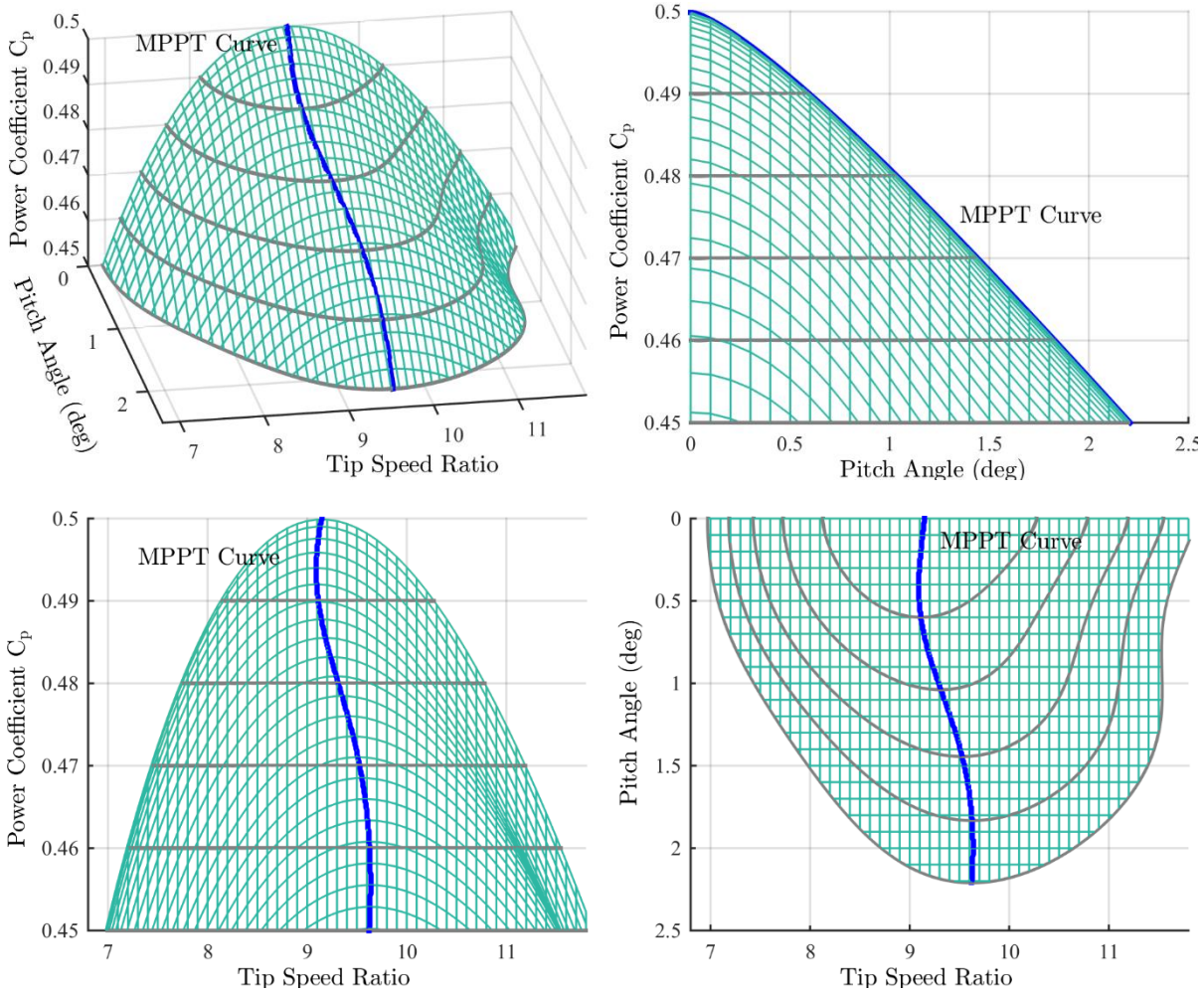

Figure 4-15: Power coefficient versus pitch angle and tip speed ratio.

Albeit the non-linear relation of CP with respects to pitch angles and tip speed ratio, it is clear that the C_P has a linear relationship with pitch angle for the deloading amount greater than 2%, as shown in up right hand side of Figure 4-15. In this interval, this CP can be estimated by a second-order polynomial as follows:

$$C_P^{MPPT} \approx -0.00256\,\Theta^2 - 0.01776\,\Theta + 0.5012 \qquad 0 \le \Theta \le 2.5 \text{ deg} \tag{4.28}$$

The relationship between C_P and pitch angle can be converted to the linear expression (4.29) with a little bit error in estimation process.

$$C_P^{MPPT} \approx -0.02342\,\Theta + 0.50325 \qquad 0 \le \Theta \le 2.5 \text{ deg} \tag{4.29}$$

This linear equation can reduce the computation burden and also provide network operator a fact and reasonable outlook for the relationship between the reserve powers and pitch angle of WTs. As it is explained for Figure 4-13, the reference power can be determined using MPPT curve shown in right hand side of Figure 4-12 in term of WT speed, if the pitch angle value is zero. While the pitch angle is set to a value more than zero for the sake of deloading WT, the pitch angle should be also integrated into reference power determination. Whereas the operating point is specified by MPPT curve in Figure 4-15, it is noteworthy that this figure is plotted in term of tip speed ratio not WT speed. While the wind speed is available, the operating point can be selected directly using Figure 4-15. However, the need to measure wind speed is one of the main disadvantage of this WT controlling approach. In order to get rid of this drawback, MPPT should be defined in a way that WT speed replaces with tip speed ratio. To this end, it is supposed that wind speed is fixed to a specific value, so that

MPPT curve is obtained from Figure 4-15 in terms of pitch angles and WT speed. In an iterative process for all considered wind speeds, a MPPT surface can be obtained instead of MPPT curve, as shown in left hand side of Figure 4-16. It is to be noticed that the wind speed is not required in this approach. The right hand side of Figure 4-16 is similar to the left one with this difference that power axis is replaced with speed. This figure is utilised to determine the initial conditions in PowerFactory software.

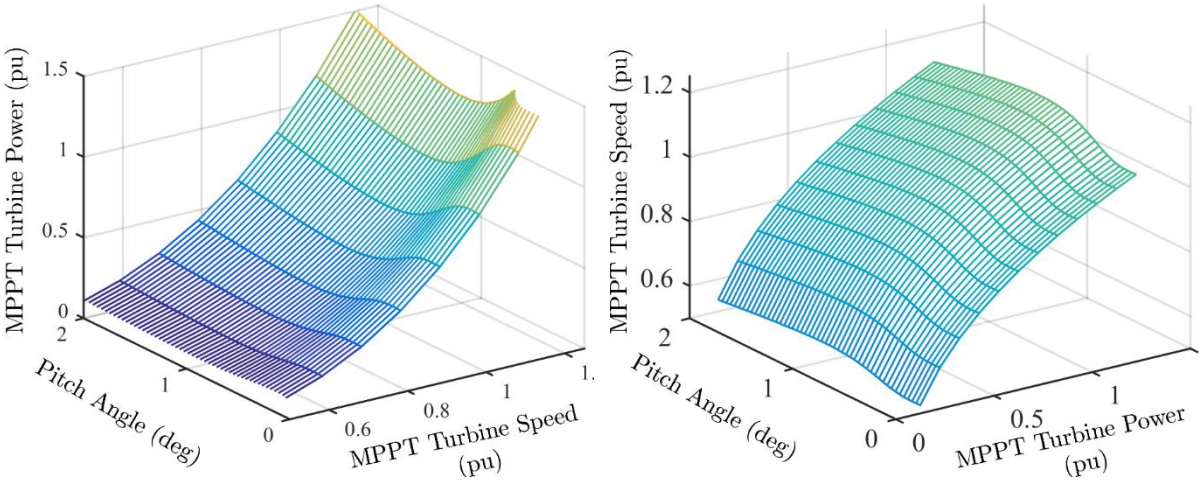

Figure 4-16: MPPT turbine power versus pitch angle and MPPT turbine speed (Left) and MPPT turbine speed versus pitch angle and MPPT turbine power (Right).

Figure 4-17 show the whole structure of controlling pitch angle to determine the operating point of VSWT and keep the additional available power as reserve for it. Therefore, the reference pitch angles are determined by primary controller in proportion of reserve power. Consequently, the pitch controller tunes the pitch angle using servo motors. The pitch angle variation rate is set to 10 degrees per second [6]. Finally, the MPPT Surface regulates reference power in terms of WT speed and pitch angle based on left hand side of Figure 4-16.

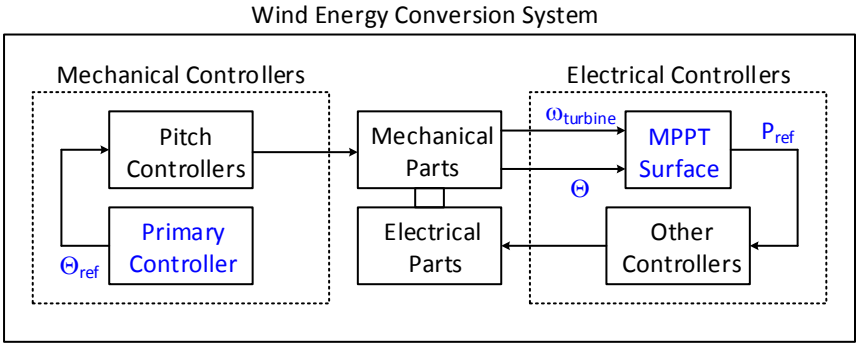

Figure 4-17: Operating point selection by MPPT surface in WECS.

It is to be noted that although a MPPT point shouldn't be necessarily selected as the operating point and it can be from the grey horizontal curves depicted in Figure 4-15 in order to utilize pitch angle control to deload WT, two objective functions are essential in operating point selection process: i) WT speed change required for reserve power should be small; and ii) The maximum power in lowest amount of time injects to the grid. At first glance, it is supposed that from the viewpoint of reserve power injection speed to the grid based on deloaded MPPT curve in Figure 4-14, this WT speed based method is better as compared to pitch angle strategy due to the lower value of electrical time constant with respect to mechanical one. However, the first objective function has the worse situation in WT speed based method in comparison with pitch angle based technique for WT deloading procedure. It can be summarized that a compromised or trade-off between these two objective functions should be made to determine operating point. To this end, selecting the operating points on MPPT curve of Figure 4-15 can be the compromised or trade-off ones.

4.7 Principle of stator voltage oriented control

The DFIG based WTs offers a flexible controlling mechanism that makes them pretty attractive for variable speed WTs. The block diagram of control structure of a DFIG based WT (Type C) including the back-to-back converters is shown in Figure 4-18. As it can be seen, it is controlled by two separate controller blocks which are related to the grid side converter (GSC) and rotor side converter (RSC). The DC link voltage is controlled by the GSC which is set it to a predefined level. Also, it draws/feeds slip power from/into the grid during the sub-synchronous and super-synchronous operation, respectively. The RSC provides the possibility of decoupling the active and reactive power control of WT. The interested readers may refer to [6] for more details.

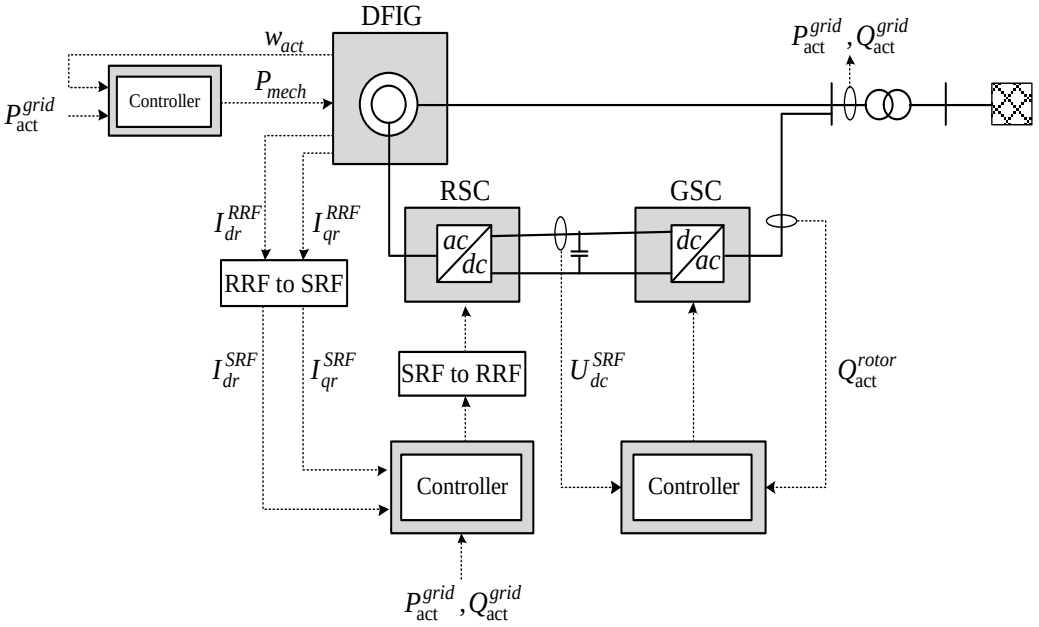

Figure 4-18: Layout of DFIG based WT.

Depending on the rotor speed, there are two modes of operation for DFIG: i) super-synchronous mode, in which the rotor speed of the generator is bigger than the synchronous speed; and (2) sub-synchronous mode, in which the generator operates below the synchronous speed. The slip is negative in the super-synchronous mode and becomes positive in the sub-synchronous mode. In the other hand, the relationship between the rotor power (P_r) and stator power (P_s) neglecting the core and cupper losses is as follows:

$$P_r \approx -sP_s \tag{4.30}$$

It means that the rotor can inject power to the grid in the super-synchronous mode and vice versa. This is illustrated in Figure 4-19.

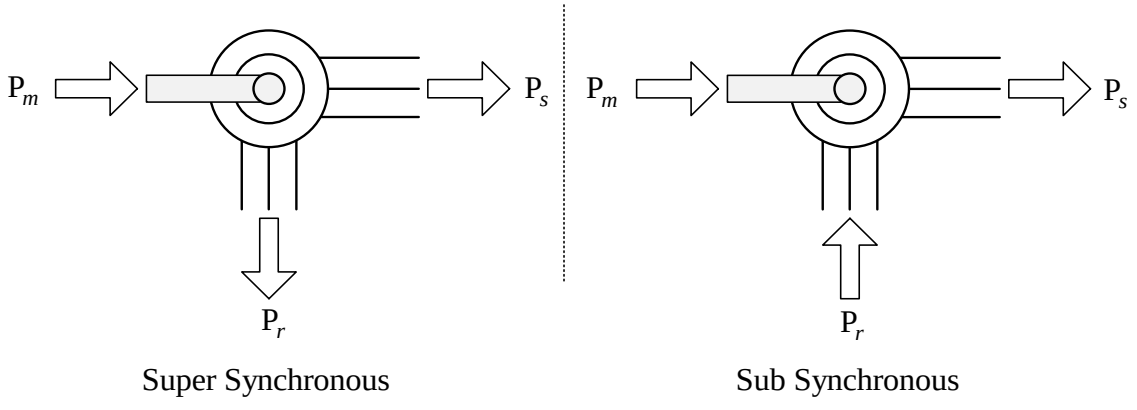

Figure 4-19: Power flow path in super- and sub-synchronous modes.

In the DFIG based WT systems, the stator is directly connected to the grid so that its voltage and frequency are constant under the normal operations. Thus, it is convenient to deploy the stator voltage oriented (SVO) control for the power electronic converters of DFIG. Figure 4-20 illustrates its space vector diagram operating with unity power factor in super-synchronous mode. The SVO is obtained by aligning the *d*-axis of the synchronous reference frame with the stator voltage vector $\overline{v}_s$. The resultant *d*- and *q*-axis stator voltages are as follows:

$$v_{qs} = 0 \text{ and } v_{ds} = v_s \tag{4.31}$$

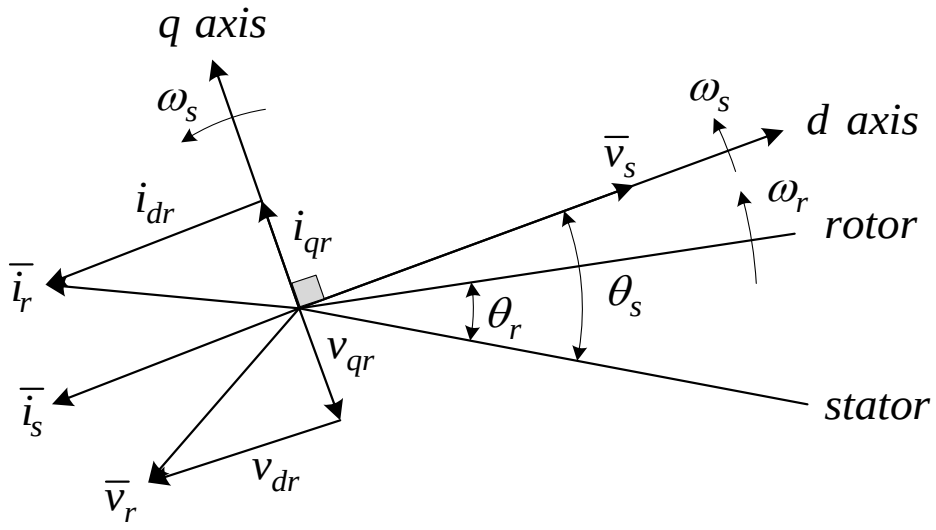

Figure 4-20: Space-vector diagram of DFIG with SVO control in the super-synchronous mode.

The stator voltage vector for the steady-state operation is as follows:

$$\vec{v}_s = R_s\vec{i}_s + j\omega_s\vec{\lambda}_s \tag{4.32}$$

The representation in dq-axis is

$$v_{ds} + jv_{qs} = R_s\left(i_{ds} + ji_{qs}\right) + j\omega_s\left(\lambda_{ds} + j\lambda_{qs}\right) \tag{4.33}$$

from which the *dq*-axis stator flux linkages are as follows:

$$\begin{cases} \lambda_{ds} = \dfrac{v_{qs} - R_s i_{qs}}{\omega_s} \\ \lambda_{qs} = -\dfrac{v_{ds} - R_s i_{ds}}{\omega_s} \end{cases} \tag{4.34}$$

Additionally, these flux linkages can be written as follows:

$$\begin{cases} \lambda_{ds} = L_s i_{ds} + L_m i_{dr} \\ \lambda_{qs} = L_s i_{qs} + L_m i_{qr} \end{cases} \tag{4.35}$$

from which the *dq*-axis stator currents are computed as follows:

$$\begin{cases} i_{ds} = \dfrac{\lambda_{ds} - L_m i_{dr}}{L_s} \\ i_{qs} = \dfrac{\lambda_{qs} - L_m i_{qr}}{L_s} \end{cases} \tag{4.36}$$

Furthermore, the stator active and reactive power can be formulated as follows:

$$\begin{cases} P_s = \dfrac{3}{2}(v_{ds} i_{ds} + v_{qs} i_{qs}) \\ Q_s = \dfrac{3}{2}(v_{qs} i_{ds} - v_{ds} i_{qs}) \end{cases} \tag{4.37}$$

Using the SVO control ($v_{qs} = 0$), it can be rewritten as follows:

$$\begin{cases} P_s = \dfrac{3}{2} v_{ds} i_{ds} \\ Q_s = -\dfrac{3}{2} v_{ds} i_{qs} \end{cases} \tag{4.38}$$

Substituting (4.34) into (4.38) gives

$$\begin{cases} P_s = \dfrac{3}{2} v_{ds}\left(\dfrac{\lambda_{ds} - L_m i_{dr}}{L_s}\right) \\ Q_s = -\dfrac{3}{2} v_{ds}\left(\dfrac{\lambda_{qs} - L_m i_{qr}}{L_s}\right) \end{cases} \tag{4.39}$$

from which

$$\begin{cases} i_{dr} = -\dfrac{2L_s}{3v_{ds}L_m} P_s + \dfrac{1}{L_m}\lambda_{ds} \\ i_{qr} = \dfrac{2L_s}{3v_{ds}L_m} Q_s + \dfrac{1}{L_m}\lambda_{qs} \end{cases} \tag{4.40}$$

Substituting the stator flux linkages from (4.34) into (4.40) and neglecting the stator resistance yields:

$$\begin{cases} i_{dr} = -\dfrac{2L_s}{3v_{ds}L_m}P_s \\ i_{qr} = \dfrac{2L_s}{3v_{ds}L_m}Q_s - \dfrac{v_{ds}}{\omega_s L_m} \end{cases} \tag{4.41}$$

This indicates that for a fixes stator voltage, the stator active and reactive powers can be controlled by the *dq*-axis rotor currents.

4.8 WECS Modelling in DIgSILENT PowerFactory

According to the above discussion, a WECS equipped with a VSWT is modelled in PowerFactory and simulated so that it quite useful for big network frequency response dynamic studies. Furthermore, the WT aerodynamic is completely and accurately modelled. Many models for VSWT based WECS is derived in [11], [17]-[19], and [29]-[35]. Each model has its own pros and cons. In the initial studies like [29] and [30], the main purpose is to model WECS and its validation. As per WECS penetration level increment in power system networks in many countries, the WECS modelling is conducted for the sake of impact on power network dynamic behaviour. However, the main target of these approaches is on voltage control modelling and short-circuits analysis with WECS in the system [31] and [32]. In the next stage, frequency control and inertial response simulation of WTs become one of the main research activities for engineering and academia [11], [17]-[19], [33]-[35]. In [33], a VSWT based WECS structure is developed by General Electric (GE) for network dynamic studies. One of the main benefits of this model is its simplicity and WT aerodynamic consideration. Furthermore, an inertial emulator is derived for WT. The comparison of the simulation results of this model with real ones increases the validity and superiority of this WECS architecture. In [34], the similar approach presented in [33] followed for WECS modelling, however, the results are not compared with real ones. In other hand, the primary frequency support by employing available reserve power under the VSWT deloaded conditions is not modelled in [33] and [34]. In [19], available inertia and droop responses from a WT to support the primary frequency control are analytically assessed. However, the derated conditions considered for primary power reserve is based on deloaded MPPT curve in left hand side of Figure 4-14 which leads to the big issue of WT speed changes. In [17] and [18], the deloading is obtained by operating the WT at pitching the blade angle to deliberately spill power so that the reserve power can be deployed for frequency control. However, the WT aerodynamic is not perfectly formulated in [17] and [18] and they need the measured wind speed data.

The proposed control scheme of VSWT based WECS is shown in Figure 4-21. This structure consists of four main modelling parts of mechanical equipment, mechanical controllers, electrical equipment and electrical controllers. This model is constructed to be appropriate for dynamic frequency studies in large scale test systems so that some simplifications are implemented. One of them is to model electrical generator and power electronic inverter of VSWT based WECS as a current resource placed in 'Wind Generator' block of Figure 4-21. In other word, this is a simple static generator in Powerfactory software. It is also to be tonted that in contrast to the conventional MPPT scheme, where the reference active power is determined based on the WT speed, the proposed MPPT strategy calculates the reference active power based on the pitch angle as well as WT speed. Then, the speed response of the MPPT loop is governed by the mechanical part's time constants. It is to be noticed that this mechanism is considered only for the times following the power deficit event. In other words, the speed response of the deployed MPPT scheme is equal to that of the conventional strategy in the normal system conditions, since the pitch angle is constant.

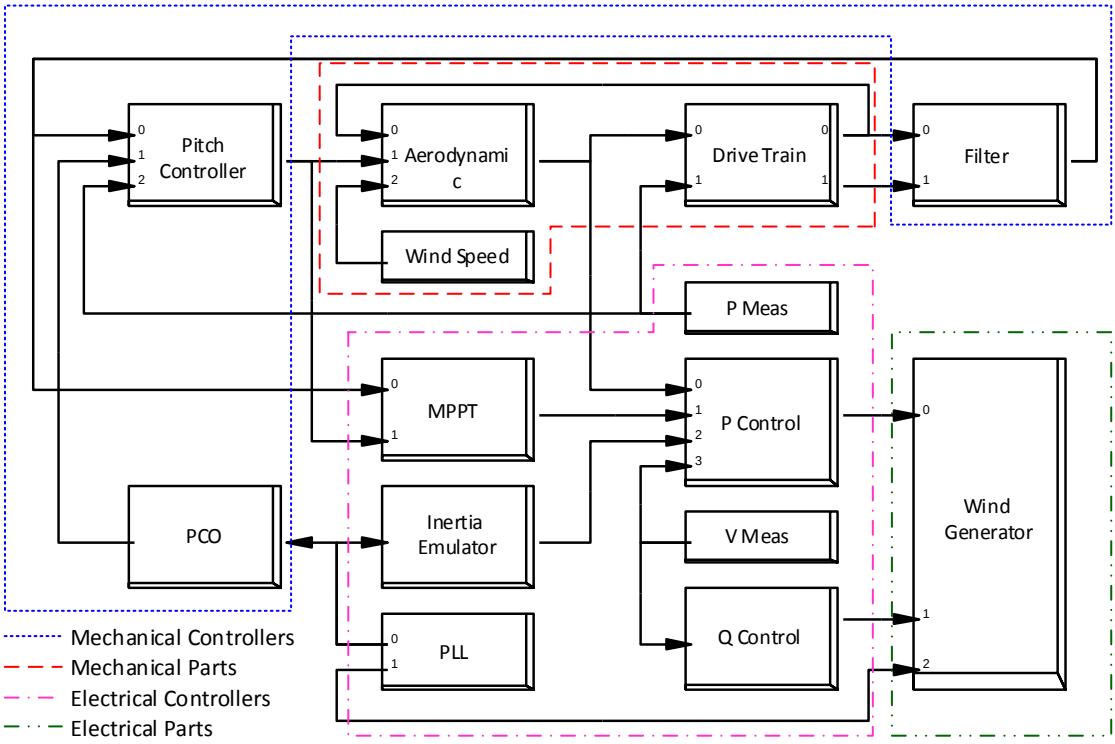

Figure 4-21: Control structure of wind energy conversion system in DIgSILENT PowerFactory.

4.8.1. WECS Primary Controller

A frequency droop control similar to the governing function in a steam turbine as WECS primary controller is simulated and shown in Figure 4-22 [35]. The input signal is the frequency deviation from its nominal value and *R* is speed regulation parameter or droop parameter, the speed at which the WECS primary controller can act. The governor delay time is Tlag and Presmax is the maximum WT reserve power margin. The rate of change of reserve power is restricted by 'Rate Limiter' block. The WECS primary controller parameters are listed in Table 4-2.

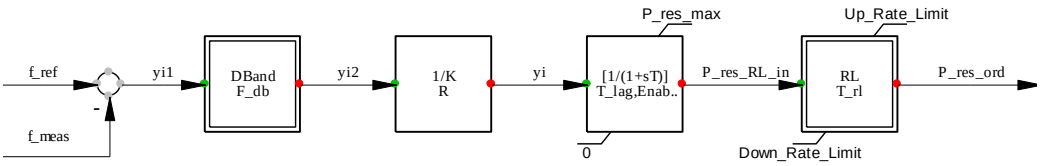

Figure 4-22: Outline of WECS Primary Controller in DIgSILENT PowerFactory.

Table 4-2: Parameters of the WECS Primary Controller.

Parameter	Value	Unit	Parameter	Value	Unit
F_{db}	0.0001	p.u.	R	0.05	p.u.
T_{lag}	1	s	$P_{res,max}$	0.1	p.u.
$Enable_{res}$	0/1	-	T_{rl}	0.02	s
Up Rate Limit	0.1	p.u./s	Down Rate Limit	-1	p.u./s

4.8.2. WECS Pitch Controller

A detailed diagram of pitch angle controller of WECS is shown in Figure 4-23. This consists of three main controllers of pitch, pitch compensation and servo motor. The reference angle is determined using the first two controllers in non-reserve power scenario. The servo motor spins the blades with the amount of reference angle [33]. Albeit the 'Primary Frequency Support' is part of 'WECS Primary Controller', this is located in 'Pitch Controller' due to similarity of PCO in WT and conventional power plant. In 'Primary Frequency Support', the reserve angle of 'Theta_res' is determined based on the available reserve power 'P_res_ava'. 'Theta_res' is the model of MPPT Curve shown in Figure 4-15. This curve is modelled based on 'Array_RT' located in 'Pitch Controller', as shown in Figure 4-24. 'RT' means that 'Reserve' specifies 'Theta'.

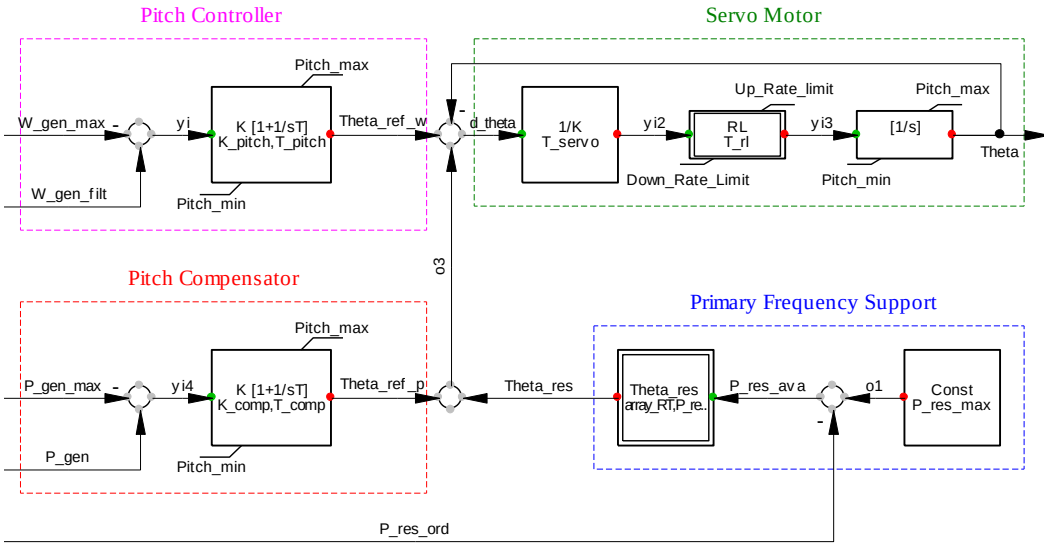

Figure 4-23: Outline of WECS Pitch Controller in DIgSILENT PowerFactory.

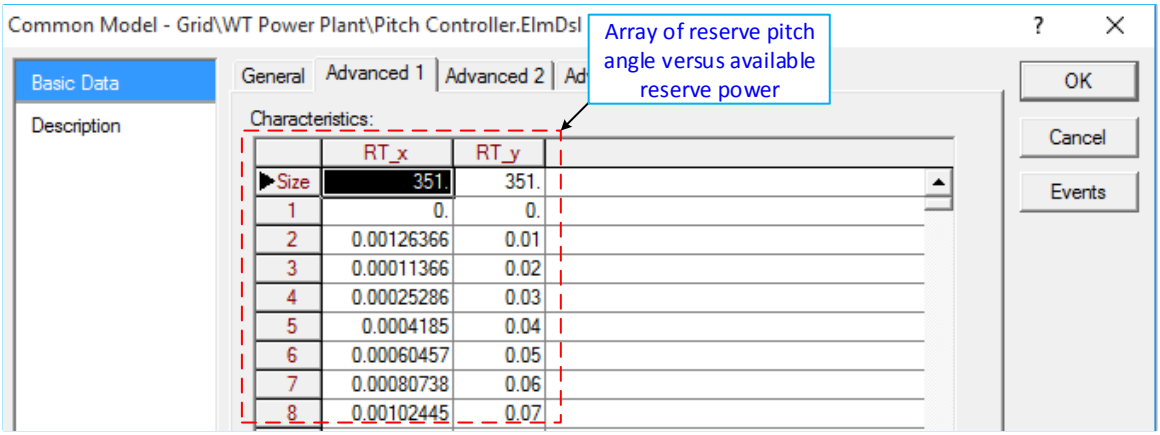

Figure 4-24: Characteristics array of reserve pitch angle versus available reserve power.

The pitch controller parameters are listed in Table 4-3. In order to avoid the reference angle oscillation following the incident and in case of low available reserve power it is presumed that if 'Theta_res' is equal to zero for 'Tpick' seconds, it will be zero for the rest 'Tdrop' seconds.

Table 4-3: Parameters of the WECS Pitch Controller.

Parameter	Value	Unit	Parameter	Value	Unit
$W_{gen,max}$	1.1	p.u.	$P_{gen,max}$	1.2	p.u.
K_{pitch}	38.6	deg/p.u.	T_{pitch}	2.2	s

K_{comp}	3	deg/p.u.	T_{comp}	0.1	s
T_{servo}	0.1	s	T_{rl}	0.05	s
$P_{res,max}$	0.1	p.u.	$Enable_{res}$	0/1	-
T_{pick}	10	s	T_{drop}	45	s
$Pitch_{min}$	0	deg	$Pitch_{max}$	27	deg
Up Rate Limit	10	p.u./s	Down Rate Limit	-10	p.u./s

4.8.3. WECS Aerodynamic

The WT aerodynamic in WECS is modelled by 'Aerodynamic' block shown in Figure 4-25. In this block, the WT power is calculated using (4.23) in terms of WT speed, wind speed and pitch angle [33].

4.8.4. WECS Drive Train

The WT blades are connected to hub which is linked to the WT shaft. The WT shaft which rotates slower than generator shaft, is connected to the generator shaft using gear box. Thus, the mechanical system of a WT is the drive train that contains of the rotating masses and the connecting shafts like a gear box. The resulting WT mechanical model is a two-mass with a connecting shaft, as indicated in Figure 4-25. This two-mass model for the mechanical dynamics of a WT is represented as follows [35]:

$$\begin{aligned}
\frac{d}{dt}\omega_{tur} &= \frac{1}{2H_{tur}}\left(T_{tur} - T_{shaft}\right) \\
\frac{d}{dt}\omega_{gen} &= \frac{1}{2H_{gen}}\left(T_{shaft} - T_{gen}\right) \\
\frac{d}{dt}\theta &= 2\pi F_{base}\left(\omega_{tur} - \omega_{gen}\right)
\end{aligned} \tag{4.42}$$

Where, T_{tur} and T_{gen} denote WT and generator torques, respectively. The torque of the shaft connecting WT and generator is T_{shaft}. The nominal frequency of WECS is F_{base}. θ illustrates the angle difference between WT (θ_{tur}) and generator (θ_{gen}) shafts as follows:

$$\theta = \theta_{tur} - \theta_{gen} \tag{4.43}$$

The turbine, generator and shaft torques can be calculated as follows:

$$T_{tur} = \frac{P_{tur}}{\omega_{tur}}, \qquad T_{gen} = \frac{P_{gen}}{\omega_{gen}}, \qquad T_{shaft} = K_{shaft}\theta + C_{shaft}\left(\omega_{tur} - \omega_{gen}\right) \tag{4.44}$$

With K_{shaft} and C_{shaft} as total shaft stiffness and total shaft damping, respectively. ω_{tur} and P_{tur} are WT speed and power, respectively. ω_{gen} and P_{gen} are generator speed and power, respectively. The state-space equation (4.42) consists of three eigenvalues in left side of imaginary axis (jw). One of this is real and other two are complex. The oscillation frequency of these eigenvalues is called as free-free frequency that can be expressed as follows:

$$f_{free-free} = \frac{1}{2\pi}\sqrt{\left(2\pi F_{base}\right)\left(\frac{K_{shaft}}{2}\right)\left(\frac{1}{H_{tur}} + \frac{1}{H_{gen}}\right)} \tag{4.45}$$

It means that shaft oscillates with $f_{free\text{-}free}$ following an imbalance between WT torque and generator torque since shaft is not perfectly stiff.

The WECS drive train is depicted by Figure 4-26 using (4.42) to (4.44). In this structure, the speed of WT's and generator's shaft is determined according to mechanical power of WT and electrical power of generator, respectively.

The WECS Drive Train is tabulated in Table 4-4 [35] so that the value of is 1.85 Hz.

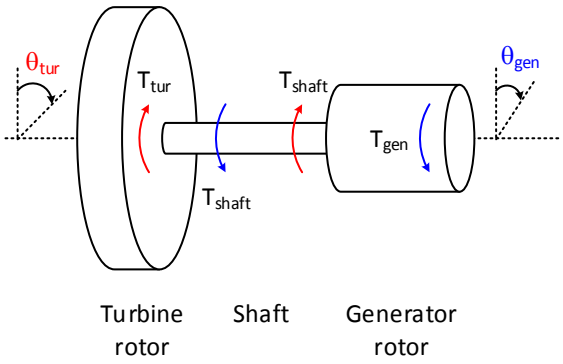

Figure 4-25: Two-mass schematic representation of the WECS Drive Train.

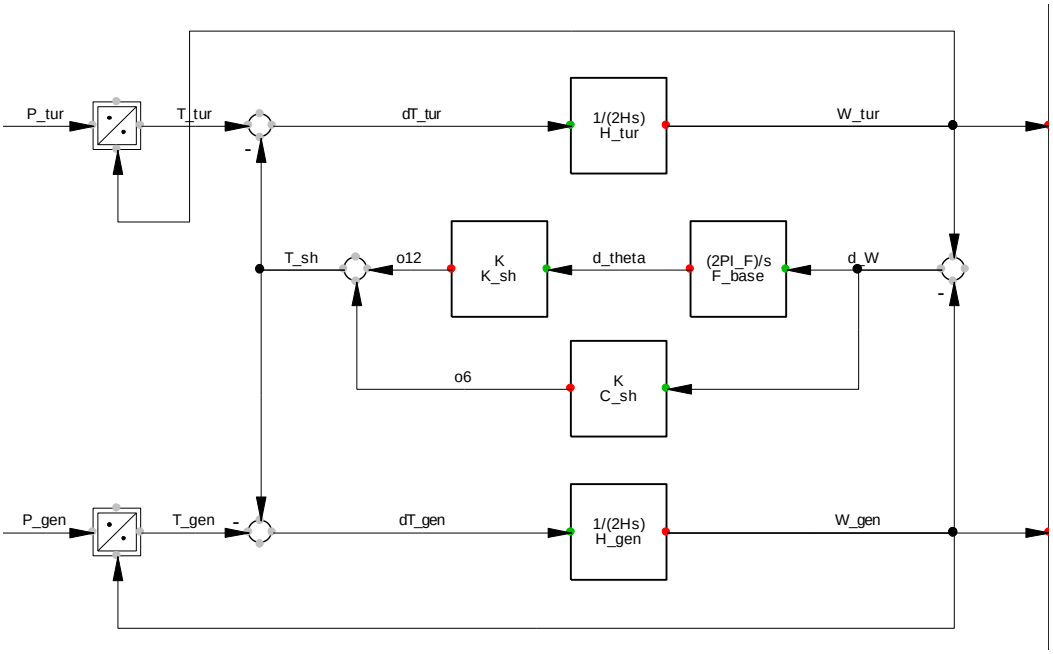

Figure 4-26: Outline of WECS Drive Train in DIgSILENT PowerFactory.

Table 4-4: Parameters of the WECS Drive Train.

Parameter	Value	Unit	Parameter	Value	Unit
F_{base}	50	Hz	H_{tur}	4.5	s
H_{gen}	0.75	s	K_{sh}	0.55	p.u./rad
C_{sh}	1.5	p.u.			

4.8.5. WECS Filter

The WECS filter is shown in Figure 4-27 in which the speeds of WT's shaft and generator are filtered by a low pass filter (LPF) with time constant of 0.2.

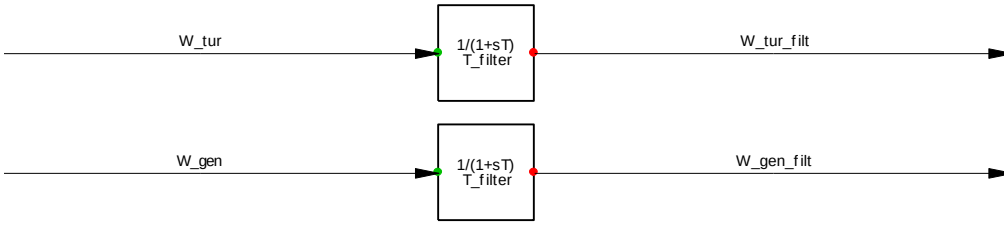

Figure 4-27: Outline of WECS Filter in DIgSILENT PowerFactory.

4.8.6. WECS Inertia Emulator

The VSWT generated power is controlled by power electronic converter. Unlike the conventional power plants, VSWTs are interfaced with the power network by power electronic converters. Thus, due the decoupled control between mechanical and electrical system, it efficiently avoids the WTs from responding to the system frequency changes. Thus, given the same disturbances, the rate of change of system frequency (RoCoF) and frequency nadir during first few seconds grows and drops rapidly with high wind penetration level. To get rid of this issue, the inertial emulator is appended into WECS controllers. The design idea of inertial emulator is to introduce a rate control which responds rapidly to the frequency change (See Figure 4-28). It is to be notified that in steady state, this controller is not activated. Firstly, the frequency error is measured so that the extra power is needed if it is low. The dead band suppresses response of the controller until the error exceeds a threshold. The purpose of the dead band is as follows: i) it prevents the control from acting on small variations (noise) and ii) it makes the controller unresponsive to the over-frequency events since they are less problematic while connecting WT into the grid. The dead band output signal is further filtered by LPF to reject measurement noise, multiplied by a Kie coefficient, passed through a 'wash out' block, and finally the rate of change and the amplitude of the generated signal limited by a 'Rate Limiter' and an amplitude limiter. In a condition that WECS should be substituted with conventional power plant with inertia constant of H, $K_{ie} \times T_{wo}$ are equal to 2H. In this figure, K_{ie} is the gain applied to the frequency deviation, and T_{lag} and T_{wo} is time constants associated with the lag and decay of the response respectively, df is the magnitude of the frequency deviation, f_{db} is the frequency dead band and Pie_{max} is the maximum power increase which can be demanded. The Up_Rate_Limit is restricted the rate of change of requested power Pie_{ord}.

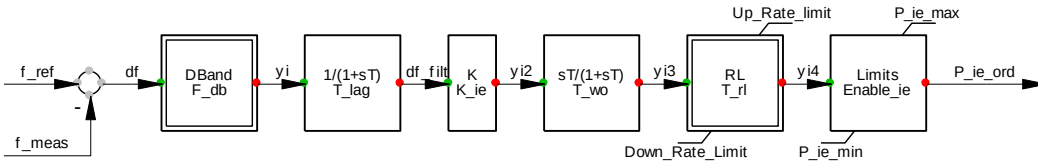

Figure 4-28: Outline of WECS Inertia Emulator in DIgSILENT PowerFactory.

The WECS inertia emulator parameters are listed in Table 4-5. The Pie_{ord} is limited to 0.1 p.u. Furthermore, the rate of change of this signal is selected as 1 p.u. per second. Baed on Kie and Two values tabulated in Table 5, the inertia constant H of synchronous generator (SG) equivalent with WT is 6.5 s.

Table 4-5: Parameters of the WECS Inertial Emulator.

Parameter	Value	Unit	Parameter	Value	Unit
F_{db}	0.0001	p.u.	T_{lag}	0.1	s
K_{ie}	130	-	T_{wo}	0.1	s
T_{rl}	0.02	s	$Enable_{ie}$	0/1	-
$P_{ie,min}$	0	p.u.	$P_{ie,max}$	0.1	p.u.
Up Rate Limit	1	p.u./s	Down Rate Limit	-1	p.u./s

4.8.7. WECS MPPT

One of the main parts of VSWT based WECS is MPPT, as shown in Figure 4-29. In this block, the P_{mppt} is determined using the generator shaft speed and blade pitch angle. Then, the rate of change of P_{mppt} is restricted by 'Rate Limiter' to a predefined value.

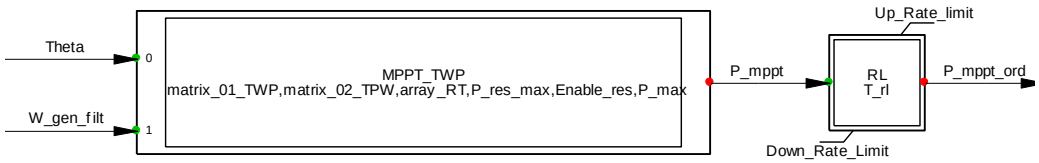

Figure 4-29: Outline of WECS MPPT in DIgSILENT PowerFactory.

In 'MPPT_TWP' depicted in Figure 4-29, two matrices are deployed to specify operating point of WT, as shown in Figure 4-30 and Figure 4-31, respectively. 'Matrix_TWP' determines power based on generator speed and pitch angle. The term 'TWP' means that both 'Theta' and 'Wgen' utilise to calculate P. In PowerFactory software, both 'Theta' and 'P_mppt' are characterised in Figure 4-29 following the load flow. As a result, another matrix is needed to determine the initial conditions of generator speed based on two aforementioned quantities, that is, 'Matrix_TPW' shown in Figure 4-31. Note, the matrices shown in Figure 4-30 and Figure 4-31 are the numeric representation of right and left sides' curves of Figure 4-16.

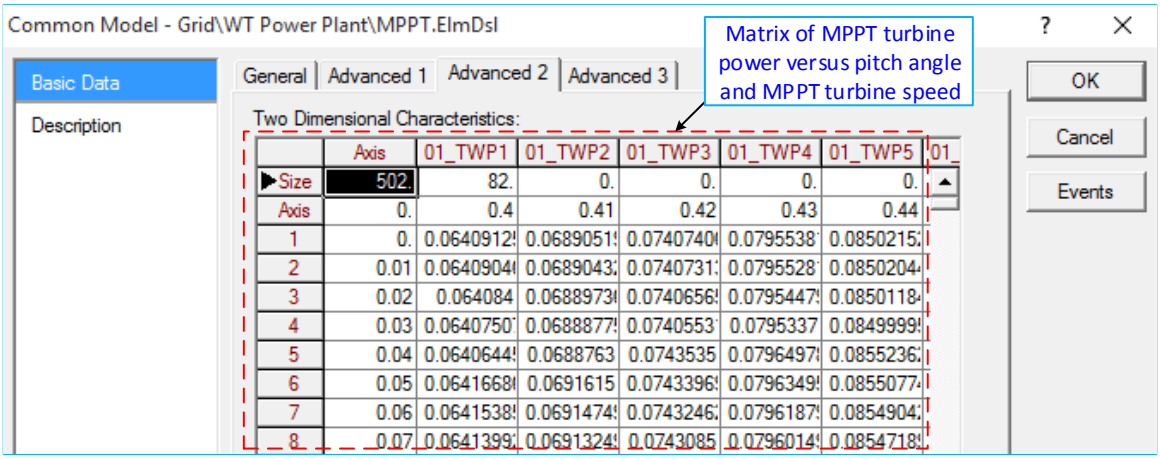

Figure 4-30: Characteristics matrix of MPPT turbine power versus pitch angle and MPPT turbine speed.

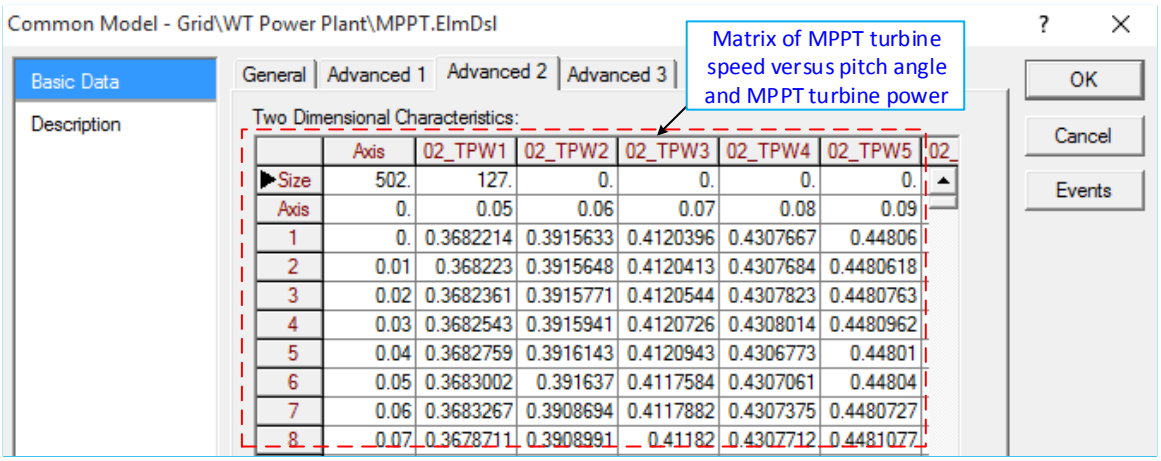

	Axis	02_TPW1	02_TPW2	02_TPW3	02_TPW4	02_TPW5	02_
▶Size	502.	127.	0.	0.	0.	0.	
Axis	0.	0.05	0.06	0.07	0.08	0.09	
1	0.	0.3682214	0.3915633	0.4120396	0.4307667	0.44806	
2	0.01	0.368223	0.3915648	0.4120413	0.4307684	0.4480618	
3	0.02	0.3682361	0.3915771	0.4120544	0.4307823	0.4480763	
4	0.03	0.3682543	0.3915941	0.4120726	0.4308014	0.4480962	
5	0.04	0.3682759	0.3916143	0.4120943	0.4306773	0.44801	
6	0.05	0.3683002	0.391637	0.4117584	0.4307061	0.44804	
7	0.06	0.3683267	0.3908694	0.4117882	0.4307375	0.4480727	
8	0.07	0.3678711	0.3908991	0.41182	0.4307712	0.4481077	

Figure 4-31: Characteristics matrix of MPPT turbine speed versus pitch angle and MPPT turbine power.

The WECS's MPPT parameters are given in Table 4-6.

Table 4-6: Parameters of the WECS MPPT.

Parameter	Value	Unit	Parameter	Value	Unit
T_{rl}	0.02	s	$Enable_{res}$	0/1	-
$P_{res,max}$	0.1	p.u.	P_{max}	1	p.u.
Up Rate Limit	0.1	p.u./s	Down Rate Limit	-1	p.u./s

4.8.8. WECS P Control

As discussed above, the proposed WECS needs to be appropriate for frequency response studies of large-scale networks and some simplifications are considered. One of them is to remove the current and power control loops in electrical controllers related to power electronic converters of WECS. After which, the active power control structure of WECS is converted to that shown in Figure 4-32. The input signals are the MPPT power, reference inertial power and the terminal voltage amplitude of WECS. The d-axis current component of static generator is the output signal of this controller that is equal to reference active power divided by voltage amplitude.

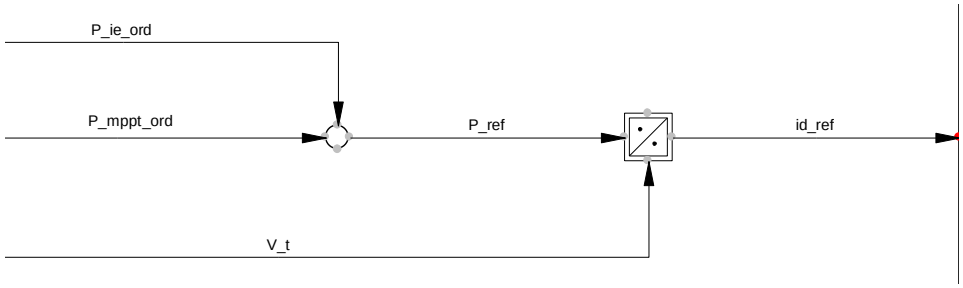

Figure 4-32: Outline of WECS P Control in DIgSILENT PowerFactory .

4.8.9. WECS Q Control

The reactive power controller design is illustrated in Figure 4-33 in which the reference power is obtained in order to control terminal voltage of WECS. The relevant parameters are taken from Table 4-7. The voltage controller is similar to static excitation system of conventional power plant. While Ka parameter is non-zero and zero, the WECS terminal type would be PV and PQ, respectively.

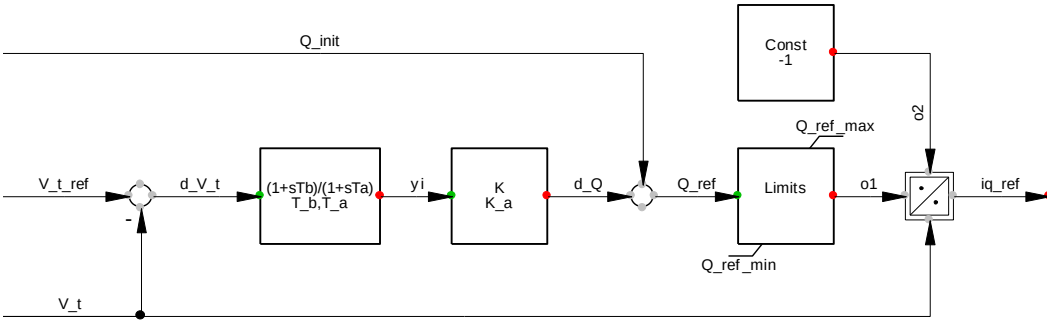

Figure 4-33: Outline of WECS Q Control in DIgSILENT PowerFactory.

Table 4-7: Parameters of the WECS Q Control.

Parameter	Value	Unit	Parameter	Value	Unit
T_a	1	s	T_b	10	s
K_a	200	-	$Q_{ref,min}$	-0.435	p.u.
$Q_{ref,max}$	0.435	p.u.			

4.8.10. WECS Phase Locked Loop (PLL)

The PLL is utilised to measure voltage angle and frequency of WECS terminal. The PLL structure which is shown in Figure 4-34 is a synchronous reference frame (SRF) PLL [36]. The Kp and Ki parameters of this PLL are 5 and 100, respectively.

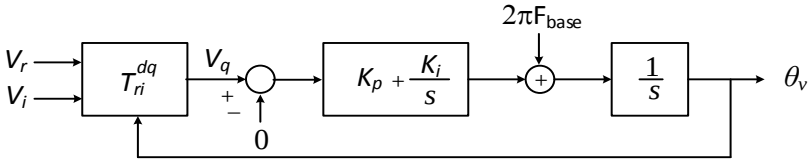

Figure 4-34: Outline of PLL in DIgSILENT PowerFactory.

4.9 Analysis of Two-Area System Considering WECS Integration

In this section, the frequency response of a modified version of the Klein-Rogers-Kundur (KRK) two-area multi-machine as the test system in two different scenarios of WT 25% and WT 50% is evaluated. The single line diagram of this benchmark system is shown in Figure 4-35. The total load demand of the network is 2734 MW and 200 Mvar. In non-WECS scenario, all the load demands are supplied by conventional power plants. It is to be noticed that 11 out of 12 units connected to buses 1, 2 and 4 are RST types. The SG 44 is hydroelectric unit. All four units connected to bus 3 are combined cycle gas turbine (CCGT). The nominal apparent power of all these units is 225 MVA and they inject 175 MW to the grid. The SG 11 is also considered as slack unit. In WT 25% scenarios, two units connected to bus 2 and two power plants from bus 4 are replaced with four WECSs. In WT 50% scenario, the reminding 4 units connected to buses 2 and 4 are substituted with 4 WECSs. In these two scenarios, the Q control of WECS is not activated.

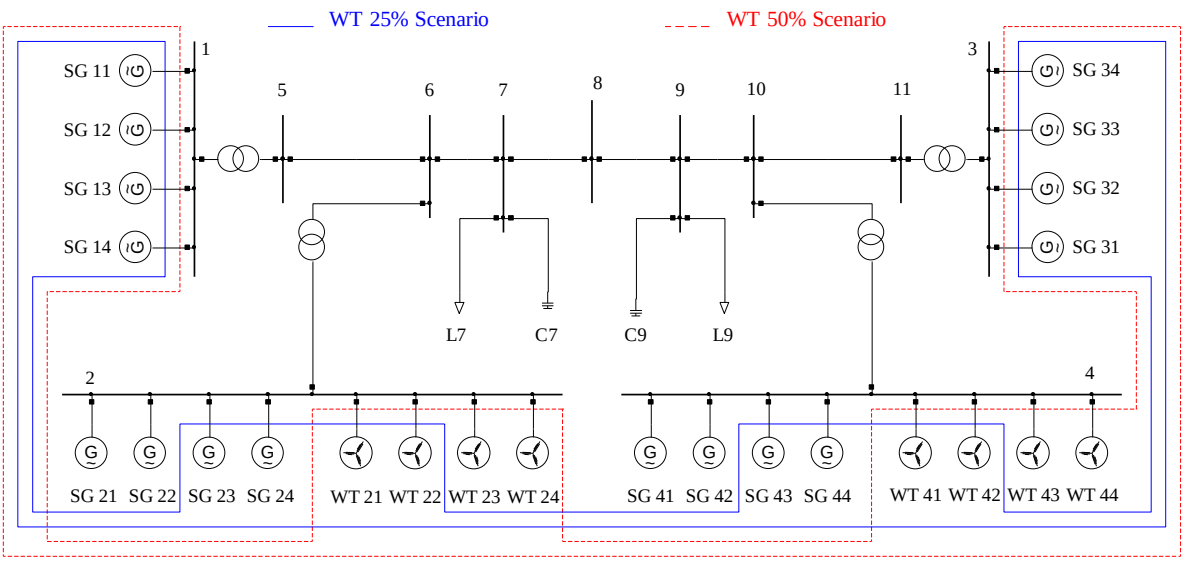

Figure 4-35: Single line diagram of the two area system.

4.9.1. Modal Analysis of Two-Area System Considering WECS Integration

This section investigates the application of the proposed WECSs design to the proposed two-area test system with high wind power penetration level and its effect on electromechanical modes using modal analysis in DIgSILENT PowerFactory. Figure 4-36 shows the system electromechanical modes for three aforementioned scenarios. In each scenario, there are 15 electromechanical modes. The six left hand side modes are related to buses 1 and 3 and they are like two groups of three modes with similar damping 5. As discussed above, since WECSs are not located in these two buses, these modes' location is not changed with increasing the numbers of WECSs. In WT 25% scenario with replacement of 4 conventional units with 4 WECSs, 4 modes of WECS with damped frequency of 2 Hz are substituted with 4 SGs' modes. It is noteworthy that the main reason behind of the different between frequencies of WT modes with 1.85 Hz in previous parts is that system frequency of two-area test system is considered to be 60 Hz. As a result, the contribution of SGs' modes is reduced from 15 to 11. Six out of these 11 modes are those six left hand side and the rest five are in right hand side with blue colour. In WT 50% scenario with replacement of all 8 units in buses 2 and 4 with 8 WECSs, the SGs' modes number is dropped down from 15 to 7. The red colour mode located in right hand side with the damping of 1.25 is one of these 7 modes. This mode is an inter-area mode between power plants connected to bus 1 and those in bus 3.

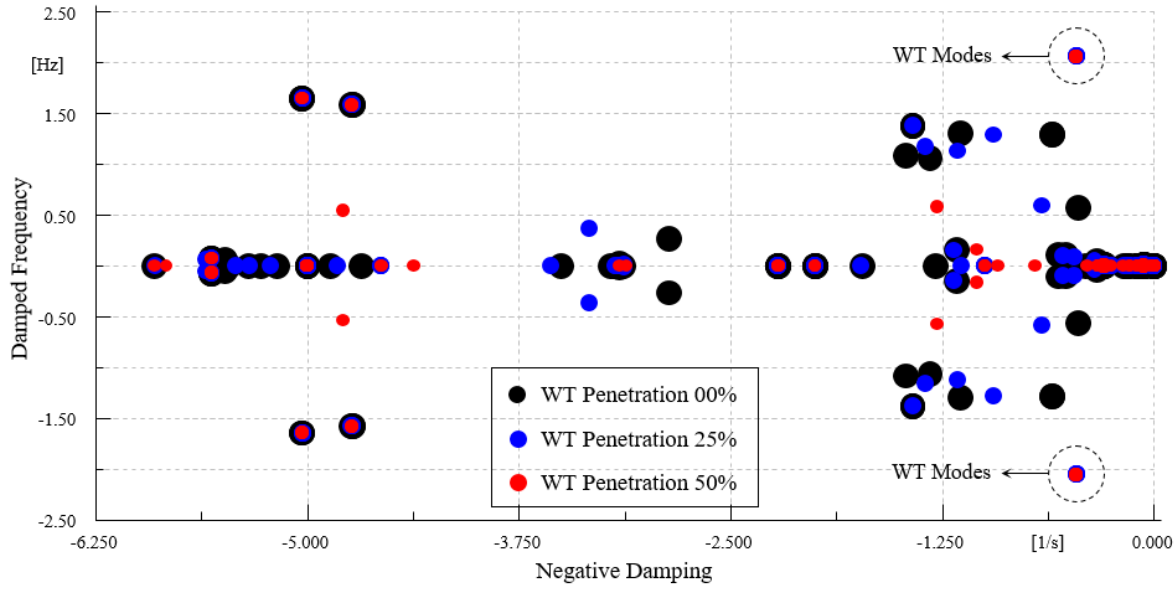

Figure 4-36: Electromechanical modes of the two area system with different WT penetration levels.

Figure 4-37 shows the impact of increasing the penetration of wind on damping the slowest electromechanical mode. Note, its damping is increased by WECS's numbers increment; however, its damped frequency is approximately fixed. The main reason for damping growth can be reduction of negative influence of SGs' exciters connected to buses 2 and 4 with increasing the numbers of WECSs.

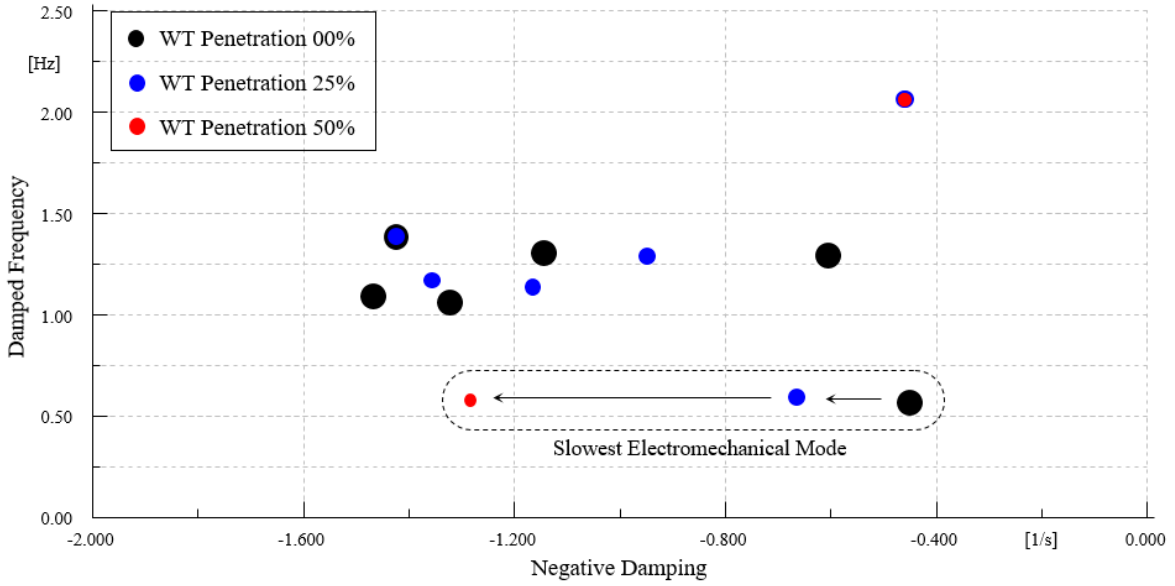

Figure 4-37: Slowest electromechanical mode of the two area system with different WT penetration levels.

4.9.2. Frequency Response of Two-Area System with Low Penetration of WECSs

In this subsection, the frequency response of two-area test system for low penetration of wind energy resources is investigated. Therefore, it is presumed that SG 14 unit is disconnected abruptly after 1 s after the simulation

start time. The simulation results related to WT 00% and WT 25% scenarios are shown in Figure 4-38 to Figure 4-43.

In order to accurately investigate WECSs, the WT 25% scenario is also divided into three sub-scenarios. In the first sub-scenario WT 25% I, the inertia emulator and PCO are deactivated for all WECSs. In the second sub-scenario WT 25% II, all inertial emulators are activated for all WECSs. Therefore, they are able to instantaneously inject power to the network following the event in order to reduce the RoCoF of COI. It is notable that the main idea of the controller is to respond quickly to frequency variation and enhance the frequency nadir as well as RoCoF. In last sub-scenario WT 50% III, both PCO and inertial emulator are activated to provide ancillary services to frequency event. The reserve power of WECSs is 10% of its generated power.

The COI frequency and RoCoF are shown in Figure 4-38 and Figure 4-39 for 4 abovementioned scenarios. The inertial power change and sum of turbine power variations of all conventional and WECSs are plotted in Figure 4-40 and Figure 4-41. It can be seen that the frequency nadir and steady-state frequency deviation are deteriorated for WT 25% I and WT 25% II scenarios compared to WT 00% one. However, the frequency response condition in terms of these two quantities in WT 25% III scenario is better than others. The frequency response in term of RoCoF for scenarios WT 25% II and WT 25% III which WTs are able to inject inertial power to the grid following the event, are located between WT 00% and WT 25% I scenarios. From the viewpoint of WTs power changes following the incident depicted in Figure 4-41, it is to be notified that frequency control support burden on SGs is apparently reduced for scenarios of WT 25% I and WT 25% II scenarios with respect to WT 00% one. However, what should be under scored is that the SGs' number are 12 and 16 for the first two scenarios and WT 00% scenario, respectively.

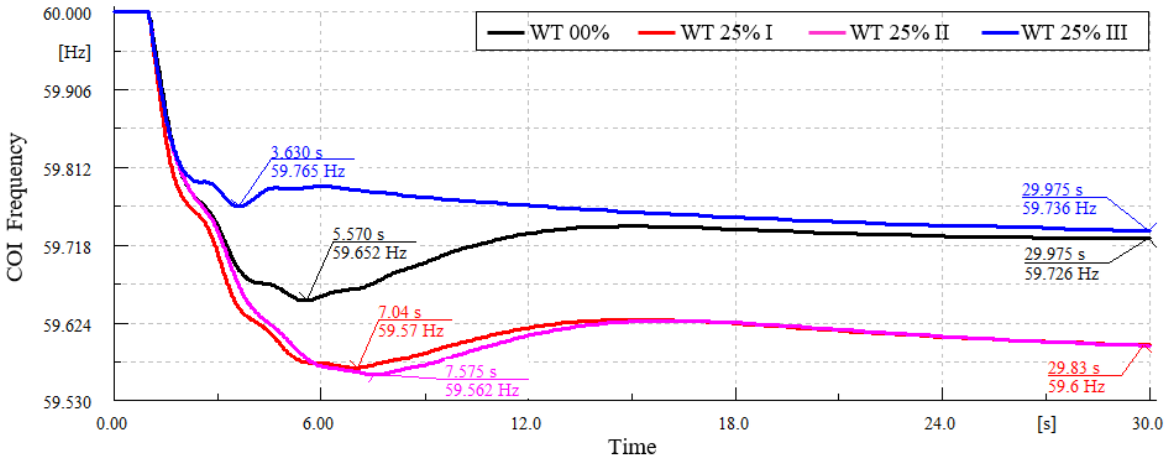

Figure 4-38: Frequency response with loss of 175 MW generation for WT 00% and WT 25% scenarios.

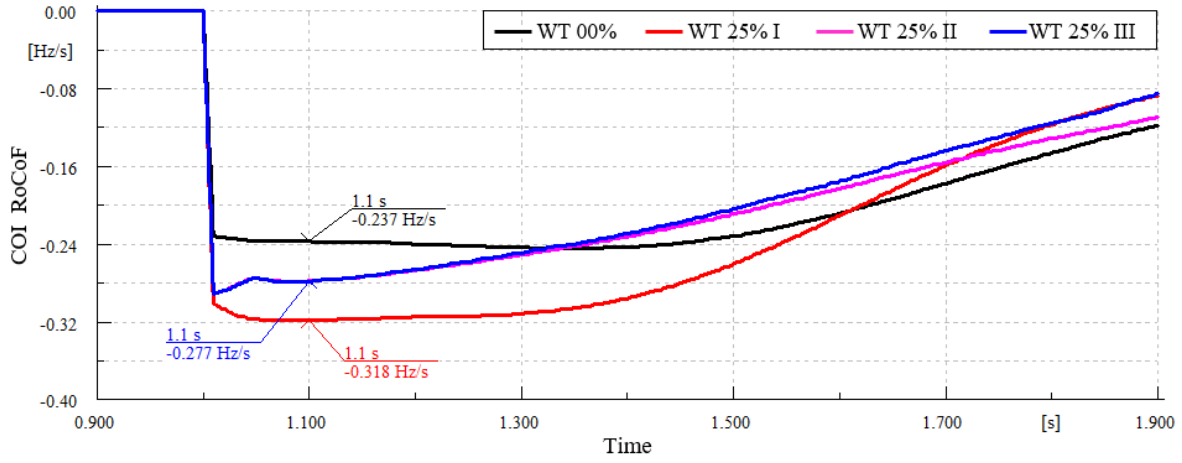

Figure 4-39: RoCoF with loss of 175 MW generation for WT 00% and WT 25% scenarios.

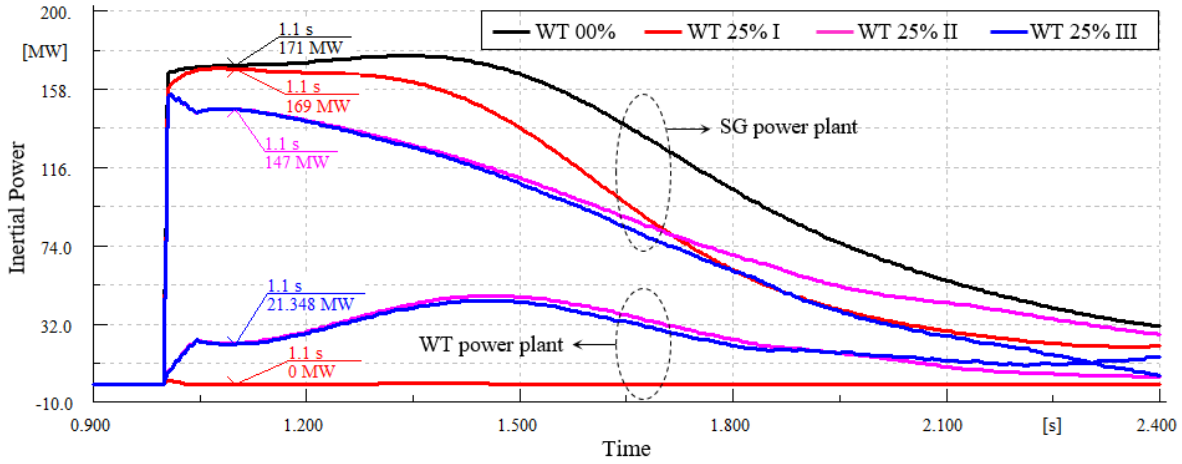

Figure 4-40: Inertial power changes with loss of 175 MW generation for WT 00% and WT 25% scenarios.

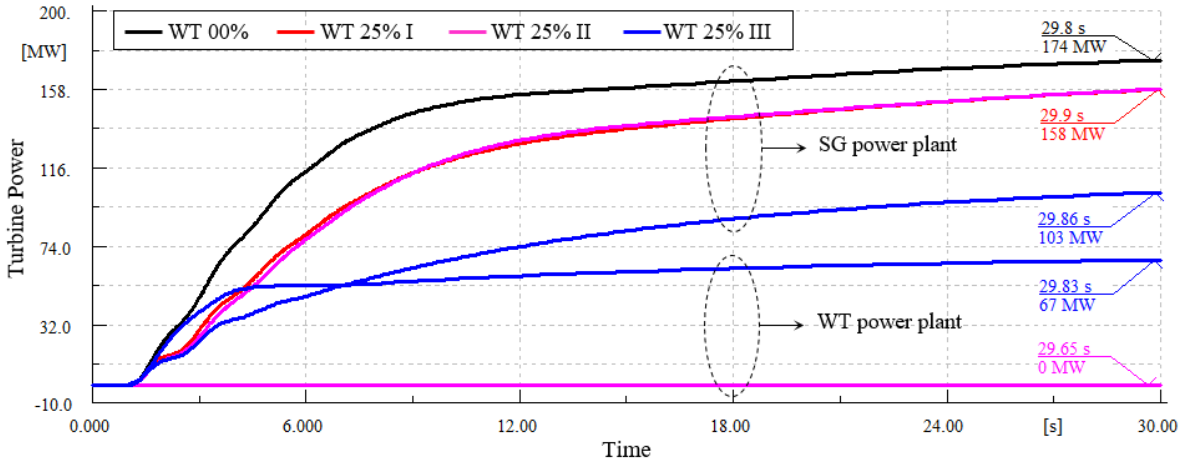

Figure 4-41: Turbine power changes with loss of 175 MW generation for WT 00% and WT 25% scenarios.

For the sake of more investigation, the WECS' quantities are shown in Figure 4-42 and Figure 4-43 for WT 25% scenario. Figure 4-42 portrays WT pitch angle, WT speed, power coefficient and WT reserve power changes. The pitch angle versus tip speed ratio and power coefficient versus pitch angle trajectories are also

shown in Figure 4-43. It is clear that the WTs' reserve power is mitigated from 10% to 1.4% in WT 25% III scenario. This in turn leads to WT speed reduction in this scenario.

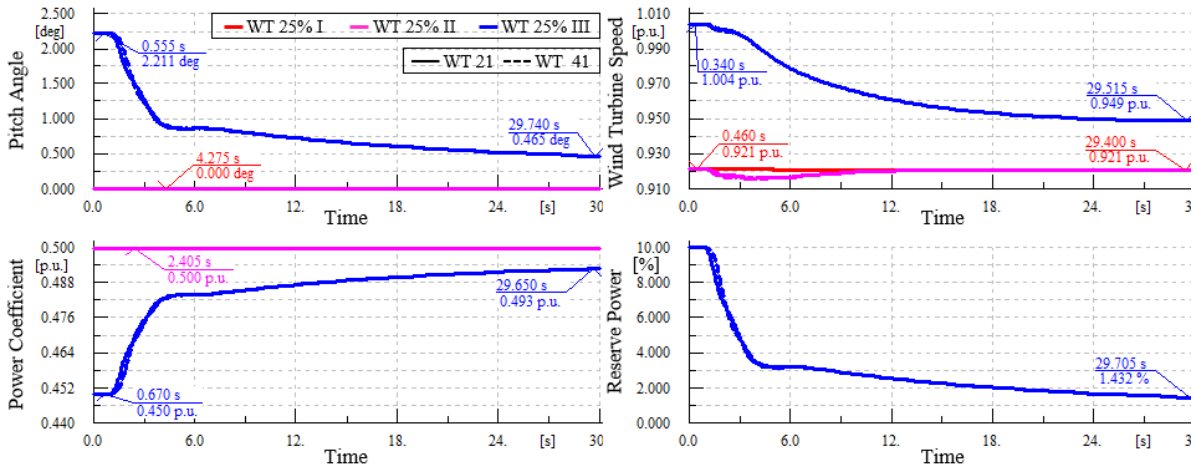

Figure 4-42: WT pitch angle, WT speed, power coefficient and WT reserve power changes with loss of 175 MW generation for WT 00% and WT 25% scenarios.

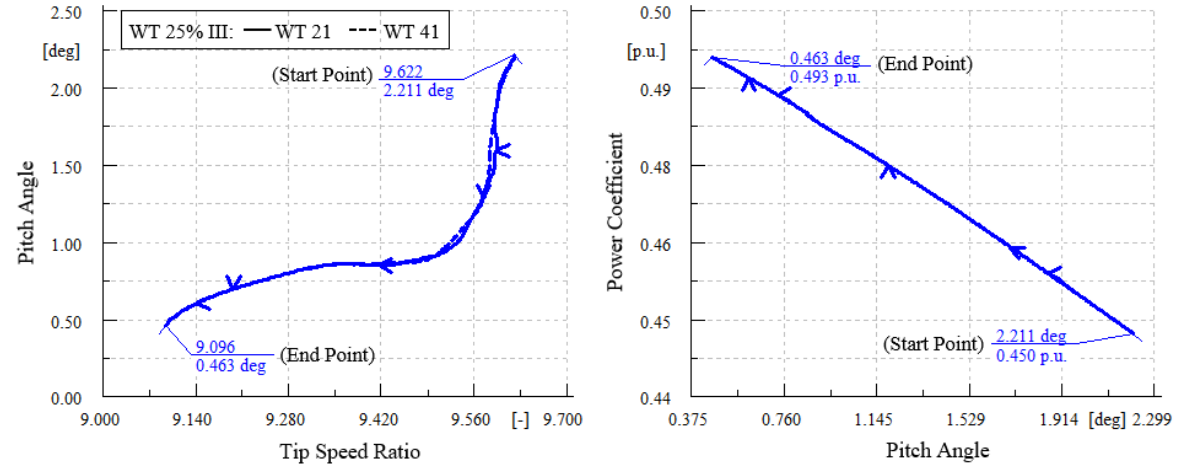

Figure 4-43: Pitch angle versus tip speed ratio, and power coefficient versus pitch angle trajectories with loss of 175 MW generation for WT 00% and WT 25% scenarios.

4.9.3. Frequency Response of Two-Area System with Medium Penetration of WECSs

In this subsection, the system frequency response for increasing the wind power penetration from 25% to 50% is investigated following SG 41. In both scenarios, all WECSs are equipped with inertial response and reserve power and the relevant results are shown in Figure 4-44 to Figure 4-49. It is observable that frequency nadir and steady-state frequency deviation are improved by increasing the WECS capacity from 25% to 50%. It means that a higher wind penetration yields a more responsive frequency regulation of the system, provided that the WECSs are equipped with the proposed governing function. This is in part because the inverter-based interfaces of WECSs are more flexible and can provide faster frequency response than conventional power plants. However, the system COI RoCoF is deteriorated. This is due to the fact that the WECSs have a lower rate of increment of inertial power than the conventional ones. Therefore, the inertial response of the WTs should not be exaggerated to trigger the conventional generators to increase their power output. Moreover, it should not be misunderstood that WECS based governor response has no impact on RoCoF entirely. Additionally, the WTs

reserve power at the end of simulation interval in WT 50% scenario is almost 0.8% larger than WT 25% one, as shown in Figure 4-48. It is to be noted that this value for the former scenario should be apparently two times compared to the later one. However, the WECSs' primary frequency support speed increment is higher than conventional ones.

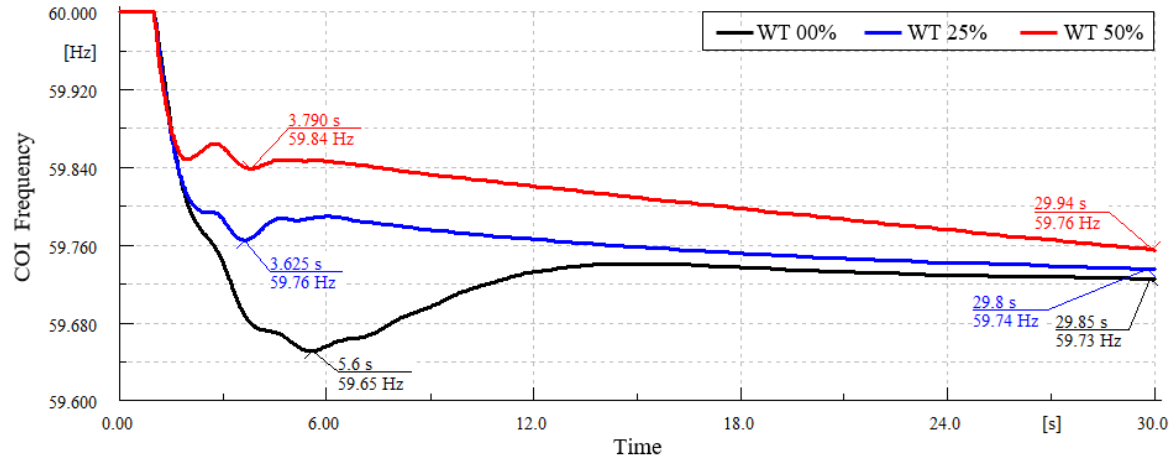

Figure 4-44: Frequency response with loss of 175 MW generation for WT 25% and WT 50% scenarios.

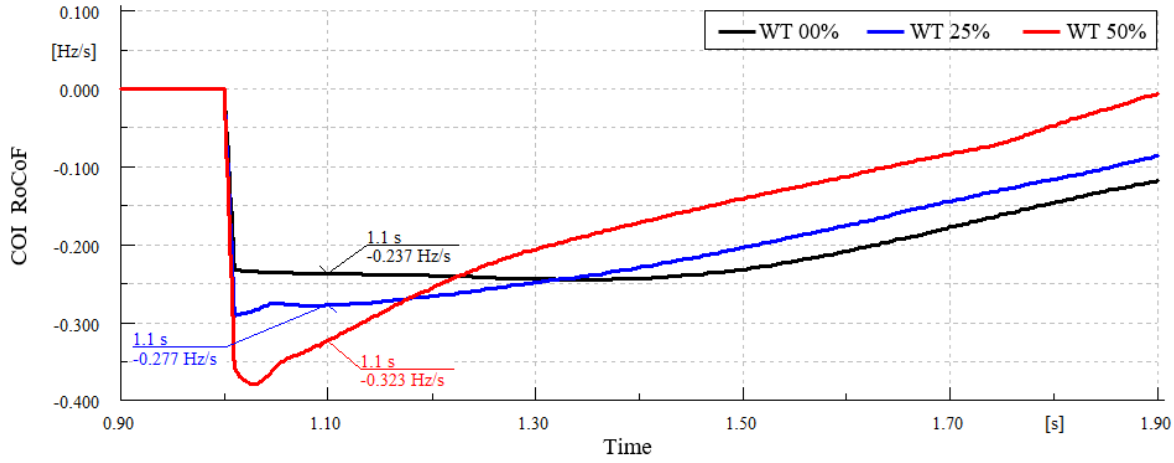

Figure 4-45: RoCoF with loss of 175 MW generation for WT 25% and WT 50% scenarios.

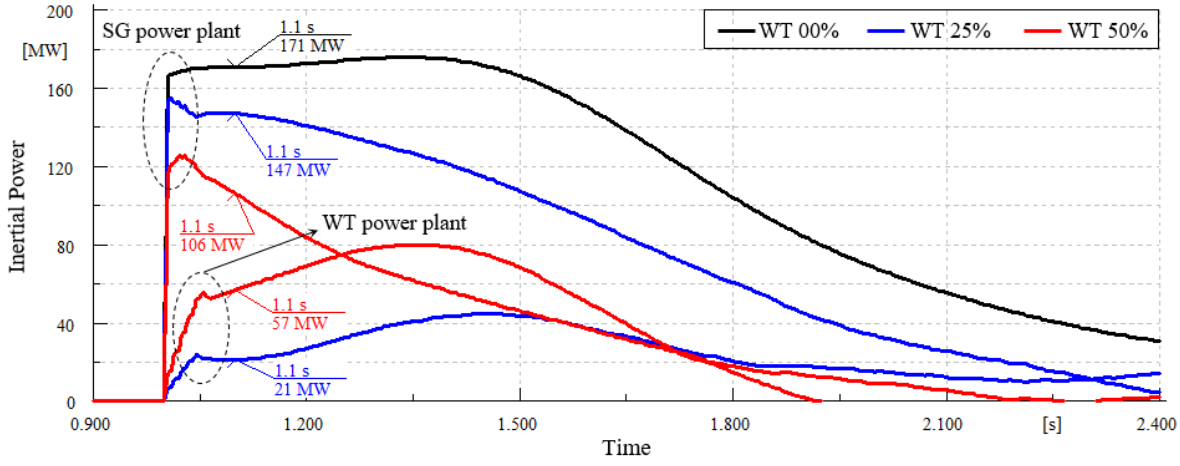

Figure 4-46: Inertial power changes with loss of 175 MW generation for WT 25% and WT 50% scenarios.

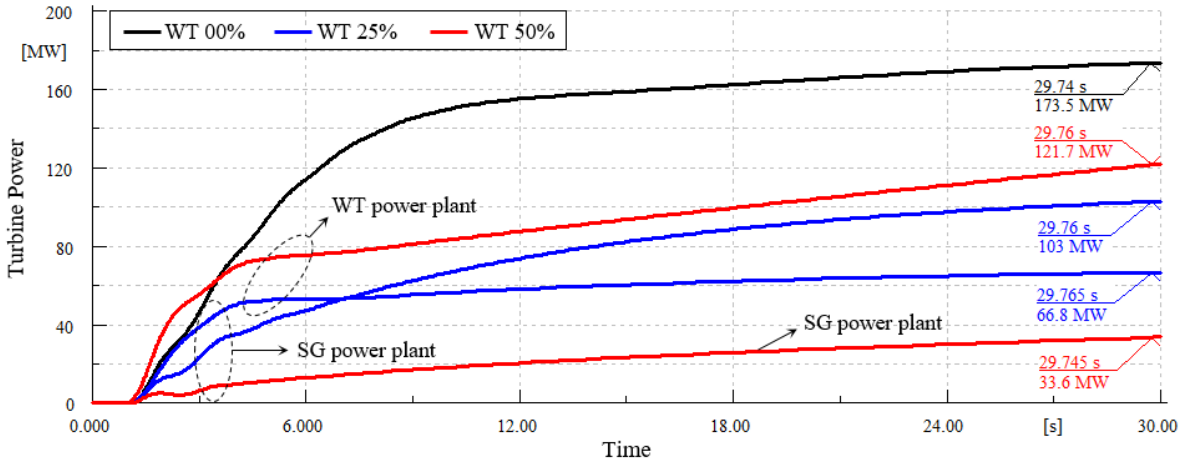

Figure 4-47: Turbine power changes with loss of 175 MW generation for WT 25% and WT 50% scenarios.

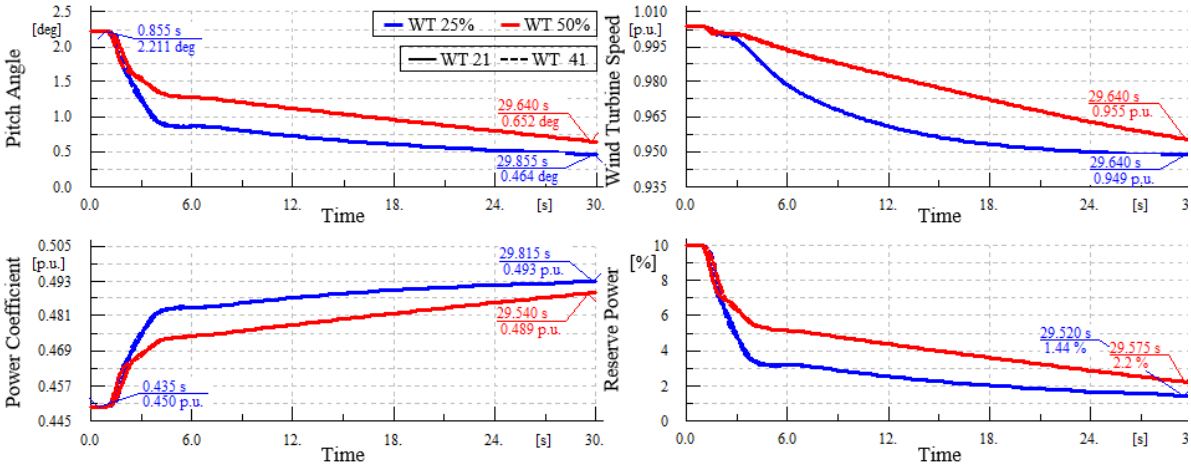

Figure 4-48: WT pitch angle, WT speed, power coefficient and WT reserve power changes with loss of 175 MW generation for WT 25% and WT 50% scenarios.

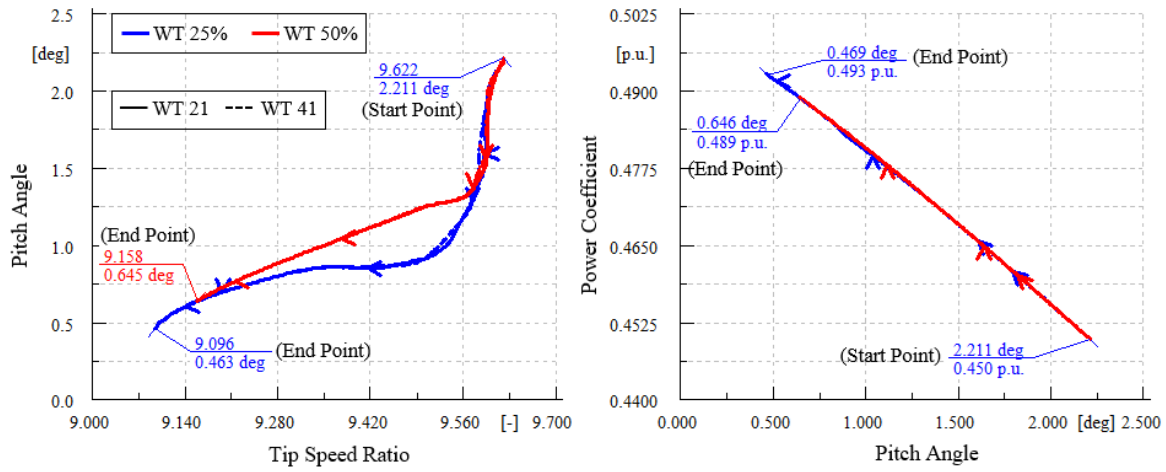

Figure 4-49: Pitch angle versus tip speed ratio, and power coefficient versus pitch angle trajectories with loss of 175 MW generation for WT 25% and WT 50% scenarios.

4.9.4. Executive Summary of Integrating WT in Two-Area test System

The dynamics of power system frequency are studied in this project study. A valid dynamic model of a VSWT based WECS is developed in DIgSILENT PowerFactory. The proposed WECS model performance in frequency response studies is investigated using modal analysis and time domain simulation approach. The proposed model is integrated into different benchmark systems including single-machine-infinite-bus, a simple multi-machine and modified 2-area KRK model. It is observed from the results that this model has two complex pairs related to drive train so that their damped frequency and damping are approximately independent of WECS loading and dependent just on drive train parameters. In time domain simulation analysis, it is found that once WT reserve power is considerably sufficient compared to the disturbance size so that WECS reserve power after the event is not zero, the network frequency response in terms of frequency response and steady-state frequency deviation is enhanced with respect to non-WECS case. However, the RoCoF is deteriorated. In two-area KRK test system, it is observed that the frequency nadir and steady-state frequency deviation are deteriorated for WT 25% I and WT 25% II scenarios compared to WT 00% one. However, the frequency response condition in terms of these two quantities in WT 25% III scenario is better than others. The frequency response in term of RoCoF for scenarios WT 25% II and WT 25% III which WTs are able to inject inertial power to the grid following the event, are located between WT 00% and WT 25% I scenarios. It is observable that frequency nadir and steady-state frequency deviation are improved by increasing the WECS capacity from 25% to 50%. It means that a higher wind penetration yields a more responsive frequency regulation of the system, provided that the WECSs are equipped with the proposed governing function. However, the system COI RoCoF is deteriorated. This is due to the fact that the lower rate of increment of inertial power than the conventional ones is considered for WECSs.

4.10 Analysis of 36-Zone GB Network Considering WECS based DFIG Integration

In this section, the WECS described in previous section is integrated into 36-zone GB network. It means that they contribute to supply 36-zone GB network load demand. The impact of DFIGs and a number of varying system conditions like high/low wind generation level, emulated inertia control and governor-like controls as PCO from WECS for several contingency events is investigated. In this regard, the generation level and geographical distributions of conventional power plants and WECSs across the network is firstly evaluated under their low and high penetration levels.

The generations and geographical distribution of conventional power plants in 36-zone GB network for three different scenarios of 0% (WT 00% scenario), 25% (WT 25% scenario) and 50% (WT 50% scenario) wind penetration levels are plotted in Figure 4-50. It can be seen that 90% of generated power is located in bottom i.e. England and Wales, while Scotland supplies only 10% of total load demand of 36-Zone GB network. It is obvious that the largest generating unit is nuclear power plant placed on zone 12 so that supplies 13% of total network load demand. The accurate power generation of each region and unit is tabulated in Table 4-8.

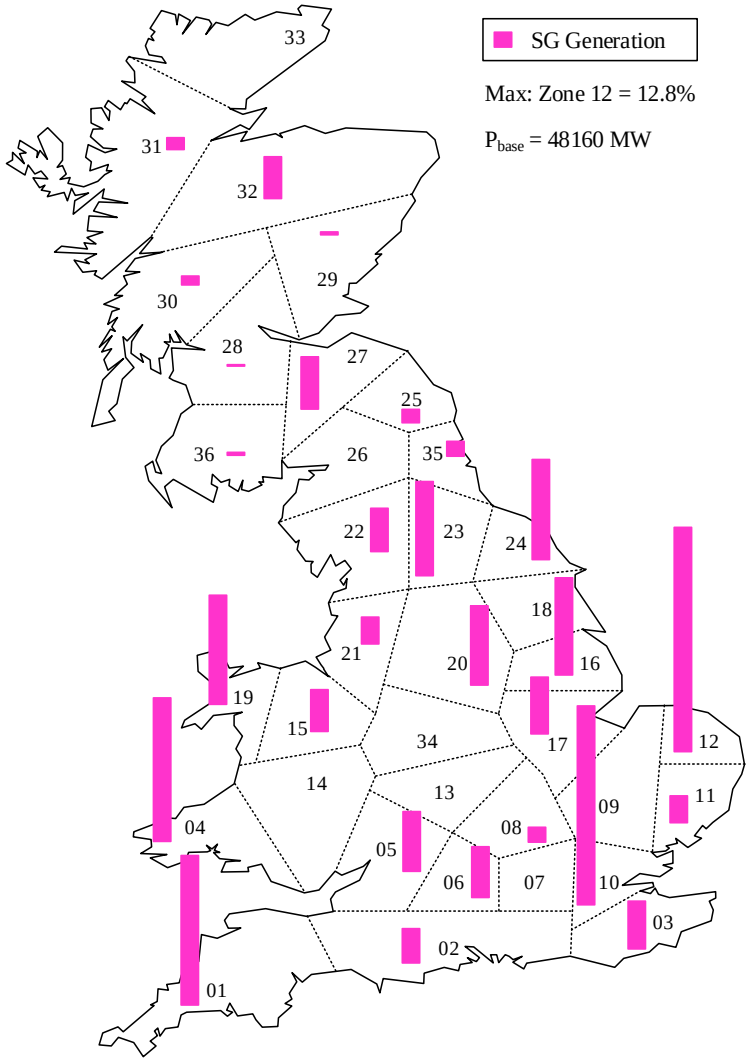

Figure 4-50: Geographic distribution of SG generation.

It is to be noted that two discrepant low and high penetration of wind units i.e. WT 25% Scenario and WT 50% Scenario are considered to investigate the effect of replacement of conventional generating units with WECSs. In these two scenarios, 25% and 50% of load demand are supplied by WECSs, respectively. Since total load demand of 36-zone GB network is 40 GW, total power generated by WECSs are 10 GW and 20 GW in aforementioned two scenarios. The accurate generated power of conventional power plants and WECSs are listed in Table 4-8 and Table 4-9. As shown, albeit the combined cycle gas turbines' (CCGTs') power capacity is reduced in consequence of WECSs' penetration level increment, the capacity of other conventional units is fixed. It is to be noted the power capacity of WECSs is zero in WT 00% Scenario.

Table 4-8: Active power of conventional power plants in two scenarios

No.	Type	Zone	Active Power in WT 00% Sc. (MW)	Active Power in WT 25% Sc. (MW)	Active Power in WT 50% Sc. (MW)
01	Gas	01	809	531	252
02	**Nuclear**	**01**	**3337**	**3343**	**3468**
03	Gas	02	946	620	294
04	Nuclear	03	1299	1301	1350
05	**Gas**	**04**	**3941**	**2585**	**1226**
06	BioMass	05	100	100	100
07	Gas	05	1575	1033	490
08	Gas	06	1385	909	431

09	Gas	08	420	276	131
10	BioMass	10	741	742	742
11	Gas	10	4732	3105	1473
12	Gas	11	751	493	234
13	Gas	12	1609	1055	501
14	Nuclear	12	4548	4555	4726
15	Gas	15	1180	774	367
16	Gas	16	2704	1774	841
17	Gas	17	1544	1013	481
18	Gas	19	617	405	192
19	**Nuclear**	**19**	**2398**	**2400**	**2400**
20	Gas	20	2172	1425	676
21	Gas	21	724	475	225
22	Nuclear	22	1202	1204	1249
23	**BioMass**	**23**	**1722**	**1724**	**1724**
24	Gas	23	858	563	267
25	Gas	24	2759	1810	859
26	BioMass	25	366	366	366
27	BioMass	27	120	120	120
28	Gas	27	107	70	33
29	**Nuclear**	**27**	**1214**	**1216**	**1261**
30	Gas	28	18	12	6
31	BioMass	29	52	52	52
32	Gas	29	14	9	4
33	Hydro	30	232	233	233
34	Hydro	31	321	322	322
35	Gas	32	11	7	3
36	Hydro	32	535	536	536
37	**Pump Storage**	**32**	**611**	**612**	**612**
38	BioMass	35	280	280	280
39	Gas	35	126	83	39
40	BioMass	36	45	45	45
41	Hydro	36	33	33	33
Total Active Power (MW)			48157	38209	28644

Table 4-9: Active power of wind power plants in two scenarios

Zone	Active Power in WT 25% Sc. (MW)	Active Power in WT 50% Sc. (MW)	Zone	Active Power in WT 25% Sc. (MW)	Active Power in WT 50% Sc. (MW)
01	**403**	**805**	**19**	**812**	**1624**
02	42	84	20	44	88
03	268	537	21	92	184
04	502	1003	22	440	880
05	23	45	23	183	366
06	12	24	24	706	1412
07	0	1	25	56	112
08	1	2	26	148	297
09	1	2	**27**	**827**	**1653**
10	164	328	28	294	589
11	23	45	29	106	212
12	**1448**	**2896**	30	93	186
13	91	183	31	228	455
14	28	57	**32**	**969**	**1938**
15	226	451	33	272	544
16	331	661	34	1	1
17	0	1	35	492	985
18	8	16	36	667	1334
			Total	10000	20000

In order to clearly understand how traditional generators are substituted with WECSs, the power change of these units for two scenarios of WT 25% and WT 50% with respect to base scenario of WT 00% is portrayed in Figure 4-51. It is to be noticed that the maximum variation is related to gas unit located in zone 10 so that its power generation in scenario WT 50% is dropped down by 70% compared to base scenario 00% WT. It can be also deduced that the power generation contribution of northern area is increased with respect to WT 00% scenario. It means that the replacement procedure is accomplished in a way to balance the geographical distribution of network generation between south and north of 36-zone GB model.

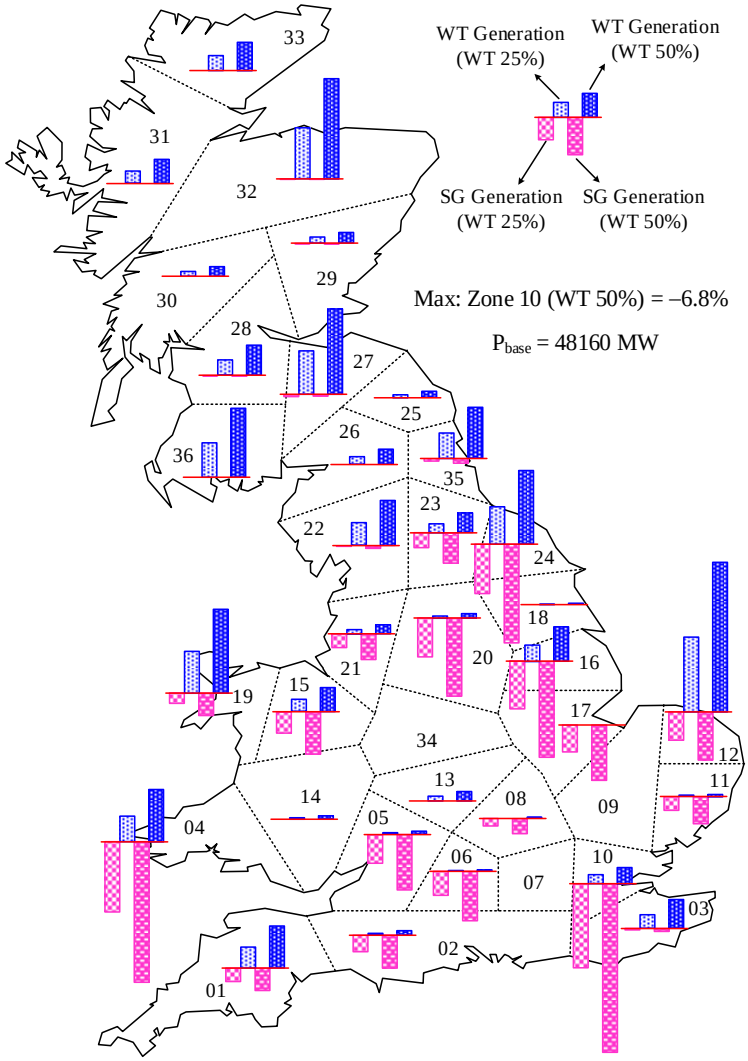

Figure 4-51: SG and WT generation deviations in “WT 25%” and “WT 50%” scenarios.

4.10.1. Modal Analysis of 36-Zone GB Network Considering WECS Integration

Figure 4-52 shows the variation of the electromechanical modes for three aforementioned scenarios with different wind conditions. It is to be noticed that some electromechanical modes are replaced with WT modes related to two-mass drive train once conventional power plants are substituted with WECSs. It is notable that their inertial and dynamic behaviour is also dependent on wind turbulence and the mechanical states of the drive train and tower. As can be seen from this figure, all electromechanical modes can be divided into two general categories of SG modes and WT modes. They represent dynamic behaviour of rotor for SG and WT,

respectively. The SG modes' damping and frequency are approximately fixed or slightly increased with wind penetration level increment.

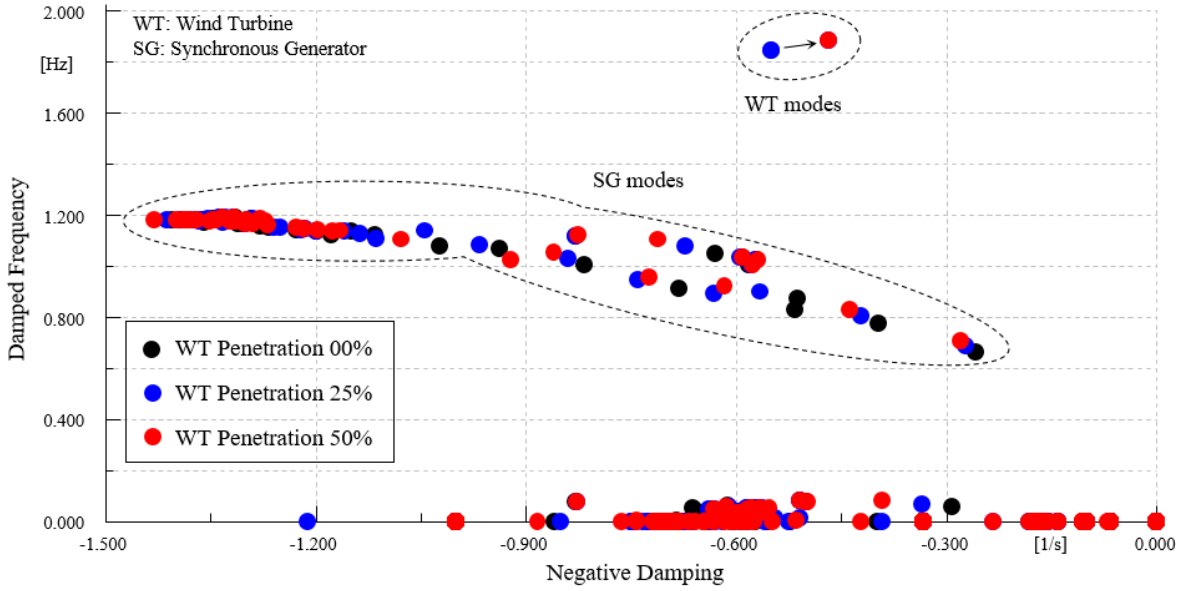

Figure 4-52: Effect of WECS integration in electromechanical modes.

Figure 4-53 portrays the influence on the electromechanical modes from the wind penetration level increment specifically for two slowest electromechanical modes from different scenarios. It can be deduced from the results presented in this figure that a higher wind penetration yields a more responsive frequency regulation of the network, provided that the damping and frequency pf electromechanical modes are increased. This is due to the fact that negative effect of conventional generating unit i.e. damping reduction is reduced since some part of their capacities is replaced with WECSs.

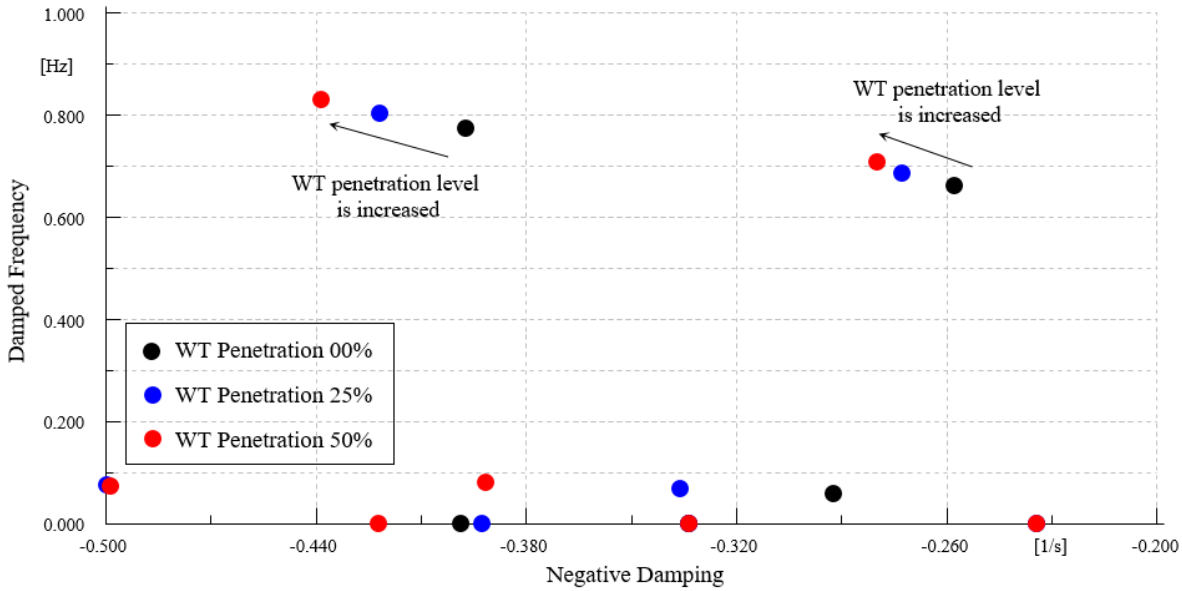

Figure 4-53: Effect of WECS integration in two slowest electromechanical modes.

4.10.2. Frequency Response of 36-Zone GB Network with Low Penetration of Wind Energy Conversion Systems

In this section, the GB system frequency response following loss of some generators is investigated for low penetration of WECSs. To this end, 6 different losses of generators from discrepant parts of the network are selected as depicted in Figure 4-54. In the following, different criteria related to SFR like the centre of inertia (COI) frequency variation and RoCoF change for loss of generator at time equal to one second for 30 seconds after the event are evaluated for two scenarios of WT 00% and WT 25%. It is to be notified that step size for time domain simulation is equal to 0.005 s.

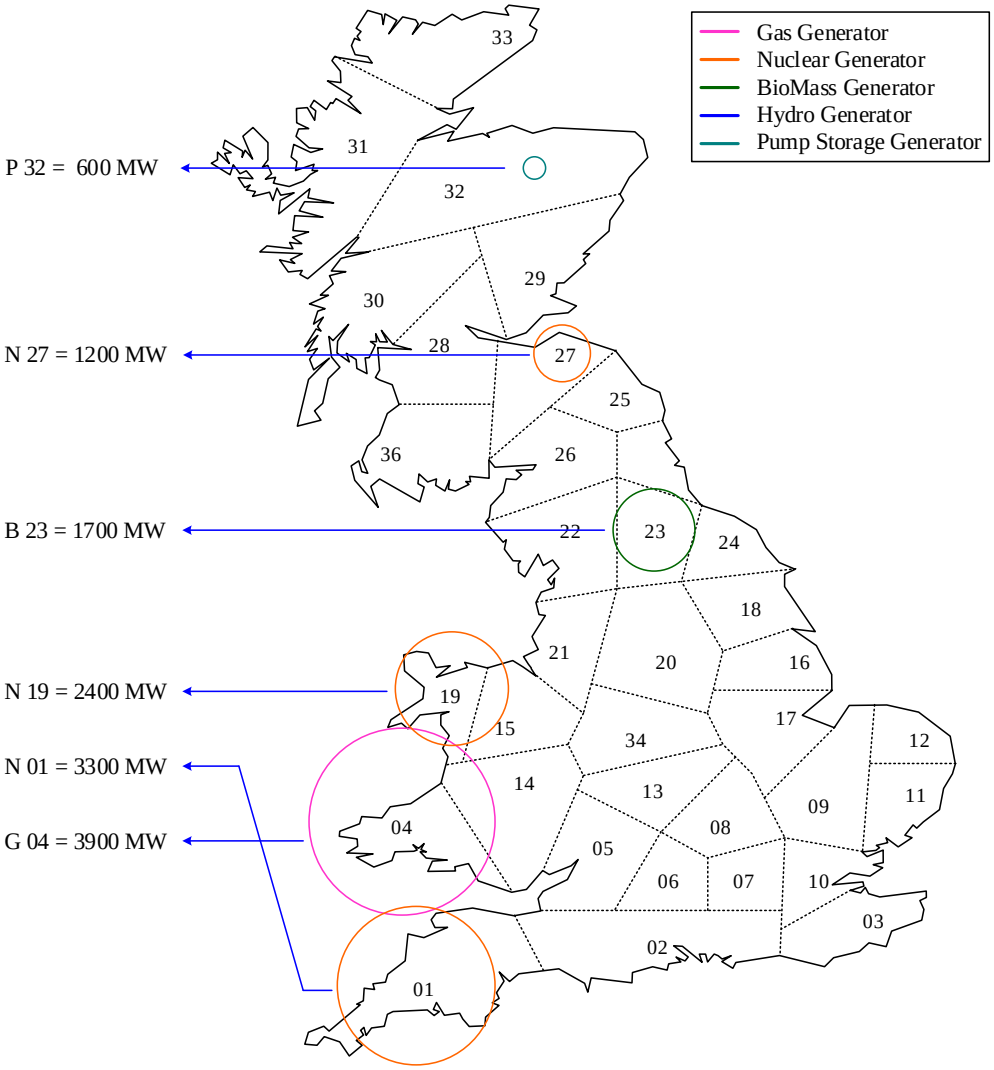

Figure 4-54: Geographic distribution of selected loss of generation.

In order to monitor and investigate the system frequency response of WECSs alongside of conventional units' response, the 36-zone GB network is divided into 5 geographical regions, as shown in Figure 4-55. In each region, the frequency response curves and quantities of WECSs highlighted by 'Measurement Point' are tabulated for each incident.

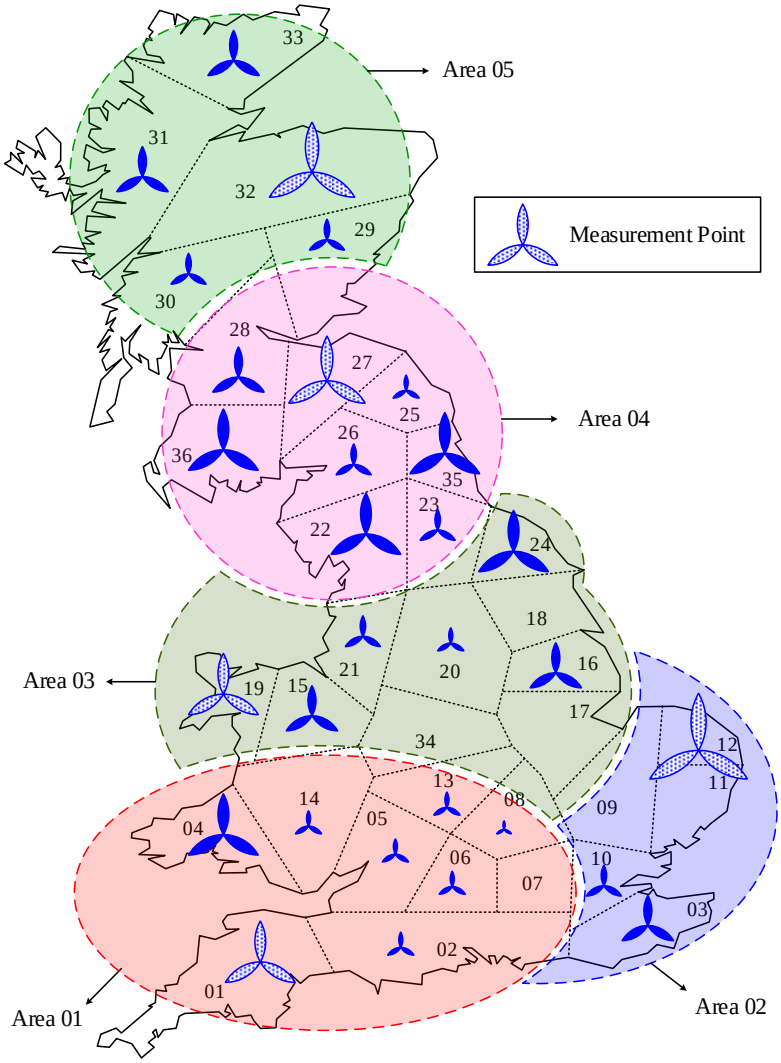

Figure 4-55: Area boundaries and measurement points.

4.10.3. Loss of 1,700 MW Generation in Zone 23

In this event, the biomass unit located in zone 23 with the capacity of 1,700 MW is abruptly disconnected. The results are illustrated in Figure 4-56 to Figure 4-58 for WT 00% and WT 25% scenarios. The expression of (1722-1724 MW) in these figures indicates the loss of generators for these respective two scenarios i.e. 1722 MW and 1724 MW. In order to accurately investigate WECSs, the WT 25% scenario is also divided into three sub-scenarios. In the first sub-scenario WT 25% I, the inertia emulator and PCO are deactivated for all WECSs. It means that the power output of WECS is independent of network frequency deviation and it is fixed in both pre- and post-contingency states. In the second sub-scenario WT 25% II, all inertial emulators are activated for all WECSs. Therefore, they are able to instantaneously inject power so-called 'Inertial Power' to the network following the event in order to reduce the RoCoF of COI. It is notable that the main idea of the controller is to respond quickly to frequency variation and enhance the frequency nadir as well as RoCoF. In last sub-scenario WT 25% III, both PCO and inertial emulator are activated to provide ancillary services to frequency event. Whilst both synchronous (PCO) and emulated inertial responses of WECSs act in the time-frame before the full governor droop response provision, there is a delay due to a dead-band in inertial emulator to prevent false triggering. It is to be noticed that PCO is considered to support the WECSs for participating in the frequency response and the WECSs should operate at partial load, ensuring sufficient reserve power at any instant. This is

de-loading mode that can be deployed to tune the active power output of WT. Then, the active power obtained by each WT can drop down or up to complement the system frequency deviations. It is also notable that this power is injected simultaneously with inertial power following the in-feed.

The COI frequency change for the above mentioned four scenarios is shown in Figure 4-56 and Figure 4-57. The COI RoCoF variation for the first few seconds after the event is portrayed in Figure 4-68. Based on Figure 4-56 and Figure 4-57, it can be seen that system frequency of WT 00% scenario is more than WT 25% I for the first six seconds following the disturbance, while it is less than that after this interval. The main reason for this phenomenon is that the initial power in WT 25% I is less than WT 00% due to replacement of gas turbines with WECSs without inertial emulator. Consequently, this can lead to the situation that COI RoCoF in WT 25% I scenario is more than other, as shown in Figure 4-58. For the sake of comparison of system frequency for the interval 4 to 30 s, the system frequency of WT 25% I should be apparently less than that of WT 00% since some of conventional units are replaced with WECSs which are not equipped with reserve power. However, as it can be seen from Figure 4-56 and Figure 4-57, it is not true. The main reason for this matter is that WTs are replaced with CCGTs. These units work based on their base load operation mode before the disturbance and their power outputs will be dropped down following the frequency excursion. As a result, the replacement of these power plants with WECSs (Even WECSs without primary frequency support ability) can enhance primary frequency control support. Moreover, the SGs' turbine power in WT 25% I in WT 25% I is less than those of WT 00% scenario. Therefore, the steady state value of frequency in first scenario is more than the second one.

In scenario WT 25% II, the inertial emulator of all WECSs are activated. Therefore, all WECSs inject inertial power to grid following the event. This can reduce COI RoCoF with respect to WT 25% I. However, the frequency nadir and steady-state value of frequency are not changed compared to WT 25% I since reserve power is neglected for WECSs. Finally, all PCO blocks are activated in WT 25% III scenario and reserve power is incorporated. The R parameter in PCO block is 0.05 for all WECSs. As a result, 640 MW out of 1500 MW primary frequency responses is generated by WECSs in this scenario. This reduces frequency nadir and its steady state value by 40% and 40% compared to WT 25% II scenario.

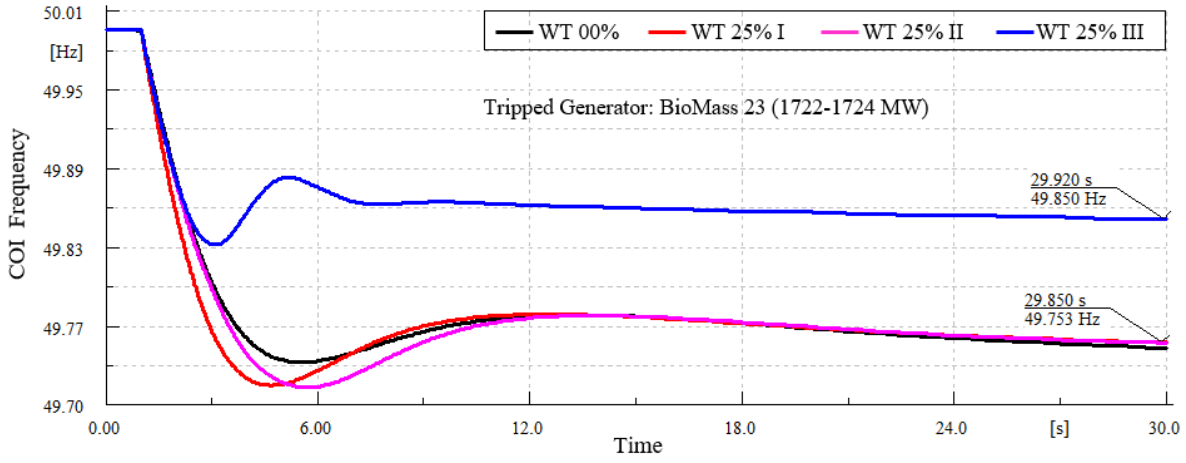

Figure 4-56: Frequency response with loss of 1700 MW generation in middle of network (Zone 23).

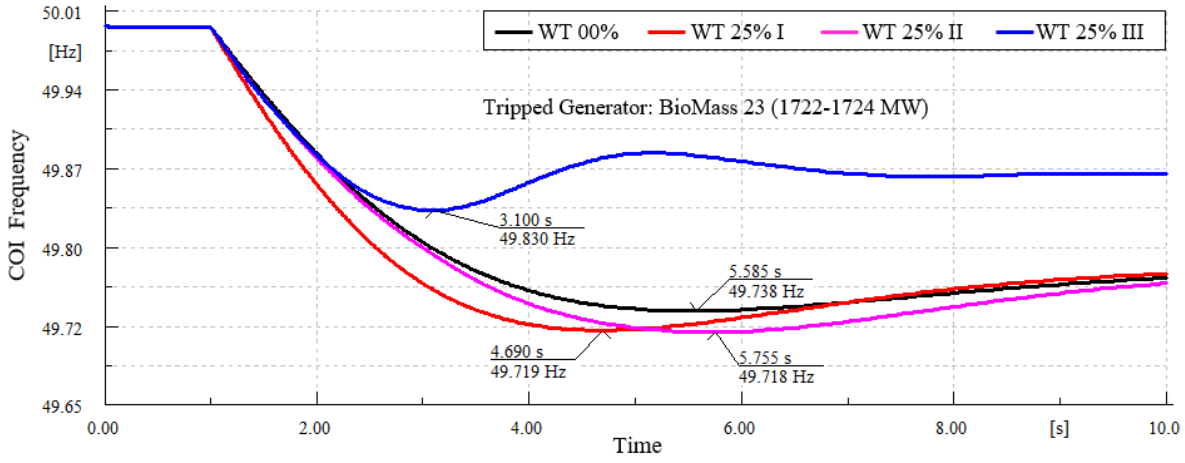

Figure 4-57: Frequency nadir with loss of 1700 MW generation in middle of network (Zone 23).

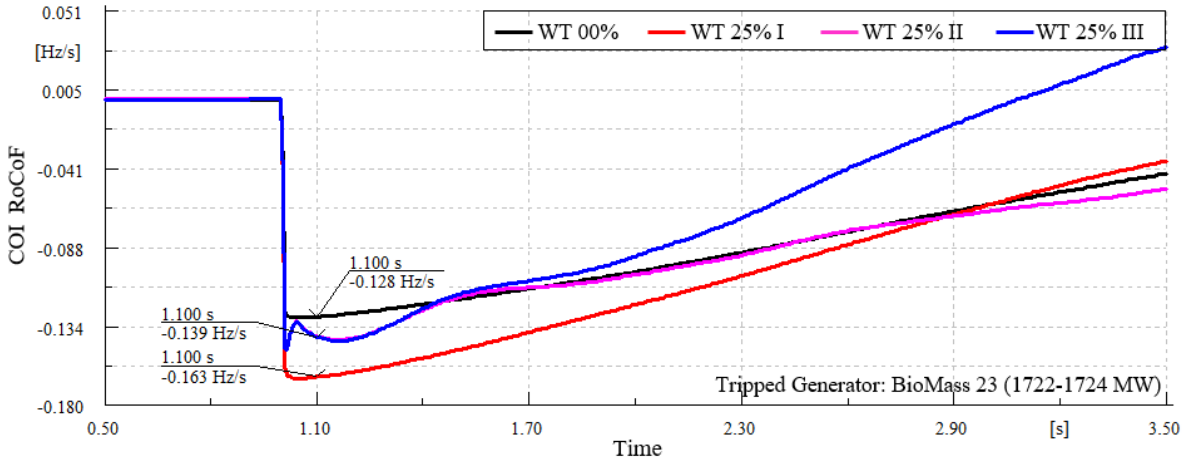

Figure 4-58: RoCoF deviations with loss of 1700 MW generation in middle of network (Zone 23).

4.10.4. Loss of 2,400 MW Generation in Zone 19

In this event, the nuclear unit located in zone 19 with the capacity of 2,400 MW is abruptly disconnected. The results are illustrated in Figure 4-59 to Figure 4-61 for WT 00% and WT 25% scenarios. The expression of (2398-2400 MW) in these figures indicates the loss of generators for these respective two scenarios i.e. 2398 MW and 2400 MW. In order to accurately investigate WECSs, the WT 25% scenario is also divided into three sub-scenarios. In the first sub-scenario WT 25% I, the inertia emulator and PCO are deactivated for all WECSs. It means that the power output of WECS is independent of network frequency deviation and it is fixed in both pre- and post-contingency states. In the second sub-scenario WT 25% II, all inertial emulators are activated for all WECSs. Therefore, they are able to instantaneously inject power so-called 'Inertial Power' to the network following the event in order to reduce the RoCoF of COI. It is notable that the main idea of the controller is to respond quickly to frequency variation and enhance the frequency nadir as well as RoCoF. In last sub-scenario WT 25% III, both PCO and inertial emulator are activated to provide ancillary services to frequency event. Whilst both synchronous (PCO) and emulated inertial responses of WECSs act in the time-frame before the full governor droop response provision, there is a delay due to a dead-band in inertial emulator to prevent false triggering. It is to be noticed that PCO is considered to support the WECSs for participating in the frequency response and the WECSs should operate at partial load, ensuring sufficient reserve power at any instant. This is

de-loading mode that can be deployed to tune the active power output of WT by rotor speed control. Then, the active power obtained by each WT can drop down or up to complement the system frequency deviations. It is also notable that this power is injected simultaneously with inertial power following the in-feed.

The COI frequency change for the above mentioned four scenarios is shown in Figure 4-59 and Figure 4-60. The COI RoCoF variation for the first few seconds after the event is portrayed in Figure 4-61. Based on Figure 4-59 and Figure 4-60, it can be seen that system frequency of WT 00% scenario is more than WT 25% I for the first 5.5 seconds following the disturbance, while it is less than that after this interval. The main reason for this phenomenon is that the initial power in WT 25% I is less than WT 00% due to replacement of gas turbines with WECSs without inertial emulator. Consequently, this can lead to the situation that COI RoCoF in WT 25% I scenario is more than other. For the sake of comparison of system frequency for the interval 4 to 30 s, the system frequency of WT 25% I should be apparently less than that of WT 00% since some of conventional units are replaced with WECSs which are not equipped with reserve power. However, as it can be seen from Figure 4-59 and Figure 4-60, it is not true. The main reason for this matter is that WTs are replaced with CCGTs. These units work based on their base load operation mode before the disturbance and their power outputs will be dropped down following the frequency excursion. As a result, the replacement of these power plants with WECSs (Even WECSs without primary frequency support ability) can enhance primary frequency control support. Moreover, the SGs' turbine power in WT 25% I in WT 25% I is less than those of WT 00% scenario. Therefore, the steady state value of frequency in first scenario is more than the second one.

In scenario WT 25% II, the inertial emulator of all WECSs are activated. Therefore, all WECSs inject inertial power to grid following the event. This can reduce COI RoCoF with respect to WT 25% I. However, the frequency nadir and steady-state value of frequency are not changed compared to WT 25% I since reserve power is neglected for WECSs. Finally, all PCO blocks are activated in WT 25% III scenario and reserve power is incorporated. The R parameter in PCO block is 0.05 for all WECSs. As a result, 930 MW out of 2130 MW primary frequency responses is generated by WECSs in this scenario. This reduces frequency nadir and its steady state value by 44% and 40% compared to WT 25% II scenario.

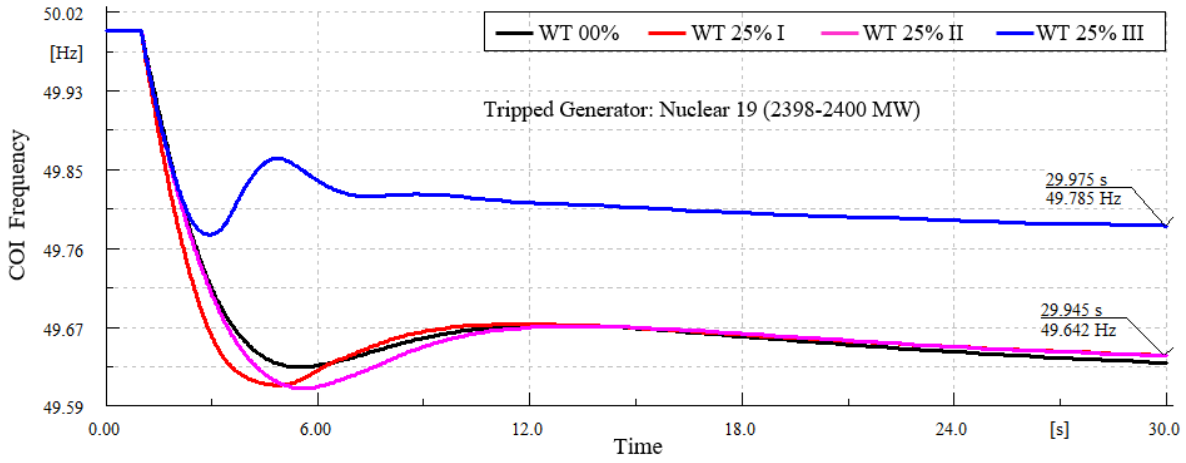

Figure 4-59: Frequency response with loss of 2400 MW generation in middle of network (Zone 19).

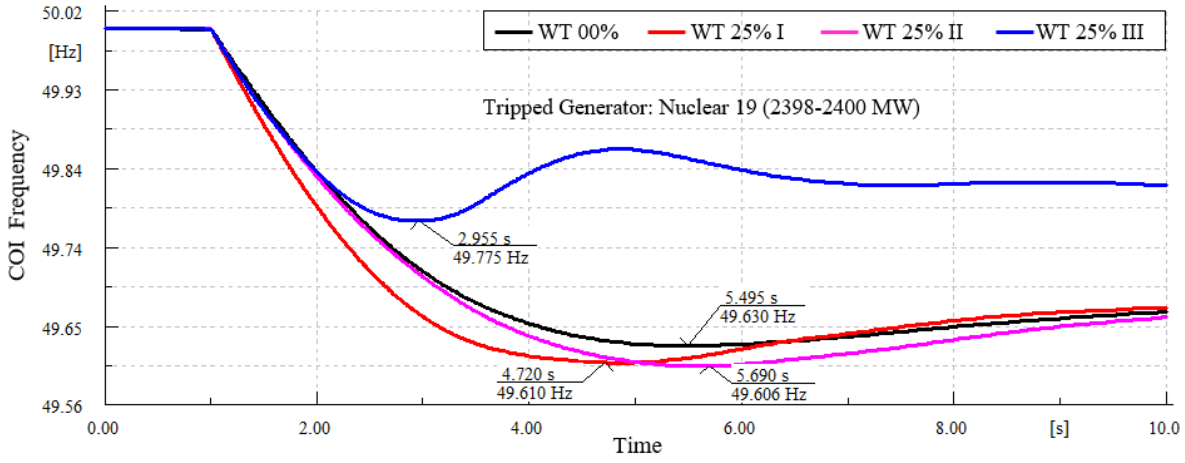

Figure 4-60: Frequency nadir with loss of 2400 MW generation in middle of network (Zone 19).

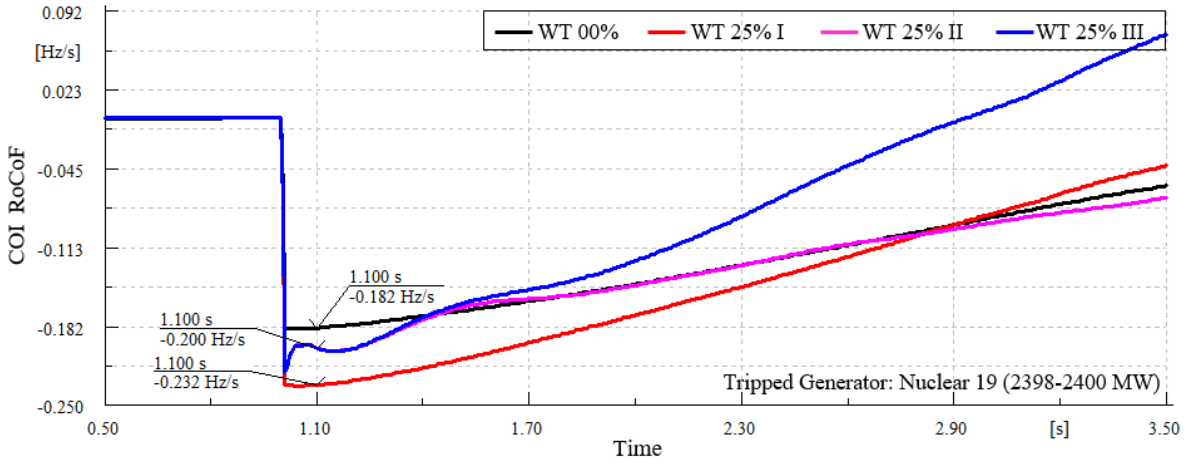

Figure 4-61: RoCoF deviations with loss of 2400 MW generation in middle of network (Zone 19).

4.10.5. Loss of 3,900 MW Generation in Zone 4

In this event, the CCGT unit located in zone 4 with the capacity of 3,900 MW in scenario WT 00% and 2600 MW in scenario WT 25% is abruptly disconnected. The results are illustrated in Figure 4-62 to Figure 4-64 for WT 00% and WT 25% scenarios. The expression of (3941-2585 MW) in these figures indicates the losses of generators are 3941 MW and 3343 MW for respective WT 00% and WT 25% scenarios. The main reason for this difference compared to other 5 events is that CCGTs are substituted with WECSs and despite others the incident is the loss of CCGT unit. In order to accurately investigate WECSs, the WT 25% scenario is also divided into three sub-scenarios. In the first sub-scenario WT 25% I, the inertia emulator and PCO are deactivated for all WECSs. It means that the power output of WECS is independent of network frequency deviation and it is fixed in both pre- and post-contingency states. In the second sub-scenario WT 25% II, all inertial emulators are activated for all WECSs. Therefore, they are able to instantaneously inject power so-called 'Inertial Power' to the network following the event in order to reduce the RoCoF of COI. It is notable that the main idea of the controller is to respond quickly to frequency variation and enhance the frequency nadir as well as RoCoF. In last sub-scenario WT 25% III, both PCO and inertial emulator are activated to provide ancillary services to frequency event. Whilst both synchronous (PCO) and emulated inertial responses of WECSs act in the time-frame before the full governor droop response provision, there is a delay due to a dead-band in inertial

emulator to prevent false triggering. It is to be noticed that PCO is considered to support the WECSs for participating in the frequency response and the WECSs should operate at partial load, ensuring sufficient reserve power at any instant. This is de-loading mode that can be deployed to tune the active power output of WT by rotor speed control. Then, the active power obtained by each WT can drop down or up to complement the system frequency deviations. It is also notable that this power is injected simultaneously with inertial power following the in-feed.

The COI frequency change for the above mentioned four scenarios is shown in Figure 4-62 and Figure 4-63. The COI RoCoF variation for the first few seconds after the event is portrayed in Figure 4-64. Based on Figure 4-62 and Figure 4-63, it can be seen that system frequency of WT 00% scenario is considerably less than WT 25% I for all times following the disturbance. This can be justified by bigger value of disturbance for first scenario with respect to the second one. The main reason for this phenomenon is that the initial power in WT 25% I is less than WT 00% due to replacement of gas turbines with WECSs without inertial emulator. Consequently, this can lead to the situation that COI RoCoF in WT 25% I scenario is more than other, as shown in Figure 4-64. For the sake of comparison of system frequency for the interval 4 to 30 s, the system frequency of WT 25% I should be apparently less than that of WT 00% since some of conventional units are replaced with WECSs which are not equipped with reserve power. However, as it can be seen from Figure 4-62 and Figure 4-63, it is not true. The main reason for this matter is that WTs are replaced with CCGTs. These units work based on their base load operation mode before the disturbance and their power outputs will be dropped down following the frequency excursion. As a result, the replacement of these power plants with WECSs (Even WECSs without primary frequency support ability) can enhance primary frequency control support. Moreover, the SGs' turbine power in WT 25% I in WT 25% I is less than those of WT 00% scenario. Therefore, the steady state value of frequency in first scenario is more than the second one.

In scenario WT 25% II, the inertial emulator of all WECSs are activated. Therefore, all WECSs inject inertial power to grid following the event. This can reduce COI RoCoF with respect to WT 25% I. However, the frequency nadir and steady-state value of frequency are not changed compared to WT 25% I since reserve power is neglected for WECSs. Finally, all PCO blocks are activated in WT 25% III scenario and reserve power is incorporated. The R parameter in PCO block is 0.05 for all WECSs. As a result, 920 MW out of 2360 MW primary frequency responses is generated by WECSs in this scenario. This reduces frequency nadir and its steady state value by 42% and 37% compared to WT 25% II scenario.

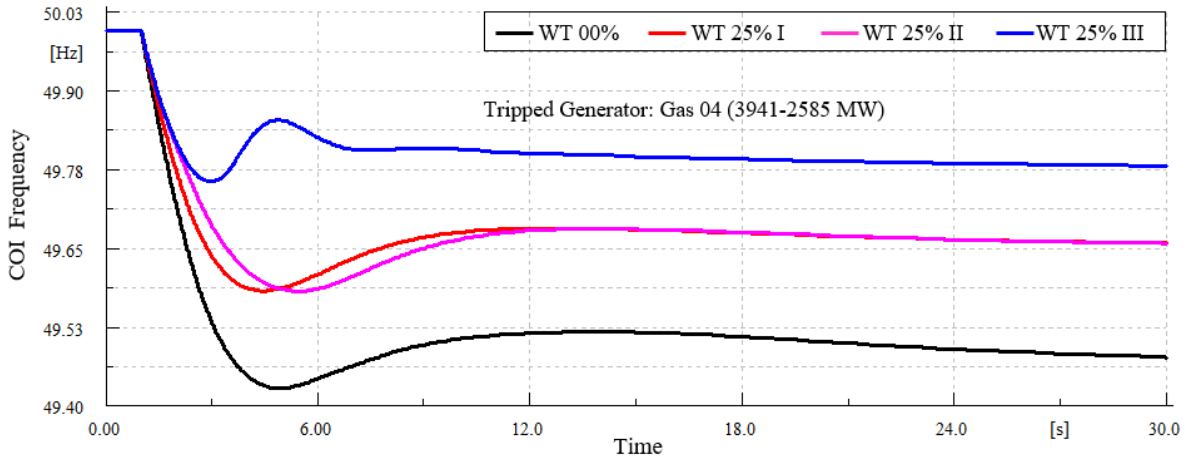

Figure 4-62: Frequency response with loss of 2600 MW generation in left bottom of network (Zone 04).

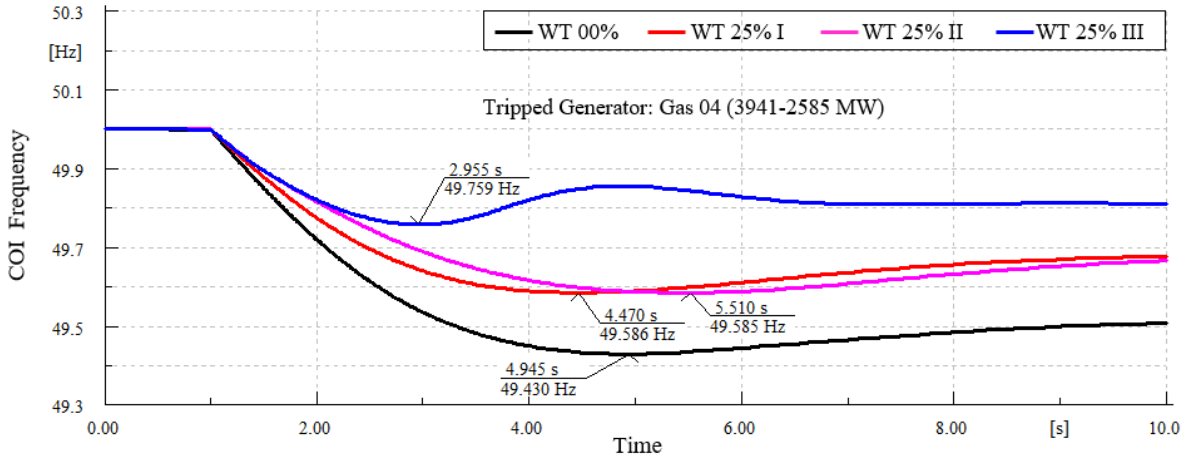

Figure 4-63: Frequency nadir with loss of 2600 MW generation in left bottom of network (Zone 04).

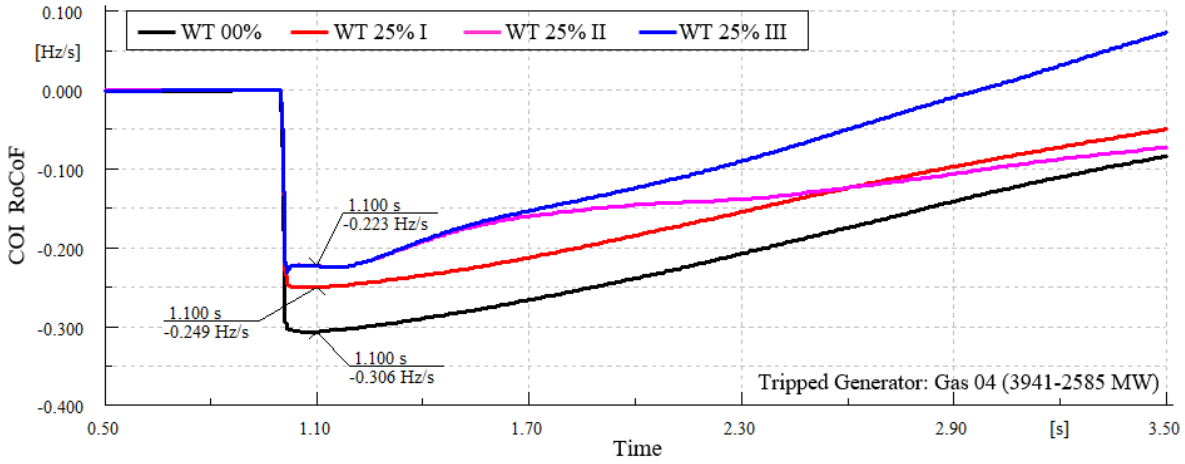

Figure 4-64: RoCoF deviations with loss of 2600 MW generation in left bottom of network (Zone 04).

4.10.6. Frequency Response of 36-Zone GB Network with Medium Penetration of Wind Energy Conversion Systems

In this section, the GB system frequency response following loss of some generators is investigated for medium penetration of WECSs. To this end, the system frequency response for abovementioned event and for two scenarios of WT 50% and WT 25% are investigated. The accurate generated powers of WECSs in WT 50% are listed in Table 4-8 and Table 4-9. In the following, different criteria related to SFR like the centre of inertia (COI) frequency variation and RoCoF change for loss of generator at time equal to one second for 30 seconds after the event are evaluated for two scenarios of WT 25% and WT 50%. It is to be notified that step size for time domain simulation is equal to 0.005 s.

In order to monitor and investigate the system frequency response of WECSs alongside of conventional units' response, the 36-zone GB network is divided into 5 geographical regions, as shown in Figure 4-55. In each region, the frequency response curves and quantities of WECSs highlighted by 'Measurement Point' are tabulated for each incident.

In each scenario, all WECSs are able to inject inertial and reserve power to the grid. The marginal reserve power for all WECSs are considered to be similar to the previous case i.e. 10%

4.10.6.1. First Event: Loss of 2,400 MW Generation in Zone 19

In the first event, the nuclear unit located in zone 19 with the capacity of 2,400 MW is abruptly disconnected. The results are illustrated in Figure 4-65 to Figure 4-67 for WT 25% and WT 50% scenarios. The expression of (2400-2400 MW) in these figures indicates the loss of generators for these respective two scenarios i.e. 2400 MW.

The COI frequency change for the above mentioned scenarios is shown in Figure 4-65 and Figure 4-66. The COI RoCoF variation for the first few seconds after the event is portrayed in Figure 4-67. While the penetration of wind power is increased from 25% to 50%, the frequency nadir and its steady state value are mitigated by 15% and 30%, respectively. More wind power is injected to the grid faster than conventional units once the penetration level of WECSs is increased. It is notable that making the penetration of WECSs twice can reduce burden on primary frequency support of conventional units by 25%. In other hand, the system frequency response in term of COI RoCoF get worse, as shown in Figure 4-65. This is because that 2343 MW and 2314 MW inertial power are injected to the network after 100 ms from disturbance occurrence based on Figure 4-66, respectively. It is noticeable that less inertial power injection to the grid in the first few moments of in-feed can lead to RoCoF increment.

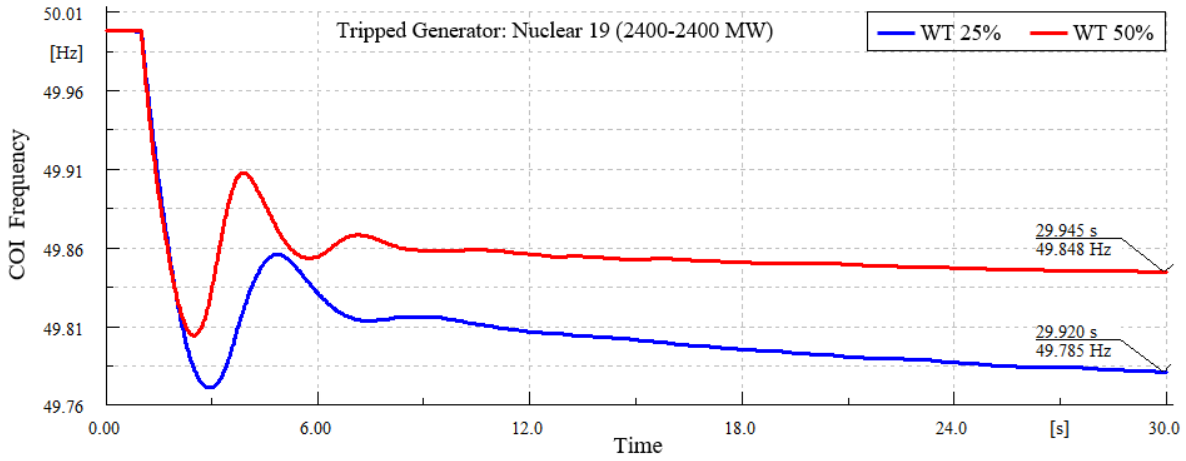

Figure 4-65: Frequency response with loss of 2400 MW generation in middle of network (Zone 19).

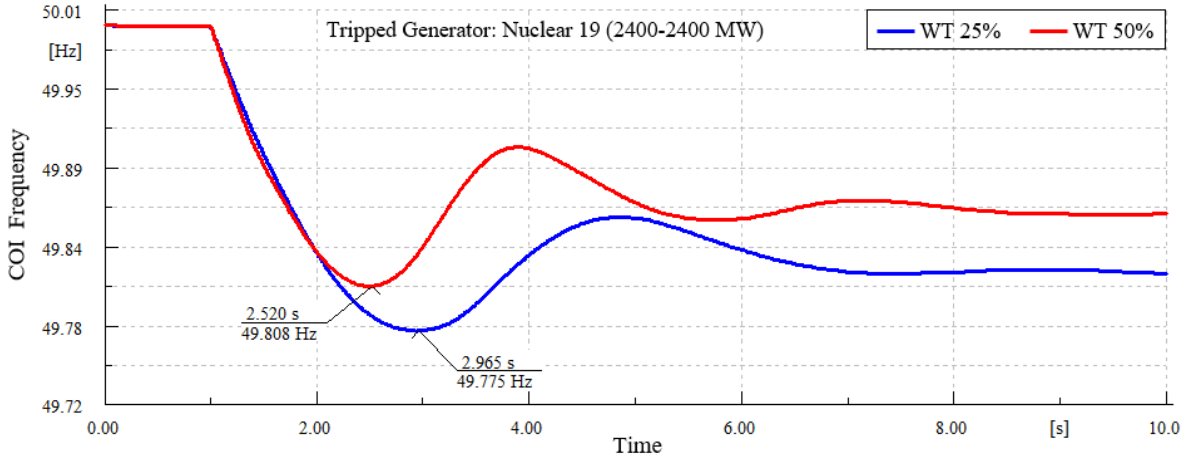

Figure 4-66: Frequency nadir with loss of 2400 MW generation in middle of network (Zone 19).

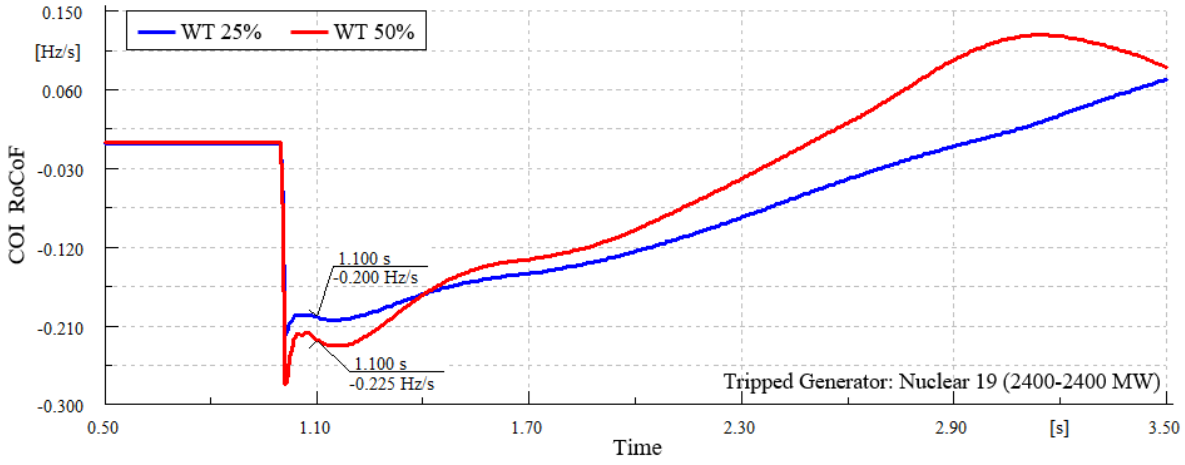

Figure 4-67: RoCoF deviations with loss of 2400 MW generation in middle of network (Zone 19).

4.10.6.2. Second Event: Loss of 3,900 MW Generation in Zone 04

In the second event, the CCGT located in zone 04 with the capacity of 3,900 MW is abruptly disconnected. The results are illustrated in Figure 4-68 to Figure 4-70 for WT 25% and WT 50% scenarios. The expression of (2585-1266 MW) in these figures indicates the loss of generators for WT 25% and WT 50% scenarios are 2585 MW and 1266 MW, respectively.

The COI frequency change for the above mentioned scenarios is shown in Figure 4-68 and Figure 4-69. The COI RoCoF variation for the first few seconds after the event is portrayed in Figure 4-70. While the penetration of wind power is increased from 25% to 50%, the frequency nadir and its steady state value are enhanced. Similar to the previous event, more wind power is injected to the grid faster than conventional units once the penetration level of WECSs is increased. Since the loss of generation for WT 50% scenario is about half of WT 25% one, therefore, one reason for frequency nadir as well as steady-state frequency deviation enhancement can be incident decrement. Additionally, the system frequency response in term of COI RoCoF is enhanced almost twice, as shown in Figure 4-68.

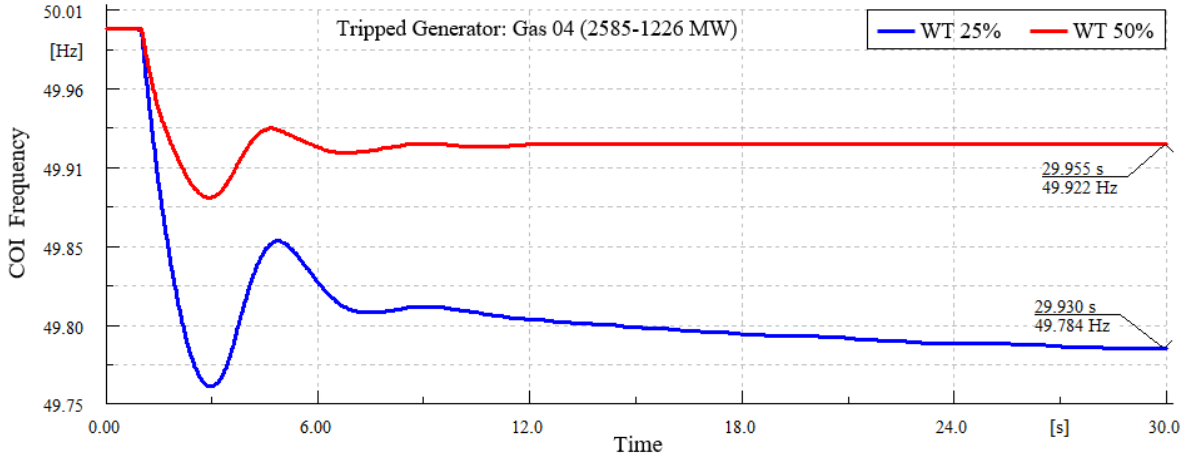

Figure 4-68: Frequency response with loss of 2600-1200 MW generation in left bottom of network (Zone 04).

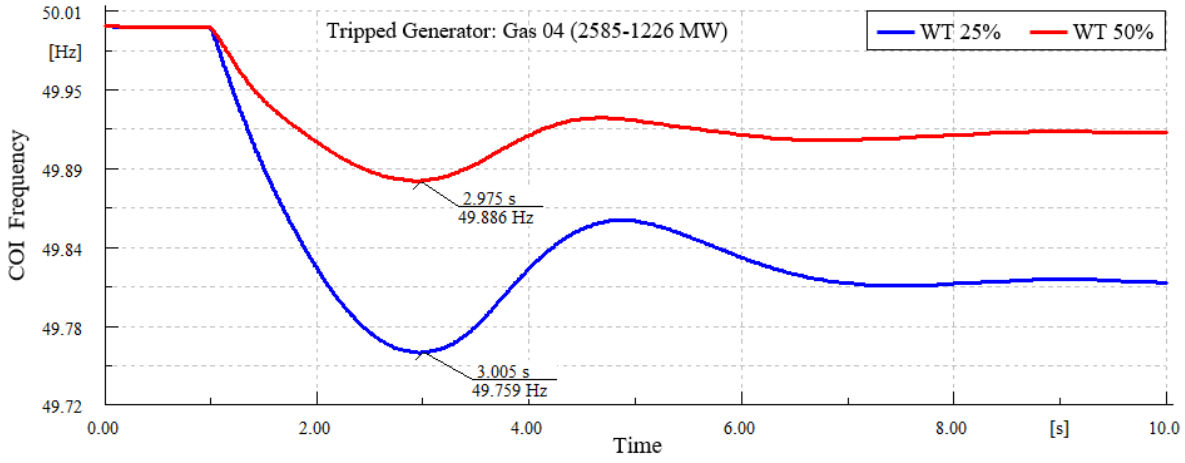

Figure 4-69: Frequency nadir with loss of 2600-1200 MW generation in left bottom of network (Zone 04).

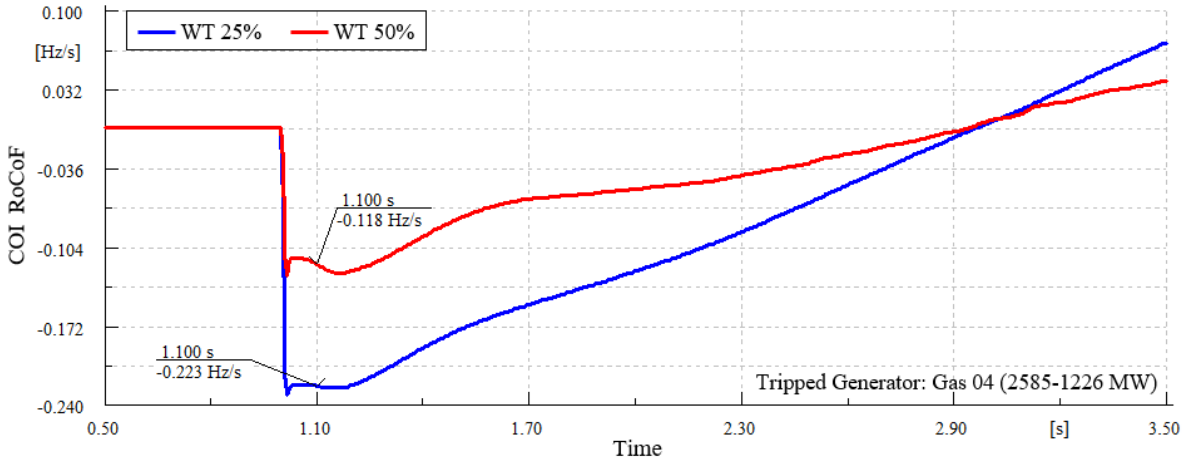

Figure 4-70: RoCoF deviations with loss of 2600-1200 MW generation in left bottom of network (Zone 04).

4.10.7. Frequency Response of 36-Zone GB Network with Different Reserve Powers of Wind Energy Conversion Systems

In all previous case studies, reserve power of WECSs before the loss of generation is equal to 10% of their generated power. However, considering this fixed value for all hours a day is not possible and reasonable due to the widely varied wind speeds. To this end, the GB system frequency response is investigated for different reserve powers of WECSs. The considered event is that the nuclear unit located in zone 19 with the capacity of 2,400 MW is abruptly disconnected. The simulation results are shown in Figure 4-71 to Figure 4-82 for three different reserve power levels of 2%, 6% and 10%. The corresponding wind speed values are portrayed in Figure 4-71.

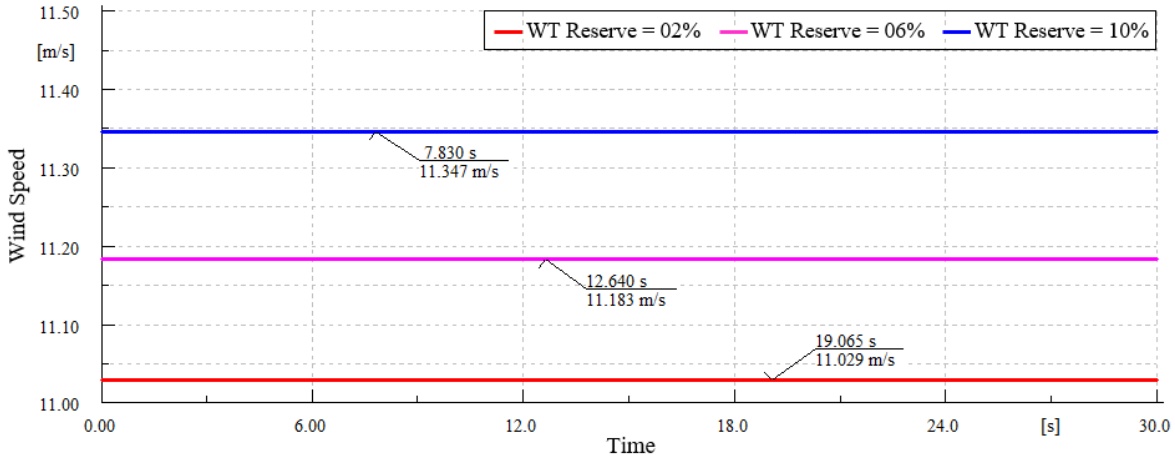

Figure 4-71: Wind speeds with different wind turbine reserve powers.

The COI frequency changes for the above mentioned reserve levels are shown in Figure 4-72 and Figure 4-73. The COI RoCoF variation for the first few seconds after the event is portrayed in Figure 4-74. Figure 4-75 shows the initial power of all conventional (SG power plants) and all WT units (WT power plants) in 36-zone GB network. The turbine power deviations with respect to pre-contingency state are plotted in Figure 4-76 for both conventional and WECS power plants.

By comparing the results of power reserve of 2% and 10%, it can be noticed that frequency nadir and steady-state frequency are improved with reserve power growth. Additionally, based on Figure 4-76, power reserve increment from 2% to 10 % can reduce burden on primary frequency support of conventional units by 50%. In other hand, the system frequency response in term of COI RoCoF get a little bit worse, as shown in Figure 4-74. In other hand, the system frequency response for power reserve of 6% is abnormal for the first 10 seconds following the event compared to reserve power of 10%. Therefore, the COI frequency for the first scenario is more than the second one.

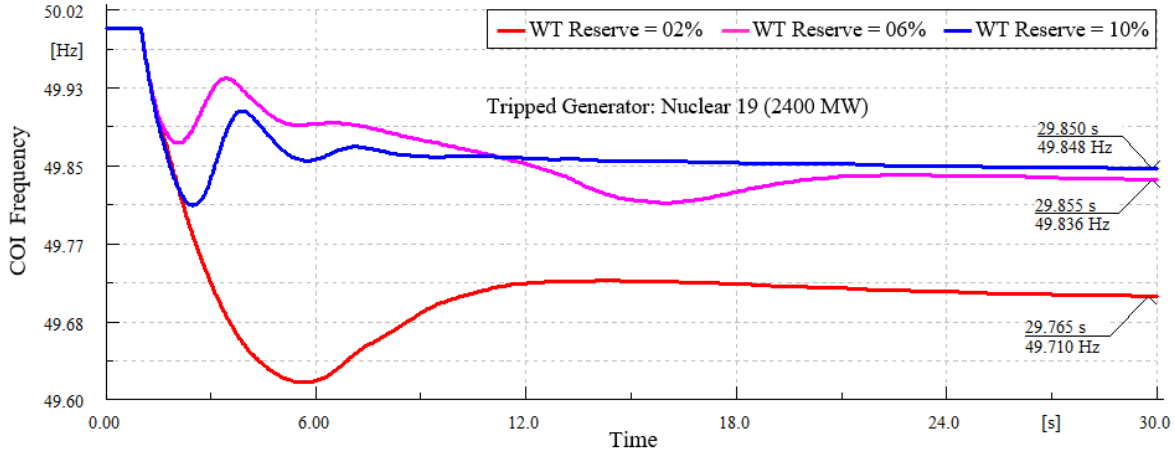

Figure 4-72: Frequency response with different wind turbine reserve powers.

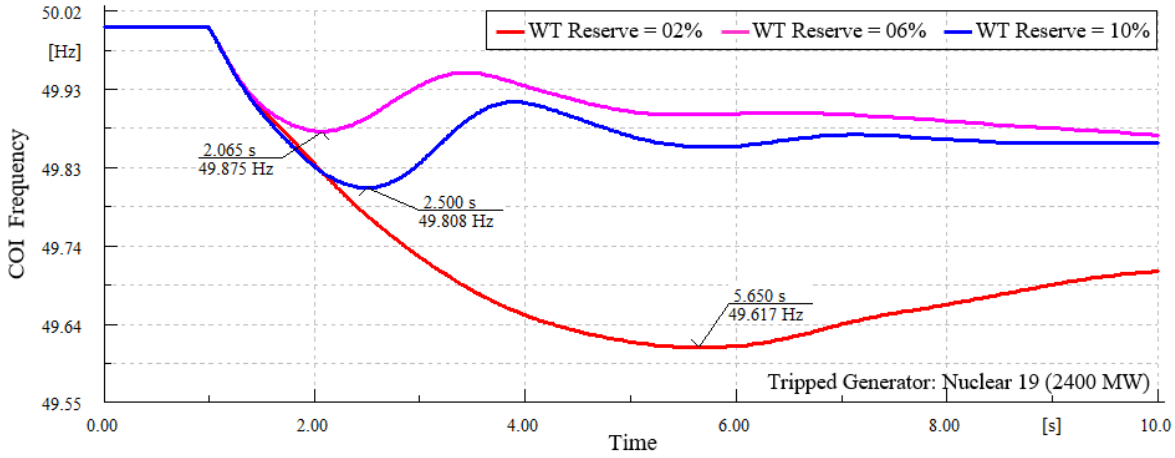

Figure 4-73: Frequency nadir with different wind turbine reserve powers.

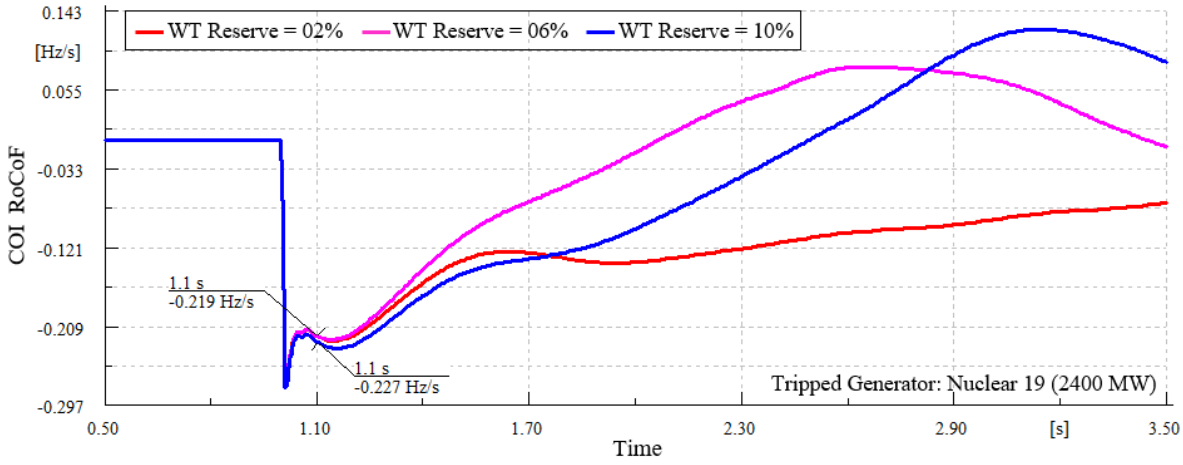

Figure 4-74: RoCoF deviations with different wind turbine reserve powers.

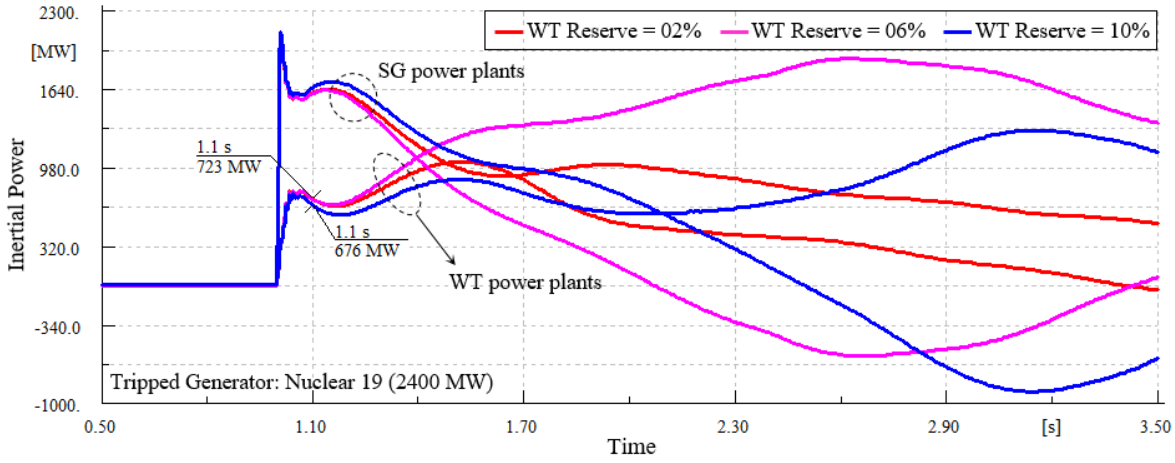

Figure 4-75: Inertial power changes with different wind turbine reserve powers.

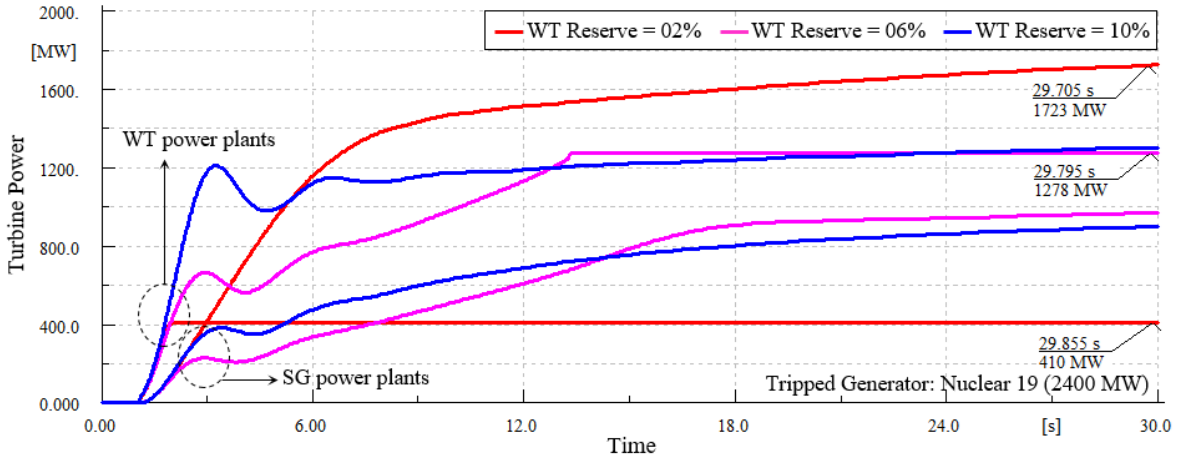

Figure 4-76: Turbine power deviations with different wind turbine reserve powers.

In order to more efficiently investigate the frequency response of WECSs for different reserve powers, several quantities related to frequency response of 5 WECSs depicted in Figure 4-55, are shown in Figure 4-77 to Figure 4-82. The turbine power change of WECSs is plotted in Figure 4-77. It is to be noticed that before the event, the WECSs are intentionally spill power and work on power equal 0.8 p.u. (Partial mode), so that the reserve energy can be used for frequency regulation, akin to the governing function. As the generation lost is huge, all reserve power of WECSs in two scenarios of 2% and 6% are injected to the grid. It is to be noted that in 2% scenario, the reserve power is equal to 2% of generated power not rated power. This point is illustrated in Figure 4-77 for the scenario of 25 in which reserve power is equal to 0.016 p.u. Additionally, WT spinning speed variations are shown in Figure 4-78. As can be seen, the WT speed is reduced for the first scenario i.e. 2% reserve and reduced for the rest.

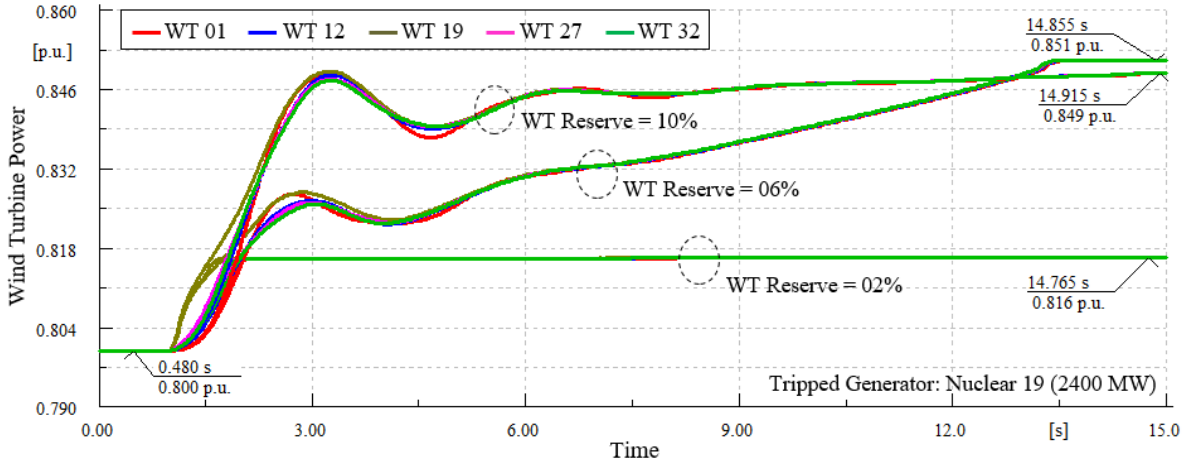

Figure 4-77: Wind turbine power changes with different wind turbine reserve powers.

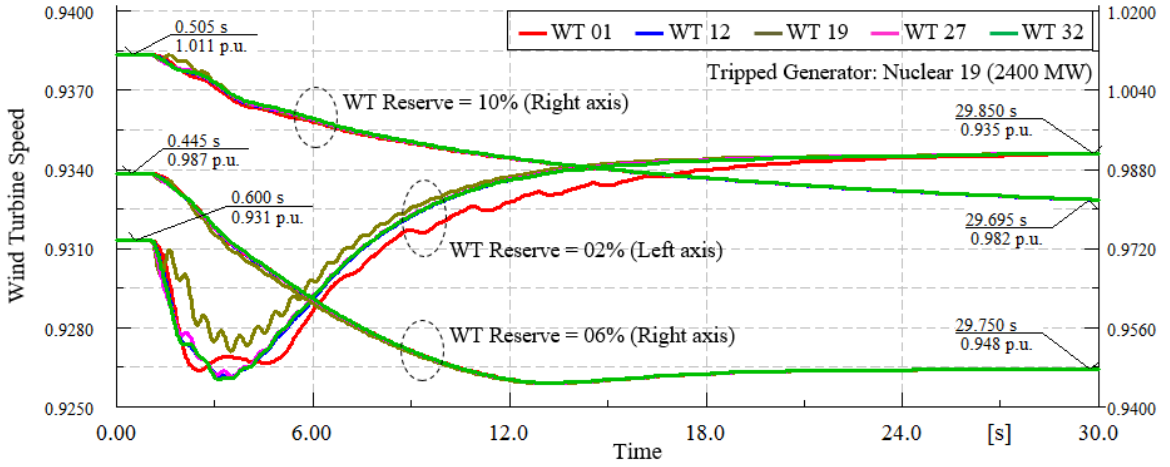

Figure 4-78: Wind turbine speed changes with different wind turbine reserve powers.

The pitch angle and *Cp* change for five WECSs are respectively shown in Figure 4-79 and Figure 4-80. It is clear-cut that pitch angles of WTs for different reserve power values is different before the incident so that the pitch angle is tuned in a bigger value in proportion of reserve power increment. After the disturbance, the pitch angle is dropped down for all scenarios for the sake of reserve power injection to the network. It is noteworthy that the pitch angle is reached to zero value over the time for reserve power levels of 2% and 6%. It means that all available reserve power is fed to the grid in these two scenarios.

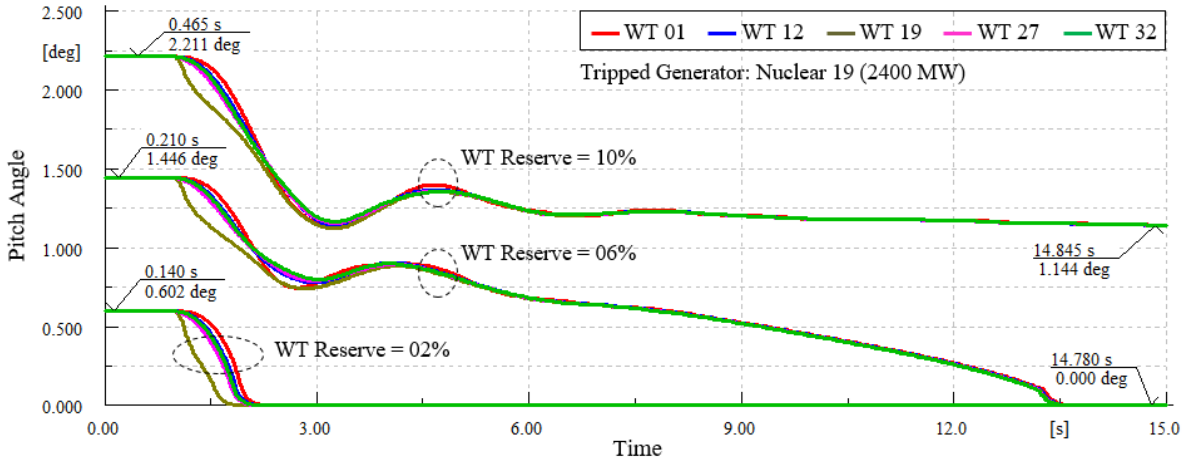

Figure 4-79: Pitch angle changes with different wind turbine reserve powers.

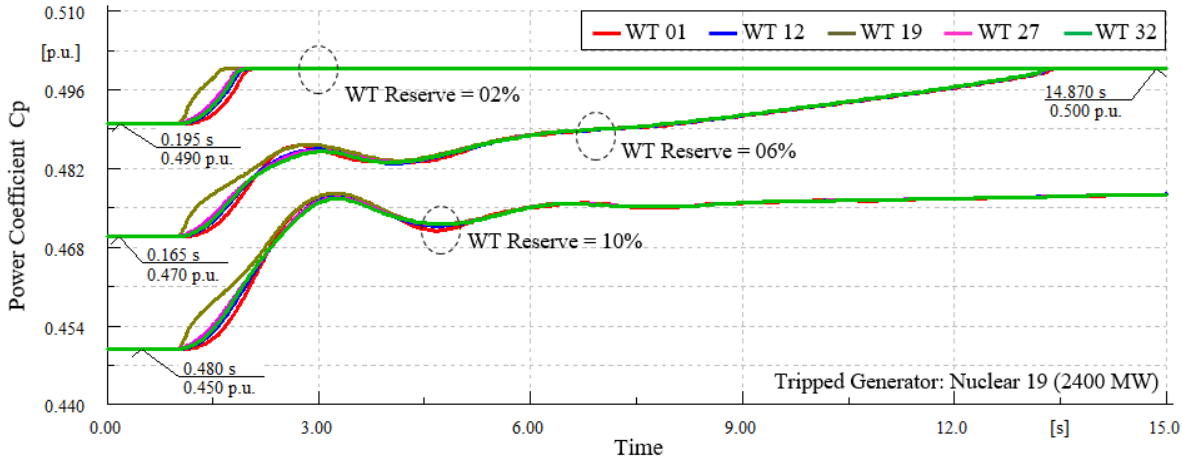

Figure 4-80: Power coefficient changes with different wind turbine reserve powers.

In order to monitor the change of equilibrium point for WTs before and after the loss of generation, some trajectories related to WECS located in zone 1 are shown in Figure 4-81. Moreover, the WECSs' equilibrium point in pre- and post-contingency state is shown on MPPT curve in Figure 4-82. In scenario of 10% reserve power, 6% of reserve power is injected to the grid by reducing pitch angle to 1.1°. In other hand, the pitch angle is reduced by 1.45° and 0.6° to reach zero and inject the whole reserve for other two scenarios of 2% and 6% reserve power, respectively. Moreover, this fact that WT's speeds are different for discrepant values of reserve power level before and after the event as shown in Figure 4-78, are coincided with equilibrium points specified in Figure 4-82.

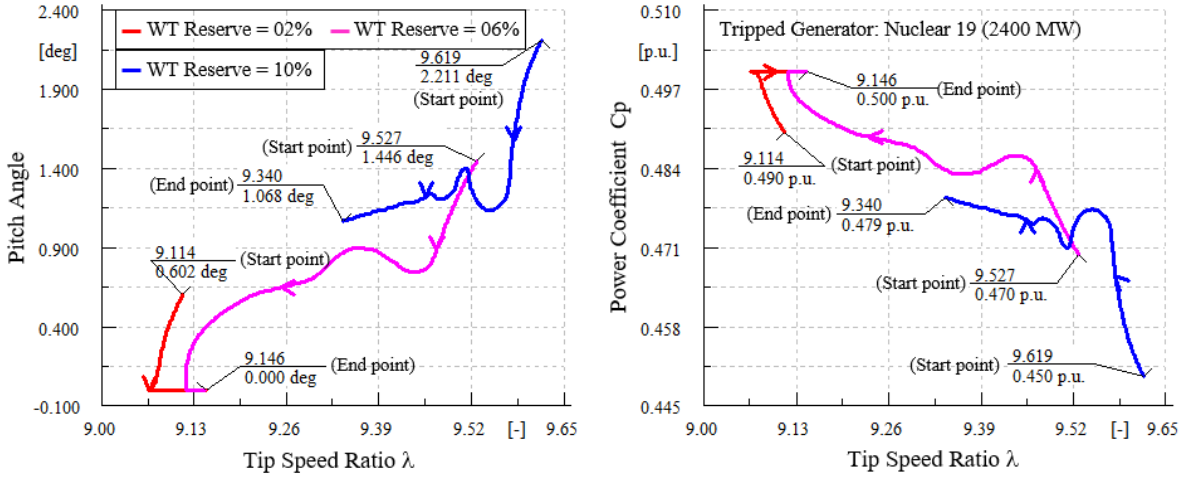

Figure 4-81: Pitch angle and power coefficient versus tip speed ratio trajectories of wind power plant 01 with different wind turbine reserve powers.

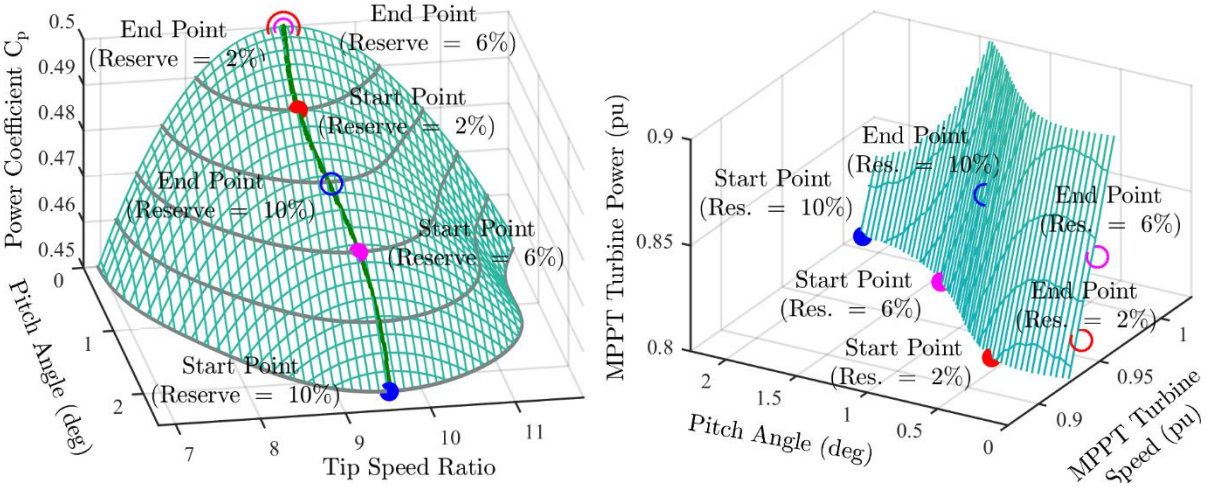

Figure 4-82: Location of pre- and post-event operating points of WECSs on MPPT characteristics with different wind turbine reserve powers: power coefficient versus pitch angle and tip speed ratio (Left), MPPT turbine power versus pitch angle and MPPT turbine speed (Right).

4.10.8. Frequency Response of 36-Zone GB Network with Different Inertial Power of Wind Energy Conversion Systems

In all previous case studies, the effect of different values of wind penetration level as well as reserve power of WECSs on GB system frequency response is investigated. In all of these circumstances, it is observed that COI

RoCoF is raised by increasing these criteria. In other word, albeit the increment rate of primary frequency response of WECSs is more than conventional units, the rate of inertial power increment of WECSs is limited to 1 p.u./s which is less than conventional units. In this regard, the impact of inertial power increment rate of WECSs on GB system COI RoCoF is evaluated. The considered event is that the nuclear unit located in zone 19 with the capacity of 2,400 MW is abruptly disconnected. The penetration level is fixed to 50%. The step size of time domain simulation and time constant of inertial emulator of WECSs are both equal to 0.001 s. The GB system frequency response for the initial moments of event occurrence for different values of 'Up Rate Limit' in Inertial Emulator blocks of WECSs are illustrated in Figure 4-83 and Figure 4-88. For the sake of better comparison, the results of WT 00% scenario are also appended into the figures. The change of COI frequency and COI RoCoF are portrayed in Figure 4-83 and Figure 4-84. It is clear-cut that the RoCoF is reduced with increasing inertial power rate of WECSs. To be accurate, The RoCoF values are dropped down by 17% and 27% with the Up Rate Limit growth from 1 pu/s to 3 pu/s and 1 pu/s to 6 pu/s, respectively, as shown in Figure 4-85.

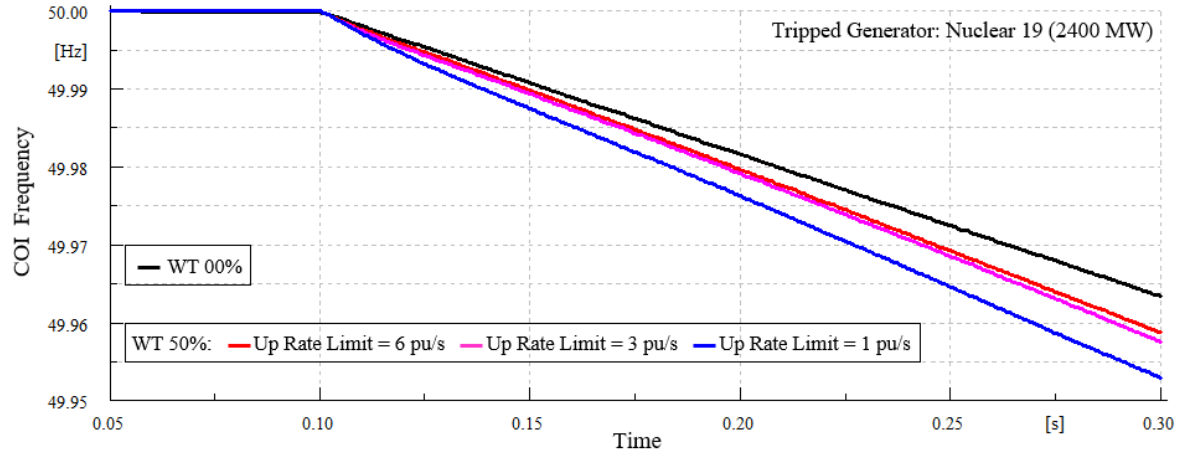

Figure 4-83: Frequency response with different up rate limits of inertial emulator.

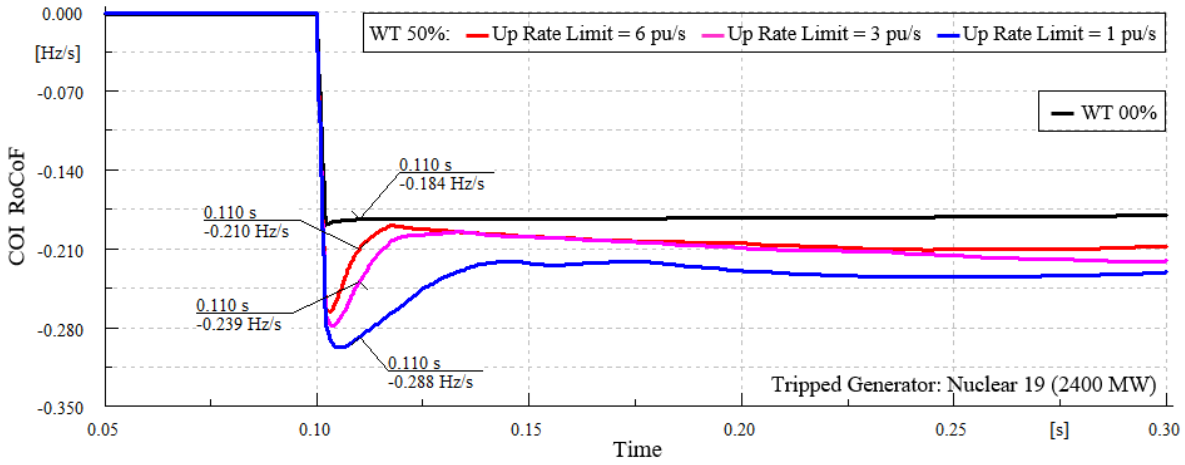

Figure 4-84: RoCoF deviations with different up rate limits of inertial emulator.

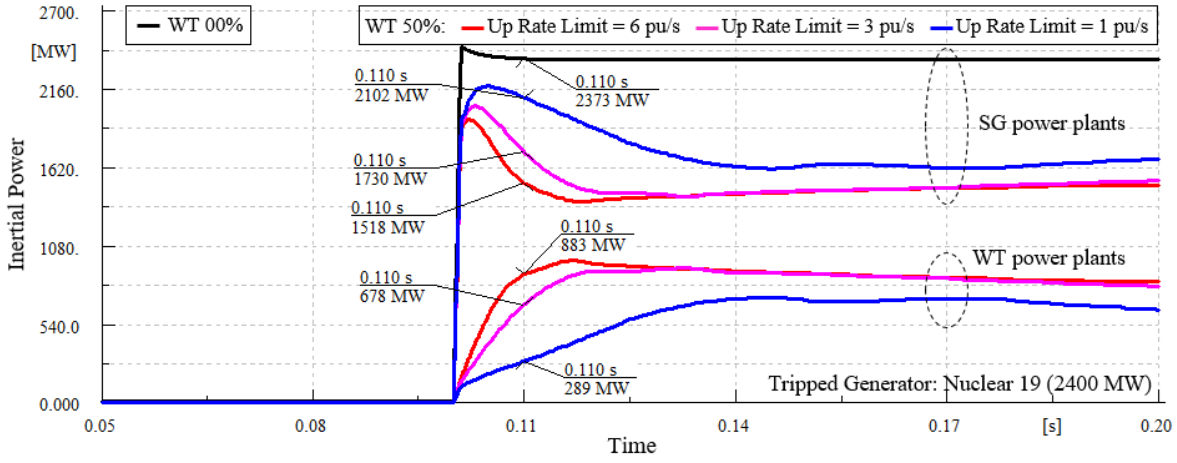

Figure 4-85: Inertial power changes with different up rate limits of inertial emulator.

In order to more efficiently investigate the frequency response of WECSs under different values of initial power increment rate, several quantities related to frequency response of 5 WECSs depicted in Figure 4-55, are shown in Figure 4-86 to Figure 4-88. The inertial power order change extracted from inertial emulator block is plotted in Figure 4-77. In this figure, the lower and upper limits of this signal are 0 and 0.1 pu, respectively. As can be seen, the closest WT to the event i.e. WT 19 is reached to the upper limitation. The initial times following the disturbance are zoomed in Figure 4-87. This figure evidently shows that the considered Up rate limit is quite matched with WT located in zone 19. In addition, it is quite clear that the algebraic summation of all WECSs of GB network is 20 GW or 25 GVA with power factor of 0.8. Therefore, the inertial power of WECSs needs to be increased by 25 GW per second or 250 MW per 0.01 second for Up rate limit equal to 1 pu/s. The corresponding values for Up rate limits of 3 and 6 should be made 3 times and 6 times. The numerical values specified in Figure 4-85 for WECS with Up rate limit of 1 and 3 have 15% and 10% difference with pre-determined values. This is due to terminal voltage change of WECSs and their active power variation in consequence. However, this difference is 40% for Up rate limit of 6. In other word, the analytical value of inertial power for WECSs should be 1500 MW per 0.01 second, however, this value is 880 MW based on Figure 4-85. In order to clarify this matter, two vital items need to be pointed out:

i) The value of 1500 MW is the maximum inertial power for WECSs not the necessary amount. It means it is possible that the generation lost value is small so that system RoCoF can't change the inertial power increment rate of all WECSs to this maximum limit.

ii) It is possible that the WT distance to the incident is huge and the local RoCoF measured by this unit can't change the inertial power increment rate of all WECSs to this maximum limit. This pint is illustrated in Figure 4-85 so that in case of Up rate limit of 6 pu/s, the only unit's inertial power which is reached to the maximum value is WT located beside the disturbance in zone 19. Therefore, the inertial power of this unit needs to be less than 1500 MW in this case.

iii) The WT speed for the first moments of event is depicted in Figure 4-88 for discrepant values of Up rate limit. What should be underscored is that whilst the COI RoCoF is reduced with increasing the inertial power rate increment, the WT rotor oscillation especially for the WECSs located nearer to the in-feed is increased.

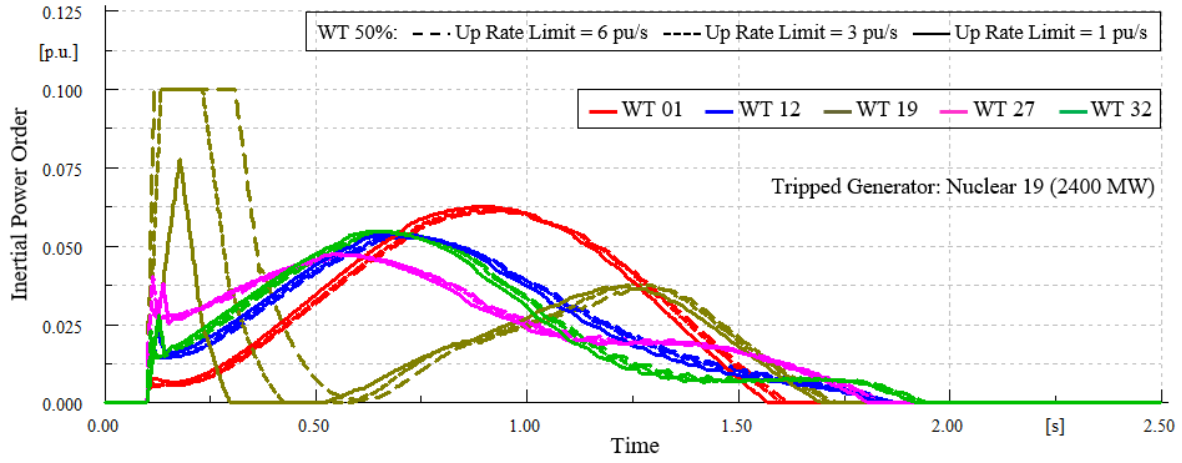

Figure 4-86: Inertial power order changes with different up rate limits of inertial emulator.

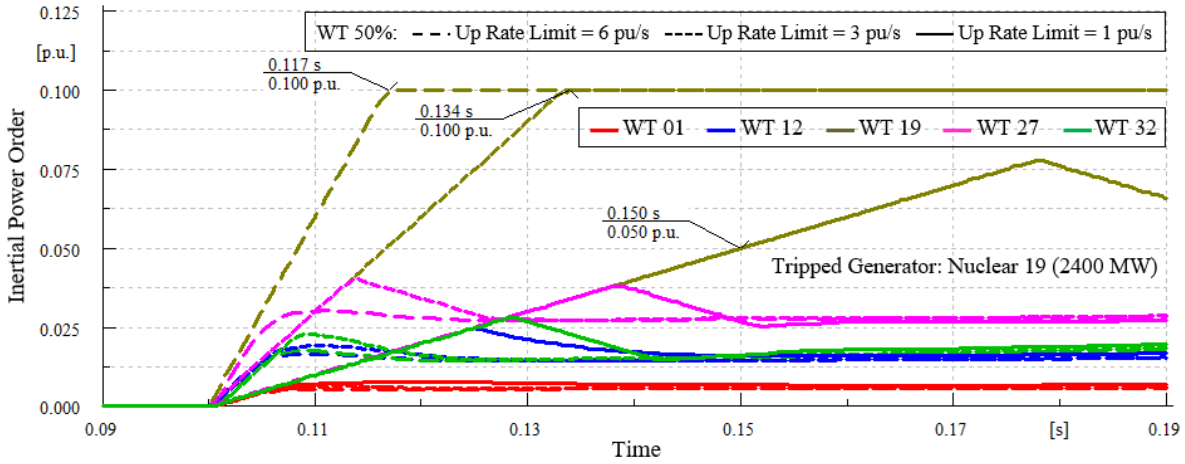

Figure 4-87: Up rate limits of inertial power order with different up rate limits.

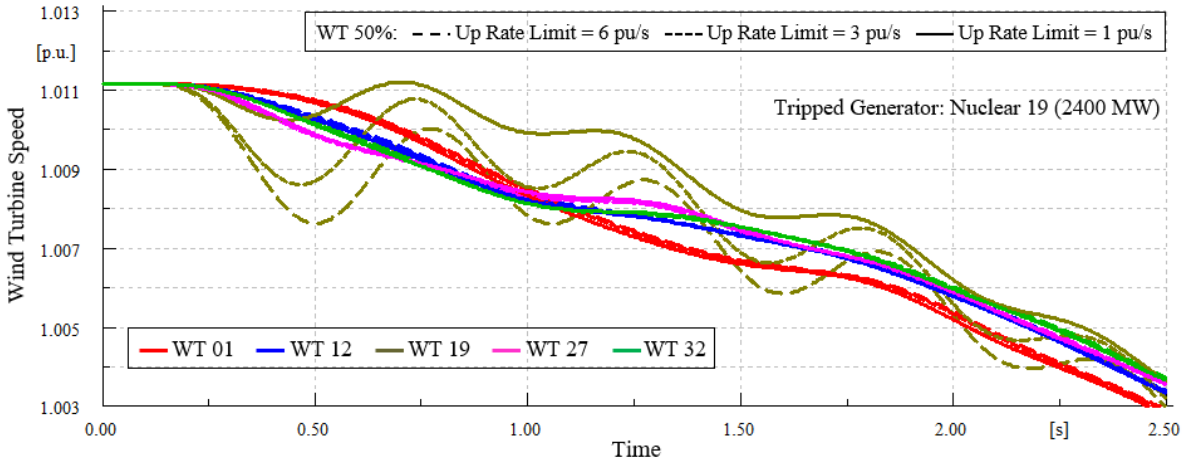

Figure 4-88: Wind turbine speed changes with different up rate limits of inertial emulator.

4.10.9. Frequency Response of 36-Zone GB Network with Different Wind Speeds of Wind Energy Conversion Systems

In order to solve load flow problem, the power generated by WECSs are tuned in a known value in DIgSILENT PowerFactory. After which, wind speed is determined based on this power as well as assigned value to reserve power. However, in practice, wind speed determines the generated power and its reserve for each WECS. To further demonstrate the effectiveness and applicability of the proposed control in practical cases, the GB system frequency response is investigated considering discrepant scenarios for wind speed. The penetration level of WECSs in this scenario is 50% and reserve power margin of 10% is assigned to all of them. The wind speed deviations percentage of five different areas depicted in Figure 4-55 are tabulated in Table 4-10 for three scenarios. The wind speed of all regions in all time horizon is fixed in Wind Speed I scenario. In Wind Speed II scenario, the wind speed is dropped down in some areas and decreased in others. It means that wind speed is increased in zones 2 and 4 and mitigated in other three regions. The maximum drop is intentionally considered as -10% in zone 3. Finally, the worst case in term of available reserve power is simulated in Wind speed III with wind speed reduction of all areas.

Table 4-10: Percentage of wind speed deviations in wind speed scenarios

Scenario	Area 01	Area 02	Area 03	Area 04	Area 05
Wind Speed I	0%	0%	0%	0%	0%
Wind Speed II	-5%	2%	-10%	3%	-5%
Wind Speed III	-5%	-4%	-5%	-2%	-5%

4.10.9.1. First Scenario: Increasing/Decreasing Wind Speed of All WECSs

In this subsection, the 36-zone GB system frequency response for the scenario of Wind Speed II following the loss of nuclear power located in zone 19 is investigated. The relevant results beside Wind Speed I scenario are illustrated in Figure 4-89 to Figure 4-100. The simulation time interval is 50 seconds. Moreover, wind speed values are changed at t=1 s for all five regions depicted in Figure 4-55, as shown in Figure 4-89. The maximum wind speed reduction -10% is related to Area 03 where disturbance location is located in zone 19. The loss of generator is simulated at t=20 s.

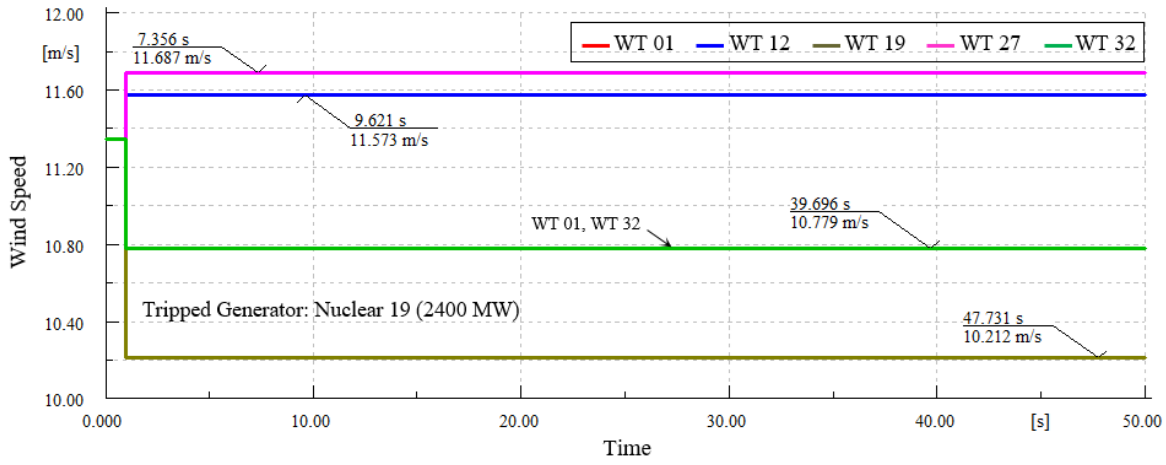

Figure 4-89: Wind speed of wind turbines in Wind Speed II scenario.

The COI frequency and COI RoCoF of GB network are shown in Figure 4-90 and Figure 4-91, respectively. Furthermore, the inertial power variations of conventional unit as well as WECS are illustrated in Figure 4-92 for the initial times of disturbance occurrence. Figure 4-93 illustrates conventional and WT turbine power change. As discussed above, the wind speed variation can change power generated by WECSs and vary reserve power, consequently. In this context, the reserve powers of all 5 regions depicted in Figure 4-55 are shown in Figure 4-94 and Figure 4-95 including of their algebraic summation. The reserve power variation of all four regions where the disturbance is not happened are shown in Figure 4-94. In other hand, the corresponding values of Area 03 (Disturbance is occurred in this region) and the power summation of all areas are shown in Figure 4-95 for Wind Speed I and Wind Speed II.

Applying the wind speed change of Wind Speed II depicted in Figure 4-89 on WECSs leads to output power reduction of WECSs by 1200 MW. This in turn can abruptly mitigate reserve power of WECSs, as shown in Figure 4-94 and Figure 4-95. As can be seen form right hand side of Figure 4-95, the amount of this reduction for the whole network is 120 MW which is quite match to 10% reserve power of WECSs. This wind speed variation is like loss of wind power leading to system frequency mitigation, as depicted in Figure 4-90. Due to this fact, output powers of conventional units and WECSs increase following the event as shown in Figure 4-93. As a result, some part of WECSs' reserve power is occupied to compensate WECSs' power reduction in consequent of wind speed changes. The reserve power of WECSs reduces by 28% from 2000 MW to 1440 MW in t=20 s. This is because the frequency nadir and steady-state frequency deviation in Wind Speed II scenario are dropped down by 11% and 60% compared to Wind Speed I, respectively. However, the COI RoCoF is equal in both scenarios. Note, the residual reserve power of all WECS is 160 MW at the end of simulation time.

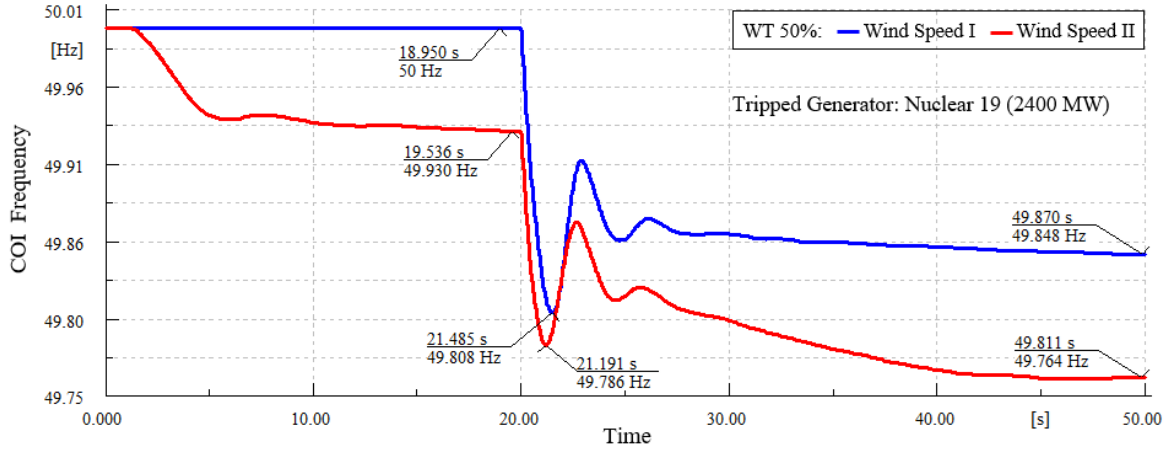

Figure 4-90: Frequency responses in "Wind Speed I" and "Wind Speed II" scenarios.

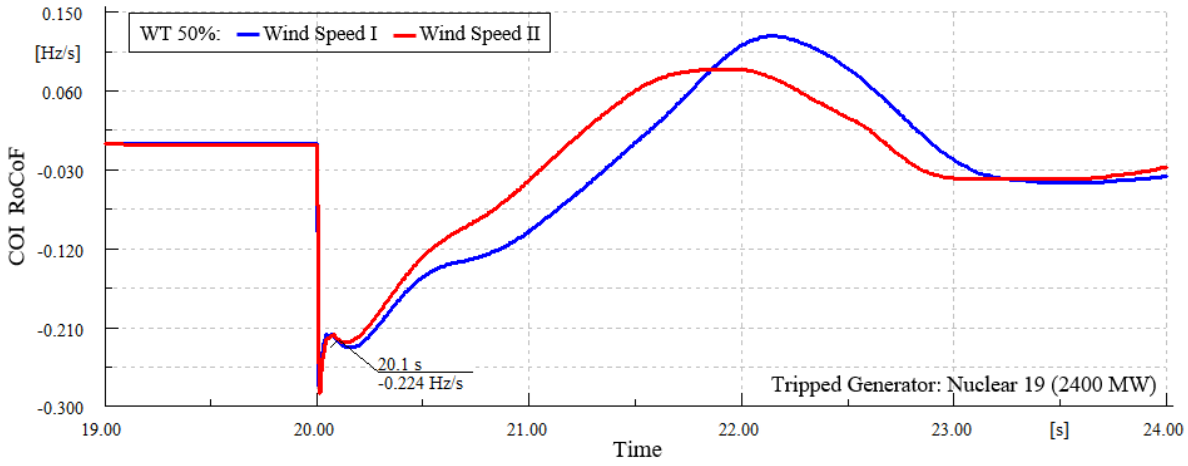

Figure 4-91: RoCoF deviations in “Wind Speed I” and “Wind Speed II” scenarios.

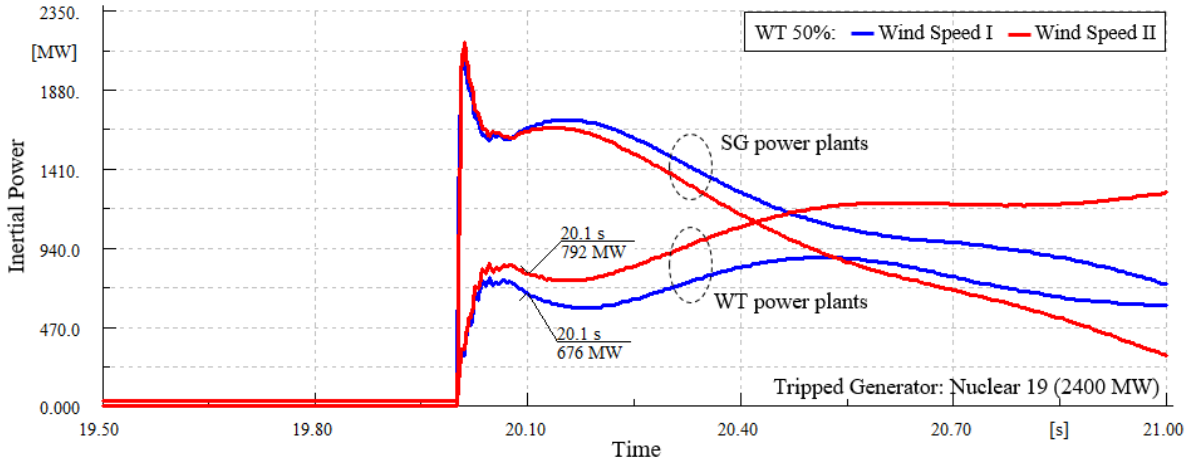

Figure 4-92: Inertial power changes in “Wind Speed I” and “Wind Speed II” scenarios.

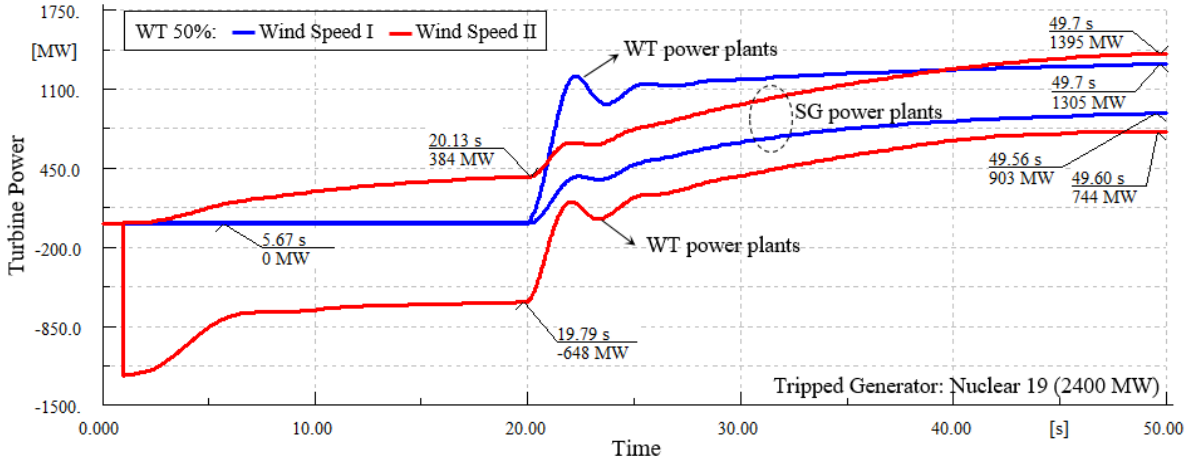

Figure 4-93: Turbine power deviations in “Wind Speed I” and “Wind Speed II” scenarios.

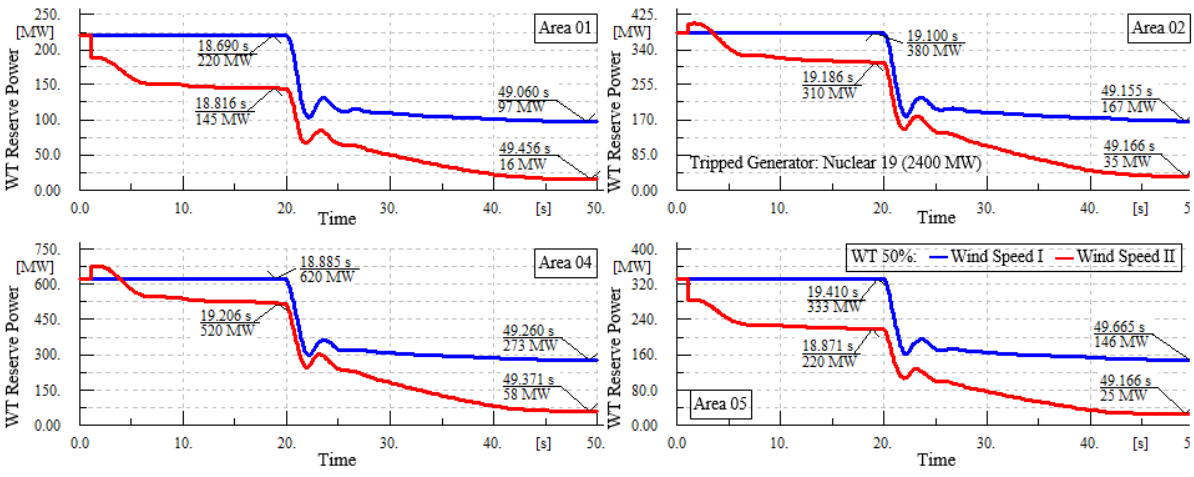

Figure 4-94: Wind turbine reserve power changes of area 01, area 02, area 04 and area 05 in “Wind Speed I” and “Wind Speed II” scenarios.

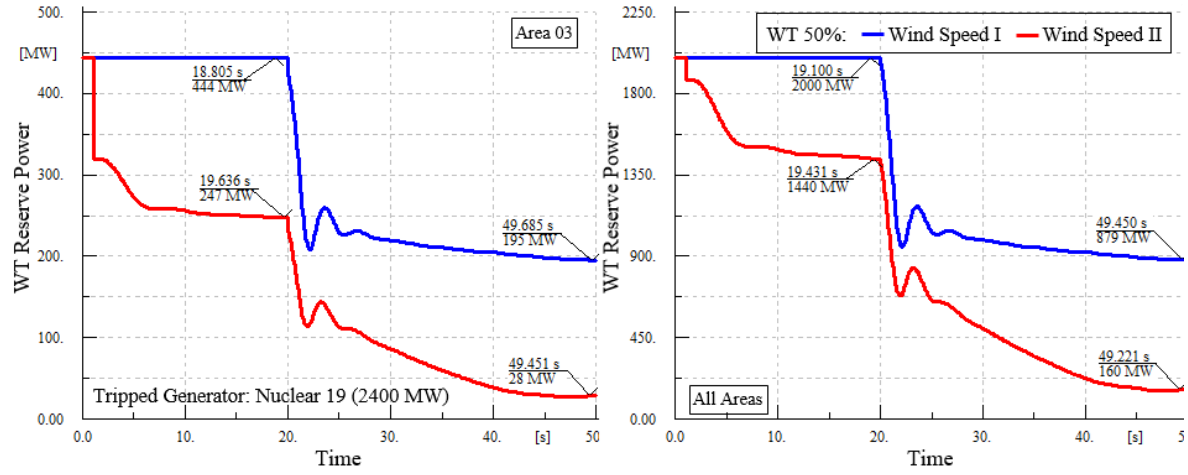

Figure 4-95: Wind turbine reserve power changes of area 03 and all areas in "Wind Speed I" and "Wind Speed II" scenarios.

In order to accurately investigate the above matter, some quantities related to 5 WECSs specified in Figure 4-55, are shown in Figure 4-96 to Figure 4-100. The rotor speed, power coefficient and turbine power variations of WECSs are portrayed in Figure 4-96, Figure 4-97 and Figure 4-98, respectively. Furthermore, pitch angle and power coefficient versus tip speed ratio trajectories are plotted in Figure 4-99 for Wind Speed (WS) II scenario. The equilibrium points of 5 WECSs on MPPT curves are determined for three times of start point, midpoint (M) and end point (E) which are 0 s, 20 s and 50 s, respectively. It is clear that the sudden increment and decrement of wind speed in t=1 lead to rotor speed boost and buck, respectively. This can be justified based on tip speed ratio equality of initial and mid equilibrium points of left hand side of Figure 4-100 in Wind Speed II ratio. It is to be notified that five WECSs have dissimilar rotor speed and identical pitch angle in t=20 s. These can be observed in left and right hand side of Figure 4-99 and Figure 4-100, respectively. It is noteworthy that 2.5% out of 10% of reserve power of all WECS is fed to grid in midpoint. The pitch angle of all WECSs located in zone 19 decreases in order to grow their generated power following the incident. As can be seen from Figure 4-96, WTs' speeds mitigate after t=20 s. This decrement can be visibly observed according to the new equilibrium points of WECSs in right hand side of Figure 4-100 at the end of simulation time.

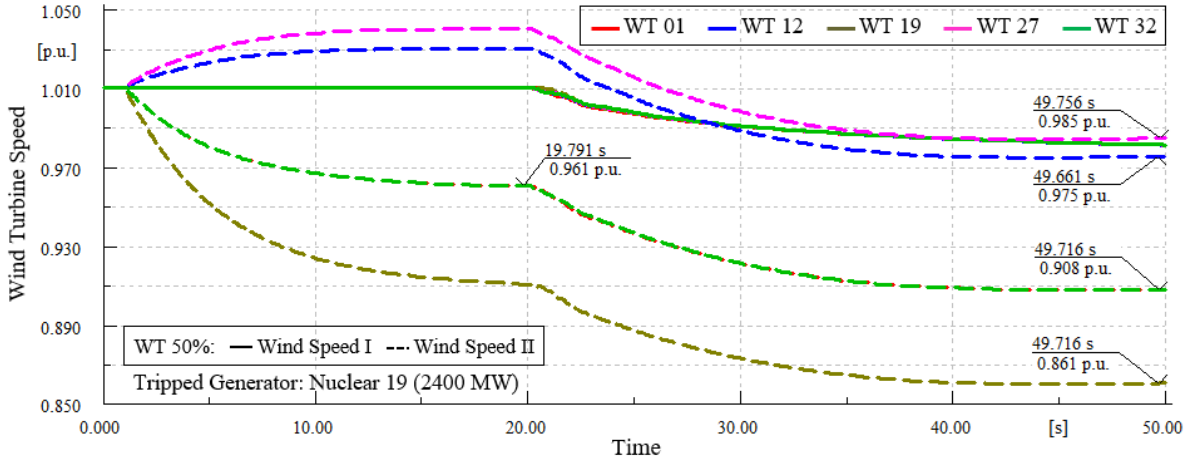

Figure 4-96: Wind turbine speed changes in "Wind Speed I" and "Wind Speed II" scenarios.

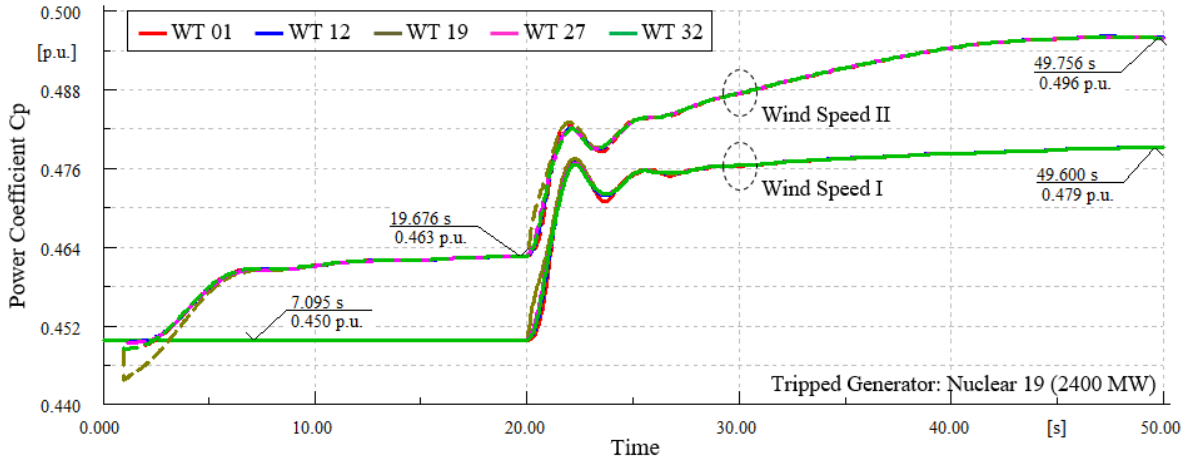

Figure 4-97: Power coefficient changes in “Wind Speed I” and “Wind Speed II” scenarios.

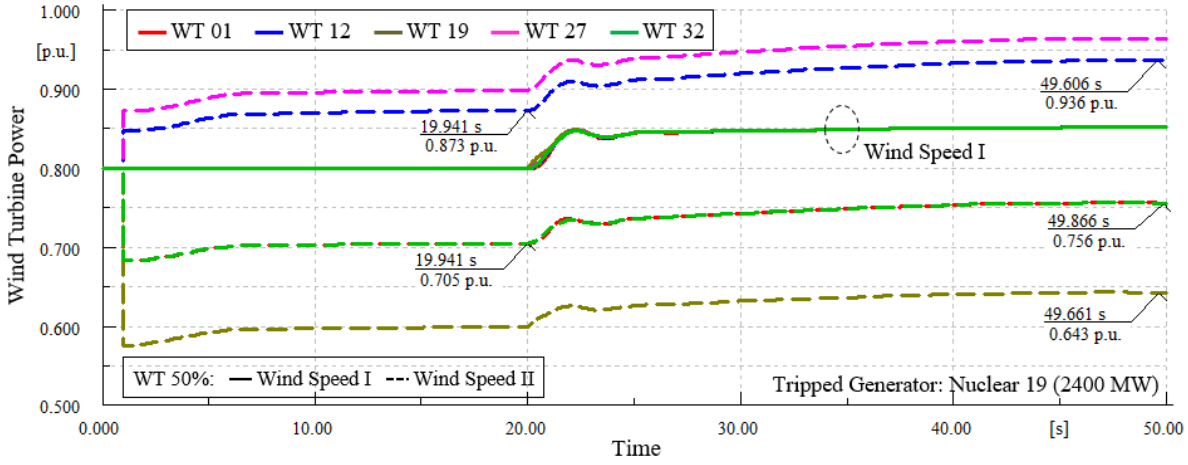

Figure 4-98: Wind turbine power changes in “Wind Speed I” and “Wind Speed II” scenarios.

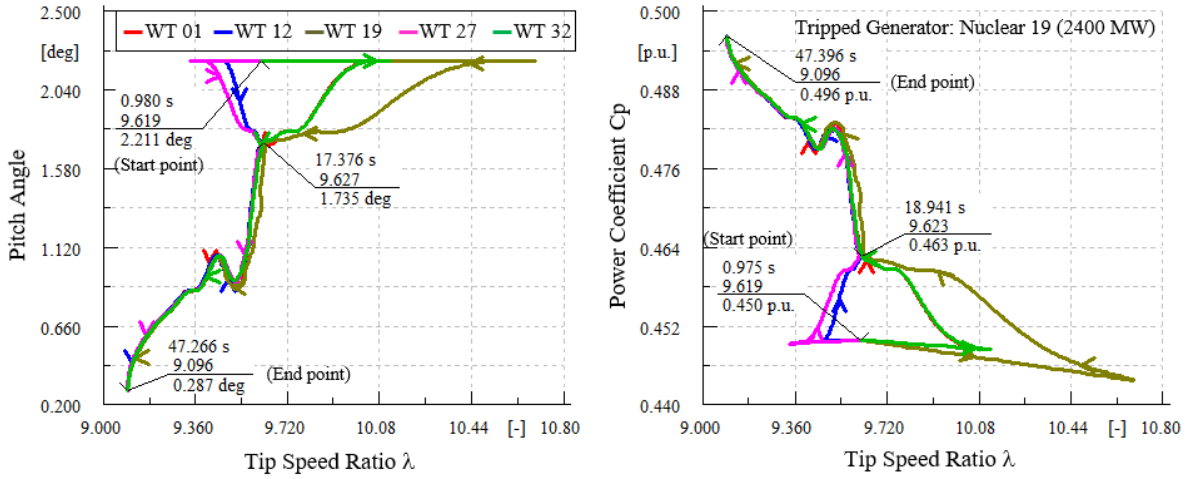

Figure 4-99: Pitch angle and power coefficient versus tip speed ratio trajectories in “Wind Speed I” and “Wind Speed II” scenarios.

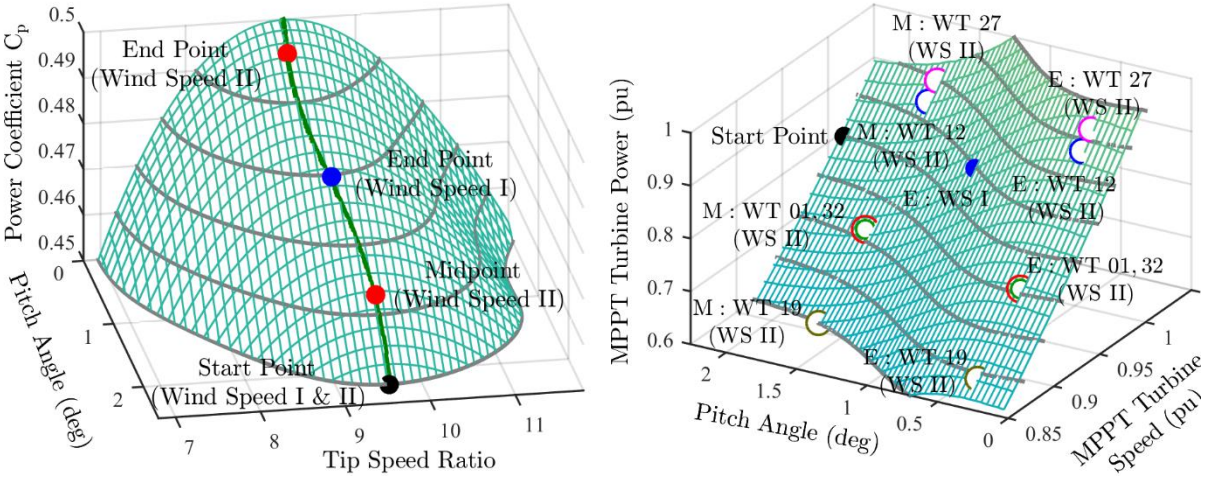

Figure 4-100: Location of pre- and post-event operating points of WECSs on MPPT characteristics in "Wind Speed I" and "Wind Speed II" scenarios: power coefficient versus pitch angle and tip speed ratio (Left), MPPT turbine power versus pitch angle and MPPT turbine speed (Right).

4.10.9.2. Second Scenario: Decreasing Wind Speed of All WECSs

In this subsection, the 36-zone GB system frequency response for the scenario of Wind Speed III following the loss of nuclear power located in zone 19 is investigated. The relevant results beside Wind Speed I scenario are illustrated in Figure 4-101 to Figure 4-110. The simulation time interval is 50 seconds. Moreover, wind speed values are changed at t=1 s for all five regions depicted in Figure 4-55, as shown in Figure 4-101. Despite Wind Speed II scenario, wind speed of Wind Speed III scenario for all regions of GB network reduces simultaneously. The loss of generator is simulated at t=20 s.

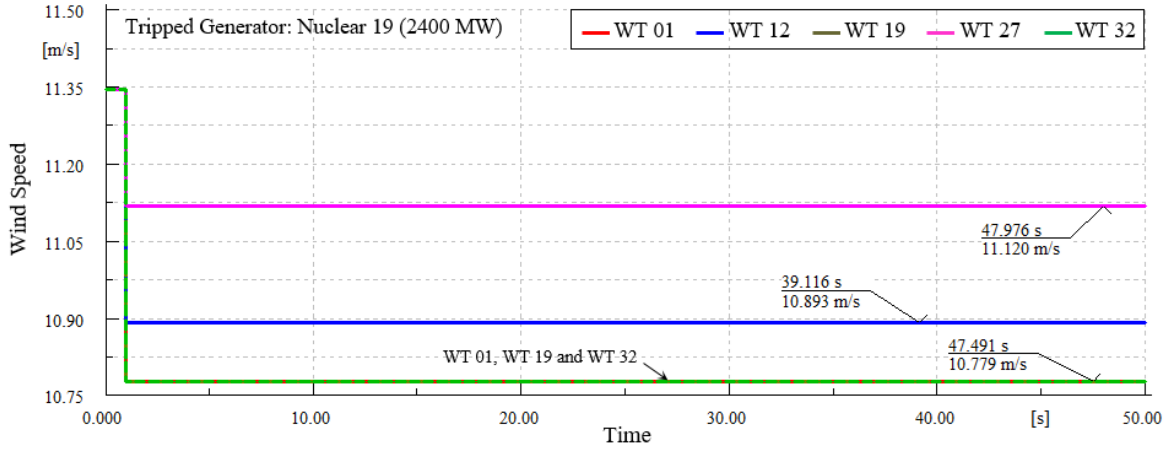

Figure 4-101: Wind speed of wind turbines in Wind Speed III scenario.

The COI frequency and COI RoCoF of GB network are shown in Figure 4-102 and Figure 4-103, respectively. Furthermore, the inertial power variations of conventional unit as well as WECS are illustrated in Figure 4-104 for the initial times of disturbance occurrence. Figure 4-105 illustrates conventional and WT turbine power change. The reserve powers of all 5 regions depicted in Figure 4-55 are shown in Figure 4-106 and Figure 4-107 including of their algebraic summation. The reserve power variation of all four regions where the disturbance is not happened are shown in Figure 4-106. In other hand, the corresponding values of Area 03 (Disturbance is occurred in this region) and the power summation of all areas are shown in Figure 4-107 for Wind Speed I and Wind Speed III.

Applying the wind speed change of Wind Speed II depicted in Figure 4-101 on WECSs leads to output power reduction of WECSs by 2250 MW. This in turn can abruptly mitigate reserve power of WECSs, as shown in Figure 4-106 and Figure 4-107. As can be seen form right hand side of Figure 4-107, the amount of this reduction for the whole network is 225 MW which is quite match to 10% reserve power of WECSs. This wind speed variation is like loss of wind power leading to system frequency mitigation, as depicted in Figure 4-102. Due to this fact, output powers of conventional units and WECSs increase following the event as shown in Figure 4-105. As a result, some part of WECSs' reserve power is occupied to compensate WECSs' power reduction in consequent of wind speed changes. The reserve power of WECSs reduces by 52% from 2000 MW to 960 MW in t=20 s. This is because the frequency nadir and steady-state frequency deviation in Wind Speed II scenario are dropped down by 30% and 165% compared to Wind Speed I, respectively. However, the COI RoCoF is equal in both scenarios. Note, the residual reserve power of all WECS is 160 MW at the end of simulation time. The simultaneous wind speed reduction across GB network in Wind Speed III reduces reserve power of all WECSs to zero value within 5 seconds from the disturbance occurrence time.

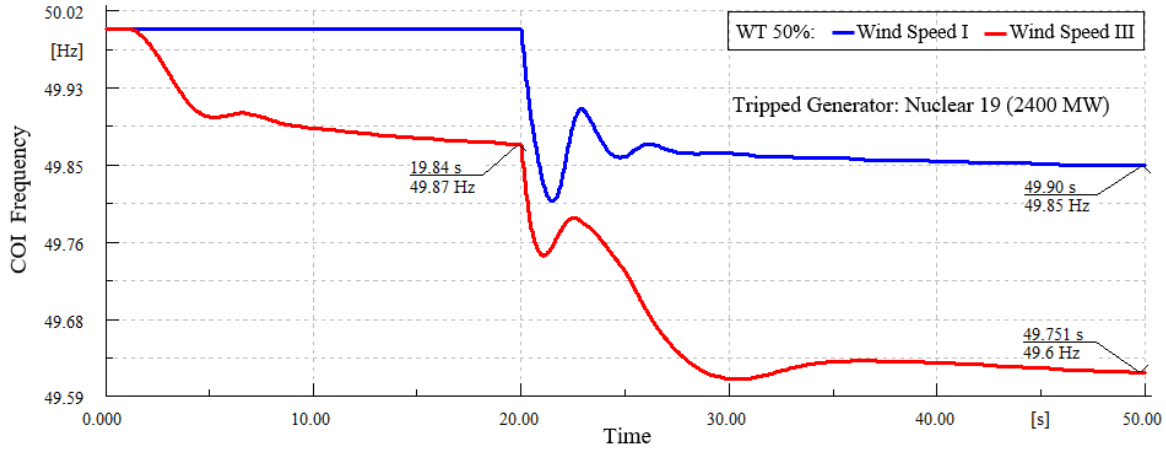

Figure 4-102: Frequency responses in "Wind Speed I" and "Wind Speed III" scenarios.

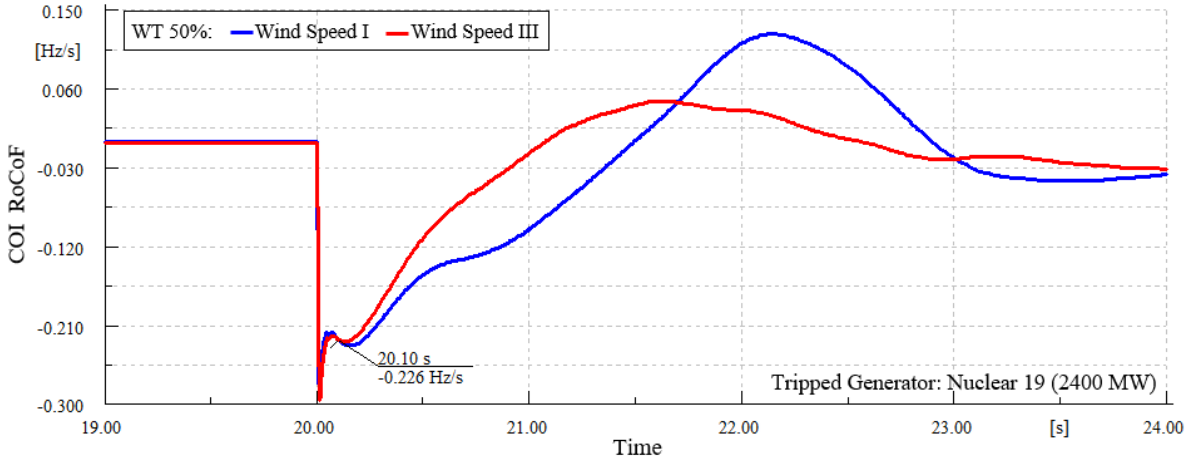

Figure 4-103: RoCoF deviations in "Wind Speed I" and "Wind Speed III" scenarios.

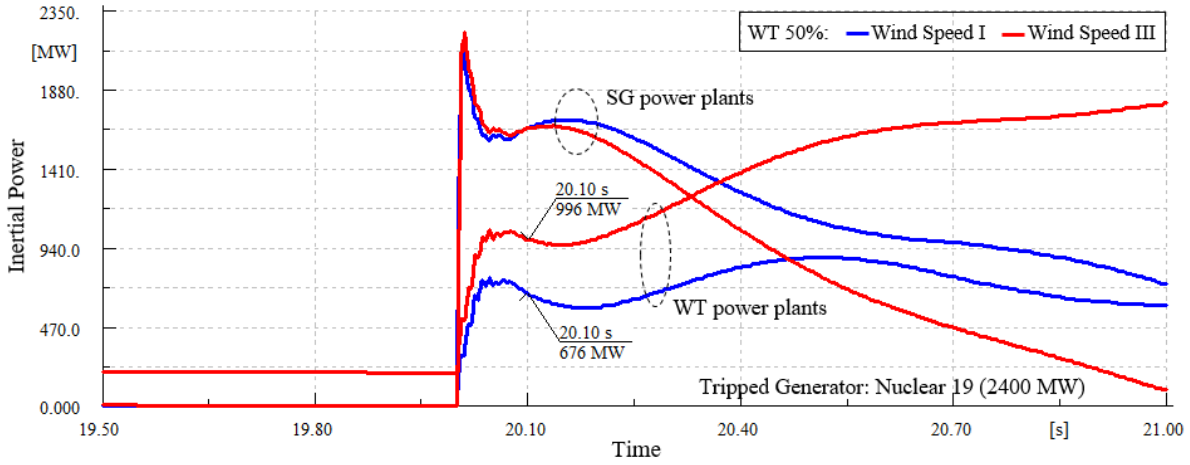

Figure 4-104: Inertial power changes in “Wind Speed I” and “Wind Speed III” scenarios.

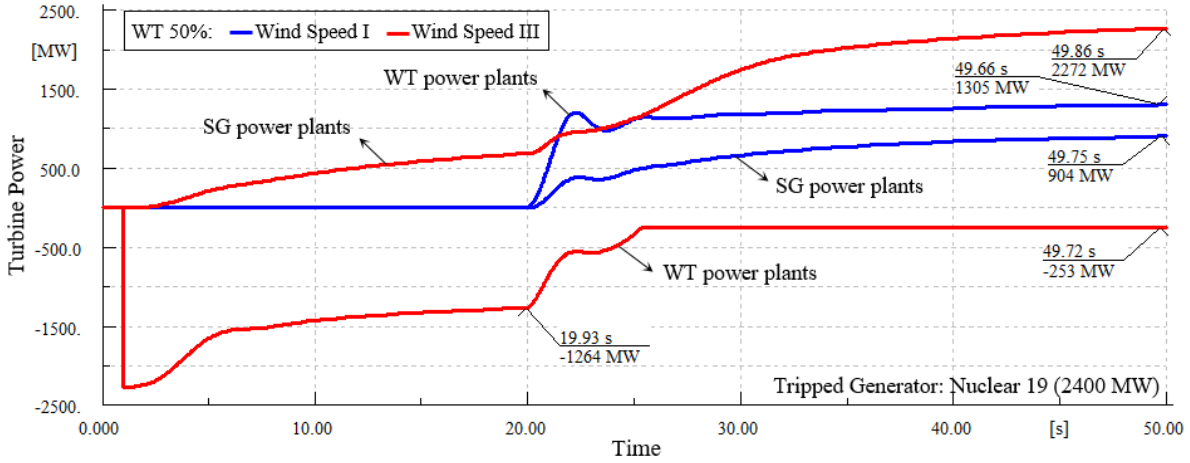

Figure 4-105: Turbine power deviations in “Wind Speed I” and “Wind Speed III” scenarios.

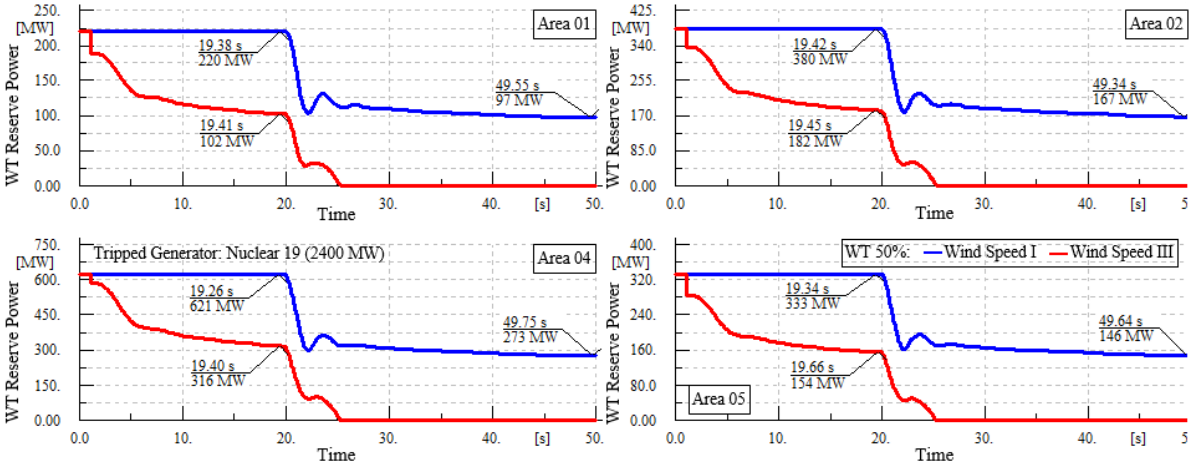

Figure 4-106: Wind turbine reserve power changes of area 01, area 02, area 04 and area 05 in “Wind Speed I” and “Wind Speed III” scenarios.

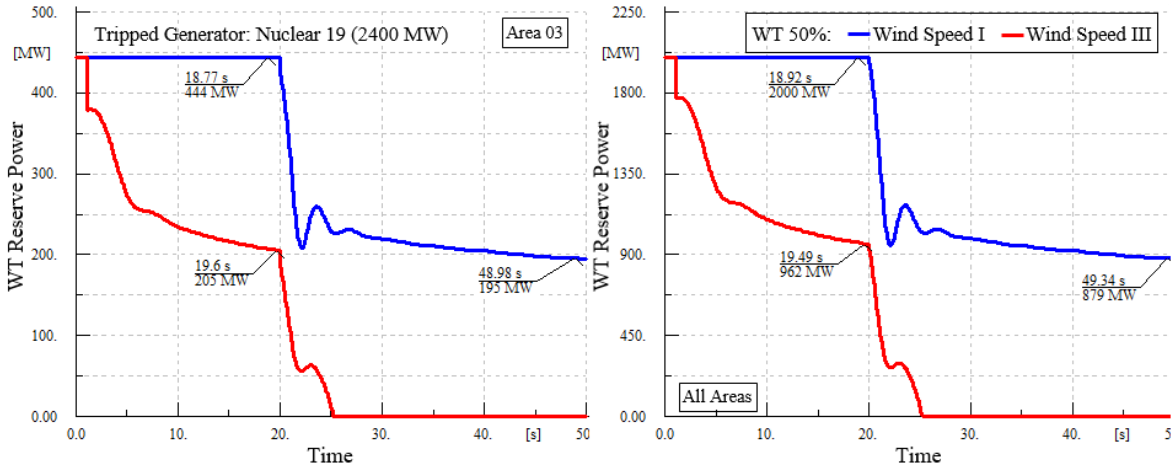

Figure 4-107: Wind turbine reserve power changes of area 03 and all areas in "Wind Speed I" and "Wind Speed III" scenarios.

In order to accurately investigate the above matter, some quantities related to 5 WECSs specified in Figure 20, are shown in Figure 4-108 to Figure 4-112. The rotor speed, power coefficient and turbine power variations of WECSs are portrayed in Figure 4-108, Figure 4-109 and Figure 4-110, respectively. Furthermore, pitch angle and power coefficient versus tip speed ratio trajectories are plotted in Figure 4-110 for Wind Speed III scenario. The equilibrium points of 5 WECSs on MPPT curves are determined for three times of start point, midpoint (M) and end point (E) which are 0 s, 20 s and 50 s, respectively. It is clear that the sudden decrement of wind speed in t=1 leads to rotor speed buck. This can be justified based on tip speed ratio equality of initial and mid equilibrium points of left hand side of Figure 4-112 in Wind Speed III scenario. It is to be notified that five WECSs have dissimilar rotor speed and identical pitch angle in t=20 s. These can be observed in left and right hand side of Figure 4-99 and Figure 4-112, respectively. It is noteworthy that 4.5% out of 10% of reserve power of all WECS is fed to grid in midpoint. The pitch angle of all WECSs located in zone 19 decreases in order to grow their generated power following the incident. As can be seen from Figure 4-108, WTs' speeds mitigate after t=20 s. This decrement can be visibly observed according to the new equilibrium points of WECSs in right hand side of Figure 4-112 at the end of simulation time. In addition, it can be clearly seen from Figure 4-112 that pitch angle and reserve power of all WECSs reach to zero in Wind Speed III scenario.

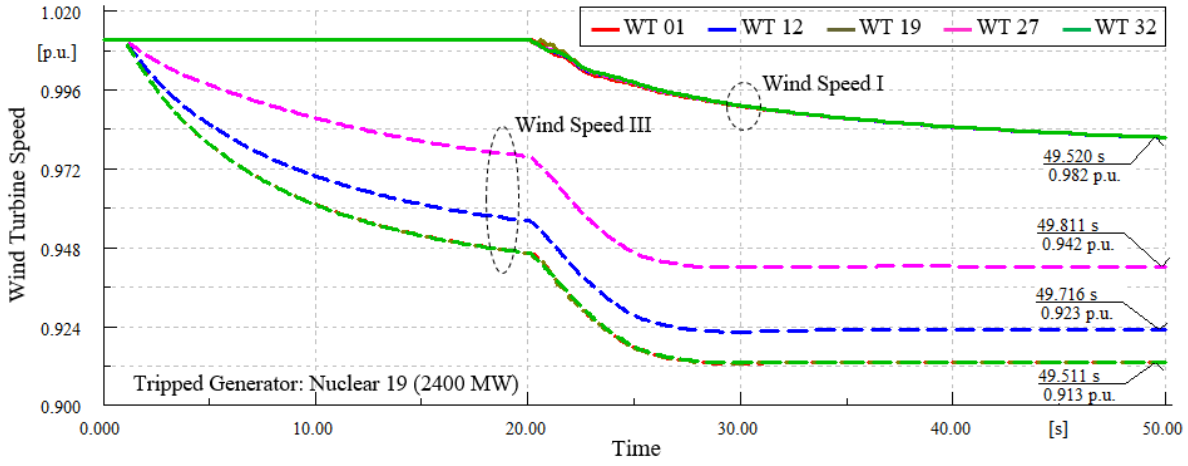

Figure 4-108: Wind turbine speed changes in "Wind Speed I" and "Wind Speed III" scenarios.

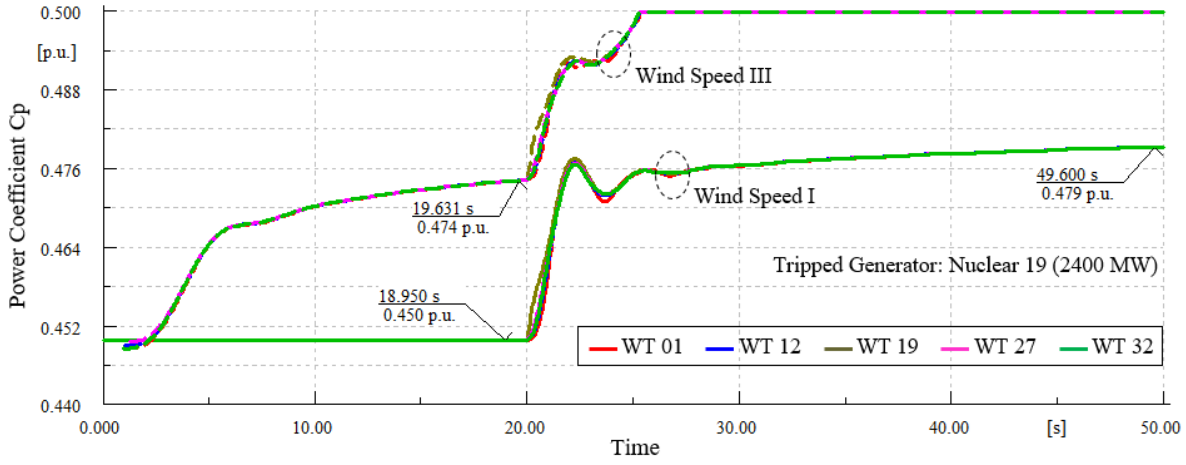

Figure 4-109: Power coefficient changes in “Wind Speed I” and “Wind Speed III” scenarios.

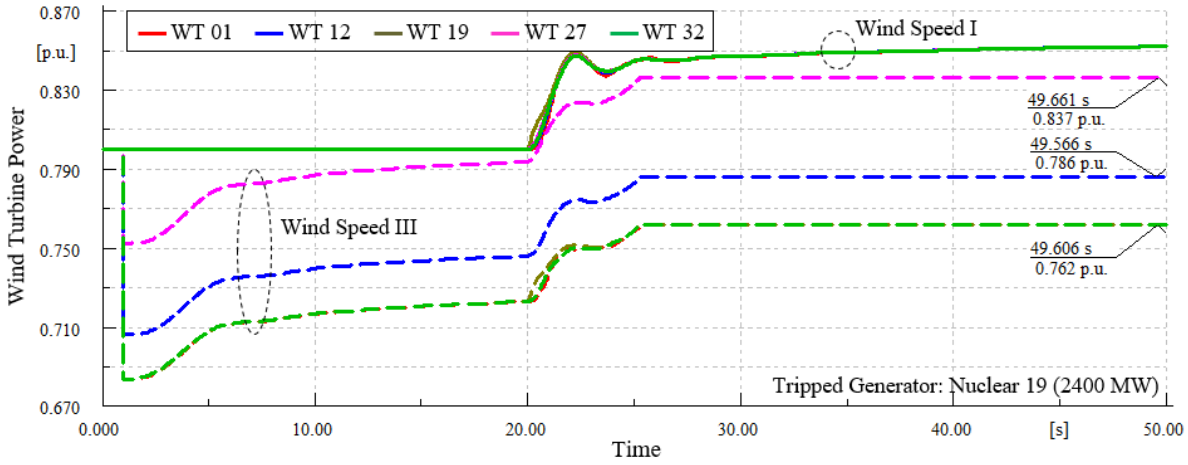

Figure 4-110: Wind turbine power changes in “Wind Speed I” and “Wind Speed III” scenarios.

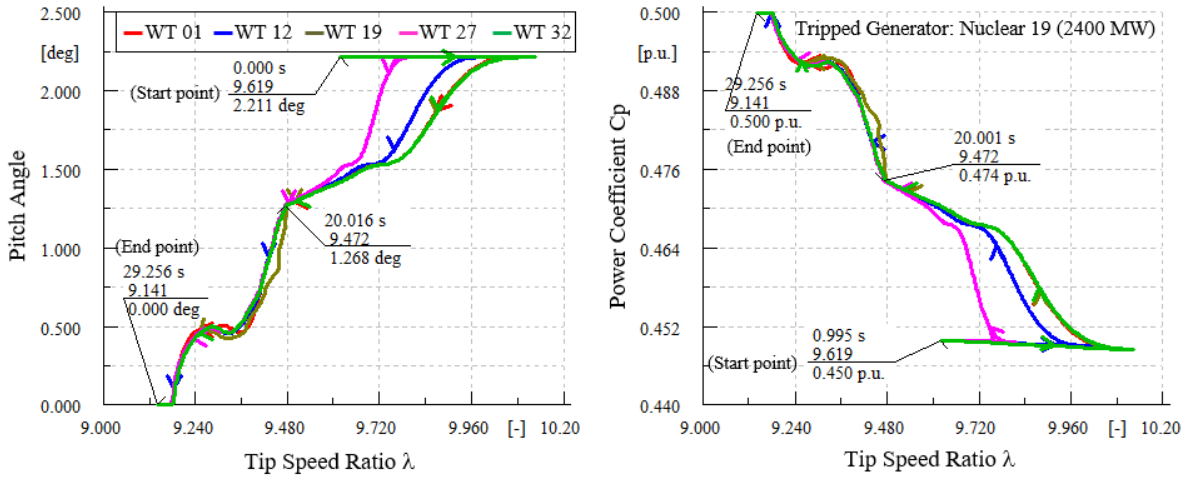

Figure 4-111: Pitch angle and power coefficient versus tip speed ratio trajectories in “Wind Speed I” and “Wind Speed III” scenarios.

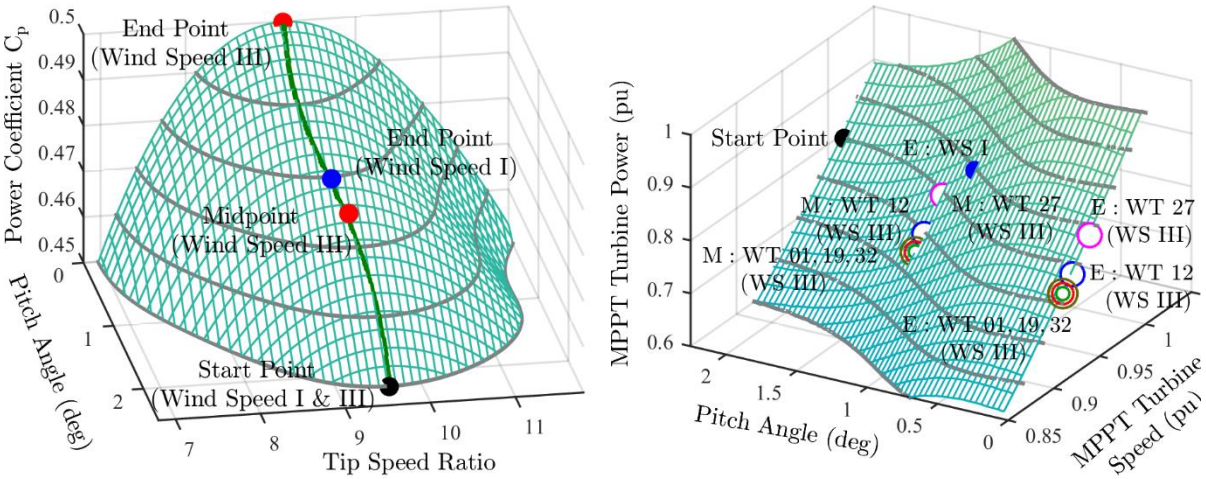

Figure 4-112: Location of pre- and post-event operating points of WECSs on MPPT characteristics in "Wind Speed I" and "Wind Speed III" scenarios: power coefficient versus pitch angle and tip speed ratio (Left), MPPT turbine power versus pitch angle and MPPT turbine speed (Right).

4.10.10. Executive Summary of Deploying WT in GB Test System

The dynamics of power system frequency are studied in this project study. A valid dynamic model of a WECS is developed in DIgSILENT PowerFactory. This WECS model is incorporated to the 36-zone GB network in order to study the influence of low and medium penetrations of WECSs on frequency control following the loss of generation.

The system frequency response of 36-zone GB network while 25% of load demand is satisfied by WECSs using time domain simulation is investigated and the results are compared with non-WECSs case. In this regard, six different losses of generators with different power capacity and location are implemented. The simulations results are provided for three main scenarios i.e. WECSs without inertial emulator and reserve power, only inertial emulator and with both inertial emulator and reserve power. A comparison between the non-WECSs and WECSs without inertial power and reserve power clearly shows that both RoCoF and frequency nadir are deteriorated in case of WECSs without inertial power and reserve power. Furthermore, it can be deduced that the steady-state frequency deviation in these two scenarios are almost identical. However, conventional units generate more power in WT 00% scenario compared to WT 25%. In case that WECSs are able to provide inertial power, the system RoCoF is improved, however, it is still worse than WT 00%. Moreover, it is observed that inertial power generated by WECSs has a slight influence on frequency nadir improvement. By taking the WT operating characteristics and conditions into account, the available inertial power and reserve power are utilized in a rational manner, and therefore the system frequency stability in terms of frequency nadir and steady-state frequency deviation compared to WT 00%, WT 25% I and WT 25% II is enhanced by 30% to 40%. This is in part because the inverter-based interfaces of WECS are more flexible and can release reserve power quicker than conventional unit. However, the system RoCoF in WT 25% scenario is still worse than WT 00%. The reason is that the increment rate of WTs' inertial power is restricted by 1 p.u. per second.

Furthermore, the system frequency response of 36-zone GB network is investigated for WT 50% and WT 25% scenarios. In this regard, two different losses of generators with different power capacity and location i.e. zone 19 and zone 4 is implemented. A comparison between these two scenarios clearly shows that both RoCoF and frequency nadir are enhanced by 15% and 305 with increment of wind power penetration. However, the COI RoCoF in WT 50% is deteriorated two times compared to WT 25%. By taking the WT operating characteristics and conditions into account, the available inertial and reserve power are utilized in a rational manner, and therefore the system frequency stability in terms of frequency nadir and steady-state frequency deviation with

wind power penetration level increment is enhanced. However, the system RoCoF gets worse, while the increment rate of WTs' inertial power is restricted by 1 p.u. per second.

The system frequency response of 36-zone GB network is also investigated for different values of reserve powers for WECSs. A comparison between the scenarios clearly shows that steady-state frequency deviation is reduced by increasing the reserve power level. Additionally, this can reduce burden on primary frequency support of conventional units. This claim can be also used for frequency nadir for most of the cases. Finally, it is observed that reserve power has a slight effect on COI frequency so that RoCoF is slightly increased with reserve power increment.

The wind speed variations impact on GB system frequency response under 50% penetration of wind power is investigated. It is observed that while the average value of wind speed variations per each MW wind power capacity installation is negative, the reserve power of WECSs is dropped down. As a result, once a generator is disconnected, the frequency nadir and steady-state frequency deviation is deteriorated compared to the fixed wind speed case. In addition, when the wind speed reduces in such a way that available reserve power of all WECSs before the event is less than half a generation lost, this reserve power will be dropped down to zero after the event. This half a power can be inferred according to 50% penetration level of WECSs and equal value of R i.e. 0.05 in PCO of WECSs and conventional units. However, it is clearly shown that reserve power changes of WECSs caused by wind speed variation have a minor effect on system RoCoF.

4.11. Load Frequency Control in Presence of WT

Wind power generation has reached extensive interest and penetration in more power systems over the last decade. On the other hand, todays, unavoidable development of wind power (WP) as a sustainable and cheap source of energy adds more difficulty and challenges to the power system frequency stability by importing another source of fluctuations, in addition to load. More importantly, this type of asynchronous generation does not contribute to the entire system inertia leading to the faster and larger frequency decay. Within this context, the system operator needs new control techniques/algorithms for existing and future hybrid power systems [37].

The main purpose of this chapter is to improve the current power system's load frequency control (LFC) by implementing a flexible fine-tuning fuzzy controller instead of conventional ones and adding the inertia emulators (IEs) to doubly-fed induction generator (DFIG) based wind turbines (WTs). These strategies can support the grid in terms of inertial, governor and secondary responses. In a large scale interconnected system, all the units are electromagnetically connected to each other through the network and in a steady state have the same nominal system frequency. So, the classical-based LFC is not an effective way to return the frequency to its nominal value after a perturbation occurrence [38]. In this regard, several variable structure controllers and adaptive control techniques are proposed for LFC in [39] and [40], respectively. One of the main drawbacks of these controllers is that they are very slow. Thus, the PID controller is suggested as an alternative strategy and vastly utilized due to its appropriate robustness and simple realization. However, its performance is highly dependent on the suitable tuning of its coefficients [41]. Accordingly, the heuristic based controllers using fuzzy logic, neural network and Kalman filter strategies are suggested in [42]-[44], respectively. Kalman filters are computationally very complex as compared to the fuzzy logic controllers. Moreover, in complex multivariable non-linear systems in which the full mathematical model may even not be available, the application of fuzzy logic controllers is particularly useful in comparison to other controllers. In this work, the fuzzy PID controller is implemented due to its simple features. Furthermore, an online Jaya algorithm (JA) is utilized to simultaneously optimize the factors of input and output membership functions for the proposed controller's coefficients. The essential concept of this new powerful is that the solution provided in search space of a problem should move towards the best agent and avoid the worst one [45]. The main feature of this algorithm which makes it distinguished in comparison of other similar algorithms is that it does not require tuning any algorithmic parameter. The superiority of the JA over the other optimization techniques in terms of computational time and optimality of the solution like genetic algorithm, particle swarm optimization,

differential evolution and teaching-learning-based optimization has recently been established in [45] (on 54 benchmark functions).

Recently, some control strategies have been provided by researchers for providing frequency support. The de-loading operation strategy as well as genetic algorithm based optimization of control parameters are proposed in [46] and [47], respectively. Supporting wind generator with battery energy storage system is another solution proposed in [48]. Also, incorporating an IE to the controlling loop of DFIG is suggested in [49]. This IE is contained of two fast and slow high-pass filters and employed to provide a non-wasting energy inertial response in a small power system. In this study, a new loop of differential lag filter is added to the previous one in order to accelerate the arresting process of frequency oscillation in a large power system. This IE has the ability to reduce the system frequency deviation (Δf), maximum frequency excursion (f^{nadir}) and the rate of change of frequency (RoCoF, $\Delta f / \Delta t$). Therefore, a new robust and efficient controlling solution for the threat of reduced inertia is provided by coordination of these new controllers. The simulation results in the DIgSILENT PowerFactory software verify the feasibility and efficiency of the projected control architecture.

4.11.1 Load frequency control

The aim of load frequency control (LFC) is to contain the initial dynamic evolution of frequency within the defined security thresholds. Moreover, according to the standard prescribes, the acceptable RoCoF is in the range of [0, 0.125] Hz/s [50], and f^{nadir} should be 49.2 Hz (for 50Hz system). To better clarify this issue, a typical primary frequency response of a large grid to a disturbance is portrayed in Figure 4-113. In the event of a power imbalance, the frequency drop is partly supported by the stored kinetic energy in the rotating masses of the synchronous units which are directly connected to the grid. At this condition, the RoCoF can be formulated as [51]:

The aim of load frequency control (LFC) is to contain the initial dynamic evolution of frequency within the defined security thresholds. Moreover, according to the standard prescribes, the acceptable RoCoF is in the range of [0, 0.125] Hz/s [50], and f^{nadir} should be 49.2 Hz (for 50Hz system). To better clarify this issue, a typical primary frequency response of a large grid to a disturbance is portrayed in Figure 4-113. In the event of a power imbalance, the frequency drop is partly supported by the stored kinetic energy in the rotating masses of the synchronous units which are directly connected to the grid. At this condition, the RoCoF can be formulated as:

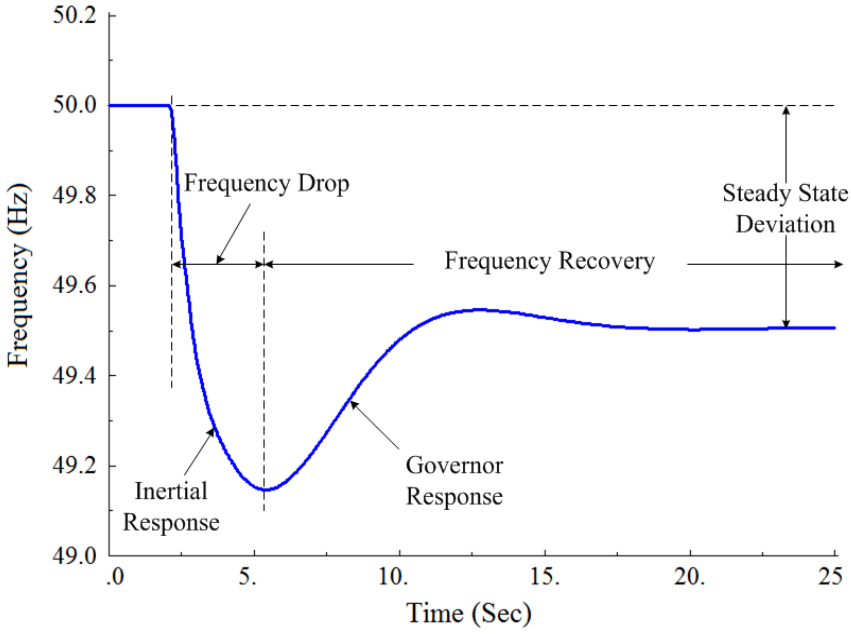

Figure 4-113: Typical primary frequency of a large grid.

$$\frac{\Delta f}{\Delta t} = \frac{\Delta P_{\text{tie}}}{2H_{\text{sys}}} \tag{4.46}$$

where, H_{sys} is the system inertia in seconds and ΔP_{tie} is calculated as follows:

$$\Delta P_{\text{tie}} = \sum_{i=1}^{N} \left(P_{\text{tie,act}_i} - P_{\text{tie,sch}_i} \right) \tag{4.47}$$

where, $P_{\text{tie,act}_i}$ and $P_{\text{tie,sch}_i}$ are the actual and scheduled power flows for a given area with N tie lines, respectively. So, the smaller the inertia of a power system, the larger the RoCoF as well as Δf . It can be concluded that the slower the inertial response of units, the lower the RoCoF. When the frequency stops reducing, i.e. the f^{nadir} is provided. It should be also mentioned that the slower the governor response, the lower the f^{nadir} . Therefore, the LFC should be smart enough to handle any disturbance and restore frequency.

4.11.2 Proposed inertia emulator (IE) for primary frequency support of DFIG

The integration of WTs to networks causes the system inertia reduction. This is because the rotating masses of these types of generations are decoupled from the grid and they do not contribute inertia to the system. One of the main solutions for handling this problem is to consider an IE in order to simulate the new scheduled wind power which will be affected by the grid frequency. As shown in Figure 4-114, it can be located between the speed controller and the P-Q controller of RSC. In this figure, w_{sch} and w_{act} are the scheduled (rated) and actual wind speed, respectively. Also, $P^{old}_{\text{tie-W,sch}}$ and $P^{new}_{\text{tie-W,sch}}$ are the scheduled wind power before and after applying IE, respectively. f_{act} is the actual frequency of the system.

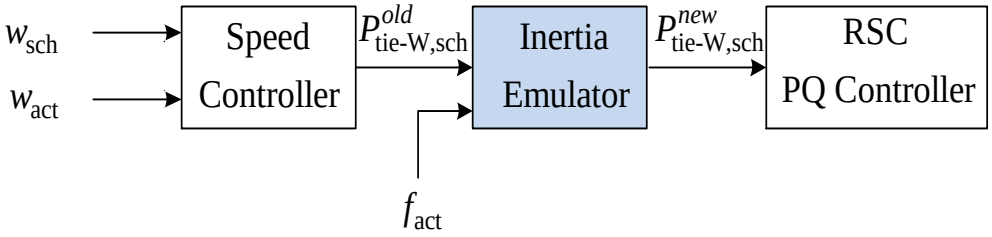

Figure 4-114: The WT controller considering IE.

The previous version of IE which is employed in [49] and the proposed IE are shown in Figure 4-115(a) and Figure 4-115(b), respectively. The previous IE which is called Dual DT1 filter can decrease the RoCoF. However, the governor response is sacrificed since the RoCoF reduction and frequency recovery is done slowly in this IE. In the proposed IE, the slow DT1 filter is replaced with a lag-differential lag filter. The equivalent electrical circuit of the proposed series filter is shown in Figure 4-116 and its Laplacian transfer function is formulated as follows:

$$G(s)=\frac{U_{out}(s)}{U_{in}(s)}=\frac{sRC}{1+sRC}\frac{1+sR_2C_1}{1+sC_1(R_1+R_2)} \tag{4.48}$$

$$G(s)=K\frac{sT}{1+sT}\frac{1+sT_b}{1+sT_a} \tag{4.49}$$

The step response of the proposed filter and a lag filter is depicted in Figure 4-117. The time constant of T_{lag} is considered to be equal to T_{slow} and set to 10-*s* in this work. Moreover, T_a, T_b and K are set to 1, 0.1 and 3, respectively. The suggested IE can simultaneously improve both the inertial and governor responses. The simulation results will confirm this claim.

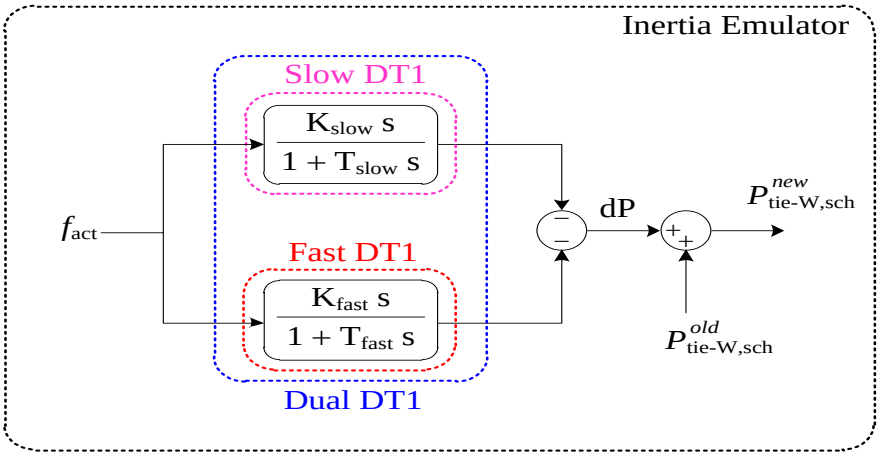

(a)

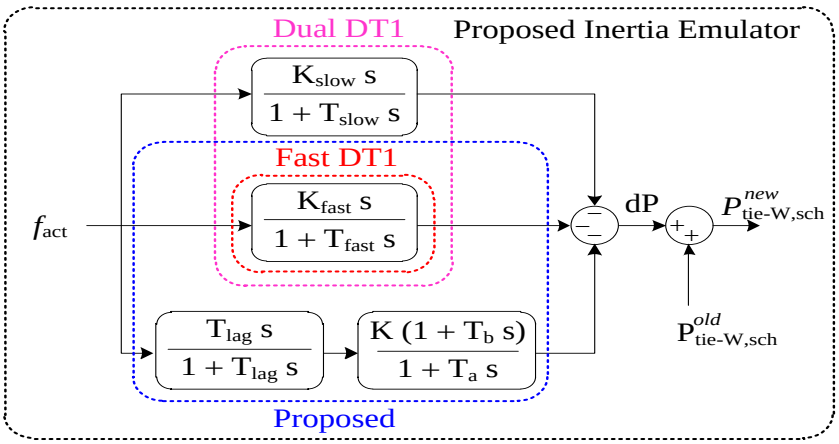

(b)

Figure 4-115: (a) The IE suggested in [49] and (b) The proposed IE.

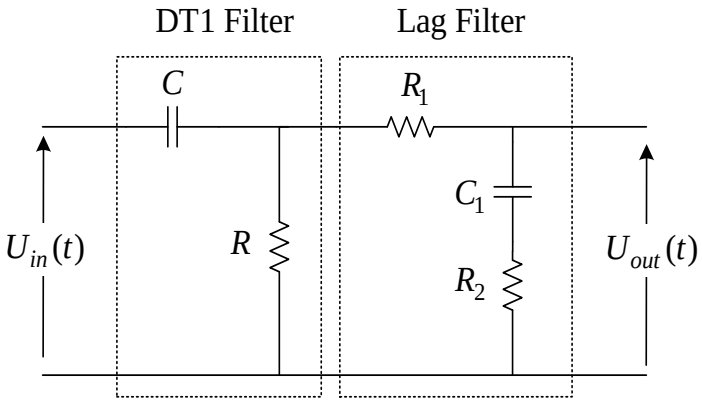

Figure 4-116: The equivalent electrical circuit of lag-differential lag filter.

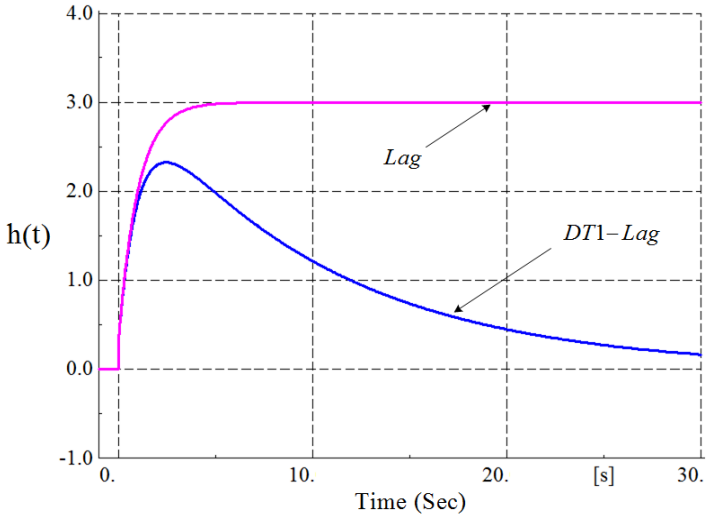

Figure 4-117: Step response of the lag-differential lag filter and lag one.

4.11.3 JA method for optimizing fuzzy PID controller

In the conventional one, the reference power of hydro or thermal units in each area is continuously controlled to be set to its nominal amount through an integral controller with the input of $\mathrm{ACE} = \delta\Delta f + \Delta P_{\mathrm{tie}}$ so-called Area Control Error (ACE) in which δ is the frequency bias.

The updated ACE with the consideration of significant penetration of WTs can be expressed as follows:

$$\Delta P_{\mathrm{tie}} = \Delta P_{\mathrm{tie\text{-}C}} + \Delta P_{\mathrm{tie\text{-}W}} = \sum_{i=1}^{N}\left(P_{\mathrm{tie\text{-}C,act}_i} - P_{\mathrm{tie\text{-}C,sch}_i}\right) + \sum_{i=1}^{N}\left(P_{\mathrm{tie\text{-}W,act}_i} - P_{\mathrm{tie\text{-}W,sch}_i}\right) \tag{4.50}$$

Where, $P_{\mathrm{tie\text{-}C,act}_i}$ and $P_{\mathrm{tie\text{-}C,sch}_i}$ are the conventional actual and scheduled power of tie line *i*, respectively. $P_{\mathrm{tie\text{-}W,act}_i}$ and $P_{\mathrm{tie\text{-}W,sch}_i}$ are the actual and scheduled wind tie line power *i*, respectively. The ACE can be reformulated as follows:

$$\mathrm{ACE} = \delta\Delta f + \sum_{i=1}^{N}\left(P_{\mathrm{tie\text{-}C,act}_i} - P_{\mathrm{tie\text{-}C,sch}_i}\right) + \sum_{i=1}^{N}\left(P_{\mathrm{tie\text{-}W,act}_i} - P_{\mathrm{tie\text{-}W,sch}_i}\right) \tag{4.51}$$

As mentioned, the traditional PID controllers are mostly used in the LFC of multi-area networks and their parameters are usually adjusted according to pre-determined operating points. This can lead to an undesirable point that is not suitable for any disturbance. So, the fuzzy logic architecture is implemented to adjust the parameters of PID. The suggested JA-fuzzy PID controller is shown in Figure 4-118. It consists of two main parts those are fuzzy logic unit as well as a PID controller. As it can be seen, the first level uses the input scaling factors α and β, the output scaling factors (ξ, γ and λ) and the input signals of ACE and ΔACE to tune the parameters of second level, i.e. K_P, K_I and K_D.

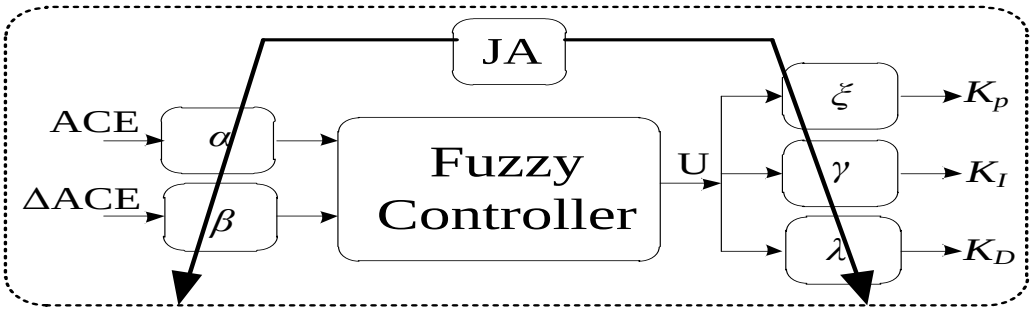

Figure 4-118: JA-fuzzy PID controller.

The fuzzy logic on the basis of Mamdani type gives a tool for translating a linguistic control technique based on expert knowledge into an automatic control strategy. It consists of four parts: fuzzification, fuzzy rule base, inference engine, and defuzzification. In order to achieve the full potential of the fuzzy systems in our concerned problem, it is crucial to design the fuzzy logic controller properly. Its designing can be divided into four steps: 1) selecting suitable kind of membership functions (MFs), 2) selecting the inputs/outputs of the system and tuning the range in which each fuzzified variable lies, 3) selecting the optimal number of MFs and 4) tuning the parameters of the MFs. These steps are explained hereinafter.

According to the investigations applied on various MFs in the LFC, the triangular one is selected because it can provide a trade-off between the accurateness and computational burden. The MFs' number has commonly an odd value and mainly depends on the sensitivity of the output variables, inputs variations and their discourse universe. Also, as mentioned, two scaling factors α and β are used to normalize the range of inputs to a discourse universe in which MFs are specified. The three scaling factors ξ, γ and λ are implemented in order to

change the normalized control efforts to their practical point. The last step is to tune the parameters of MFs. Thus, a powerful optimization method based on JA is employed. Each MF depending on its type should be defined by a number of parameters. The MFs used in our study, i.e. triangular, are defined by three parameters. Therefore in total, there are 9 (3×3) parameters for ACE, 9 (3×3) parameters for ΔACE and 12 (4×3) parameters for output variable named U. The total number of design variables considering five scaling factors would be 9+9+12+5=35 which should be optimized by JA.

The JA is a new population-based optimization algorithm which is proposed by Rao in [45]. In this technique, the fitness function of optimization algorithm should be firstly determined. As the main purpose of this study is to reduce the frequency deviation in very short time scale, the following objective function *F* is selected.

$$F = 10^2 \int t \left(\sum_{j=1}^{M} \left| \Delta \mathrm{ACE}_j \right| \right) dt \tag{4.52}$$

where, *M* is the total number of areas in the system. After which, it is assumed that there are *Nvar* number of design variables (*n*=1,…,*Nvar*) in each candidate solution *m* (*m*=1,…,*Ncan*) in each iterate *iter* (*iter*=1,…,*Niter*). Accordingly, each candidate solution can be defined as $X_{m,iter}=[x_{1,m,iter},\ldots, x_{n,m,iter},\ldots,x_{Nvar,m,iter}]$. The initial candidate solutions are randomly generated and the JA modifies them iteration by iteration according to the following equation [45]:

$$x_{n,m,iter}^{new} = x_{n,m,iter} + r1_{n,m,iter}\left(x_{n,iter}^{best} - \left|x_{n,iter}\right|\right) - r2_{n,m,iter}\left(x_{n,iter}^{worst} - \left|x_{n,m,iter}\right|\right); \forall n,m,iter \tag{4.53}$$

where, $x_{n,m,iter}^{best}$ and $x_{n,m,iter}^{worst}$ are the *n*th variables of the respective best and worst solutions in iterate *iter*. The $r1_{n,m,iter}$ and $r2_{n,m,iter}$ are two random numbers generated in the range of [0,1] corresponding to each element. The $x_{n,m,iter}^{new}$ is the new generated element *n* for candidate solution *m* in iteration *iter*. The new candidate $X_{m,iter}^{new}$ is accepted and became the input to the next iteration if it gives better fitness function value. The optimization procedure of JA is clarified in the following Pseudo-Code.

for $m = 1 : Ncan$
  Initialize $X_{m,0}$
end for
for $iter = 1 : Niter$
  for $m = 1 : Ncan$
    Update $X_{m,iter}$ **using (7.5 - 2)**
  end for
end for
Return the best solution $\mathbf{X}_{Niter}^{best}$ **with the minimum objective value (4.48).**

The MFs of two inputs and output variable obtained by JA are shown in Figure 4-119. Based on the above mentioned strategies for LFC, the fuzzy rules for the fuzzy controller are also given in Table 4-11. For instance, the first rule has the following form:

IF (ΔACE is N) and (ACE is N) *THEN* U is NL

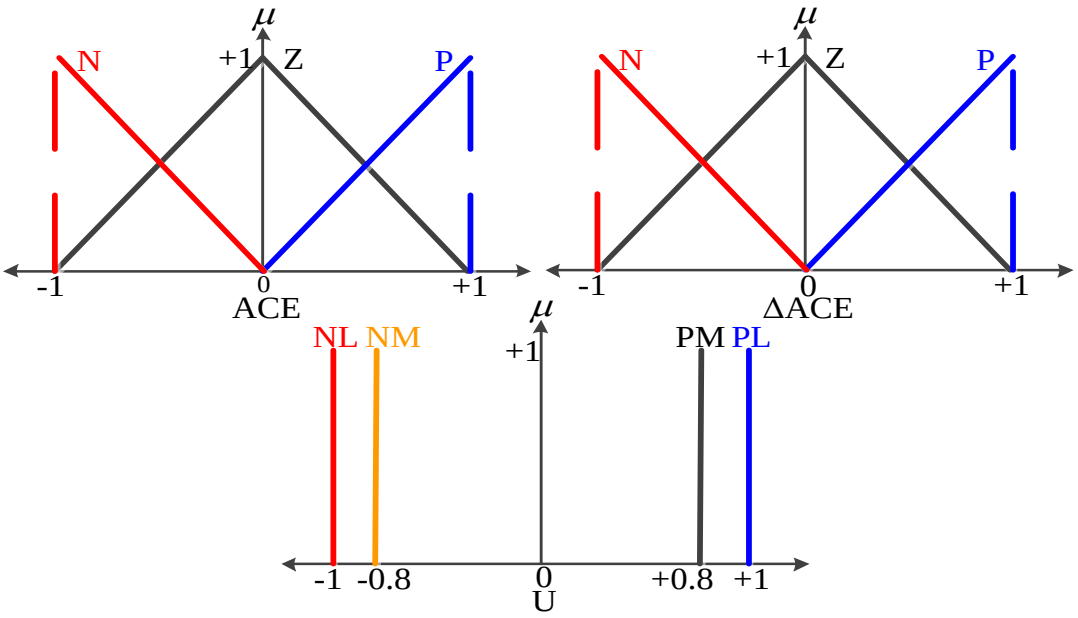

Figure 4-119: Fuzzy MFs.

Table 4-11: Fuzzy rule base.

ΔACE	ACE		
	N	Z	P
N	NL	NM	Z
Z	NM	Z	PM
P	Z	PM	PL

4.11.4 Simulation Results to apply LFC for IEEE 39-Bus Test System

4.11.4.1.Multi-area interconnected power system configuration

Performance of the suggested controller is evaluated to certify its efficiency in a wide range of operation conditions by the simulations carried out in the DIgSILENT PowerFactory software.

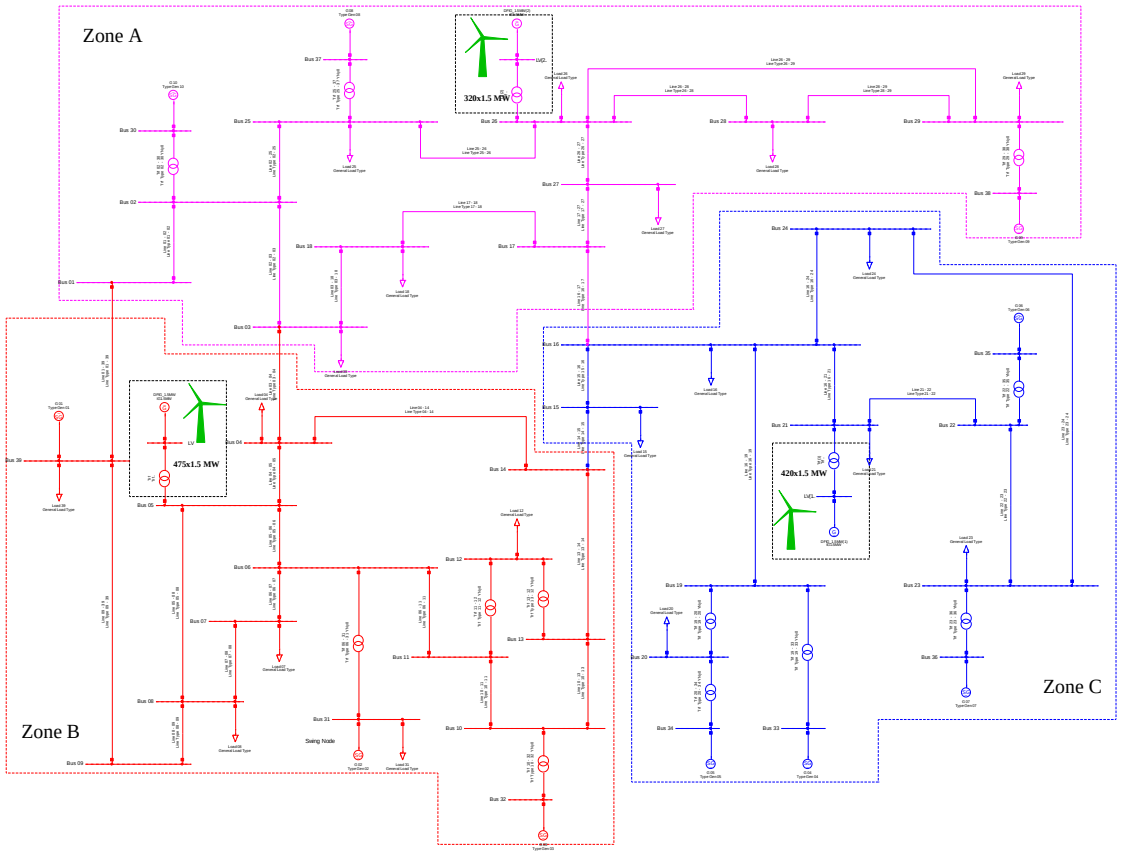

Figure 4-120: Single-line diagram of New England test system with three wind farms.

A multi-area system which is considered in some papers like [40], consists of three areas with three thermal units and one area with a hydro unit which are connected through four tie lines. However, this type of configuration is not practical and the New England power system including three strongly meshed areas, 10 thermal generators, 19 load nodes, 34 lines and 12 transformers is considered in this study and its single line diagram is shown in Figure 4-120. As shown, three wind farms comprising of 475 1.5-MW DFIG based WTs, 420 1.5-MW DFIG based WTs and 320 1.5-MW DFIG based WTs are connected to buses #5, #21 and #26, respectively. These connections are done by three power transformers. The total penetration level of wind power generation is 30%. Moreover, the wind speed variability is also considered to show the applicability purpose. The start-up and rated wind speed for these three wind farms are considered to be 8.16 and 14 m/s, respectively. All the practical constraints imposed by the physical dynamics of the system like the generation rate, governor dead band and so on are considered to be satisfied. The data of this system can be extracted from [37].

4.11.4.2.Discussion

In order to verify the effectiveness of the suggested JA-fuzzy PID controller, it is compared to original PID controller. In this regard, three step load oscillations are instantaneously applied to the abovementioned meshed zones at 10 *s*: i) In zone A: 4.56% of total load of zone, ii) In zone B: 8% of total area load in the zone, and iii) In zone C: 8% of total area load. First of all, the parameters of the fuzzy PID are optimized using the JA algorithm. The optimized scaling factors as well as PID parameters for the traditional PID controller and proposed JA-fuzzy PID controller are tabulated in Table 4-12. Their corresponding fitness function values are 23.14 and 2.31. It is evident that the fitness function of proposed technique is better than the traditional PID control strategy. It should be mentioned that the maximum number of iteration and population are set to 20 and 30, respectively.

Table 4-12: Adjusted parameters of two controllers

Proposed JA-fuzzy PID					PID		
α	β	ξ	γ	λ	K_P	K_I	K_D
1.99	2.99	7.97	5.93	0.31	7.42	3.87	1.39

In Figure 4-121, the tie-line power flows and frequency variation in the case of JA-fuzzy PID-based LFC and traditional PID controller are shown for all areas. It is clear that the results of traditional PID show more fluctuations in maintaining the tie-line flows in the acceptable bands close to the predefined amounts. It means that the proposed approach is successful in arresting the frequency deviation.

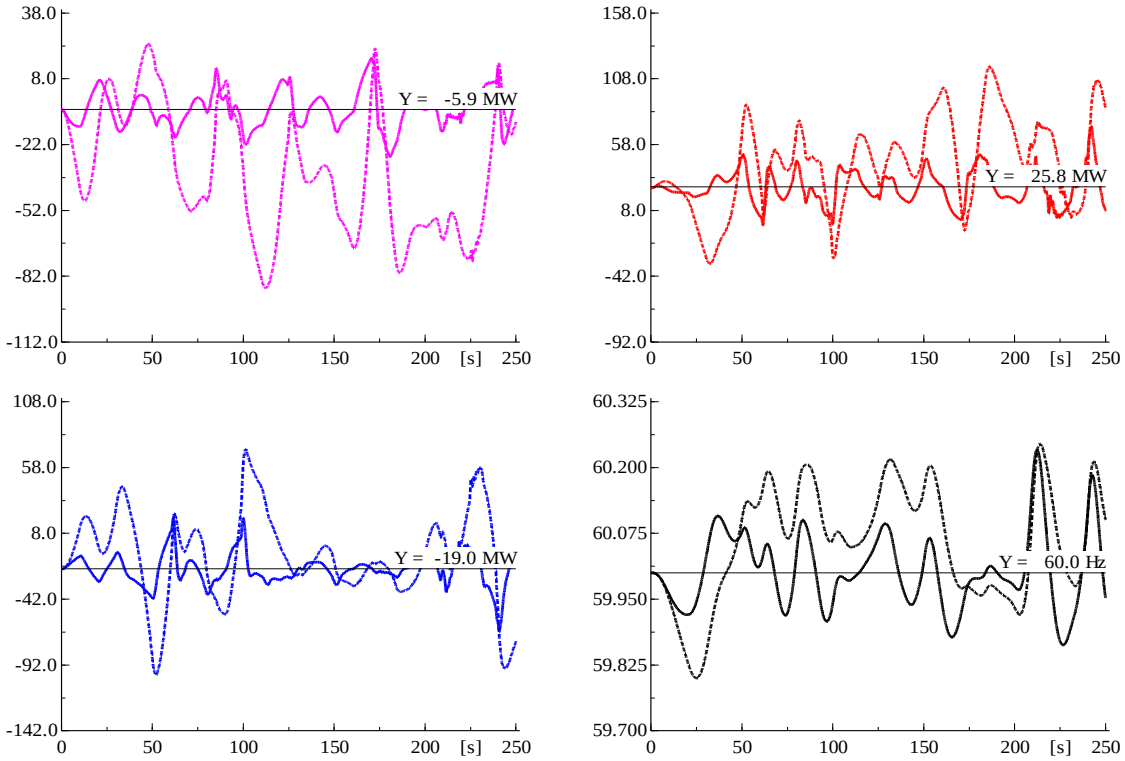

Figure 4-121: Interchange flow: Zone A (Up-Left), Zone B (Up-Rigth) and Zone C (Down-Left) with proposed JA-fuzzy PID controller (Solid) and with conventional PID controller (Dashed); System frequency (Down-Right).

The improvement in inertial response using the proposed IE for DFIG-based WTs is established by simulations in three different cases: 1) proposed IE, 2) IE presented in [49] and 3) without IE. The wind farms active power in p.u. and system frequency for these cases with 224 MW step increase of network's load are portrayed in Figure 4-122. The f^{nadir} is improved by about 0.04 Hz from 59.6 Hz (case #1) from 59.56 Hz (case #3) due to the suggested IE. It is also clear that f^{nadir} is enhanced in case #1 with respect to case #2, due to the involvement of proposed filter. As shown, the governor response of the proposed IE is considerably improved with respect to case #2. The IE makes it possible that all wind farms feed more power into the grid to restore frequency.

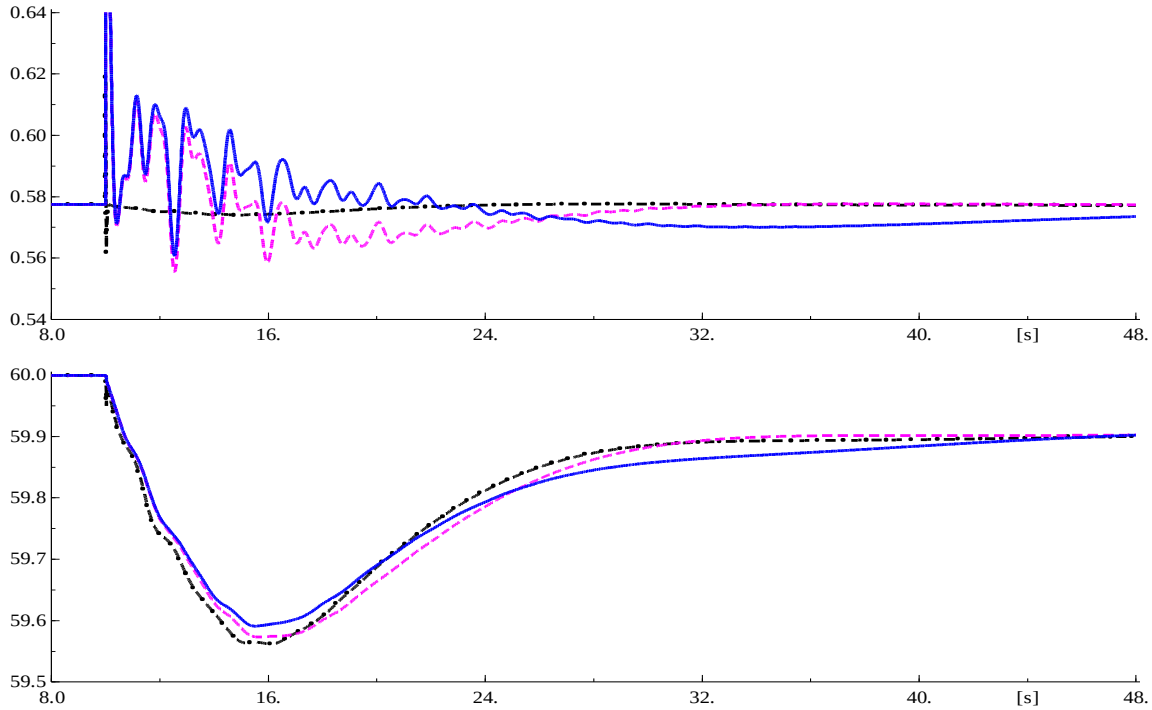

Figure 4-122: Wind farm active power in p.u. (Up) and system frequency in Hz (Down); (without IE (dot-dashed), with conventional IE (dashed) and with proposed IE (solid)).

As it mentioned, replacing conventional power generating units by non-inertia energy sources like WTs will lead to a lower inertia and increased RoCoF. So, the power system inertia has been significantly reduced and high frequency fluctuations are expected. In this regard, the previous LFC should be smartly updated to arrest frequency deviation. In response to this challenge, in this study two control strategies are suggested to improve LFC in an interconnected multi-area system. The inertial response of DFIG based WTs is enhanced by means of a new Inertia Emulator (IE) filter. Moreover, an adaptive JA-fuzzy PID controller is proposed for LFC which is designed by the new JA method. The developed LFC is applied to the IEEE New England power system test case. The simulation results provide this insight that in comparison with conventional PID controller and IE, the new JA-fuzzy PID controller and IE demonstrate superior performance.

4.11.5. Executive Summary of Deploying Modified LFC in IEEE 39-Bus Test System

Replacing conventional power generating units by noninertia energy sources like WTs will lead to a lower inertia and increased RoCoF. So, the power system inertia has been significantly reduced and high frequency fluctuations are expected. In this regard, the previous LFC should be smartly updated to arrest frequency deviation. In response to this challenge, in this chapter two control strategies are suggested to improve LFC in an interconnected multi-area system. The inertial response of DFIG based WTs is enhanced by means of a new Inertia Emulator (IE) filter. Moreover, an adaptive JA-fuzzy PID controller is proposed for LFC which is designed by the new JA method. The developed LFC is applied to the IEEE New England power system test case. The simulation results provide this insight that in comparison with conventional PID controller and IE, the new JA-fuzzy PID controller and IE demonstrate superior performance.

4.12. References

[1] G. Lalor, A. Mullane, and M. O'Malley, "Frequency control and wind turbine technologies," IEEE Trans. Power Syst., vol. 20, no. 4, pp. 1905-1913, Nov. 2005.

[2] L. Zeni, A. Rudolph, J. Münster-Swendsen, I. Margaris, A. Hansen, and P. Sørensen, "Virtual inertia for variable speed wind turbines," Wind Energy, vol. 16, no. 8, pp. 1225–1239, 2013.

[3] Ruttledge L, Flynn D. Emulated inertial response from wind turbines: gain scheduling and resource coordination. IEEE Transactions on Power Systems. 2016 Sep;31(5):3747-55.

[4] M. Tsili and P. S. Pathanassiou, "A review of grid-code technical requirements for wind farms," IET Renew. Power Gener., vol. 3, no. 3, pp. 308–332, Nov. 2009.

[5] National Grid, Innovation, Enhanced Frequency Control Capability, Available: http://www2.nationalgrid.com/UK/Our-company/Innovation/NIC/EFCC/

[6] Clark K, Miller NW, Sanchez-Gasca JJ. Modeling of GE wind turbine-generators for grid studies. GE Energy. 2010 Apr 16;4.

[7] National Grid, Innovation, Enhanced Frequency Control Capability, Available: http://www2.nationalgrid.com/UK/Our-company/Innovation/NIC/EFCC/

[8] UK Wind Energy Database, http://www.renewableuk.com/page/UKWEDhome

[9] F. M. Hughes, O. Anaya-Lara, N. Jenkins, and G. Strbac, "Control of DFIG-based wind generation for power network support," IEEE Trans. Power Syst., vol. 20, no. 4, pp. 1958-1966, Nov. 2005.

[10] F. W. Koch, I. Erlich, and F. Shewarega, "Dynamic simulation of large wind farms integrated in a multimachine network," in Proc. IEEE Power Eng. Soc. General Meeting, 2003.

[11] M. Kayikçi and J. V. Milanović, "Dynamic contribution of DFIG-based wind plants to system frequency disturbances," IEEE Trans. Power Syst., vol. 24, no. 2, pp. 859-867, May 2009.

[12] J. M. Mauricio, A. Marano, A. Gómez-Expósito, and J. L. Martinez-Ramos, "Frequency regulation contribution through variable-speed wind energy conversion systems," IEEE Trans. Power Syst., vol. 24, no. 1, pp. 173-180, Feb. 2009.

[13] J. Morren, S. W. De Haan, W. L. Kling, and J. Ferreira, "Wind turbines emulating inertia and supporting primary frequency control," IEEE Trans. Power Syst., vol. 21, no. 1, pp. 433-434, Feb. 2006.

[14] Li Y, Xu Z, Wong KP. "Advanced control strategies of pmsg-based wind turbines for system inertia support," IEEE Trans. Power Syst., 2016 Oct 12.

[15] J. Van de Vyver, J. D. De Kooning, B. Meersman, L. Vandevelde, T. L. Vandoorn, "Droop control as an alternative inertial response strategy for the synthetic inertia on wind turbines," IEEE Trans. Power Syst., vol. 31, no. 2, pp. 1129-1138, Mar. 2016.

[16] J. Lee, G. Jang, E. Muljadi, F. Blaabjerg, Z. Chen, and Y. C. Kang, "Stable short-term frequency support using adaptive gains for a dfig-based wind power plant," IEEE Trans. Energy Convers., vol. 31, no. 3, pp. 1068-1079, Sep. 2016.

[17] S. Ghosh, S. Kamalasadan, N. Senroy, and J. Enslin, "Doubly fed induction generator (DFIG)-based wind farm control framework for primary frequency and inertial response application," IEEE Trans. Power Syst., vol. 31, no. 3, pp. 1861-1871, May 2016.

[18] Wilches-Bernal F, Chow JH, Sanchez-Gasca JJ. A Fundamental Study of Applying Wind Turbines for Power System Frequency Control. IEEE Transactions on Power Systems. 2016 Mar;31(2):1496-505.

[19] Ye H, Pei W, Qi Z. Analytical modeling of inertial and droop responses from a wind farm for short-term frequency regulation in power systems. IEEE Transactions on Power Systems. 2016 Sep;31(5):3414-23.

[20] Wu Z, Gao W, Zhang H, Yan S, Wang X. Coordinated Control Strategy of Battery Energy Storage System and PMSG-WTG to Enhance System Frequency Regulation Capability. IEEE Transactions on Sustainable Energy. 2017 Mar 8.

[21] De Almeida RG, Lopes JP. Participation of doubly fed induction wind generators in system frequency regulation. IEEE transactions on power systems. 2007 Aug;22(3):944-50.

[22] Arani MM, Mohamed YA. Analysis and Damping of Mechanical Resonance of Wind Power Generators Contributing to Frequency Regulation. IEEE Transactions on Power Systems. 2016 Oct 19.

[23] Vidyanandan KV, Senroy N. Primary frequency regulation by deloaded wind turbines using variable droop. IEEE Trans. Power Systems. 2013 May;28(2):837-46.

[24] I. Erlich and M. Wilch, “Primary frequency control by wind turbines,” in Proc. 2010 IEEE Power and Energy Soc. General Meeting, 2010, pp. 1-8.
[25] R. Gasch and J. Twele, Windkraftanlagen, Grundlagen, Entwurf, Planung und Betrieb, B. Teubner, 2005.
[26] Betz, A., (1919). Schraubenpropeller mit geringstem energieverlust. Gottinger Nachr., Germany.
[27] S. Heier, Grid Integration of Wind Energy Conversion Systems, 2nd Edition, Wiley, April 2006
[28] Fortmann, Jens. Modeling of wind turbines with doubly fed generator system. Springer, 2014.
[29] R. Pena, J. C. Clare and G. M. Asher, "Doubly fed induction generator using back-to-back PWM converters and its application to variable-speed wind-energy generation," in IEE Proceedings - Electric Power Applications, vol. 143, no. 3, pp. 231-241, May 1996.
[30] J. G. Slootweg, S. W. H. de Haan, H. Polinder and W. L. Kling, "General model for representing variable speed wind turbines in power system dynamics simulations," in IEEE Transactions on Power Systems, vol. 18, no. 1, pp. 144-151, Feb 2003.
[31] Akhmatov, Vladislav. "Analysis of dynamic behaviour of electric power systems with large amount of wind power." Electrical Power Engineering (2003).
[32] Yazhou Lei, A. Mullane, G. Lightbody and R. Yacamini, "Modeling of the wind turbine with a doubly fed induction generator for grid integration studies," in IEEE Transactions on Energy Conversion, vol. 21, no. 1, pp. 257-264, March 2006.
[33] Shao, M., et al. Modeling of GE Wind Turbine-Generator for Grid Studies, Version 4.6. Tech. Rep., General Electric International, Inc, 2013.
[34] Hansen, Anca Daniela, and Ioannis D. Margaris. Type IV wind turbine model. DTU Wind Energy, 2014.
[35] Ackermann, Thomas, ed. Wind power in power systems. Vol. 140. Chichester, UK: John Wiley, 2005.
[36] Karimi-Ghartema, Masoud. Enhanced phase-locked loop structures for power and energy applications. John Wiley & Sons, 2014.
[37] H. Bevrani, M. Watanabe, and Y. Mitani, Power System Control: Fundamentals and New Perspectives, Wiley-IEEE press, 2014.
[38] G. Delille, B. Francois, G. Malarange, “Dynamic frequency control support by energy storage to reduce the impact of wind and solar generation on isolated power system inertia,” IEEE Trans. Sustain. Energy, vol. 3, no. 4, pp. 931-939, Oct. 2012.
[39] N. N. Benjamin and W. C. Chan “Variable structure control of electric power generation,” IEEE Trans. Power App. Syst., vol. 101, no. 2, pp. 376-380, Feb. 1982.
[40] W. Tan “Decentralized load frequency controller analysis and tuning for multi-area power systems,” Energy Convers. Manage., vol. 52, no. 5, pp. 2015-2023, May 2011.
[41] C. Knospe, “PID control,” IEEE Control Syst. Mag., vol. 26, no. 1, pp. 30-31, Feb. 2006.
[42] S. Zhang, Y. Mishra, and M. Shahidehpour, “Fuzzy-logic based frequency controller for wind farms augmented with energy storage systems,” IEEE Trans. Power Syst., vol. PP, no. 99, 2015.
[43] S. M. Malik, S. Yingyun, A. Z. Khan, “Implementation of intelligent AGC in PSAT for optimal use in smart grids,” 2014 IEEE Int. Conf. Intel. Energy Power Syst. (IEPS), pp. 186-191,
[44] L. Ding and S. K. Jayaweera, “Optimal stochastic tracking for primary frequency control in an interactive smart grid infrastructure,” IEEE Syst. J., vol. 9, no. 3, pp. 978-988, Aug. 2014.
[45] R. Rao, “Jaya: A simple and new optimization algorithm for solving constrained and unconstrained optimization problems,” Int. J. Ind. Eng. Comput., vol. 7, no. 1, pp. 19-34, 2016.
[46] F. D. Gonzalez, M. Hau, A. Sumper, and O. G. Bellmunt, “Participation of wind power plants in system frequency control: Review of grid code requirements and control methods,” Renew. Sustain. Energy Rev., vol. 34, pp. 551-564, June 2014.
[47] C. D. Das, A. K. Roy, and N. Shinha,“GA based frequency controller for solar thermal diesel wind hybrid energy generation energy storage system,” Int. J. Elect. Power Energy Syst., vol. 43, no. 1, pp. 262-279, Dec. 2012.

[48] A. Esmaili, B. Novakovic, A. Nasiri, and O. Abdel-Baqi, “A hybrid system of Li-lon capacitors and flow battery for dynamic wind energy support,” IEEE Trans. Ind. Appl., vol. 49, no. 4, pp. 1649-1657, Jul. 2013.

[49] M. Marinelli, S. Massucco, A. Mansoldo, and M. Norton, “Analysis of inertial response and primary power-frequency control provision by doubly fed induction generator wind turbines in a small power system,” In Proc. 17th Power Syst. Comput. Conf., Aug. 2011.

[50] Energy Networks Association and National Grid, Frequency Changes During Large Disturbances and Their Impact on the Total System, 2013.

[51] Altimania, Mohammad Rashed "Modelling of doubly-fed induction generators connected to distribution system based on eMEGASim® real-time digital simulator", 2014 [Available online] http://www.opal-rt.com/sites/default/files/technical_papers/Modeling%20of%20Doubly-Fed%20Induction%20Generators%20Connected%20to%20Distribu.pdf

5. Reserve Power and Inertial Emulator Based PV System: Development and Formulation

A suitable model of PV system for studying its short-term dynamic response to a system frequency deviation is developed. In the chapter, the concentration is on describing the main component of PV system and its relevant equations. Available inertial and droop responses based on de-loading from the PV system to help supporting the primary frequency control in power system networks are also analytically investigated. Then the model is utilised in conjunction with a simple but practical two-area Klein-Rogers-Kundur (KRK) power system and GB models to study the impact of increasing levels of wind energy conversion system (WECS) generation on frequency control. The modal analysis and dynamic time-domain simulation to study the power system frequency response and investigate how the PV systems can impact this response on a test power system with high penetration of WECSs.

5.1. Literature Review

Photovoltaic (PV) power plants penetration is increasing at high rate to become one of the most popular sustainable energy sources nowadays [1]. It is reported that in 2017, the overall UK solar PV capacity is increased by 6% compared to 2016 to stand at about 12 GW, and that there are many more planned plants across the Great Britain (GB) network [2], [3]. However, PVs do not contribute to the whole inertia of the network since they do not have rotational mass. Furthermore, the I-V and P-V characteristics of PV system are nonlinear in terms of PV module temperature and solar irradiance level [4]. In order to get rid of these issues, grid codes impose growing ancillary service requirements to PV power plants which increasingly extend to the frequency regulation provision [5]. Additionally, it is necessary to deload the maximum power point tracking to the sub-optimal one in order to maintain active power reserves and deploy inertial emulator to support frequency regulation.

In principle, two control strategies exist to implement frequency regulation capabilities of the PVs: either installing battery energy storage (BES) to enhance inertial response and droop controller [6], [7], at price of increased system cost and complicatedness, or employing the most cost-effective deloaded technique [8] to deploy in droop based primary frequency regulation. In the case of latter approach which modifies the maximum power point tracking (MPPT) techniques to operate PV at a suboptimal power than at the MPP [9], [10], the capacitors of the DC link are usually characterized by high rate of charging and thus the frequency response challenge is transferred to the PV generator and its control scheme. The literature on PV power control without deploying internal BES is still restricted.

Frequency regulation becomes even a more challenging topic for two-stage PV module from a control perspective since the PV inverter's DC link voltage is decoupled from the voltage of PV generator [11]. However, the droop-type control proposed in [12] is the only method in this area, a control strategy is introduced in [13] to adjust the PV operating point below the MPP, by regulating the PV module voltage to a specific portion of its open circuit voltage. However, this fraction is not determined in relation to the reserve power stipulated by power system operator or grid codes. In addition, a proportional-integral (PI) based grid frequency control strategy is presented in [14], without noticing how to follow external reserve margin. A fuzzy based controller to regulate PV power output for frequency regulation is proposed in [6] in which the PV switches from the MPPT mode to the frequency regulation mode and vice versa.

A sufficiently detailed PV model to providing all required frequency regulation functionalities is still missing from the state-of-the-art literatures. In this chapter, an average but accurate model for the PV system is derived where the inertial and droop based frequency regulations can be obtained. As a short time interval has to be simulated to investigate the PV model for dynamic frequency studies, the detailed model, which models all the switching procedures results in an overly-long simulation time. Therefore, an averaged but accurate model of the PV system is deployed, where the voltage source inverter is treated as a current source in the proposed PV model. In this way, the simulation time is shortened while at the same time retaining enough precision. One of

the key features of this PV system is that the real behavior of PV module is modelled. Additionally, the MPPT which is one of the most vital parts of real PV systems' control architecture is deployed in the proposed model. In order to deload the PV module for primary frequency response, its required voltage needs to be increased. The MPP voltage is calculated using Newton-Raphson technique due to non-linear relationship of voltage and current of PV module. The DC-DC boost converter is deployed to regulate the duty cycle, to tune the PV module voltage on the predetermined voltage of MPPT block and meet the reserve requirement. The proposed framework has this ability to greatly track the solar irradiance and module temperature variation and capture maximum producible power from PV module. Regarding inertial frequency response, this inertial power is taken from dc link capacitor by adjusting the dc link reference voltage. As releasing some portion of energy stored in dc link capacitor leads to its voltage reduction, a new voltage recovery strategy is proposed and appended into dc link voltage controller. The main advantage of this method is that it has almost no influence on generated power of the PV system.

5.2. Motivation

Photovoltaic (PV) power has reached extensive interest and penetration in more power systems over the last decade. Therefore, a lot of power industries like UK (EFCC project) have deployed PV systems. On the other hand, todays, unavoidable development of PVs as a sustainable and cheap source of energy adds more difficulty and challenges to the power system frequency stability by importing another source of fluctuations, in addition to load. More importantly, this type of asynchronous generation does not contribute to the entire system inertia leading to the faster and larger frequency decay. In addition, the conventional types of PVs operate in their maximum power point tracking (MPPT) curve so that reserve power is unavailable. Thus, PVs naturally can provide small or even no contributions to the frequency control of power networks [15].

The reduction of synchronous inertia results in faster and more considerable changes in system frequency response (SFR), rate of change of frequency (RoCoF) and the frequency deviation following the incidents. In the EFCC project, the main focus is on fast system frequency control support immediately after a power mismatch. These controllers can be divided into two major parts those are emulated inertial response (EIR) and de-loading operation. The former one deploys the energy stored in DC link capacitor of PV systems to obtain a temporary injection of power [16], while the later one makes PVs to operate over a de-loaded MPPT curve to provide reserve power. In this context, it is to be noted that for PVs operated above MPP voltage and not dropped down before the disturbance, their injection power is followed by the energy recovery phase as PVs track back to their MPPT.

With high integrations of PVs into power systems especially Great Britain (GB) transmission network, frequency instability is a prominent challenge, and therefore the expectation of transmission system operator (TSO) i.e. National Grid (NG) in U.K. is also that the PVs could take part in the frequency response [17], [18].

This chapter tries to discuss and illustrate the PV system model in DIgSILENT PowerFactory. Developing the mathematical model of the PV system and its modelling derived in DIgSILENT simulation language (DSL) and DIgSILENT programming language (DPL) for power system frequency studies are the main aims of this chapter.

5.3. Photovoltaic System

5.3.1. The Electrical Characteristic of a PV Module

The basic building block for PV applications is a module consisting of a number of cells in series to deliver much higher voltage than that of an individual cell. The semiconductor materials are utilized in PV to convert sunlight into electrical power. The equipment is so closely pertinent to the solid-state technologies deployed to

make transistors, diodes, and all of other semiconductor switches. The starting point for most of the world's current generation of PV devices, as well as almost all semiconductors, is pure crystalline silicon. A PV cell is a *p-n* junction, as shown in left side of Figure 5-1.

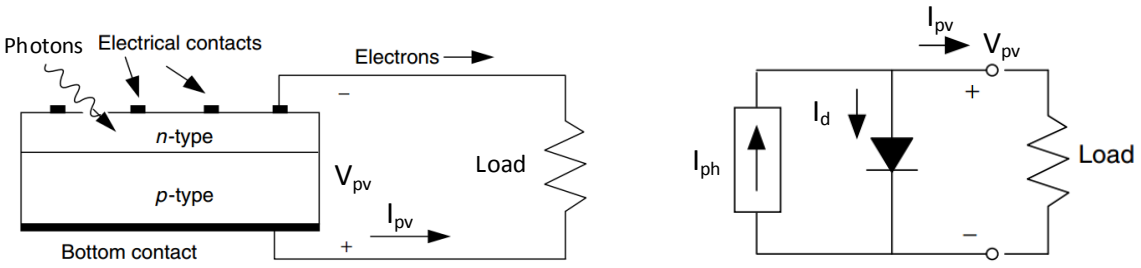

Figure 5-1: A photovoltaic cell (left) and the simplest equivalent circuit for it (right).

When this junction is exposed to the sunlight, this energy can be transferred to the electrons in vicinity of this junction. As photons are absorbed, the hole-electron pairs can be formed and the created voltage from the holes and electrons movement provides current. The energy that an electron needs to jump from the forbidden band to the conduction one is called the band-gap energy, indicated by *Eg* in electron-volts (eV). The band-gap energy of a silicon is 1.1 eV (1 eV = 1.6×10^{-19} J) [19].

A simple equivalent circuit for a PV cell comprises of a diode in anti-parallel with a current source, as depicted in right side of Figure 5-1. The voltage-current characteristic of PV module is described by the following Shockley's diode equation [19]:

$$I_{pv} = I_{sc} - I_{rs}\left(\exp\left(\frac{q}{kAT}V_{pv}\right) - 1\right) \tag{5.1}$$

where V_{pv} is the voltage applied across the PV cell, I_{sc} is the short-circuit current (light-induced current), I_{rs} is the reverse saturation current of the diode, q is the electron charge, k is Boltzmann's constant, T is the absolute temperature of PV cell, and A is the diode quality factor which accounts for different mechanisms responsible for moving carriers across the module's junction. q is the electron charge ($q = 160 \times 10^{-21}$ C). The short-circuit current is function of absolute temperature of PV cell and solar irradiance as follows:

$$I_{sc} = \left(I_{sc}^{stc} + k_i\left(T - T_{stc}\right)\right)\left(\frac{G}{G_{stc}}\right) \tag{5.2}$$

where I_{sc}^{stc} is the short-circuit current at standard test conditions (STC), k_i is the temperature coefficient of the current, T_{stc} is the reference temperature, G is the irradiance, and G_{stc} is the reference irradiance. The reverse saturation current can be formulated as follows:

$$I_{rs} = I_{rs}^{stc}\left(\frac{T}{T_{stc}}\right)^3 \exp\left(\frac{1}{kA}\left(\frac{E_g^{stc}q}{T_{stc}} - \frac{E_g}{T}\right)\right) \tag{5.3}$$

Where I_{rs}^{stc} and E_g^{stc} are the reverse saturation current and the band-gap energy under standard test conditions (STC), respectively. The band-gap energy is as follows:

$$E_g = E_g^{stc}q\left(1 + k_g\left(T - T_{stc}\right)\right) \tag{5.4}$$

Where, k_g is the temperature coefficient of the band-gap energy.

Figure 5-2 portrays the generic I–V and P-V curves for a PV module, pinpointing several key parameters such as the open-circuit voltage V_{oc}^{stc} and I_{sc}^{stc} in STC. Furthermore, the product of voltage and current is the delivered power by the module. The maximum power point (MPP) is the point close to the knee of I–V curve at which the power is in its maximum value. The current and voltage at the MPP are indicated as I_{mmp}^{stc} and V_{mmp}^{stc}. The voltage and current at the MPP are considered as rated voltage and rated current.

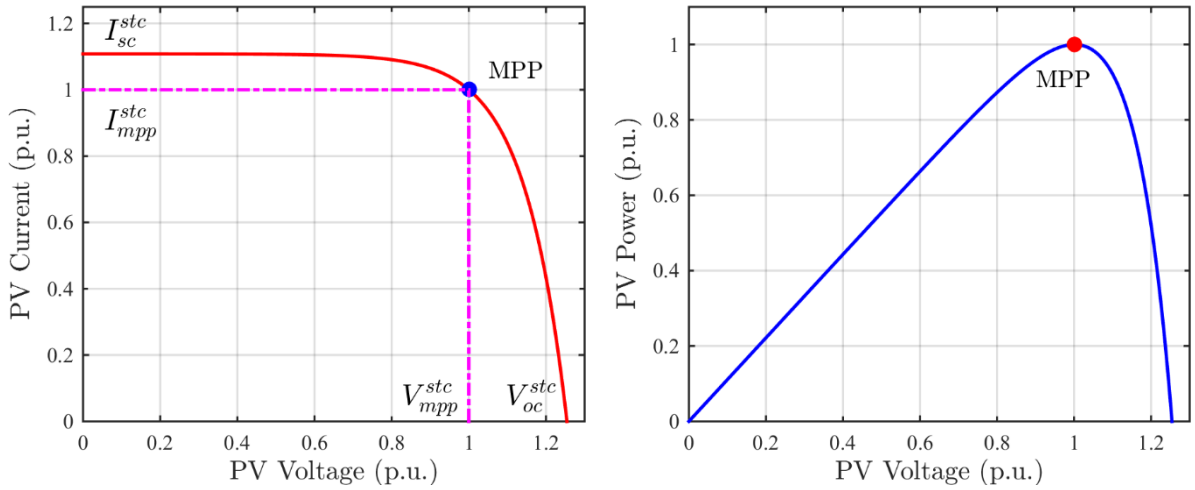

Figure 5-2: PV current versus PV voltage characteristic (Left), PV power versus PV voltage characteristic (Right).

The I_{rs} at STC and the A parameter can be calculated as follows [20]:

$$\begin{bmatrix} \ln\left(I_{rs}^{stc}\right) \\ \dfrac{q}{kAT} \end{bmatrix} = \begin{bmatrix} 1 & V_{mpp}^{stc} \\ 1 & V_{oc}^{stc} \end{bmatrix}^{-1} \begin{bmatrix} \ln\left(I_{sc}^{stc} - I_{mpp}^{stc}\right) \\ \ln\left(I_{sc}^{stc}\right) \end{bmatrix} \tag{5.5}$$

Therefore, I_{rs}^{stc} is given as follows:

$$I_{rs}^{stc} = \exp\left(\frac{-V_{oc}^{stc}}{V_{mpp}^{stc} - V_{oc}^{stc}}\right)\ln\left(I_{sc}^{stc} - I_{mpp}^{stc}\right) + \left(\frac{V_{mpp}^{stc}}{V_{mpp}^{stc} - V_{oc}^{stc}}\right)\ln\left(I_{sc}^{stc}\right) \tag{5.6}$$

And A at temperature T can be determined as follows:

$$A = \left(\frac{q}{kT}\right)\left(\frac{\ln\left(I_{sc}^{stc} - I_{mpp}^{stc}\right)}{V_{mpp}^{stc} - V_{oc}^{stc}} - \frac{\ln\left(I_{sc}^{stc}\right)}{V_{mpp}^{stc} - V_{oc}^{stc}}\right)^{-1} \tag{5.7}$$

Finally, the open circuit voltage at a specific operating condition can be calculated as follows:

$$V_{oc} = \left(\frac{kAT}{q}\right)\ln\left(\frac{I_{sc} + I_{rs}}{I_{rs}}\right) \tag{5.8}$$

The parameters of PV module studied in this chapter are listed in Table 5-1. The module is modeled as 36 cells in series, with a cell temperature of 25 ◦C and E_g^{stc} is 1.11 eV per cell. Therefore, this is 39.96 eV for the PV module. The I-V and P-V characteristics of a PV module, of the type in Table 5-1, are plotted in Figure 5-3 for different solar irradiance. The short-circuit current of module is proportional to solar irradiance based on (2), as

clearly shown in left side of Figure 5-3. As can be seen, the MPP is approximately proportional to the irradiance as well.

Table 5-1: Parameters of the studied PV module [21].

Parameter	Symbol	Value	Unit
Module Open Circuit Voltage at STC	V_{oc}^{stc}	21.7	V
Module Short Circuit Current at STC	I_{sc}^{stc}	8	A
Module MPP Voltage at STC	V_{mpp}^{stc}	17.3	V
Module MPP Current at STC	I_{mpp}^{stc}	7.22	A
Isc Temperature Coefficient	k_i	3.18	mA/K
Band-gap Energy Temperature Coefficient	k_g	-0.2677	meV/K.C
Band -gap Energy of PV Module at STC	E_g^{stc}	39.96	eV
Module Temperature at STC	T_{stc}	25	C
Irradiance at STC	G_{stc}	1000	W/m2

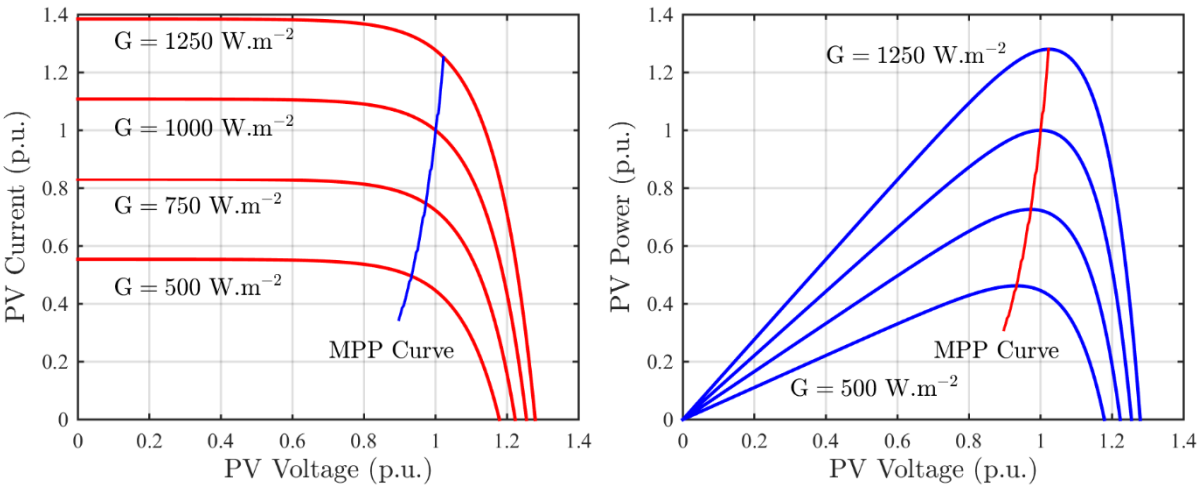

Figure 5-3: PV current versus PV voltage characteristics (Left), PV power versus PV voltage characteristics (Right) at standard temperature condition.

The effect of temperature variation on I–V and P-V curves that show how the curves shift as the cell temperature changes is investigated. Figure 5-4 shows examples for the curves for the abovementioned typical module. The irradiance level is 1000 W/m^2. As the ki coefficient (5.2) is negligible, the short-circuit current is identical for discrepant temperatures. This is obviously depicted in left side of Figure 5-4. As the cell temperature increases, the open-circuit voltage decreases substantially. Whereas this should be increased based on (5.8), it is to be noted that *A* has a reverse relation with temperature so that the *ln* term in (5.8) determines the temperature dependency of open circuit voltage. The net result when cells heat up is the MPP decreases.

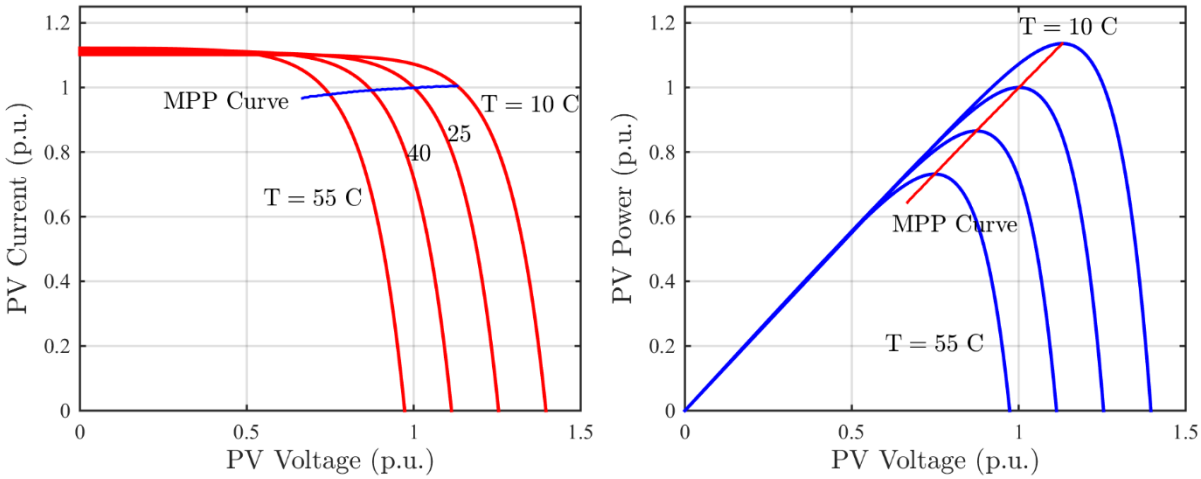

Figure 5-4: PV current versus PV voltage characteristics (Left), PV power versus PV voltage characteristics (Right) at standard irradiance condition.

5.3.2. PV System Modelling in DIgSILENT PowerFactory

In this chapter, a generic grid connected two stages PV system with boost stage is deployed and shown in Figure 5-5 [22]. In this two-stage structure, two power electronic converters in cascade are used to convert the generated power of PV module to AC power. As a result, the DC-DC boost converter increases the voltage of PV modules and the maximum power can be simultaneously captured by setting the voltage of PV module to MPP [23]. In the next stage, the voltage source inverter converts the DC link voltage to three-phase AC one that can be reached to the network voltage using a transformer. In practice, a LCL filter that is effective in the reduction of switching frequency harmonics is located between the inverter's output side and transformer which is not shown in Figure 5-5.

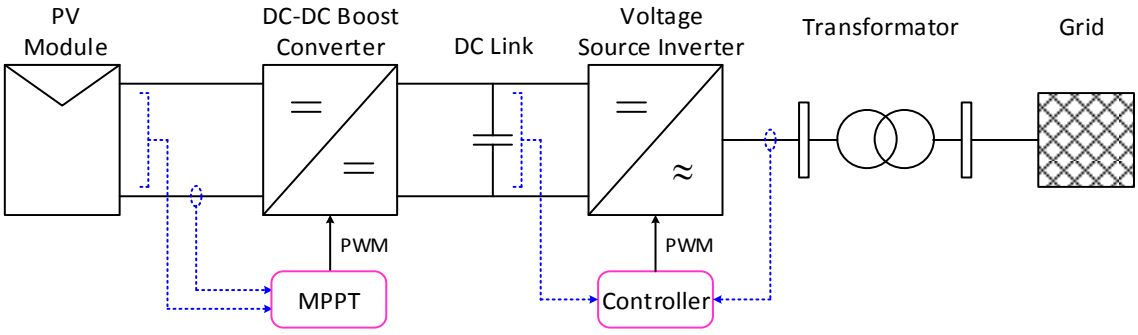

Figure 5-5: Control structure for a grid connected two stages PV system [22].

In the following, a grid connected PV system is simulated in PowerFactory software based on the above mentioned explanations. As a short time interval has to be simulated to investigate the PV model for dynamic frequency studies especially in large scale test systems, the detailed model, which models all the switching procedures results in an overly-long simulation time. Therefore, an averaged but accurate model of the PV system is deployed, where the voltage source inverter is treated as a current source in the proposed PV system model. In this way, the simulation time is shortened while at the same time retaining enough precision. Moreover, the PV module physics is modelled accurately. The developed control structure of grid connected PV system is depicted in Figure 5-6. The output voltage and power of inverter are measured by *V Meas* and *P Meas*, respectively. The *PLL* is used to calculate the output frequency of the inverter.

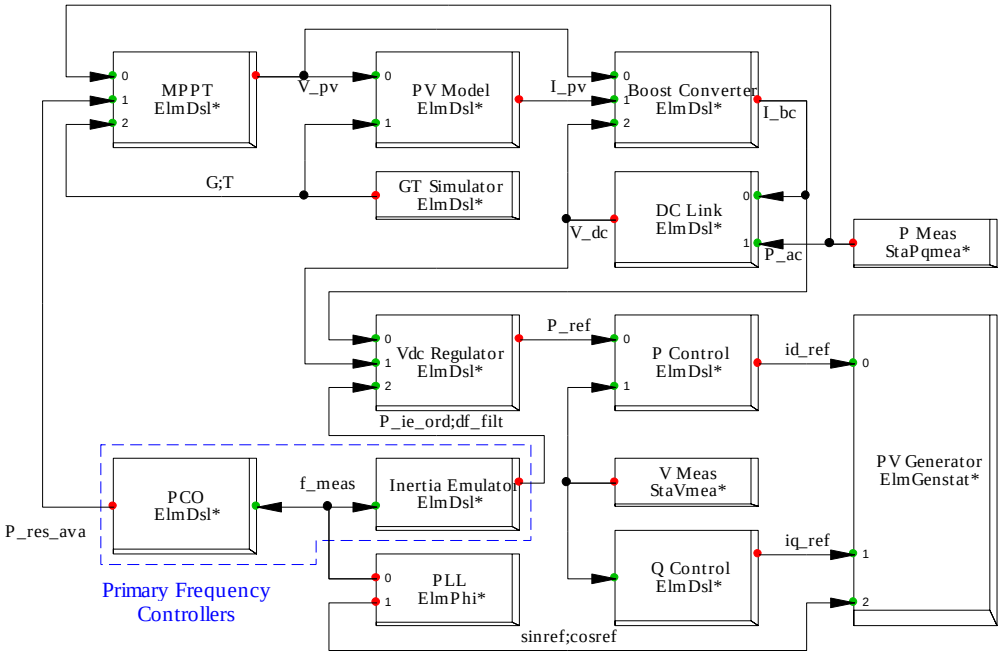

Figure 5-6: Control structure for a grid connected two stages PV system in DIgSILENT PowerFactory.

5.3.2.1. Inertial Emulator

The PV systems are interfaced with the power network by power electronic converters and the generated power of these power plants is controlled by these devices. Thus, due to the buffer, i.e. power electronic converter, between PV modules and electrical system, it efficiently avoids the inertia of PV systems, if any, from responding to the system frequency excursions. But, unlike the conventional power plants or wind energy conversion systems (WECSs), the photovoltaic systems do not have rotating shaft. Thus, given the same disturbances, the rate of change of system frequency (RoCoF) and frequency nadir during first few seconds grows and drops rapidly with high photovoltaic penetration level. To get rid of this issue, the inertial emulator is appended into PV system controllers. The design idea of inertial emulator is to introduce a rate control which responds rapidly to the frequency change (See Figure 5-7). It is to be notified that in steady state, this controller is not activated. Firstly, the frequency error is measured so that the extra power is needed if it is low. The dead band suppresses response of the controller until the error exceeds a threshold. The purpose of the dead band is as follows: i) it prevents the control from acting on small variations (noise) and ii) it makes the controller unresponsive to the over-frequency events since they are less problematic while connecting PV systems into the grid. The dead band output signal is further filtered by LPF to reject measurement noise, multiplied by a Kie coefficient, passed through a 'wash out' block, and finally the rate of change and the amplitude of the generated signal limited by a 'Rate Limiter' and an amplitude limiter, respectively. In a condition that PV system should be substituted with conventional power plant with inertia constant of H, $K_{ie} \times T_{wo}$ are equal to 2H. In this figure, K_{ie} is the gain applied to the frequency deviation, and T_{lag} and T_{wo} is time constants associated with the lag and decay of the response respectively, df is the magnitude of the frequency deviation, f_{db} is the frequency dead band and Pie_{max} is the maximum power increase which can be demanded. The Up_Rate_Limit is restricted the rate of change of requested power Pie_{ord}.

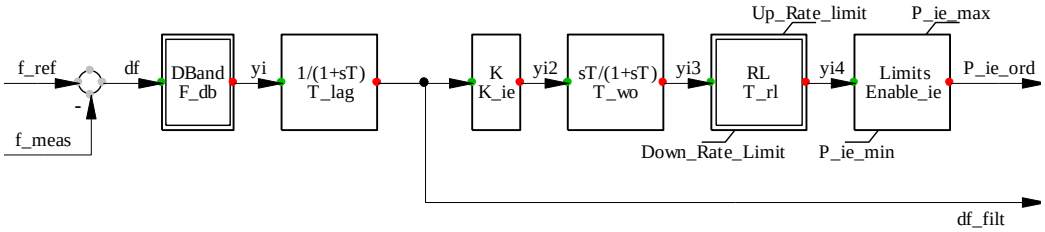

Figure 5-7: Outline of the "Inertial Emulator" of PV system in DIgSILENT PowerFactory.

The PV system inertia emulator parameters are listed in Table 5-2. The Pie_{ord} is limited to 0.1 p.u. Furthermore, the rate of change of this signal is selected as 1 p.u. per second. Baed on Kie and Two values tabulated in Table 5-2, the inertia constant H of synchronous generator (SG) equivalent with WT is 6.5 s.

Table 5-2: Parameters of the "Inertial Emulator" of PV system.

Parameter	Value	Unit	Parameter	Value	Unit
F_{db}	0.0001	p.u.	T_{lag}	0.1	s
K_{ie}	130	-	T_{wo}	0.1	s
T_{rl}	0.0025	s	$Enable_{ie}$	0/1	-
$P_{ie,min}$	0	p.u.	$P_{ie,max}$	0.1	p.u.
Up Rate Limit	1	p.u./s	Down Rate Limit	-1	p.u./s

5.3.2.2. Primary Controller

A frequency droop control, similar to the governing function in a steam turbine, as PV system primary controller (PCO) is simulated and shown in Figure 5-8. The input signal is the frequency deviation from its nominal value and *R* is speed regulation parameter or droop parameter. The governor virtual delay time is Tlag and Presmax is the maximum PV system reserve power margin. The rate of change of reserve power is restricted by 'Rate Limiter' block. The "P_res_int" is set to the maximum PV system reserve power margin. The PV system primary controller parameters are listed in Table 5-3.

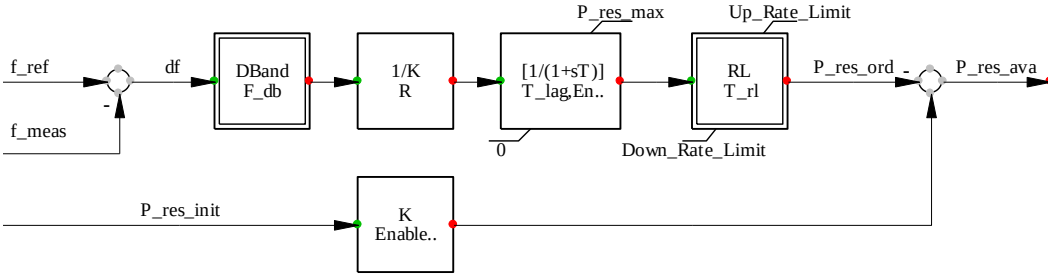

Figure 5-8: Outline of the "PCO" of PV system in DIgSILENT PowerFactory.

Table 5-3: Parameters of the WECS Primary Controller.

Parameter	Value	Unit	Parameter	Value	Unit
F_{db}	0.0001	p.u.	R	0.05	p.u.
T_{lag}	1	s	$P_{res,max}$	0.1	p.u.
$Enable_{res}$	0/1	-	T_{rl}	0.02	s
Up Rate Limit	0.1	p.u./s	Down Rate Limit	-1	p.u./s

5.4. Analysis of Two-Area System Considering PV Integration

In this section, the modal analysis and frequency response of a modified version of the Klein-Rogers-Kundur (KRK) two-area multi-machine as the test system in different scenarios is evaluated. The single line diagram of this benchmark system is shown in Figure 5-9. The total load demand of the network is 2517 MW and 200 Mvar. In non-WTPV scenario, all the load demands are supplied by conventional power plants. It is to be noticed that 11 out of 12 units connected to buses 1, 2 and 4 are reheat steam turbine (RST) types. The *SG 44* is a hydroelectric unit. All four units connected to bus 3 are combined cycle gas turbine (CCGT) power plants. The nominal apparent power of all these units is 225 MVA. The *SG 11* is also considered as slack unit. In WTPV 50% scenarios, all SG units connected to bus 2 and bus 4 are replaced with eight wind turbine (WT) power plants. In WTPV 75% scenario, the two middle units connected to buses 1 and 3 are substituted with four PV power plants. The active power generation of each unit is tabulated in Table 5-4, for mentioned scenarios. In these scenarios, all SG units connected to bus 1 and 3 are equipped with power system stabilizers (PSS) and all SG units have automatic voltage regulator (AVR) controllers. Also, the "Q control" of WT and PV power plants is not activated. Furthermore, the *Kp* and *Ki* parameters of PLLs in WT and PV power plants are set to 100 and 2000, respectively.

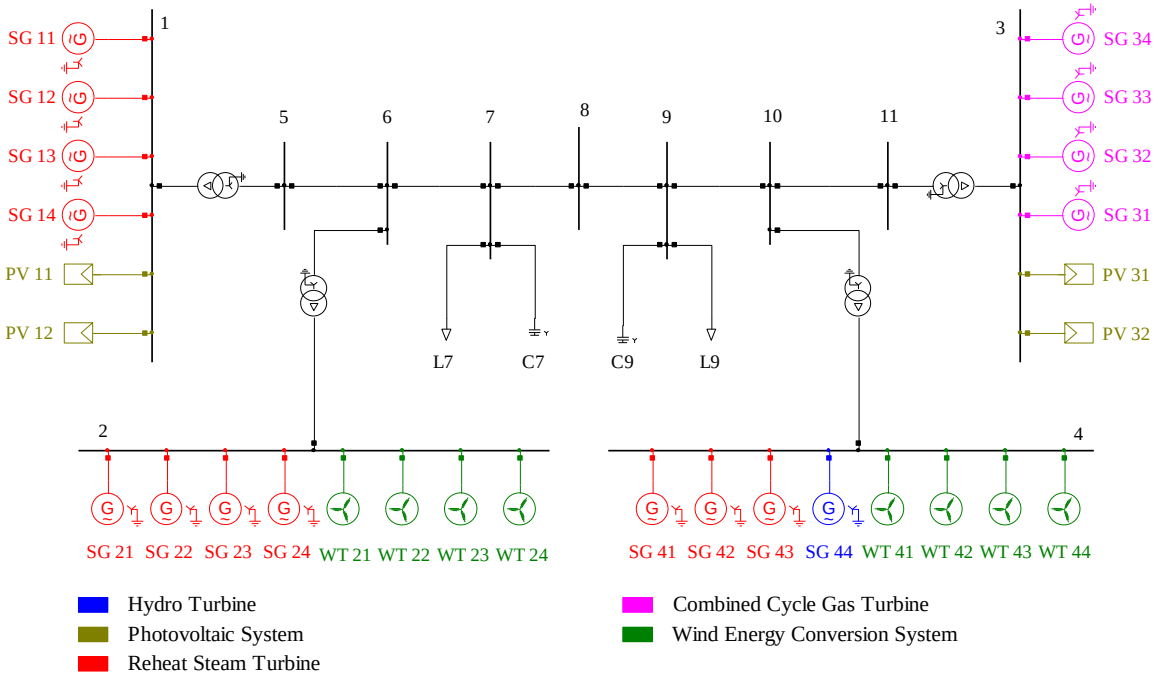

Figure 5-9: Single line diagram of the two area system.

Table 5-4: Active power of power plants in the defined scenarios

Unit	WTPV 00% (MW)	WTPV 50% (MW)	WTPV 75% (MW)
SG 11	17	17	27
SG 12	175	175	-
SG 13	175	175	-
SG 14	**100**	**100**	**100**
SG 21	175	-	-
SG 22	175	-	-
SG 23	175	-	-
SG 24	175	-	-
SG 31	165	165	165
SG 32	180	180	-
SG 33	180	180	-
SG 34	180	180	180
SG 41	175	-	-
SG 42	175	-	-
SG 43	175	-	-
SG 44	175	-	-
WT 21	-	175	175
WT 22	-	175	175
WT 23	-	175	175
WT 24	-	175	175
WT 41	-	175	175
WT 42	-	175	175
WT 43	-	175	175
WT 44	-	175	175
PV 11	-	-	175
PV 12	-	-	175
PV 31	-	-	175
PV 32	-	-	175
Sum	2572	2572	2572

5.4.1. Modal Analysis of Two-Area System Considering PV Integration

This section investigates the application of the proposed PV system model design to the proposed two-area test system with high wind and photovoltaic power penetration levels and its effect on electromechanical modes using modal analysis tool in DIgSILENT PowerFactory. Figure 5-10 shows the system electromechanical modes for three aforementioned scenarios. In each scenario, there are 15 electromechanical modes.

There are 15 electromechanical modes in WTPV% scenario those are highlighted in Figure 5-10 with black colour. The slowest mode with damping frequency of 0.65 Hz is an inter-area mode and all SGs participate in this mode. In WTPV 50% scenario, as 8 SGs connected to buses 2 and 4 are substituted with 8 WTs, the electromechanical modes of SG units reduced from 15 to 7 so that the rest 8 belongs to WTs. All these modes are highlighted with blue colour in Figure 5-10. In the next stage, two middle units connected to buses 1 and 3 are replaced with 4 PVs in WTPV 75% scenario and the associated modes are bolded with red colour. In this scenario, 8, 4 and 3 modes are pertinent to WTs, dc link and SGs, respectively. Additionally, the PSSs of all SGs operated in buses 1 and 3 participates in the left side mode with damping of 7.5 s.

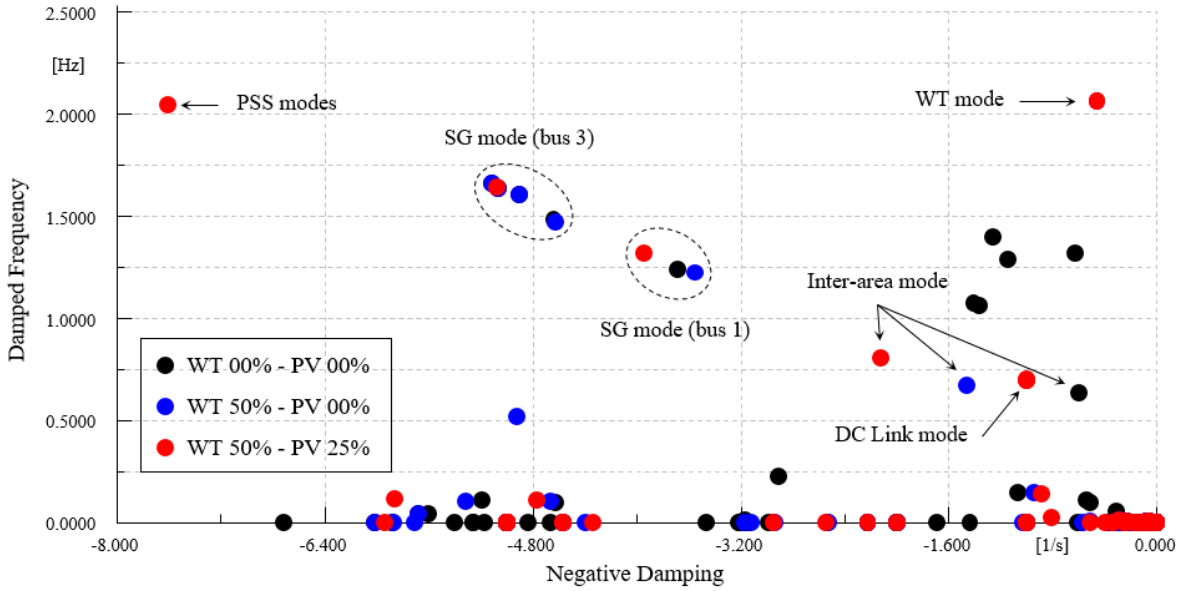

Figure 5-10: Electromechanical modes of the two area system with different WT and PV penetration levels.

The effect of wind and photovoltaic penetration levels on damping of slowest electromechanical mode associated with SG units are shown in Figure 5-11. It is clear-cut that whilst its damping increases with increasing of wind energy conversion systems and PV penetrations, the damped frequency is approximately fixed. The main reason of damping growth is the negative influence of automatic voltage regulator of SGs connected to buses 2 and 4 in case of renewable energy sources integration increment.

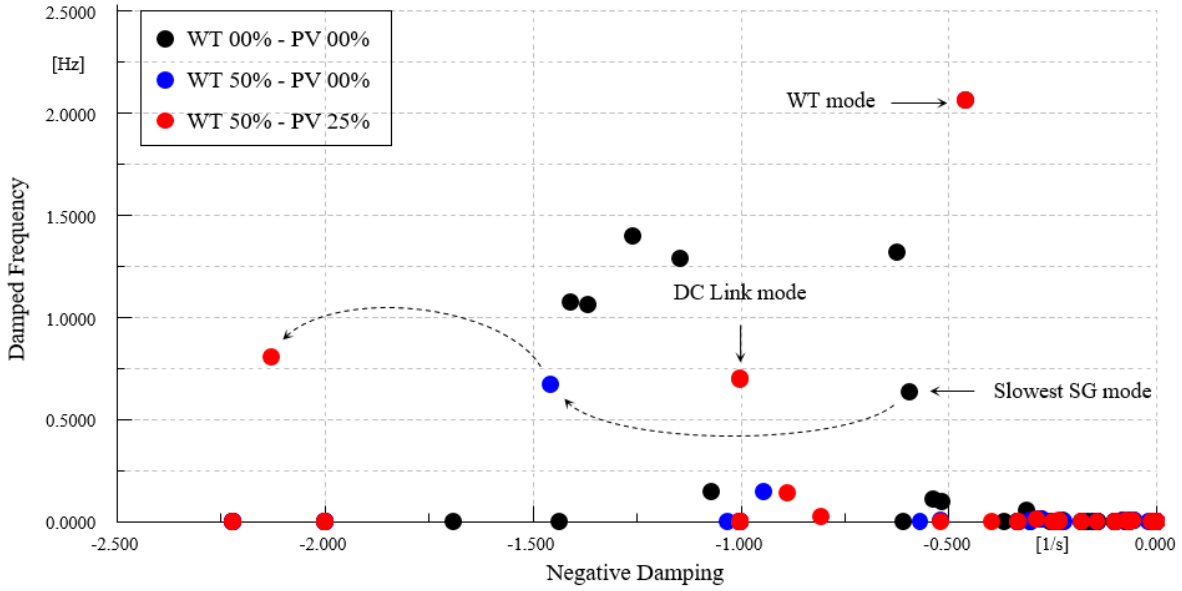

Figure 5-11: Slowest SG mode of the two area system with different WT and PV penetration levels.

5.4.2. Frequency Response of Two-Area System Considering PV Integration

5.4.2.1. PV Inertia Emulator and Primary Frequency Controller

In this subsection, the dynamic performance of inertia emulator and primary frequency control of the PV systems and their impacts on system frequency regulation following the generation trip of *SG 14* is investigated. In this regard, the WTPV 75% scenario is divided into three sub-scenarios. In WTPV 75% I scenario, only WTs are equipped with inertia emulator and droop based controller. The inertia emulator of the PV systems are activated beside the inertia emulator and reserve based primary frequency response of the WTs in WTPV 75% II scenario. Finally, the WTPV 75% III consists of PVs and WTs with inertia emulator and primary frequency based reserve power. It is observed that the frequency controller objective is accomplished as shown in Figure 5-12 because the frequency nadir and steady-state frequency variations performance of the system is further improved considering reserve power for the PV systems.

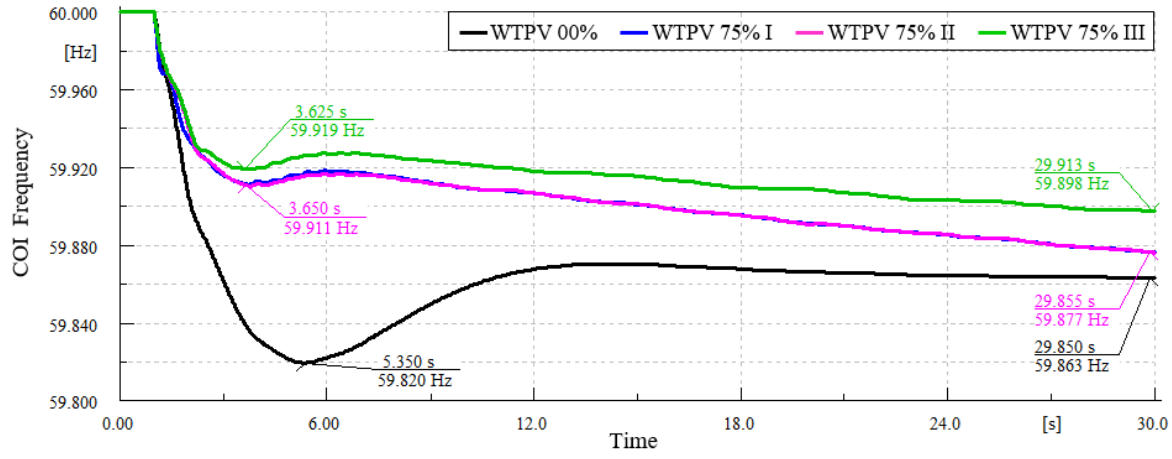

Figure 5-12: Frequency response with loss of 100 MW generation for WTPV 00% and WTPV 75% scenarios.

The COI RoCoF changes are portrayed in Figure 5-13. As can be seen, the COI RoCoF of the system is significantly enhanced when the proposed controller, including the transient part of inertia emulation control, is included in the PVs alongside of WECSs with inertia emulator.

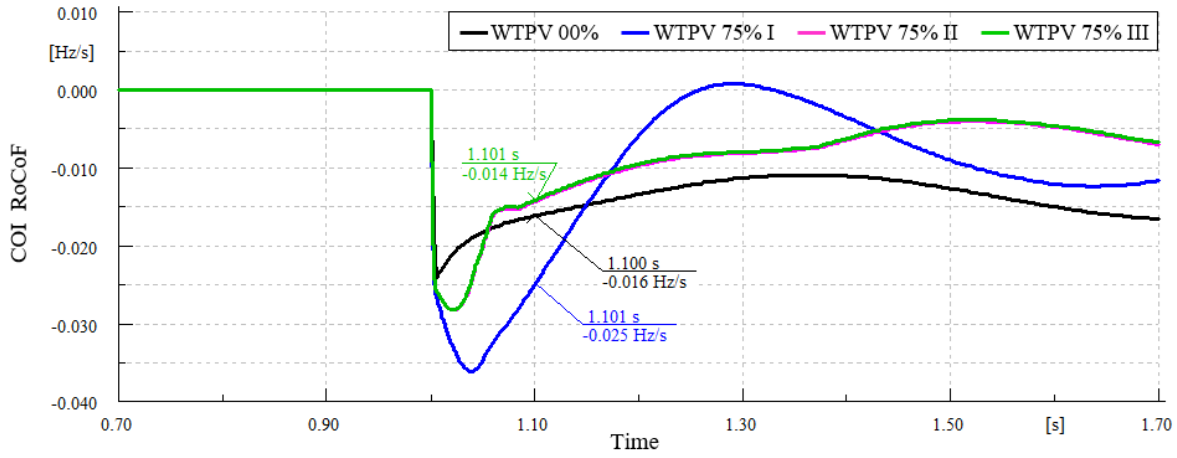

Figure 5-13: RoCoF with loss of 100 MW generation for WTPV 00% and WTPV 75% scenarios.

In order for clear investigation of the PV systems dynamic behaviour following the loss of *SG 14*, the variables related to the *PV 11* and *PV 31* are shown in Figure 5-14 for WTPV 75% scenario. As can be seen from Figure 5-14, the *PV 11* shows higher frequency variation in the first few seconds as compared to the *PV 31* due to its nearer distance to incident.

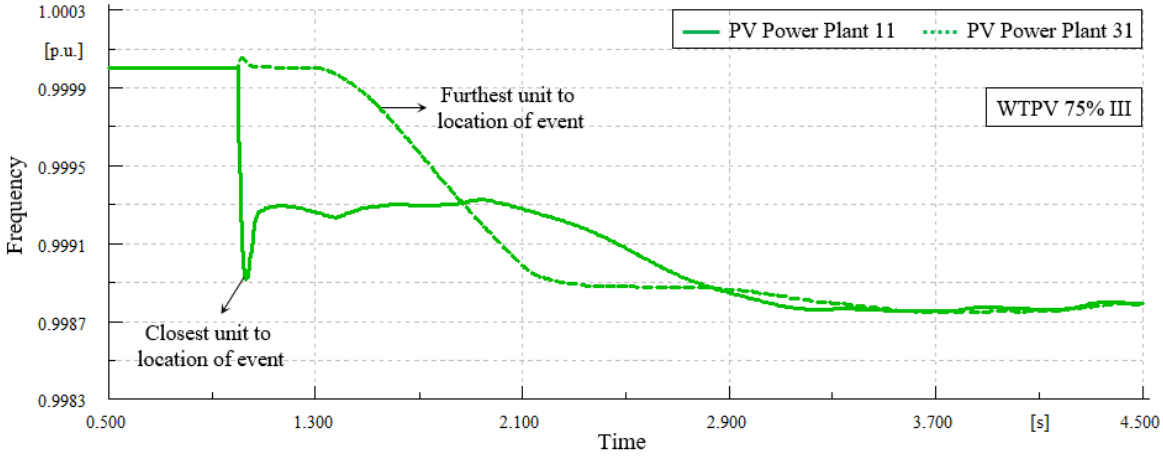

Figure 5-14: Frequency of PV power plant 11 and PV power plant 13 for WTPV 75% III scenario.

5.4.2.2. Frequency Response with Different Droop Parameters

In the previous system frequency response studies, the PCOs' droop coefficient of all power plants is uniformly set to 5%. In this subsection, this parameter is reduced a tenth for renewable energy sources and its effect on system frequency response is analysed. The reason for considering this different droop setting is to investigated their responses and reserve generation capability when they are overrated than the others. Once again, the loss of the *SG 14* is considered as an event. The simulation results are shown in Figure 5-15 and Figure 5-16 for two different values of droop parameter in WTPV 75% III scenario. As shown in Figure 5-15, the frequency nadir and steady state frequency deviation are reduced considerably with droop reduction of the PVs and WTs due to renewable energy sources power increment. In such a scenario, the power plants with lower droop setting are responsible for a larger contribution to primary frequency response. Moreover, in order to practically increase the primary frequency support of the deloaded WTs and PVs, their droop parameters should be as low as possible. Therefore, a change in the system frequency would force them to increase their power output. In other hand, this change of droop parameter has slight influence on COI RoCoF (See Figure 5-16).

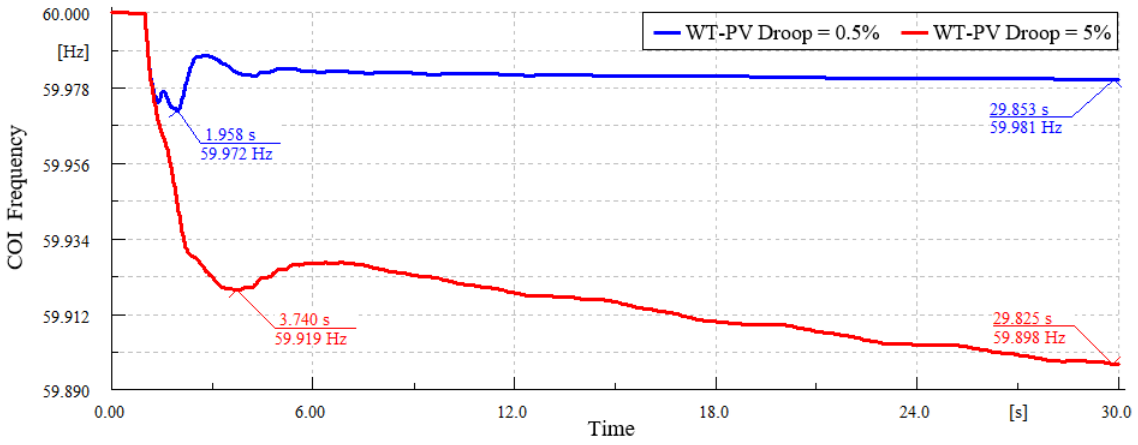

Figure 5-15: Frequency response with loss of 100 MW generation for different WT-PV droop parameters.

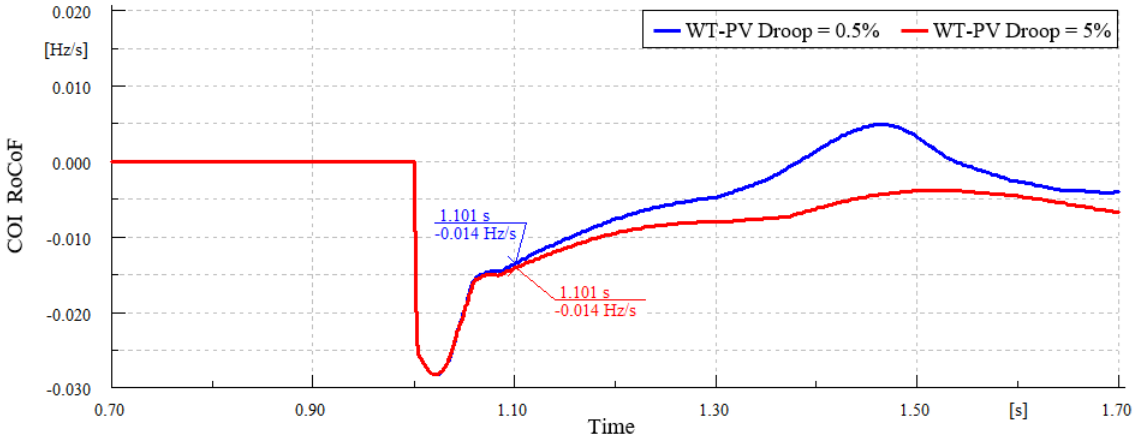

Figure 5-16: RoCoF with loss of 100 MW generation for different WT-PV droop parameters.

5.4.3. Executive Summary of Deploying PV in Two-Area test System

The main goal of this chapter is to investigate the effect of PV systems integration on frequency response of power systems which their load demands are supplied by conventional CCGT, thermal and hydro units as well as renewable energy sources like WTs. In this context, an average and accurate dynamic model of PV system is firstly derived and its dynamic performance and behaviour is analysed. One of the key features of this model is that the real behaviour of the PV module is modelled.

The effect of PV model on frequency response of two-area KRK system is analysed. It is observed from the results that in the power systems with PV systems which share the responsibilities of frequency control with the conventional generation indicate how to enhance the overall system frequency response and mitigate the stresses over the SGs and WTs in the system. The two-area system with PV units supplying mandatory frequency response enhanced with reserve and inertial power have a direct impact also over the global indicators of frequency quality: RoCoF, frequency nadir and steady-state frequency deviation. From the small-signal analysis, it is found that modelling of dc link for PV system leads to a DC Link mode in eigenvalues of original two-area system. Furthermore, this mode results in inter-area oscillations of some variables like dc link voltage and power output of PV system. In order to remove this oscillation, a damping controller can be designed and added to the dc link voltage regulator of PV systems. In this chapter, the droop coefficient reduction of PVs' PCOs and its primary frequency support in consequence can quickly damp these inter-area oscillations of dc link in PV systems. Moreover, the chapter performs other time-domain evaluation combined with a sensitivity analysis to demonstrate the power system stability margin enlargement and the primary frequency regulation benefits brought by the added ancillary services like reserve based droop controller and inertia emulator to prove their requirement with increased levels of PV penetration.

5.5. Analysis of 36-Zone GB Network Considering PV Integration

In this section, the system frequency response of 36-zone GB network integrated CCGT, WTs and PVs under the proposed PV system model following an abrupt and sever power disturbance. In this regard, the generation level and geographical distribution of conventional power plants, PVs and WTs considering 50% penetration level of WECSs and 25% of PVs (Total renewable energy sources penetration is equal to 75%) are investigated. After which, the modal analysis is deployed to show the PV and WT integration impact on electromechanical modes of 36-zone GB network. The time-domain based system frequency response following the sudden and sever in-feed is applied on several system scenarios.

The generation power and geographical distribution of traditional plants are shown in Figure 5-17. It is to be noted that almost 90% of network generation is located in the southern part of UK i.e. England & Wales and Scotland supplies only 10% of whole system load demand. As mentioned, the largest unit is the nuclear power plant located in zone 12 which supplies 13% of whole system generation. The accurate generation of each zone is tabulated in Table 5-5 in MW.

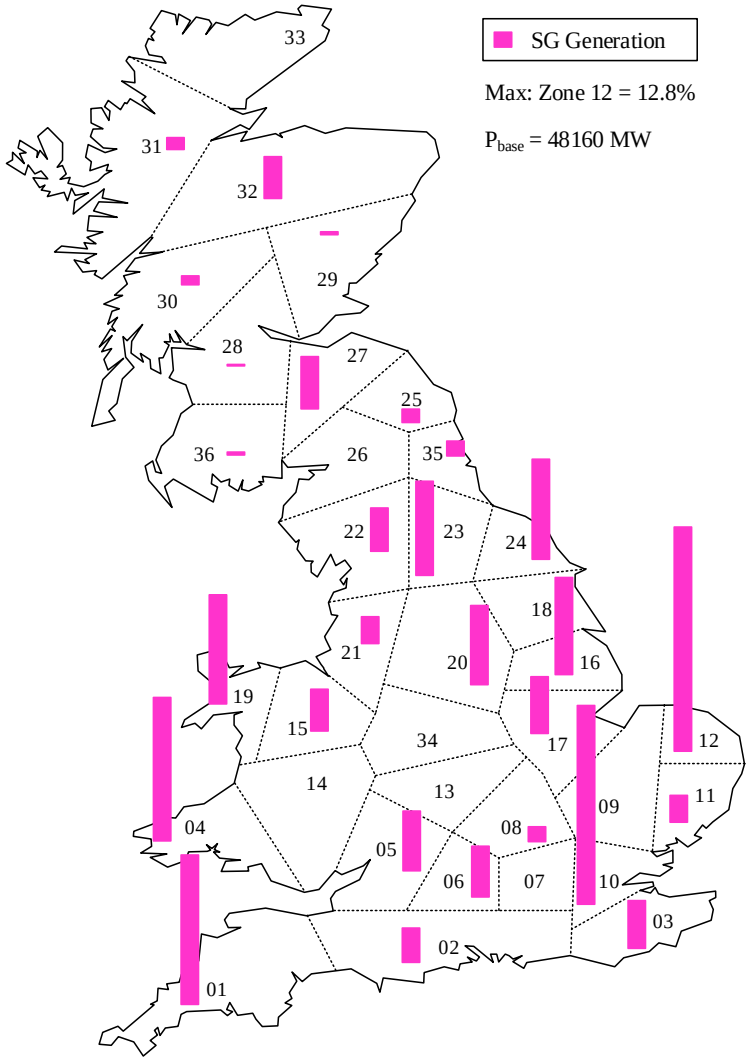

Figure 5-17: Geographic distribution of SG generation in "WTPV 00%" scenario.

In order to analyse the effect of conventional power plants' replacement with PV and WT power plants, two scenarios of WTPV 00% and WTPV 75% are considered. In first scenario, the whole system load is satisfied by conventional SGs. In the second scenario, the PVs and WTs supply 25% and 50% of GB network demand, respectively. Since the total load demand of the network is 40 GW, the power generation of PVs and WTs are 10 GW and 20 GW, respectively. The precise generation of SGs, PVs and WTs are tabulated in Table 5-5 and Table 5-6. As can be seen, as the penetration of renewable energy sources increases, the gas turbines are removed while other conventional units' capacity is fixed. However, the capacity of pumped storage unit located in zone 32 is zero in WTPV 75% scenario.

Table 5-5: Active power of conventional power plants in two scenarios

No.	Type	Zone	WTPV 00% (MW)	WTPV 75% (MW)
01	Gas	01	809	-
02	Nuclear	01	3337	3474

03	Gas	02	946	-
04	Nuclear	03	1299	1352
05	Gas	04	3941	
06	BioMass	05	100	100
07	Gas	05	1575	-
08	Gas	06	1385	-
09	Gas	08	420	-
10	BioMass	10	741	742
11	Gas	10	4732	-
12	Gas	11	751	-
13	Gas	12	1609	-
14	Nuclear	12	4548	4735
15	Gas	15	1180	-
16	Gas	16	2704	-
17	Gas	17	1544	-
18	Gas	19	617	-
19	Nuclear	19	2398	2400
20	Gas	20	2172	-
21	Gas	21	724	-
22	Nuclear	22	1202	1251
23	**BioMass**	**23**	**1722**	**1724**
24	Gas	23	858	-
25	Gas	24	2759	-
26	BioMass	25	366	366
27	BioMass	27	120	120
28	Gas	27	107	-
29	Nuclear	27	1214	1264
30	Gas	28	18	-
31	BioMass	29	52	52
32	Gas	29	14	-
33	Hydro	30	232	158
34	Hydro	31	321	218
35	Gas	32	11	-
36	Hydro	32	535	363
37	Pump Storage	32	611	-
38	BioMass	35	280	280
39	Gas	35	126	-
40	BioMass	36	45	45
41	Hydro	36	33	22
Total Active Power (MW)			48157	18666

Table 5-6: Active power of PV and WT power plants in WTPV 75% scenario.

Zone	PV (MW)	WT (MW)	Zone	PV (MW)	WT (MW)
01	509	805	19	162	1624
02	539	84	20	520	88
03	114	537	21	346	184
04	334	1003	22	169	880
05	425	45	23	493	366
06	311	24	24	143	1412
07	335	1	25	179	112
08	917	2	26	43	297
09	490	2	27	150	1653
10	123	328	28	170	589
11	119	45	29	141	212
12	380	2896	30	94	186

13	607	183	31	15	455
14	404	57	32	94	1938
15	646	451	33	102	544
16	46	661	34	114	1
17	40	1	35	247	985
18	272	16	36	207	1334
			Total	10000	20000

The geographical distribution of generated power of all units is shown in Figure 5-18 for WTPV 75%. By comparing this figure and Figure 5-17, it is clearly observable that the conventional units placed beside the coast i.e. nuclear units and the biomass power plants located in the middle part of GB network are considered while the gas turbine units of middle-down part of GB network, that is, the high-densely consumption region are substituted with PVs. Moreover, in order to supply all deliverable power of gas turbines in the top areas and coasts of network i.e. low-densely consumption region, the WTs are installed and connected to the associated buses.

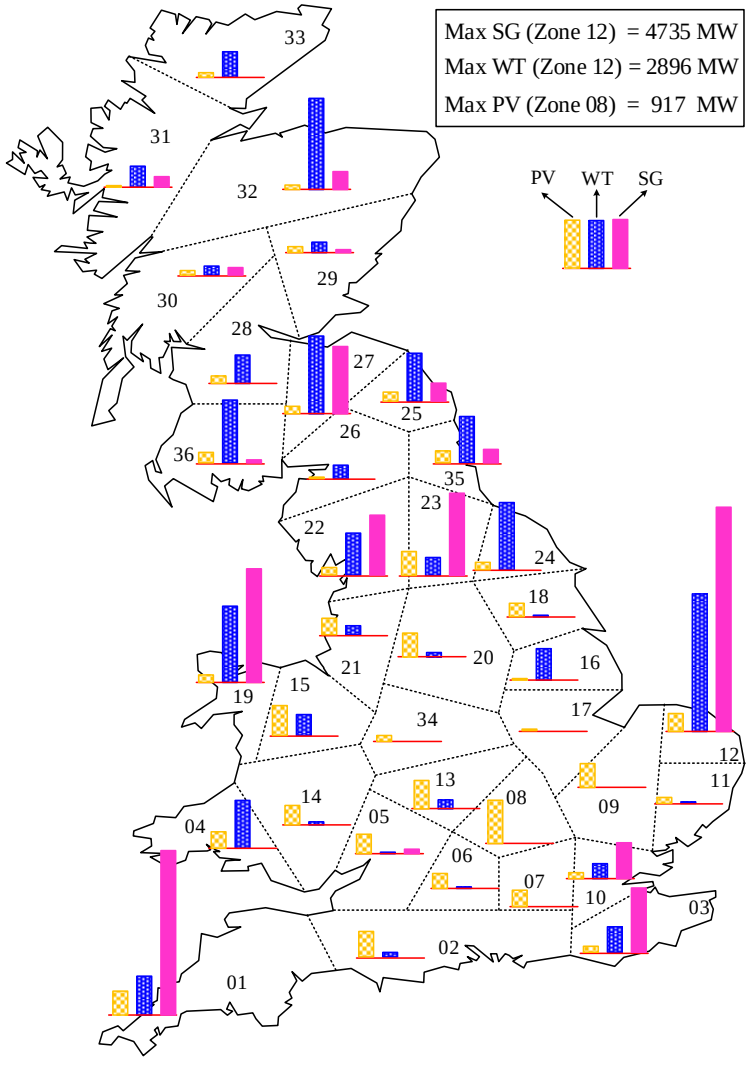

Figure 5-18: Geographic distribution of power plant's generations in "WTPV 75%" scenario.

5.5.1. Modal Analysis of 36-Zone GB Network Considering PV Integration

Once the conventional generating units substitute with the PVs and WTs, some electromechanical modes of the network related to the motion equation of the SG's rotor are replaced with double-mass drive train modes of WTs. The electromechanical modes of 36-zone GB network for four different cases are shown in Figure 5-19. They are divided into two groups of SG modes and WT modes which are representative of dynamic behaviour of the SG's rotor and WTs. The frequency and damping of SG modes are approximately fixed or slightly increased in consequence of increasing PVs and WTs penetration levels.

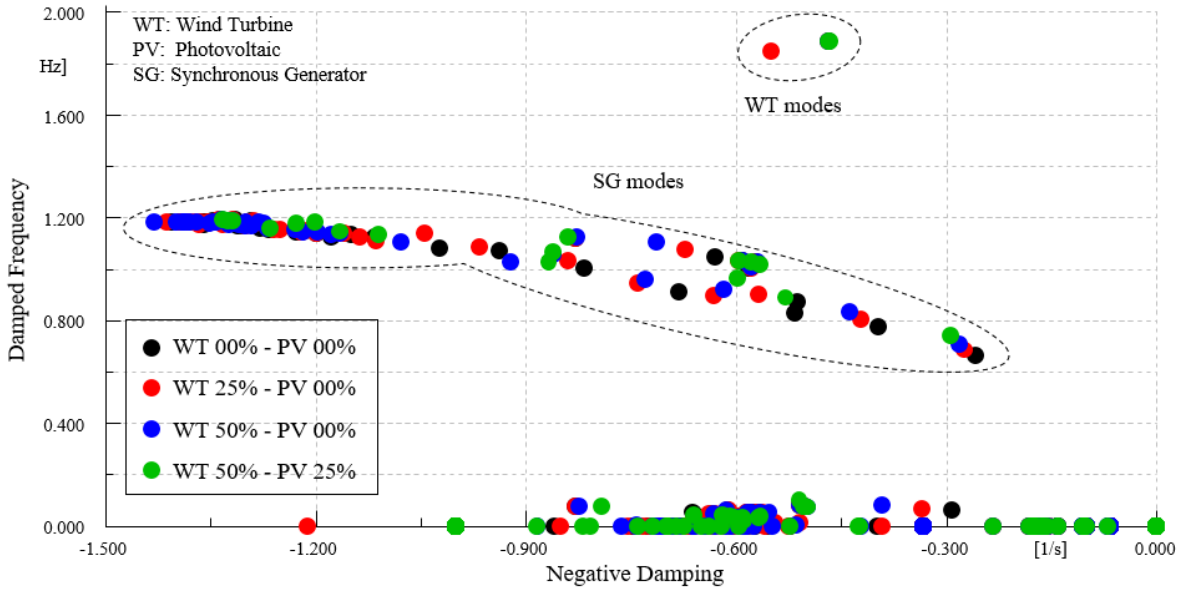

Figure 5-19: Effect of WECS and Photovoltaic integration in electromechanical modes.

In order to accurately observe and investigate the effect of growing renewable energy sources penetration levels on electromechanical modes in the 36-zone GB network, two slowest modes are shown in Figure 5-20 for different scenarios. It is clear-cut that damping and frequency of these two modes are increased following the penetration levels increment. This is due to the fact that the AVRs of CCGTs are removed after CCGTs replacement procedure and their negative influence on electromechanical modes i.e. damping reduction mitigates and their damping increases.

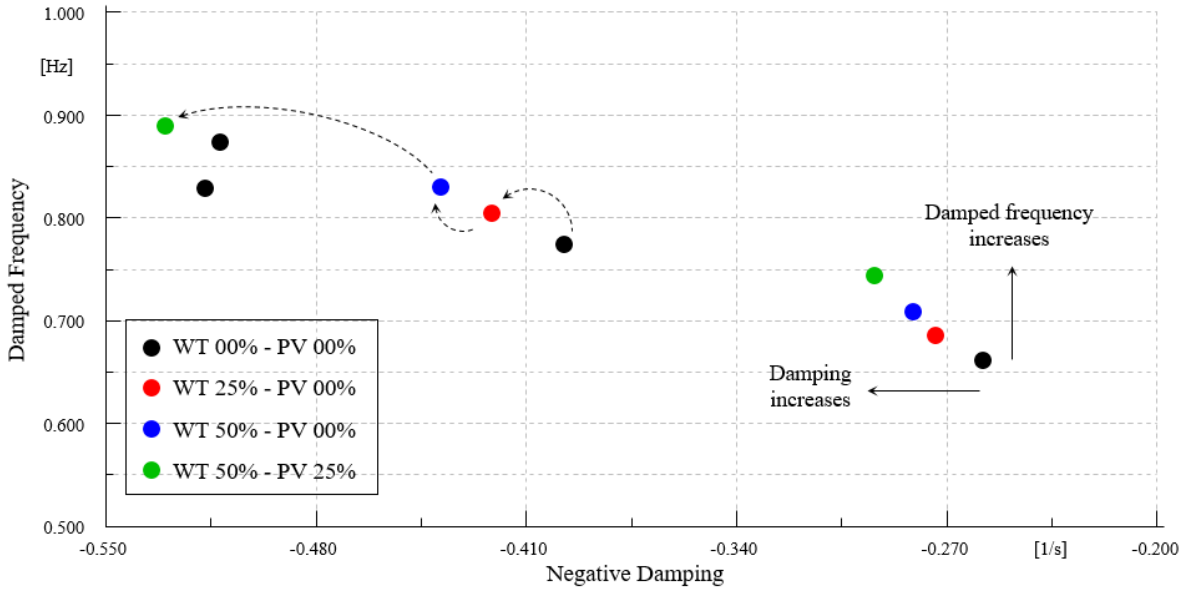

Figure 5-20: Effect of WECS and Photovoltaic integration in two slowest electromechanical modes.

5.5.2. Frequency Response of 36-Zone GB Network Considering PV Integration

In this section, the GB system frequency response is validated following the biomass 23 generation lost. The main reason of selecting this unit is that its capacity is fixed after integration of the PV systems and WT units. In simulation results, different quantities like centre of inertia (COI) frequency and RoCoF changes are shown for 30 s following the disturbance at t = 1 s in two case studies of WTPV 00% and WTPV 75%. The step size parameter of time-domain simulations is equal to 0.0025 s. In the following results, the COI frequency is illustrated beside the SGs' frequencies based on the following relation:

$$F_{COI} = \frac{\sum_{i=1}^{N} H_i S_i F_i}{\sum_{i=1}^{N} H_i S_i} \tag{5.9}$$

Where, H_i, S_i and F_i are the inertia constant, apparent power and frequency of the *i*th SG, respectively.

5.5.2.1. Loss of 1700 MW Generation in Zone 23

The biomass unit located in zone 23 with the capacity of 1700 MW is abruptly disconnected from the grid. The simulation results are shown in Figure 5-21 to Figure 5-23 for two scenarios of WTPV 75% and WTPV 00%. In order to investigate the dynamic performance of PVs and WTs, the WTPV 75% scenario is divided into four sub-scenarios. In WTPV 75% I, the inertia emulator and PCO are deactivated for all PVs and WECSs. In scenario of WTPV 75% II, the WTs are equipped with the reserve and inertial powers. It is to be pointed out that the PVs don't have these abilities. In WTPV 75% III scenario, the PV units are equipped with inertia emulators as well. Finally, the reserve power are considered for all PVs in WTPV 75% IV scenario.

According to Figure 5-21 to Figure 5-23, it is clearly observed that the RoCoF increases expressively once renewable energy sources don't have inertial power feature (in WTPV 75% I) compared to the scenario of non-

renewable energy sources (in WTPV 00%). This can lead to frequency nadir increment. It is due to the fact that they don't contribute in the inertial frequency regulation of GB system. In other hand, in WTPV 75% II and (WTPV 75% III and IV) scenarios with respective inertial response releasement of WTs and (both WTs and PVs), the RoCoF and the frequency nadir are considerably decreased.

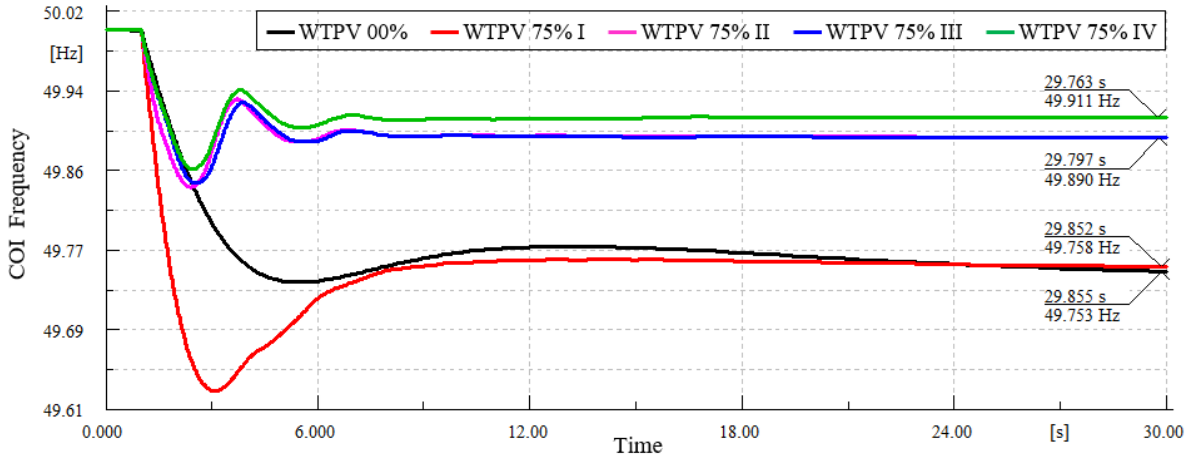

Figure 5-21: Frequency response with loss of 1700 MW generation in middle of network (Zone 23).

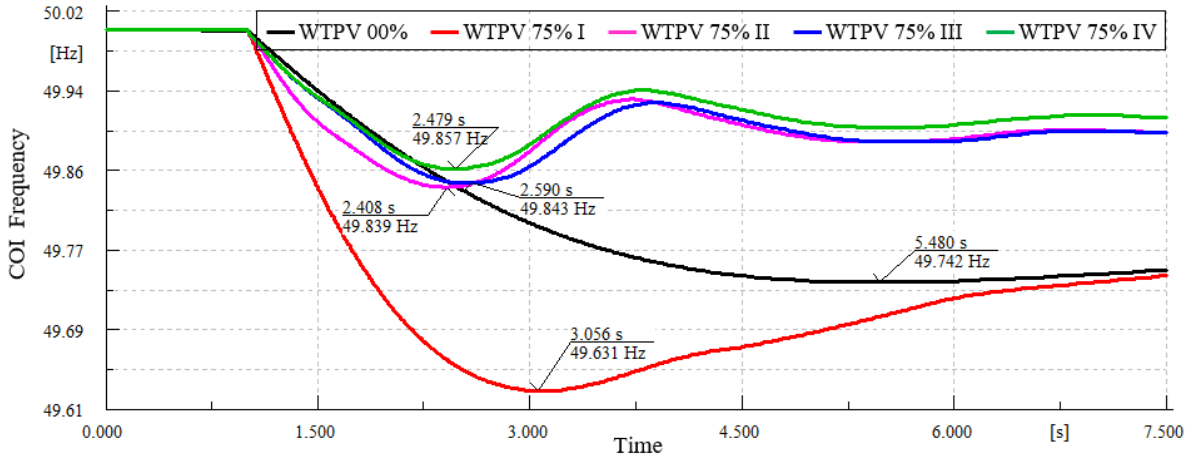

Figure 5-22: Frequency nadir with loss of 1700 MW generation in middle of network (Zone 23).

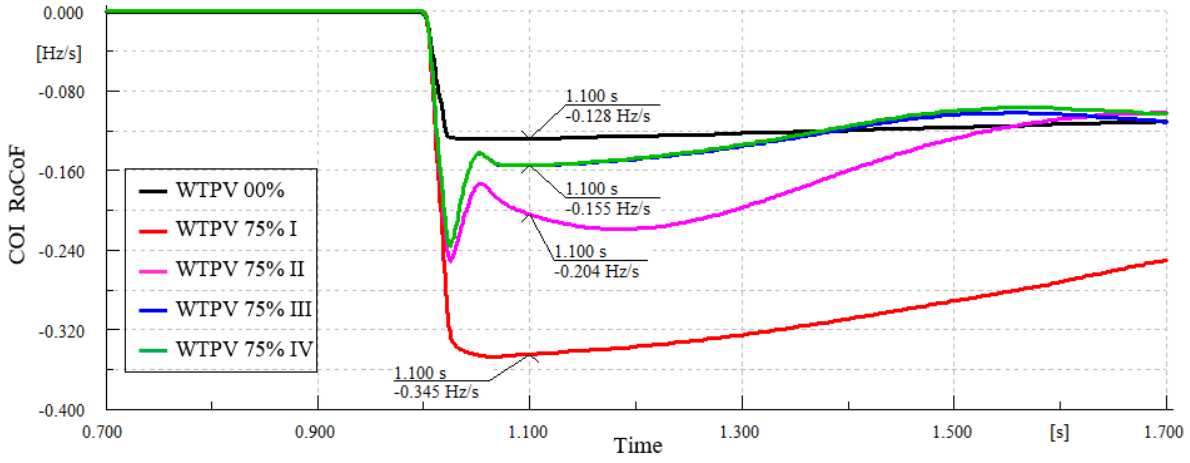

Figure 5-23: RoCoF deviations with loss of 1700 MW generation in middle of network (Zone 23).

In order to precisely investigate the dynamic performance of the PV systems in response of generation trip, the variables associated with five PV units from different locations of GB networks are shown in Figure 5-24. In this figure, frequency measured in corresponding locations is portrayed. The maximum and minimum RoCoF are respectively pertinent to the *PV 23* and *PV 01* which is quite matched with their electrical distance to incident.

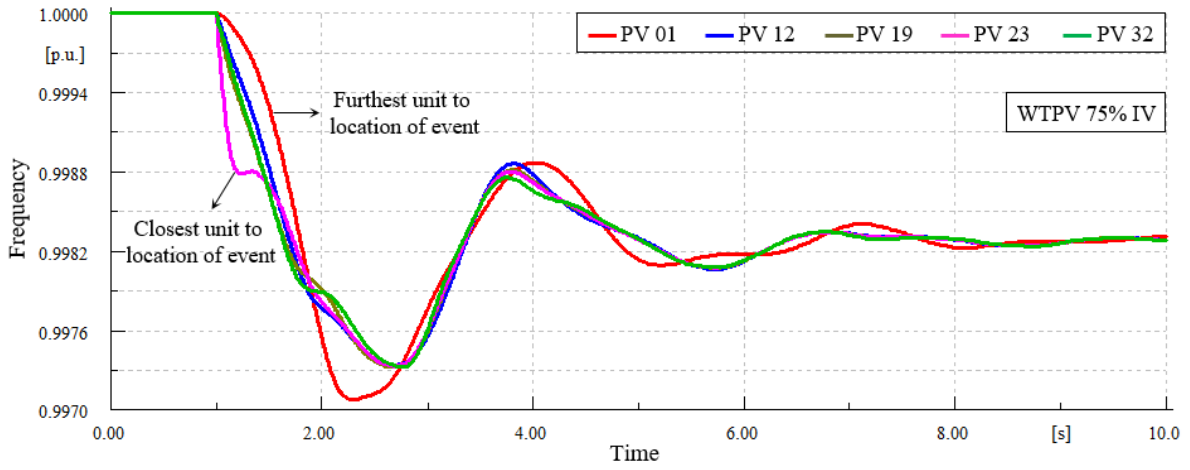

Figure 5-24: Frequency of PV power plants with loss of 1700 MW generation in middle of network.

5.5.3. Executive Summary of Deploying PV in GB Test System

In this chapter, the dynamic performance of the proposed PV system is investigated through 36-zone GB system frequency response. According to system studies in different scenarios, the WT and PV integration influences are separately analysed for system frequency response following the large contingency in the middle part of the GB network. It is observed that the PV system with reserve and inertial frequency support capabilities can enhance frequency stability criteria like RoCoF, frequency nadir and steady-state frequency deviation. In addition, the primary frequency support burden on the conventional units and or WTs is mitigated accordingly. It is also deduced that closeness of the PV units to the disturbance location has considerable impact on their inertial frequency response so that the nearer units inject more inertial power to the grid.

5.6. References

[1] B. K. Bose, "Global warming: Energy, environmental pollution, and the impact of power electronics," IEEE Ind. Electron. Mag., vol. 4, no. 1, pp. 6-17, Mar. 2010.

[2] Monthly deployment of all solar photovoltaic capacity in the United Kingdom, Available: https://www.gov.uk/government/statistics/solar-photovoltaics-deployment

[3] National Grid, Innovation, Enhanced Frequency Control Capability, Available: http://www2.nationalgrid.com/UK/Our-company/Innovation/NIC/EFCC/

[4] M. T. Ameli, S. Moslehpour, and M. Shamlo, "Economical load distribution in power networks that include hybrid solar power plants," Electr. Power Syst. Res., vol. 78, no. 7, pp. 1147-1152, Jul. 2008.

[5] M. Garcia-Gracia, N. El Halabi, H. Ajami, and M. P. Comech, "Integrated control technique for compliance of solar photovoltaic installation grid codes," IEEE Trans. Energy Convers., vol. 27, no. 3, pp. 792-798, Sep. 2012.

[6] M. Datta, T. Senjyu, A. Yona, T. Funabashi, and C. H. Kim, "A frequency-control approach by photovoltaic generator in a PV-diesel hybrid power system," IEEE Trans. Energy Convers., vol. 26, no. 2, pp. 559-571, Jun. 2011.

[7] N. Kakimoto, S. Takayama, H. Satoh, and K. Nakamura, "Power modulation of photovoltaic generator for frequency control of power system," IEEE Trans. Energy Convers., vol. 24, no. 4, pp. 943-949, Dec. 2009.

[8] W. A. Omran, M. Kazerani, and M. M. A. Salama, "Investigation of methods for reduction of power fluctuations generated from large grid-connected photovoltaic systems" IEEE Trans. Energy Convers., vol. 26, no 1, pp. 318-327, Mar. 2011.

[9] H. Xin, Y. Liu, Z. Wang, D. Gan, and T. Yang, "A new frequency regulation strategy for photovoltaic systems without energy storage," IEEE Trans. Sustain. Energy, vol. 4, no. 4, pp. 985-993, Oct. 2013.

[10] D. Wu, F. Tang, T. Dragicevic, J. C. Vasquez, and J. M. Guerrero, "Autonomous active power control for islanded AC microgrids with photovoltaic generation and energy storage system," IEEE Trans. Energy Convers., vol. 29, no. 4, pp. 882-892, Dec. 2014.

[11] L. Chen, A. Amirahmadi, Q. Zhang, N. Kutkut, and I. Batarseh, "Design and implementation of three-phase two-stage grid-connected module integrated converter," IEEE Trans. Power Electron., vol. 29, no. 8, pp. 3881-3892, Aug. 2014.

[12] A.F. Okou, O. Akhri, R. Beguenane, and M. Tarbouchi, "Nonlinear control strategy insuring contribution of PV generator to voltage and frequency regulation," In Proc. 6th IET Int. Conf. Power Electron. Machines and Drives (PEMD), March 27-29, Bristol, UK, 2012, pp. 1-5.

[13] V.A.K. Pappu, B. Chowdhury, and R. Bhatt, "Implementing frequency regulation capability in a solar photovoltaic power plant," In Proc. North American Power Symp. (NAPS), Sep. 26-28, Arlington, TX, 2010, pp. 1-6.

[14] L. D. Watson, and J.W. Kimball, "Frequency regulation of a microgrid using solar power," In Proc. 26th IEEE Annual Appl. Power Electron. Conf. Expos. (APEC), March 6-11, Fort Worth, TX, 2011, pp. 321-326.

[15] Crăciun BI, Kerekes T, Séra D, Teodorescu R. Frequency support functions in large PV power plants with active power reserves. IEEE Journal of Emerging and Selected Topics in Power Electronics. 2014 Dec;2(4):849-58.

[16] Batzelis E, Kampitsis G, Papathanassiou S. Power Reserves Control for PV Systems with Real-Time MPP Estimation via Curve Fitting. IEEE Transactions on Sustainable Energy. 2017 Feb 24.

[17] Monthly deployment of all solar photovoltaic capacity in the United Kingdom, Available: https://www.gov.uk/government/statistics/solar-photovoltaics-deployment

[18] National Grid, Innovation, Enhanced Frequency Control Capability, Available: http://www2.nationalgrid.com/UK/Our-company/Innovation/NIC/EFCC/

[19] Masters, Gilbert M. Renewable and efficient electric power systems. John Wiley & Sons, 2013.

[20] S. B. Kjær, "Design and control of an inverter for photovoltaic applications," Ph.D. dissertation, Dept. Energy Technol., Inst. Energy Technol., Aalborg Univ., Aalborg, Denmark, 2005.

[21] S. B. Kjær, "Evaluation of the “Hill Climbing” and the “Incremental Conductance” Maximum Power Point Trackers for Photovoltaic Power Systems," in IEEE Transactions on Energy Conversion, vol. 27, no. 4, pp. 922-929, Dec. 2012.
[22] Teodorescu, Remus, Marco Liserre, and Pedro Rodriguez. Grid converters for photovoltaic and wind power systems. Vol. 29. John Wiley & Sons, 2011.

6. Assessment of the Fast Frequency Support of BES

A suitable model of battery energy storage system (BESS) system for studying its short-term dynamic response to a system frequency deviation is developed. In the chapter, the concentration is on describing the main component of the BESS system and its relevant equations. Available inertia and droop responses from the BESS system to help supporting the primary frequency control in power system networks are also analytically investigated. Then the model is utilised in conjunction with a simple but practical two-area Klein-Rogers-Kundur (KRK) power system as well as 36-zone GB network to study the impact of increasing levels of wind energy conversion system (WECS) and photovoltaic (PV) generations on frequency control. The modal analysis and dynamic time-domain simulation tools are utilised to study the power system frequency response and investigate how the BESS can impact this response on a test power system with high penetration of the wind turbines (WTs) and PV systems.

6.1. Literature Review

Battery energy storage systems (BESS) are regularly tested and integrated into the practical power systems to serve discrepant functionalities especially frequency regulation. For instance, the installations of BESS have reached over 600 MW in US since October 2015 based on the U.S. Department of Energy Global Energy Storage Database [1]. BESS can be used to smoothen and arbitrage the renewable energy source (RES) power output to enhance grid reliability and frequency stability. Additionally, the hybridized BESS with a primary frequency control of the RES can be a comprehensive solution to outperform the frequency control issues. In the UK, there are three frequency frameworks including the secure frequency controller, mandatory frequency response and frequency control by demand side management. WTs and PVs should deploy inertial emulator to release stored kinetic energy in their respective shaft and dc link capacitor or apply deloaded maximum power point tracking in order to control their output power following the frequency disturbance [2].

The contribution of RES to the network frequency regulation becomes a matter of attention for many researchers in the field. For example, the inertial emulator and droop controllers are proposed in [3]-[7] for wind energy conversion system (WECS), while similar approaches can be seen in [8] for BESS, PV-BESS [9], [10] and WECS-BESS [11]. Regarding the WECS's inertial emulator, the classical MPPT is selected as the operation mode of WECS and inertial power stored in its shaft is released. However, in droop controller, the WECS operates in a deloaded manner achieved by either operating at the suboptimal rotor speed [12] or pitching the angle of blade [13] to deliberately spill power so that the reserve power will be deployed for the primary frequency regulation.

Additionally, other converter-connected based sources like PVs which do not inherently have a stored energy source, can deliver the emulated inertial response once a satisfactory energy stored in their converter systems [14]. However, all the state-of-the-art approaches have some drawbacks that need further studies. Further, UK National Grid needs to come up with this issue that due to the variability of wind speed and solar radiation, how a WT and PV can obtain a consistent frequency response for large scale test system. BESS is efficiently appropriate to address the incipient challenges due to its high ramp rate and fast response [15]. In Danish network, the primary frequency provided by BESS is found to be the most beneficial service [16]. A BESS are deployed in micro-grid to sustain the output power, voltage, and frequency [17], [18]. The frequency response of UK power systems might be significantly enhanced by electric vehicle based BESS [19], however, a large number of electric vehicles can potentially put at risk the system frequency stability [20]. A BESS is deployed in [21] as an effective regulation source to instantaneously respond to the frequency excursion. It is notable that the widespread BESS employment is constrained by high capital costs. Thus, the vanadium-redox battery (VRB) is applicable for this purpose because of their fast response, high scalability, long life, low maintenance costs and high efficiency.

An average but precise VRB model equipped with the inertial and droop based frequency regulation is derived in this chapter. As a very short time interval has to be simulated to evaluate the developed VRB model, the detailed model with all switching procedure leads to the prolong simulation time. Therefore, an average but precise VRB model is provided in which a current source is deployed instead of voltage source inverter. Thus, the execution time is decreased while at the same time maintaining enough precision. The DC-DC boost

converter is also appended to the battery model to regulate the duty cycle, to tune the output current of converter and meet the reserve requirement. It is notable that the current regulator regulates the output current magnitude of DC-DC boost converter taking state of charge limitations and reserve power into account. Further, the inertial power is captured from the capacitor of DC link by tuning the reference voltage of DC link. As releasing some portion of energy stored in DC link capacitor leads to its voltage reduction, a new voltage recovery strategy is proposed and added to the DC link voltage controller. The main advantage of this approach is that it has almost no impact on power generated by BESS. Additionally, a frequency droop control, similar to the governing function of the conventional synchronous generator is provided for the proposed VRB system.

6.2. VRB Introduction, Physical Model and Requirement

Due to significantly increasing the penetration level of renewable energy sources like wind turbines and photovoltaics, decreasing the inertia of the whole system and frequency response reserve impose a hard challenge for power system operators to maintain the balance between system demand and generation. Frequency response support from asynchronously connected generating units, like the batteries, pumped hydro, deloaded WTs and PVs could deliver supplementary primary frequency support. For instance, the Federal Energy Regulatory Commission in the USA released Order No. 819 to revise frequency regulations so that the system operators have to stimulate renewable energy sources to take part in multiple forms of grid frequency support like inertial and primary frequency, thereby mitigating the primary frequency support burden of synchronous generators (SGs) and enhancing system reliability and stability [22]. In the UK, there are three frequency mechanisms comprising of firm frequency response, mandatory frequency response and frequency control by demand management. WTs and PVs should have primary frequency control by deploying the stored kinetic energy (inertia emulator) of WTs or energy stored in dc link capacitor of PV systems or deloaded maximum power point tracking for both WTs and PVs to regulate their output following the frequency excursion [23].

In order to reach the above noticed goal in practical cases, National Grid need to come up with this challenge that due to the variability and uncertainty of wind speed and solar irradiance, how a WT and PV can provide a reliable frequency response. Battery energy storage system is optimally suitable to meet the incipient challenge due to its fast response and high ramp rate [24]. Global BESS installations have reached over 600 MW in the USA as of October 2015 [25]. Primary frequency support is found to be the most beneficial service by BESSs on the Danish network [26] and Li-ion BESSs can fulfil this ancillary service. However, the widespread BESS employment is restricted by high capital costs. Vanadium-Redox battery (VRB) is a solution to support primary frequency response due to its fast response. Therefore, this chapter derives an appropriate model of VRB-based BESS for the sake of primary frequency regulation.

This chapter tries to discuss and illustrate the BESS model in DIgSILENT PowerFactory software. Developing the mathematical model of the VRB-based BESS and its modelling derived in DIgSILENT simulation language (DSL) and DIgSILENT programming language (DPL) for power system frequency studies are the main aims of this chapter.

Generally, in order to improve BESS efficiency and dynamic performance, VRB model deploys a controlled pump to induce flow. This type of BESS can be utilized in power system networks with large integration of wind energy conversion systems and PV power plants [27]. The main differences of the VRB with respect to Li-Ion battery [28] are as follows:

1) Utilizing an ion exchange membrane to make a larger fraction of internal resistance constant.
2) Deploying pump and controlling devices for better circulation.
3) Implementing electrolyte tanks to enlarge BESS capacity.
4) Interdependency between energy and power rating.
5) Lengthy lifetime.

As can be seen, the power and energy are thus not related, and this allows for easy scaling of the battery specifications as required. According to the experimental results, constant resistive values comprising of parasitic and internal resistances are used in literature to model different VRB losses [29]. The internal resistance represents all losses related to reaction kinetics and resistance of mass transport, membrane, solution, electrode and bipolar plate. However, consumed power by recirculation pumps, the system controller and power loss from cell-stack by-pass currents are represented by parasitic resistance.

Furthermore, it is to be noticed that the total energy stored in BESS associates with the state of charge (SOC) and the active chemicals value. In other hand, total electrode area within the cell stacks determines total BESS's available power. The presented VRB model can be deployed in system energy content and transient responses process.

Speaking of complexity, the BESS model should be accurate enough to manage large system simulations. There should be an acceptable trade-off between executional time and complicatedness. From the scale viewpoint, the BESS model needs to be adaptable to practical voltage and power levels with integration of renewable energy sources (RESs) like wind energy conversion system and PV power plants.

6.3. VRB Model Specifications

Figure 6-1 shows the studied VRB model. In this model, the effects of fixed loss, variable loss due to re-circulation pumps, state of charge representation and transients, and Various battery characteristics are examined, including the power rating, cell stack voltage, pump losses, internal and parasitic resistance losses, state of charge representation and transients. As a consequence, the fixed loss including the resistance of mass transport, membrane, solution and electrode are modelled using two resistances of $R_{reaction}$ and $R_{resistive\ losses}$. The resistance of $R_{fixed\ losses}$ and current source of $I_{pump\ losses}$ are considered to represent variable loss associated with re-circulation pump. The battery transients are modelled by $I_{pump\ losses}$. The internal voltage of battery is dependent on SOC and can be calculated using Nernst equation [30], [31]:

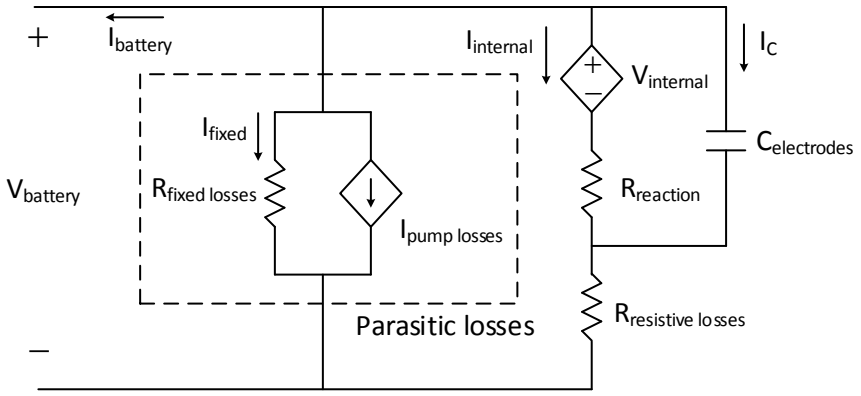

Figure 6-1: VRB electrical model [30].

$$V_{internal} = N_{cell}\left(V_{eq} + 2\frac{RT}{F}\ln\left(\frac{SOC}{100 - SOC}\right)\right) \tag{6.1}$$

where, N_{cell} is the number of series cells in VRB, V_{eq} is the cell voltage at a SOC of 50%, T is the temperature of battery, F and R are the Faraday and universal gas constants, respectively. The power flows dependent voltage source in Figure 6-1, could be expressed as equation (6.2):

$$P_{internal} = V_{internal} I_{internal} \tag{6.2}$$

The SOC can be determined using the power flow amount of depended voltage source of $V_{internal}$.

$$SOC = \frac{100 \int P_{internal} dt}{P_{battery} \left(\frac{E_{battery}}{\eta_{battery} / 100} \right) \left(\frac{SOC_{\max} - SOC_{\min}}{100} \right)} \tag{6.3}$$

where, $\eta_{battery}$ is the stack efficiency, $P_{battery}$ is the stack nominal power, $E_{battery}$ is the capacity of electrolyte tank, SOC_{min} and SOC_{max} are the minimum and maximum values of SOC in linear operating region, respectively. The current amplitude of depended current source $I_{pump\ losses}$ can be obtained in terms of internal current of VRB and SOC as follows:

$$I_{pump\ losses} = K_{pump} \frac{|I_{internal}|}{SOC} \tag{6.4}$$

where, K_{pump} is the pump current gain. The internal current of VRB model is derived as follows:

$$I_{internal} = \frac{V_C - V_{internal}}{R_{reaction}} \tag{6.5}$$

where, V_C is the voltage across electrodes capacitor $C_{electrodes}$. In order to calculate the current flows through R_{fixed} resistor, a Kirchhoff's Voltage Law (KVL) is applied to equivalent circuit of Figure 6-1. It yields:

$$R_{fixed} I_{fixed} = V_C - R_{resistive\ losses} \left(I_{internal} + I_{pump\ losses} + I_{fixed} \right) \tag{6.6}$$

Then, I_{fixed} can be written as follows:

$$I_{fixed} = \frac{V_C - R_{resistive\ losses} \left(I_{internal} + I_{pump\ losses} \right)}{R_{fixed} + R_{resistive\ losses}} \tag{6.7}$$

The capacitor current can be represented by other currents using a Kirchhoff's Current Law (KCL) as follow:

$$I_C = -I_{internal} - \left(I_{fixed} + I_{pump\ losses} + I_{internal} \right) \tag{6.8}$$

When capacitor current is determined, capacitor voltage can be computed by solving first order differential equation (6.9).

$$\frac{d}{dt} V_C = \frac{I_C}{C_{electrodes}} \tag{6.9}$$

Finally, the VRB terminal voltage is computed as follows:

$$V_{battery} = R_{fixed} I_{fixed} \tag{6.10}$$

The parameters of studied VRB battery model in this project are tabulated in Table 6-1. It is to be mentioned that the nominal current and voltage quantities are deployed to represent the input and output variables of the VRB model in per unit values.

Table 6-1: Parameters of studied VRB model [30].

Parameter	Symbol	Value	Unit

Stack Nominal Power	$P_{battery}$	3.3	kW
Capacity of Electrolyte Tank	$E_{battery}$	1	hour
Battery Efficiency	$\eta_{battery}$	79	%
Battery Equilibrium Voltage	V_{eq}	1.4	V
Gas Constant	R	8.31451	J/(mol.K)
Battery Temperature	T	298	K
Faraday Constant	F	96485	C/mol
Number of Cells in Series	N_{cell}	39	-
Pump Current Gain	K_{pump}	1.0126	-
Minimum State Of Charge	$SOC_{\min}$	20	%
Maximum State Of Charge	$SOC_{\max}$	80	%
Reaction Losses Resistor	$R_{reaction}$	0.061	ohm
Resistive Losses Resistor	$R_{resistive}$	0.04	ohm
Fixed Losses Resistor	R_{fixed}	21	ohm
Electrodes Capacitor	$C_{electrodes}$	0.15	F
Nominal Current of Battery	I_{nom}	80	A
Nominal Voltage of Battery	V_{nom}	50	V

6.4. The VRB Modelling in DIgSILENT PowerFactory

The grid connected two-stage BESS system is shown in Figure 6-2. The reason that this model is called two-stage is that two power electronic converters are used in cascade to convert generated direct current (DC) power of VRB to alternating current (AC) power. The DC-DC boost converter increases the battery terminal voltage and at the same time a current regulator, controls the active power of the VRB by controlling the output current amplitude. In the next stage, a voltage source inverter converts DC link voltage to three phase AC voltage. Finally, the inverter voltage output level is increased to the system one using a step-up transformer. However, in order to remove the high frequency harmonics generated by inverter switching, a low pass filter LCL is deployed between inverter and transformer.

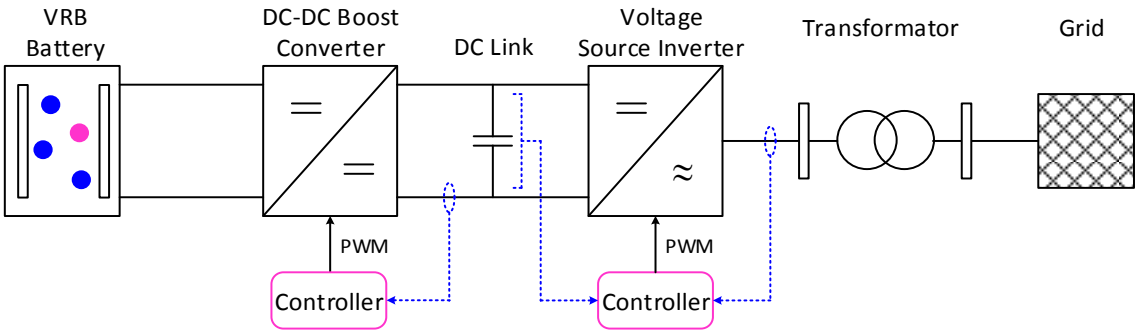

Figure 6-2: Control structure for a grid connected two stages battery energy storage system.

According to the above mentioned explanations, a grid connected BESS is simulated in DIgSILENT PowerFactory so that it can be appropriate for studying dynamic frequency response of large scale systems and at the same time the VRB physical modelling is properly modelled. The controlling structure of the proposed grid connected BESS is shown in Figure 6-3. The voltage source inverter shown in Figure 6-2 is modelled as 'BESS Generator'. Indeed, this is a 'Static Generator' or a simple current source of DIgSILENT PowerFactory

software. The power and voltage output of the inverter can be measured by 'P Meas' and 'V Meas', respectively. Furthermore, the PLL measures the output frequency of the inverter.

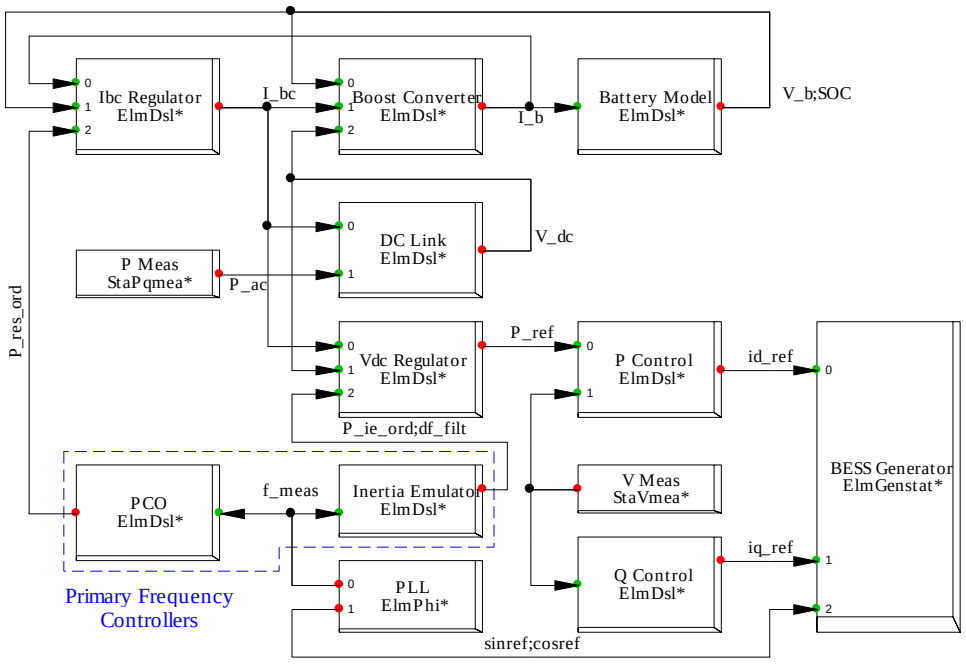

Figure 6-3: Control structure for a grid connected two stages BESS in DIgSILENT PowerFactory.

6.4.1. Inertia Emulator

The BESSs are interfaced with the power network by power electronic converters and the generated power of these power plants is controlled by these devices. Thus, due to the buffer, i.e. power electronic converter, between BESS and electrical system, it efficiently avoids the inertia of the BESS, if any, from responding to the system frequency excursions. But, unlike the conventional power plants or wind energy conversion systems, the BESS do not have rotating shaft. To get rid of this issue, the inertia emulator is appended into the BESS controllers as shown in Figure 6-4. The design idea of inertia emulator is to introduce a rate control which responds rapidly to the frequency change. It is to be notified that in steady state, this controller is not activated. Firstly, the frequency error is measured so that the extra power is needed if it is low. The dead band suppresses response of the controller until the error exceeds a threshold.. The dead band output signal is further filtered by a low pass filter (LPF) to reject measurement noise, multiplied by a K_{ie} coefficient, passed through a 'wash out' block, and finally the rate of change and the amplitude of the generated signal limited by a 'Rate Limiter' and an amplitude limiter, respectively. In a condition that the BESS system should be substituted with conventional power plant with inertia constant of H, $K_{ie} \times T_{wo}$ are equal to 2H. In this figure, K_{ie} is the gain applied to the frequency deviation, and T_{lag} and T_{wo} is time constants associated with the lag and decay of the response respectively, df is the magnitude of the frequency deviation, f_{db} is the frequency dead band and Pie_{max} is the maximum limit of power increase which can be demanded. The Up_Rate_Limit is the restricted rate of change of requested power Pie_{ord}.

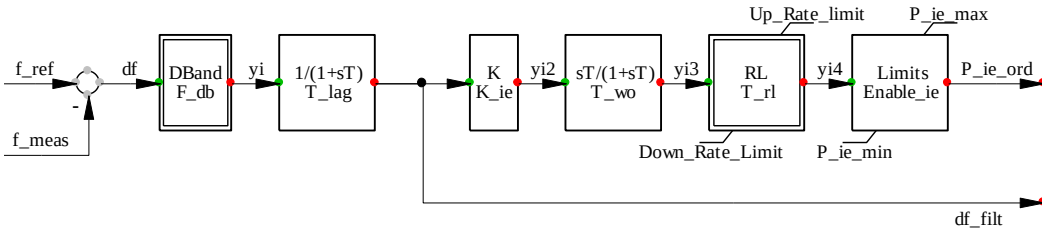

Figure 6-4: Outline of the "Inertial Emulator" in the BESS model in DIgSILENT PowerFactory.

The BESS model's inertia emulator parameters are listed in Table 6-2. The Pie_{ord} is limited to 0.1 p.u. Furthermore, the rate of change of this signal is selected as 1 p.u. per second. Based on K_{ie} and T_{wo} values tabulated in Table 6-2, the inertia constant H of synchronous generator (SG) equivalent with the BESS is 6.5 s.

Table 6-2: Parameters of the "Inertia Emulator" in the BESS model.

Parameter	Value	Unit	Parameter	Value	Unit
F_{db}	0.0001	p.u.	T_{lag}	0.1	s
K_{ie}	130	-	T_{wo}	0.1	s
T_{rl}	0.005	s	$Enable_{ie}$	0/1	-
$P_{ie,min}$	0	p.u.	$P_{ie,max}$	0.1	p.u.
Up Rate Limit	1	p.u./s	Down Rate Limit	-1	p.u./s

6.4.2. Primary Controller

A frequency droop control, similar to the governing function in a steam turbine power plant, as BESS primary controller (PCO) is simulated and shown in Figure 6-5. The input signal is the frequency deviation from its nominal value and *R* is speed regulation parameter or droop parameter. The governor virtual delay time is T_{lag} and P_{resmax} is the maximum BESS system reserve power margin. The rate of change of reserve power is restricted by 'Rate Limiter' block. The "P_res_int" is set to the maximum BESS reserve power margin. The BESS primary controller parameters are listed in Table 6-3.

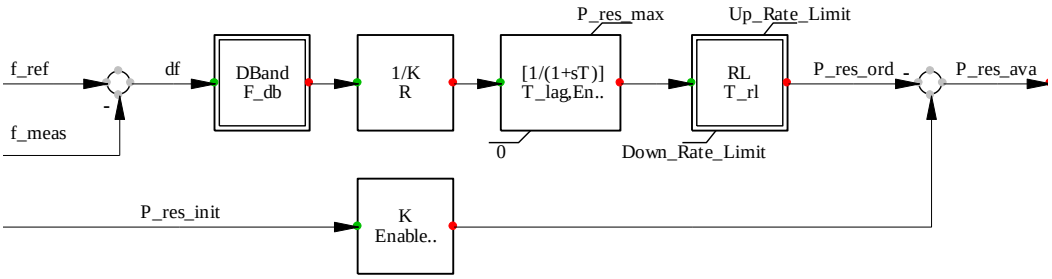

Figure 6-5: Outline of the "PCO" in the BESS in DIgSILENT PowerFactory.

Table 6-3: Parameters of the BESS Primary Controller.

Parameter	Value	Unit	Parameter	Value	Unit
F_{db}	0.0001	p.u.	R	0.05	p.u.
T_{lag}	1	s	$P_{res,max}$	0.1	p.u.
$Enable_{res}$	0/1	-	T_{rl}	0.02	s
Up Rate Limit	0.1	p.u./s	Down Rate Limit	-1	p.u./s

6.5. Analysis of Two-Area System Considering BESS Integration

In this section, the modal analysis and time domain frequency response of a modified version of the Klein-Rogers-Kundur (KRK) two-area multi-machine as the test system in different scenarios is evaluated. The single line diagram of this benchmark system is shown in Figure 6-6. The total load demand of the network is 2,517 MW and 200 Mvar. In non-WTPV scenario, named "WTPV 00%", all the load demands are supplied by conventional power plants. It is to be noticed that 11 out of 12 units connected to buses 1, 2 and 4 are reheat steam turbine (RST) types. The 'HT 44' is a hydroelectric unit. All four units connected to bus 3 are combined cycle gas turbine (CCGT) power plants. The nominal apparent power of all these units is 225 MVA. The 'RST 11' is also considered as slack unit. In "WTPV 75%" scenarios, all the synchronous generator (SG) units connected to bus 2 and bus 4 are replaced with eight WT power plants. In addition, the two middle units connected to buses 1 and 3 are substituted with four PV power plants. The active power generation of each unit is tabulated in Table 6-4, for above mentioned scenarios. In these scenarios, all SG units connected to bus 1 and 3 are equipped with power system stabilizers (PSSs) and all sixteen SG units have automatic voltage regulator (AVR) controllers. Also, the "Q control" of WT and PV power plants is not activated. Furthermore, the Kp and Ki parameters of PLLs in the PV power plants are set to 10 and 200, respectively. In order to evaluate the effects of the BESSs on frequency response of the two-area system, two BESS units are connected to bus 1 and 3. The nominal ratings of the both units are 100 MVA and 10 MWh. In other words, a BESS unit can supply 100 MW for 6 minutes.

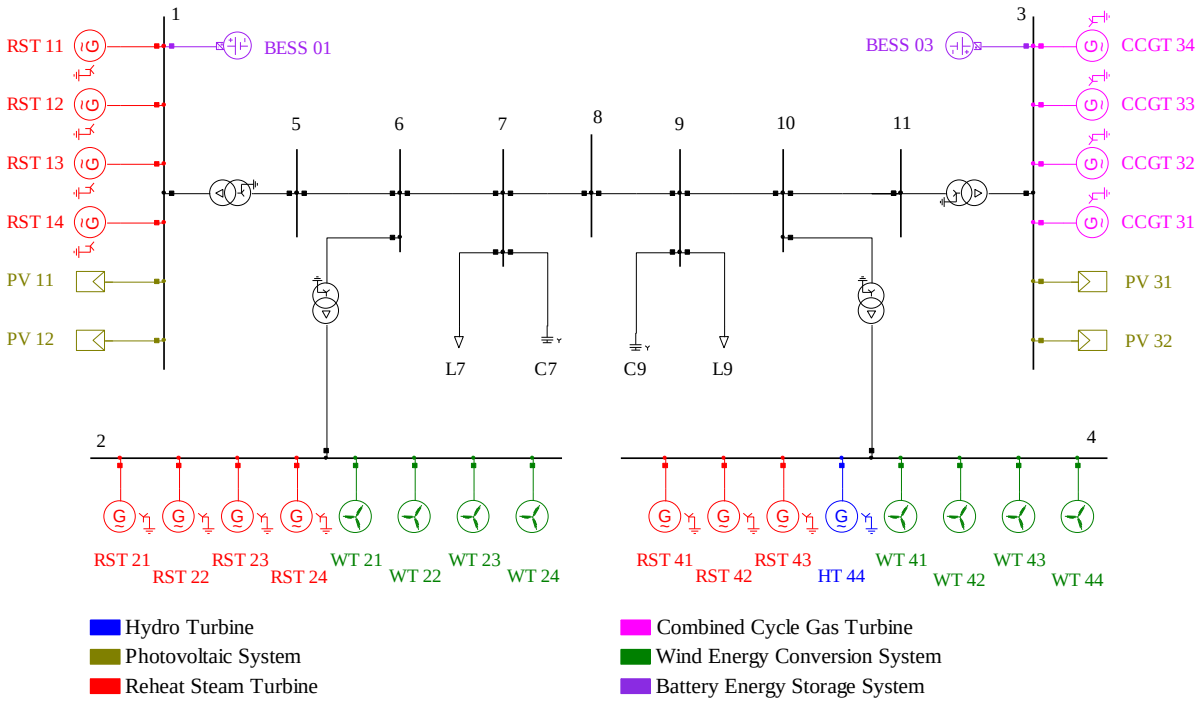

Figure 6-6: Single line diagram of the two-area system.

Table 6-4: Active power of power plants in defined scenarios (in MW)

Unit	WTPV 00%	WTPV 75%	Unit	WTPV 00%	WTPV 75%
RST 11	11	11	RST 42	175	-
RST 12	175	-	RST 43	175	-
RST 13	175	-	HT 44	175	-
RST 14	**100**	**100**	WT 21	-	175
RST 21	175	-	WT 22	-	175
RST 22	175	-	WT 23	-	175

RST 23	175	-	WT 24	-	175
RST 24	175	-	WT 41	-	175
CCGT 31	180	180	WT 42	-	175
CCGT 32	180	-	WT 43	-	175
CCGT 33	180	-	WT 44	-	175
CCGT 34	180	180	PV 11	-	175
RST 41	175	-	PV 12	-	175
			Sum	2581	2571

6.5.1. Modal Analysis of Two-Area System Considering BESS Integration

This section investigates the effects of the BESS on electromechanical modes of the studied two-area test system with high wind and photovoltaic power penetration levels using modal analysis tool in DIgSILENT PowerFactory. Figure 6-7 shows the electromechanical modes of two-area KRK system for predefined scenarios. In each scenario, there are 15 electromechanical modes. In first scenario which all 16 units are SGs, there exist 15 electromechanical modes as highlighted with distinct black colour in Figure 6-7. The slowest mode with damped frequency of 0.6 Hz is inter-area mode where all the SGs are participated in this mode. In the second scenario, the SGs' electromechanical modes highlighted as pink colour are reduced from 15 to 7 as eight SGs are substituted with eight WECSs in buses 2 and 4. It means that other 8 modes are associated with WTs. In third scenario, the SGs' electromechanical modes are mitigated from 7 to 3 since 4 SGs of nodes 1 and 3 are replaced with four PV units, as highlighted by blue colour. The electromechanical modes of fourth scenario are highlighted with green colour which are coincided with all modes of third scenario. Additionally, a BESS DC Link mode is appeared with damped frequency of 1.6 Hz.

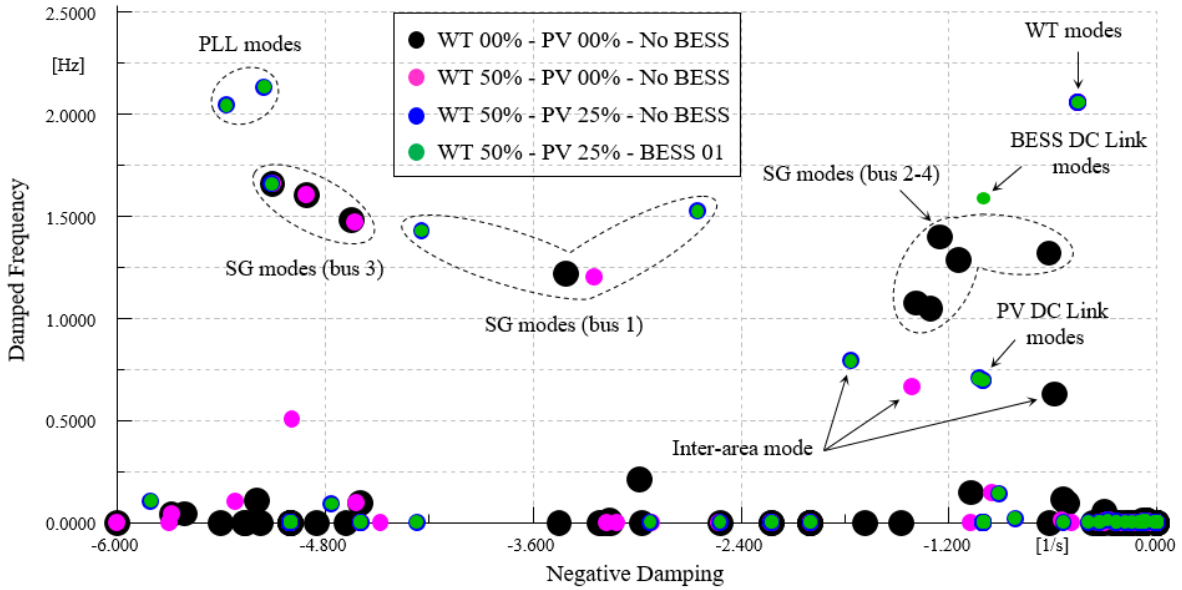

Figure 6-7: Electromechanical modes of the two-area system with different scenarios.

The impact of penetration levels of wind and photovoltaic generations on the damping of slowest electromechanical modes related to the SGs is shown in Figure 6-8. It is clearly observed that the damping of this mode is increased by increasing the number of installed WECSs and PVs, however, its damped frequency is almost fixed. The main reason of damping increment is negative effect increment of AVR systems of SGs on buses 2 and 4 following renewable energy sources increment in the grid.

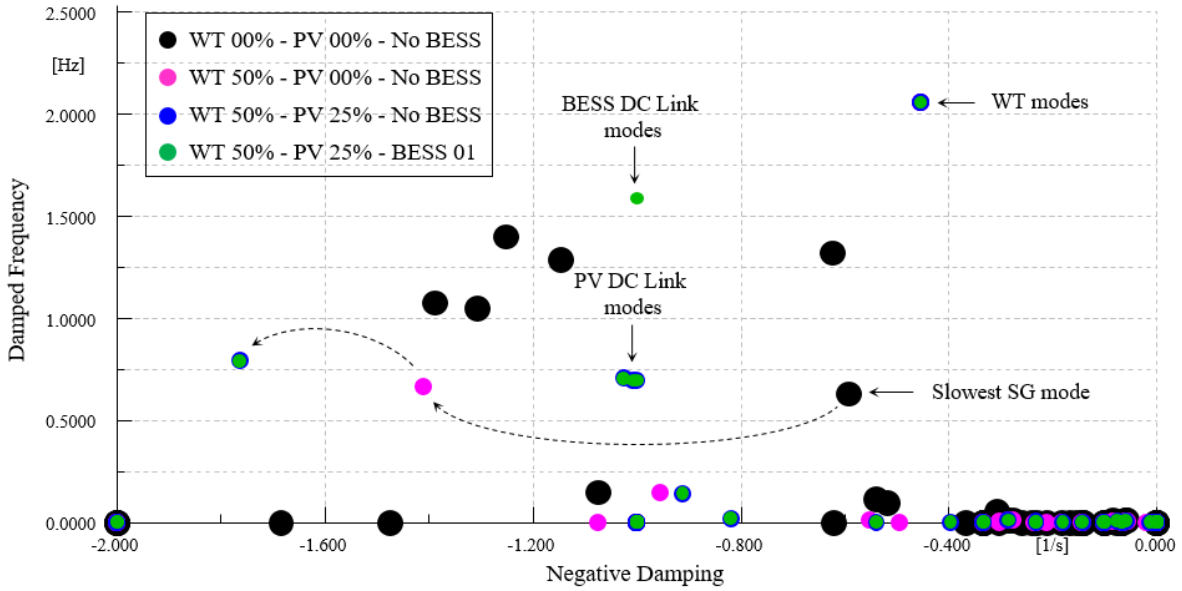

Figure 6-8: Slowest SG mode of the two-area system with different scenarios.

6.5.2. Frequency Response of Two-Area System

6.5.2.1. Effect of the BESS on Frequency Response of Two-Area System

In this subsection, dynamic performance of the inertia emulator and the BESS primary frequency controller and their impact on system frequency response is investigated following the abrupt loss of 'RST 14'. To this end, the 'WTPV 75%' is divided into three sub-scenarios. In WTPV 75% I scenario, only WTs are equipped with inertia emulator and droop based controller. The inertia emulator of the PV systems are activated beside the inertia emulator and reserve based primary frequency response of the WTs in WTPV 75% II scenario. Finally, in WTPV 75% III, the 'BESS 01' connected to node 1 is participated in system primary frequency control. The inertial and reserve powers of PVs and WECSs are limited to 0.1 p.u. consists of the PVs and WTs with inertia emulator and primary frequency based reserve power. It is observed that the frequency controller objective is accomplished as shown in Figure 6-3 because the frequency nadir and steady-state frequency variations of the system is further improved considering reserve power for the PV systems. Moreover, their ramp rates are 1 p.u./s and 0.1 p.u./s, respectively. In other hand, the inertia emulator's parameters of the 'BESS 01' are identical to those of PVs and WECSs, however, the maximum reserve power limitation and its ramp rate are set to 1 p.u. and 2 p.u./s, respectively. The droop coefficient of all generating units and the 'BESS 01' are chosen as 5% and 0.05%, respectively. The simulation results related to above mentioned scenarios are shown in Figure 6-9 to Figure 6-11. The COI frequency is presented in Figure 6-9 and Figure 6-10. The COI RoCoF changes are portrayed in Figure 6-11.

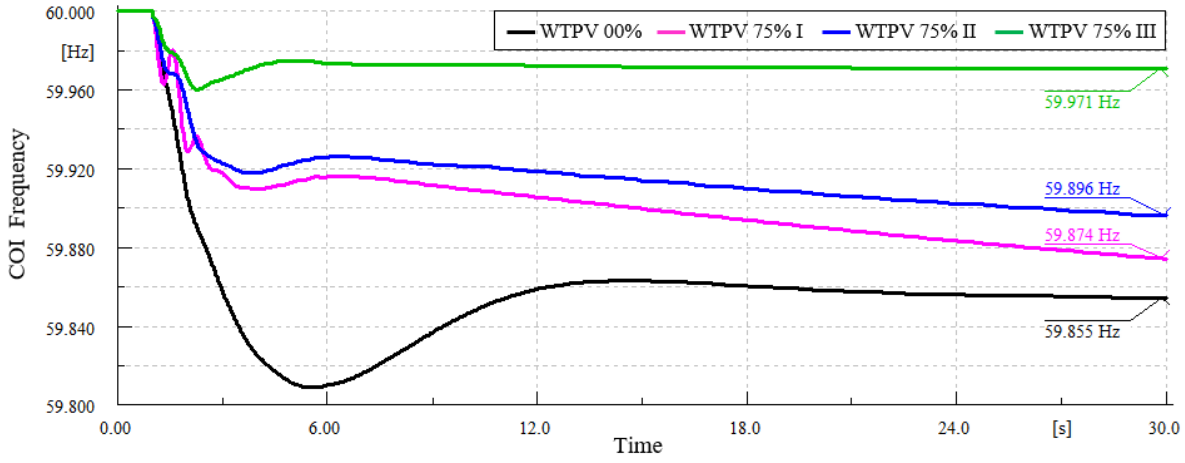

Figure 6-9: Frequency response with loss of 100 MW generation for different scenarios.

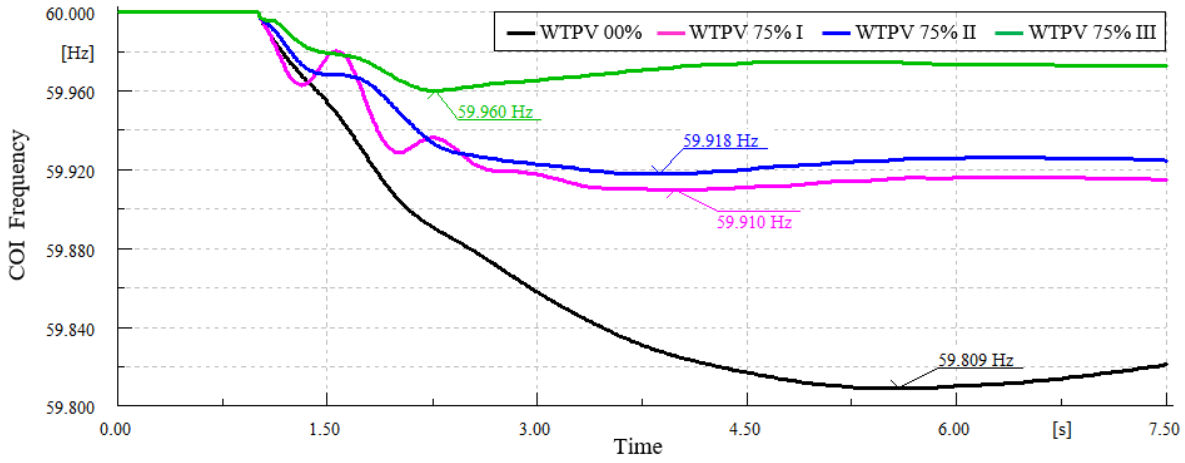

Figure 6-10: Frequency nadir with loss of 100 MW generation for different scenarios.

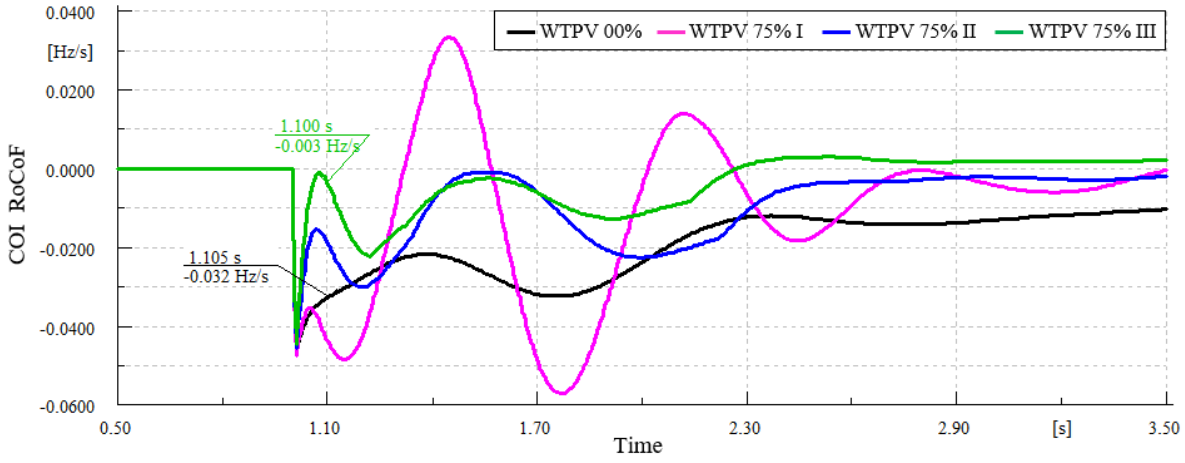

Figure 6-11: COI RoCoF with loss of 100 MW generation for different scenarios.

6.5.2.2. Effect of the BESS Droop on Frequency Response of Two-Area System

In this section, the effect of droop parameter of *R* on primary frequency support of the 'Primary Controller' in 'BESS 01' as well as system frequency response of two-area KRK network is investigated. In this regard, the simulation results of four scenarios for loss of generator 'RST 14' are shown in Figure 6-12 to Figure 6-14. The first scenario which is highlighted by blue colour is identical to the third scenario in the previous section. It is to be mentioned that the main purpose of selecting infinite value for droop coefficient is to deactivate it. In this scenario, all the RSTs, WTs and PVs are equipped with primary frequency controller. The fourth scenario highlighted by green colour is identical to fourth scenario in the previous section in which the 'BESS 01' is also participated in frequency regulation (its parameter *R* is set to 0.05%). The third scenario highlighted by black colour is similar to fourth scenario, however, *R* is equal to 0.5% for the 'BESS 01'. Finally, this parameter is set to 5% for the 'BESS 01' in second scenario which is specified by red colour. As can be seen from simulation results, the system frequency is changed slightly with respect to non-BESS case while the droop parameter of the 'BESS 01' is identical to other units.

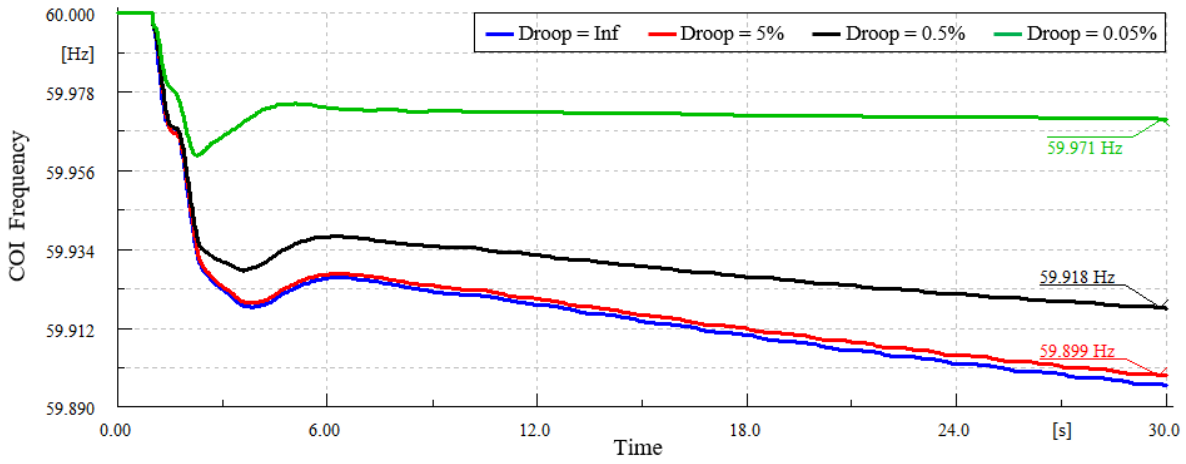

Figure 6-12: Frequency response with loss of 100 MW generation for different BESS droop.

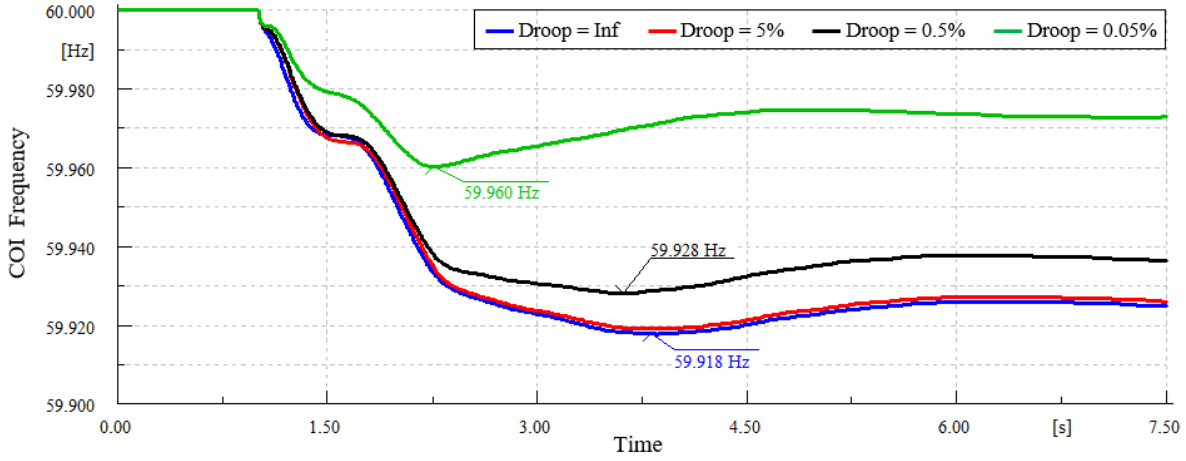

Figure 6-13: Frequency nadir with loss of 100 MW generation for different BESS droop.

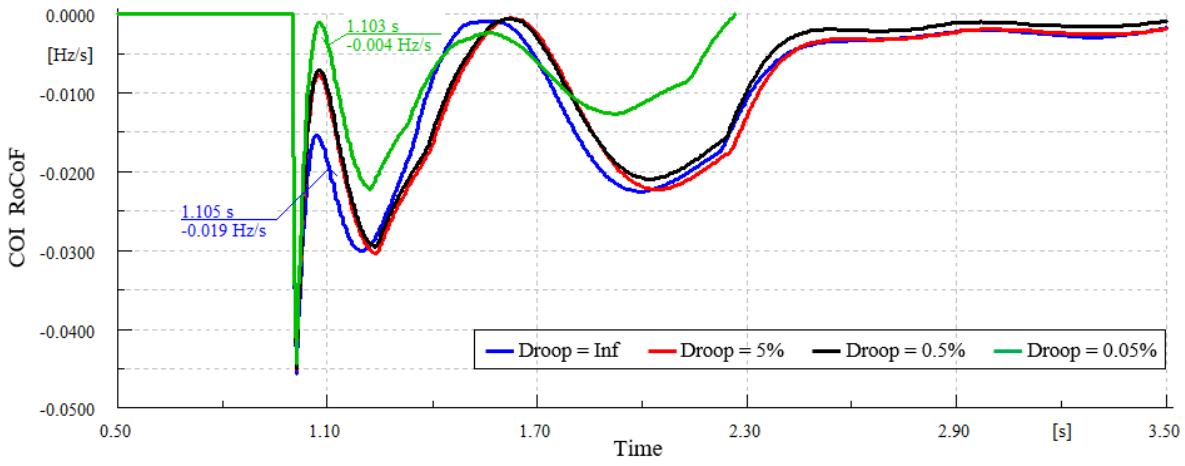

Figure 6-14: COI RoCoF with loss of 100 MW generation for different BESS droop. Effect of The BESS Location on Frequency Response of Two-Area System

6.5.2.3. Effect of the BESS Location on Frequency Response of Two-Area System

In this section, the impact of installation location of the BESS on primary frequency control support and system frequency response of two-area test system is analysed. In this regard, the following two discrepant scenarios are defined: 1) The 'BESS 01' is the only energy storage of the grid and 2) The BESS connected to bus 3 i.e. 'BESS 03' is the only energy storage of the network. The droop parameters of both BESSs are set to 0.05%. The results of these two scenarios following the loss of 'RST 14' unit are portrayed in Figure 6-15 to Figure 6-17. As can be seen from Figure 6-15 and Figure 6-16, the system COI frequency is almost similar for both scenarios after t=10 s. In other word, the location of the BESS and its distant to the event has the highest influence on the system frequency for the first few seconds of disturbance. Therefore, the RoCoF and frequency nadir become smaller and greater if the BESS distance to the incident is lower compared to other cases.

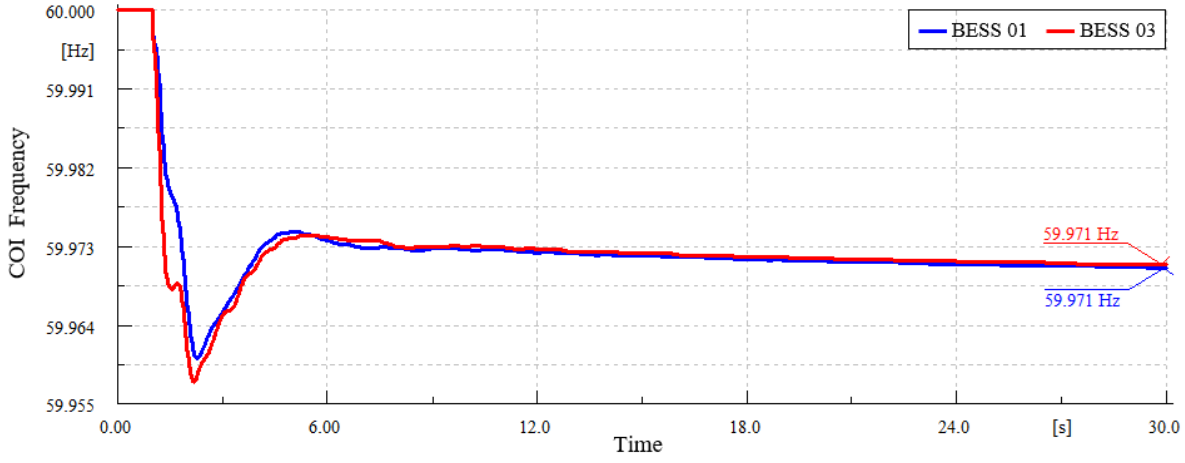

Figure 6-15: Frequency response with loss of 100 MW generation for different BESS location.

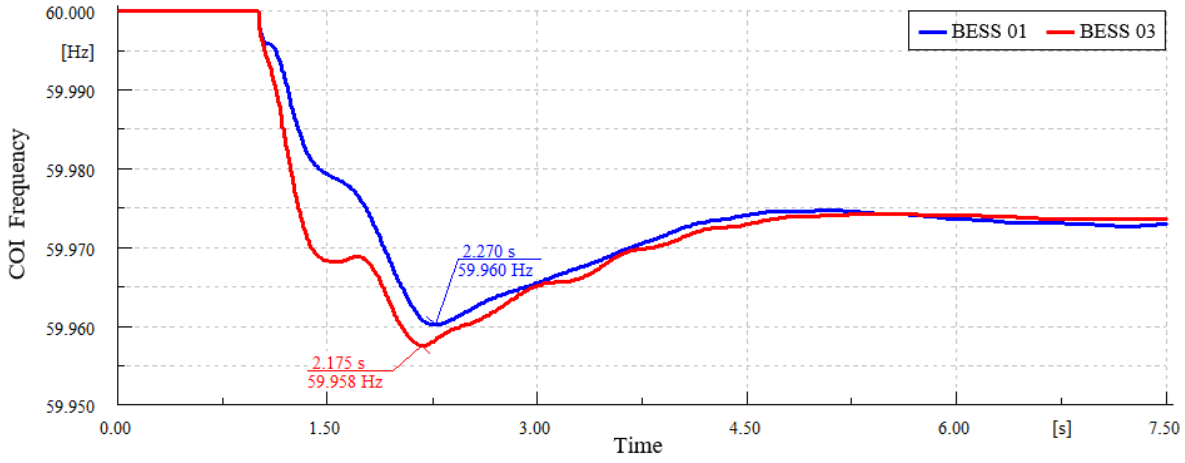

Figure 6-16: Frequency nadir with loss of 100 MW generation for different BESS location.

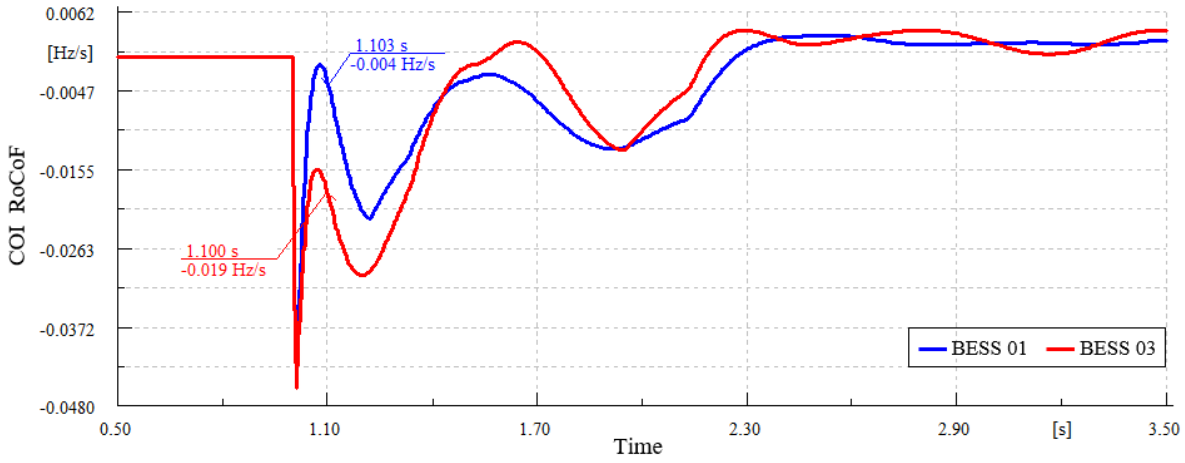

Figure 6-17: COI RoCoF with loss of 100 MW generation for different BESS location.

6.5.3. Executive Summary of Deploying BES in Two-Area test System

The main goal of this chapter was to investigate the effect of the BESS integration on frequency response of power systems which their load demands are supplied by conventional CCGT, thermal and hydro units as well as renewable energy sources like WTs and PVs. In this context, an average and accurate dynamic model of the BESS system was firstly derived in DIgSILENT PowerFactory and its dynamic performance and behaviour were analysed.

The effect of BESS on frequency response of two-area KRK system is analysed. It is observed from the results that in the power systems with the BESSs which share the responsibilities of frequency control with the conventional generation indicate how to enhance the overall system frequency response and mitigate the stresses over the SGs, WTs and PVs in the system. The two-area system with BESSs supplying mandatory frequency response enhanced with reserve and inertial power have a direct impact also over the global indicators of frequency quality: RoCoF, frequency nadir and steady-state frequency deviation. Furthermore, the influence of BESS's droop coefficient and its installation location on primary frequency support is investigated. It is observed that the location of the BESS doesn't have considerable effect on its performance; however, droop parameter has considerable impact on primary frequency support of it. Consequently, while the droop coefficient of the BESS is equal to SGs, the system frequency response is not meaningfully changed after BESS

installation due to lower capacity of BESSs with respect to power plants. In other hand, if the BESS's droop coefficient is set approximately one-hundredth of SG's one, the participation level of this unit in primary frequency support will be considerably increased and system frequency response will be accordingly enhanced.

6.6. Analysis of 36-Zone GB Network Considering BESS Integration

In this section, the system frequency response of 36-zone GB network integrated CCGT, WTs, PVs and BESSs under the proposed BESS model following an abrupt and sever power disturbance. In this regard, the generation level and geographical distribution of conventional power plants, PVs and WTs are investigated. After which, the modal analysis is deployed to show the PV, WT and BESS integration impact on electromechanical modes of 36-zone GB network. The time-domain based system frequency response following the sudden and sever in-feed loss is applied on several system scenarios.

The generation power and geographical distribution of traditional plants are shown in Figure 6-18. It is to be noted that almost 90% of network generation is located in the southern part of UK i.e. England & Wales and Scotland supplies only 10% of whole system load demand. As mentioned, the largest unit is the nuclear power plant located in zone 12 which supplies 13% of whole system generation. It is to be noticed that 60% and 305 of conventional generating unit are CCGT and nuclear power plants, respectively. The remained 10% generating units are included of 10% biomass and 3% hydro turbine. The accurate generation of each zone is tabulated in Table 6-5 in MW.

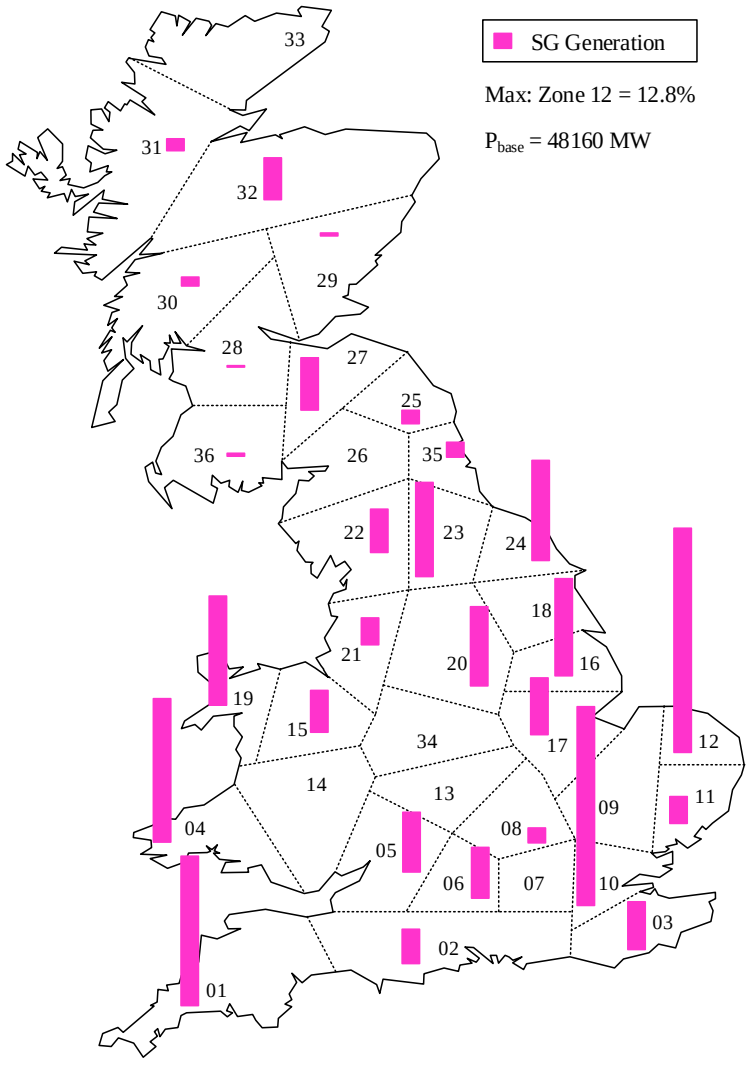

Figure 6-18: Geographic distribution of SG generation in "WTPV 00%" scenario.

In order to analyse the effect of conventional power plants' replacement with PV and WT power plants, two different scenarios of WTPV 00% and WTPV 60% are considered. In first scenario, the whole system load is satisfied by conventional SGs. In the second scenario, the PVs and WTs supply 20% and 40% of GB network demand, respectively. Since the total load demand of the network is 40 GW, the power generation of PVs and WTs are 8 GW and 16 GW, respectively. The precise generation of SGs, PVs and WTs are tabulated in Table 6-5 and Table 6-6. As can be seen, as the penetration of renewable energy sources increases, the capacity of gas turbines based CCGT are decreased while other conventional units' capacity is fixed. The capacity of CCGTs is 5 GW and i.e. 12.5% of load demand in WTPV 60% scenario. In other hand, 27.5% of load is supplied by nuclear, biomass and hydro-turbine power stations in this scenario.

Table 6-5: Active power of conventional power plants in two scenarios

No.	Type	Zone	WTPV 00% (MW)	WTPV 60% (MW)
01	Gas	01	809	140
02	Nuclear	01	3337	3436
03	Gas	02	946	164
04	Nuclear	03	1299	1337
05	Gas	04	3941	683
06	BioMass	05	100	100
07	Gas	05	1575	273
08	Gas	06	1385	240
09	Gas	08	420	73
10	BioMass	10	741	742
11	Gas	10	4732	820
12	Gas	11	751	130
13	Gas	12	1609	279
14	Nuclear	12	4548	4683
15	Gas	15	1180	204
16	Gas	16	2704	469
17	Gas	17	1544	268
18	Gas	19	617	107
19	Nuclear	19	2398	2400
20	Gas	20	2172	376
21	Gas	21	724	125
22	Nuclear	22	1202	1238
23	**BioMass**	**23**	**1722**	**1724**
24	Gas	23	858	149
25	Gas	24	2759	478
26	BioMass	25	366	366
27	BioMass	27	120	120
28	Gas	27	107	19
29	Nuclear	27	1214	1250
30	Gas	28	18	3
31	BioMass	29	52	52
32	Gas	29	14	2
33	Hydro	30	232	233
34	Hydro	31	321	322
35	Gas	32	11	2
36	Hydro	32	535	536
37	Pump Storage	32	611	612
38	BioMass	35	280	280
39	Gas	35	126	22
40	BioMass	36	45	45
41	Hydro	36	33	33

Total Active Power (MW)	48157	24534

Table 6-6: Active power of PV and WT power plants in WTPV 60% scenario.

Zone	PV (MW)	WT (MW)	Zone	PV (MW)	WT (MW)
01	407	609	19	129	1312
02	431	61	20	416	95
03	92	459	21	277	198
04	267	824	22	135	641
05	340	49	23	395	394
06	249	26	24	114	1025
07	268	1	25	144	121
08	734	2	26	34	299
09	392	2	27	120	1251
10	98	252	28	136	511
11	95	49	29	113	221
12	304	2096	30	75	138
13	486	197	31	12	335
14	323	61	32	75	1469
15	517	438	33	82	426
16	37	578	34	91	1
17	32	1	35	198	781
18	218	17	36	165	1060
			Total	8000	16000

The geographical distribution of generated power of all units is shown in Figure 6-19 for WTPV 60%. Furthermore, the CCGT participation in supplying load demand is separately shown. By comparing this figure and Figure 6-18, it is clearly observable that the conventional units placed beside the coast i.e. nuclear units and the biomass power plants located in the middle part of GB network are considered while the gas turbine units of middle-down part of GB network, that is, the high-densely consumption region are substituted with PVs. Moreover, in order to supply all deliverable power of gas turbines in the top areas and coasts of network i.e. low-densely consumption region, the WTs are installed and connected to the associated buses.

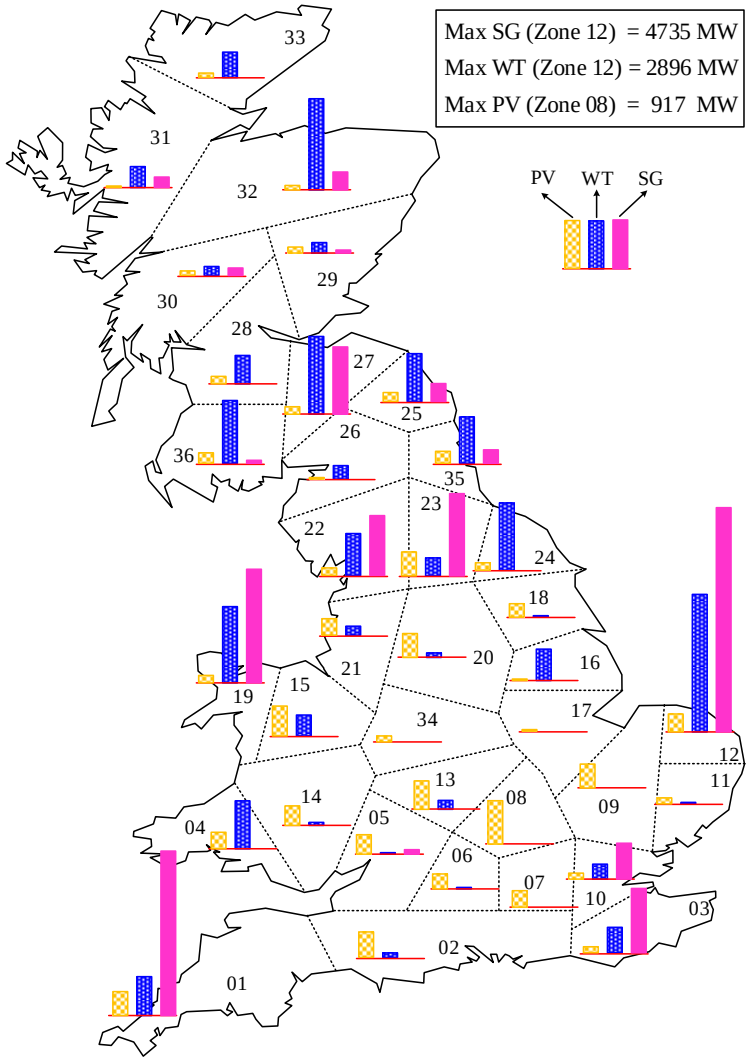

Figure 6-19: Geographic distribution of power plant's generations in "WTPV 60%" scenario

6.6.1. Modal Analysis of 36-Zone GB Network Considering BESS Integration

The electromechanical modes of the system are shown in Figure 6-20 for four discrepant scenarios. All load demand is supplied by conventional units in first scenario. In second one, 40% of load is supplied by WTs and the rest by conventional units. The WTs and PVs are supplied 40% and 20% of load demand in third scenario. In the last and fourth scenario, a BESS with 500 MVA and 50 MWh capacities is also connected to the network in zone 23 compared to the previous scenario. Once the conventional generating units substitute with the PVs and WTs, some electromechanical modes of the network related to the motion equation of SG's rotor are replaced with double-mass drive train modes of WTs and DC link modes of PV systems. These sort of modes are representative of rotor dynamics of SGs and WTs as well as dc link dynamic of PV systems. Installing BESS can just append one mode with damping frequency of 1.6 Hz to the eigenvalues of the whole network. This is also the case for PV system. The frequency and damping of SG modes are approximately fixed or slightly increased in consequence of increasing PVs and WTs penetration levels. It is to be noted that the initial condition of dependent function of 'Ramp' in 'Vdc Regulator' of PV and BESS are set to 1 for the sake of calculating the eigenvalues of GB system. The dc link modes will be located on the origin once they are set to zero.

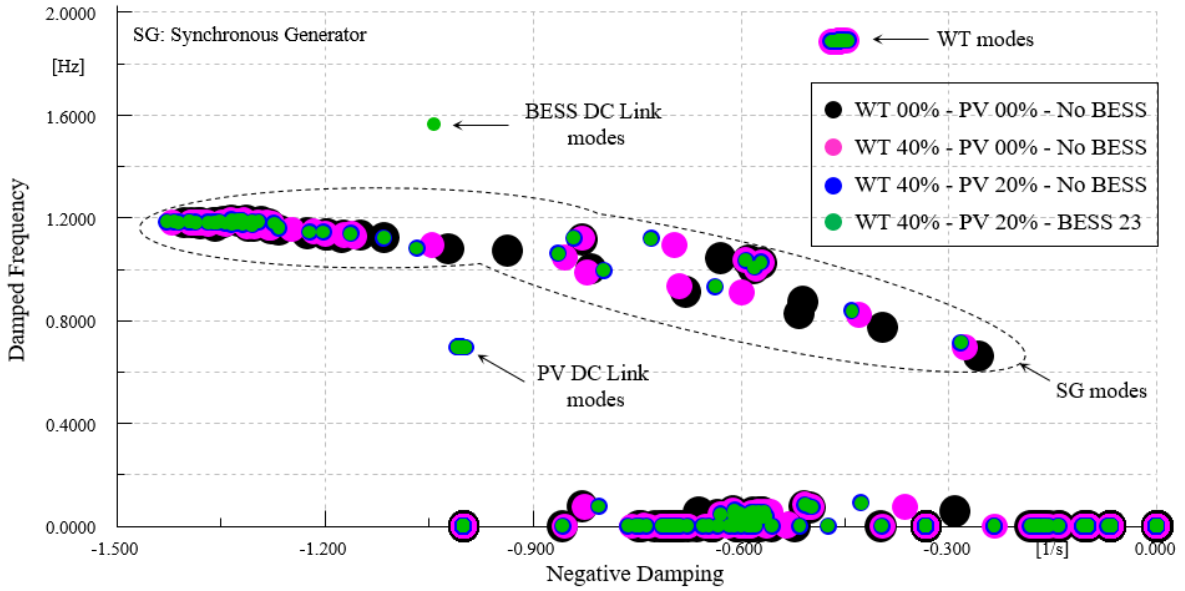

Figure 6-20: Effect of WECS, Photovoltaic and BESS integration in electromechanical modes.

In order to accurately observe and investigate the effect of growing renewable energy sources penetration levels on electromechanical modes in the 36-zone GB network, two slowest modes are shown in Figure 6-21 for different scenarios. It is clear-cut that damping and frequency of these two modes are increased following the penetration levels increment. This is due to the fact that the AVRs of CCGTs are removed after CCGTs replacement procedure and their negative influence on electromechanical modes i.e. damping reduction mitigates and their damping increases.

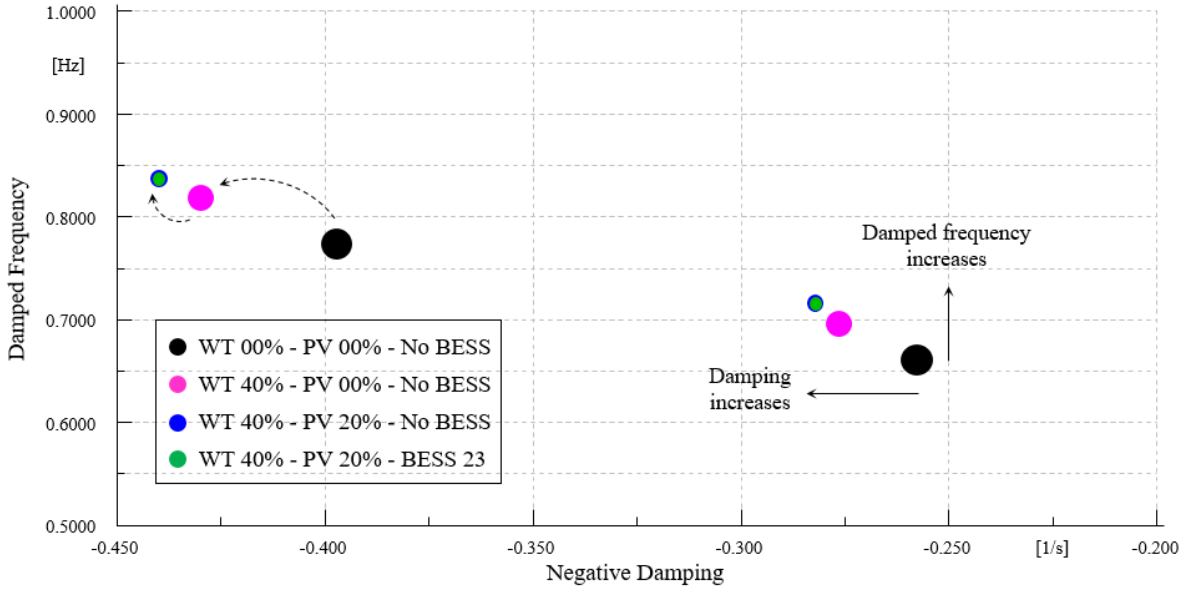

Figure 6-21: Effect of WECS, Photovoltaic and BESS integration in two slowest electromechanical modes.

6.6.2. Frequency Response of 36-Zone GB Network Considering BESS Integration

In this section, the GB system frequency response is validated following the biomass 23 generation lost. The main reason of selecting this unit is that its capacity is fixed after integration of PVs and WTs. In simulation results, different quantities like centre of inertia (COI) frequency and RoCoF changes are shown for 30 s following the disturbance at t=1 s in two case studies of WTPV 00% and WTPV 60%. The step size parameter of time-domain simulations is equal to 0.005 s. In the following results, the COI frequency is illustrated beside the SGs' frequencies based on the following relation:

$$F_{COI} = \frac{\sum_{i=1}^{N} H_i S_i F_i}{\sum_{i=1}^{N} H_i S_i} \tag{6.11}$$

Where, H_i, S_i and F_i are the inertia constant, apparent power and frequency of the *i*th SG, respectively.

6.6.2.1. Loss of 1700 MW Generation in Zone 23

The effect of BESS with nominal values of 500 MVA and 50 MWh located in zone 23 on GB system frequency response is investigated hereinafter. The biomass unit located in zone 23 with the capacity of 1700 MW is abruptly disconnected from the grid. The simulation results are shown in Figure 6-22 to Figure 6-24 for two scenarios of WTPV 60% and WTPV 00%. In order to investigate the dynamic performance of the PVs, WTs and the BESS, the WTPV 60% scenario is divided into four sub-scenarios. In WTPV 60% I, the inertia emulator and PCO are deactivated for all PVs and WECSs. In scenario of WTPV 60% II, the WTs are equipped with the reserve and inertial powers. It is to be pointed out that the PVs don't have these abilities. In WTPV 60% III scenario, the PV units equip with inertia emulator and reserve power as well. Finally, the proposed BESS model are considered in WTPV 60% IV scenario. The inertial and reserve powers of WTs and PVs are restricted to 0.1 p.u. The inertial and reserve ramp rates of these units are 1 p.u. per second and 0.1 p.u. per second, correspondingly. In contrast, the parameters of inertia emulator of the 'BESS 23' are considered to be similar to WTs and PVs, however, its maximum reserve power is assumed to be 1 p.u and it can be increased by 2 p.u. per second. The droop coefficient of all units are 5%, however, this is selected as 0.05% for the BESS unit.

According to Figure 6-22 to Figure 6-24, it is clearly observed that the COI frequency criteria like RoCoF and frequency nadir are significantly aggravated in WTPV 60% I compared to WTPV 00% due to considerable decrement of system inertial power. However, steady-state frequency deviation is identical. This is because that the inertia drop in WTPV 60% results in steady-state frequency deviation increment following the first few seconds of disturbance occurrence so that the SGs can generate much more power and make the frequency closer to that of the WTPV 00% scenario.

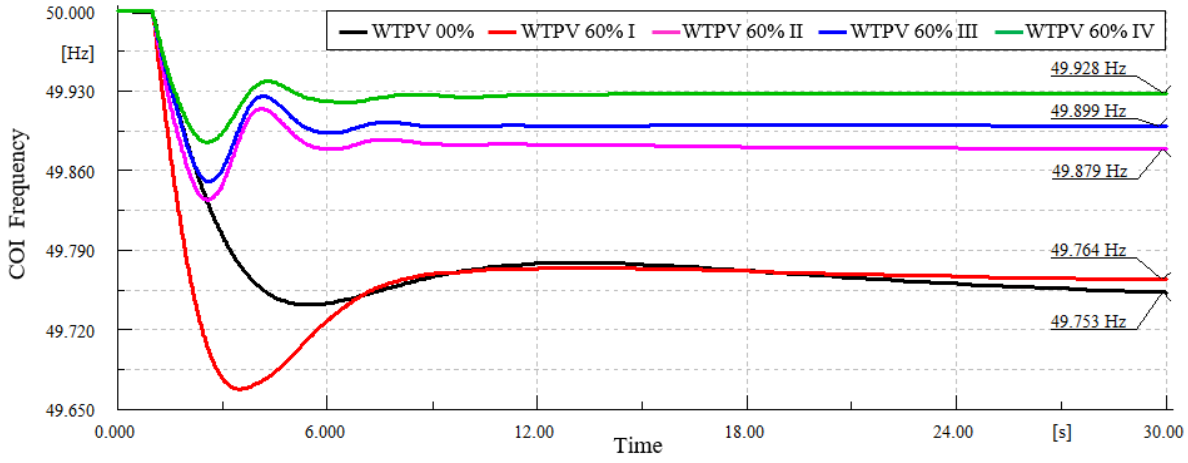

Figure 6-22: Frequency response with loss of 1700 MW generation in middle of network.

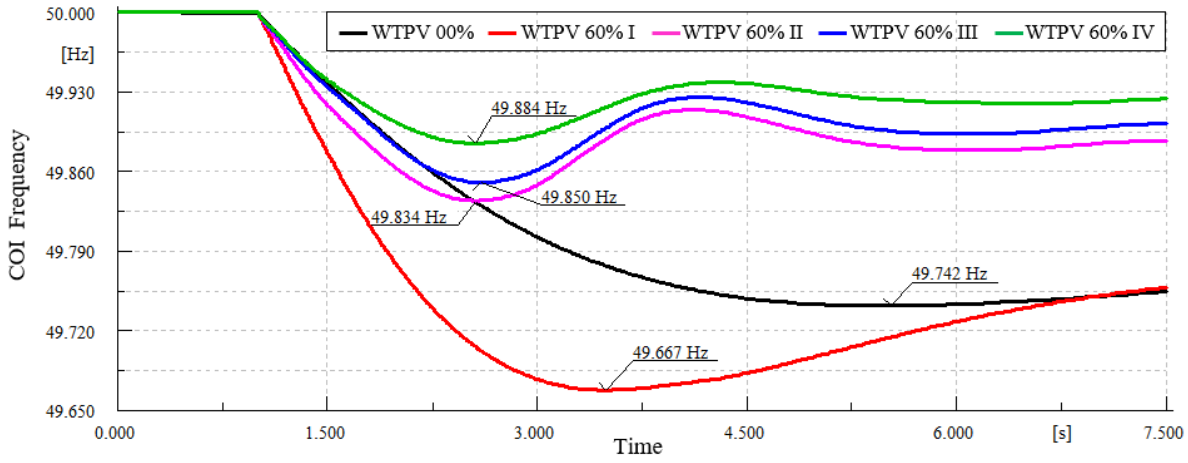

Figure 6-23: Frequency nadir with loss of 1700 MW generation in middle of network (Zone 23).

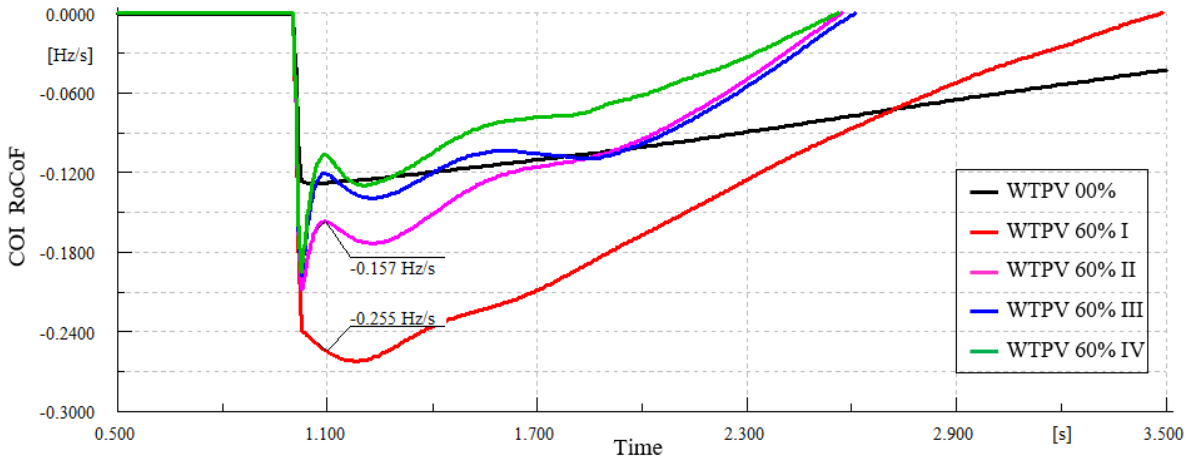

Figure 6-24: RoCoF deviations with loss of 1700 MW generation in middle of network.

6.6.2.2. Effect of BESS Droop on Frequency Response of 36-Zone GB Network

In this subsection, the influence of droop parameter (*R*) of the Primary Controller of the 'BESS 23' on GB system frequency response is analysed. In this context, the results of four aforementioned scenarios following loss of biomass unit located in zone 23 are shown in Figure 6-25 to Figure 6-27. The first scenario highlighted with blue traces is identical to WTPV 60% III in previous section. In this scenario, all SGs, WTs and PVs have primary frequency support. It is noteworthy that selection an infinite droop for the BESS means it is deactivated. The fourth scenario highlighted with green traces is identical to WTPV 60% IV in previous section in which the droop amount of the 'BESS 23' is 0.05% . The third scenario is highlighted with black traces is similar to fourth scenario, except that the droop parameter for the 'BESS 23' is set to 0.5%. Finally, in second scenario which is highlighted by red traces, is similar to third scenario except that the droop parameter of the 'BESS 23' is considered to be 5%. As can be seen from simulation results, the network frequency is just slightly changed if the droop parameter of the 'BESS 23' is equal to other units, compared to when it is deactivated. This change is, as a result of increased primary frequency support of network with the 'BESS 23' installation, in order to make the system frequency closer to its nominal one. In other hand, in third scenario where the droop parameter of the BESS 23 is one-tenth of other units, the power output of this storage unit is increased from 0.04 p.u. to 0.34 p.u. This leads to 10% and 5% enhancement of steady-state frequency deviation and frequency nadir respectively with respect to second scenario. Finally, while the droop parameter of the BESS 23 is considered to be one-hundredth of other units in fourth scenario, about 30% of generation lost is supplied by this energy storage unit. This results in 21% and 18% improvement of steady-state frequency deviation and frequency nadir respectively in comparison of third scenario.

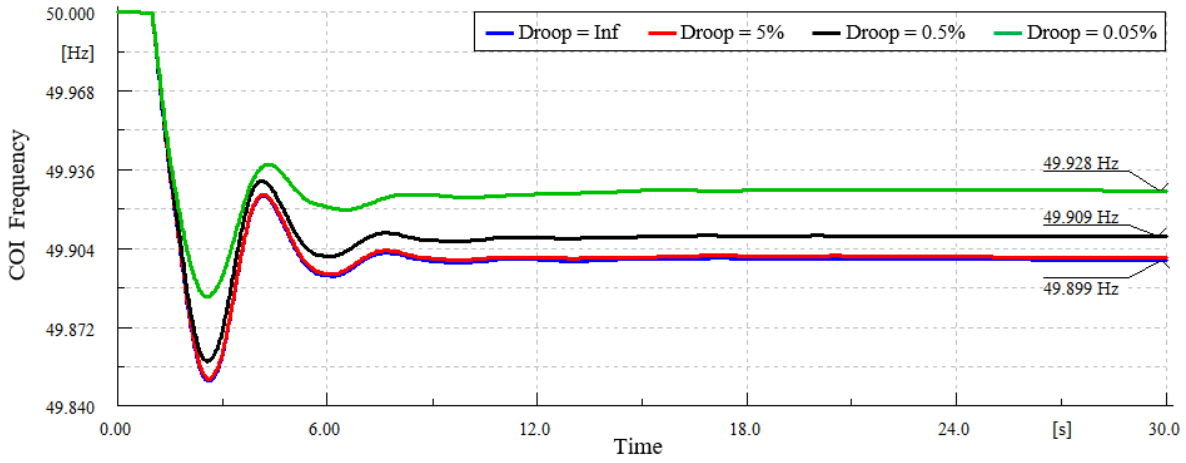

Figure 6-25: Frequency response with loss of 1700 MW generation in middle of network for different BESS droop.

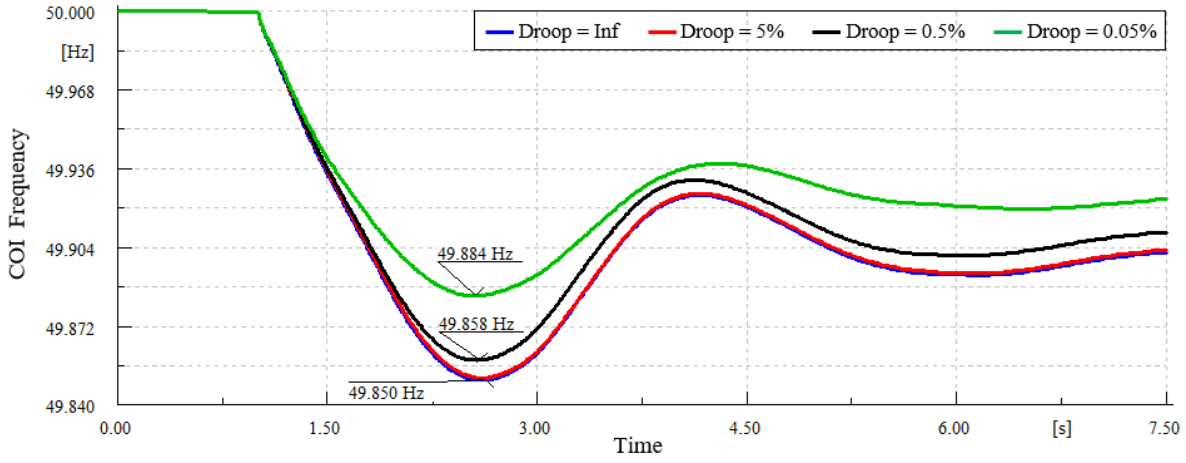

Figure 6-26: Frequency nadir with loss of 1700 MW generation in middle of network for different BESS droop.

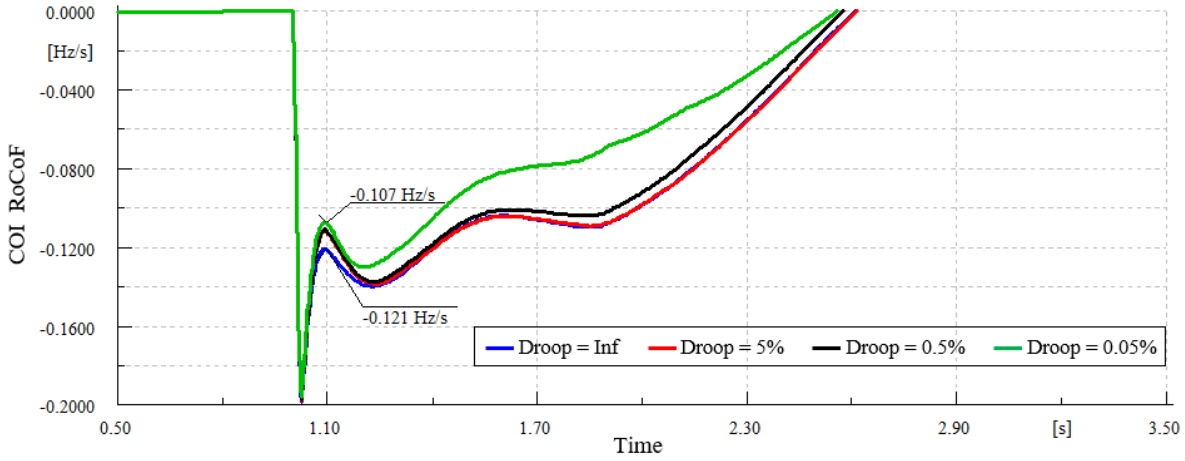

Figure 6-27: RoCoF deviations with loss of 1700 MW generation in middle of network for different BESS droop.

6.6.3. Executive Summary of Deploying BES in GB System

In this chapter, the dynamic performance of the proposed BESS system is investigated through 36-zone GB system frequency response. According to system studies in different scenarios, the WT and PV integration influences are analysed for system frequency response following the large power contingency in the middle part of network. It is observed that the BESS system with reserve and inertial frequency support capabilities can enhance frequency stability criteria like RoCoF, frequency nadir and steady-state frequency deviation. However, this enhancement is proportional to the ratio of the BESS nominal power and power disturbance size. In addition, the primary frequency support burden on conventional units and or WTs and PVs is mitigated accordingly.

6.7. References

[1] FERC Order No. 819: Third-Party Provision of Primary Frequency Response Service. (2015). [Online]. Available: https://www.ferc.gov/ whats-new/commmeet/2015/111915/E-1.pdf

[2] IEC White Paper, "Grid integration of large-capacity renewable energy sources and use of large-capacity electrical energy storage," Int. Electrotech. Comm., Geneva, Switzerland, Tech. Rep., 2012.

[3] J. Zhao, X. Lyu, Y. Fu, X. Hu, and F. Li, "Coordinated microgrid frequency regulation based on DFIG variable coefficient using virtual inertia and primary frequency control," IEEE Trans. Energy Conver., vol. 31, no. 3, pp. 833-845, Sep. 2016.

[4] J. Van de Vyver, J. D. De Kooning, B. Meersman, L. Vandevelde, T. L. Vandoorn, "Droop control as an alternative inertial response strategy for the synthetic inertia on wind turbines," IEEE Trans. Power Syst., vol. 31, no. 2, pp. 1129-1138, Mar. 2016.

[5] H. Ye, W. Pei, and Z. Qi, "Analytical modeling of inertial and droop responses from a wind farm for short-term frequency regulation in power systems," IEEE Trans. Power Syst., vol. 31, no. 5, pp. 3414-3423, Sep. 2016.

[6] S. I. Nanou, G. N. Patsakis, and S. A. Papathanassiou, "Assessment of communication-independent grid code compatibility solutions for VSC–HVDC connected offshore wind farms," Electric Power Syst. Res., vol. 121, pp. 38-51, Apr. 2015.

[7] M. F. Arani and E. F. El-Saadany, "Implementing virtual inertia in DFIG-based wind power generation," IEEE Trans. Power Syst., vol. 28, no. 2, pp. 1373-1384, May 2013.

[8] G. Delille, B. Francois, and G. Malarange, “Dynamic frequency control support by energy storage to reduce the impact of wind and solar generation on isolated power system's inertia,” IEEE Trans. Sustain. Energy, vol. 3, no. 4, pp. 931-939, Oct. 2012.
[9] M. Datta, T. Senjyu, A. Yona, T. Funabashi, and C. H. Kim, “A frequency-control approach by photovoltaic generator in a PV–diesel hybrid power system,” IEEE Trans. Energy Convers., vol. 26, no. 2, pp. 559-571, Jun. 2011.
[10] N. Kakimoto, S. Takayama, H. Satoh, and K. Nakamura, “Power modulation of photovoltaic generator for frequency control of power system,” IEEE Trans. Energy Convers., vol. 24, no. 4, pp. 943-949, Dec. 2009.
[11] V. Knap, S. K. Chaudhary, D. I. Stroe, M. Swierczynski, B. I. Craciun, R. Teodorescu, “Sizing of an energy storage system for grid inertial response and primary frequency reserve,” IEEE Trans. Power Syst., vol. 31, no. 5, pp. 3447-3456, Sep. 2016.
[12] P.-K. Keung, P. Li, H. Banakar, and B. T. Ooi, “Kinetic energy of wind-turbine generators for system frequency support,” IEEE Trans. Power Syst., vol. 24, no. 1, pp. 279–287, Feb. 2009.
[13] R. G. De Almeida and J. A. Peças Lopes, “Participation of doubly fed induction wind generators in system frequency regulation,” IEEE Trans. Power Syst., vol. 22, no. 3, pp. 944-950, Aug. 2007.
[14] J. Driesen and K. Visscher, “Virtual synchronous generators,” in Proc. IEEE PES General Meeting, Pittsburgh, PA, Jul. 2008.
[15] P. Mercier, R. Cherkaoui, and A. Oudalov, "Optimizing a Battery Energy Storage System for Frequency Control Application in an Isolated Power System," IEEE Trans. Power Syst., vol. 24, no. 3, pp. 1469-1477, 2009.
[16] M. Swierczynski, D. I. Stroe, A. I. Stan, R. Teodorescu, and D. U. Sauer, “Selection and performance-degradation modeling of LiMO2/Li4Ti5O12 and LiFePO4/C battery cells as suitable energy storage systems for grid integration with wind power plants: An example for the primary frequency regulation service,” IEEE Trans. Sustain. Energy, vol. 5, no. 1, pp. 90-101, Jan. 2014.
[17] B. Lian, A. Sims, D. Yu, C. Wang, and R. W. Dunn, “Optimizing LiFePO4 battery energy storage systems for frequency response in the UK system,” IEEE Trans. Sustain Energy, vol. 8, no. 1, pp. 385-394, Jan., 2017.
[18] X. Tang, X. Hu, N. Li, W. Deng, and G. Zhang, “A novel frequency and voltage control method for islanded microgrid based on multienergy storages,” IEEE Trans. Smart Grid., vol. 7, no. 1, pp. 410-419, Jan. 2016.
[19] Y. Mu, J. Wu, J. Ekanayake, N. Jenkins, and H. Jia, “Primary frequency response from electric vehicles in the Great Britain power system, IEEE Trans. Smart Grid, vol. 4, no. 2, pp. 1142-1150, Jun. 2013.
[20] M. R. V. Moghadam, R. Zhang, and R. T. Ma, “Distributed frequency control via randomized response of electric vehicles in power grid,” IEEE Trans. Sustain. Energy, vol. 7, no. 1, pp. 312-324, Nov. 2016.
[21] S. Chen, T. Zhang, H. B. Gooi, R. D. Masiello, and W. Katzenstein, “Penetration rate and effectiveness studies of aggregated BESS for frequency regulation,” IEEE Trans. Smart Grid, vol. 7, no. 1, pp. 167-177, Jan. 2016.
[22] FERC Order No. 819: Third-Party Provision of Primary Frequency Response Service. (2015). [Online]. Available: https://www.ferc.gov/ whats-new/commmeet/2015/111915/E-1.pdf
[23] IEC White Paper, “Grid integration of large-capacity renewable energy sources and use of large-capacity electrical energy storage,” Int. Electrotech. Comm., Geneva, Switzerland, Tech. Rep., 2012.
[24] P. Mercier, R. Cherkaoui, and A. Oudalov, "Optimizing a Battery Energy Storage System for Frequency Control Application in an Isolated Power System," IEEE Trans. Power Syst., vol. 24, no. 3, pp. 1469-1477, 2009.
[25] Office of Electricity Delivery & Energy Reliability. (2015, Oct.). DOE global energy storage database. [Online]. Available: http://www.energystorageexchange.org
[26] M. Swierczynski, D. I. Stroe, A. I. Stan, R. Teodorescu, and D. U. Sauer, “Selection and performance-degradation modeling of LiMO2/Li4Ti5O12 and LiFePO4/C battery cells as suitable energy storage systems for grid integration with wind power plants: An example for the primary frequency regulation service,” IEEE Trans. Sustain. Energy, vol. 5, no. 1, pp. 90–101, Jan. 2014.

[27] A. Shibata, S. Kanji et al., "Development of Vanadium Redox Flow Battery for Photovoltaic Generation System", Conference Record of the Twenty-Fourth IEEE Photovoltaic Specialists Conference, Volume: 1, Page(s): 950-953, December 1994.
[28] S. Buller, M. Thele et al. "Impedance-Based Simulation Models of Supercapacitors and LiIon Batteries for Power Electronic Applications", IEEE Transactions on Industry Applications, Volume: 41, Number: 3, Page(s): 742-747, May 2005.
[29] M. Gatrell and N. Gupta, "Developing a simple flow battery model - Initial concepts", Electricity Storage Systems Project, National Research Council Canada (NRC) document.
[30] Chahwan, J., C. Abbey, and G. Joos. "VRB modelling for the study of output terminal voltages, internal losses and performance." Electrical Power Conference, 2007. EPC 2007. IEEE Canada. IEEE, 2007.

7. Smart Induction Motor Variable Frequency Drive Systems for Frequency Regulation

A smart induction motor variable frequency drive system for studying its short-term dynamic response to a system frequency deviation is proposed and developed. In the chapter, the concentration is on describing the main component of the smart induction motor and its relevant equations. Available inertia and droop responses from the proposed smart induction motor to help supporting the primary frequency control in power system networks are also analytically investigated. Then the model is utilised in conjunction with a simple but practical two-area Klein-Rogers-Kundur (KRK) power system and 36-Zone GB system to study the impact of it on frequency control by time domain simulation tool in DIgSILENT PowerFactory software.

7.1. Literature Review

Renewable energy sources (RESs) have been extensively developed in many areas in last decades due to environmental and energy security risks, however, the system inertia is decreased and frequency response imposes a new challenge for power system operators to maintain power quality. The inertial response (IR) and droop based primary frequency response (PFR) using available spinning reserve power are inherently deployed in conventional power plants (CPPs) to restore sudden frequency deviations. However, power converter interfaces decouple the network frequency from the rotational part of wind energy conversion systems (WECs). In addition, the photovoltaic (PV) units have static dc generators. Thus, these generating units, by themselves, neither obtain the IR nor participate in PFR mechanism [1].

WECSs and PVs are commonly operated in maximal power point tracking (MPPT) level. Several methodologies for providing PFR and or IR from these power plants are proposed in [2], [3]. However, the MPPT can't be achieved by following these approaches that is extremely unattractive [4]. Moreover, deployment of momentary increase in the output power of WECS for the sake of IR results in rotor speed decrement and operating point variation. Furthermore, it may lead to a second frequency dip once the rotor speed is recovering [5] as well as grid instability [6]. Battery energy storage system (BESS) is another solution to meet the emergent challenges due to its fast ramp up/down rate and high efficiency [7]. PFR has been studied to be the most beneficial ancillary service employing BESSs in Danish electricity market [8], however, the extensive range installation of BESS is limited by its high capital costs. Whilst the vehicle-to-grid and grid-to-vehicle are proposing by electric vehicles to support system frequency response [9]-[11], their fleets are currently pretty small. It is to be noted that the BESS and electric vehicles can also provide a suitable IR [4], [12] and PFR [13], [14]. These solutions could be economically more feasible than the RESs curtailment or load shedding [15].

There is also a growing motivation for loads to participate in system frequency regulation under the concept of demand response (DR) or demand side management (DSM) [16]-[20]. DR is usually deployed by operation management of delay tolerant loads or over direct on/off thermostatic loads control such as freezers and refrigerators [21], [22] or load scheduling on the basis of market price signals [23]. Most of the traditional DR frameworks except thermostatic loads are designed for peak load shifting and shaving. In other hand, albeit the direct on/off thermostatic loads control mitigate the average consumed power therewith, system frequency response in shorter time intervals, they cannot be implemented in other load types like large motors, lighting, and etc. which the smart loads (SLs) can be worthwhile [24]. A power converter interface is usually used to decouple the SL from the supply or grid to permit the voltage/frequency across it to be handled over a broader range to develop short-term reserve power based on their dependency to voltage (for static loads) or frequency (for motor loads) [24].

The SLs based series compensator or electric spring and its dynamic modelling and control are derived in [25], [26]. The distributed voltage control potential of SLs is compared with STATCOM in [27]. The superiority of SLs in PFR considering just a MV/LV network segment is investigated in [17]. Over the last decades, a vast majority of researchers have focused on induction motor drive systems [28], while a little attention has been paid to the smart induction motor [1], [24]. In [1], the concept of other types of static smart loads is generalized and also the drive connected motor load is also implemented. The motor SL proposed in [1] is an induction motor variable frequency drive (VFD) system with a modified speed controller. In this structure, the measured

deviation in grid frequency and rate of change of frequency (RoCoF) is deployed to change the supply frequency reference for the motor so that the motor speed and its consumption power are mitigated following the abrupt frequency dropt. Whilst the control block for primary frequency support apparently emulates the governor action of synchronous generator and inertial response of direct on line (DOL) induction motors, there are many inconsistencies in the proposed model. For instance, one of the outputs of this model is inverter reference frequency instead of reference power. Another shortcoming of the proposed structure in [1] is that motor inertial power is not suitably emulated. Instead of RoCoF change, the grid frequency variation should be directly added to the inverter reference frequency. One of the main cons of smart motor load proposed in [1] is that the inertia load is neglected. Consequently, the rate of change of reserve rotor speed is selected to be the huge value of 0.4 p.u. per sec. However, the load inertia is generally ten times of motor shaft, it is impossible to ignore it from induction motor VFD drive.

In order to overcome the above noticed shortages, a new speed controller is derived in this chapter for smart induction motor. In this architecture, the reserve rotor speed of primary controller is calculated based on grid frequency changes to be added to reference rotor speed. After which, this signal us updated by multiplying in a drop gain. The output signal is passed through a low pass filter (LPF) and a rate limiter to determine reserve power. The reserve rotor speed signal is calculated using this reserve power and the rotor speed before the frequency excursion. This reserve rotor speed is negative and is subtracted from rotor speed to specify the reduced amount of motor consumption power. However, it is to be noted that the rate of change of reserve rotor speed should be imposed by a rate limiter. This rate should be cleared according to motor active power and load inertia. Moreover, an inertia emulator is considered to provide IR. In this structure, there is only one low pass filter in inertia emulator to remove high frequency oscillation of frequency signal not RoCoF.

This chapter tries to discuss and illustrate the proposed smart induction motor variable frequency drive system in DIgSILENT PowerFactory. Developing the mathematical model of the smart induction motor and its modelling derived in DIgSILENT simulation language (DSL) and DIgSILENT programming language (DPL) for power system frequency studies are the main aims of this chapter.

7.2. Formulation and Development of Smart Induction Motor Variable Frequency Drive Systems

The open loop speed control of an induction motor by constant volt-per-hertz strategy is the most popular method of speed control drive in industry because of its simplicity and cost effectiveness [29], [30]. This drive system has two main types, the passive front-end (PFE) and the active front-end (AFE) VFD systems. Figure 7-1 illustrates a typical configuration for the induction motor passive front-end VFD system. A 6-pulse diode rectifier is commonly employed as a front end in this drive systems. In the other hand, an active inverter supplies the variable frequency voltage to the induction motor that is needed to take it to the required speed. The DC link of the PFE-VFD systems is composed of a DC capacitor and a DC inductor. There is no voltage controller to regulate the DC link voltage in these simple drive systems. Although, a PFE-VFD system is a simple and cost effective solution for most industrial applications, there is no energy reversibility capability in regeneration mode and a dynamic braking chopper is used in its DC link to dissipate regeneration energy. Also, the passive rectifier creates harmonic currents in the power grid.

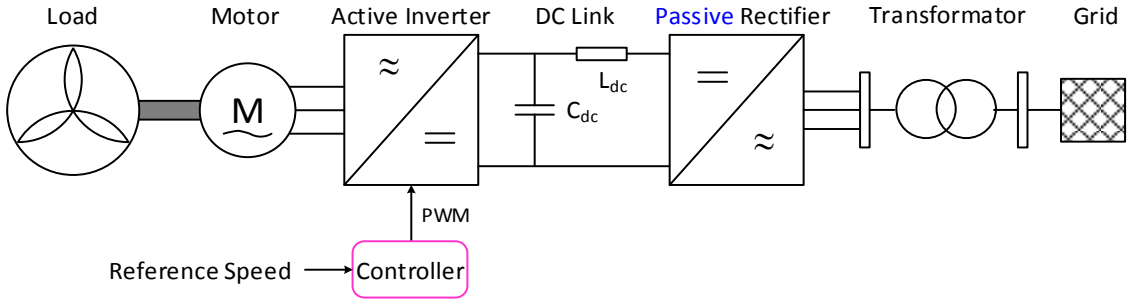

Figure 7-1: Induction motor passive front-end variable frequency drive system.

For applications with stringent harmonic requirements or with energy reversibility capability, an active front-end VFD system can be used. A typical configuration for this drive system is shown in Figure 7-2. Its front-end rectifier is a bi-directional converter composed of controllable switches. The active rectifier regulates amplitude of the DC link voltage by controlling drawn power from the power grid. Although, the AFE-VFD system is more expensive than the PFE-VFD system, it has energy reversibility capability and considerable energy saving can be obtained when this drive is adopted.

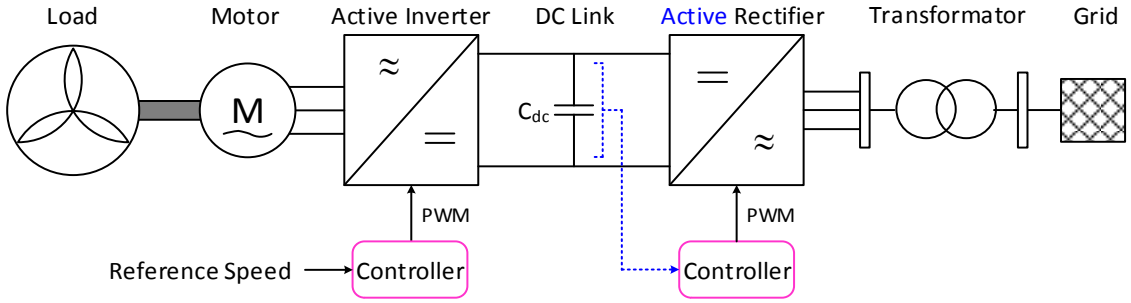

Figure 7-2: Induction motor active front-end variable frequency drive system.

7.2.1. The Induction Motor Modelling

The induction motor is main component of a variable speed drive system. In this subsection, the modelling procedure of a three phase squirrel cage induction motor is described in details. The equivalent circuit for steady-state operation of an induction motor is shown in Figure 7-3. This circuit is regardless of the operation frequency and it is suitable for variable frequency drive applications [29].

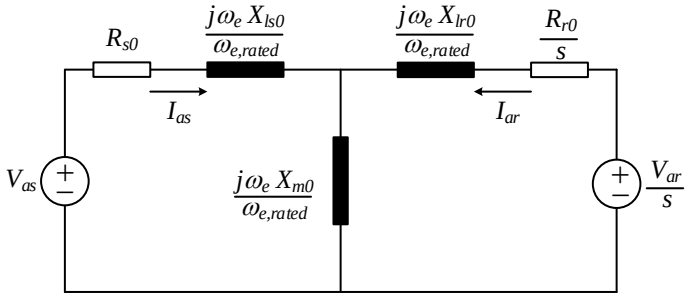

Figure 7-3: Equivalent circuit for steady-state operation of an induction motor [29].

where the slip s is defined as

$$s = \frac{\omega_e - \omega_r}{\omega_e} \tag{7.1}$$

The angular frequencies and impedances are in radians per second and ohm respectively, in equivalent circuit shown in Figure 7-3. The subscript zero indicates given parameter is pertinent to rated frequency and voltage operation. Using this circuit steady-state electromagnetic torque can be calculated as

$$T_e = 3\left(\frac{P}{2}\right)\left(\frac{X_{m0}^2}{\omega_{r,rated}}\right)\mathrm{Re}\left[jI_{as}^* I_{ar}\right] \tag{7.2}$$

where I_{as}^* is the conjugate of I_{as}.

For a squirrel cage induction motor, V_{ar} is zero. With this assumption, the steady-state electromagnetic torque generated by an induction motor can be expressed as

$$T_e = \frac{3\left(\frac{P}{2}\right)\left(\frac{\omega_e}{\omega_{r,rated}}\right)\left(\frac{X_{m0}^2}{\omega_{r,rated}}\right)R_{r0}sV_{as}^2}{\left[R_{s0}R_{r0} + s\left(\frac{\omega_e}{\omega_{r,rated}}\right)^2\left(X_{m0}^2 - X_{ss0}X_{rr0}\right)\right]^2 + \left(\frac{\omega_e}{\omega_{r,rated}}\right)^2\left[R_{r0}X_{ss0} + sR_{s0}X_{rr0}\right]^2} \tag{7.3}$$

Where P is number of poles of motor and

$$X_{ss0} = X_{ls0} + X_{m0}, \quad X_{rr0} = X_{lr0} + X_{m0} \tag{7.4}$$

The torque in (7.3) is in N.M. In per unit, (3) becomes

$$T_e = \frac{\omega_e X_{m,pu}^2 R_{r,pu} sV_{as,pu}^2}{\left[R_{s,pu}R_{r,pu} + s\omega_e^2\left(X_{m,pu}^2 - X_{ss,pu}X_{rr,pu}\right)\right]^2 + \omega_e^2\left[R_{r,pu}X_{ss,pu} + sR_{s,pu}X_{rr,pu}\right]^2} \tag{7.5}$$

Note that ω_e is in per unit, in (7.5).

In order to simulate dynamic behavior of induction motor in time-domain, it is quite comment to deploy the synchronous reference farm based equations. The current or linkage flux can be considered as state variables. As the number of derivative operators as per each relation for flux linkage case is half of the current one, thus, they are selected as state variable in this chapter. With the assumption, the q-axis equations can be written as follows:

$$\begin{aligned}
\frac{d}{dt}\psi_{qs} &= \omega_{e,rated}\left(V_{qs} - \omega_e\psi_{ds} - \frac{R_{s,pu}}{X_{ls,pu}}\left(\psi_{qs} - \psi_{mq}\right)\right) \\
\frac{d}{dt}\psi_{qr} &= \omega_{e,rated}\left(V_{qr} - (\omega_e - \omega_r)\psi_{ds} - \frac{R_{r,pu}}{X_{lr,pu}}\left(\psi_{qr} - \psi_{mq}\right)\right) \\
\psi_{mq} &= X_{M,pu}\left(\frac{\psi_{qs}}{X_{ls,pu}} + \frac{\psi_{qr}}{X_{lr,pu}}\right) \\
I_{qs} &= \frac{1}{X_{ls,pu}}\left(\psi_{qs,pu} - \psi_{mq}\right), \quad I_{qr} = \frac{1}{X_{lr,pu}}\left(\psi_{qr} - \psi_{mq}\right)
\end{aligned} \tag{7.6}$$

And the d-axis equations can be expressed as

$$\begin{aligned}
\frac{d}{dt}\psi_{ds} &= \omega_{e,rated}\left(V_{ds} + \omega_e\psi_{qs} - \frac{R_{s,pu}}{X_{ls,pu}}\left(\psi_{ds} - \psi_{md}\right)\right) \\
\frac{d}{dt}\psi_{dr} &= \omega_{e,rated}\left(V_{dr} + (\omega_e - \omega_r)\psi_{qs} - \frac{R_{r,pu}}{X_{lr,pu}}\left(\psi_{dr} - \psi_{md}\right)\right) \\
\psi_{md} &= X_{M,pu}\left(\frac{\psi_{ds}}{X_{ls,pu}} + \frac{\psi_{dr}}{X_{lr,pu}}\right) \\
I_{ds} &= \frac{1}{X_{ls,pu}}\left(\psi_{ds} - \psi_{md}\right), \quad I_{dr} = \frac{1}{X_{lr,pu}}\left(\psi_{dr} - \psi_{md}\right)
\end{aligned} \tag{7.7}$$

Where resistances and reactances in per unit are

$$R_{s,pu}=\frac{R_{s0}}{Z_{base}},\qquad R_{r,pu}=\frac{R_{r0}}{Z_{base}},\qquad X_{ls,pu}=\frac{X_{ls0}}{Z_{base}},\qquad X_{lr,pu}=\frac{X_{lr0}}{Z_{base}},$$
$$X_{m,pu}=\frac{X_{m0}}{Z_{base}},\qquad X_{M,pu}=\left(\frac{1}{X_{ls,pu}}+\frac{1}{X_{lr,pu}}+\frac{1}{X_{m,pu}}\right)^{-1} \tag{7.8}$$

The base impedance Z_{base} is for an arbitrary operation frequency. In order to determine this parameter, the base quantities pertinent to rated operation frequency and voltage are defined as

$$V_{base,0}=\frac{V_{rated,0}}{\sqrt{3}},\qquad V_{dq,base,0}=\sqrt{2}\ V_{base,0}$$
$$I_{dq,base,0}=\frac{P_{rated}\times 746}{1.5\ V_{dq,base,0}},\qquad Z_{base,0}=\frac{3\ V_{base,0}^2}{P_{rated}\times 746} \tag{7.9}$$

Then the base quantities for an arbitrary frequency can be calculated as follow.

$$V_{base}=V_{base,0},\qquad V_{dq,base}=\sqrt{2}\ V_{base}$$
$$I_{dq,base}=\frac{P_{rated}\times 746}{1.5\ V_{dq,base}},\qquad Z_{base}=\frac{3\ V_{base}^2}{P_{rated}\times 746} \tag{7.10}$$

The equivalent circuits for an induction motor in synchronous reference frame related to equations (7.6) and (7.7) is shown in Figure 7-4.

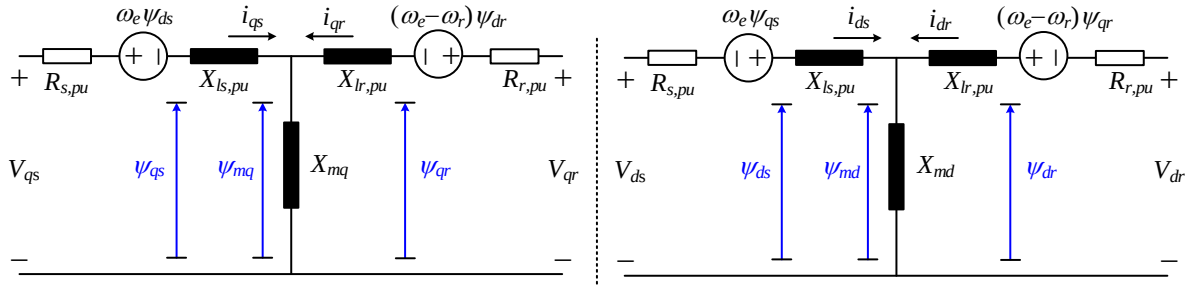

Figure 7-4: Synchronous reference frame equivalent circuits for an induction motor.

The initial conditions of the state and output variables must be calculated in a time domain simulation. To this end, the derivatives in equations (7.6) and (7.7) are set to zero. By applying this rule to mentioned equations, the initial conditions of the flux linkages and the currents can be calculated as

$$\psi_{qs}^{init}=\frac{X_{ls}V_{qs}^{init}}{R_s-K_8R_s+K_{12}\omega_eX_{ls}-K_{12}K_9R_s}$$
$$\psi_{ds}^{init}=K_{12}\psi_{qs}^{init}$$
$$\psi_{mq}^{init}=K_8\psi_{qs}^{init}+K_9\psi_{ds}^{init}$$
$$\psi_{md}^{init}=K_{10}\psi_{qs}^{init}+K_{11}\psi_{ds}^{init}$$
$$\psi_{qr}^{init}=\frac{1}{D_r}\left(R_r^2\psi_{mq}^{init}-sR_rX_{lr}\psi_{md}^{init}\right) \tag{7.11}$$
$$\psi_{dr}^{init}=\frac{1}{D_r}\left(sR_rX_{lr}\psi_{mq}^{init}+R_r^2\psi_{md}^{init}\right)$$
$$I_{qs}^{init}=\frac{1}{X_{ls}}\left(\psi_{qs}^{init}-\psi_{mq}^{init}\right),\qquad I_{ds}^{init}=\frac{1}{X_{ls}}\left(\psi_{ds}^{init}-\psi_{md}^{init}\right)$$
$$I_{qr}^{init}=\frac{1}{X_{lr}}\left(\psi_{qr}^{init}-\psi_{mq}^{init}\right),\qquad I_{dr}^{init}=\frac{1}{X_{lr}}\left(\psi_{dr}^{init}-\psi_{md}^{init}\right)$$

where

$$D_r = R_{r,pu}^2 + s^2 X_{lr,pu}^2, \quad K_1 = \frac{D_r X_{lr,pu} - X_M R_{r,pu}^2}{D_r X_{lr,pu}}, \quad K_2 = \frac{D_r X_{lr,pu} - X_{M,pu} R_{r,pu}^2}{s R_{r,pu} X_{lr,pu} X_{M,pu}}$$

$$K_3 = \frac{D_r}{s R_{r,pu} X_{ls,pu}} K_1, \quad K_4 = \frac{s R_{r,pu} X_{M,pu}}{D_r}, \quad K_5 = \frac{X_{M,pu}}{X_{ls,pu}}, \quad K_6 = K_2$$

$$K_7 = \frac{K_3}{K_1}, \quad K_8 = \frac{K_5 K_6}{K_4 + K_1 K_2}, \quad K_9 = \frac{K_3 K_6}{K_4 + K_1 K_2} - K_7 \tag{7.12}$$

$$K_{10} = \frac{K_5}{K_4 + K_1 K_2}, \quad K_{11} = \frac{K_3}{K_4 + K_1 K_2}, \quad K_{12} = \frac{K_{10} R_{s,pu} + \omega_e X_{ls,pu}}{R_{s,pu}\left(1 - K_{11}\right)}, \quad s = \omega_e - \omega_r$$

The electromagnetic torque in terms of synchronous reference frame variables becomes

$$T_e = \psi_{ds} I_{qs} - \psi_{qs} I_{ds} \tag{7.13}$$

Finally, the rotor speed is determined by the equation of motion as follow.

$$\frac{d}{dt}\omega_r = \frac{1}{2H}\left(T_e - T_L\right) \tag{7.14}$$

where T_L is the load torque. The H is inertia constant in seconds and its value is

$$H = \frac{1}{2}\left(\frac{J}{\mathrm{P}_{rated} \times 746}\right)\left(\frac{2}{P}\omega_{e,rated}\right)^2 \tag{7.15}$$

where J is the total moment of inertia of motor and load in $kg.m^2$. The P_{rated} is the rated mechanical power of motor in hp.

7.2.2. Scalar Speed Control of Induction Motors

The elementary constant volt-per-hertz control is simplest scalar induction motor drive system [29]. In this speed control method, based two approximations i.e. rotor speed is equal to operation electrical frequency and the magnitude of the stator flux linkage is proportional to the ratio of stator voltage to electrical frequency, the reference q-axis stator voltage is selected to be as follows:

$$V_{qs,ref} = \omega_e \tag{7.16}$$

where ω_e is the electrical frequency of applied stator voltage in per unit. Then, the base voltage will be updated based on equation (7.16) as follows:

$$V_{base} = V_{qs,ref} \; V_{base,0} \tag{7.17}$$

The steady-state characteristics of a 50 hp and a 500 hp induction motors with elementary volt-per-hertz control are shown in Figure 7-5 and Figure 7-6, respectively [29]. The motor's load assumed to be a constant torque load that its value shown with dot dashed red traces. With this load type, the 50 hp induction motor can operate with speeds larger than 0.4 per unit. However, efficiency of the motor is considerably reduced for low-speed operations. In contrast, the 500 hp induction motor can never start this load because of its starting torque is lower than that of load for whole operation electrical frequencies.

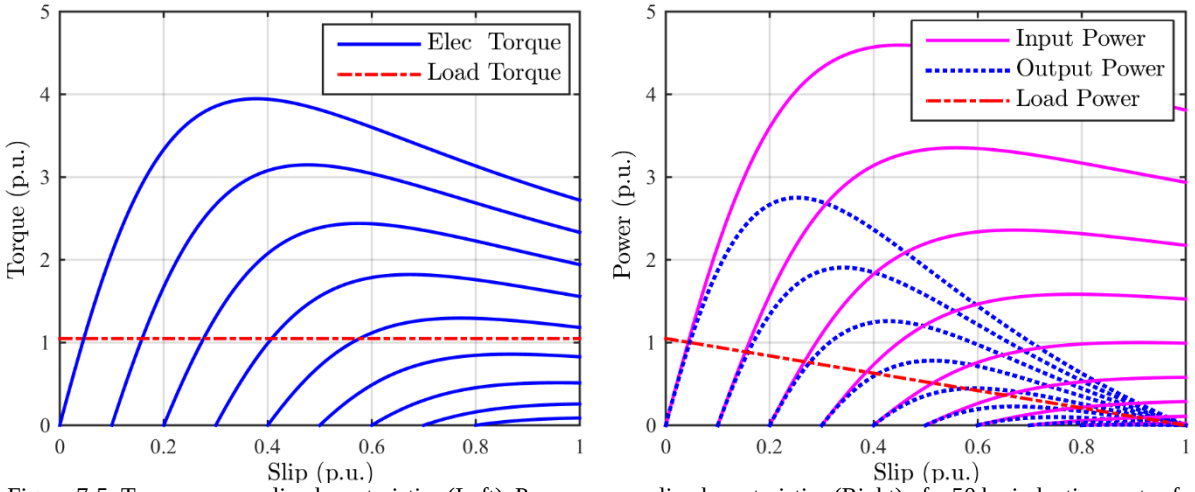

Figure 7-5: Torque versus slip characteristics (Left), Power versus slip characteristics (Right) of a 50 hp induction motor for various electrical frequencies with elementary volt-per-hertz control.

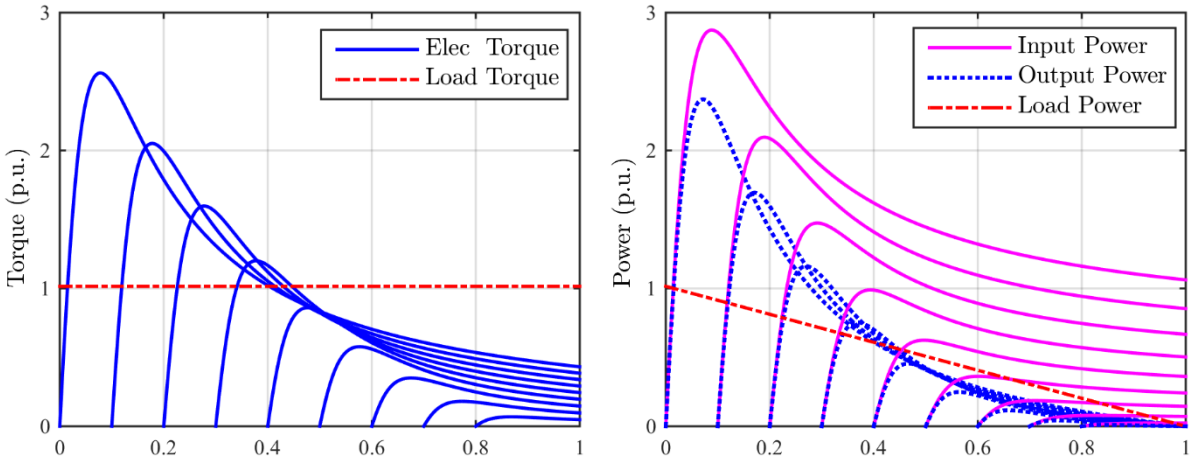

Figure 7-6: Torque versus slip characteristics (Left), Power versus slip characteristics (Right) of a 500 hp induction motor for various electrical frequencies with elementary volt-per-hertz control.

The low-speed performance of elementary volt-per-hertz speed control can be improved in a compensated volt-per-hertz speed control. This improvement is obtained by selecting the stator voltage in such a way that the slope of torque-slip characteristics at synchronous speed becomes independent of the stator electrical frequency [29]. This can be done as follows. Taking the derivative of (7.3) with respect to slip at synchronous speed for an arbitrary electrical frequency yields

$$\left.\frac{\partial T_e}{\partial s}\right|_{s=0} = \frac{K\omega_e V_{as}^2}{R_{r0}^2\left[R_{s0}^2 + \omega_e^2 X_{ss0}^2\right]} \tag{7.18}$$

where

$$K = 3\left(\frac{P}{2}\right)\left(\frac{X_{m0}^2}{\omega_{e,rated}^2}\right)R_{r0} \tag{7.19}$$

Equation (7.18) for base and an arbitrary electrical frequencies are calculated in equations (7.20) and (7.21), respectively.

$$\left.\frac{\partial T_e}{\partial s}\right|_{s=0,\ \omega_e=\omega_{e,rated}} = \frac{K\omega_{e,rated}V_{as}^2}{R_{r0}^2\left[R_{s0}^2+X_{ss0}^2\right]} \tag{7.20}$$

$$\left.\frac{\partial T_e}{\partial s}\right|_{s=0,\ \omega_e=\omega_e} = \frac{K\omega_e V_{as}^2}{R_{r0}^2\left[R_{s0}^2+\left(\frac{\omega_e}{\omega_{e,rated}}\right)^2 X_{ss0}^2\right]} \tag{7.21}$$

Setting (7.20) equal to (7.21) yields

$$V_{as} = V_{as0}\sqrt{\left(\frac{\omega_{e,rated}}{\omega_e}\right)\frac{R_{s0}^2+\left(\frac{\omega_e}{\omega_{e,rated}}\right)^2 X_{ss0}^2}{R_{s0}^2+X_{ss0}^2}} = V_{as0}\sqrt{\left(\frac{\omega_{e,rated}}{\omega_e}\right)\frac{R_{s0}^2+\omega_e^2 L_{ss0}^2}{R_{s0}^2+\omega_{e,rated}^2 L_{ss0}^2}} \tag{7.22}$$

In per unit parameters, (7.22) becomes

$$V_{qs,ref} = \sqrt{\left(\frac{1}{\omega_e}\right)\frac{R_{s0,pu}^2+\omega_e^2 X_{ss0,pu}^2}{R_{s0,pu}^2+X_{ss0,pu}^2}} \tag{7.23}$$

It is worth to mention that the ratio of the rated frequency to arbitrary frequency term in right hand side of equation (7.22) is missed in [29]. The steady-state characteristics of a 50 hp and a 500 hp induction motors with compensated volt-per-hertz speed control are shown in Figure 7-7 and Figure 7-8, respectively. It can be seen that the slope of torque-slip curves at synchronous speed is identical for all operation frequencies. Also, the reduction in the maximum torque with reduction in operation frequency is considerably more than that of elementary volt-per-hertz control. In addition, the 500 hp motor can drive the constant torque load with this compensated scalar speed control.

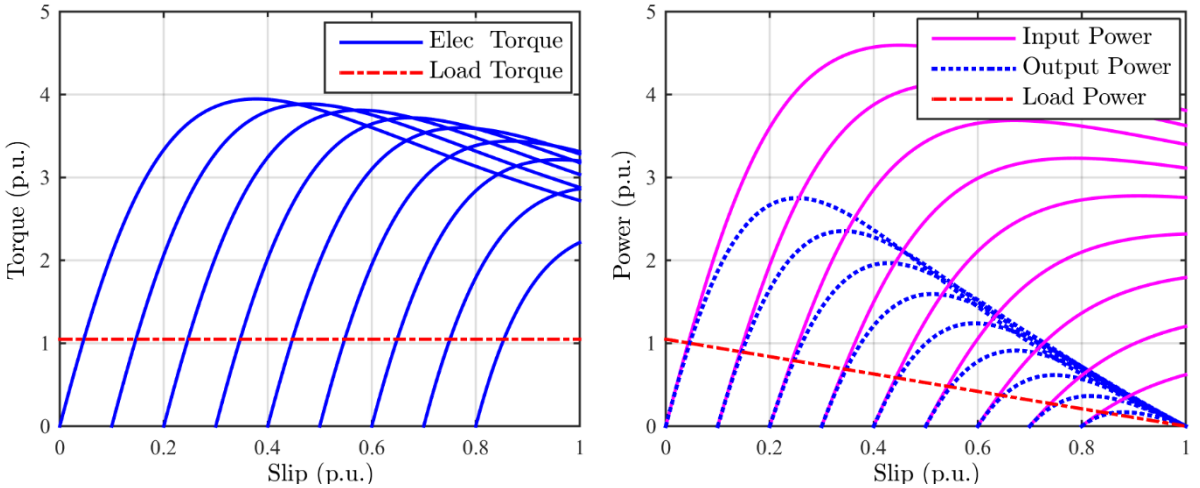

Figure 7-7: Torque versus slip characteristics (Left), Power versus slip characteristics (Right) of a 50 hp induction motor for various electrical frequencies with compensated volt-per-hertz control.

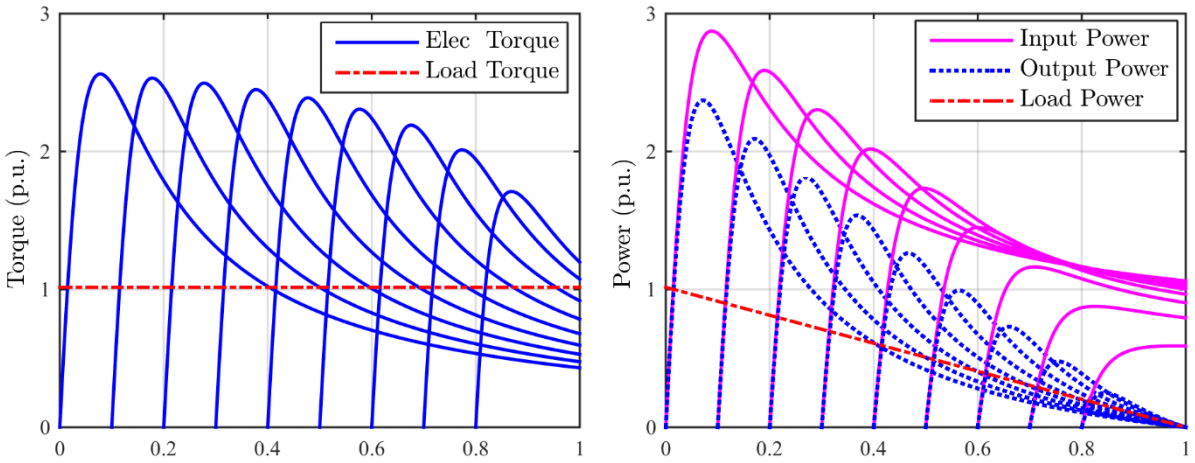

Figure 7-8: Torque versus slip characteristics (Left), Power versus slip characteristics (Right) of a 500 hp induction motor for various electrical frequencies with compensated volt-per-hertz control.

7.3. Proposed Smart Induction Motor Variable Frequency Drive Systems

Over the last decades, a vast majority of researchers have focused on induction motor drive systems, while a little attention has been paid to the smart induction motor [31]-[32]. In [32], the concept of other types of static smart loads is generalized and also the drive connected motor load is also implemented. The motor smart load proposed in [32] is an induction motor VFD system with a modified speed controller. In this structure, the measured deviation in grid frequency and rate of change of frequency (RoCoF) is deployed to change the supply frequency reference for the motor so that the motor speed and its consumption power are mitigated following the abrupt frequency dropt. Whilst the control block for primary frequency support apparently emulates the governor action of synchronous generator and inertial response of direct on line (DOL) induction motors, there are many inconsistencies in the proposed model. For instance, one of the outputs of this model is inverter reference frequency instead of reference power. Practically, the reference reserve power should be initially determined based on grid reference change and then reference rotor speed must be calculated using this reference power. Finally, the final value of inverter reference frequency i.e. f_{mot}^{*} should be computed using reference rotor speed. Additionally, the main reason of deploying PI controller in the proposed structure in Figure 5 of [32] (See Figure 7-9) is to diminish the middle stages procedures. It is to be noticed that there are no PI controller in the arcitechre of conventional governor (However, there is a PI controller in isochronous governor deployed in islanded micro-grids).

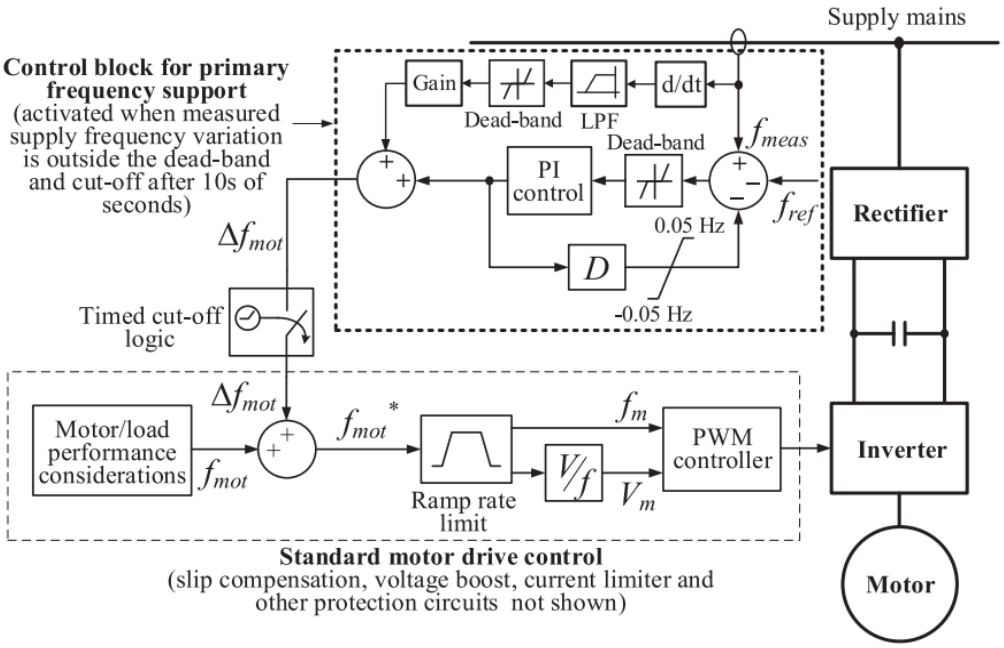

Figure 7-9: Motor type smart load with modified drive control [32].

Another shortcoming of the proposed structure is that motor inertial power is not suitably emulated. In other word, the main purpose of the derived model in [32] is to determine inverter reference frequency on the basis of abrupt grid RoCoF so that the power drawn by rectifier from the grid in response of grid frequency variations should be identical to DOL induction motors. However, instead of RoCoF change, the grid frequency variation should be directly added to the inverter reference frequency.

In order to overcome the above noticed shortages, a new speed controller is derived in this chapter for smart induction motor, as shown in Figure 7-10. In this architecture, the reserve rotor speed of primary controller block is calculated based on grid frequency changes to be added to reference rotor speed. After which, this signal is updated by multiplying in a drop gain. The output signal is passed through a low pass filter (LPF) and a rate limiter to determine reserve power. The reserve rotor speed signal is calculated using this reserve power and the rotor speed before the frequency excursion. This reserve rotor speed i.e. $\omega_{r,res}$ is negative and is subtracted from rotor speed to specify the reduced amount of motor consumption power i.e. Pres. However, it is to be noted that the rate of change of reserve rotor speed should be imposed by a rate limiter. This rate should be cleared according to motor active power and load inertia.

One of the main cons of smart motor load proposed in [32] is that the inertia load is neglected. Consequently, the rate of change of reserve rotor speed is selected to be the huge value of 0.4 p.u. per sec. However, the load inertia is generally ten times of motor shaft, it is impossible to ignore it from induction motor VFD drive. This is due to the fact that amplitude of electromagnetic torque variation and motor stator's current variation would be largely underestimated. This is investigated further in validation section. In the next stage, the reference frequency of inverter voltage is determined in the open loop speed controller using the new value of reference rotor speed. The 'Wr2We' can be considered as a coefficient with the value of one while the rotor speed error is reasonable, otherwise, its output signal can be determined using (7.24). The *'C_1'* and 'C_2' would be discrepant for different induction motors and could be specified based on their steady-state characteristics. However, they are typically more than 0.9 and less than 0.1, respectively.

$$\omega_{e,ref} = C_1 \omega_{r,ref} + C_2 \tag{7.24}$$

It is to be pointed out that the output signal of 'Wr2We' block is summed up with the output of inertial emulator. In this structure, there is only one LPF in inertia emulator to remove high frequency oscillation of frequency signal not RoCoF.

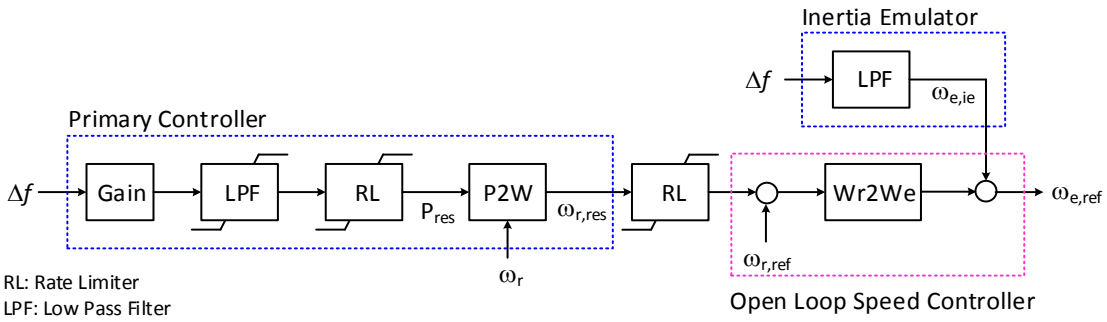

Figure 7-10: Proposed speed control in the smart induction motor variable frequency drive system.

7.4. Smart Induction Motor Modelling in DIgSILENT PowerFactory

According to the above mentioned explanations, the proposed smart induction motor systems is simulated in DIgSILENT PowerFactory so that it can be appropriate for dynamic frequency response of large scale systems and at the same time the dynamic behaviour of induction motor and power electronic converters are properly modelled. Firstly, a smart induction motor with passive front-end VFD system is addressed because of that it is commonly used in most drive applications. In the following, a smart induction motor with active front-end VFD system is modelled by applying some changes to passive front-end VFD system.

7.4.1. Smart IM PFE-VFD

The control structure of the Smart IM PFE-VFD system is shown in Figure 7-11. In this structure, the "Induction Motor" simulates an induction motor by a fifth order differential equation set. The input signals of this block are load torque, electrical frequency and stator voltage. And its output signals are rotor speed and input power of motor which is inverter power. The torque of load is determined by "Load Torque" block based on rotor speed. The "Speed Controller" is a compensated volt-per-hertz speed controller. The amplitude and frequency of inverter output voltage is determined by this speed controller based on an updated reference rotor speed. The "DC Link" block simulates a RLC circuit and calculates rectifier input power based on the inverter power. Note that there is no PowerFactory's induction motor and power converter elements in this structure and all of them are simulated using DIgSILENT Simulation Language. The main advantage of this method is that this induction motor VFD system can be integrated to power systems by the "General Load" element in PowerFactory. To this end, the rectifier power which is determined by "DC Link" block is modified by "IM2Load" block in such a way that it can be an input signal for the "General Load" element. This element is "Load" block. The "IM2Load" block in addition to convert P_{rec} in per unit to P_{ext} in MW, it can determine what portion of general load is modelled as IM VFD load type. The "Smart" term in smart IM VFD is constitute by the "PCO" and the "Inertia Emulator" blocks based on the proposed speed control shown in Figure 7-10. Finally, the frequency of power system is measured at rectifier input terminal (i.e. General Load terminal) by "PLL" measurement block. The detailed description of each block in Figure 7-11 is deferred to following subsections.

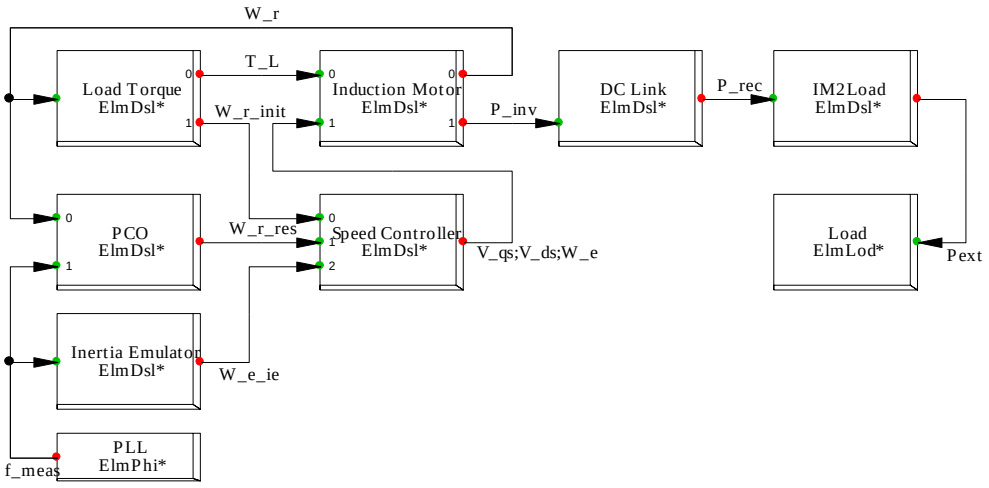

Figure 7-11: Control structure of the Smart IM PFE-VFD in DIgSILENT PowerFactory.

7.4.2. Induction Motor

The 'Induction Motor' shown in Figure 7-11, is detailed in Figure 7-12. It contains two block references named "IM Equations" and "Swing Equation". The former calculates stator and rotor currents, and electromagnetic torque using a fourth order state space model with the flux linkages as state variables based on equations (7.6) to (7.13). The rotor speed is determined in "Swing Equation" reference block based on equations (7.14) and (7.15). All variables shown in Figure 7-12 are in per unit. Note that the "P_{in}" output signal is the "P_{inv}" signal in Figure 7-11. The parameters of two studied induction motors are tabulated in Table 7-1.

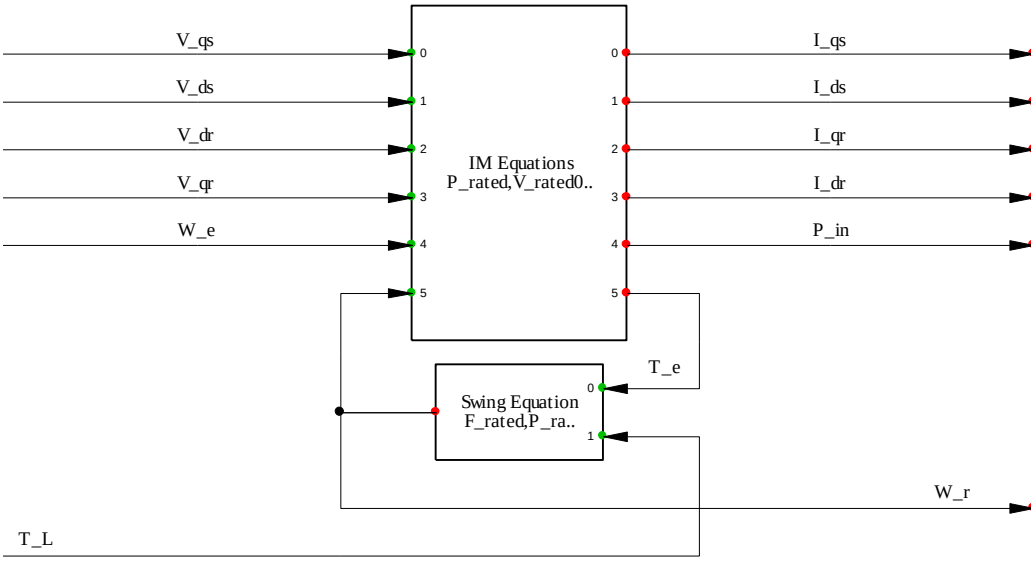

Figure 7-12: Outline of the "Induction Motor" in the Smart IM PFE-VFD in DIgSILENT PowerFactory.

Table 7-1: Parameters of the induction motors [29].

Parameter	50 hp	500 hp	Unit
Rated Line to Line Voltage	460	2300	Vrms
Rated Mechanical Power	50	500	Hp

Rated Electrical Frequency	60	60	Hz
Rated Stator Resistance	0.087	0.262	Ohm
Rated Rotor Resistance	0.228	0.187	Ohm
Rated Stator Leakage Reactance	0.302	1.206	Ohm
Rated Rotor Leakage Reactance	0.302	1.206	Ohm
Rated Magnetizing Reactance	13.08	56.02	Ohm
Number of Poles	4	4	-
Motor Moment of Inertia	1.662	11.08	kg.m2
Load Moment of Inertia*	30	700	kg.m2

* this parameter is not borrowed from [29]

7.4.3. Load Torque

The considered load in this study is a constant torque load which its value is set to the rated torque of induction motor. The outline of "Load Torque" shown in Figure 7-11, is detailed in Figure 7-13. It contains one block reference named "Torque Equation". The load torque is calculated by this block. Its equations is shown in Figure 7-14. Initially, the rated slip is calculated using S1 to S8 internal variables. Then the rated torque is calculated according to equation (7.5) with rated slip. Note that rotor speed as input signal is used only for initial rotor speed output signal that is sent to the "Speed Controller".

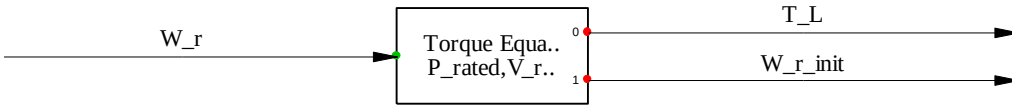

Figure 7-13: Outline of the "Load Torque" in the Smart IM PFE-VFD in DIgSILENT PowerFactory.

```
S1 = R_r0_pu * sqr(X_m0_pu)
S2 = R_r0_pu * R_s0_pu
S3 = sqr(X_m0_pu) - X_ss0_pu*X_rr0_pu
S4 = R_r0_pu * X_ss0_pu
S5 = R_s0_pu * X_rr0_pu
S6 = S1+sqr(S3)+sqr(S5)
S7 = 2*S2*S3 + 2*S4*S5 - S1
S8 = sqr(S2) + sqr(S4)

s_rated = (-S7-sqrt(sqr(S7)-4*S6*S8))/(2*S6)

T_rated = (R_r0_pu*s_rated*sqr(X_m0_pu))/
&          (sqr(R_r0_pu*R_s0_pu+s_rated*(sqr(X_m0_pu)-X_ss0_pu*X_rr0_pu)) +
&          sqr(R_r0_pu*X_ss0_pu+s_rated*R_s0_pu*X_rr0_pu))

T_L = T_rated
W_r_init = 1*W_r
```

Figure 7-14: Equations of the "Torque Equation" in the "Load Torque".

7.4.4. Speed Controller

The "Speed Controller" shown in Figure 7-11, is portrayed in Figure 7-15. This controller is a compensated volt-per-hertz speed controller and determines the amplitude and frequency of the inverter output voltage in such a way that the rotor speed tracks its reference value, i.e. the "W_r_ref" signal [29]. In the normal operation of power system, the input and output of the rate limiter block are zero, and reference rotor speed is only

determined by its initial value, i.e. the "W_r_ref_init" signal. In other hand, the reference rotor speed is updated by its reserve value in a sudden reduction of power system frequency. Then, this updated rotor speed is limited through a min-max limiter. The limiter output is used to calculate reserve electrical frequency by equation (7.24). Finally, this value is added to inertia emulator electrical frequency to determine the electrical frequency of the inverter, i.e. the output signal named "W_e". Also, the amplitude of q-axis stator voltage is calculated by equation (7.23) based on the reserve electrical frequency. The parameters of the "Speed Controller" are tabulated in Table 7-2.

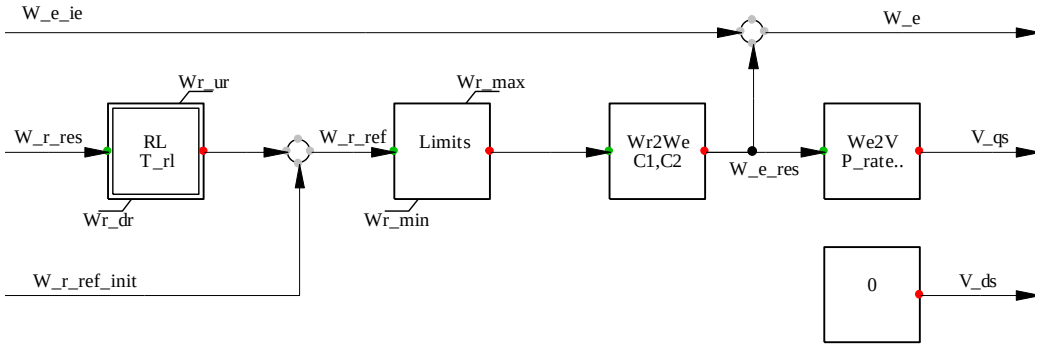

Figure 7-15: Outline of the "Speed Controller" in the Smart IM PFE-VFD in DIgSILENT PowerFactory.

Table 7-2: Parameters of the "Speed Controller" in the Smart IM PFE-VFD system.

Parameter	50 hp	500 hp	Unit
Wr_dr	-0.1	-0.04	p.u./s
Wr_ur	0.1	0.04	p.u./s
Wr_min	0	0	p.u.
Wr_max	1	1	p.u.
C1	0.9928	0.9969	-
C2	0.0520	0.0175	-

7.4.5. DC Link in PFE-VFD

The circuit located between the rectifier and the inverter is called DC link. The DC link circuit in a passive front-end VFD system is shown in Figure 7-16. In this VFD system, the DC link is a DC RLC circuit. There is no voltage controller to regulate the DC link voltage, i.e. "V_{dc}", in this type of VFD systems. A DC inductor is placed between the rectifier and the DC capacitor. This inductor can be treated such as a current source which counteracts with the DC link voltage variations. For example, if the inverter power is increased in results of an ordered increase in motor speed, then the DC link voltage will be reduced. In the following, the inductor holds a new equilibrium point between mid-point voltage, "V_{mp}", and the DC link voltage by increasing the rectifier current. In this new equilibrium point the (averaged) value of the mid-point and DC link voltages are equal. The DC resistor, "R_{dc}", accounts for ohmic losses of the inductor. It is noteworthy to mention that this RLC DC link circuit adds a complex pair eigenvalue to the system which will be unstable when DC resistor is zero.

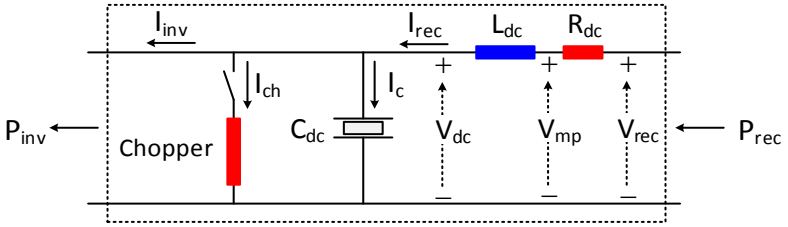

Figure 7-16: Electrical circuit of the DC link in the smart IM PFE-VFD system.

The outline of the "DC Link" in the Smart IM PFE-VFD is shown in Figure 7-17 based on Figure 7-16. In the conventional passive front-end VFD system there is no chopper circuit. This circuit is integrated to the DC link to prevent extreme increase in its voltage when the inverter current is reversed (in regeneration mode). The output signal of the "Chopper" reference block is determined by first row of equation (7.25). In other words, the inverter current will be dissipated by the chopper when it is negative. In this case, the absolute amplitude of the chopper current is equal to that of the inverter current. Therefore, the capacitor and rectifier currents will be zero. Otherwise, the value of this auxiliary signal is set to zero and then the chopper current will be zero. The dissipated energy by the chopper is calculated by two bottom rows of equation (7.25) in pu.s.

$$
\begin{aligned}
I_{ch} &= \text{select}(I_{inv} < 0,\ -I\_inv,\ 0) \\
\frac{d}{dt} x\_E_{ch} &= I_{ch} V_{dc} \\
E_{ch} &= x\_E_{ch}
\end{aligned}
\tag{7.25}
$$

The parameters of the "DC Link" in the smart IM PFE-VFD system are tabulated in Table 7-3.

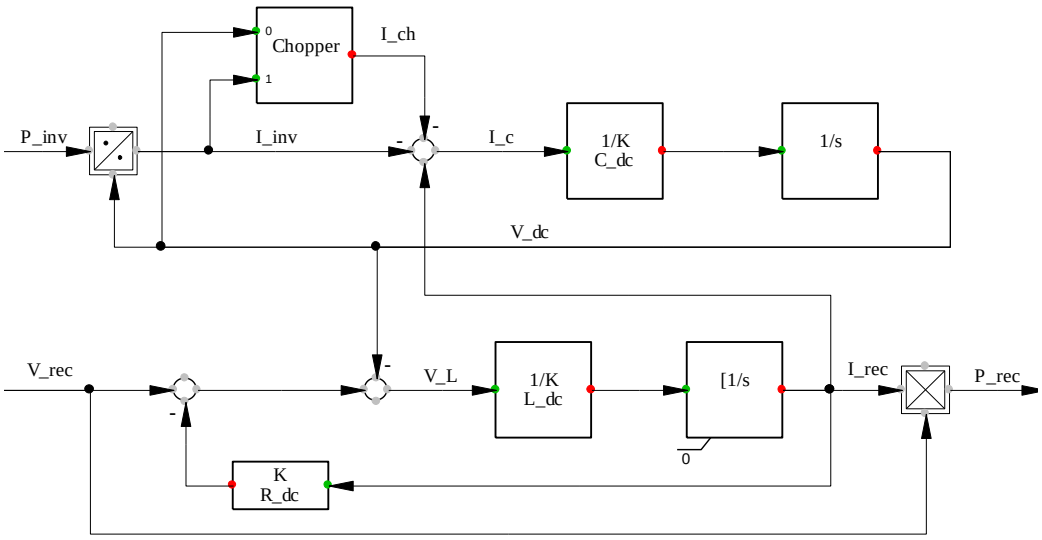

Figure 7-17: Outline of the "DC Link" in the Smart IM PFE-VFD in DIgSILENT PowerFactory.

Table 7-3: Parameters of the "DC Link" in the Smart IN PFE-VFD system.

Parameter	Value	Unit	Parameter	Value	Unit
R_dc	0.01	p.u.	C_dc	1	s
L_dc	5e□5	s			

7.4.6. IM to Load

As mentioned above, the smart induction motor VFD system is integrated to power system by a "General Load" element in PowerFactory. The active power input signal of this element must be in MW unit. The "IM2Load" block that is shown in Figure 7-18 converts the rectifier power in per unit to the load power, "P_load", in MW. The corresponding load's type is selected constant power in order to guarantee voltage variations of the load terminal do not change the ordered rectifier power ("P_rec"). Also, parameter "K" determines what portion of the corresponding load is assumed to be an induction motor type. This parameter can accept values from zero (no motor load) to one (full motor load).

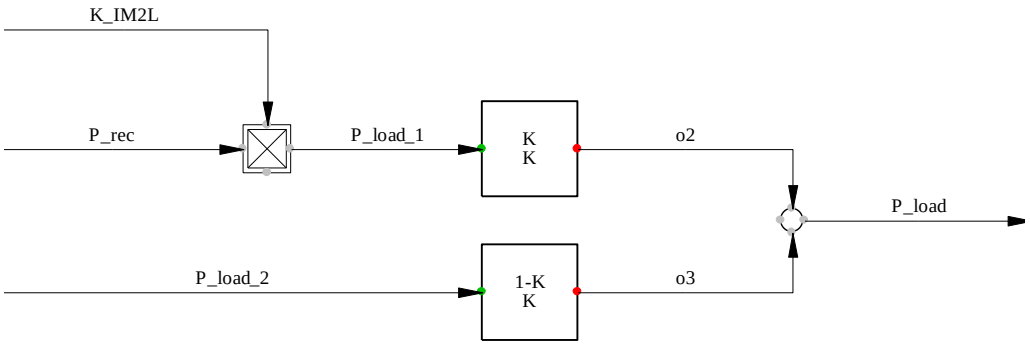

Figure 7-18: Outline of the "IM2L" in the Smart IM PFE-VFD in DIgSILENT PowerFactory.

7.4.7. Inertia Emulator

There is an important note in designing an inertia emulator for an induction motor VFD system. However, this load is interfaced by power electronic converters to power system like photovoltaic systems (PVs) or full scale wind energy conversion systems (WECSs), its inertia emulator differs with that of the PVs or WECSs. To describe this difference, the power trajectory of a DOL induction motor connected to an infinite bus after an abrupt frequency change is shown in Figure 7-19. The power trajectory versus frequency and the power trajectory versus time are shown in left and right figures, respectively. Before frequency event, the induction motor operates in point "A". Note that only linear region of the power-frequency curves near to synchronous speed, in an exaggerated manner, are shown. After a sudden frequency reduction, the operation frequency is changed from f_{old} to f_{new} immediately because of infinite bus assumption. This results in a transient reduction in input power of the induction motor corresponding to point "B". Afterwards, motor's speed will decrease to new equilibrium point "C" in a given time interval. At the same time, input power of the induction motor will increase in comparison with point "B". Meanwhile, inertial energy of the rotor is subtracted from the motor's input energy. This temporary reduction in motor's input energy will moderated rate of change of frequency (RoCoF) in the power system. In addition, the power system demand will be decreased by steady-state power reduction of the induction motor.

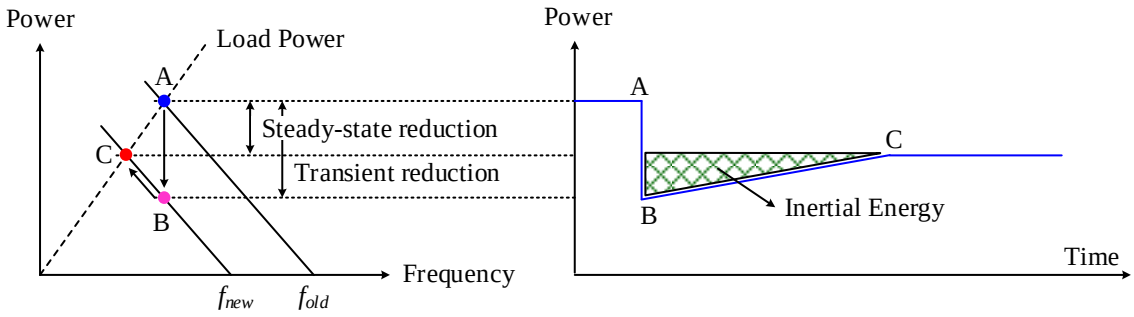

Figure 7-19: Power trajectory of a DOL induction motor after an abrupt frequency change.

According to above explanations, a suitable inertia emulator for a IM PFE-VFD system is proposed. The outline of this emulator is shown in Figure 7-20. It contains only a dead band block and a low pass filter (LPF) to filter undesirable signals from the measured frequency. Note that there is no derivative block in this emulator in comparison with that of PVs or WECSs. The time constant "T_{lag}" is assumed to be 0.01 s, in this chapter.

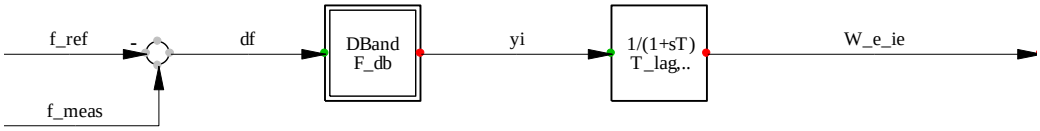

Figure 7-20: Outline of the proposed "Inertia Emulator" in the Smart IM PFE-VFD in DIgSILENT PowerFactory.

7.4.8. Primary Controller

A reserve speed control, based on the governing function in a steam turbine power plant [33], as primary controller (PCO) is simulated for the smart induction motor VFD system and shown in Figure 7-21. The measured frequency deviation is passed through a dead band then it is divided by the droop parameter, i.e. "R". The resulted signal is filtered and limited to a maximum limit by a first order low pass filter (LPF). The output signal of the LPF is preliminary reserve power order. The rate of change of this preliminary signal is restricted by a rate limiter. The rate limiter's output is the reserve power order, i.e. "P_res_ord". This variable which is in per unit determines that what portion of the pre-event motor's input power must be reduced. However, the reserve power order cannot be directly sent to the "Speed Controller" and it must be translated to a speed order signal. This is done by the "P2W" block. It determines a reserve speed based on the pre-fault motor's speed and the reserve power order by equation (7.26). The minus sign indicates that for a positive reduction in power a negative reserve speed must be added to the pre-fault motor's speed.

$$\omega_{r,res} = -\omega_{r,init} P_{res,ord} \tag{7.26}$$

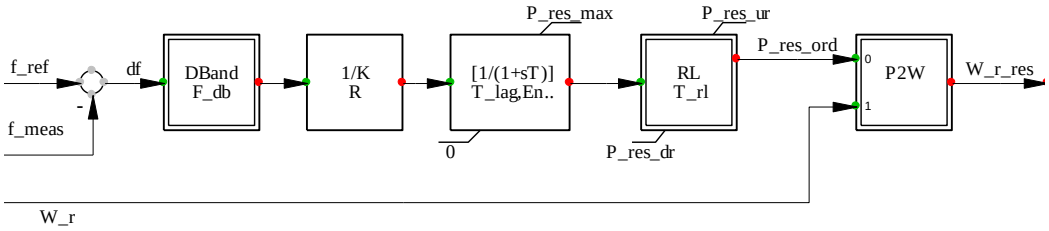

Figure 7-21: Outline of the "PCO" in the Smart IM PFE-VFD in DIgSILENT PowerFactory.

In order to prevent undesirable oscillations in the reserve power order at post-fault operation, the LPF's equations is modified as equation (27). The internal variables "Flag" and "yo1" are added to original equations. When the "yo1" reaches to the maximum limit of reserve power, the "Flag" will change immediately from zero to one and it holds this value for "T_{drop}" seconds (in this study, 30 s). The LPF's output variable, i.e. the preliminary reserve power, will be fixed to its maximum limit while the "Flag" is one. The "Primary Controller" parameters are listed in Table 7-4.

$$\begin{aligned} x. &= \text{Enable}_{res} \times (yi - yo)/T \\ yo1 &= \text{limstate}(x, y_{min}, y_{max}) \\ \text{Flag} &= \text{picdro}(yo1 >= y_{max},\ 0,\ T_{drop}) \\ yo &= \text{select}(\text{Flag} > 0.5,\ y_{max},\ yo1) \end{aligned} \tag{7.27}$$

Table 7-4: Parameters of the "PCO" in the Smart IM PFE-VFD system.

Parameter	Value	Unit	Parameter	Value	Unit
T_drop	30	s	R	0.0005	p.u.
T_lag	1	s	P_res_max	0.25/0.1*	p.u.
Enable_{res}	0/1	-	T_rl	0.02	s
P_res_ur	0.1	p.u./s	P_res_dr	-1	p.u./s

* These values are for 50 hp and 500 hp motor, respectively

7.4.9. Phase Locked Loop (PLL)

The PLL is utilised to measure the frequency of the rectifier terminal in a smart IM VFD system. The PLL structure which is shown in Figure 7-22 is a synchronous reference frame (SRF) PLL [34]. The Kp and Ki parameters of this PLL are 10 and 200, respectively.

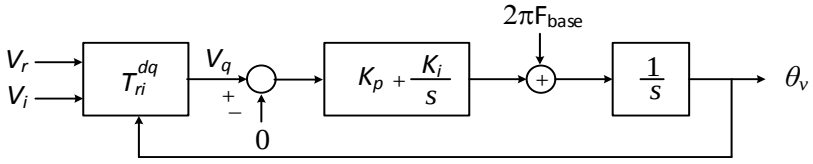

Figure 7-22: Outline of the "PLL" in DIgSILENT PowerFactory.

7.5. Smart IM AFE-VFD

The control structure of the Smart IM AFE-VFD system is shown in Figure 7-23. This structure is similar to that of a Smart IM PFE-VFD system shown in Figure 7-11. However, the its "DC Link" is not a RLC circuit and it is created by only a DC capacitor. Also, the "Vdc Regulator" block is added to the AFE-VFD system in comparison with the PFE-VFD system in order to regulate amplitude of the DC link voltage. Because of mentioned similarity between the Smart IM AFE-VFD system and the Smart IM PFE-VFD system, only the "DC Link" and the "Vdc Regulator" blocks are described in the following subsections.

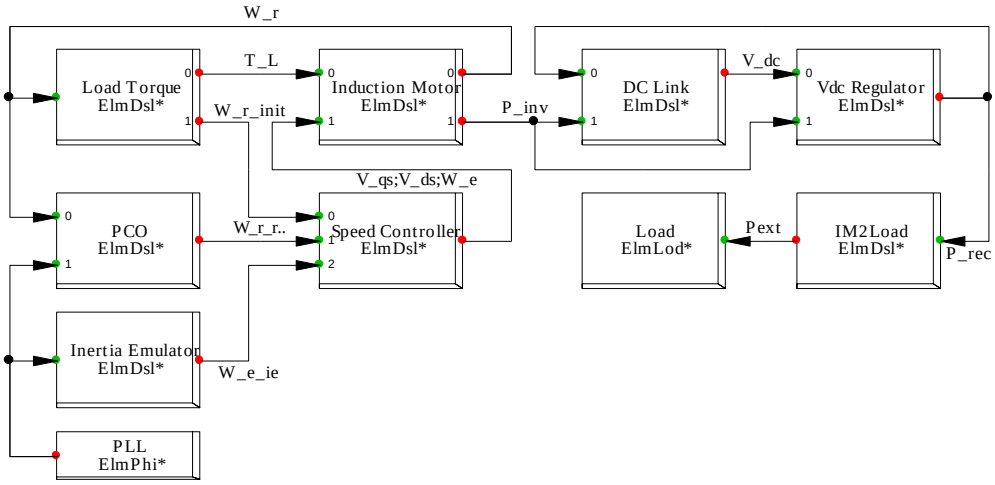

Figure 7-23: Control structure of the Smart IM AFE-VFD in DIgSILENT PowerFactory.

7.5.1. DC Link in AFE-VFD

The DC link circuit in an active front-end VFD system is shown in Figure 7-24. In this VFD system, the DC link is a DC capacitor. The capacitance of this capacitor is 1 s in this study. The outline of the "DC Link" in the Smart IM AFE-VFD is shown in Figure 7-25 based on Figure 7-24. In the conventional active front-end VFD system there is no chopper circuit. This circuit is integrated to the DC link to prevent power injection to grid in the regeneration mode. Although, the chopper can be enabled or disabled by a parameter named "Enable_ch".

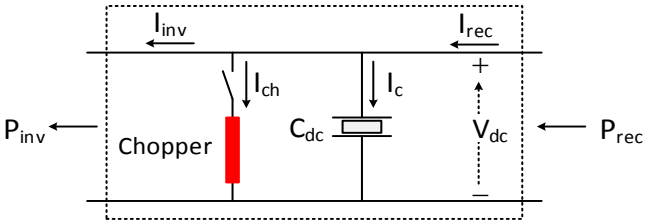

Figure 7-24: Electrical circuit of the DC link in the smart IM AFE-VFD system.

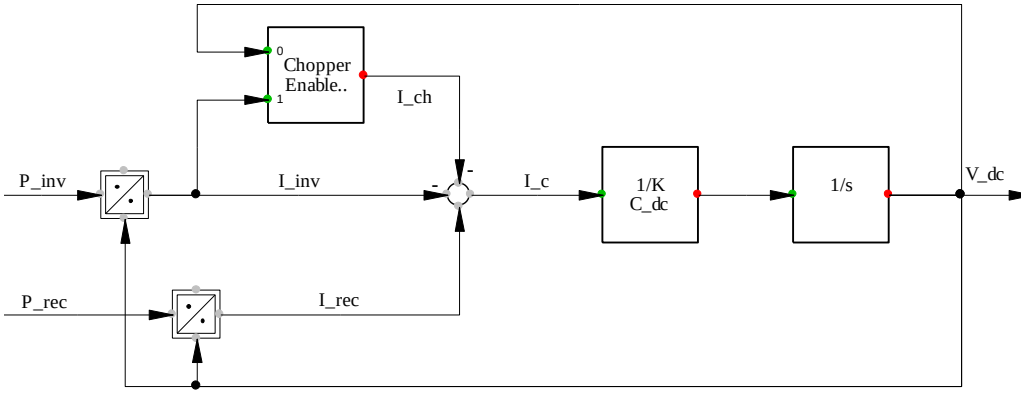

Figure 7-25: Outline of the "DC Link" in the Smart IM AFE-VFD in DIgSILENT PowerFactory.

7.5.2. Voltage Regulator

In an AFE-VFD system, as its name indicates its rectifier is composed by controllable switches which can be on and off programmatically in order to meet an objective function. This objective function is minimum deviation in the DC link voltage of the AFE-VFD system. To meet this function, a voltage regulator is designed using the DC link power balance equation given as [35]:

$$\frac{d}{dt}\left(\frac{1}{2}C_{dc}V_{dc}^{2}\right)=P_{rec}-P_{inv} \tag{7.28}$$

The outline of this voltage regulator is shown in Figure 7-26. The error between the DC link voltage square and its reference square value is passed through a proportional-integrator (PI) controller. Its output is the rectifier power order. The switches of rectifier will be control in such a way that its power be equal to the PI's output, i.e. "P_rec". The K_{Vdc} and T_{Vdc} parameters of the PI are 100 and 20, respectively in this study.

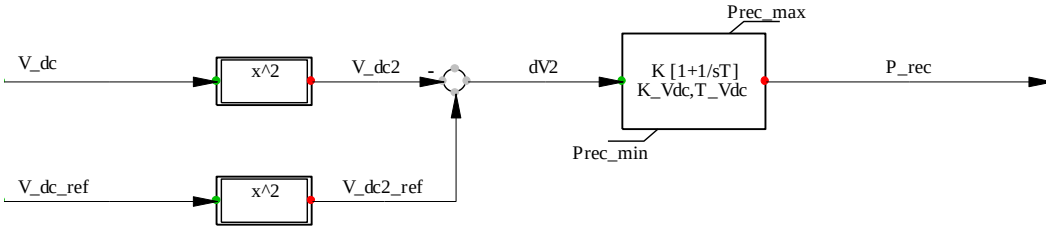

Figure 7-26: Outline of the "Vdc Regulator" in the Smart IM AFE-VFD in DIgSILENT PowerFactory.

7.6. Analysis of Two-Area System Considering Smart Induction Motors

In this section, effect of the proposed smart induction motor VFD systems on primary frequency response of a modified version of the Klein-Rogers-Kundur (KRK) two-area multi-machine as the test system [33] is evaluated. The single line diagram of this benchmark system is shown in Figure 7-27. The total load demand of the network is 2,525 MW and 200 Mvar. Two operation scenarios are defined for the studied two-area system. In non-WTPV scenario, named "WTPV 00%", all the load demands are supplied by conventional power plants. It is to be noticed that 11 out of 12 units connected to buses 1, 2 and 4 are reheat steam turbine (RST) types. The unit "HT 44" is a hydroelectric unit. All four units connected to bus 3 are combined cycle gas turbine (CCGT) power plants. The nominal apparent power of all these units is 225 MVA. The unit "RST 11" is also considered as slack unit. In "WTPV 75%" scenarios, all the synchronous generator (SG) units connected to bus 2 and bus 4 are replaced with eight WT power plants. In addition, the two middle units connected to buses 1 and 3 are substituted with four PV power plants. Also, the battery energy storage system (BESS) connected to bus 1 is activated in this scenario. The nominal ratings of this storage system are assumed to be 100 MVA and 10 MWh. The active power generation of each unit is tabulated in Table 7-5, for above mentioned scenarios. In these scenarios, all SG units connected to bus 1 and 3 are equipped with power system stabilizers (PSS) and all sixteen SG units have automatic voltage regulator (AVR) controllers. Also, the "Q control" of the WT and PV power plants is not activated.

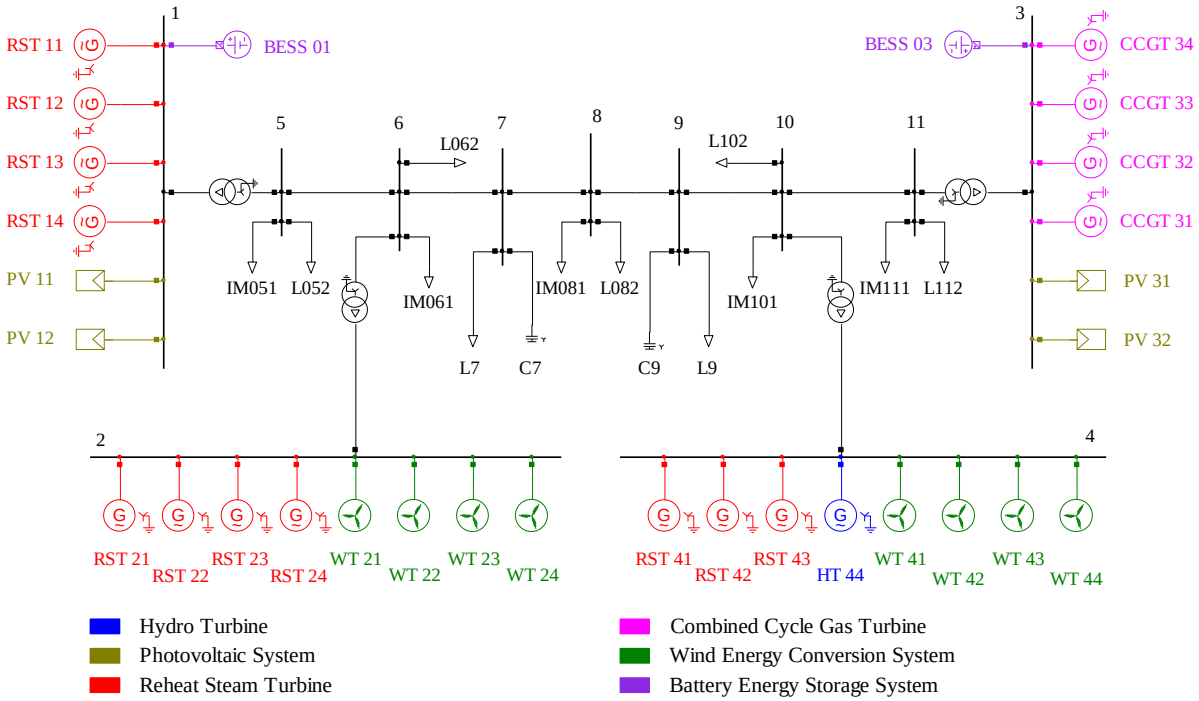

Figure 7-27: Single line diagram of the two-area system.

Table 7-5: Active power of power plants in defined scenarios (in MW).

Unit	WTPV 00%	WTPV 75%	Unit	WTPV 00%	WTPV 75%
RST 11	11	11	RST 42	175	-
RST 12	175	-	RST 43	175	-
RST 13	175	-	HT 44	175	-
RST 14	**100**	**100**	WT 21	-	175
RST 21	175	-	WT 22	-	175
RST 22	175	-	WT 23	-	175
RST 23	175	-	WT 24	-	175
RST 24	175	-	WT 41	-	175
CCGT 31	180	180	WT 42	-	175

CCGT 32	180	-	WT 43	-	175
CCGT 33	180	-	WT 44	-	175
CCGT 34	180	180	PV 11	-	175
RST 41	175	-	PV 12	-	175
			Sum	2581	2571

7.6.1. Frequency Response of Two-Area System Considering Smart Induction Motors

In this subsection, the impact of proposed smart motor loads on primary frequency response of two-area test system is studied. In this regard, five motor loads with the demand of 5% of total load demand of the grid are connected to discrepant buses, as shown as IM in Figure 7-27. Furthermore, five static loads with the algebraic sum of demand equal to 2% of network load demand are connected to the IM buses. The accurate information of networks' loads is taken from Table 7-6. It is to be pointed out that the amount of 10 extra loads added to the network is subtracted from the main loads connected to nodes 7 and 9 so that the network demand is fixed.

Table 7-6: Active and reactive powers of loads (in MW-Mvar).

Load	Act. Power	Rea. Power	Load	Act. Power	Rea. Power
L7	900	100	IM081	25	0
L9	1450	75	L082	10	5
IM051	25	0	IM101	25	0
L052	10	5	L102	10	5
IM061	25	0	IM111	25	0
L062	10	5	L112	10	5

The data of smart motor loads' types and their operation criteria before the loss of generation are shown in Table 7-7 so that two out of five motor loads are PFE type. Additionally, three 50 hp and two 500 hp motors are integrated to the system. The maximum reserve powers of small and large motors are set to 0.2 p.u. and 0.1 p.u., respectively. Moreover, different pre-contingency motors' speed and speed rate limits are taken into consideration since the operation modes and speed control potentials of network's motor loads are discrepant.

Table 7-7: Operation parameters of the smart IM VFD systems.

Load	PFE or AFE	Motor Power (hp)	Maximum Reserve (pu)	Speed Rate Limit (pu/s)	Pre-fault Speed (pu)
IM051	AFE	50	0.2	0.05	0.85
IM061	PFE	500	0.1	0.01	0.9
IM081	AFE	50	0.2	0.04	1
IM101	PFE	50	0.2	0.03	0.9
IM111	AFE	500	0.1	0.01	1

The simulation results related to the loss of RST 14 unit with rated active power of 100 MW for different scenarios are shown in Figure 7-28 to Figure 7-43. The results of first scenario i.e. WTPV 00% is highlighted with black traces. The WTPV 75% scenario is divided into two specific sub-scenarios so that all load demands are non-motoric in the first sub-scenario highlighted with green traces. In other hand, five out of 12 loads of the network are chosen from smart motor loads tabulated in Table 7-7 in the second sub-scenario depicted by blue traces. By comparing non-WTPV and WTPV scenarios, it is clear-cut that the primary frequency control criteria in terms of RoCoF, frequency nadir, and steady-state frequency deviation are significantly enhanced in second scenario. This is due to the fact that frequency response of renewable energy sources and BESS is faster than conventional units in primary frequency support. The COI frequency of two sub-scenarios associated with WTPV 75% is shown in Figure 7-29. It can be observed that the system frequency is closer to its nominal value while 5% of load demand is considered to be the proposed smart motor loads. The frequency nadir and steady-

state frequency deviations are improved by 40% and 10%, respectively. In contrast, the RoCoF of these two sub-scenarios is similar for the first few seconds after the incident, as shown in Figure 7-30. This is because of lower inertia of motors compared with that of power plants. As can be seen from Figure 7-31 to Figure 7-34, the smart motor loads can reduce the primary frequency support burden on conventional power plants, renewable energy sources and BESS by 10% to 15%, correspondingly.

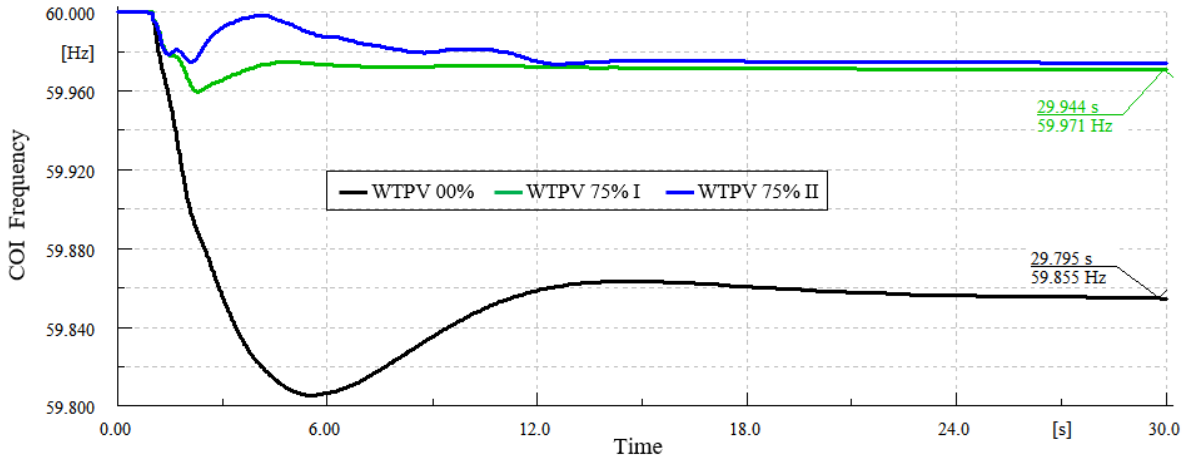

Figure 7-28: The COI frequency response with loss of 100 MW generation for different scenarios.

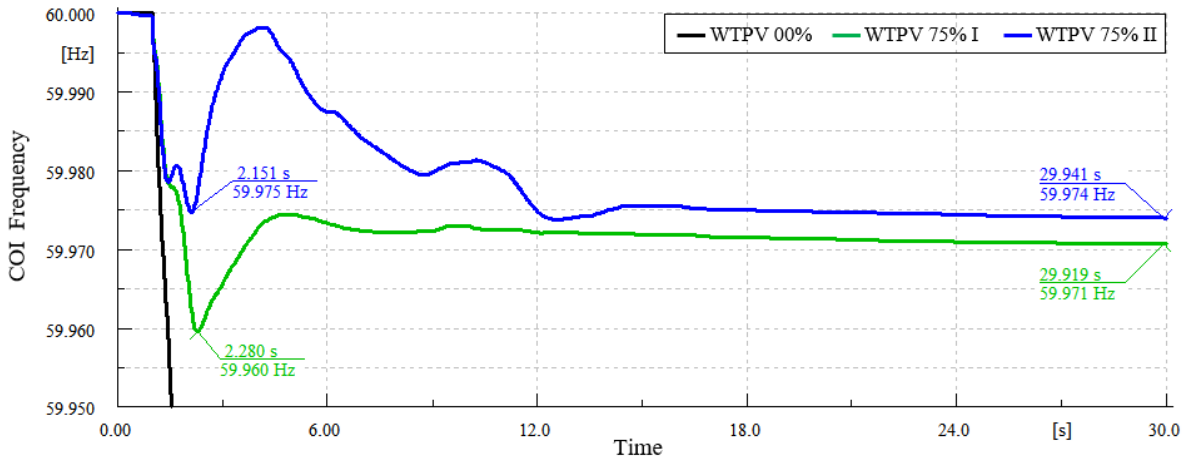

Figure 7-29: Frequency nadir and steady-state frequency deviation for different scenarios.

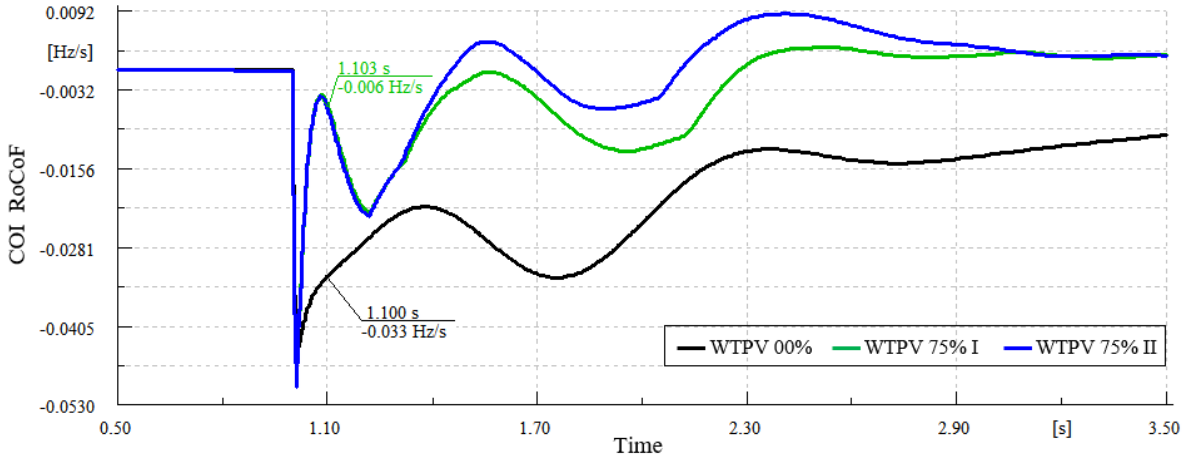

Figure 7-30: The COI RoCoF with loss of 100 MW generation for different scenarios.

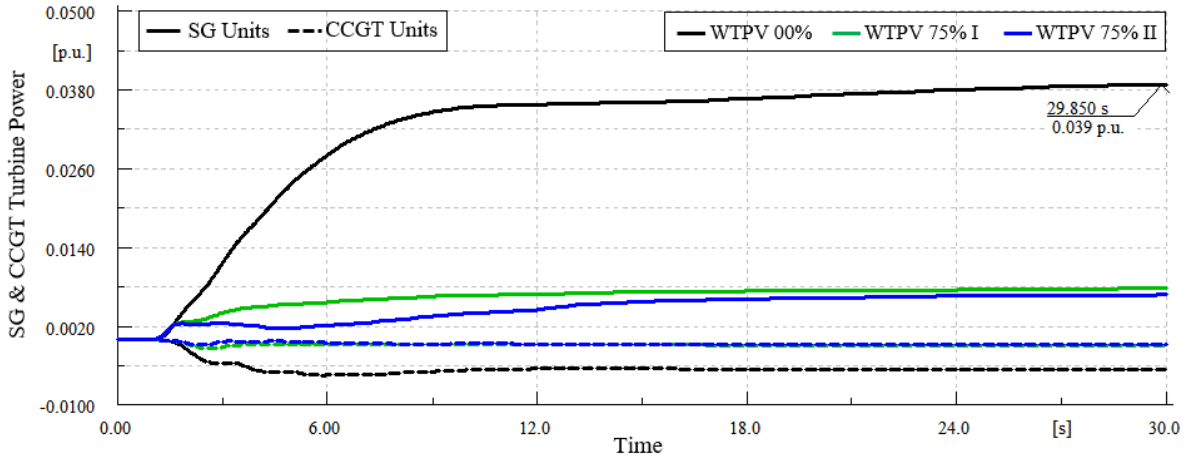

Figure 7-31: Turbine power changes of SG and CCGT units with loss of 100 MW generation for different scenarios.

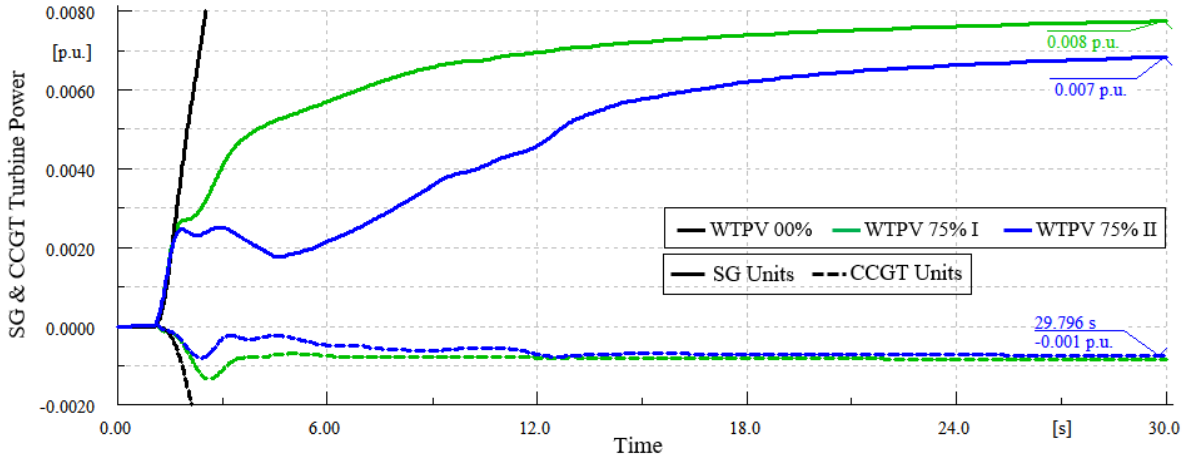

Figure 7-32: Turbine power changes of SG and CCGT units with loss of 100 MW generation for different scenarios.

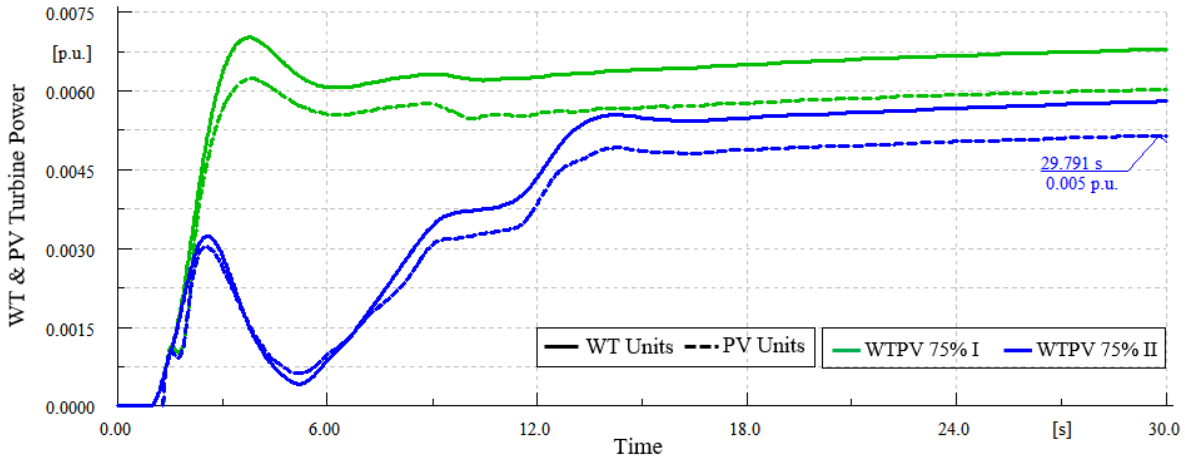

Figure 7-33: Turbine power changes of WT and PV units with loss of 100 MW generation for different scenarios.

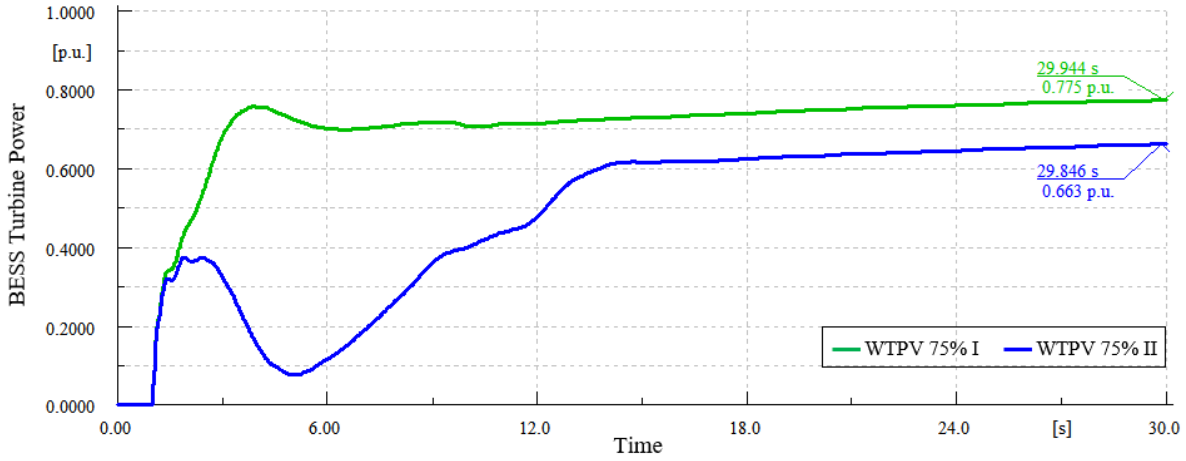

Figure 7-34: The BESS power changes with loss of 100 MW generation for different scenarios.

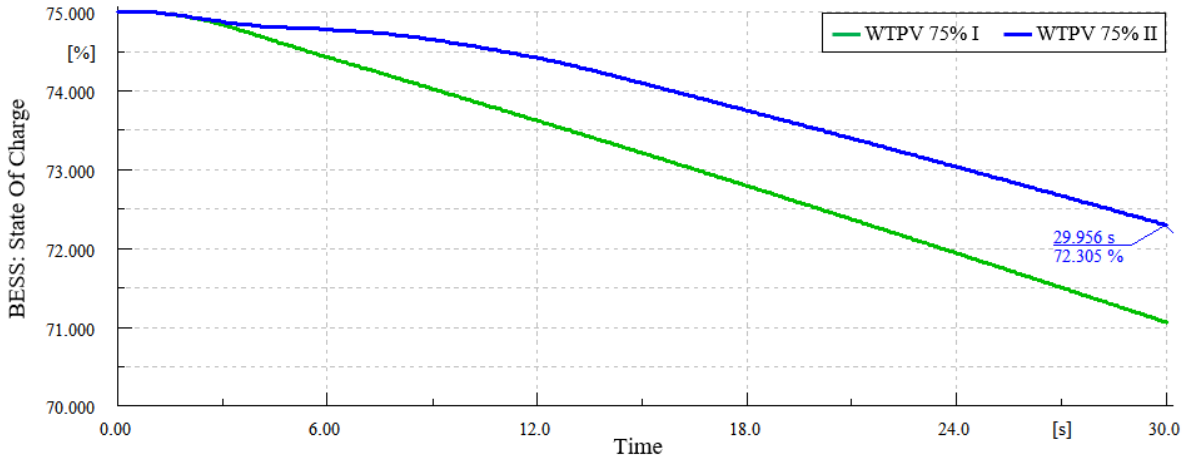

Figure 7-35: The BESS state of charge with loss of 100 MW generation for different scenarios.

In order to precisely analyse the performance of primary frequency support capability of proposed smart motor loads, the dynamic behaviour of these systems following the generation lost are shown in Figure 7-36 to Figure 7-43 for WTPV 75% II. The reserve power order and corresponding reserve rotor speed are shown in Figure 7-36 and Figure 7-37, respectively. It is observed that two units of IM101 and IM111 respond lately since they have farthest electrical distance to the disturbance location. The response of IM061 is slower than IM081 as the ramp up rate of reserve power of smart loads are chosen in a way that maximum reserve power could be reachable within 1 sec. According to Figure 7-38, the rotors speeds are mitigated based on determined reserve speeds. The difference among pre-fault rotor speeds is illustrated in this Figure. The electrical frequency which is determined by the inertia emulators of the smart induction motors is shown in Figure 7-39. As mentioned in previous sections, this frequency is only the filtered measured frequency not its derivative. The smart motors order in terms of distant to the incident location is clearly observable in this Figure. The electromagnetic torque variations, stator current and smart motors' power following the disturbance occurrence are shown in Figure 7-40 to Figure 7-42. As can be seen, the dynamic behavior of two 500 hp motors is identical. The response difference between these two motors is due to different pre-fault rotor speeds; however, they don't work in regeneration mode. In other hand, three 50 hp motors are seen sever changes due to higher amount of speed rate limits, so that two motors of IM051 and Im081 which are equipped with AFE-VFD

systems work in regeneration mode. It is to be noted that the chopper of these units are deactivated. The algebraic summation of network active power reduction happened by smart motors is shown in Figure 7-43. It is clear that sever changes of motors' power following the first few seconds of event leads to the reduction of consumed power of the grid equal to the generation lost amount (100 MW). This is due to considering load inertias of motors connected to the grid. In addition, 17 MW out of 125 MW consumed power of motoric loads is reduced after transient state.

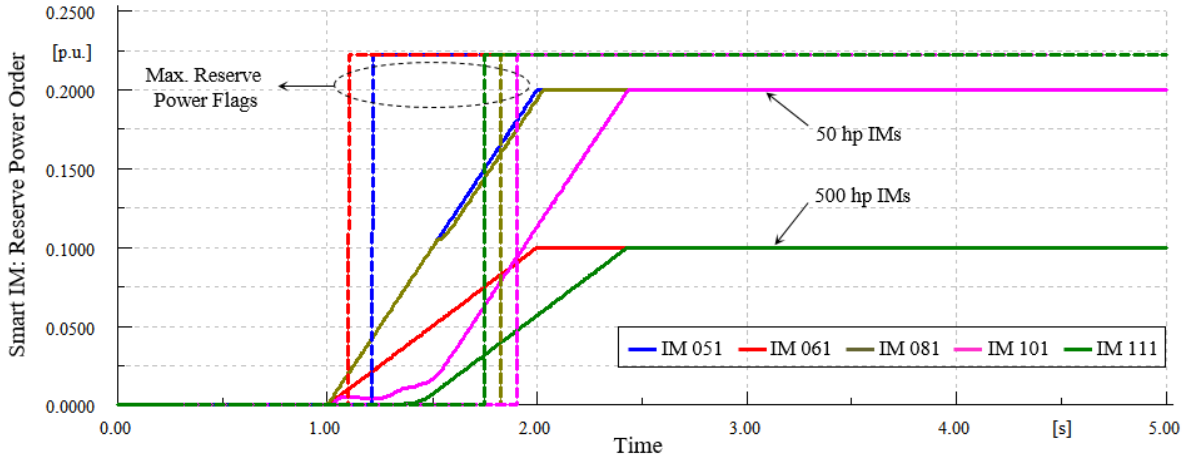

Figure 7-36: Reserve power order of the smart induction motors with loss of 100 MW generation.

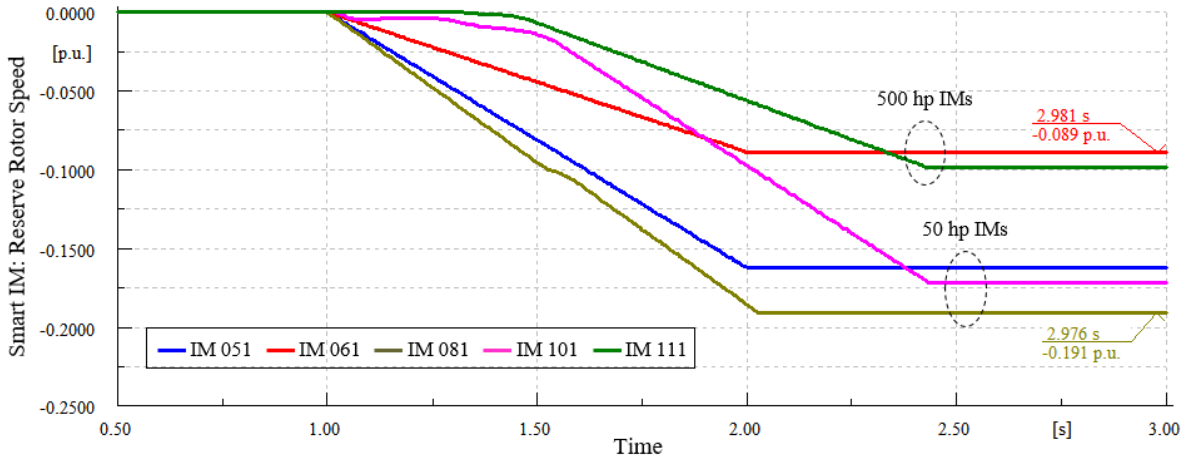

Figure 7-37: Reserve rotor speed of the smart induction motors with loss of 100 MW generation.

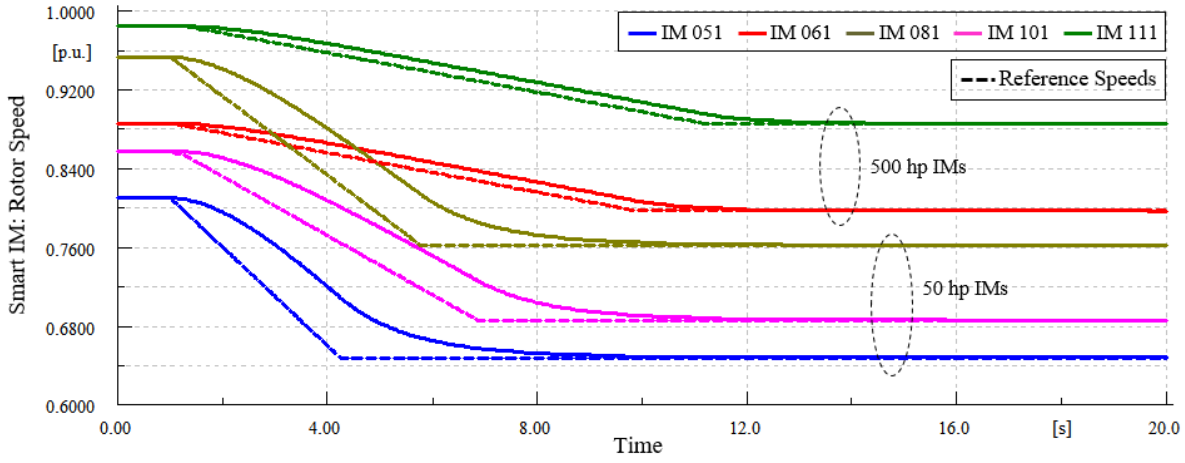

Figure 7-38: Rotor speed of the smart induction motors with loss of 100 MW generation.

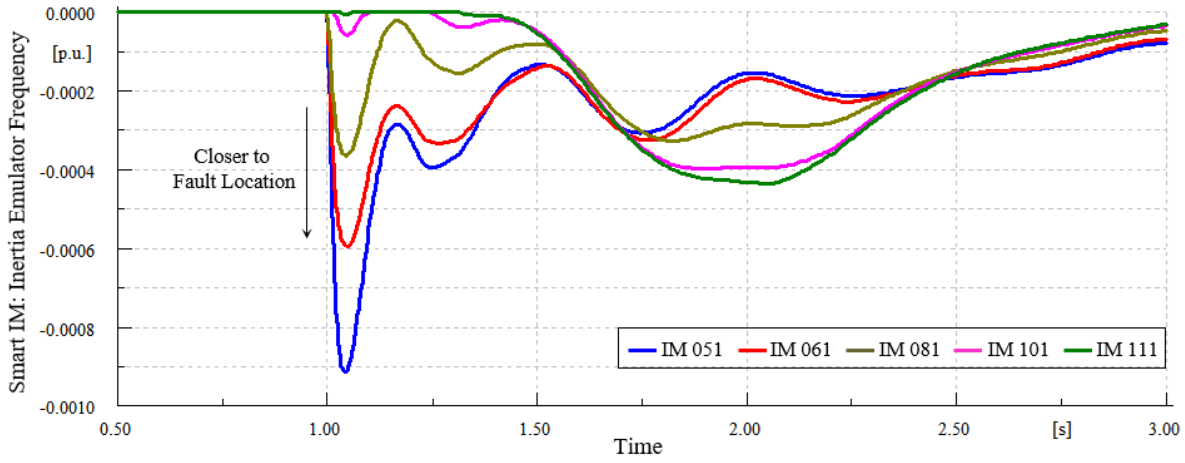

Figure 7-39: Electrical frequency of the inertia emulators of the smart induction motors.

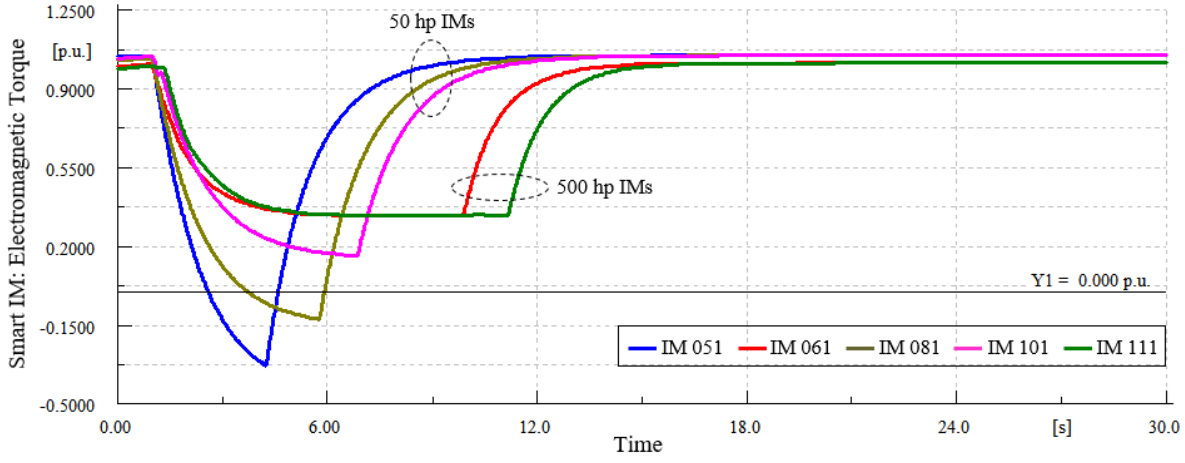

Figure 7-40: Electromagnetic torques of the smart induction motors with loss of 100 MW generation.

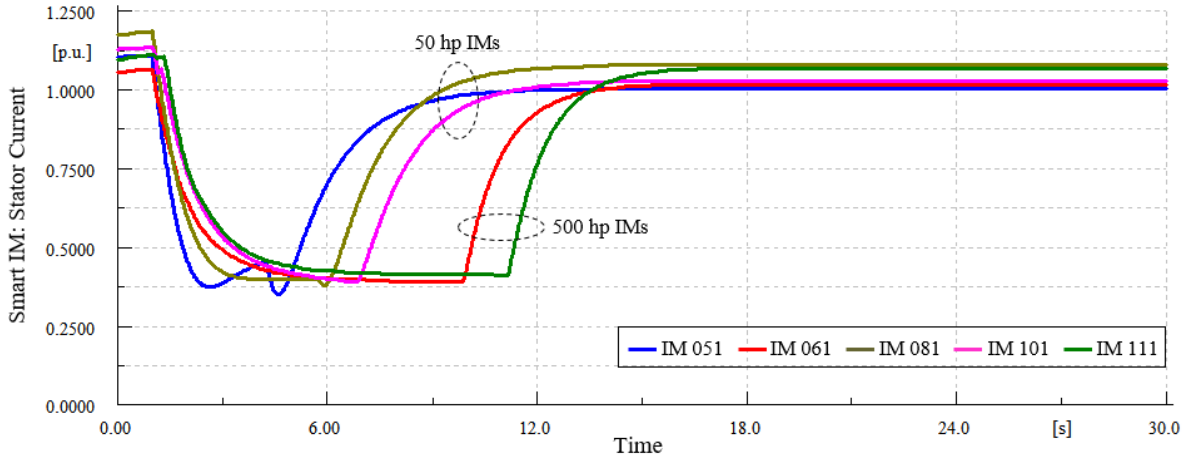

Figure 7-41: Stator currents of the smart induction motors with loss of 100 MW generation.

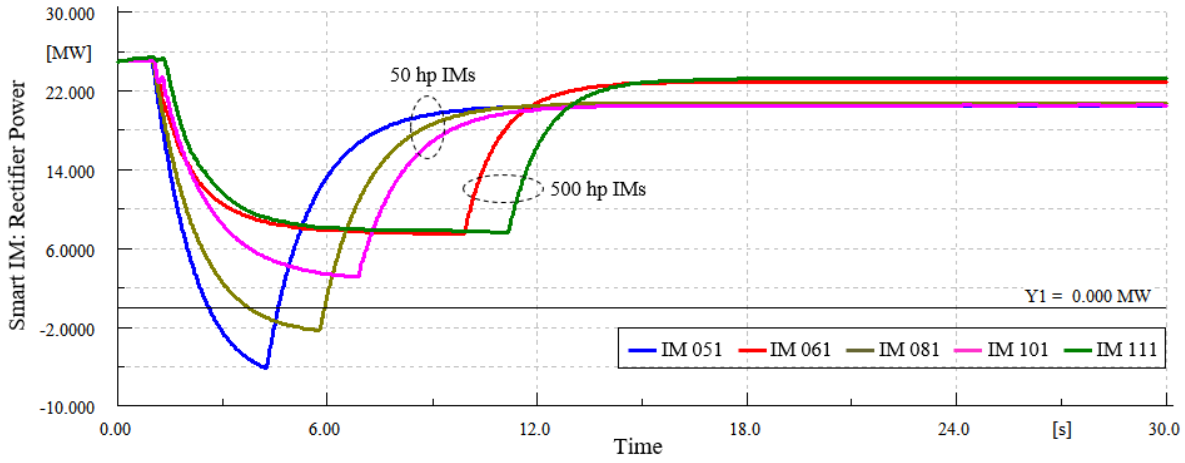

Figure 7-42: Rectifier power of the smart induction motors with loss of 100 MW generation.

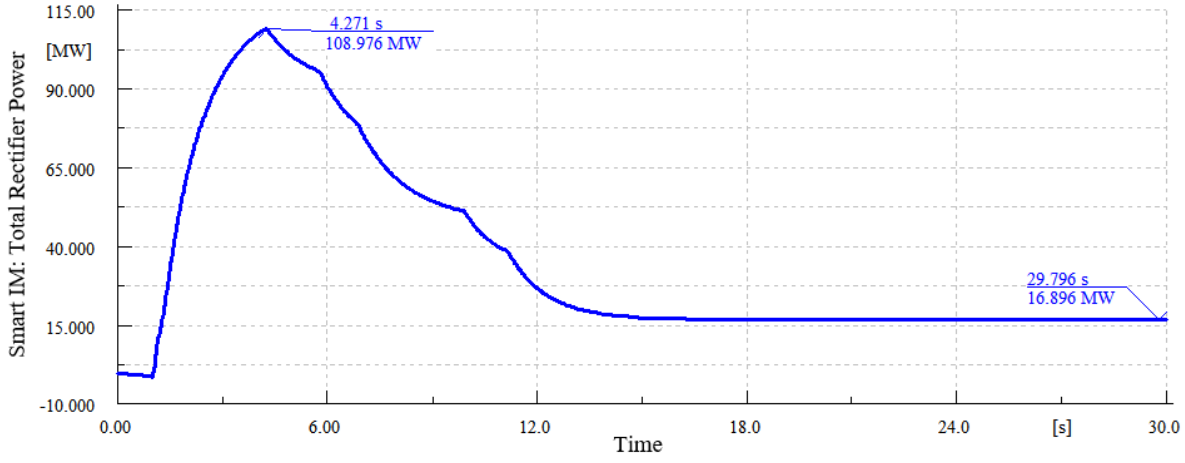

Figure 7-43: Total rectifier power of the smart induction motors with loss of 100 MW generation.

7.6.2. Executive Summary of Deploying SIM in Two-Area Kundur System

The main purpose of this chapter is to investigate primary frequency support of power systems considering smart loads in the network. In this regard, a smart induction motor is propsed and simulated in DIgSILENT PowerFactory. This model is developed by modifying induction motor variable frequency drive systems in order to participate in primary frequency support. This modelled is suggested for both systems of passive front-end and active front-end. In model validation, it is illustrated the derived model can provide all expected capabilities. Further, a new inertia emulator is proposed to properly inspire the inertial response of VFD systems. In the developed IM VFD systems model, it is illustrated that moment of inertia of motor's load has significant influence on dynamic behaviour of these systems following the loss of generator. As a result, the appropriate selection of motors' reserve power and the corresponding speed can be achieved by considering the above noticed parameters. It is also shown the variation amplitude of motors' variables like electromagnetic torques and stator current become twofold by doubling the response speed of smart motors in consequent of power reduction. In other hand, it is illustrated that motors' reserve power increment doesn't have considerable influence on the above mentioned variables of motors and the loss of energy is increased in chopper.

The primary frequency control of two-area network is investigated integrating smart loads. In this regard, it is assumed that 5% of network demand is supplied by five smart motors with different operational parameters. In this context, it is illustrated that whereas the integration of these kinds of loads into the grid doesn't have meaningful impact on RoCoF, the frequency nadir and steady-state frequency deviation are significantly enhanced. Additionally, it is observed that the power equivalent to consumed power of smart motors is subtracted from network demand due to initial consumption power of smart motors following the loss of generation in consequence of considering load inertia. This can also result to the reduction of primary frequency support burden on conventional and or renewable and BESS units. In other word, these units require lower ramp rate to increase their powers following the incident.

7.7. Analysis of 36-Zone GB Network Considering Smart Induction Motors

In this section, the primary frequency control in 36-zone GB network with the proposed smart induction motors as dynamic loads are evaluated. In this regard, two operation scenarios are defined. In first scenario, named "WTPV 00%", all network demand is supplied by conventional power plants like nuclear or combined cycle gas turbine (CCGT) power plants. The generation power and geographical distribution of these plants are shown in Figure 7-44. It is to be noted that almost 90% of network generation is located in the southern part of UK i.e. England & Wales and Scotland supplies only 10% of whole system load demand. The largest unit is the nuclear power plant located in zone 12 which supplies about 13% of whole system generation. It is to be noticed that 60% and 30% of conventional generating unit are CCGT and nuclear power plants, respectively. The remained 10% generating units are included of 10% biomass and 3% hydro turbine. The accurate generation of each zone is tabulated in Table 7-8 in MW.

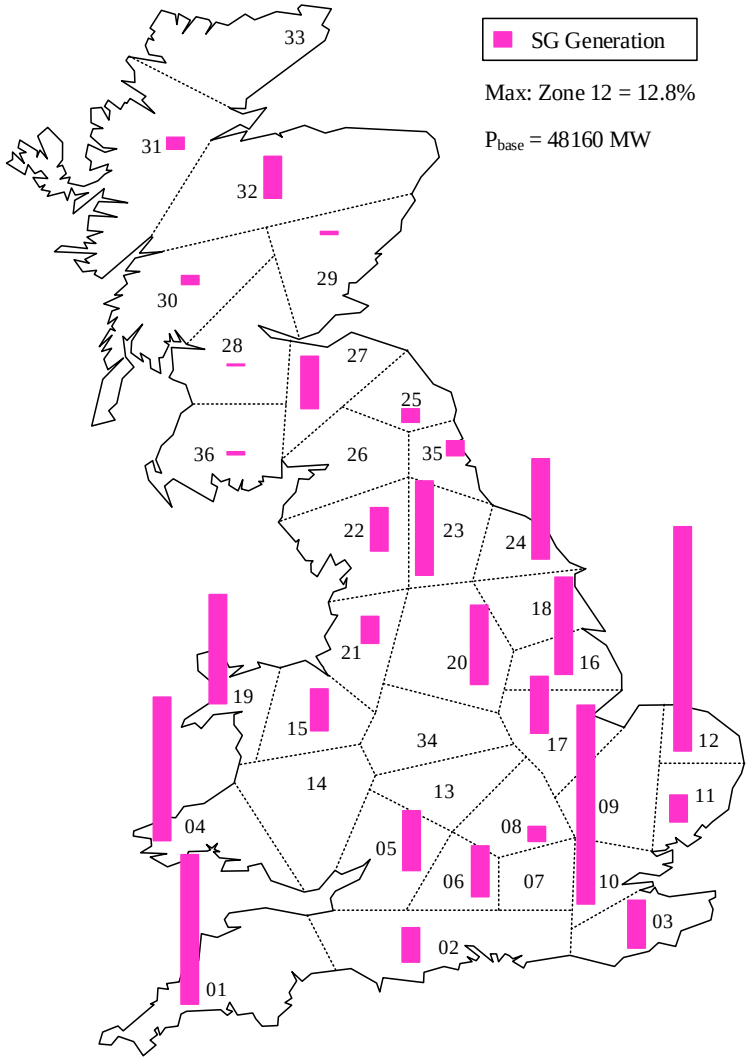

Figure 7-44: Geographic distribution of SG generation in "WTPV 00%" scenario.

In the second scenario, named "WTPV 60%", the PVs and WTs supply 20% and 40% of GB network demand, respectively. Since the total load demand of the network is 40 GW, the power generation of PVs and WTs are 8 GW and 16 GW, respectively. The precise generation of SGs, PVs and WTs are tabulated in Table 7-8 and Table 7-9. As can be seen, as the penetration of renewable energy sources increases, the capacity of gas turbines based CCGT are decreased while other conventional units' capacity is fixed. The capacity of CCGTs is 5 GW and i.e. 12.5% of the network demand. In other hand, 27.5% of load is supplied by nuclear, biomass and hydro-turbine power stations in this scenario. In addition, a battery energy storage system (BESS) with ratings 500 MW and 50 MWh is installed in zone 23 in order to support primary frequency control, in this scenario.

Table 7-8: Active power of conventional power plants in defined scenarios

No.	Type	Zone	WTPV 00% (MW)	WTPV 60% (MW)
01	Gas	01	809	140
02	Nuclear	01	3337	3436
03	Gas	02	946	164
04	Nuclear	03	1299	1337
05	Gas	04	3941	683
06	BioMass	05	100	100
07	Gas	05	1575	273
08	Gas	06	1385	240
09	Gas	08	420	73

10	BioMass	10	741	742
11	Gas	10	4732	820
12	Gas	11	751	130
13	Gas	12	1609	279
14	Nuclear	12	4548	4683
15	Gas	15	1180	204
16	Gas	16	2704	469
17	Gas	17	1544	268
18	Gas	19	617	107
19	Nuclear	19	2398	2400
20	Gas	20	2172	376
21	Gas	21	724	125
22	Nuclear	22	1202	1238
23	**BioMass**	**23**	**1722**	**1724**
24	Gas	23	858	149
25	Gas	24	2759	478
26	BioMass	25	366	366
27	BioMass	27	120	120
28	Gas	27	107	19
29	Nuclear	27	1214	1250
30	Gas	28	18	3
31	BioMass	29	52	52
32	Gas	29	14	2
33	Hydro	30	232	233
34	Hydro	31	321	322
35	Gas	32	11	2
36	Hydro	32	535	536
37	Pump Storage	32	611	612
38	BioMass	35	280	280
39	Gas	35	126	22
40	BioMass	36	45	45
41	Hydro	36	33	33
Total Active Power (MW)			48157	24534

Table 7-9: Active power of PV and WT power plants in “WTPV 60%” scenario.

Zone	PV (MW)	WT (MW)	Zone	PV (MW)	WT (MW)
01	407	609	19	129	1312
02	431	61	20	416	95
03	92	459	21	277	198
04	267	824	22	135	641
05	340	49	23	395	394
06	249	26	24	114	1025
07	268	1	25	144	121
08	734	2	26	34	299
09	392	2	27	120	1251
10	98	252	28	136	511
11	95	49	29	113	221
12	304	2096	30	75	138
13	486	197	31	12	335
14	323	61	32	75	1469
15	517	438	33	82	426
16	37	578	34	91	1
17	32	1	35	198	781
18	218	17	36	165	1060
			Total	8000	16000

The geographical distribution of generated power of all units is shown in Figure 7-45 for “WTPV 60%” scenario. Furthermore, the CCGT participation in supplying the network demand is separately shown. By comparing this figure with Figure 7-44, it is clearly observable that the conventional units placed beside the

coast, i.e. nuclear units and the biomass power plants, located in the middle part of GB network are considered while the CCGT units of middle-down part of GB network, that is, the high-densely consumption region are substituted with PVs. Moreover, in order to supply all deliverable power of the CCGT units in the top areas and coasts of network, i.e. low-densely consumption region, the WTs are installed and connected to the associated buses.

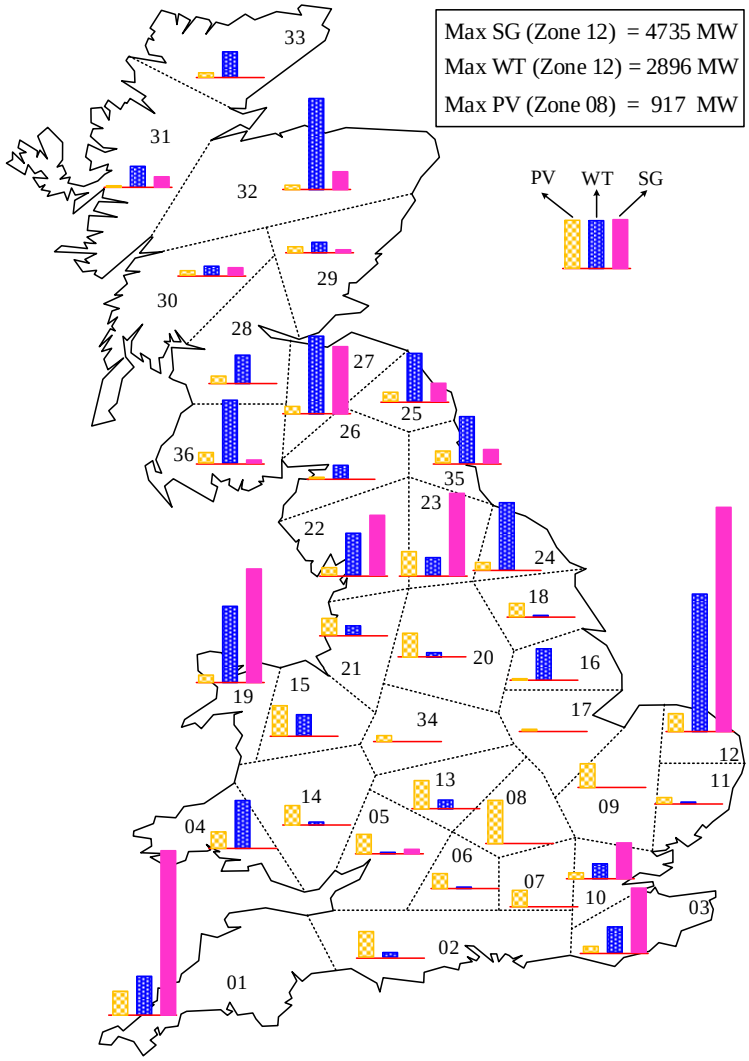

Figure 7-45: Geographic distribution of power plant's generations in "WTPV 60%" scenario

7.7.1. Frequency Response of 36-Zone GB Network Considering Smart Induction Motors

In this section, the GB system frequency response is validated following the biomass 23 generation lost. The main reason of selecting this unit is that its capacity is fixed after integration of the PVs and WTs power plants. In simulation results, different quantities like centre of inertia (COI) frequency and rate of change of frequency (RoCoF) changes are shown for 30 seconds following the disturbance which occurred at $t = 1\ s$. The step size parameter of time-domain simulation is equal to 0.005 seconds. In the following results, the COI frequency is illustrated based on the following relation:

$$F_{COI} = \frac{\sum_{i=1}^{N} H_i S_i F_i}{\sum_{i=1}^{N} H_i S_i} \tag{7.29}$$

Where, H_i, S_i and F_i are the inertia constant, apparent power and frequency of the *i*th SG, respectively.

In order to examine effect of the proposed smart induction motor loads on primary frequency control, the "WTPV 60%" is divided to two sub-scenario specified by "I" and "II" suffixes. In "WTPV 60% I" sub-scenario, all loads in GB 36-zone network are assumed to be non-smart loads. The 20%, 35% and 45% of these loads are modelled as constant power, constant current and constant impedance respectively. Also, active power of these loads will be reduced 1% for 1% reduction in frequency. In other hand, 5% of network demand are assumed to be the proposed smart loads, in "WTPV 60% II" sub-scenario. The type, motor power and operation parameters of these 36 smart loads are tabulated in Table 7-10. The 23 smart loads are passive front-end (PFE) and others are active front-end (AFE) types. Also, the 9 smart loads adopt large 500 hp induction motors and others adopt medium 50 hp induction motors. The maximum reserve power (i.e. allowed reduction in motor' power) is assumed to be limited to 0.1 or 0.2 per unit. The parameters of induction motors are borrowed from [32].

Table 7-10: Operation parameters of the smart induction motor loads in "WTPV 60% II" scenario.

Zone	Type	Motor Power (hp)	Maximum Reserve (pu)	Speed Rate Limit (pu/s)	Zone	Type	Motor Power (hp)	Maximum Reserve (pu)	Speed Rate Limit (pu/s)
01	**AFE**	**500**	**0.10**	**0.01**	19	AFE	500	0.10	0.01
02	AFE	50	0.10	0.02	20	AFE	50	0.10	0.02
03	AFE	500	0.10	0.01	21	PFE	50	0.20	0.02
04	PFE	50	0.20	0.02	22	PFE	500	0.10	0.01
05	AFE	50	0.10	0.02	**23**	**PFE**	**50**	**0.20**	**0.02**
06	PFE	50	0.20	0.02	24	PFE	500	0.10	0.01
07	PFE	50	0.20	0.02	25	PFE	50	0.20	0.02
08	**AFE**	**50**	**0.10**	**0.01**	26	PFE	50	0.20	0.04
09	AFE	50	0.10	0.02	27	PFE	50	0.20	0.02
10	AFE	500	0.10	0.01	28	AFE	50	0.10	0.02
11	PFE	50	0.20	0.02	29	AFE	500	0.10	0.01
12	PFE	50	0.20	0.02	30	PFE	50	0.20	0.02
13	PFE	50	0.20	0.01	31	PFE	50	0.20	0.02
14	AFE	50	0.10	0.02	32	AFE	50	0.10	0.02
15	**PFE**	**50**	**0.20**	**0.01**	33	PFE	50	0.20	0.02
16	**PFE**	**500**	**0.10**	**0.01**	34	PFE	50	0.20	0.04
17	PFE	50	0.20	0.02	35	PFE	50	0.20	0.02
18	**PFE**	**500**	**0.10**	**0.01**	36	PFE	50	0.20	0.02

The simulation results with loss of "BioMass 23" unit for the three defined scenarios are shown in Figure 7-46 to Figure 7-60. The COI frequency and COI RoCoF are depicted in Figure 7-46 and Figure 7-47, respectively. The primary frequency response of the GB network is considerably improved in "WTPV 60% I" scenario in comparison with "WTPV 00%" scenario, by equipping renewable power plants with primary frequency support capability. The turbine power changes of SG and CCGT power plants after infeed loss are shown in Figure 7-48. According to this figure, the mentioned improvement in primary frequency response is along with reduced burden in primary frequency support of the non-renewable power plants. It is worth noting that the negative turbine power change of the CCGT units are because of its unique dynamic behaviour in full load operation following an abrupt frequency reduction. In other words, generated power of a full load CCGT power plant will be reduced in response of an infeed loss. As mentioned, 5% of GB network's demand assumed to be smart loads with primary frequency support capability in scenario "WTPV 60% II". The simulation results of this scenario is specified by blue coloured traces. It can be seen that the proposed smart loads can mitigate COI frequency respect to non-smart load case, i.e. "WTPV 60% I" scenario. The turbine power changes of WTs and PVs power plants and that of the BESS unit are shown in Figure 7-49 and Figure 7-50 for renewable scenarios. Note that

turbine power of the BESS unit is its battery power. It can be clearly seen that primary frequency support burden of these units are reduced by the smart loads. This reduction is significant in 3-12 seconds time interval. The lower energy production with the BESS unit results in higher state of charge (see Figure 7-51).

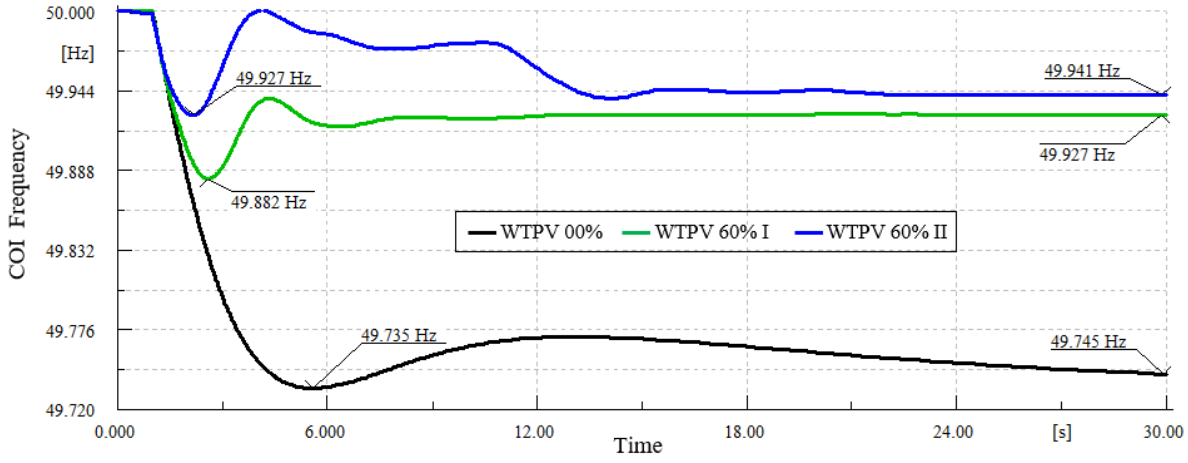

Figure 7-46: COI frequency response with loss of 1700 MW generation in middle of network.

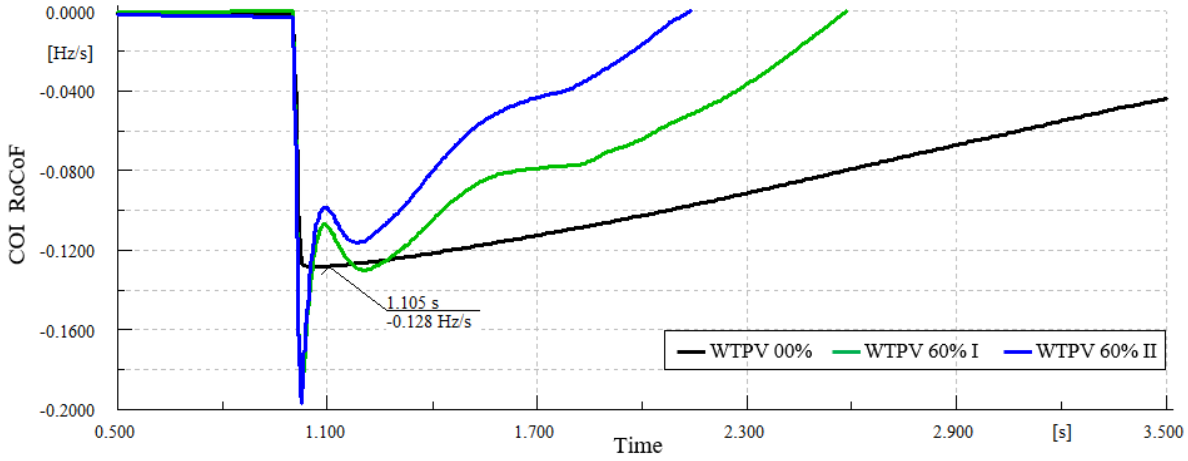

Figure 7-47: COI RoCoF deviations with loss of 1700 MW generation in middle of network.

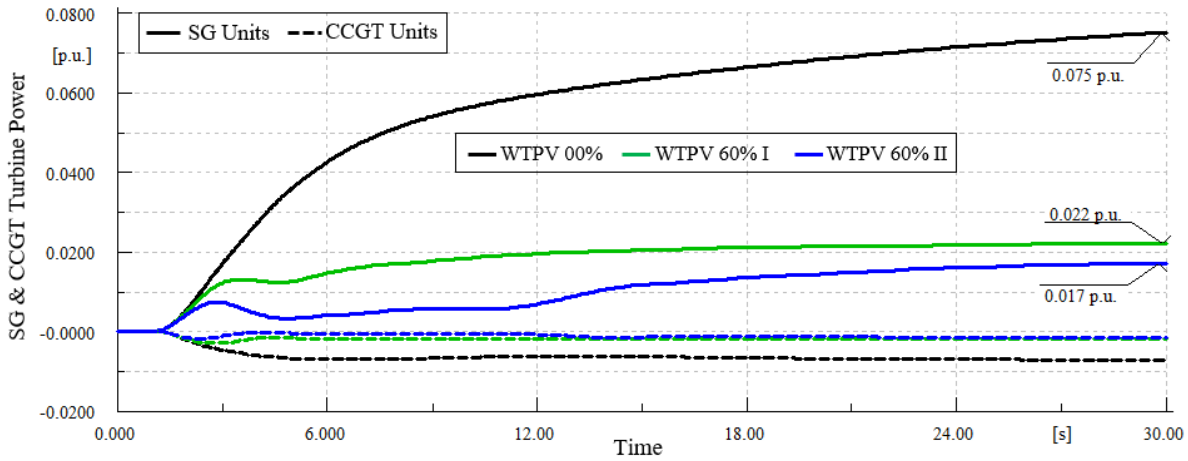

Figure 7-48: Turbine power changes of SG and CCGT units with loss of 1700 MW generation in middle of network.

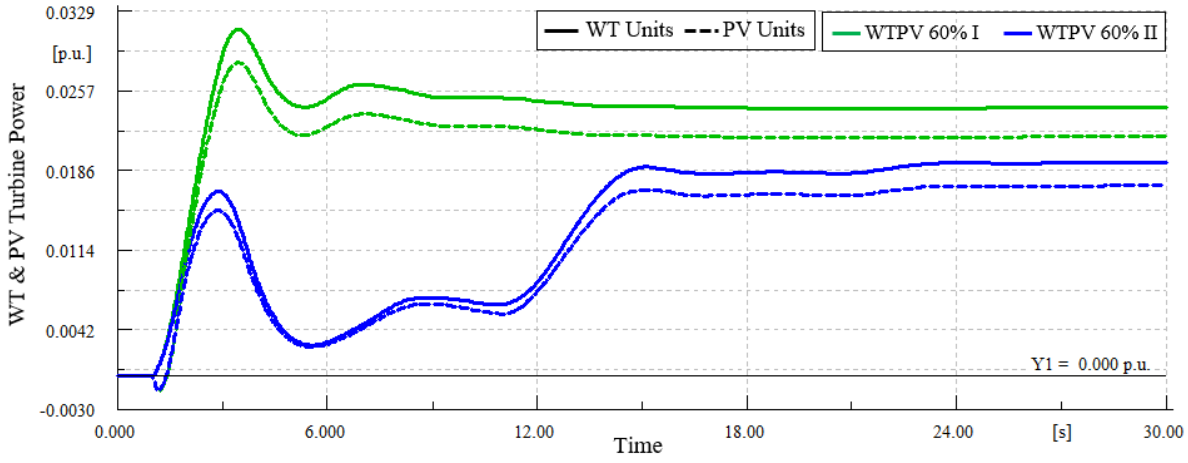

Figure 7-49: Turbine power changes of WT and PV units with loss of 1700 MW generation in middle of network.

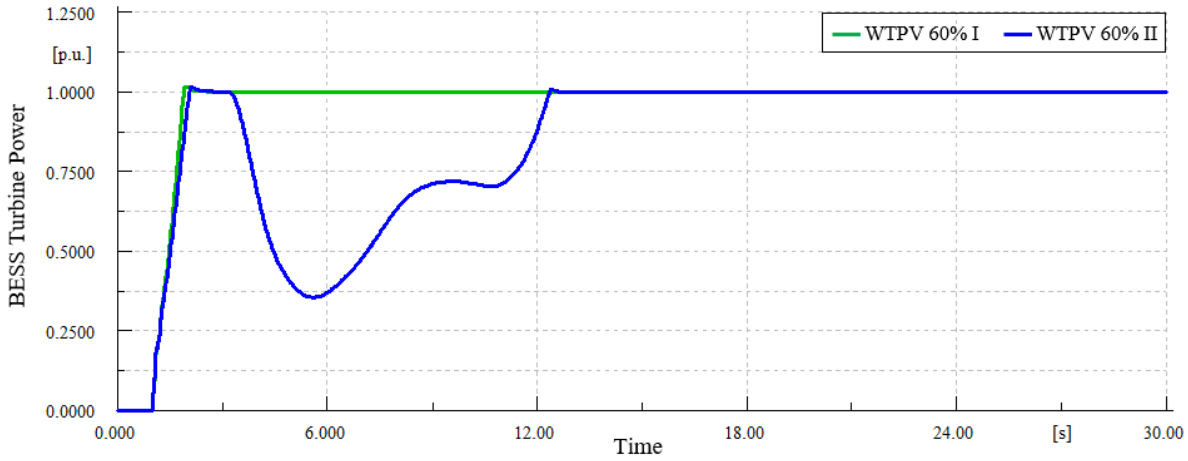

Figure 7-50: Turbine power changes of the BESS 23 with loss of 1700 MW generation in middle of network.

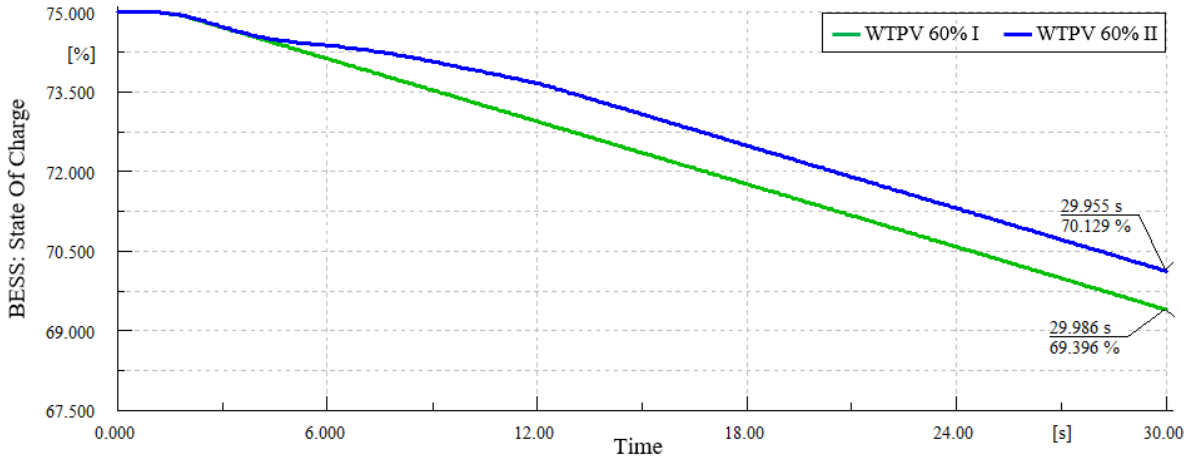

Figure 7-51: State of charge of the BESS 23 with loss of 1700 MW generation in middle of network.

In order to further discussion and better understanding of the proposed smart load's dynamic performance following an abrupt frequency reduction, some variables of six smart induction motors (IMs) are shown in Figure 7-52 to Figure 7-62 for "WTPV 60% II" scenario. These six smart IMs are deliberately selected with different electrical distance to infeed loss's location, i.e. zone 23. These loads are bolded in Table 7-10. The

reserve power orders and their relative reference rotor speed are depicted in Figure 7-52 and Figure 7-53, respectively. The power orders are reached to their maximum limit in one second after infeed loss. The reserve power order of "Smart IM 15" and "Smart IM 23" are limited to 0.2 per unit and those of other four smart IMs are limited to 0.1 per unit. The reference rotor speeds are proportional to reserve power orders because of that motor's mechanical loads are assumed to be constant torque loads. In other words, a 10% reserve power needs to a 10% motor's speed reduction. These values stated in "%" instead of "pu" because they are determined as a portion of pre-fault operating point of induction motors. The reference rotor speeds of all six smart IMs are reached to determined post-fault values in about 10 seconds after infeed loss event, except the "Smart IM 15". As mentioned, this smart load and "Smart IMs 23" can reduce their power to 0.2 pu, but speed rate limit of later load is double that of "Smart IM 15". This difference results in what is shown in Figure 7-51 for the smart load in zone 15.

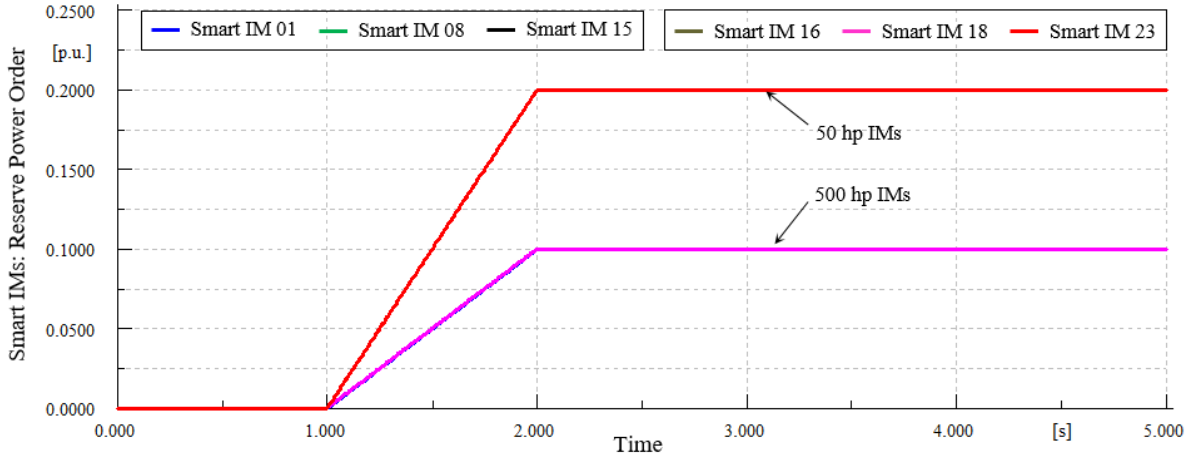

Figure 7-52: Reserve power order of the smart induction motors with loss of 1700 MW generation.

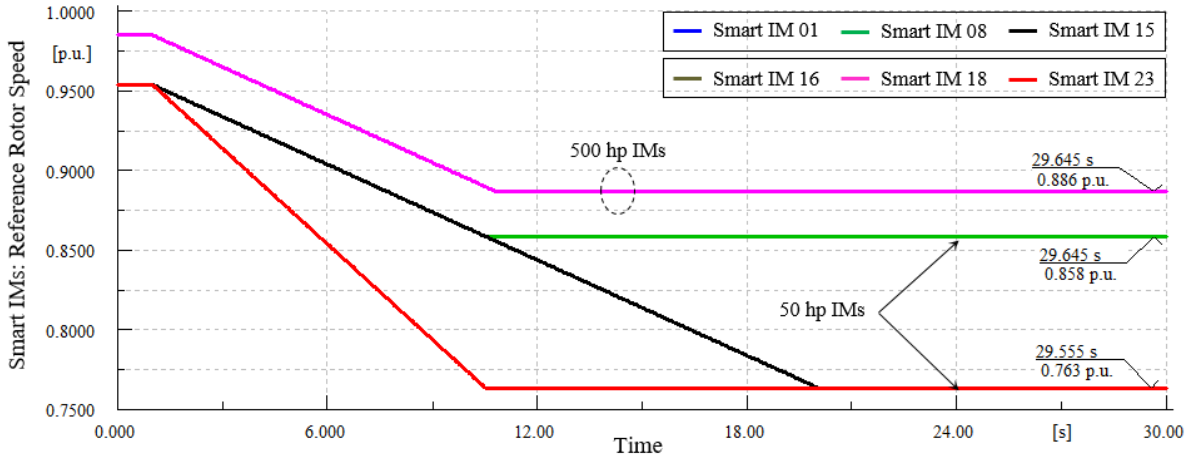

Figure 7-53: Reference rotor speeds of the smart induction motors with loss of 1700 MW generation.

The output signal of inertia emulator of the smart loads is depicted in Figure 7-54 and Figure 7-55. This signal, that emulates dynamic behaviour of a direct on line (DOL) induction motor, will be added to reserve electrical frequency to generate electrical frequency of inverter in variable frequency drive systems. How this signal changes determine electrical distance of related smart load to location of infeed loss. This can be clearly seen in Figure 7-55. According to reference rotor speed a reserve electrical frequency is calculated. By adding this reserve frequency to inertia emulator frequency, the reference electrical frequency, i.e. frequency of inverters in VFD systems, will be determined. This frequency is shown for the six smart loads in Figure 7-56. Note that magnitude of inverter's voltage is also changed proportional to frequency to get a constant flux linkage.

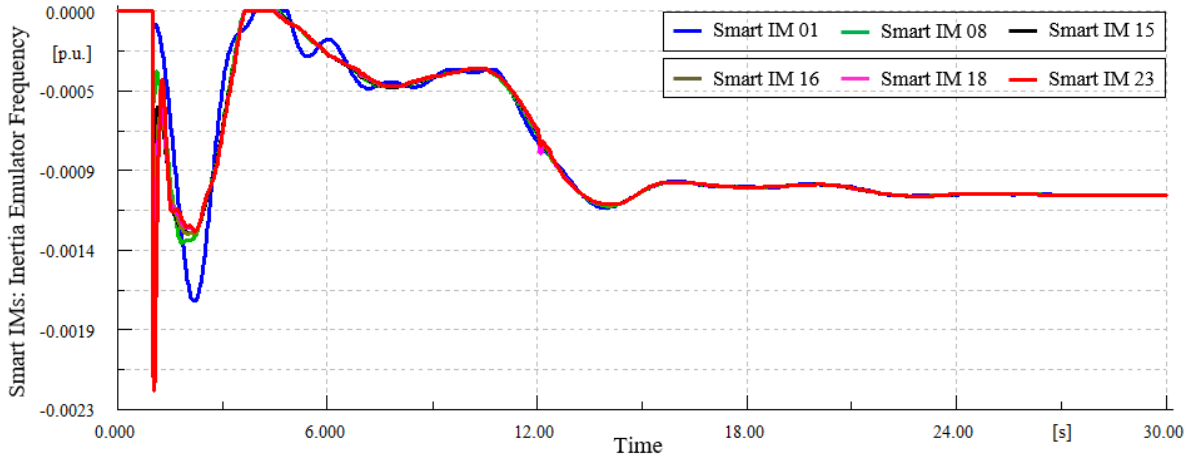

Figure 7-54: Inertia emulators electrical frequency of the smart IMs with loss of 1700 MW generation.

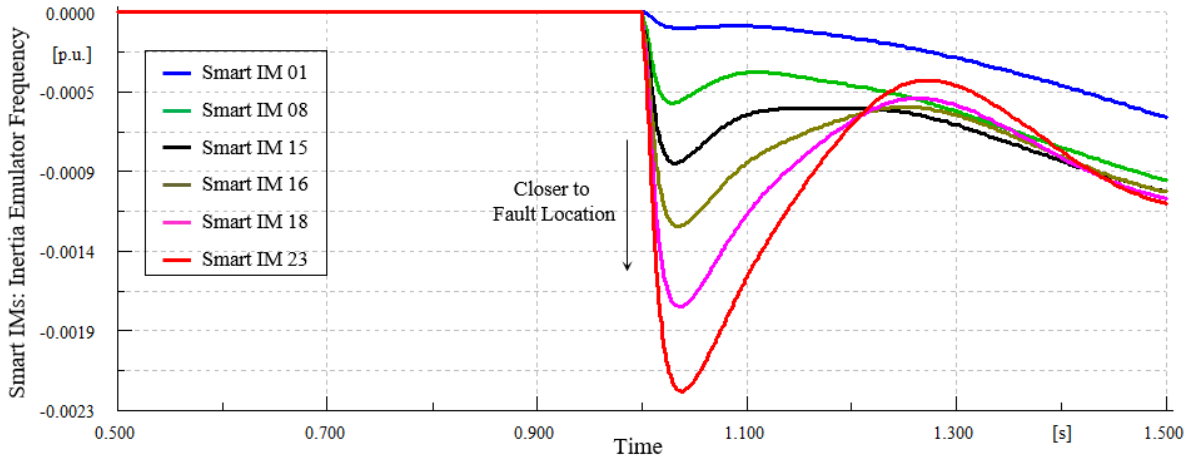

Figure 7-55: Inertia emulators electrical frequency of the smart induction motors with loss of 1700 MW generation (immediately after event).

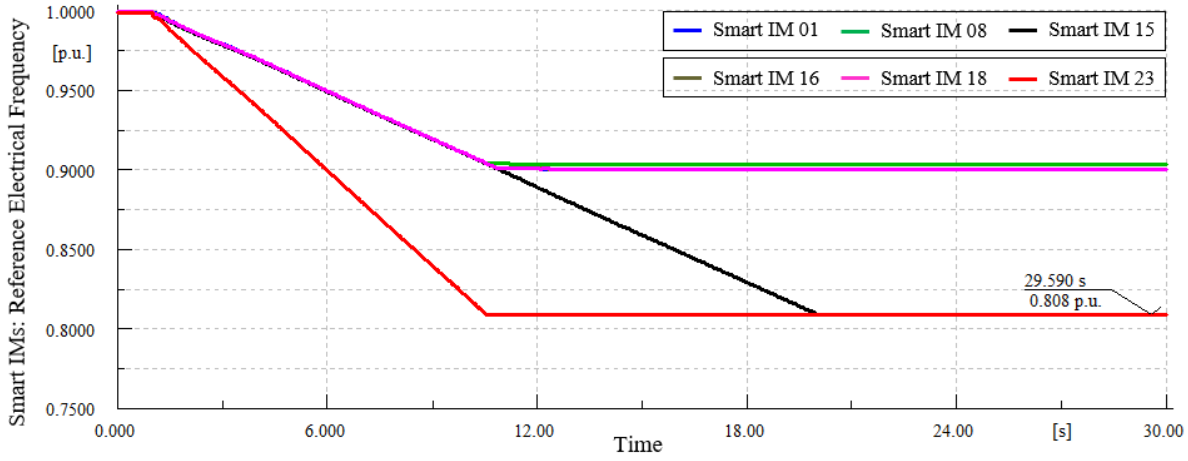

Figure 7-56: Reference electrical frequency of the smart induction motors with loss of 1700 MW generation.

When electrical frequency and voltage magnitude of the inverters change based on required reserve power, the operating point of induction motors on steady-state torque-slip characteristics will changes. As shown in Figure 7-57, this operating point change results in rotor speed reduction which in turn will result in

electromagnetic torque and stator current variations (see Figure 7-58 and Figure 7-59). Finally, active power of smart induction motors will change as shown in Figure 7-60. It is worth noting that mechanical load's inertia causes temporary variations of electromagnetic torques and stator currents to be significant. These variations, which are larger for a faster speed reduction, limit speed down rate to a value below 0.05 pu per seconds. The electromagnetic variations of 500 hp motor are bigger than that of 50 hp motors because of higher load inertia and steeper linear region of torque-slip characteristic in former. In other hand, more reserve power, like "Smart IM 15", results in wider time interval for temporary variation. Also, the active power of all three 500 hp motors in the given six motors reached to zero at about 5 seconds after infeed loss event. The "Smart IM 01" is equipped with an active front-end drive system and it operates in regeneration mode at 7-10 seconds time span.

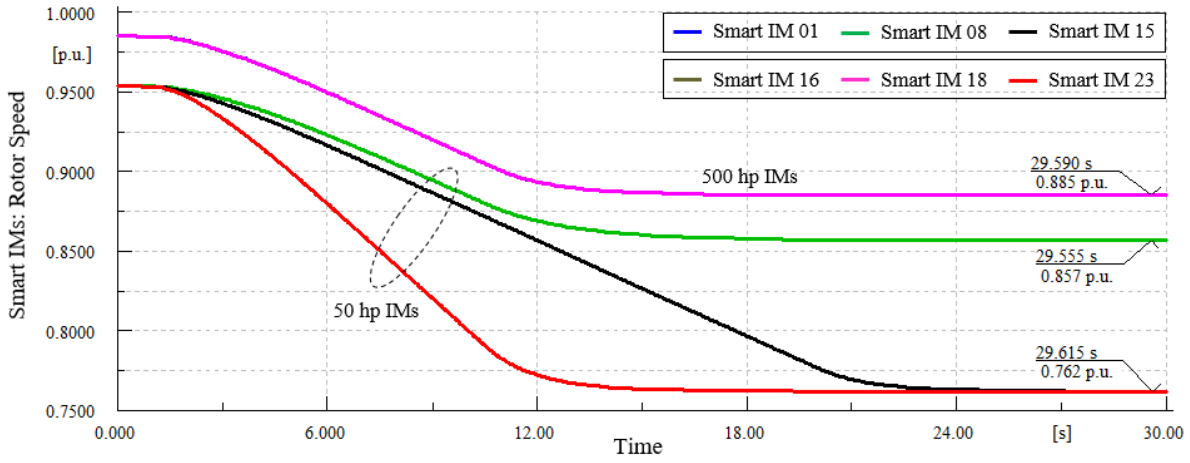

Figure 7-57: Rotor speeds of the smart induction motors with loss of 1700 MW generation.

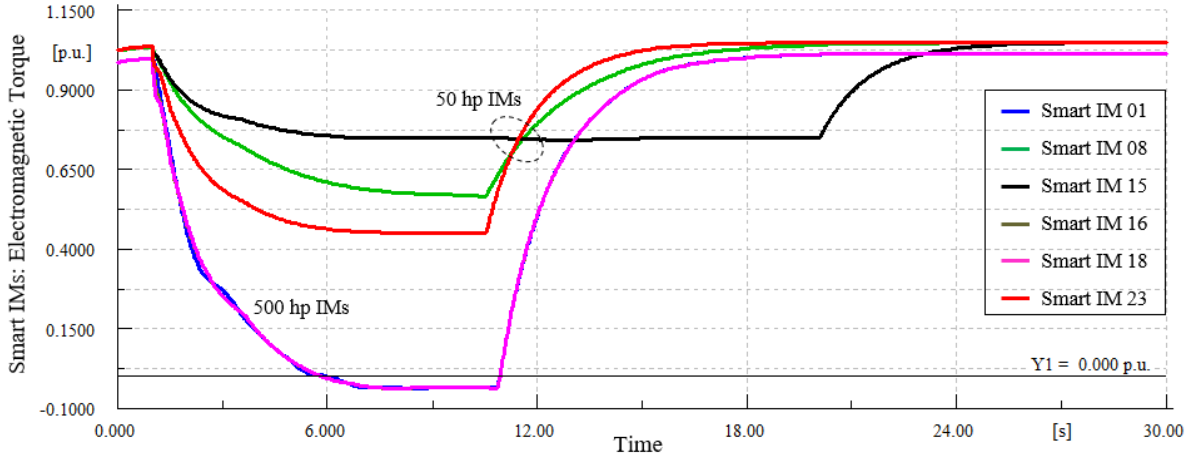

Figure 7-58: Electromagnetic torques of the smart induction motors with loss of 1700 MW generation.

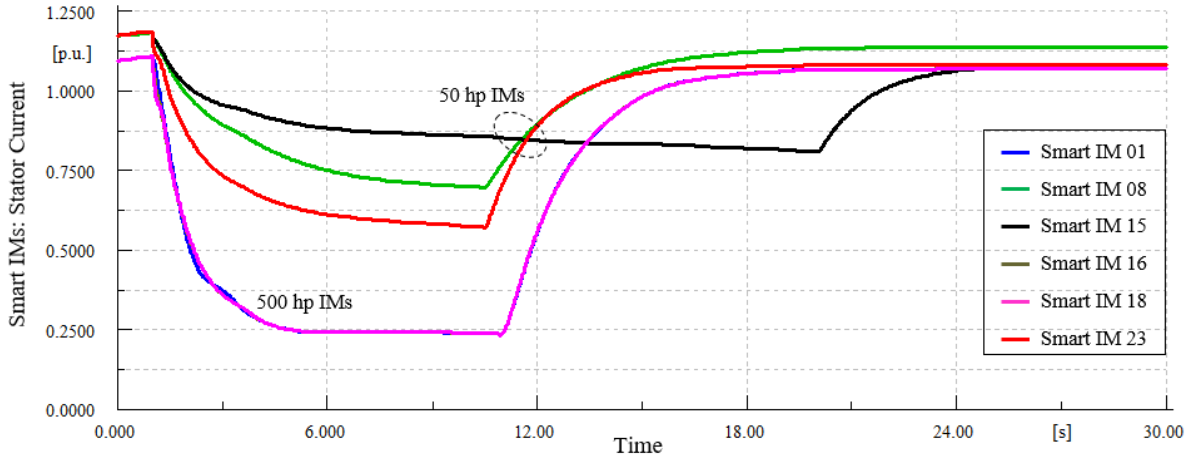

Figure 7-59: Stator currents of the smart induction motors with loss of 1700 MW generation.

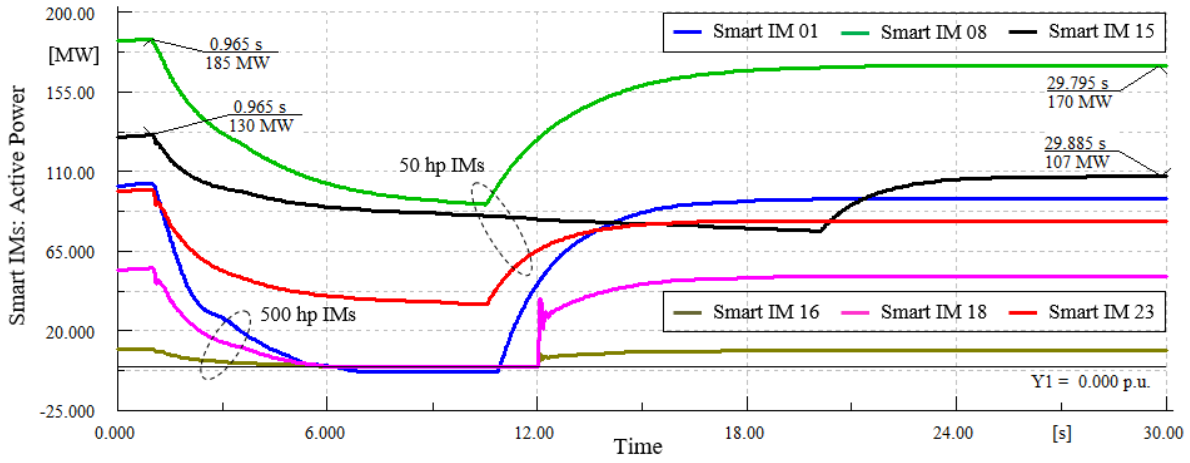

Figure 7-60: Active powers of the smart induction motors with loss of 1700 MW generation.

The total active power reduction of all 36 smart induction motors following infeed loss is shown in Figure 7-61. This trace has five time intervals. In first 5 seconds after event, active power of all smart induction motors is decreased. At about 5 seconds after infeed loss, active power of 50 hp motors with speed rate limit equal to 0.02 pu per seconds reached to their minimum values and then increase (for example see Figure 7-62). At time 10 s, active power of 50 and 500 hp motors equipped with AFE drive systems, with reserve power and speed rated limit equal to 0.1 pu and 0.01 pu per second, respectively, increase from their minimum value to post-fault steady-state operating points. This time is about 12 seconds for smart motors equipped with PFE drive systems. Finally, smart motors with reserve power and speed rated limit equal to 0.2 pu and 0.01 pu per second, respectively, like "Smart IM 15", start recovery from its minimum active power at t=20 s. As mentioned, the total smart motors demand is assumed to be 5% of total network demand, i.e. 2 GW. Therefore, maximum temporary power reduction from smart motors can be 2 GW when power of all of them reduced to zero. However, this value is about 1365 MW in this scenario as shown in Figure 7-61. Also, total steady-state active power reduction from all smart motors is 238 MW or about 12% of total pre-fault motor consumptions.

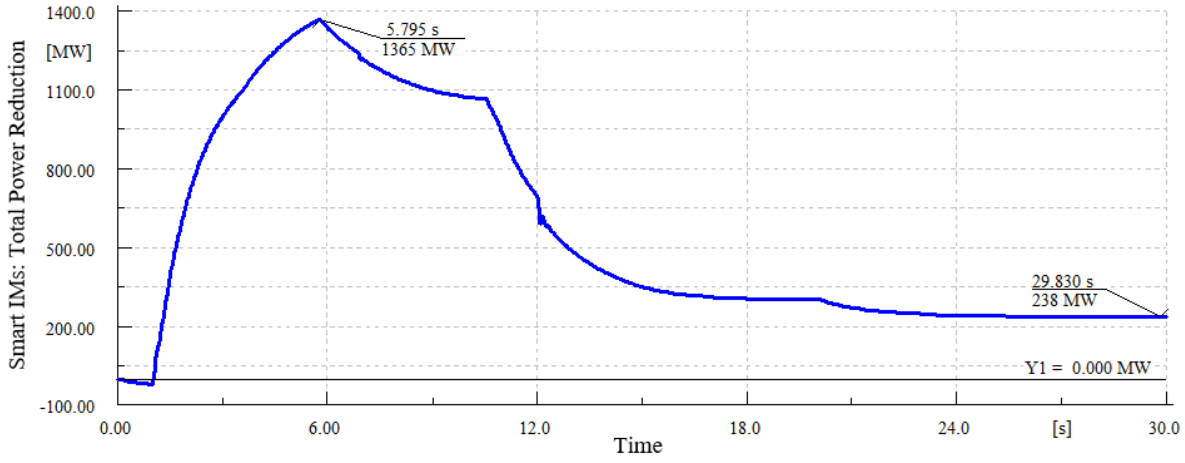

Figure 7-61: Total active power reduction of the smart induction motors with loss of 1700 MW generation.

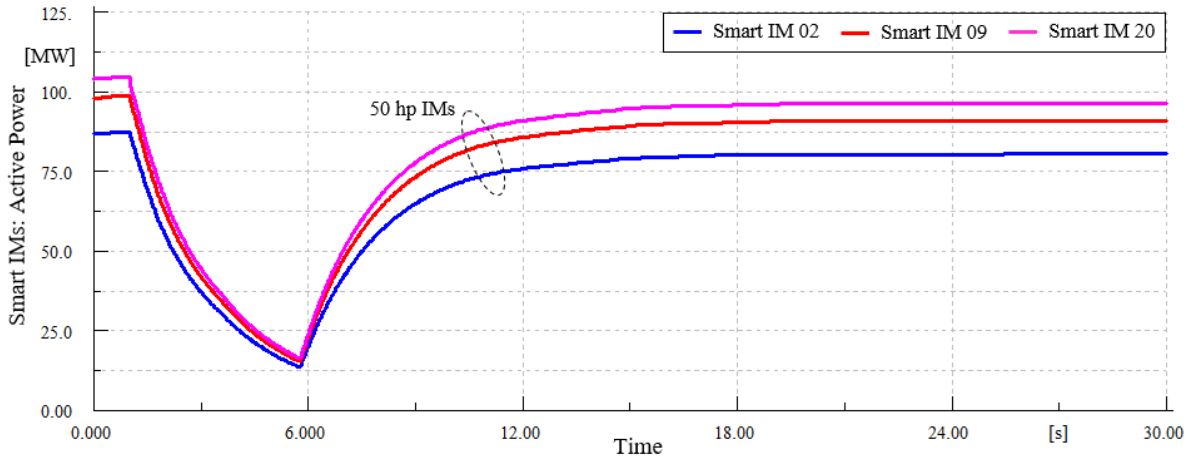

Figure 7-62: Active powers of the smart induction motors with loss of 1700 MW generation.

7.7.2. Executive Summary of Deploying SIM in 36-Zone GB System

In this chapter, the dynamic performance of the proposed smart induction motor in primary frequency control is investigated through 36-zone GB system frequency response. According to system studies in different scenarios, it is observed that the proposed smart load with primary frequency support capability can enhance frequency stability of the GB system. This results in, the primary frequency support burden on conventional power plants and or WTs and PVs units, also on BESS system is mitigated accordingly. This mitigation is significant in first seconds after infeed loss because of temporary large variations in active power consumption of smart induction motors. It is also deduced that closeness of the smart load to the disturbance location has not considerable impact on its primary frequency support if the droop parameter of its primary controller be smaller than that of power plants.

7.8. References

[1] V. Trovato, I. M. Sanz, B. Chaudhuri, and G. Strbac, "Advanced control of thermostatic loads for rapid frequency response in Great Britain," IEEE Trans. Power Syst., vol. 32, no. 3, pp. 2106-2117, May 2017.

[2] H. Xin, Y. Liu, Z. Wang, D. Gan, and T. Yang, "A new frequency regulation strategy for photovoltaic systems without energy storage," IEEE Trans. Sustain. Energy, vol. 4, no. 4, pp. 985-993, Oct. 2013.
[3] X. Yuan and Y. Li, "Control of variable pitch and variable speed directdrive wind turbines in weak grid systems with active power balance," IET Renew. Power Gener., vol. 8, no. 2, pp. 119-131, Mar. 2014.
[4] V. Knap, S. K. Chaudhary, D. I. Stroe, M. Swierczynski, B. I. Craciun, and R. Teodorescu, "Sizing of an energy storage system for grid inertial response and primary frequency reserve, IEEE Trans. Power Syst., vol. 31, no. 5, pp. 3447-3456, Sep. 2016.
[5] H. Geng, X. Xi, L. Liu, G. Yang, and J. Ma, "Hybrid modulated active damping control for dfig based wind farm participating in frequency response," IEEE Trans. Energy Convers., Feb. 2017.
[6] J. Van de Vyver, J. D. De Kooning, B. Meersman, L. Vandevelde, T. L. Vandoorn, "Droop control as an alternative inertial response strategy for the synthetic inertia on wind turbines," IEEE Trans. Power Syst., vol. 31, no. 2, pp. 1129-1138, Mar. 2016.
[7] X. Li, D. Hui, and X. Lai, "Battery energy storage station (BESS)-based smoothing control of photovoltaic (PV) and wind power generation fluctuations," IEEE Trans. Sustain. Energy, vol. 4, no. 2, pp. 464-473, Apr. 2013.
[8] M. Swierczynski, D. I. Stroe, A. I. Stan, R. Teodorescu, and D. U. Sauer, "Selection and performance-degradation modeling of LiMO2/Li4Ti5O12 and LiFePO4/C battery cells as suitable energy storage systems for grid integration with wind power plants: An example for the primary frequency regulation service," IEEE Trans. Sustain. Energy, vol. 5, no. 1, pp. 90-101, Jan. 2014.
[9] T. Masuta and A. Yokoyama, "Supplementary load frequency control by use of a number of both electric vehicles and heat pump water heaters, IEEE Trans. Smart Grid., vol. 3, no. 3, pp. 1253-1262, Sep. 2012.
[10] H. Liu, Z. Hu, Y. Song, J. Wang, and X. Xie, "Vehicle-to-grid control for supplementary frequency regulation considering charging demands", IEEE Trans. Power Syst., vol. 30, no. 3, pp. 3110-3119, Nov. 2015.
[11] S. Izadkhast, P. Garcia-Gonzalez, and P. Frías, "An aggregate model of plug-in electric vehicles for primary frequency control", IEEE Trans. Power Syst., vol. 30, no. 3, pp. 1475-1482, May 2015.
[12] G. Delille, B. Francois, and G. Malarange, "Dynamic frequency control support by energy storage to reduce the impact of wind and solar generation on isolated power system's inertia," IEEE Trans. Sustain. Energy, vol. 3, no. 4, pp. 931-939, Oct. 2012.
[13] D. I. Stroe, V. Knap, M. Swierczynski, A. I. Stroe, and R. Teodorescu, "Operation of a grid-connected lithium-ion battery energy storage system for primary frequency regulation: A battery lifetime perspective," IEEE Trans. Industry Appl., vol. 53, no. 1, pp. 430-438, Jan. 2017.
[14] P. Mercier, R. Cherkaoui, and A. Oudalov, "Optimizing a battery energy storage system for frequency control application in an isolated power system," IEEE Trans. Power Syst., vol. 24, no. 3, pp. 1469-1477, Aug. 2009.
[15] L. S. Vargas, G. Bustos-Turu, and F. Larraín, "Wind power curtailment and energy storage in transmission congestion management considering power plants ramp rates," IEEE Trans. Power Syst., vol. 30, no. 5, pp. 2498-2506, Sep. 2015.
[16] M. R. Moghadam, R. T. Ma, and R. Zhang, "Distributed frequency control in smart grids via randomized demand response, IEEE Trans. Smart Grid, vol. 5, no. 6, pp. 2798-2809, Nov. 2014.
[17] Z. Akhtar, B. Chaudhuri, S. Y. Hui, "Primary frequency control contribution from smart loads using reactive compensation," IEEE Trans. Smart Grid, vol. 6, no. 5, pp. 2356-2365, Sep. 2015.
[18] M. Bayat, K. Sheshyekani, M. Hamzeh, and A. Rezazadeh, "Coordination of distributed energy resources and demand response for voltage and frequency support of MV microgrids," IEEE Trans. Power Syst., vol. 31, no. 2, pp. 1506-1516, Mar. 2016.
[19] C. K. Lee, N. R. Chaudhuri, B. Chaudhuri, and S. R. Hui, "Droop control of distributed electric springs for stabilizing future power grid," IEEE Trans. Smart Grid, vol. 4, no. 3, pp. 1558-1566, Sep. 2013.
[20] X. Chen, Y. Hou, S. C. Tan, C. K. Lee, and S. Y. Hui, "Mitigating voltage and frequency fluctuation in microgrids using electric springs, IEEE Trans. Smart Grid, vol. 6, no. 2, pp. 508-515, Mar. 2015.
[21] S. H. Tindemans, V. Trovato, and G. Strbac, "Decentralized control of thermostatic loads for flexible demand response," IEEE Trans. Control Syst. Tech., vol. 23, no. 5, pp. 1685-1700, Sep. 2015.
[22] D. Angeli and P. A. Kountouriotis, "A stochastic approach to 'dynamic demand' refrigerator control," IEEE Trans. Control Syst. Technol., vol. 20, no. 3, pp. 581-592, May 2012.
[23] A. H. Mohsenian-Rad, V. W. S. Wong, J. Jatskevich, R. Schober, and A. Leon-Garcia, "Autonomous demand-side management based on game-theoretic energy consumption scheduling for the future smart grid," IEEE Trans. Smart Grid, vol. 1, no. 3, pp. 320-331, Dec. 2010.
[24] D. Chakravorty, B. Chaudhuri, and S. Y. Hui, "Rapid frequency response from smart loads in Great Britain power system," IEEE Trans. Smart Grid, Oct. 2016.

[25] N. R. Chaudhuri, C. K. Lee, B. Chaudhuri, and S. R. Hui, “Dynamic modeling of electric springs,” IEEE Trans. Smart Grid, vol. 5, no. 5, pp. 2450-2458, Sep. 2014.
[26] C. K. Lee and S. Y. Hui, “Reduction of energy storage requirements in future smart grid using electric springs,” IEEE Trans. Smart Grid, vol. 4, no. 3, pp. 1282-1288, Sep. 2013.
[27] X. Luo, Z. Akhtar, C. K. Lee, B. Chaudhuri, S. C. Tan, S. Y. Hui, “Distributed voltage control with electric springs: Comparison with STATCOM,” IEEE Trans. Smart Grid, vol. 6, no. 1, pp. 209-219, Jan. 2015.
[28] Z. Liu, Z. Zheng, and Y. Li, “Enhancing fault-tolerant ability of a nine-phase induction motor drive system using fuzzy logic current controllers,” IEEE Trans. Energy Convers., Apr. 2017.
[29] Krause, Paul, et al. Analysis of electric machinery and drive systems. Vol. 75. John Wiley & Sons, 2013.
[30] Bimal K. Bose. Modern power electronics and AC drives. 2002.
[31] D. Chakravorty; B. Chaudhuri; S. Y. R. Hui, "Rapid Frequency Response From Smart Loads in Great Britain Power System," in IEEE Transactions on Smart Grid, vol.PP, no.99, pp.1-10.
[32] V. Trovato, I. M. Sanz, B. Chaudhuri and G. Strbac, “Advanced Control of Thermostatic Loads for Rapid Frequency Response in Great Britain,” in IEEE Transactions on Power Systems, vol. 32, no. 3, pp. 2106-2117, May 2017.
[33] Kundur P. Power system stability and control. Balu NJ, Lauby MG, editors. New York: McGraw-hill; 1994 Jan 1.
[34] Karimi-Ghartema, Masoud. Enhanced phase-locked loop structures for power and energy applications. John Wiley & Sons, 2014.
[35] Yazdani, Amirnaser, and Reza Iravani. Voltage-sourced converters in power systems: modeling, control, and applications. John Wiley & Sons, 2010.

8. A New Approach to the On-line Estimation of the Loss of Generation Size in Power Systems

Following an unintended disconnection of a synchronous generator (SG) from the power system, what is also known as a loss of generation (LoG), it is not trivial to precisely estimate the post-event power system's inertia and the LoG size. One of reasons for that is that both of them are a function of the unknown inertia reduction. To solve this challenging problem, this paper presents an analytical method based on the rate-of-change-of-frequency (RoCoF). The method relies on a modified swing equation, allowing a simultaneous estimation of both unknowns independently. To this end, the values of mechanical starting time, apparent power and loading of lost generator are formulated for the power system under study. In a practical application, the method can use RoCoF measured by phasor measurement units (PMUs). The paper discusses the impact of various frequency estimation approaches to the proposed LoG estimation. Furthermore, a new method for LoG size estimation, based on the interpolated estimated inertial response, is proposed. The efficiency of the proposed approach is validated through extensive simulations with Matlab/Simulink using a simple power system and the IEEE 39-bus test network.

8.1. Literature Review

Loss of generation (LoG) can cause frequency instability and this phenomenon is of particular interest for future power systems characterized by high penetration of power-electronic-interfaced renewable generation that produces a reduction of the system's inertia [1]. Enhanced frequency control mechanisms are expected to provide fast frequency response to mitigate the consequences associated to the system inertia reduction and these control mechanisms do require a suitable coupling with wide-area monitoring and control systems [1]-[2]. As well-known, the inertial response (IR) in power systems comes from the kinetic energy stored in the rotating shaft of SGs and rotating electrical motors from the demand side. Immediately after a LoG, the lost power is supplied by the IR and after that by the SGs governors [3]. In the other hand, under-frequency load shedding (UFLS) has been commonly used for preventing frequency instability following severe contingencies. In conventional UFLS schemes, non-critical loads are sequentially shed, based on a-priori assumptions and past experience [4]. However, it is essential to minimize the amount of load to be shed using adaptive mechanisms [5]-[9]. In the framework introduced in [5], the optimal load shedding plan can be created based on the estimated power imbalance using the swing equation. In [6], the LoG size is estimated by considering voltage dependency of the loads for adjusting the adaptive UFLS schemes in order to utilize as much as possible the primary frequency support. In [7] a strategy for updating the estimated LoG during load shedding process through the system's inertia constant estimation is introduced. In [8], load shedding amount is analytically derived by solving the swing equation considering ramp-shape governor response to achieve minimal load shed. Recently, an improved UFLS is presented. It is based on the calculation of power imbalance during load shedding process using equivalent swing equation of power system [9].

Therefore, power system dynamic modelling and the estimation of the system' inertia and LoG size, play the critical roles in deriving adaptive load shedding schemes. In this context, in [10] the inertial, governor and automatic generation control responses, following a LoG event, are investigated by Lotfalian, et al.. The IR is determined using the system's inertia and the RoCoF. However, this approach assumes that the RoCoF is the same for all the SGs following the LoG event. The inertia constant of a Japanese power system is estimated in [11] using the swing equation with frequency and LoG size as known input variables. Terzija, et al. proposed a framework relying on a PMU-based Wide Area Monitoring System (WAMS) to estimate the magnitude of active power disturbances in distribution networks [12]. In this study, particular reference is given to the inclusion of wind farms. However, in [12], it is considered that the loss of the up-stream grid as the main LoG

contingency and it is assumed that the total inertia of the isolated distribution network is available for the LoG size estimation process. In [13], the time of the LoG disturbance and post-event power system's inertia are simultaneously estimated using synchronized on-line WMAS. However, the measured active power mismatch after the frequency event is used to estimate the loss of inertia not disturbance size. Similarly, Ashton, et al., proposed a method to estimate the inertia of the residual resources in the Great Britain power system based on the known and estimated LoG sizes [14]. The inertia of Nordic power system is estimated through the modeling the power variation after a frequency event using a) RoCoF data [15] or b) an average system's voltage [16], under known power imbalance value. Recently, a method to estimate power mismatch after an abrupt incident has been proposed, based on the generalized injection shift factors concept [17]. However, instead of an infeed loss, the study focuses on a loss of load. Finally, the approaches to model the frequency and voltage dependencies of the power variation following a LoG event proposed in [15] and [16], are combined in [18] to better estimate the system's inertia constant.

In most of these studies, the system inertia is estimated using the well-known swing equation with the SGs' rotor speed as available measurements and LoG size as inputs. Additionally, the LoG size is estimated using the system inertia assumed as a known parameter. Regardless of the estimated variable, an improper common practice in the inertia or LoG size estimation is to neglect the reduction of the system inertia. It can be shown that this deficiency, i.e., the underestimating the system inertia reduction, results in a percentage error roughly equal to the lost power size normalized to the system's base power. In order to bridge this gap, this chapter proposes an analytical and on-line approach that allows improving the accuracy of the LoG active power size estimation via formulating the lost inertia in the swing equation. In this regard, the estimated lost inertia is subtracted from the pre-event system's inertia to give an estimation of the post-event system's inertia, through the definition of dedicated auxiliary parameters associated with the SGs. Initially, the inertia constant, apparent power and loading of the unknown lost SG, are formulated using pre-event system's operational data in order to modify the conventional swing equation-based LoG size estimation approach. Then, through an on-line estimation procedure, the post-event system's inertia and the IR are simultaneously can be determined. In the computer-aided simulation tools, whereas the LoG estimation can be conducted using mechanical speed of SGs, this variable is not practically measurable. In fact, the frequencies measured by PMUs which are installed at the terminals of SGs are the input data for the proposed estimation process. Theoretically, the IR value gives the LoG size immediately following the LoG event [16]. However, this may not be a practical solution to quantify the lost power in view of the uncertainties of measurements immediately after the event [11]. In this respect, a simple and reliable technique based on the IR interpolation is deployed to obtain the LoG size estimation. To be more specific, a 5th order interpolation is applied on the estimated IR to compensate for the potential unreliability of data measured right after the event and achieve accurate LoG.

The chapter also addresses the associated implementation challenges of the estimation process using WAMS systems [19], [20]. A LoG event is accompanied with the voltage angle jump, then it negatively affects frequencies measured by PMUs immediately after the disturbance [21]. Consequently, the efficacy of the proposed LoG size estimation approach is studied using real PMUs in which a commercially-available synchrophasor estimation algorithm is deployed. Further, the PMU reporting latency is also taken into account [22]. The efficacy of the proposed approach is verified by a simple test system and, then, IEEE 39-bus system in Matlab/Simulink software under two scenarios of SG's rotor speeds and PMUs' frequencies as input variables for the estimation process.

8.2. Loss of Generation Size Estimation: The Conventional Approach

According to the Newton's second law of motion, if there is an imbalance between the mechanical's prime mover torque of a synchronous generator, T_m, and its load electromagnetic torque, T_e, the SG's rotor mechanical angular speed ω_m, can be calculated by the swing differential equation [3]:

$$T_m - T_e = \frac{d}{dt}\left(J\omega_m\right) \approx J\frac{d}{dt}\left(\omega_m\right) \tag{8.1}$$

where, J is the total moment of inertia of the SG's rotor and the turbine's shaft in [kg·m^2]. In (8.1), it is assumed that the rotor is solid, so that its moment of inertia variation over time can be ignored. Here, the torques and rotor speed are expressed in [N·m] and [rad/sec], respectively. In power system studies, it is preferable to define a per-unit inertia constant H, as the kinetic energy in [W·s] at the rated speed divided by the [VA] base. For the sake of simplicity, $2H$ is defined as the *mechanical starting time M*, as follows [3]:

$$M = 2H = 2\left[\left(0.5J\omega_{mb}^2\right)\left(S_b\right)^{-1}\right] \tag{8.2}$$

where, ω_{mb} and S_b are the base mechanical speed and the apparent power in [rad/sec] and [VA], respectively. Consequently, the units of H and M would be seconds. By using the above definitions, (8.1) becomes:

$$T_m - T_e = \frac{S_b M}{\omega_{mb}^2}\frac{d}{dt}\left(\omega_m\right) = \frac{S_b M}{\omega_{mb}}\frac{d}{dt}\left(\bar{\omega}_m\right) \tag{8.3}$$

where, $\bar{\omega}_m$ is mechanical speed in per-unit. In order to explain how to conventionally estimate the LoG size, let us consider a typical power system with n SGs actuated by n turbines and supplying m electrical loads (see Figure 8-1).

The swing equation (8.3) can be modified to consider a small perturbation around the equilibrium point denoted in (8.4) by zero subscript for the i-th generator.

$$\left(T_{m0,i} + \Delta T_{m,i}\right) - \left(T_{e0,i} + \Delta T_{e,i}\right) = \frac{S_{b,i}}{\omega_{mb}} M_i \frac{d}{dt}\left(\bar{\omega}_{m0,i} + \Delta\bar{\omega}_{m,i}\right) \tag{8.4}$$

Since at the equilibrium point the SG's speed is constant and electromagnetic torque is equal to the mechanical torque, the following equation can be obtained:

$$\Delta T_{m,i} - \Delta T_{e,i} = \frac{S_i}{\omega_{mb}} M_i \frac{d}{dt}\left(\Delta\bar{\omega}_{m,i}\right) \tag{8.5}$$

Let us assume that the j-th generator has been abruptly disconnected from the grid. The sudden disconnection of the j-th SG means that its generated electromagnetic torque is null following its sudden disconnection. This phenomenon can be expressed by (8.6) and considered in (8.4).

$$\Delta T_{e,j} = -T_{e0,j} \tag{8.6}$$

Since the post-event averaged voltage variation in the entire power system is negligible, the lost electromagnetic torque supplied by the rest of SGs can be interpreted as:

$$\sum_{i=1,\neq j}^{n} \Delta T_{e,i} = -\Delta T_{e,j} \tag{8.7}$$

The participation of each on-line generator to the lost electromagnetic torque generation depends on its respective rating and electrical distance to the disconnected generator. Thus, the following equation is yielded by extending (8.5) to all the generators except the lost one:

$$\sum_{i=1,\neq j}^{n} \Delta T_{m,i} - \sum_{i=1,\neq j}^{n} \Delta T_{e,i} = \frac{1}{\omega_{mb}} \sum_{i=1,\neq j}^{n} \left(S_{b,i} M_i \frac{d}{dt}\left(\Delta\bar{\omega}_{m,i}\right)\right) \tag{8.8}$$

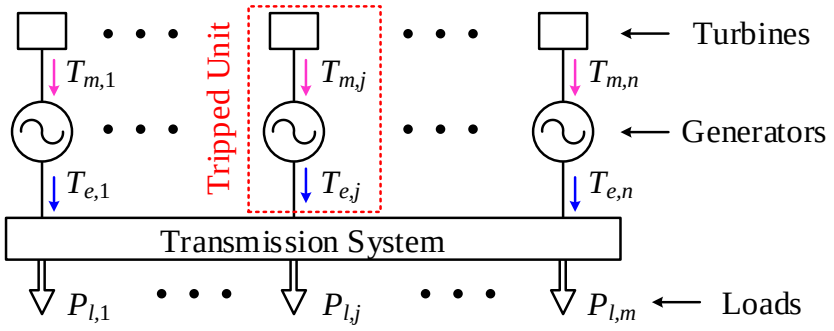

Figure 8-1: A typical power system containing *n* generators and *m* loads.

Since the tripped SG is unknown, it is impossible to remove the *j*-th index from the right-hand side of (8.8). As an approximation in the conventional LoG size estimation, the right-hand side of (8.8) can be rewritten in terms of the angular speed of the equivalent centre of inertia (COI), defined as [23]:

$$\bar{\omega}_m^{COI} = \left(\sum_{i=1}^{n}\left(S_i M_i \bar{\omega}_{m,i}\right)\right)\left(\sum_{i=1}^{n}\left(S_i M_i\right)\right)^{-1} \tag{8.9}$$

As a result, by substituting (8.9) in (8.8), one obtains:

$$\sum_{i=1,\neq j}^{n} \Delta T_{m,i} - \sum_{i=1,\neq j}^{n} \Delta T_{e,i} \approx \frac{1}{\omega_{mb}}\left(\sum_{i=1}^{n}\left(S_{b,i} M_i\right)\right)\frac{d}{dt}\left(\Delta\bar{\omega}_m^{COI}\right) \tag{8.10}$$

Since the tripped SG is unknown, the almost equal sign is used. In other words, the left-hand side of (8.10) corresponds to the (*n*-1) SGs which are on-line after the event, while its right one associates with all the *n* SGs including the tripped unit. It is worth observing that in the first few seconds following the event, the first term of the left-hand side of (8.10), which is pertinent to the mechanical parts of the power plants, can be ignored due to the slow-changing mechanical torque relative to the electromagnetic torque [3]. With this assumption, by using (8.6) and (8.7), the lost electromagnetic torque can be estimated as follows:

$$T_{e0,j} \approx -\frac{1}{\omega_{mb}}\left(\sum_{i=1}^{n}\left(S_i M_i\right)\right)\frac{d}{dt}\left(\Delta\bar{\omega}_m^{COI}\right) \tag{8.11}$$

Finally, the LoG size expressed in terms of the active power imbalance can be conventionally estimated as follows:

$$P_{e0,j} = \omega_m^{COI} T_{e0,j} \approx \omega_{mb} T_{e0,j} = -SM_{pre-event}\frac{d}{dt}\left(\Delta\bar{\omega}_m^{COI}\right) \tag{8.12}$$

where,

$$SM_{pre-event} = \sum_{i=1}^{n}\left(S_i M_i\right) \tag{8.13}$$

Each SG in Figure 8-1 is representative of one or a group of power plants. They are also composed by a set of synchronous machines that are not necessarily identical. In other words, parameters of equivalent SGs should be calculated by the COI concept.

8.3. Loss of Generation Size Estimation: A New Approach

The novelty of the proposed approach lies in the possibility of directly assessing the reduced inertia to be used in (11) in order to improve the accuracy of the estimation of the power imbalance, i.e., the lost active power. Thus, (8.12) can be rewritten as:

$$P_{e0,j} = -SM_{post-event}\frac{d}{dt}\left(\Delta\bar{\omega}_m^{COI}\right) \tag{8.14}$$

where, $SM_{post\text{-}event}$ denotes the post-event system's inertia considering the lost inertia, which can be rewritten as:

$$SM_{post-event} = SM_{pre-event} - S_{b,j}M_j \tag{8.15}$$

Unlike in (8.12), the *j*-th index of inertia has been removed from the algebraic summation on the right-hand side of (8.15). However, determining the exact amount of the reduced inertia $S_{b,j}M_j$, is impossible. In order to resolve this barrier, an online method is proposed hereinafter. The pre-event active power loading of the tripped generator is employed to replace the unknown $S_{b,j}$ with a known term in (8.15). In this regard, the pre-event active power loading of the lost unit can be calculated as:

$$L_j = P_{e0,j}\left(S_j\right)^{-1} \tag{8.16}$$

Combining (8.15) and (8.16), $SM_{post\text{-}event}$ can be rewritten as follows:

$$SM_{post-event} = SM_{pre-event} - P_{e0,j}M_j\left(L_j\right)^{-1} \tag{8.17}$$

Next, combining (8.14) and (8.17) yields:

$$P_{e0,j} = -\left(SM_{pre-event} - P_{e0,j}M_j\left(L_j\right)^{-1}\right)\frac{d}{dt}\left(\Delta\bar{\omega}_m^{COI}\right) \tag{8.18}$$

Note that $P_{e0,j}$ appears in both the left- and right-hand sides of (8.18), showing the estimated and real values of the LoG, respectively. By substituting the real value with the estimated one, (8.18) becomes:

$$P_{e0,j} = -\frac{SM_{pre-event}\frac{d}{dt}\left(\Delta\bar{\omega}_m^{COI}\right)}{1-\frac{M_j}{L_j}\frac{d}{dt}\left(\Delta\bar{\omega}_m^{COI}\right)} \tag{8.19}$$

This can be further simplified as follows:

$$P_{e0,j} = -K_{SM}SM_{pre-event}\frac{d}{dt}\left(\Delta\bar{\omega}_m^{COI}\right) \tag{8.20}$$

where,

$$K_{SM} = \left(1-\frac{M_j}{L_j}\frac{d}{dt}\left(\Delta\bar{\omega}_m^{COI}\right)\right)^{-1} \tag{8.21}$$

Eq. (8.20) represents a new approach for on-line LoG size estimation which results in a more accurate estimation of LoG size, compared to the conventional approach expressed through (8.12). In (8.21), the speed deviation derivative is a negative quantity, so that the reduced inertia coefficient K_{SM} is lower than 1. In the conventional approach, it is equal to 1. In other words, this reduced inertia coefficient K_{SM} models the system

inertia reduction after the event in the proposed LoG size estimation. Recall that on one hand, the estimated post-event system's inertia is:

$$SM_{post-event} = K_{SM} SM_{pre-event} \tag{8.22}$$

In the other hand, the lost inertia can be estimated as:

$$SM_{LoG} = \left(1 - K_{SM}\right) SM_{pre-event} \tag{8.23}$$

At this point, it is instructive to have a deeper insight into the proposed estimation process associated with inertia reduction and LoG size. In this context, let us assume that $P_{e0,j}$ is the estimated LoG in both-hand sides of (8.18). It can be deduced that the post-event system's inertia and the LoG size can be consequently estimated in real-time state. For the sake of explanation, the following off-line recursive rules mimicking the proposed LoG size estimation are provided:

For $k = 1$ **to** $N_{\max}$

Calculate

$$\begin{aligned} SM_{post-event}(k) &= SM_{pre-event} - \left(L_j\right)^{-1} M_j P_{e0,j}(k-1) \\ P_{e0,j}(k) &= -\left[SM_{post-event}(k)\right] \frac{d}{dt}\left(\Delta\bar{\omega}_m^{COI}(k)\right) \end{aligned} \tag{8.24}$$

End For

where, $P_{e0,j}(0)$ is equal to zero, N_{max} is the total number of sampling periods within the estimation time interval. At the first observation, the post-event inertia is equal to its pre-event value. In contrast, the LoG size $P_{e0,j}$ is greater than zero. In the second observation, the post-event inertia will be updated based on the estimated LoG size at the pervious window. In addition, $P_{e0,j}$ will be determined using the updated post-event inertia. This loop repeats for N_{max} windows. Note that, as mentioned, (8.20) has an on-line nature and the rules presented in (8.24) are provided only for the sake of a more detailed clarification of (8.20). In other words, the post-event system inertia and the LoG size estimations should be done simultaneously and independently using (8.20) to (8.22).

Note that M_j and L_j deployed in (8.15) to (8.21) are unknown. Since all the equations and parameters are adaptively updated in the proposed method, the sensitivity of the derived technique to the above-mentioned parameters is minor. However, the rough but reasonable initial values should be selected for M_j and L_j. For instance, the pre-event system's loading can be selected for L_j as follows:

$$L_j^{init} = \left(\sum_{i=1}^{n} P_{e0,i}\right)\left(\sum_{i=1}^{n} S_i\right)^{-1} \tag{8.25}$$

where, L_j^{init} is the initial value of L_j. In the other hand, the initial value of M_j is set to the mechanical time constant of the unit with highest forced outage rate (FOR):

$$M_j^{init} = M \text{ of unit with highest FOR} \tag{8.26}$$

Note that these initialized parameters will not be updated during the estimation process (i.e., they are constant). It is useful to obtain the sensitivity of the estimated LoG size by the proposed method to these parameters as follows:

$$\frac{\partial P_{e0,j}}{\partial M_j} \propto \frac{\partial K_{SM}}{\partial M_j} = L_j^{-1}\left(1 - M_j L_j^{-1}\frac{d}{dt}\left(\Delta\bar{\omega}_m^{COI}\right)\right)^{-2}\frac{d}{dt}\left(\Delta\bar{\omega}_m^{COI}\right) \tag{8.27}$$

$$\frac{\partial P_{e0,j}}{\partial L_j} \propto -M_j L_j^{-2}\left(1 - M_j L_j^{-1}\frac{d}{dt}\left(\Delta\bar{\omega}_m^{COI}\right)\right)^{-2}\frac{d}{dt}\left(\Delta\bar{\omega}_m^{COI}\right) \tag{8.28}$$

Equations (8.27) and (8.30) indicate that the slope of the estimated LoG size (or its estimation error) with respect to M_j and L_j variations has the negative and positive value, respectively (see Figure 8-9 and Figure 8-12). In other words, by increasing M_j (or L_j) with regard to its real value, the estimated LoG size tends to be lower (greater) than its true value. These sensitivity analyses are validated in the simulation results section.

8.4. Loss of Generation Size Estimation: Implementation Considerations

This section firstly investigates the effect of different load models on the proposed LoG size estimation. Furthermore, it quantifies the impact related to the errors associated to the frequency measured by PMUs. With respect to the latter aspect, an appropriate solution is proposed and discussed.

8.4.1. Impact of the Load Characterization

Load characteristics have a key role in power system dynamics studies such as the LoG size estimation [24]. Usually, the voltage-dependency of loads is modelled as [25]:

$$P_L = \sum_{j=1}^{m}\left(p_{1,j}\bar{V}_j^{\,2} + p_{2,j}\bar{V}_j + p_{3,j}\right)P_{L0,j} \tag{8.29}$$

where, $P_{L0,j}$ and V_j represent the nominal power and voltage of j-th load in per-unit, respectively. The $p_{1,j}$, $p_{2,j}$, and $p_{3,j}$ denote the proportion of constant impedance loads (CILs), constant current loads (CCLs) and constant power loads (CPLs) in the j-th load, respectively. The frequency-dependency of the loads can be represented as follows [26]:

$$P_L = \sum_{j=1}^{m}\left(1 + K_{pf,j}\Delta f_j\right)P_{L0,j} \tag{8.30}$$

where, $K_{pf,j}$ is the load damping constant of load j typically in the range of 0 to 3 [24], Δf_j is frequency deviation at the j-th load bus. By assuming an efficient voltage control in the entire power system, the power variation of the CILs and CCLs can be ignored and the load's power deviation can be estimated as:

$$\Delta P_L \approx \sum_{j=1}^{m}\left(K_{pf,j}\Delta f_j\right)P_{CPL,j} \tag{8.31}$$

where, $P_{CPL,j}$ is the CPL load for the j-the demand. As mentioned, the lost energy is supplied by the on-line SGs which initially provide the IRs. Following the IR, the SGs' governor responses (GRs) limit the change in frequency by providing the lost energy and part of the released IR while the frequency deviation exceeds a pre-defined threshold. Therefore, the LoG size estimation must be accomplished before the GRs initiation otherwise the first term in the left-hand side of (8.10) would be unknown. Then, the LoG should be estimated using the frequency data before GRs' initiation. In this time interval, the deviation in generation side, i.e., P_{LoG} plus deviation in demand side, i.e., ΔP_L is supplied by inertial responses on the on-line SGs P_{IR}. This means:

$$IR = P_{LoG} + \Delta P_L \tag{8.32}$$

In other words, the IR is also dependent to the load's power deviation. Frequency and load's power deviations, along with the IR following a LoG event, are qualitatively shown in Figure 8-2. As can be seen, Δf decreases linearly before the GRs initiation which in turn results in an increased reduction in the load's power. The P_{IR} is determined by subtracting this power reduction from the lost power. Note that if the lost power is known, then an approximated P_{IR} (not its true value) can be achieved by substituting (8.31) in (8.32). The approximated IR is used for the comparison purpose in the simulation results. In view of the above discussion, relations (8.12) and (8.20) estimate the IR power, but not the LoG size. Theoretically, immediately following a frequency event the P_{IR} value gives the LoG size. However, this is not a practical solution to determine the lost power because of the inevitable considerable transients in measurements immediately after the event. In this respect, we here discuss a simple and robust method to estimate LoG size based on the estimated P_{IR}. In Figure 8-3 the true and approximated IRs for a typical LoG event are shown. Regardless of initial transients due to the impact of voltage angle jump on loads' dynamic behaviour, the approximated IR (black solid) can roughly represent its real value (dashed). In the simulation environment, another source of the initial transients is the non-ideality of the CPL loads modelling. The estimated IR using (8.12) or (8.20) is shown in blue solid trace where the estimated values are updated every 20 ms, what corresponds to the PMUs reporting rates [27], explaining the discrete nature of the estimation. Surely, its value after the event does not give a reliable estimation of the LoG size. As a solution to this problem, an interpolated IR is used to compensate the unreliability of data measured in the initial moments after the LoG event and obtain a near-to-real LoG size. This method is robust enough to the initial transients. The time interval D is PMU's delay that is addressed in the next section.

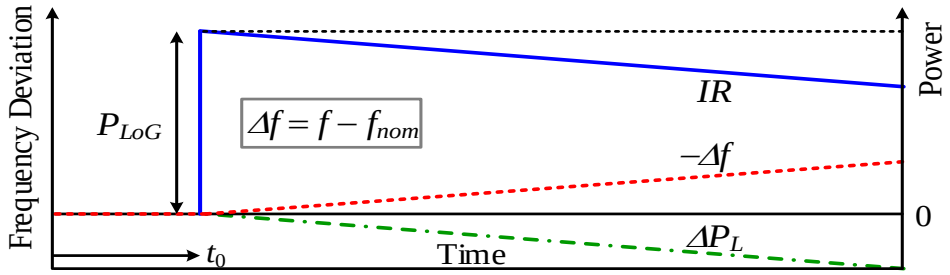

Figure 8-2: Frequency deviation, load's power deviation and IR in a LoG event.

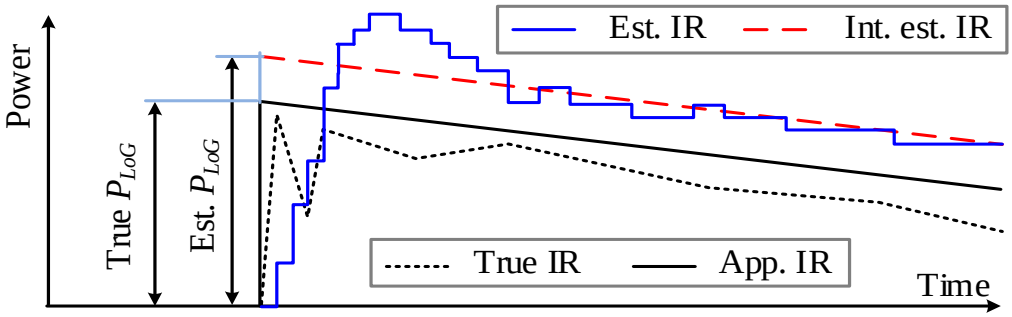

Figure 8-3: The proposed method to estimate LoG size from the estimated IR.

8.4.2. Impact of the Frequency Measured by PMUs

According to the IEEE Std. C37.118, PMUs are devices that provide an estimation of the voltage and current synchrophasors, frequency and RoCoF, all based on the common coordinated universal time reference [27]. These devices estimate synchrophasors assuming a constant frequency signal model and are usually relying on the discrete Fourier transform [28]. A simple and consistent method to estimate frequency is through the phasor time derivation [29]. However, it yields implausible spike in the frequency when voltage angle abruptly jumps due to the electrical transients such as LoG events or numerical derivatives. This may induce instabilities if the

control actions are taken based on it. Averaging over several phase angle samples is used as a simple solution to mitigate undesirable transients' effect, which results in a delay in the frequency estimation [21]. Moreover, in PMU-based WAMS applications, phasor data concentrator (PDC) reporting latency is one of the main design parameters. The PDC reporting latency is composed by the PMU reporting latency, the communication network latency and the PDC latency [22].

The implemented PMU in [28] deploys an enhanced-interpolated discrete Fourier transform (e-IpDFT) algorithm that iteratively compensates the impacts of the spectral interference created by the negative image of main spectrum tone. This can provide an optimal trade-off between synchrophasor estimation accurateness, response time, and computational complication. The e-IpDFT algorithm combines three discrepant approaches to decrease the influence of the sources of error (aliasing and spectral leakage): 1) windowing; 2) DFT-interpolation; and 3) iterative procedure for the compensation of the spectral interference made by the negative image of the main frequency component of signal. The performances of the e-IpDFT algorithm, in both static and dynamic circumstances, might be affected by two factors: 1) its sampling frequency f_s and 2) its window length T. The signal is sampled by the PMU each $t_s = 1/f_s$ (being f_s the PMU sampling frequency), and collected over the time window $T = N \cdot ts$ sufficiently short so that the signal can be presumed stationary within it. The optimal selection of f_s and T is restricted by several factors, mainly represented by: 1) assumptions behind the algorithm formulation; 2) accuracy and response time requirements defined in the IEEE Std. C37.118.1-2011 [27]; and 3) the computational limitations of the chosen hardware platform which are taken into account. It is to be noted the advantages of this PMU algorithm refer to the relatively simple application and low-computational difficulty capable of attaining reasonable exactness and response times after a careful choice of the algorithm parameters. It extends the DFT-interpolation scheme proposed in [30] considering the impacts of the spectral interference created by the negative image of the main spectrum tone and compensating it by iterative procedure presented in [31]. An analytical comparison between the classical IpDFT and the proposed e-IpDFT approach and the description of the algorithm deployment into an FPGA-based PMU prototype are also provided in [28]. A complete metrological characterization of the developed PMU on the basis of the static and dynamic tests nedded by the IEEE Std. C37.118.1-2011 is provided in [28]. The proposed PMU algorithm in [28] and its prototype exhibits peculiar characteristics enabling their use in several applications for both transmission and distribution networks.

The aforementioned undesirable characteristics of the PMU sensing infrastructure, i.e., the PMU frequency undershoot and the delay in the frequency estimation, are illustrated in Figure 8-4 for a simulated LoG. A solution to mitigate this undershoot is setting a tolerance on an allowable change in phase angle between samples [21]. As another solution, in this study the interpolation technique is deployed to circumvent the frequency undershoots. The PMU measurement reporting latency is also taken into account in the proposed LoG estimation process. It is assumed that the frequency data are gathered up to one second following the incident time and this window can be divided into two time intervals. The first interval is from the disturbance instant t_0, to the first time of crossing of SGs' speeds or PMUs' frequencies with the COI ones t_1. The second interval is from t_1 to the second crossing time t_2. After which, the 5^{th} order interpolation is applied on the selected data contains the event instant and second time interval in order to get rid of unreliable information from the first time interval. The proposed interpolation technique needs two data sets in order to achieve COI frequency at the first moments following the loss of generation event. The former one is only the event occurrence data in terms of its time instant and COI frequency value (which is identical with the pre-event point). The later one comprises of time interval from the first crossing point of the measured frequencies to the second crossing point. These data sets are easily available through the PMU data. Further details are provided in the next section.

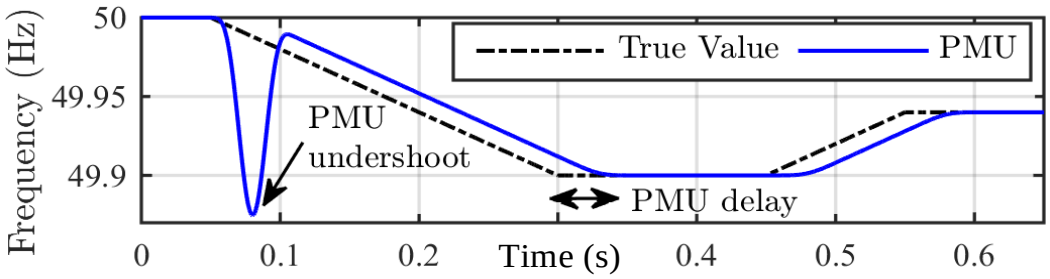

Figure 8-4: Undershoot and delay of frequency measured by PMUs in a LoG.

8.5. Simulation Results

In this section, the effectiveness of the proposed LoG size estimation is investigated using two test cases: a simple power system and the IEEE 39-bus test network. Both test systems are implemented within the MATLAB/Simulink simulation environment. In this regard, two scenarios named "Speed" and "PMU" are used. The former represents the case in which the SGs' rotor speeds are considered to be available. The latter makes reference to frequency measured by PMUs.

8.5.1. LoG Size Estimation for a Simple Power System

In the first case study shown in Figure 8-5, the LoG size estimation is conducted for the two above-mentioned scenarios. As shown in Figure 8-5, five aggregated loads are initially supplied by three SGs. All the relevant parameters are reported in Table 8-1. The total system demand plus power losses is around 1000 MW. The SG_1 and SG_2 supply 240 MW and 710 MW, respectively. Generated power by SG_3 is 5% of system demand, that is, 50 MW. L_1 and L_2 are CPL loads which consume 80% of total demand, and other loads are modelled as CILs. Frequency dependency of the CPL loads is considered by K_{pf}=2. All power system stabilizers are deliberately disabled to deteriorate inter-area oscillations. All SGs are equipped with IEEE type 1 exciter and steam turbine governors with 5% droop factor [32].

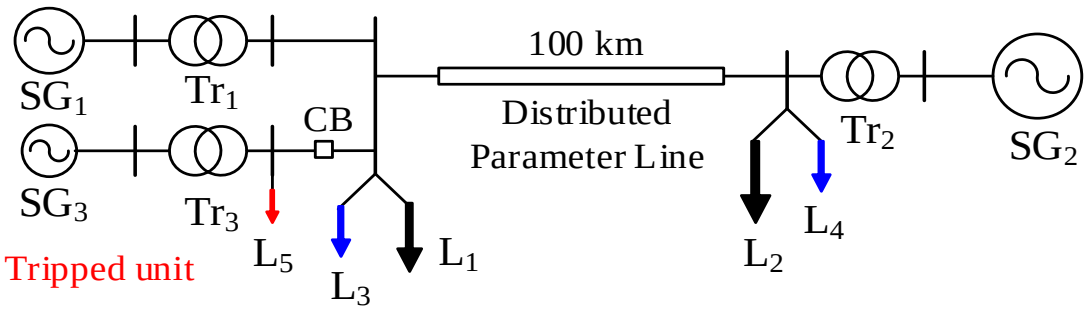

Figure 8-5: Single line diagram of the studied simple test system.

Table 8-1: Parameters of the Simple Test System

Parameter	S (MVA)	M (s)	Parameter	P (MW)	Q (Mvar)
SG_1	300	8	L_1	200	10
SG_2	900	11	L_2	600	50
SG_3	60	7	L_3	100	10
Parameter	**S (MVA)**	**X (p.u.)**	L_4	100	10
Tr_1	400	0.15	L_5	1	0
Tr_2	900	0.15	**Parameter**	**L (H/km)**	**C (F/km)**
Tr_3	100	0.15	Line	1.4e-3	8.78e-9

At t=0.1 s, the SG_3 is tripped through suddenly opening its main circuit breaker (CB). The simulation results of the 'Speed' scenario for the conventional and proposed approaches are shown in Figure 8-6 and Figure 8-7. Taking into account the local load L_5, the true value of the power imbalance caused is 49 MW. Following the sudden disconnection of the SG_3, the SG_1 and SG_2 start to oscillate against each other. Apparently, the rate of change of speed of SG_1 is about four times larger than that of SG_2, at t=0.2 s. It is worth noting that the RoCoF is calculated as the absolute value [13]. The true and approximated values of the IR power are shown in Figure 8-6 with the black dashed and solid traces, respectively. The approximated IR is calculated using (8.30). The discrepancy between all of the IRs' traces is due to the CIL's power deviation which is not considered in the approximated IR power. The red dash dot trace shows the estimated IR power by the conventional approach. This trace reaches its maximum amount after 200 ms following the event and decreases consequently. This maximum value can be selected as the estimated LoG size. However, this does not provide a reliable estimation. First, as mentioned before, the LoG size should be determined based on the estimated IR power at the event time not at any later time. Second, it will be shown later that the LoG estimation on the basis of the maximum IR results in a larger estimation error for the PMU scenario. Thus, another method is proposed in this chapter to estimate the LoG size using the estimated IR since is more reliable and less sensitive to the initial measurement transients. The background of this method is explained in Figure 8-2. Let us consider the measurement noise and transients which add uncertainty to the IR, especially immediately after the event. With this assumption, an averaged IR can be obtained by a 5^{th} order interpolation based on the estimated IR values from a time after termination of initial transient to a time before GRs initiation (up to 1 s after the event).

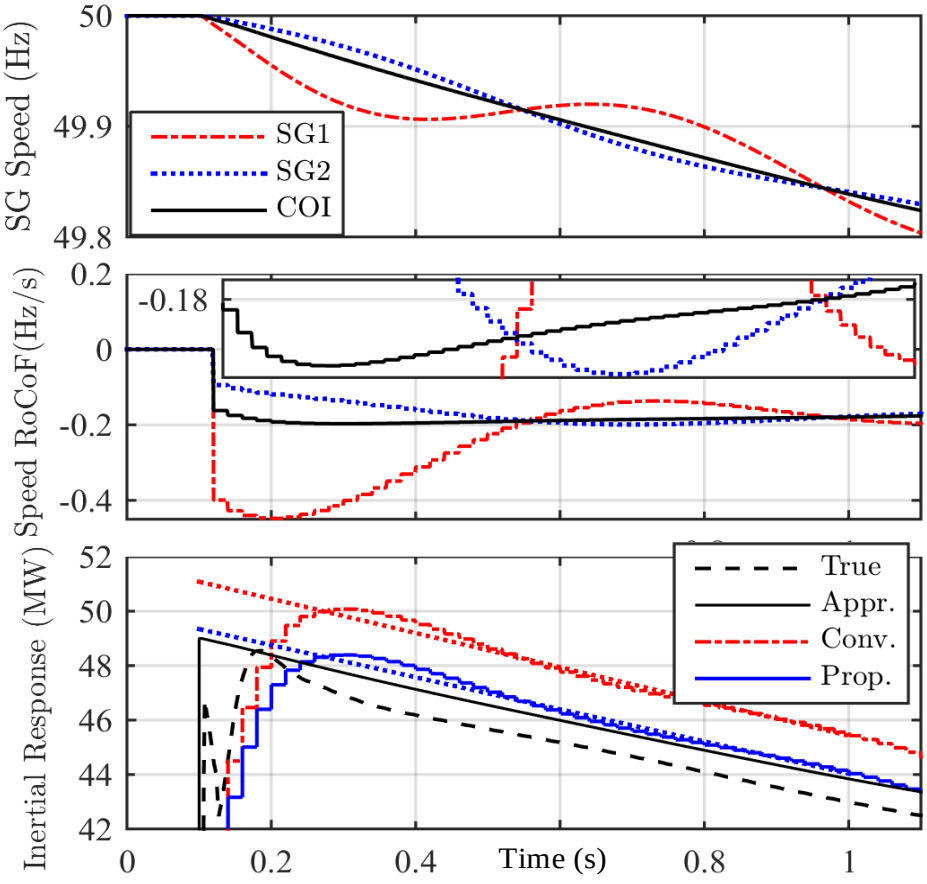

Figure 8-6: Results of the Speed scenarios for a 49 MW LoG event.

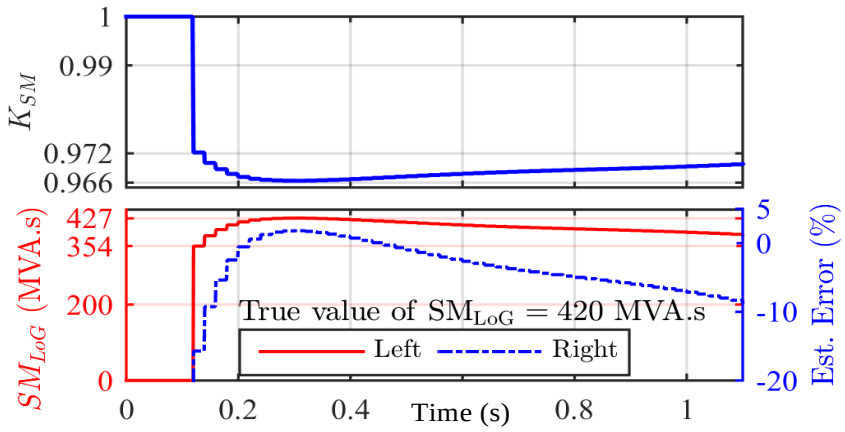

Figure 8-7: Lost inertia estimation in the Speed scenario for 49 MW LoG event.

Then, the value of this averaged IR at event time yields an estimation of the LoG size that is more reliable than that of the maximum method. The interpolated IRs are illustrated in Figure 8-6 with dotted lines. Based on the interpolated data, the estimated LoG size by conventional approach is about 51 MW. In the other hand, the estimated IR by the proposed approach is shown with blue solid trace. Here, M_j^{init} is 7 s and L_j^{init} indicates the pre-event generation loading of the whole system, i.e., 0.8. It can be seen that this estimated IR is considerably closer to the approximated one and then to the true IR compared to that of the conventional approach. The estimated LoG size using interpolation of the estimated IR is about 49.3 MW in the proposed approach. In other words, estimation error of the proposed approach is about 6 times smaller than that of the conventional method. Moreover, the lost inertia estimation, in terms of the coefficient K_{SM} and SM_{LoG}, using the proposed method are illustrated in Figure 8-7.

As mentioned in the previous sections, the 'Speed' scenario requires the rotor speed of the SGs which, in practice, are unavailable. To investigate the efficiency of the derived approach in a real-world condition, the results obtained by PMU scenario are illustrated in Figure 8-8. The measured frequencies by PMUs oscillate with the lower amplitudes in comparison with SGs rotor speeds. Moreover, they are closer to the COI frequency. This is due to SGs' internal impedance.

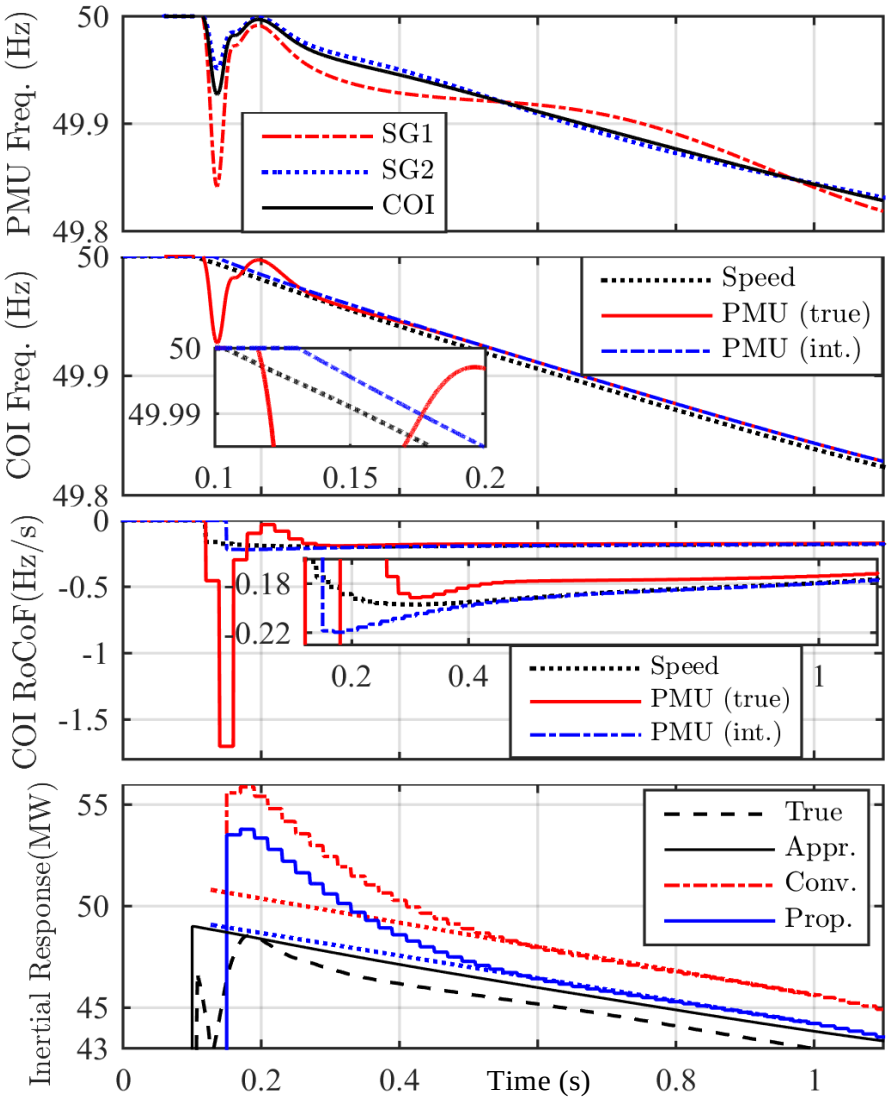

Figure 8-8: Results of the PMU scenarios for a 49 MW LoG event.

Additionally, the measured frequencies exhibit a considerable transient immediately after the event which results in an unreliable COI frequency measurement. To mitigate this aspect, an interpolated COI frequency is employed for the LoG size estimation instead of its true value. Note that the order of interpolation should be greater than one, here 5^{th} order, because of the variable COI RoCoF, as shown in Figure 8-8. For the sake of comparison, the COI speed is also shown. The PMU delay can be seen in the COI Frequency sub-figure. This delay is 30 ms which is half of the PMU's sampling window (60 ms) [27]. Based on the interpolated COI frequency, the estimated IRs along with their interpolated values are shown in Figure 8-8. The maximum values of the estimated IRs are considerably larger than the true LoG size. However, the interpolated COI frequency is used to obtain the interpolated IRs which results in much better estimation of the LoG size. Here the proposed approach gives a lower estimation error similar to the Speed scenario. As the measured frequency by PMUs has 30 ms delay, the interpolated IR is equal to the LoG size not instantly at event time, but after 30 ms from this time.

For the sake of comparison, the performance of LoG size estimation algorithms is provided in Table 8-2 for the discussed case. The SG_1 generates 240 MW in all three cases and the SG_2 supplies the residual demand as slack unit. These results reveal that the proposed approach has estimation errors 4 to 15 times smaller than that of the conventional methods.

Finally, the impact of the discrepancies between M_j^{init} and L_j^{init}, and their real values pertinent to the tripped generator, on the estimation error of the proposed method is illustrated in Figure 8-9. The horizontal axes represent variation of M_j^{init} and L_j^{init} with respect to their true values, i.e., 7 seconds and 82%. For instance, ±20% variation for M_j^{init} means that its horizontal axis ranges from 5.6 to 8.4 seconds. It can be seen that the estimation error has a linear relationship with the M_j^{init}. However, it tends to a non-linear relation especially for the negative variations of L_j^{init}. These relationships can be explained by the link of M_j and L_j with post-event system's inertia represented in (8.17). A greater (lower) value of the M_j^{init} (L_j^{init}) than its true value results in a smaller (larger) post-event system's inertia and then the estimation error tends to be negative (positive) and vice versa. In addition, Figure 8-9 shows that the estimation error of the proposed approach is always smaller than that of the conventional one even under these significant variations in M_j^{init} and L_j^{init}.

Table 8-2: LoG Size Estimation Error for Different LoG Sizes in Simple System

LoG Size	39 MW	49 MW	59 MW
Speed: Conventional	3.73%	4.25%	4.56%
Speed: Proposed	**0.91%**	**0.70%**	**0.29%**
PMU: Conventional	2.83%	3.65%	4.22%
PMU: Proposed	**0.057%**	**0.14%**	**-0.027%**

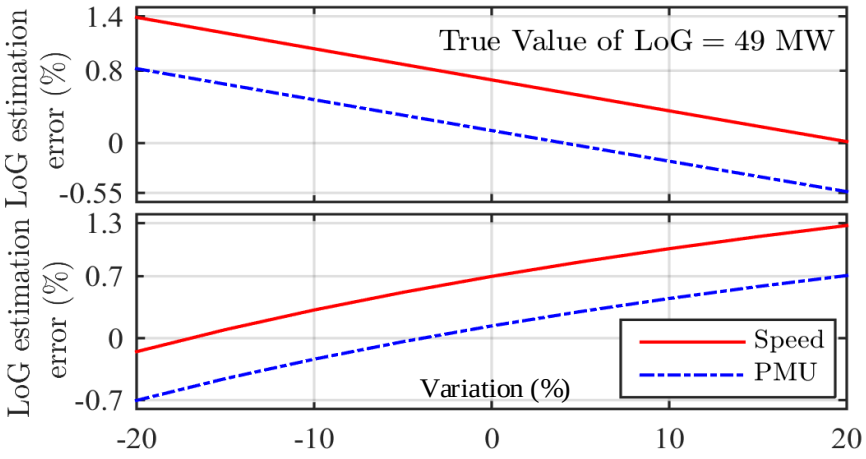

Figure 8-9: LoG estimation error with M_j^{init} (up) and L_j^{init} (down) variations.

However, it tends to a non-linear relation especially for the negative variations of L_j^{init}. Figure 8-9 shows that the estimation error of the proposed approach is always smaller than that of the conventional one even under these significant differences.

8.5.2. LoG Size Estimation for the IEEE 39-bus System

In order to prove the ability and accuracy of the proposed approach, we use a large-scale system composed by the IEEE 39-bus system [33]. The system load is about 6 GW which is supplied by 11 SGs. The SG5 is divided into two identical units with rating of 260 MVA each. Parameters of the SGs are reported in Table 8-3. Loads are composed by 80% CPL loads, with K_{pf} =2, and 20% CIL loads. All the SGs are equipped with the exciter and governor.

Table 8-3: Parameters of the IEEE 39-Bus System

Unit	S (MVA)	M (s)	P (MW)	Unit	S (MVA)	M (s)	P (MW)
SG_1	3000	13	1104	SG_6	1000	8.7	650
SG_2	1000	10.56	216	SG_7	1000	6.46	567
SG_3	1000	9.5	656	SG_8	1000	6.92	547
SG_4	1000	6.234	638	SG_9	1000	8.116	840
SG_5	520	10	508	SG_{10}	1000	6.51	261

At t=0.1 s, the SG_{52} is tripped. The simulation results of the 'Speed' scenario for the conventional and the proposed approaches are shown in Figure 8-10. Here, M_j^{init} and L_j^{init} are assumed to be 6.234 s and 0.5, respectively. A 1 MW local load is also tripped in addition to the SG_{52}, so that the true value of the lost power is 253 MW. As can be seen from Figure 8-10, the estimated IRs have considerable oscillatory behaviour in comparison with those of Figure 8-6. This is due to significant inter-area oscillations in this large system. It can be deduced that the LoG size estimation based on the maximum estimated IRs gives unreliable results. In contrast, as it can be seen from dotted traces in Figure 8-10, the proposed interpolation can result in more accurate estimation. Moreover, the estimation error of the proposed approach is about 3 times smaller than that of the conventional one (see Table 8-4).

The results related to the 'PMU' scenario with the mentioned LoG event are illustrated in Figure 8-11. Regardless of the initial undershoots; the amplitude of frequency oscillations is smaller than those of SGs rotor speeds, especially for units closer to the event location.

Table 8-4: LoG Size Estimation Error for Two Scenarios in IEEE 39-Bus System

LoG Size (MW)	Speed Scenarios		PMU Scenarios	
	Conv.	Prop.	Conv.	Prop.
253	4.4%	**1.4%**	2.78%	**- 0.11%**

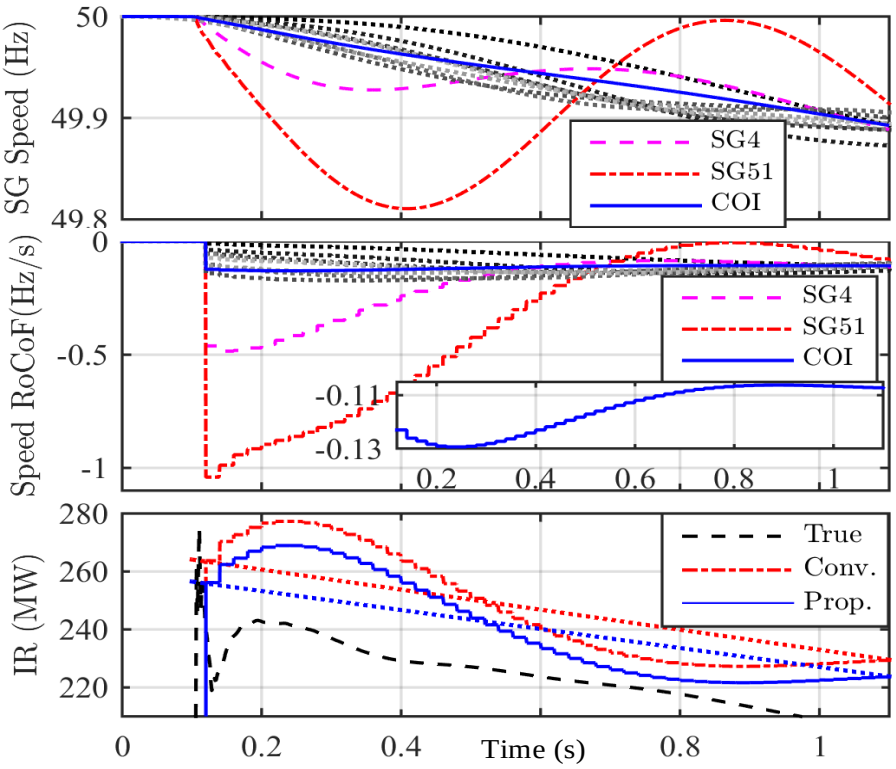

Figure 8-10: Results of the Speed scenarios for a 253 MW LoG event.

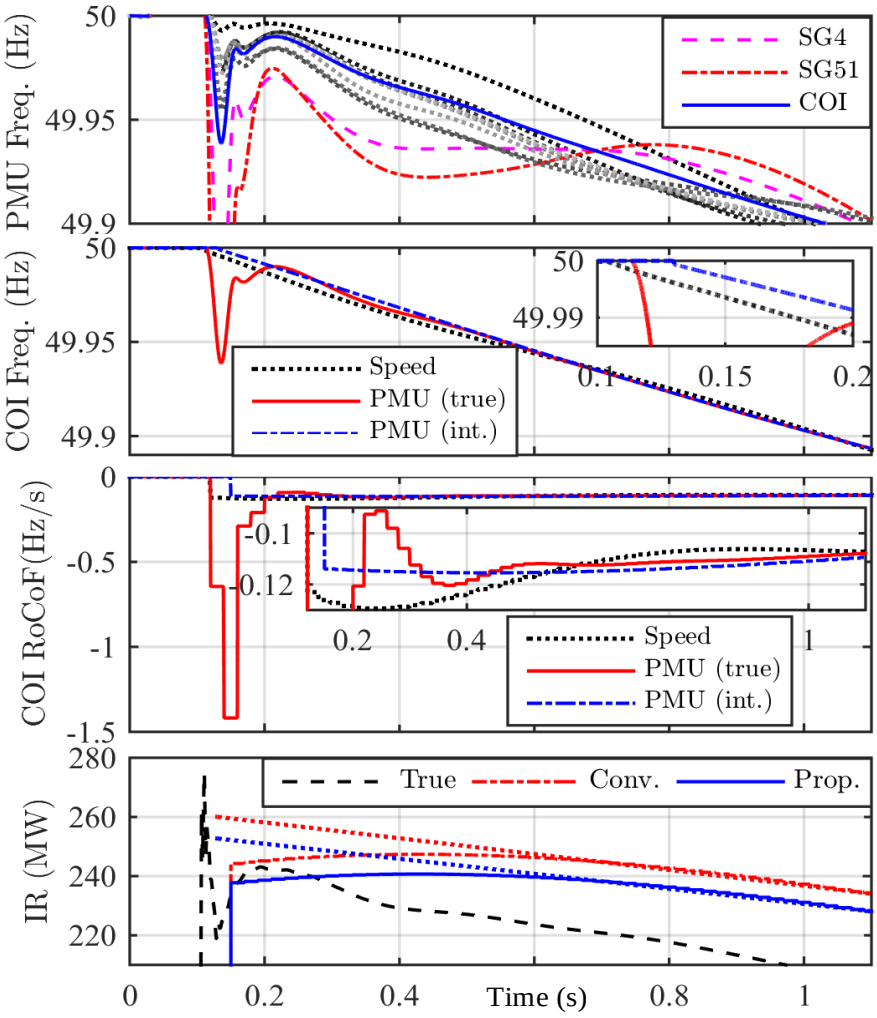

Figure 8-11: Results of the PMU scenarios for a 253 MW LoG event.

It is notable that the undershoot of the measured frequency at the terminal of the SG_{52} reaches to 49.3 Hz. The proposed approach provides more accurate LoG size estimation than that of the conventional method as previous cases (See Table 8-4).

Finally, the effect of discrepancies between the M_j^{init} and L_j^{init}, and their real values pertinent to the tripped SG, on performance of the proposed approach is shown in Figure 8-12. It can be seen that even in the worst case, i.e. -20% variation for M_j^{init}, estimation error of the proposed method is at least 2 times smaller than that of the conventional approach.

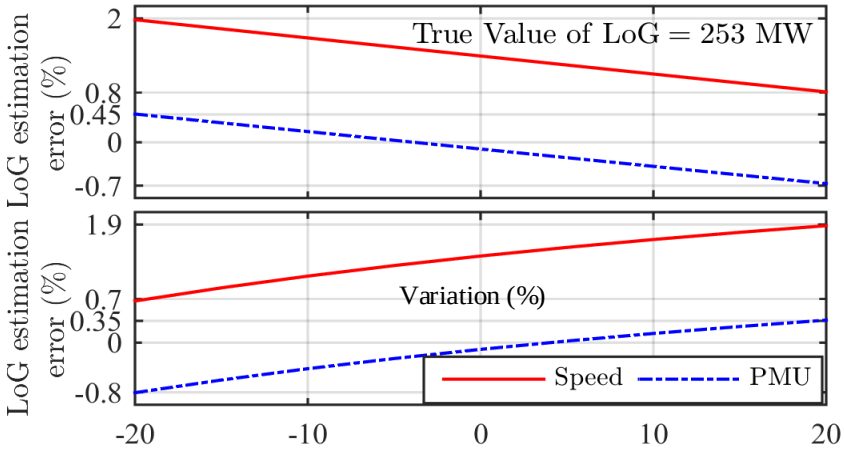

Figure 8-12: LoG Estimation error with M_j^{init} (up) and L_j^{init} (down) variations.

8.6. Executive Summary

This chapter focuses on the dynamic behavior of a power grid following a LoG event. In order to take into account the inertia reduction in the LoG size estimation, a new method for simultaneously estimating the inertial response and system's inertia is proposed. To address the practical implementation aspects of the proposed method, the load models' impact, their damping; and characteristics of the frequency measured by PMUs are thoroughly taken into account and formulated. Furthermore, a process to obtain a reliable estimation of the LoG size based on the interpolated estimated inertial response is proposed. In addition, the latency associated with data communication channels of PMUs is also modeled. Eventually, the advantage of considering inertia reduction in the LoG size estimation is adequately demonstrated through several examples and extensive testing using two different scenarios of SG's rotor speeds and PMUs' frequencies. The estimation error obtained by the proposed method is less than that of the conventional approach, showing the acceptable accuracy and superiority of the proposed estimation algorithm. This would lead to a more accurate decision on the necessity and the size of LoG, hence reduced risk of frequency instability. It should be pointed out that the derived approach can be used for advanced frequency control as well as under frequency load shedding schemes. The proposed framework can be extended in the future work by estimating of LoG and the equivalent inertia of the system, which is highly affected by the presence of converter-interfaced generations. Further studies can be done to apply power variations of the constant current loads or constant impedance loads on the LoG size estimation. Additionally, it can be followed by validating the proposed scheme with real measurement data.

8.7. References

[1] Enhanced Frequency Control Capability (EFCC), https://www.nationalgrideso.com/innovation/projects/enhanced-frequency-control-capability-efcc, accessed 01 September 2018.

[2] R. Azizipanah-Abarghooee, M. Malekpour, M. Zare, and V. Terzija, "A new inertia emulator and fuzzy-based LFC to support inertial and governor responses using Jaya algorithm. *IEEE PESGM*, pp. 1-5, 2016.

[3] P. Kundur, N. J. Balu, and M. G. Lauby, *Power System Stability and Control*. New York: McGraw-Hill, 1994.

[4] P. M. Anderson and A. A. Fouad, Power system control and stability, IEEE Press Power Engineering Series, 2003.

[5] V. V. Terzija, "Adaptive underfrequency load shedding based on the magnitude of the disturbance estimation," *IEEE Trans. Power Syst.*, vol. 21, no. 3, pp. 1260-1266, Aug. 2006.

[6] U. Rudez, and R. Mihalic, “Monitoring the first frequency derivative to improve adaptive underfrequency load-shedding schemes,” *IEEE Trans. Power Syst.*, vol. 26, no. 2, pp. 839-846, May 2011.
[7] A. Ketabi, and M. Hajiakbari Fini, “An underfrequency load shedding scheme for hybrid and multiarea power systems.” *IEEE Trans. Smart Grid*, vol. 6, no. 1, pp. 82-91, Jan. 2015.
[8] Y. Tofis, S. Timotheou and E. Kyriakides, “Minimal Load Shedding Using the Swing Equation,” *IEEE Trans. Power Syst.*, vol. 32, no. 3, pp. 2466-2467, May 2017.
[9] J. Jallad, S. Mekhilef, H. Mokhlis and J. A. Laghari, “Improved UFLS with consideration of power deficit during shedding process and flexible load selection,” *IET Renew. Power Gen.*, vol. 12, no. 5, pp. 565-575, 9 4 2018.
[10] M. Lotfalian, R. Schlueter, D. Idizior, P. Rusche, S. Tedeschi, L. Shu, and A. Yazdankhah , “Inertial, governor, and AGC/economic dispatch load flow simulations of loss of generation contingencies,” *IEEE Trans. Power App. Syst.*, vol. PAS-104, no. 11, pp. 3020-3028, Nov. 1985.
[11] T. Inoue, H. Taniguchi, Y. Ikeguchi and K. Yoshida, “Estimation of power system inertia constant and capacity of spinning-reserve support generators using measured frequency transients,” *IEEE Trans. Power Syst.*, vol. 12, no. 1, pp. 136-143, Feb. 1997.
[12] V. Terzija, M. Kayikci, and D. Cai, “Power imbalance estimation in distribution networks with renewable energy resources,” *Electr. Distrib.-Part 1, 2009. CIRED 2009. 20th Int. Conf. Exhib. 2009 (pp. 1-4). IET.*
[13] P. Wall and V. Terzija, “Simultaneous estimation of the time of disturbance and inertia in power systems,” *IEEE Trans. Power Delivery*, vol. 29, no. 4, pp. 2018-2031, Aug. 2014.
[14] P. M. Ashton, C. S. Saunders, G. A. Taylor, A. M. Carter, M. E. Bradley, “Inertia estimation of the GB power system using synchrophasor measurements,” *IEEE Trans. Power Syst.*, vol. 30, no. 2, pp. 701-709, Mar. 2015.
[15] D. Zografos and M. Ghandhari, "Estimation of power system inertia," *2016 IEEE Power and Energy Society General Meeting (PESGM)*, Boston, MA, 2016, pp. 1-5.
[16] D. Zografos and M. Ghandhari, “Power system inertia estimation by approaching load power change after a disturbance,” *2017 IEEE Power & Energy Society General Meeting*, Chicago, IL, 2017, pp. 1-5.
[17] Y. C. Chen, S. V. Dhople, A. D. Domínguez-García and P. W. Sauer, “Generalized injection shift factors,” *IEEE Tran. Smart Grid*, vol. 8, no. 5, pp. 2071-2080, Sept. 2017.
[18] D. Zografos, M. Ghandhari, and R. Eriksson, “Power system inertia estimation: Utilization of frequency and voltage response after a disturbance,” *Electr. Power Syst. Res.*, vol. 161, pp. 52-60, Aug. 2018.
[19] S. Chakrabarti, E. Kyriakides, T. Bi, D. Cai, and V. Terzija, “Measurements get together,” *IEEE Power Energy Mag.*, vol. 7, Jan. 2009.
[20] V. Terzija, G. Valverde, D. Cai, P. Regulski, V. Madani, J. Fitch, S. Skok, M. M. Begovic, and A. Phadke, “Wide-area monitoring, protection, and control of future electric power networks,” *IEEE Proc*,. vol. 99, no. 1, pp. 80-93, Jan. 2011.
[21] A. G. Phadke and B. Kasztenny, “Synchronized phasor and frequency measurement under transient conditions,” *IEEE Trans. Power Delivery*, vol. 24, no. 1, pp. 89-95, Jan. 2009.
[22] A. Derviskadic, P. Romano, M. Pignati and M. Paolone, “Architecture and experimental validation of a low-latency phasor data concentrator,” *IEEE Trans. Smart Grid*, vol. PP, no. 99, pp. 1-1, 2016.
[23] C. J. Tavora and O. J. M. Smith, “Characterization of equilibrium and stability in power systems,” *IEEE Trans. Power App. Syst.*, vol. PAS-91, no. 3, pp. 1127-1130, May 1972.
[24] C. Concordia and S. Ihara, “Load representation in power system stability studies,” *IEEE Trans. Power App. Syst.*, vol. PAS-101, no. 4, pp. 969-977, Apr. 1982.
[25] W. W. Price, C. W. Taylor, and G. J. Rogers, “Standard load models for power flow and dynamic performance simulation,” *IEEE Trans. Power Syst.*, vol. 10, no. 3, pp. 1302-1313, Aug 1995.
[26] E. Welfonder, H. Weber and B. Hall, “Investigations of the frequency and voltage dependence of load part systems using a digital self-acting measuring and identification system,” *IEEE Trans. Power Syst.*, vol. 4, no. 1, pp. 19-25, Feb 1989.
[27] *IEEE Standard for Synchrophasor Measurements for Power Systems*, IEEE Std C37.118.1-2011, Dec. 28, 2011.
[28] P. Romano and M. Paolone, “Enhanced interpolated-DFT for synchrophasor estimation in FPGAs: Theory, implementation, and validation of a PMU prototype,” *IEEE Trans. Instrum. Measur.*, vol. 63, no. 12, pp. 2824-2836, Dec. 2014.
[29] A. G. Phadke, J. S. Thorp and M. G. Adamiak, “A new measurement technique for tracking voltage phasors, local system frequency, and rate of change of frequency,” *IEEE Trans. Power App. Syst.*, vol. PAS-102, no. 5, pp. 1025-1038, May 1983.
[30] T. Grandke, “Interpolation algorithms for discrete Fourier transforms of weighted signals,” *IEEE Trans. Instrum. Meas.*, vol. 32, no. 2, pp. 350–355, Jun. 1983.

[31] A. Moriat, “System and method for estimating tones in an input signal,” U.S. Patent 6 965 068, Nov. 15, 2005.
[32] R. Boyer, “Primary governing and frequency control in ERCOT," *2007 IEEE Power Eng. Soc. General Meeting IEEE*, Tampa, FL, 2007, pp. 1-8.
[33] K. R. Padiyar, Power System Dynamics: Stability and Control. NewYork: Wiley, 1996.

9. Assessment of the Value of Wide-Area and Interim Wide-Area EFCC in GB Power Systems

In delivering enhanced frequency control capability (EFCC), the options for the control and deployment of resources based on monitoring of the electricity system can fundamentally affect the way the frequency is recovered during an event. The development of three separate forms of fast frequency response control models is critical to both describing the future benefits of fast frequency response services accurately and describing the type of frequency response necessary to achieve these benefits. In *proximity based all zone* method, the responses closest to the disturbance are preferentially delivered. We explore this and two other approaches (Equality dispatch and interim based all zone dispatch) within this report. In *equality based all zone* technique, the response evenly across the pool of resource available with no zonal priority is delivered. In *interim technique*, the zonal response whose proportions are defined ahead of the event rather than based on data available during the event required in the two mentioned approaches. Within DIgSILENT PowerFactory, 3 abovementioned forms of fast frequency control have been modelled in this report. The MCS uses available and additional data from phasor measurement units (PMUs) to monitor the system and a central control unit to provide the flexible response from the frequency service providers. Its behaviour is replicated via a proximity dispatch approach based not on weighted measurement, but rather from the inertias across the system and the frequencies behaviour as derived from the well-known swing equation of the physical behaviour of the system [1].

The simulation tests defined above can only approximate the operation of a real frequency control system, such as GE MCS, which may be subject to discrepant physical features surrounding its detailed operation. Within our initial analysis, the resources deployed are modelled as purely static load response, however, the algorithms developed are flexible to look at more complex deployments of response across all static and dynamic providers as needed. In traditional frequency controllers, most response is on the basis of the absolute value of frequency. Across all 3 modes of all zone operation, corrective responses are initiated automatically when this value violates the predefined thresholds. We have included within the simulation models consideration of sensible inherent delay to prevent spurious triggering and factors to prevent over response, which approximates settings and functions present within the GE MCS. The fully all zone (proximity dispatch) and interim EFCC approaches respectively deploy against the globally calculated rate of change of frequency (RoCoF), and the RoCoF seen by the resource itself to trigger a response as soon as an event occurs, with the delays, sampling approach and calculation approach used acting to avoid spurious triggering. They all deliver enough response across the network fast enough to contain the frequency event without over or under delivery. It is to be noted that under equality dispatch, the response is evenly spread across resources available; whereas in the other two approaches you do get more response closer to the event. The frequency response is proportional to the event size by employing frequency and RoCoF to define the extent of the required response. This methodology is characterised to be self-limiting and not over-respond.

It is to be outlined that the overall requirements of these three schemes are as follows:

i) Bound total response size to events in proximity technique.
ii) Zonal and all zone based RoCoF and power mismatch calculation time
iii) Implementing PMU data like zonal RoCoF as an indicator in fast fault detection and location in order to assist the transient stability.
iv) Speed of response.
v) Transient stability – e.g. at least not worse than without any response. Assume sparse location of resources.
vi) Utilization of available EFCC resources
vii) The ability to deal with failures in resource deployment

In this report, all zone and interim EFCC schemes are developed in DIgSILENT PowerFactory and undertaken simulations show the effect of a frequency event as well as fault upon the transmission network at both the global and zonal level. Three different scenarios comprising of loss of generation in two discrepant zones, faults followed by a loss of generation, boundary flows (i.e. loss in south, all response in north and etc.) are taken into

account. For these events, the model is able to instruct response from a range of resources. The EFCC based modelling techniques are capable to simulate the key to EFCC which is the employment of sufficient responses to meet the event. The modelling drives the right level of response in the right zone of the system to support stable system recovery. Containment of maximum active power loss within 500ms-700ms of the event is required to prevent limiting the maximum loss possible at that time. Albeit deployment of resource close to the event is beneficial, it has founded out that up to 2025 this is not mandatory so that the interim control is enough. This method is not relied on real time frequency and df/dt other than zonally received but which does need a all zone picture of the system's state prior to an incident. All of these techniques allow researchers to see the zonal and global frequency, identify how and to what extent zonal resource is important and how best to combine EFCC with other forms of frequency response. To the best of our knowledge, these problems have not been dealt with by such an accurate approach in any of the existing research projects surrounding fast frequency response deployment. The major findings of the report can be summarized as follows:

- Modelling 3 separate forms of frequency response control systems in the GB reduced system model
- Illustrating the benefit the EFCC approach has in increasing the max loss that the system can operate to
- Presenting that up to 2025 the interim control approach is most effective, but that all 3 methods work
- Testing the robustness of the control approaches against changes in simulation of RoCoF sampling, communication delay, and resource availability and have demonstrated that for >0.6 Hz/s interim technique is no longer sufficient

9.1. Introduction

This section seeks to establish a modelling basis by which the performance of future control systems used to deliver fast frequency response may be compared. The modelling approach identifies the required levels of frequency response in time, location and volume that will maintain stable and contained frequency (and voltage) disturbance events to secured levels of loss across the GB network.

The development of these models is critical to both describing the future benefits of fast frequency response services accurately and describing the type of frequency response necessary to achieve these benefits. These two factors in turn can inform a roadmap of control system implementation, which ensures the necessary functional capabilities of frequency performance are delivered to ensure the benefits identified.

A key aspect to any fast frequency control system is the ability to model and simulate the effects of that control system upon the frequency containment of the GB network. This enables the overall objectives of that control system to be articulated, in terms of the speed and volumes of frequency response required, but also the conditions of GB network inertia, scales of maximum loss and levels of Rate of Change of Frequency (RoCoF) that may be sustained by the use of the control system.

Past control system models typically represent the effects of national balancing services measuring national frequency change to deliver against national frequency containment. However, in the timescales that fast frequency response is now required, in less than 1 second, the NIC EFCC project has demonstrated the phenomena of zonal frequency and zonal RoCoF. It is therefore necessary that any fast frequency response control system model accounts for zonal frequency variation. This is achieved here by use of the DIgSILENT reduced 36 bus GB network model.

Overlaid upon the 36 bus GB network model are 3 separate forms of frequency response control system:

(i) **Proximity**: This approach features the objectives of delivering frequency response closest to the point of mismatch within the GB network model (as measured in the differences in zonal RoCoF) and prioritises frequency response resources accordingly to deliver this, subject to their availability close to the mismatch. The approach, within the timescales of a frequency event, calculates within each zone the frequency and RoCoF across all of the 36 zones, which it then weights according to the zonal inertia to derive a national RoCoF and frequency change. Against these criteria, action is taken and the scale of national power correction to be dispatched is determined - this power correction being

delivered closest to the event. In theory, this approach represents the most "ideal" stable and controlled delivery of frequency response given it limits the potential for inter-area instability across the GB network during its delivery. In practice, this approach would require wide-area features to acquire and synthesize weighted frequency measurements across the GB network to inform control action.

(ii) **Equality**: This approach distributes the required frequency response evenly across the network, subject to resource availability. The approach again calculates weighted frequency and RoCoF during the event from across the 36 network zones and again defines criteria of action based upon this information. For this control mode, there is however no consideration of the zonal priority of the frequency response delivered; the focus is only on using zonally available frequency and RoCoF to determine objectives of national frequency response, which is distributed evenly across all available resources across the network. This approach and its sensitivity studies across resource location and availability allow comparison to the Proximity mode (see above) to understand the effect, if any, a less controlled response deployment strategy has on frequency control.

(iii) **Interim:** This approach considers the effectiveness of a frequency response solution, differing to the two approaches above, by not requiring frequency data from across the GB network in real-time to inform its frequency response function. This approach, exactly as before is based on performing a national frequency and RoCoF derivation. However, in this approach, that derivation comes from taking the zonal frequency and RoCoF value within the zone and deriving from the relative inertia locations across the GB network prior to the event and delivering frequency response proportional to that distribution of inertia. Unlike the above modes of operation, this approach would not require wide-area, real-time availability of PMU data to inform frequency and RoCoF measurement during an event, nor the infrastructure to communicate this to centralized or distributed points of national calculation. Comparison of the effectiveness of the interim approach against the above two alternatives is used to identify periods of future operation which could be satisfied by the interim approach and therefore requires less extensive infrastructure.

Across all of the above control approaches, the weighting of each zones frequency and RoCoF consider perfect foresight of the inertia available and its distribution across the GB network ahead of any event. The models are however capable of being modified to examine the effect of zonal and national forecast inaccuracies. In practice PMU coverage as illustrated across the VISOR and MIGRATE projects may complement improved definition of zonal inertia in real time and the effectiveness of the above simulation approaches in reality.

The simulation models also feature user definable fields enabling a variety of real-time operational considerations and settings. For example, resource capability and availability, communication delay, data synthesizing window periods, resource activation time and delay periods before responding to set criteria across frequency and RoCoF. The setting of these parameters allows different strategies to implementation and control of a real network to be considered and the behaviour of those real networks to be more closely emulated.

The simulation approaches described above can only approximate to the operation of a real frequency control system, such as the GE MCS, which may be subject to different physical features surrounding its detailed operation. For example, the GE MCS uses a measurement focused approach to its activation and national frequency and RoCoF calculation, which requires additional measures to accommodate non-simulate-able conditions of measurement loss, error and variable and adaptive approaches to the challenges associated with measurement and its accuracy. However, such control systems will share one or more of the objectives of the models described above. For example the GE MCS delivers the range of frequency control objectives as delivered in the proximity approach and may be tested in practice to the degree in which it may achieve those objectives and the model may provide an articulation of the "target" frequency control objectives that should be achieved within the real control system.

This report forms a key element of the overall NIC EFCC project in both identifying the key stages of functional performance required by a frequency control system, providing a mechanism supporting the implementation of those objectives into a real frequency control system and clarity in the stages of implementation required in fast frequency control systems as they apply to the GB network. The models outlined in this report provide both developers of control systems and planners of future frequency control strategies the ability to better understand and quantify the effect of these control systems and optimise the delivery of fast frequency control against other more conventionally simulated services.

9.2. Interim, Equality and Proximity based Wide-Area EFCC

9.2.1. Interim EFCC

The EFCC scheme is an evolving method developed to overcome the adverse effects which comes along with the large integration of renewables, i.e. the loss of system inertia. One of the crucial components deployed to support this scheme is the zonal controller, which directly makes specific decisions and accordingly deploys resources to restore frequency after a disturbance. This is explained in Figure 9-1. In zonal case, if there is a pre-event snapshot of the zonal spread of inertia, the interim method will be triggered to deploy all within zone response proportionately as informed by all-zone inertia spread. Otherwise, the within zone mode will be activated instead only according to frequency and RoCoF which is consisting of slower and smaller response.

The Interim based EFCC scheme demands zonal controllers to work using only zonal information during the event itself, in which it only responds to the zonal measurements, without accessing the information from an all-zone calculation (AZC). This AZC performs as a brain to the EFCC scheme in all-zone mode only in its communication ahead of the event of the distribution of system inertia ahead of the event. The AZC and zonal controller calculate global and zonal Centre of Inertia (COI) calculations of df/dt in order to find the global and zonal power mismatch, respectively.. As such the proportionate zonal response can be deduced from the proportion of resources that are in that zonal area and the proportion of inertia in that area. In real time, this means that the zonal controller and its interim control system works under an “event trigger” mechanism, where the corresponding detection block will constantly receive the zonal Rate of Change of Frequency (RoCoF) and absolute frequency signals measured in a defined time period. Considering the flexible and user-defined based RoCoF calculating and reporting window, the zonal controllers can respond accordingly to secure the maximum loss on the electricity system at the time.

The zonal controllers computes the required power response, the volume of which, in each zone, is calculated based on RoCoF, for the centre of inertia (COI) and how the zonal inertia present at the point of the resource relates to that COI. The available resources in the control area, typically wind and solar energy sources, will then be dispatched by the corresponding zonal controller, according to the calculation results, to restore frequency. One of the prerequisites for this mechanism to perform its function properly is that zonal controller has the knowledge of maximum ΔP deployment prior to the fault in its pre-determined configuration (amongst resources are armed and available to meet the maximum loss that may occur on the system at the time). This seems dependent upon the RoCoF behaviour and the location of the resources. If there are no sufficient resources in all zones to help the transient stability, the other zones can potentially assist to keep system stability intact. Further testing with insufficient resources in zones in shape of worst-case scenarios of high resource in Scotland vs low resource in England will be provided in simulation results. Additionally, in order to better focus on the effects of the EFCC scheme and also for simplicity, the demonstration examples presented in this chapter are assumed to purely adopt a demand reduction action, instead of injecting wind and solar energy. However, it can be easily applied on other service providers based on these same principles.

The objective of the simulation on interim EFCC, at present, is to see if this simplified system, which is less reliant on wide-area comms and real-time calculations, but performs on a basis of zonally different RoCoF across the system during the event, is capable of deploying enough response and acting fast enough in practice.

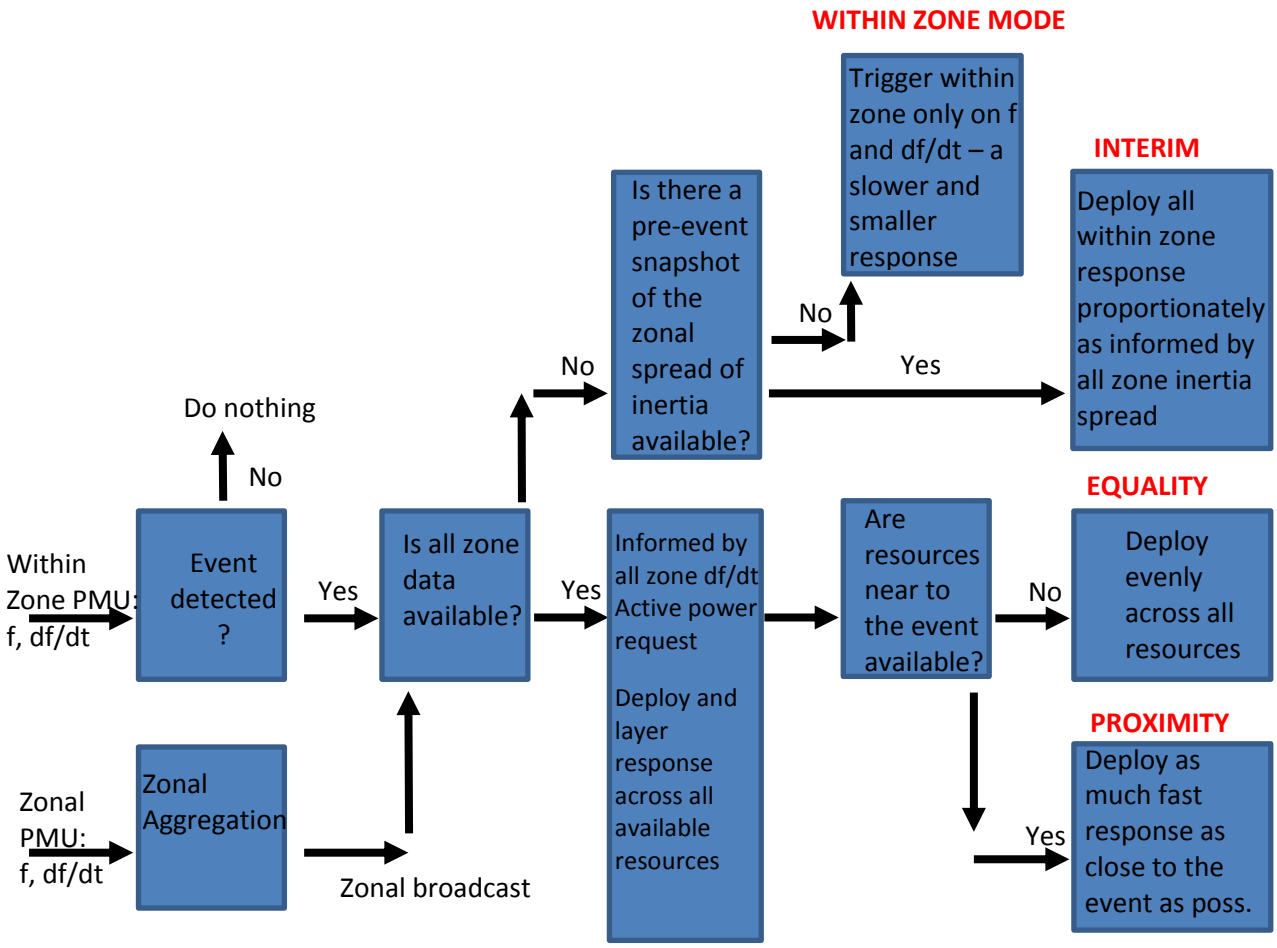

Figure 9-1: SFC control initiation work flow

9.2.2. Equality and Proximity based Wide-Area EFCC

Wide-area EFCC is a control scheme highly dependent of the interaction between the all-zone calculation, zonal calculations (ZC), and zonal controllers. The all-zone calculation is linked with plenty of zonal controllers and associated resources and measurements which it respectively arms and weights, this is represented within the DIgSILENT code by an All Zone Calculation informing the zonal controllers. Additionally, it is to be noted that zonal calculation, zonal aggregation (ZA) and zonal resource response blocks are considered with zone where zonal controller is accommodated. The outputs of zonal PMUs will be sent to zonal aggregation in order to send zonal broadcast signal to equality or proximity to give them their role across the frequency event subject to availability of all-zone data (See Figure 9-1). It is to be noticed that the resiliency and reliability of the system is improved by deploying these zonal aggregations. The within zone PMU data in terms of frequency and RoCoF will detect the event to initiate the process. In other hand, the zonal PMU data in case of frequency and RoCoF as well as inertia will be sent to the zonal aggregation. The output zonal broadcast and event detection signals will be received by either equality/proximity or interim/within zone mode to derive a frequency response. zoneI case of all-zone informed by all-zone df/dt, if there are resources near to the event available, the proximity

technique will be triggered to deploy as much fast response as close to the event as pose. Otherwise, the equality technique will deploy evenly across all resources.

In simulation coding, according to the event size and location, along with the information regarding the resources in all of zones, the all-zone calculation we have developed is going to determine the co-ordination of response, specifying which zones will take part in the reserve service and how many available resources will be allocated in each zone. The results will then propagate back to each zone, which will accordingly produce a more specific coordinated response value for each resource being deployed.

For a detected event based on within zone PMU data, a wide-area calculation is going to identify the COI RoCoF, and the level of response to be triggered. This scheme can be more specifically divided into two categories, based on the research direction of this project, according to either the resources closest to the disturbance are available to be deployed as priority (Proximity) or the resources are just evenly distributed across all the zones (Equality). The Proximity dispatch deploys the maximum zonal RoCoF difference with disturbed zone to ensure the resources are deployed closest to the disturbance being observed.

The Equality dispatch still relies on the real-time monitoring but is not reliant on having sufficient resources close to an event or in the maximum zonal RoCoF difference calculation. It is however still calculating the global Centre of Inertia (COI) need and delivering sufficient response to meet the containment of frequency. The purpose of the Equality dispatch model is to examine the benefit of wide-area control where there may be limitations in zonal resources, and to examine the effect of the proximity calculation approximating the GE MCS performance as illustrated by the difference between proximity and equality dispatch results.

9.3. Calculation of RoCoF and Loss of Generation

9.3.1.1. RoCoF Calculation Approach in EFCC

The RoCoF, which is a crucial reference for EFCC scheme to work, can also be represented by the notation *df/dt*, as it is a derivative of frequency with respect to time. However, due to the fast response requirement, the calculation process must be simplified. A short window, though, can be convenient for RoCoF calculation, provides inaccurate results with a relatively large error. As an improved approach, a "growing window method" can be adopted in this case, as demonstrated in Figure 9-2(a) and Figure 9-2(b).

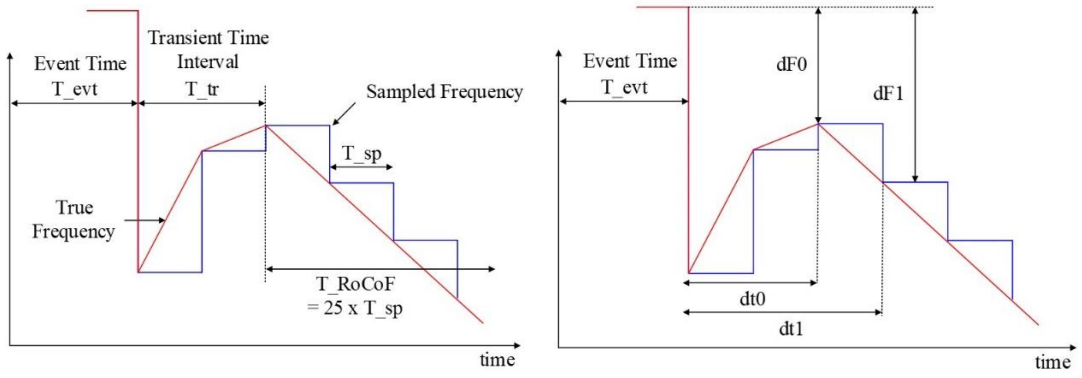

Figure 9-2: (a) RoCoF calculation using the transient times; (b) RoCoF calculation using the asscociated variables

Assume a point prior to the disturbance as time zero. The time interval between this point and the instant of event occurring is represented by T_{evt}. After that, there is a transient time interval, denoted by T_{tr}, where the frequency goes up because of the PMU measurements. The zonal aggregations start to collect samples soon after the transient period and the sampling step time T_{sp} decides the length of each short window. The maximum window size, also known as the final RoCoF calculation time interval T_{RoCoF}, is always set to be integer multiple of the sample time. The value of the multiplier K_{sp}, based on the developed equations in relevant DIgSILENT Simulation Language (DSL) macros, can be manually configured in this project. Accordingly, the value of T_{RoCoF} can be adjusted, i.e. with a 20 ms T_{sp} setting, a total T_{RoCoF} can be changed from 100 ms to 500 ms, if K_{sp} jumps from 5 to 25.

This method takes a short window of the frequency variation curve, from the starting point time zero to the end of transient period. Within this window, the initial RoCoF value can be computed by dividing the frequency difference with the time difference:

$$RoCoF(t = T_{evt} + T_{tr}) = \frac{dF_0}{dt_0} \tag{9.1}$$

As time goes by, a second window can be taken from the curve, with the same starting point and one more time step in the horizontal axis. Additionally, the corresponding RoCoF can be calculated as the average of the first and the second derivatives as follows:

$$RoCoF(t = T_{evt} + T_{tr} + T_{sp}) = \frac{\frac{dF_0}{dt_0} + \frac{dF_1}{dt_1}}{1+1} \tag{9.2}$$

Each time a new window is taken, the corresponding RoCoF can be updated with a more accurate value. When the number of smapling windows reaches the pre-set maximum window number, the best overall estimation is thus obtained, as described as follows.

$$RoCoF(t = T_{evt} + T_{tr} + \mathrm{K}_{sp} \cdot T_{sp}) = \frac{\sum_{i=0}^{\mathrm{K}_{sp}} \frac{dF_i}{dt_i}}{1 + \mathrm{K}_{sp}} \tag{9.3}$$

As can be seen, the most significant measured parameter here is the value of frequency difference at each time step. For an interim EFCC calculation, the initial frequency values, ahead of the event, along with zonal inertias are directly collected from the zonal PMUs, and put together into corresponding zonal calculation, where a synthetic value named zonal COI frequency is generated for producing zonal RoCoF. These calculations make use of the distribution of zonal inertia before the event, to define the ratios between zones of active power response delivery by the zonal resource response during the event relative to its calculation of RoCoF within zone during the event.

On the other hand, the all-zone EFCC's RoCoF calculation, whilst also following the same rule described above, uses data collected from all zonal aggregations. In this case the frequency used for computation is a global COI value, which is transmitted from the system aggregator as presented in Figure 9-3.

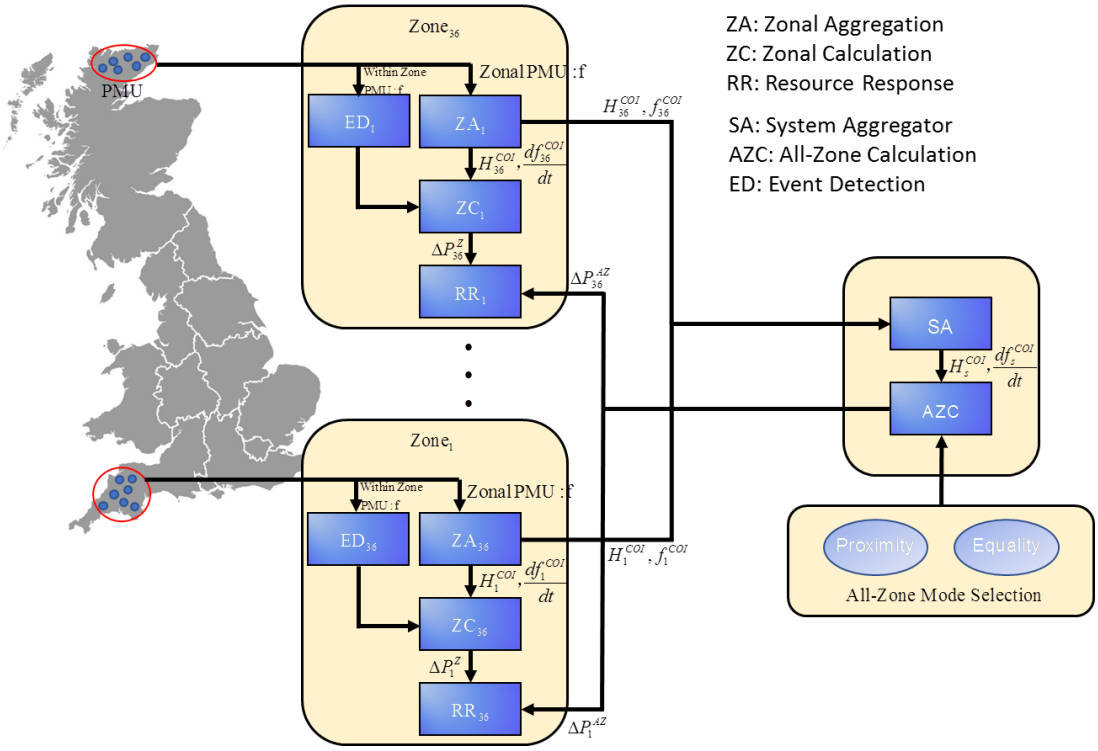

Figure 9-3: Local and wide-area SFC scheme configuration

9.3.1.2. Loss of Generation Estimation

- *Interim Response Calculation*

The loss of generation in the electrical system, also equivalent to the required power response, can be determined based upon the RoCoF and inertia. As in the calculation within the zone, the power required in each zone is calculated separately, using (9.4).

$$\Delta P_i^L = -2H_i^{COI} \cdot \frac{df_i^{COI}}{dt} \tag{9.4}$$

Where:

ΔP_i^L is the required power in zone *i*;

H_i^{COI} is the zonal COI inertia within zone *i*;

$\frac{df_i^{COI}}{dt}$ is the zonal COI RoCoF within zone *i*.

- *Wide-area Equality Mode Response Calculation*

For this mode, the basic principle for computing the total loss of generation is similar to the pre-described rule, only the concentration is on the global picture. Whilst having different distributed requirements for deploying resources, the first step for both proximity and equality modes is to identify the power loss of the entire system, which is described as follows.

$$\Delta P_s = -2H_s^{COI} \cdot \frac{df_s^{COI}}{dt} \tag{9.5}$$

Where:

ΔP_s is the required power of the entire electrical system;

H_s^{COI} is the system COI;

$\frac{df_s^{COI}}{dt}$ is the system COI RoCoF.

The idea of Equality mode is originally proposed to simplify the algorithm, so as to speed up the responding process. It follows the principle where each zone shares the same responsibility for load response, as simply presented as follows:

$$\Delta P_i^{WA} = \frac{P_s}{n} \tag{9.6}$$

Where:

ΔP_i^{WA} is the required power for zone *i* in the wide-area mode;

n is the number of zones.

- *Proximity Mode Response Calculation*

The proximity mode, however, involves a more complicated computation process. Considering the electrical distance, along with other electromagnetic effects, each zone has a different degree of influence upon the system when they provide the same amount of power response. Thus, in this section, a weight factor w is introduced to describe the relationship between the zonal and system response, so as to identify the amount of resources that are supposed to dispatch at each location. A weight factor is defined by the maximum point of RoCoF in each zone as follows:

$$w_i = \frac{RoCoF_i^{\max}}{\sum_{i=1}^{n} RoCoF_i^{\max}} \tag{9.7}$$

Since the system response is the summation of all zonal values, with the total power calculated in (9.5), each zonal MW response can be obtained by multiplying it by the weight coefficient:

$$\Delta P_i^{WA} = w_i \cdot P_S \tag{9.8}$$

9.4. Asset/Resource/Service Modelling of Interim, Equality and Proximity based EFCC Modelling

All simulations regarding interim, equality and proximity EFCC are done on 36-zone GB network in DIgSILENT PowerFactory. The single line diagram of GB network is depicted in Figure 9-4 in which the numerous generation and consummation sites are concentrated on the southern part rather than the northern one. As a matter of this fact, the zones are numbered from the bottom to top. In this case it is supposed that this load is supplied by 70 power stations consisting of gas power plants, nuclear power stations, biomass plants, hydroelectric generations and pumped storage units located in 36 zones. The electric power difference between the power output of 70 power plants plus 4 western HVDC links and grid power consumptions and losses can be transferred to the neighbourhoods using 8 eastern and southern HVDC links. The lowest and highest amounts of loads i.e. 57 MW and 3,541 MW are located in zones 31 (Northern area) and 8 (south-eastern area near to London), respectively. The 36-zone GB network can be approximately divided by three parts of bottom, middle and top where 58%, 32% and 10% are respectively assigned to them. Thus, the load demand is increased significantly from the northern area to southern one. In the EFCC modelling, the following sensitivities have been considered: 1) All-zone control (Proximity): Resources closest to event are deployed as priority and this approximates the GE's MCS in function; 2) All-zone control (Equality): Resources are evenly distributed across all zones but informed by global need; 3) Interim control: Response is zonally provided based on zonal information. It is to be noticed that this provides a pathway of EFCC optimisation to be mapped and the effect of the MCS to be simulated. Additionally, the proposed interim control has the potential to be an interim stage of EFCC deployment. It works on the principle of: i) If a "picture" of an event is needed beforehand, it can be accurately projected forward and reacted with confidence; ii) Even though, with enough information it can be still acted. The proposed interim has a reduced infrastructure requirement.

Error! Reference source not found. shows the relationship between components at different levels during the scheme operation, as laying out in the diagram, each zone is equipped with a zonal controller, which is in charge of the interim EFCC. The zonal controller connects to several zonal generators and their terminals converge at the location of the all-zone calculation. In this way, the zonal controller enables the data measured from generators to propagate through, from generators to all-zone calculation, and be utilised in the all-zone techniques as equality or proximity dispatch modes. As the resource response levels are responsible for reacting to the disturbances, they can receive the triggering signals from interim, equality and proximity modes, and execute the command to control the loads.

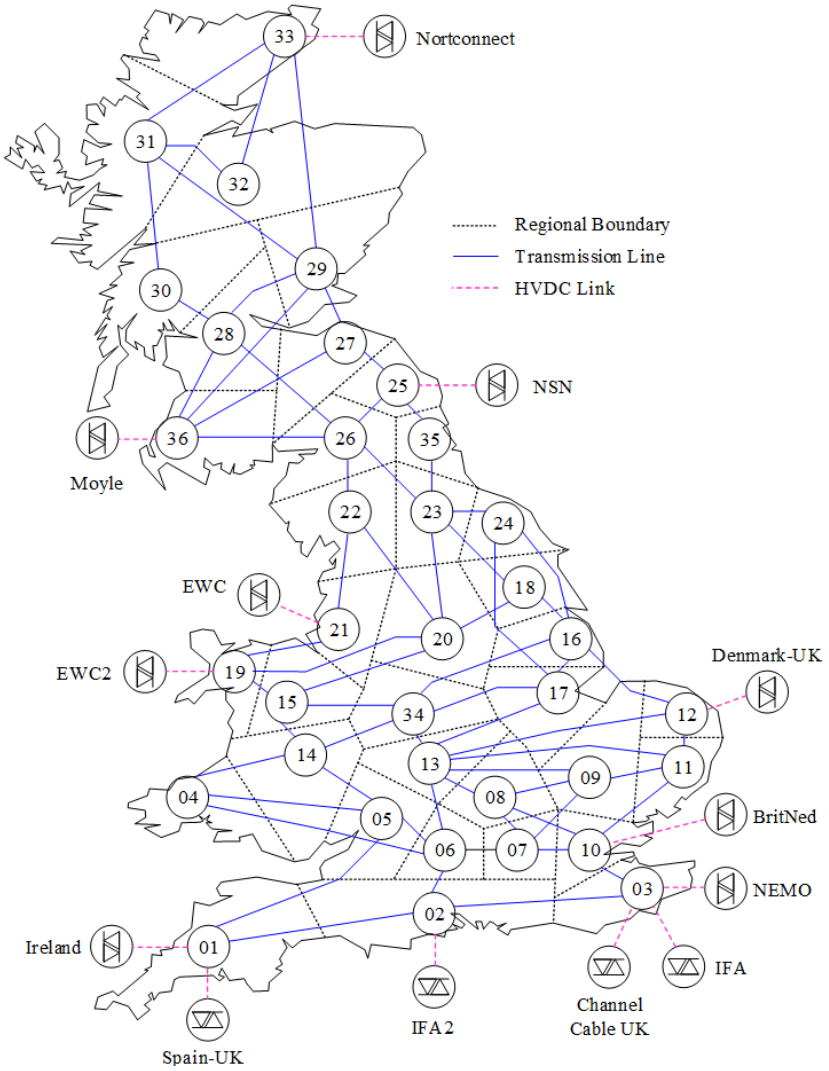

Figure 9-4: Single line diagram of 36-zone GB network

Figure 9-5is a zoomed graph of the first zone showing the specific functions of components at each level. At normal state, when the generators produce energy to match the load level, their frequency and capacity information are transmitting to the zonal controllers in a real-time frame. As the disturbance occurs, the resource response level decides either the system will be running under interim, equality and proximity modes. If the interim EFCC is selected, then the zonal aggregators in zonal controllers will compute COI frequency and RoCoF within zone, intermediate variables such as 2HS (where, H and S are inertia (s) and base power (MVA), respectively) and 2HSF (where, F is frequency (Hz)), loss of generation, as well as record the frequency nadirs and maximum RoCoF points. Otherwise, the computation process will be executed in the system aggregator (SA) of the all-zone calculation, for global counterparts of all the parameters described above. The roles of three important levels are listed as follows:

- **Interim EFCC Level**
- Calculate MS(2HS), MSF(2HSF) within zone
- Calculate COI Frequency within zone
- Calculate COI Frequency Nadir within zone
- Calculate COI RoCoF within zone
- Calculate maximum COI RoCoF within zone
- Calculate loss of generation within zone
- Calculate electrical/Mechanical power change within zone

- **Wide Area EFCC Level**
- Calculate global MS(2HS), MSF(2HSF)
- Calculate global COI Frequency
- Calculate global COI RoCoF
- Calculate maximum global COI RoCoF
- Consider the EFCC RoCoF threshold
- Calculate global loss of generation
- **WA1 (Equality):** Calculate the level of response to be triggered for each zone by equal allocation
- **WA2 (Proximity):** Calculate the level of response to be triggered by the zones closest to the disturbance
- Calculate global electrical/Mechanical power change

- **Resource Response Level**
- Select interim, equality or proximity EFCC
- Arrange ramp rate limiter of resource response
- Insert a low limiter to ensure that where load reduction calculated to be required in a zone exceeds the resources available in that zone, the resource is limited.

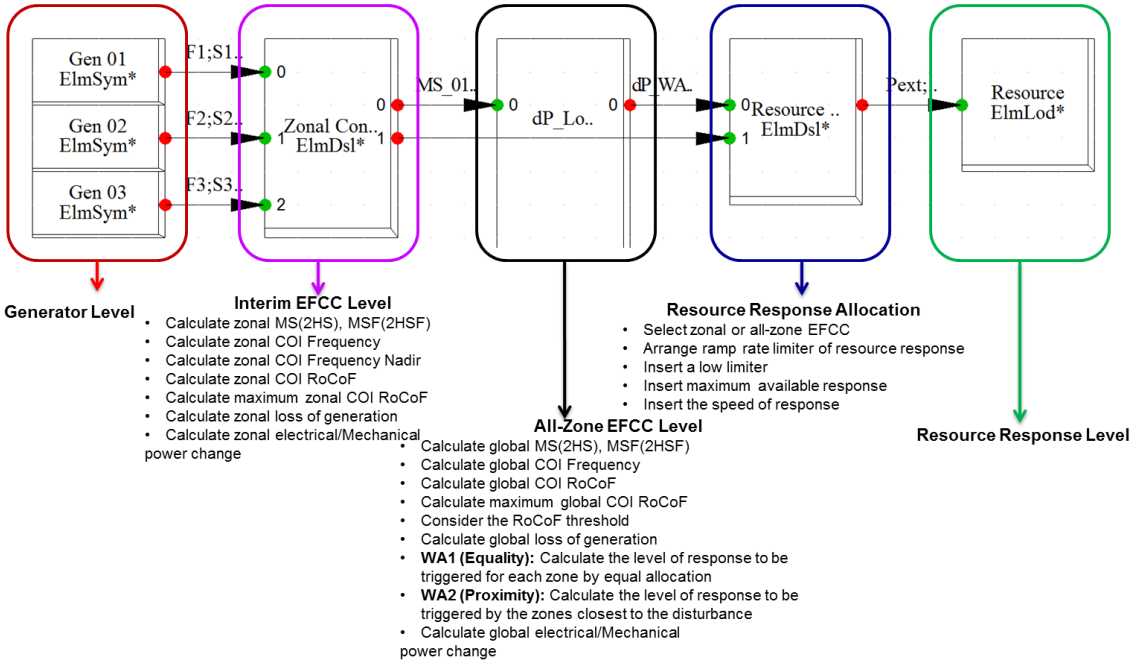

Figure 9-5: Detailed EFCC operation scheme in DIgSILENT PowerFactory.

In a detailed view, the interim EFCC function is divided into six function blocks as shown in Figure 9-6. Inertia has been also sent to zonal aggregation along with PMU frequency signal which zonal aggregation must be able to take zonal measurements and package in the suitable format for broadcasting. Under such preparation, zonal MS and MSF can be computed numerically in the red block. It is to be noted that M, S and F are mechanical time constant, base power, and frequency of generator, respectively. In the next step, the results of MS and MSF are leveraged in wide-area based EFCC level and resource response level respectively. Afterwards, on the basis of MS, the COI frequency and COI frequency nadir are computed as the key in the calculation of COI RoCoF and its minimum in the following functions. Zonal loss of generation is another production. Additionally, by the setting threshold and operating data acquired before, the electrical and mechanical power change within zone is able to be calculated here. From the diagram, it can be seen that totally 11 input ports are used to compute the zonal MF, MFS and the following processes, and additional 10 input ports are necessary for the power change calculation. As a result, the required information can be produced and outputted to the next step by the 10 output ports.

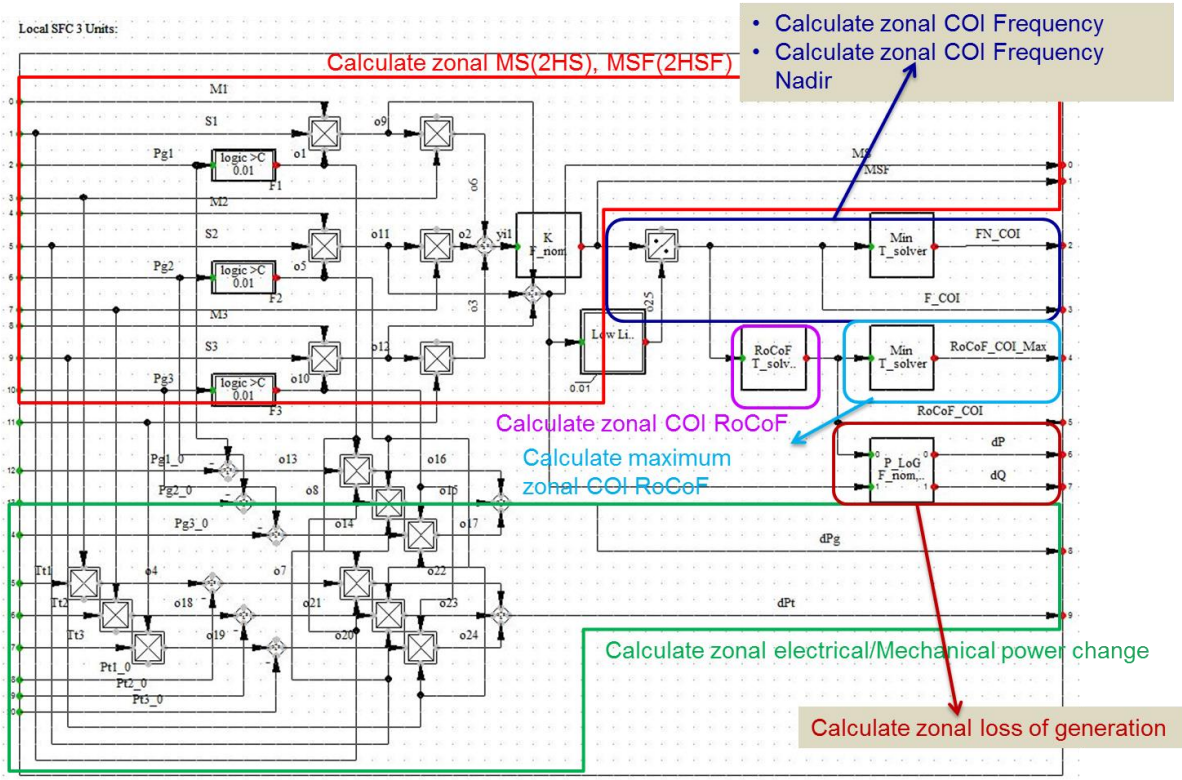

Figure 9-6: Detailed interim EFCC model in DIgSILENT PowerFactory.

It is to be noticed that based on GC0079 reference, a LF relay would trigger within 130ms being signalled for a "static service" like a tripping of demand) plus a 200ms cushion period to cover signalling and delivery. As the code presented in Figure 9-7 besides the window size described by T_{evt} , T_{tr} and $K_{sp} \cdot T_{sp}$, a communication time delay T_{cum}, results from inherent time of relay tripping and signal delivering, should be considered, when it comes to the response time of deploying resources. Thus, the time for "event trigger" and response action are respectively described as follows:

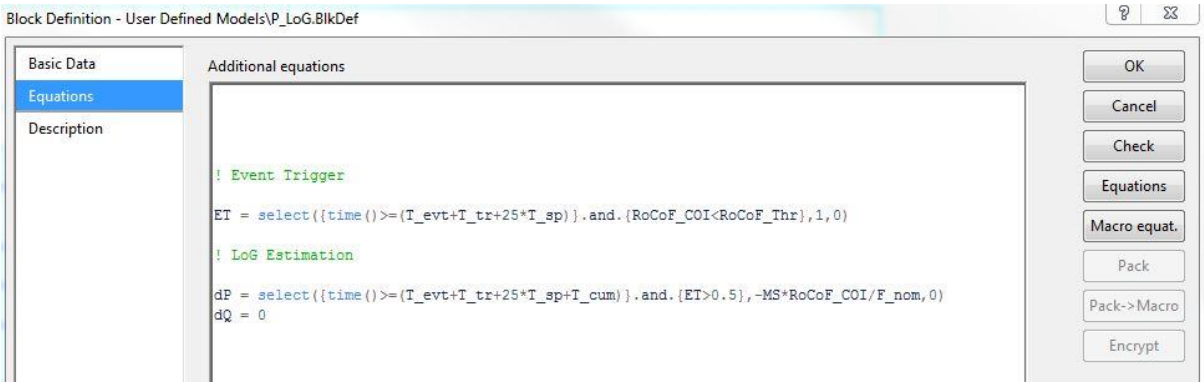

Figure 9-7: Loss of generation calculation within zone

$$t_1 = T_{evt} + T_{tr} + K_{sp} \cdot T_{sp} \tag{9.9}$$

$$t_2 = T_{evt} + T_{tr} + K_{sp} \cdot T_{sp} + T_{cum} \tag{9.10}$$

Other parameters and their values configured in this project, along with their function descriptions, are listed in Table 9-1.

Table 9-1: Parameter Settings for Running EFCC

Name	Type	Value	Unit	Description
Flag_setparam	int	0		Set parameters (>0).Run simulation(=0)
Zone_Number	string	01		Zone number of tripped generator
Generator_Name	string	NU		Name of tripped generator
T_start	double	0	s	Start time of simulation
T_stop	double	20	s	Stop time of simulation
T_solver	double	2.5	ms	Solver Time Step Size
T_evt	double	0.1	s	Time of loss of generation event
T_tr	double	200	ms	Freq Measuring Transient Time
T_sp	double	20	ms	RoCoF Sampling Period
K_sp_max	int	25		Number of Sampling for RoCoF Calculation
T_cum_local	double	0	ms	Communication Time in interim EFCC Mode
T_cum_wa	double	100	ms	Communication Time in WA EFCC Mode
RoCoF_Thr	double	-0.15	Hz/s	Threshold RoCoF
K_eff_est	double	0	%	Effective LoG Estimation Factor
P_RSR	double	600	MW/s	Active Power Rising Slew Rate in Resource Response
K_lsh_max	double	50	%	Allowable Maximum Resource Response of Each Zone
WA_Flag	int	1		Wide Area (>0), Interim (=0) Modes
dP_Flag	int	2		WA Mode: Equality Dispatch (=1). Proximity Dispatch

9.5. Test Description, Objectives and Process

9.5.1. Marginal Cases

This case is constructed from the plant dispatch for the consumer power minimum condition in the 2016 system operability framework (SOF) document data tables. This dispatch is then applied on the 36 zone GB model. Inertia assumptions by technology type are then applied based upon existing plant on GB capabilities and demand inertia assumptions for the events. The corresponding criteria can be considered:

i) no RoCoF in any zone as measured over 500ms >1Hz/s,
ii) no frequency nadir as measured in any zone of the network to fall below 49.5Hz.

This dispatch case has then flexed the size of the maximum loss of generation simulated by re-allocating MW between the following zones:

1) Test 1: Zone 1 – SW (where hinkley point C maximum loss of generation risk ultimately emerges, and where the variation between COI frequency and transient zone frequency is biggest)
2) Test 2: Zone 22 (Heysham area, where there is a lot of existing generation, some maximum loss candidates, and has the smallest variation between COI frequency and transient zone frequency).

The marginal cases based on the above criteria are obtained and shown in Table 9-2 and Table 9-3 for corresponding scenarios year 2020/21 and 2025/26. The respective system inertia is tabulated in Table 9-4. As can be seen from these Tables, all the EFCC sensitivities recover the frequency effectively for larger losses than are possible without EFCC. Up to 2025/26, interim EFCC mode is most effective however all approaches deliver acceptable results. Furthermore, with any of these 3 approaches being used under EFCC for the disturbance occurred in zone 1, a maximum system loss between 850MW and 395MW larger than possible without EFCC can be accommodated for scenarios 2020/21 and 2025/26, respectively. It is to be noticed that the amount of disturbances to reach maximum RoCoF of 1Hz/s in case of 2020/2021 are 645MW and 1290MW for zone 1 and 22, respectively.

Table 9-2: Marginal case for scenario year 2020/21

Zone	Frequency Nadir 49.5 Hz	With EFCC implemented
1	710 MW	1560 MW
22	725 MW	1685 MW

Table 9-3: Marginal case for scenario year 2025/26

Zone	Frequency Nadir 49.5 Hz	With EFCC implemented
1	530 MW	925 MW
22	555 MW	1035 MW

Table 9-4: System Inertia

Scenario year	Base Power S (MVA)	Base Power times inertia S*H (MVAs)
2020/21	27349.03	83575.14
2025/26	27259.98	48601.75

9.5.2. Comparison of of Interim, Equality and Proximity EFCC Schemes for scenario year 2020/21

All the following simulation results are associated with 1560 MW generator loss in Zone 1 in which frequency nadir reaches to its threshold i.e. 49.5 Hz.

- *System COI frequency*

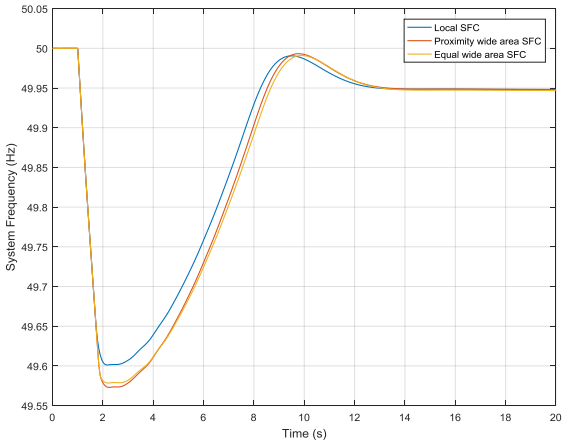

Figure 9-8: Comparison of System COI frequency using 3 modes (interim, all-zone (Proximity and equality)) of EFCC for 1560 MW loss in zone 1 in 2020/21

Figure 9-8 shows when there is 1560 MW loss in zone 1, the comparison of system COI frequency with 3 modes of EFCC. As can be seen, interim EFCC has lower frequency deviation due to less communication delay. It is clear-cut that interim EFCC can efficiently enhance the zonal frequency response of the system. This performance can be even more highlighted for test systems with lower number of zones. Furthermore, there are many user-defined parameters like transient time, RoCOF calculation time, sampling windows and etc. that can be properly tuned to highlight the superiority of interim EFCC. This sensitivity analysis is investigated in the next subsection. The proximity EFCC has the worst frequency nadir since the interim EFCC does need the zonal frequency data without communicating with other zones. Thus, the disturbance size will be quickly calculated and the required frequency response within zone will be triggered. As can be seen, the all-zone (Equality dispatch) and all-zone (Proximity Dispatch) have roughly similar frequency behaviour.

- *System COI RoCoF*

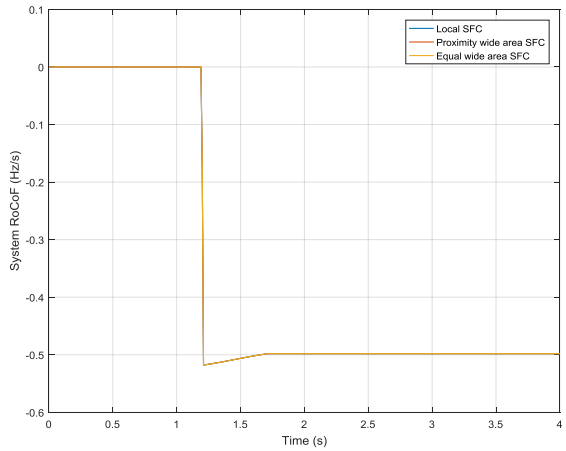

Figure 9-9: Comparison of system COI RoCoF using 3 modes (interim, all-zone (Proximity and equality)) of EFCC for 1560 MW loss in zone 1 in 2020/21

From Figure 9-9, the comparison of system COI RoCoF with 3 modes of EFCC has been shown. According to swing equation ($H = \frac{\Delta P \cdot f}{2RoCoF}$), the total system inertia excluding the tripped generator would be 72500

MW.s, since $\Delta P, f, RoCoF$ are 1,450 MW, 50 Hz and -0.5 Hz/s respectively. 3 modes of wide area have similar performance in terms of system COI RoCoF. It can be seen that the estimation error is 7% ((1560MW-1450MW)/1560MW).

- *Zone 1 frequency*

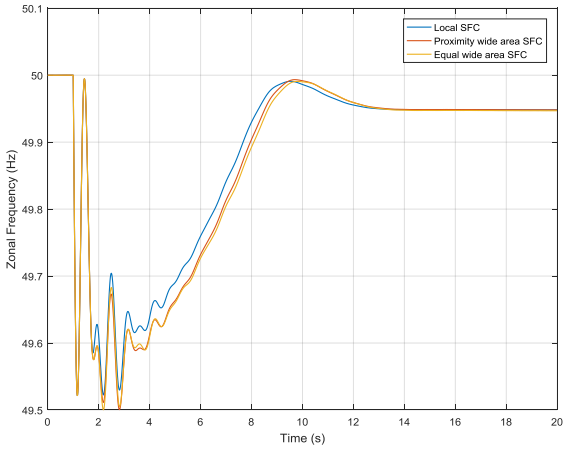

Figure 9-10: Comparison of zone 1 frequency using 3 modes (interim, all-zone (Proximity and equality)) of EFCC for 1560 MW loss in zone 1 in 2020/21

Figure 9-10 shows when there is 1560 MW loss in zone 1, the comparison of zone 1 frequency with 3 modes of EFCC. As can be seen, interim EFCC has better frequency nadir due to less communication delay. The proximity based all-zone EFCC has the worst frequency nadir. Unlike the equality and proximity modes of operation, the interim EFCC approach would not require wide-area, real-time availability of PMU data to inform frequency and RoCoF measurement during an event, nor the infrastructure to communicate this to centralized or distributed points of national calculation.

- *Total loss of generation estimation*

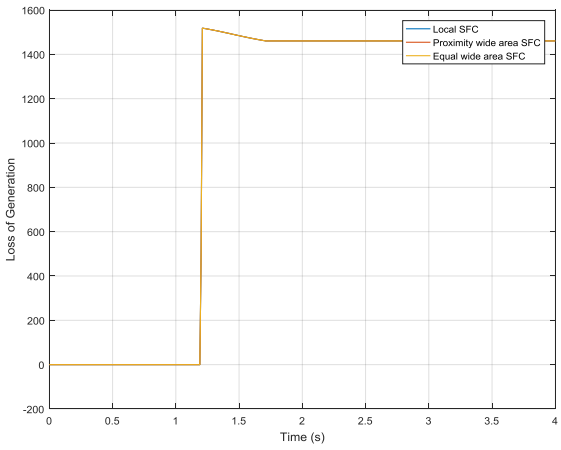

Figure 9-11: Comparison of total loss of generation estimation using 3 modes (interim, all-zone (Proximity and equality)) of EFCC for 1560 MW loss in zone 1 in 2020/21

From Figure 9-11, the comparison of total loss of generation estimation with 3 modes of EFCC has been shown. The loss of generation size i.e. 1,450MW estimated by swing equation after the RoCoF calculation window which is explained in previous section.

- *Load response of each zone*

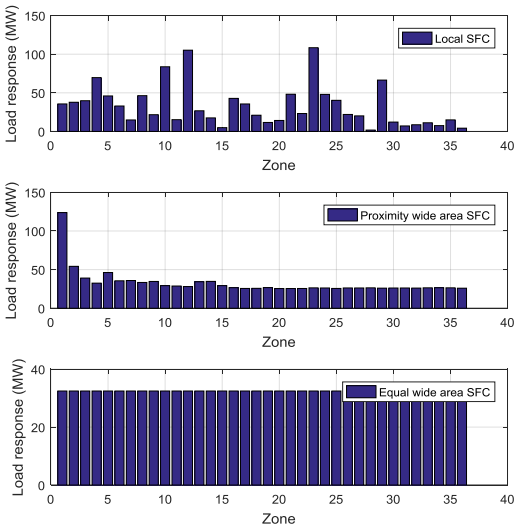

Figure 9-12: Comparison of load response of each zone using 3 modes (interim, all-zone (Proximity and equality)) of EFCC for 1560 MW loss in zone 1 in 2020/21

Figure 9-12 shows the comparison of load response with 3 modes of EFCC in each zone. As can be seen, the required power response within zone is dependent to the zonal RoCoF and inertia. The larger the inertia and RoCoF of the zone is, the larger frequency response is. For instance, the zonal frequency response burden on zones 23, 12 and 10 is higher as compared to other zones since their inertia and RoCoF are greater. In case of proximity technique, each zone has a different degree of influence upon the system considering their electrical distance. The closer to the disturbance location, the greater response is. For example, zone 1 has higher response as event is occurred in this zone. In equality mode, each zone principally shares the same responsibility for frequency response as can be seen in Figure 9-12. In case of all-zone based proximity and equality, all zonal resources are activated at the same time based on COI RoCoF. However, the zonal controllers of interim EFCC are activated based on the zonal COI RoCoF to allocate required response on resources.

9.6. Results & Testing Outcomes for scenario year 2025/26

- **Effect of Number of Sampling for RoCoF Calculation**

- *System COI Frequency*

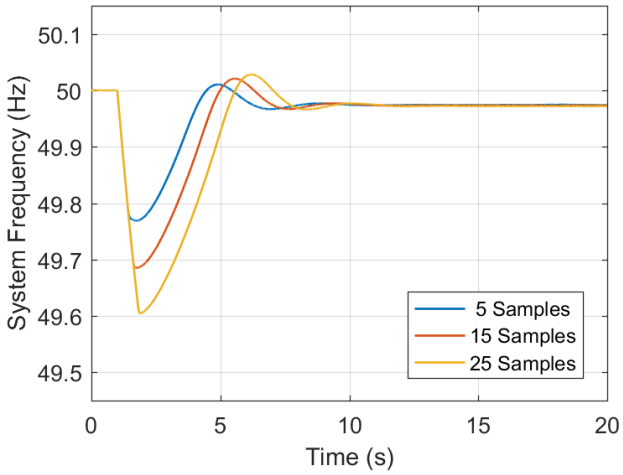

Figure 9-13: Comparison of System COI frequency with different Samples for RoCoF Calculation

Figure 9-13 presents three curves of system COI frequency variation, each of which is plotted with different number of samples taken into account. The more samples it takes, the lower frequency nadir will be obtained, accompanied with a larger overshoot. This phenomenon is caused by time delay, since in the RoCoF calculation process, involving more samples will extend the time duration for system to process the data information. The frequency is still dropping while the RoCoF and LoG remains unknown, and the resources will not be deployed until the calculation is finished. It is to be noted that at any given time it is important to get the balance right between too long a sampling period and too long a delay before deploying resource, and too short a delay and an inaccurate RoCoF for the deployment of resource.

- *System COI RoCoF*

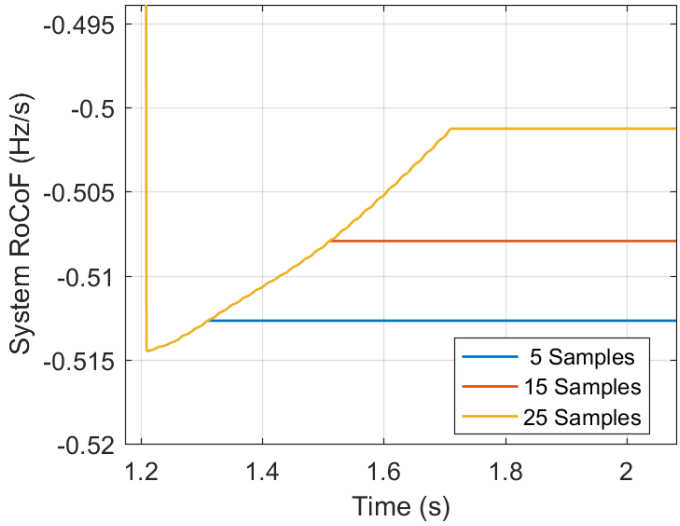

Figure 9-14: Comparison of System COI RoCoF of each zone with different Samples for RoCoF Calculation

Figure 9-14 shows the variation of system COI RoCoF, in which there is a vertical sudden drop at the initial stage. When the RoCoF decreases to around 0.515 Hz/s, it begins to rise back. Its value will be stabilised once the calculation is finished with all the samples. Therefore, since taking different number of samples differs the time period for RoCoF calculation, the three curves diverge at different time point. In case of lower sampling numbers, the time is relatively short, and thus a higher system RoCoF is observed.

- *Zone 1 frequency*

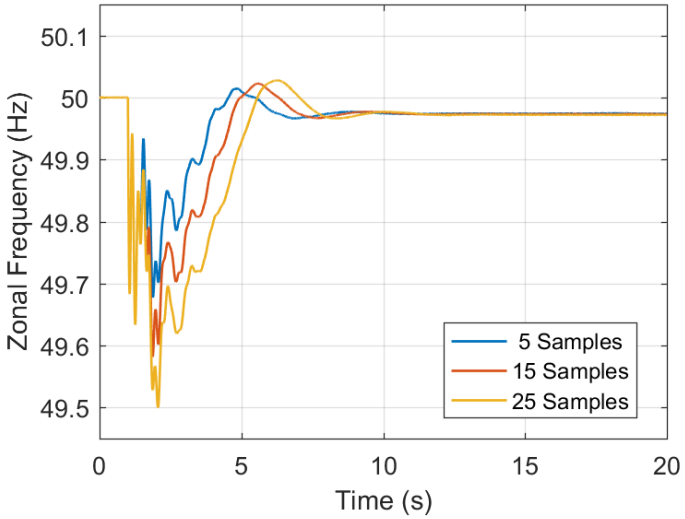

Figure 9-15: Comparison of zone 1 frequency with different Samples for RoCoF Calculation

In case of regional frequency, e.g. in zone 1, its behaviour looks just similar to its counterpart at system level, in terms of frequency nadir. Fewer samples lead to a lower nadir point and a larger overshoot calculation result. However, in the previous case, the system frequency is synthesised by data obtained from 36 zones, which has a positive effect on smoothing the curve, whilst in Figure 9-15, apparently, the graph contains much more oscillations. This is due to the local and inter-area oscillations. In power system networks, the small signal stability problems may be either local or inter-area which are dependent on the eigenvalues. The local problems involve a small portion of the system and they may be associated with rotor angle oscillation of a generator in an area against others. The inter-area problems are caused by interactions of a group of generators in one area swinging against a group in other area. However, the COI or average or system frequency is selected as the overall or representative of the whole network's frequency. Thus, this nation variable is less oscillatory in comparison with zonal frequency.

- *Total loss of generation estimation*

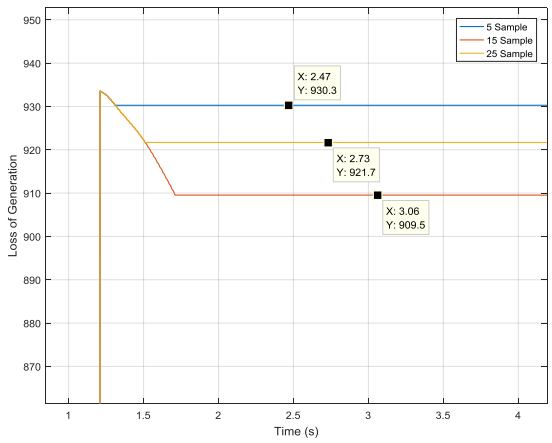

Figure 9-16: Comparison of total loss of generation estimation with different Samples for RoCoF Calculation

With the calculated system RoCoF values, the corresponding total system generation loss can be computed and plotted as shown in Figure 9-16. The LoG curves have the opposite trend, compared to the RoCoF, the smaller the sampling number, the higher the LoG value.

- **Effect of Communication Time in Interim EFCC Mode**

- *System* *COI Frequency*

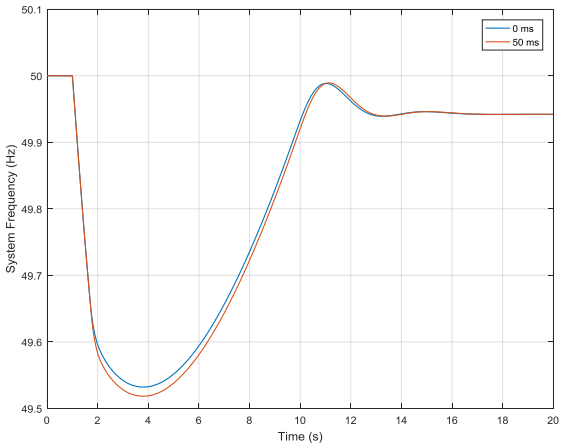

Figure 9-17: Comparison of System COI frequency with different Communication Time in inetrim EFCC Mode

In this subsection, the effects of communication time on the interim EFCC are going to be explored with the help of simulation software. These delays represent in this case delays in the communication between the zonal controller and the zonal resource without the centralised co-ordination from all-zone calculation, each LC will interchange necessary information when they co-operate to determine the deployed resources at each region, and accordingly bring about a communication delay when applying interim EFCC scheme to deal with disturbances. Obviously, according to Figure 9-17, the time delay leads to a lower nadir since it, to some extent, slows down the response speed.

- *Zone 1 frequency*

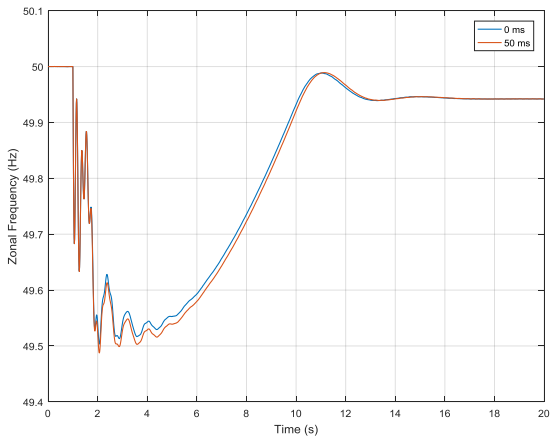

Figure 9-18: Comparison of zone 1 frequency with different Communication Time in interim EFCC Mode

Similarly, as the communication between zonal PMUs, zonal aggregation, event detection, zonal calculation, and resource response delays their responsive time, the nadir in each zonal frequency curve is also affected and becomes lower than the one with no communication time. Also, as mentioned before, both curves in Figure 9-18 contain much more oscillations than the ones of system frequency, since there is not enough amount of generation power in the neighbourhood can help stabilise the frequency behaviour in the zone.

- *Total loss of generation estimation*

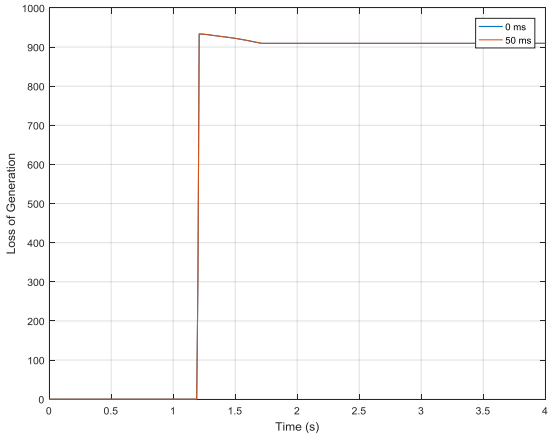

Figure 9-19: Comparison of total loss of generation estimation with different Communication Time in interim EFCC Mode

The swing based loss of generation calculation points out that the generation loss is proportional to the system RoCoF, and the multiple is determined by inertia constant, which is a fixed value once the generation units have been settled. Though communication signals slow down the process of resource response and deployment, it does not affect the RoCoF calculation as latency is mostly related to the data exchange between zonal controller and resource response block. Therefore, the RoCoF values are the same in both cases, and as can be seen in Figure 9-19, there is no difference in terms of LoG estimation.

- **Effect of Communication Time in all-zone EFCC Mode**
- *System COI Frequency*

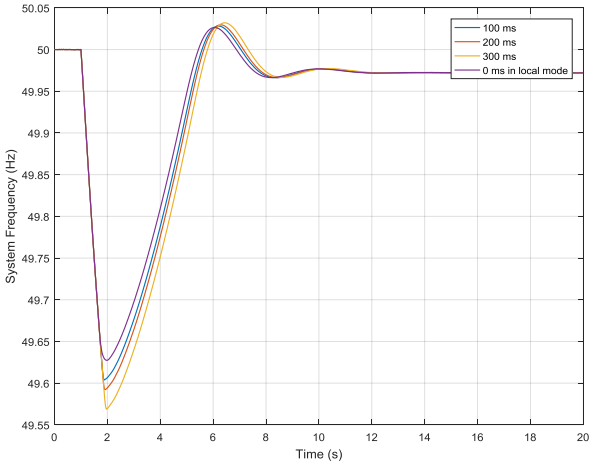

Figure 9-20: Comparison of System COI frequency with different Communication Time in all-zone EFCC Mode

In the wide-area mode, the situation is quite the same as in interim mode. The data signals transmit back and forth between all-zone calculation and each individual zonal controller, which takes much bigger time than in the previous scenario. Figure 9-20 compares four different cases with different time delay caused by signal delivering, and the possible communication delay in interim mode is neglected. The graph shows the same characteristic as before, due to faster response, in case of lower communication delay, less deviation of frequency is observed. Accordingly, the interim mode gives the best performance.

- *Zone 1 frequency*

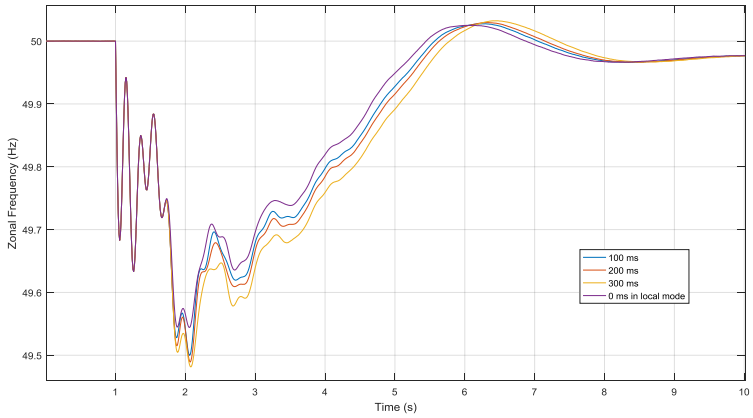

Figure 9-21: Comparison of zone 1 frequency with different Communication Time in all-zone EFCC Mode

When concentrating on the zonal performance, as shown in Figure 9-21, again, the frequency has a more oscillatory characteristic. It is worth noting that in each simulation, it can be seen that the zonezonal behaviours damp out in about 1.5s. Besides, if compared to the previous curves, with the centralised control and dispatch of all-zone calculation, the frequency oscillation in wide-area mode is more damped than in interim mode.

- *Total loss of generation estimation*

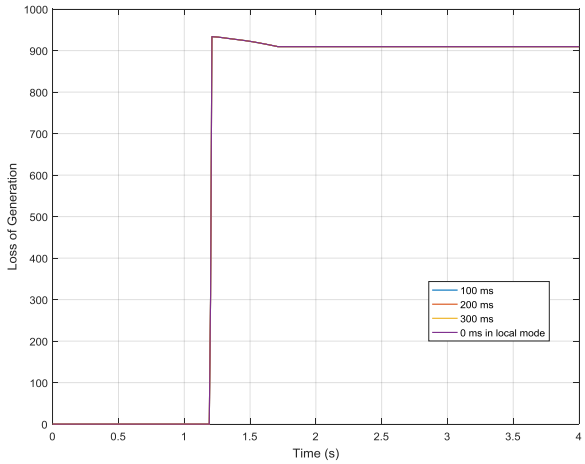

Figure 9-22: Comparison of total loss of generation estimation with different Communication Time in all-zone EFCC Mode

As explained before, the total LoG estimation only involves a fixed inertia constant and a changing RoCoF. However, the RoCoF calculation is roughly independent from the signal communication time. Thus, either working in interim mode or in wide-area one with different delay time, the LoG estimation results are all the same.

- **Effect of resource response rate in all-zone mode (Equality mode)**

- *System COI Frequency*

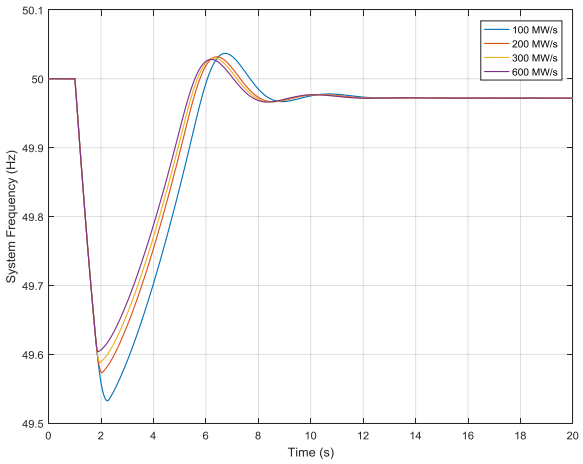

Figure 9-23: Comparison of System COI frequency with different resource response rate

Resource response rate decides how much time is required to perform full amount of function of EFCC scheme. Obviously, from Figure 9-23, there is a distinct improvement in both frequency nadir and overshoot as the rate increases from 100 MW/s to 200 MW/s. When the rate continues to go up, the situation can still be improved, nonetheless, the change gradually becomes smaller. This phenomenon results from the fact that usually only a relatively small amount of zonal load is participated in resource response and the time needed to pull the whole required amount is almost the same once the rate rises up to a certain value.

- *Zone 1 frequency*

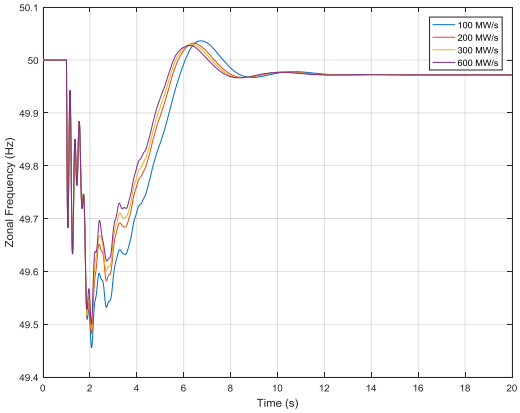

Figure 9-24: Comparison of zone 1 frequency with different resource response rate

Figure 9-24 shows the frequency changing curves of zone 1 solely, which is just similar to the system frequency behaviour. Again, with the same reason mentioned before, the zonal frequency curves have a more oscillatory characteristic.

- **Effect of Allowable Maximum resource response of Each Zone in wide area mode (Equality mode)**

- *System COI Frequency*

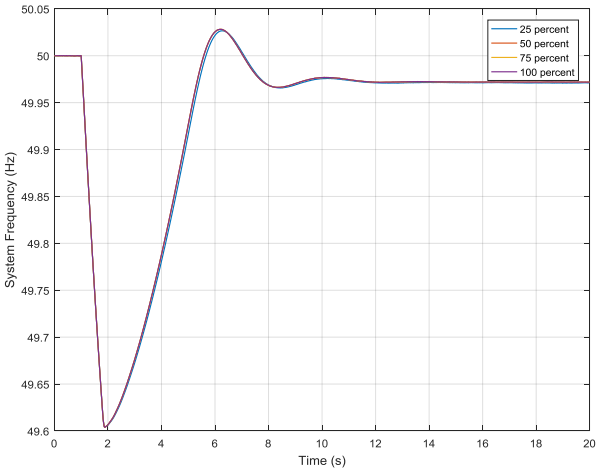

Figure 9-25: Comparison of system frequency with different Allowable Maximum Load Shedding of Each Zone

Appending this parameter is considered to indicate the allowable maximum resource response amount at each zone. The system operator can specify maximum limit of resource response which can be set to up to 100 percent of zonal resource response availability. If this is not sufficient resources available, the act of responding with resource in all zones is investigated. Considering the scenario where a maximum limit is put on the resources deployed in each zone, the effect of resource reponse limit is to be examined. The result is presented in Figure 9-25, there are only extremely small difference between different cases in terms of frequency change, as most of the zone responds less than 25% of the total amount of zonal load. It would appear that the overall response is not bounded particularly and the available resources within the zones respond sufficiently and efficiently.

- **Effect of Effective LoG Estimation Factor in all-zone mode (Equality mode)**

- *System COI Frequency*

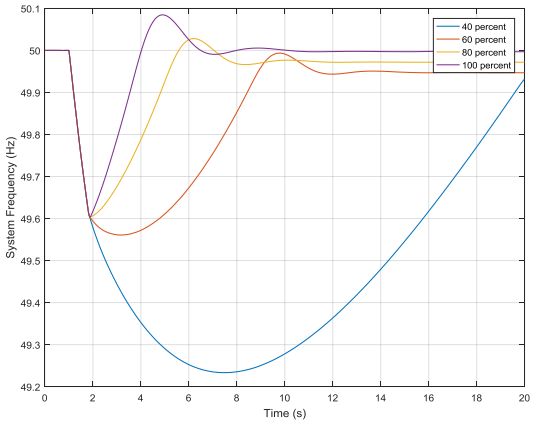

Figure 9-26: Comparison of system frequency with different Effective LoG Estimation Factor

This parameter can be tuned appropriately by the user in order to determine the contribution of EFCC scheme and online generating units' frequency response in the total estimated loss of generation. The higher the value of

'K_eff_est', the lower the frequency response burden on the online conventional units. If it is set to 40%, it means that 40% of the loss of generation is compensated by EFCC and the rest must be supplied by other power plants in the system using their inertial and primary frequency supports. This is considered to illustrate the effect of insufficient resources in all zones and its impact on frequency based transient stability. It means that the act of responding with resource in all zones, where some did not have sufficient resource, is investigated in terms of insufficient resources in zones.

In this scenario, the estimated total LoG of the system will be manually controlled by multiplying an effective estimation factor, in percentage, to the original value. The purpose of this simulation is to make a comparison between different situations where the responsibility is distributed between resource response level and on-line generating units by different ratios. For the case with higher amount of LoG estimated by swing equation, the load response called by resource response block is also higher. Since the resource responds faster than the generators, as plotted in Figure 9-26, the system frequency response performance is considerably better. On the other hand, the system frequency response burden on generating units connected to the system would be higher in case of lower resource response, and thus reduce the efficacy of the control scheme.

- *Zone 1 Frequency*

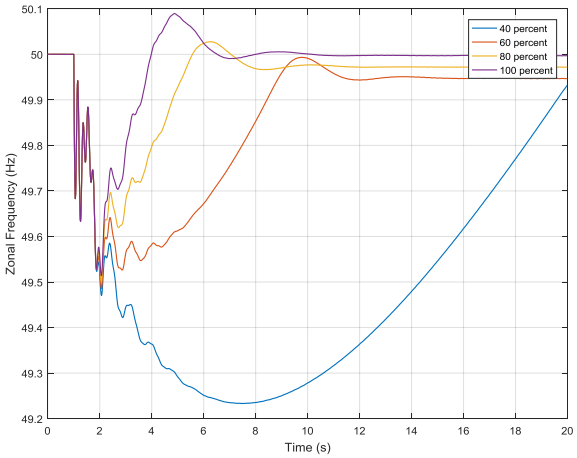

Figure 9-27: Comparison of zone 1 frequency with different Effective LoG Estimation Factor

When applying the estimation factor to the LoG, other than system frequency, the variation in interim technique shows the same characteristic as described above, as seen in Figure 9-27, except that the oscillations at initial stage are sudden and strong.

- **Effect of RoCoF Threshold in Interim EFCC mode**

- *Zone 1 Frequency*

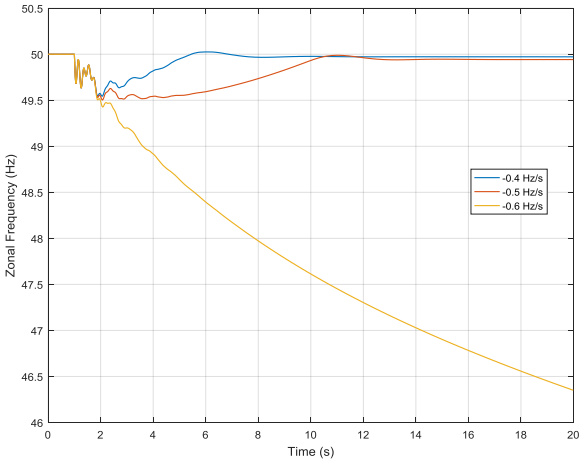

Figure 9-28: Comparison of system frequency with different RoCoF threshold

Figure 9-28 gives a clear comparison of frequency behaviour between three different RoCoF threshold situations in a zonal scenario. Apparently, as long as the trigger point of RoCoF is configured within 0.5 Hz/s, the superiority of applying EFCC scheme on the GB system can be easily recognised, since the frequency will be restored to nominal in a few seconds and its nadir can be controlled to stay above 49.5Hz. However, for a higher amount of RoCoF threshold, e.g. 0.6Hz/s, the interim EFCC based monitoring and control scheme cannot be activated and the frequency will be collapsed, as the response of online units is not sufficient to stabilize frequency. When the RoCoF is too large, the picture of the initial inertia as its distributed around the system is no longer close to the one during the event, and as such having a full wide area calculation matters is needed where there is right distribution of the resources across the system. The RoCoF threshold should be more carefully tuned in interim mode. When the threshold is set within the activating range, according to the simulation results, a smaller absolute threshold value can enable power system to possess a faster response.

- *Load response in all zones*

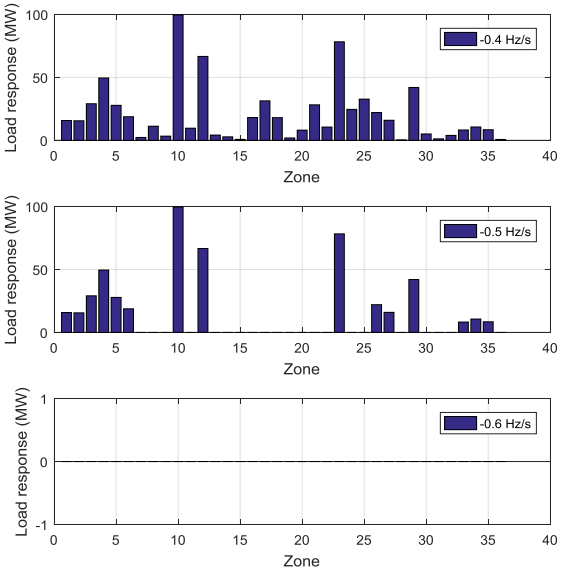

Figure 9-29: Comparison of load response with different RoCoF threshold

Expand the above simulation to all 36 zones, it can be seen that when the threshold is around -0.4 Hz/s, load response in all of zones can perform function properly. As the value increases to -0.5 Hz/s, resources in several zones located at the central area cannot be deployed. Once the RoCoF threshold reaches to -0.6Hz/s, the entire interim EFCC scheme does not work anymore because of the reasons mentioned before. To sum up, the lower amount of RoCoF threshold, the more zones will be participated in the resource response level. Additionally, since the value of LoG is determined by a fixed maximum point of RoCoF after the EFCC scheme is triggered, though larger threshold leads to more frequency drop, the deployed amount of resource in each zone remains unchanged (See Figure 9-29).

- **Effect of a 3-phase short-circuit fault followed by 1560 MW loss of generation in zone 1 for scenario year 2020/21**

A 140ms three-phase short-circuit fault (solid fault on the 400kV zone 1 busbar- no fault resistance model)) followed by a loss of generation at *t*=1s in zone 1 (SW England) of 1560 MW for scenario year 2020/21 is applied on GB test system. The developed scheme can identify the faults and act appropriately. It is also a helpful case study to recognize how significant the impacts of faults are. Zonal frequencies of all 36 zones are depicted in Figure 9-30 and Figure 9-31. The solid red line represents the COI system frequency and the blue line indicates the aggregated zone 1's frequency. The effect of short circuit fault can be seen as the frequency rises during the short circuit period. As it can be seen, the zone 1 transient frequency 50.7- 48.3 Hz is occurred during the period that the fault is being applied. It means that with a three phase fault, the system is largely impacted, and the system frequency has shown a tremendous increase due to the fault. After fault clearing time, the generator is tripped which eventually leads to an under-frequency event. The designed scheme is not affected by the frequency rising since the initial measured frequency provided by measurement is blocked from calculation by considering the interval called 'Transient time'. As such, the scheme can correctly detect the event, calculate the RoCoF and allocate the amount of response to the zones in a correct manner. As can be seen, the RoCoF calculation time set to 500 ms which can be changed to 300 ms to trigger EFCC earlier.

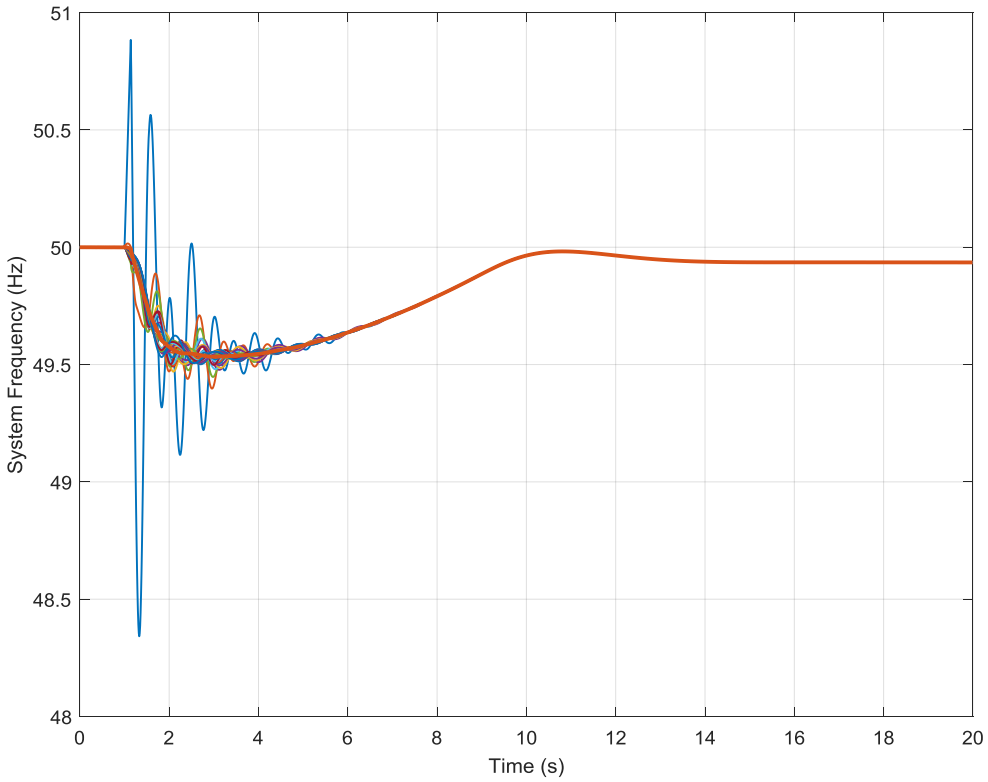

Figure 9-30: Zonal and COI frequency following loss of generation in zone 1 (SW England) of 1560 MW as a result of a 140ms 3p-e fault for scenario year 2020/2021 (Brown-COI frequency, light blue: zonal frequency of SW England)

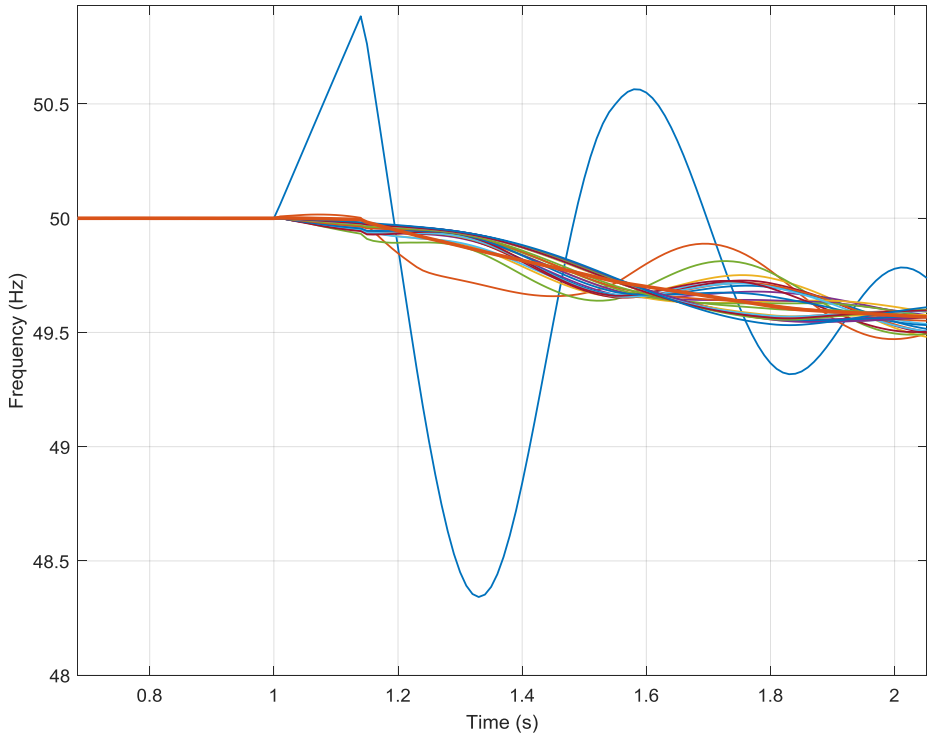

Figure 9-31: Zoomed zonal and COI frequency following loss of generation in zone 1 (SW England) of 1560 MW as a result of a 140ms 3p-e fault for scenario year 2020/2021 (Brown-COI frequency, light blue: zonal frequency of SW England)

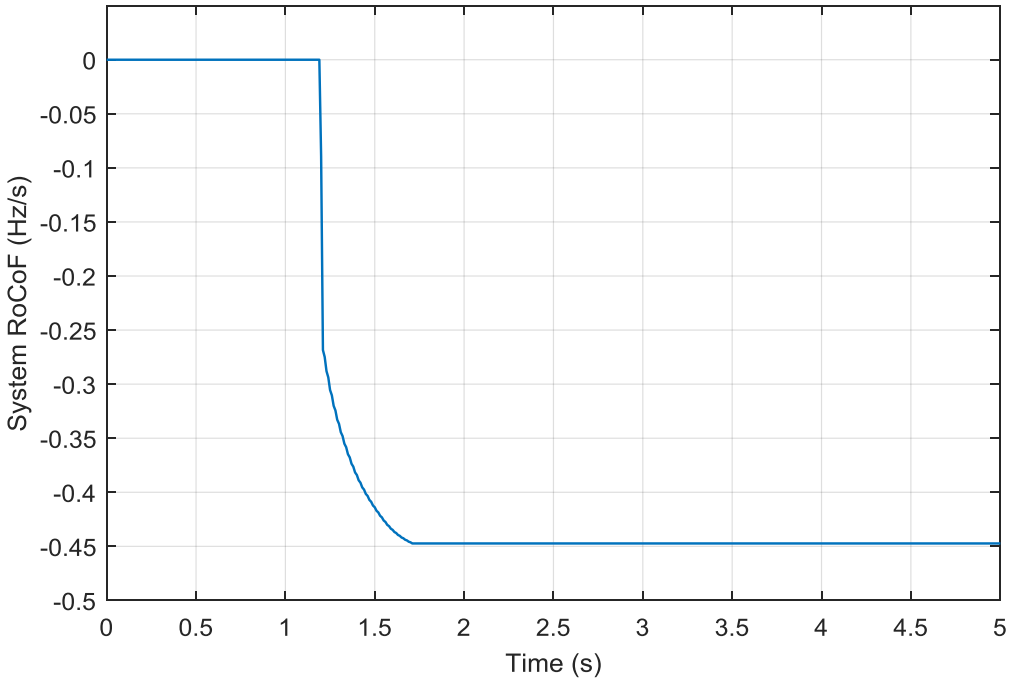

Figure 9-32: System COI RoCOF following loss of generation in zone 1 (SW England) of 1560 MW as a result of a 140ms 3p-e fault for scenario year 2020/2021

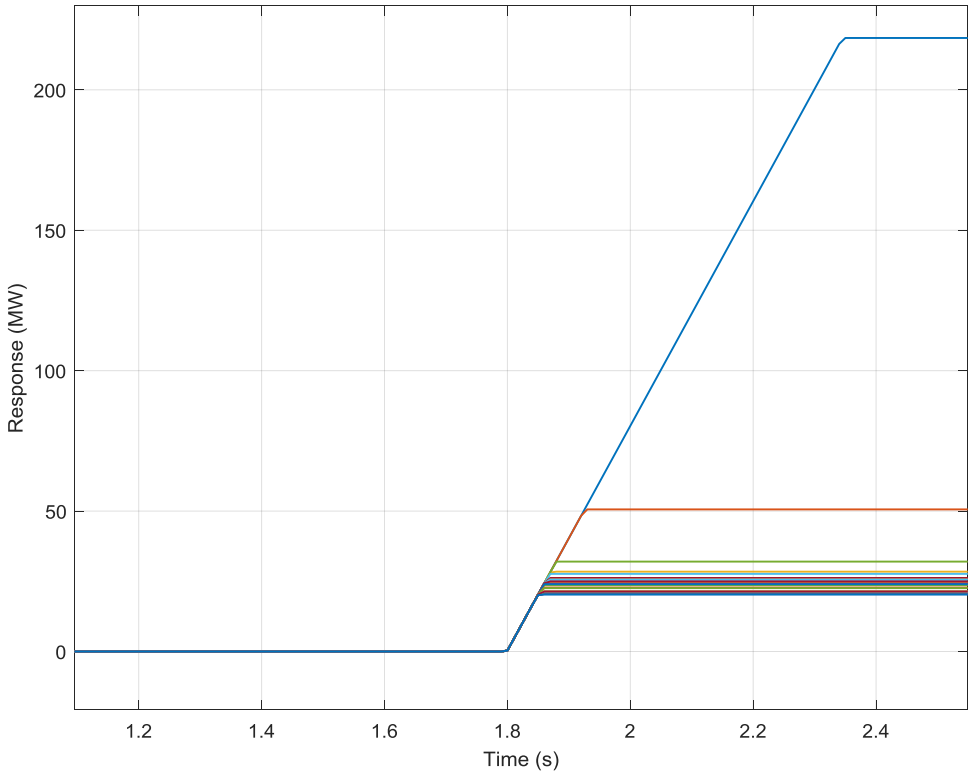

Figure 9-33: Zonal rsource response level over time following loss of generation in zone 1 (SW England) of 1560 MW as a result of a 140ms 3p-e fault for scenario year 2020/2021

In Figure 9-32, the calculated system RoCoF is shown. It can be seen the effect of short-circuit is negligible. The zonal resource response level over time following the event+fault (Light blue trend is associated with zone 1's response) is illustrated in Figure 9-33. This figure is provided to show resource deployment over a time component so it is clear how the resources are being deployed. This illustrates this fact to understand the timing sequence of resource deployment and the impact on the oscillations. As expected, the response of zone 1 is the largest (in blue) as the RoCoF of zone 1 is significantly greater than other zones. Additionally, it is confirmed that the resources are being dispatched closest to the event and evidenced in the above mentioned frequency plot.

- **Effect of 1560 MW loss in zone 1 for 2020 with unbalanced resource allocation**

This is a worst-case scenario of high resource in Scotland (8 zones) versus zero resource in England with an event at zone 1 (SW England) under loss of generation 1560 MW at *t*=1s. In the current tests, the assumption of sufficient resources in 8 zones located in Scotland and completely insufficient resources (none of England zones are participating in EFCC's response) acts to investigate the high efficiency of transient stability of EFCC. Zonal frequencies of all 36 zones are shown in Figure 9-34, which recovered after EFCC's action. Light blue trend is corresponded to zone 1's frequency while COI frequency is represented as Brown colour. The system RoCoF is also given in Figure 9-35. The results indicate that for this extreme case, the scheme would drive a short term deviation below 49.5Hz but above 49.2Hz. As an exceptional event, this would be still acceptable since the deviation is of short duration and low probability.

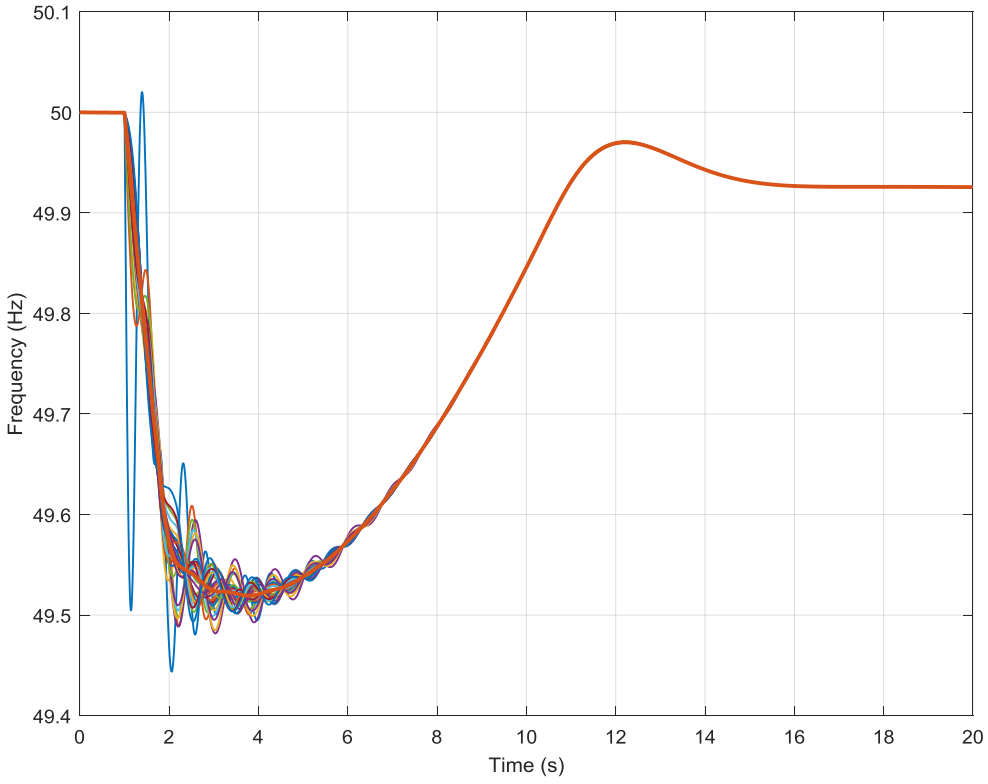

Figure 9-34: Zonal and COI frequency following loss of generation in zone 1 (SW England) of 1560 MW (Brown-COI frequency, light blue: zonal frequency of SW England) for scenario year 2020/2021 with unbalanced resource allocation

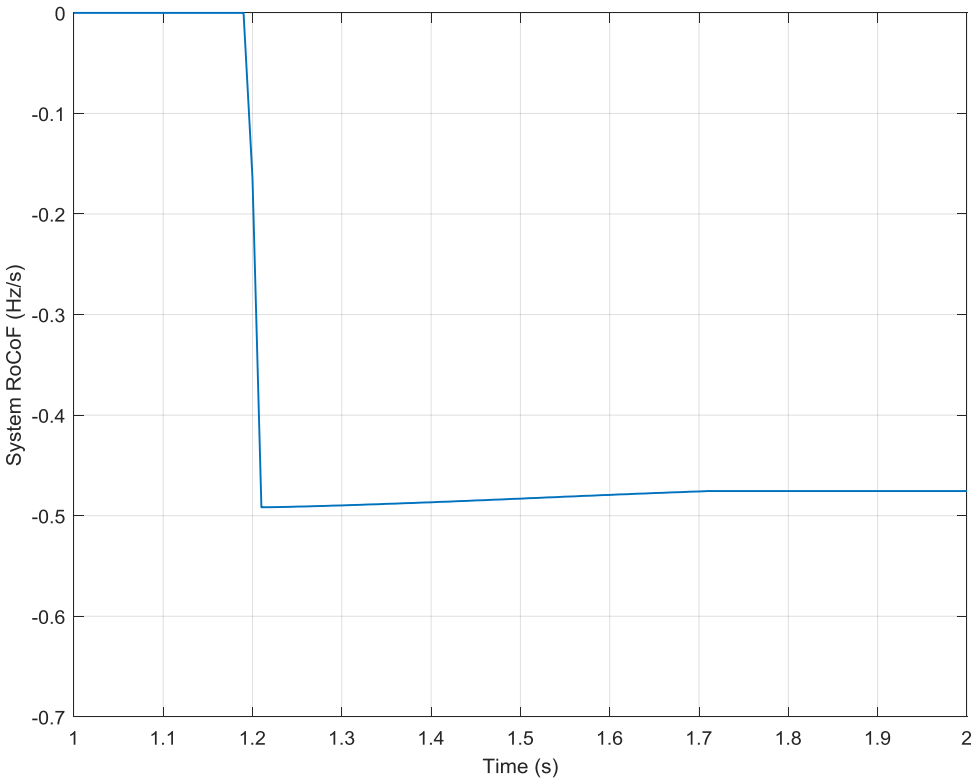

Figure 9-35: System COI RoCOF following loss of generation in zone 1 (SW England) of 1560 MW for scenario year 2020/2021 with unbalanced resource allocation

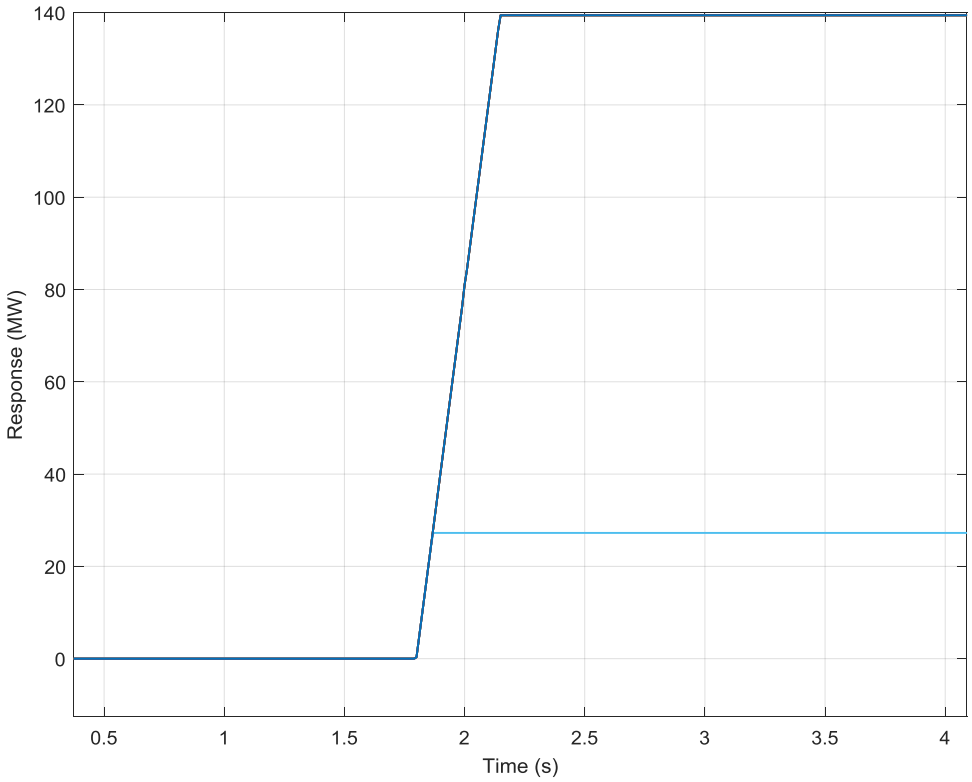

Figure 9-36: Zonal rsource response level (only 8 available zones in Scotland) over time following loss of generation in zone 1 (SW England) of 1560 MW for scenario year 2020/2021 with unbalanced resource allocation

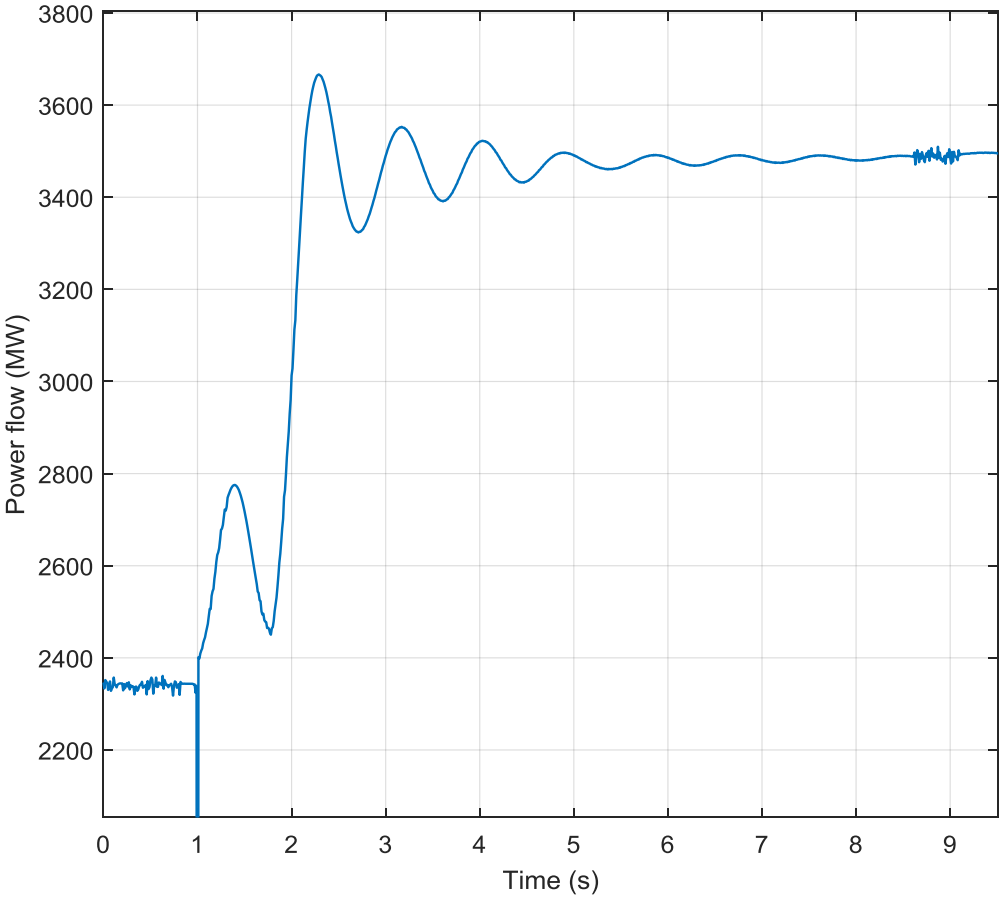

Figure 9-37: Power flow from Scotland to England (three lines located in boundary) following loss of generation in zone 1 (SW England) of 1560 MW for scenario year 2020/2021 with unbalanced resource allocation

Boundary power flow from Scotland to England (i.e. loss in SW England, no response at England, and all responses in Scotland) is shown in Figure 9-37.

9.6.1. Summary of system studies with (MCS)-Local and wide area SFCs

3 possible forms of fast frequency control have been modelled- these being Proximity dispatch (approximating the performance of the GE MCS), Equality dispatch (where deployment of resources are evenly spread across those available, irrespective of the location of the event) and Interim mode (where the picture of inertia distribution during the event is used to ensure a degree of co-ordination in the deployment of zonal resources based on frequency and RoCoF within zone during the event). These three cases respectively enabled modelling the full MCS capability, the effect of not seeking to damp inter-area effects, and finally the sensitivity of not relying on the wide area communication in real-time during the event itself. These algorithms are designed with a flexible user interface allowing settings, approximating to those deployed in the actual GE MCS to be implemented and allowed further analysis sensitivities on their selected values.

The EFCC based modelling approaches are able to simulate the key to EFCC which is the deployment of sufficient resources to meet the event. The modelling drives the right level of response in the right area of the system to support stable system recovery. Containment of maximum active power loss within 500ms - 700ms of

the event is needed to avoid restricting the maximum loss possible at that time. Whilst deployment of resource close to the event is beneficial, it has identified that up to 2025 this is not essential so that the zonal area (interim wide-area) control is sufficient. This approach is not dependent on real time frequency and df/dt other than zonally received but which does need a wide-area picture of the system's state prior to an event. Approaches allow researchers to see the zonal and global frequency, identify how and to what extent zonal resource is important and how best to combine EFCC with other forms of frequency response. EFCC requires sufficient time to deliver. The above models are designed to consider the future operation of the GB transmission system with and without fast frequency response, dispatching the reduced 36 bus model of the GB system to representative future year's inertia and generation/demand mix.

It is to be noted that following a frequency event, for a maximum of 4s, the frequency and rate of change of frequency can be seen to differ across the GB system. It is observed that the inertia declines and distribution of inertia changes in the future system operating conditions, the system frequency and rate of change of frequency become more volatile, with frequency falling more rapidly during an event. Assuming no replacement of inertia support is found from changes to current control approaches to Non-Synchronous Generation or no fast frequency services under EFCC is delivered. The DIgSILENT PowerFactory's works have demonstrated that all 3 options for fast frequency control are effective for future scenarios on the GB system up to 2025, but that at levels of RoCoF above 0.6Hz/s expected to occur more frequently beyond 2025 a solution which goes beyond interim wide area would be needed. Across the period of study, a benefit of increasing the maximum loss that the system could otherwise provide between 400MW and 850MW of additional maximum loss capability to the GB grid, avoiding the need to intervene into the GB energy market to constrain down the maximum loss.

The following points can be highlighted as the outcome of this work:

- Developing the interim, equality and proximity based EFCC schemes as the monitoring and controlling scheme for the system operator for the sake of fast frequency response which monitor the electricity networks at the global and zonal levels and instruct response from a range of resources, respectively.
- System studies of the appropriate GB network with/without monitoring and control scheme (MCS) in DIgSILENT PowerFactory
- Investigations into the causes of inter-area frequency oscillation as the GB system progresses towards low inertia operation,
- Investigation into how to best model the effects of different strategies for EFCC fast frequency delivery and to understand their benefits on the future system
- The scheme is secure against three-phase short circuit fault followed by loss of generation event.
- The high efficiency of transient stability of EFCC is proved by considering completely insufficient resources as none of England zones are participated in EFCC's response.

9.7. References

[1] P. Kundur, N. J. Balu, and M. G. Lauby, Power system stability and control. New York: McGraw-hill; 1994 Jan 1.

[2] GE resource allocation, https://www.nationalgrid.com/sites/default/files/documents/ResourceAllocationPR_v1_0.pdf

10. Thesis Summary

This thesis proposes a new SFC based local and WAMS for assessing the role and the value of service providers in the future low-variable inertia power systems with high penetration of converter-connected generating units. This chapter highlights the main contributions of this thesis and summaries the most promising opportunities for further research studies.

10.1. Introduction

The research provided in this thesis is focused on deriving several techniques for enabling the delivery of fast and robust frequency control, especially in the low-variable inertia power systems where the speed of frequency regulation is of vital importance. In this regard, a dynamically valid reduction of the GB system i.e. 36-zone GB system from National Grid (NG) data is provided. The illustrative dynamic models of generator, governor, power system stabilizer, voltage controller and static voltage controller are introduced into the network reduction for the purpose of frequency control dynamic studies. Impact of system inertia on electromechanical modes is examined using the modal analysis approach. Mode shape concept is employed to determine dominant units and contribution of different zones in network frequency oscillations. Time domain simulation studies are undertaken to validate the modal analysis results. The condition of different regions from the viewpoint of frequency nadir and maximum rate of change of frequency for contingency cases and extreme cases are examined.

In other hand, without detailed technology models, any frequency control scheme will be based on the generic assumptions about technology capabilities which may not be accurate. As such, true performance is not aligned with simulated performance. The dynamic characteristics of different forms of response provided by disparate sources like CCGT, WT, PV, BES and SIM are investigated and demonstrated. It means that one of the key aspects of the work is to test and understand the capabilities of different fast frequency service providers. The inertial and droop based controlling structures of WECSs, PVs, BESSs and SIMs are appropriately modified to make them to contribute the inertial and primary frequency responses to the system.

Smart and fast frequency control permits the system to initiate the frequency response resources before the large frequency deviation, where the frequency threshold violation will trigger the response. Faster and more robust delivery of frequency regulation mitigates the size of required frequency response and the risk of secondary incidents and ultimate cascading blackouts. Therefore, the efficiency of the local and wide-area SFC depends extremely on the timing and accurateness of the event size estimation. Following an unintended disconnection of a synchronous generator from the power system, it is quite difficult for power systems operators to correctly estimate the post-event power system's inertia and loss of generation size as they are both functions of the unknown inertia reduction. To solve this problem, the thesis presents an analytical method based on the RoCoF. The method relies on a modified swing equation that allows to directly take into account the inertia reduction and the consequent LoG estimation. In other words, the inertia reduction and LoG size estimations are accomplished simultaneously and independently. This leads to a more accurate decision on the size of fast and smart frequency response obtain by fast service providers, hence lower cost and reduced the risk of frequency instability.

After that, the suggested smart frequency based local and WAMS is proposed. The provided inertia is high enough, given the effect of an inertial loss is small in proportion to GB system difference in calculation is small in local SFC compared to wider one. That given this approach does not need real-time coms provided other than locally to resource, it would not require as significant monitoring and coms infrastructure. Additionally,

deployment of resource close to the event is beneficial in local SFC mode. At present, researches into the areas fundamental for delivering a smart frequency control, is predominantly pertinent due to the expected frequency security threat imposed by high integration of converter-connected generating units in the coming decades. Additionally, the advent of PMUs and WAMS opens opportunities to explore new approaches for power system frequency control.

10.2. Conclusions

SFC is associated with any form of fast and robust active power injection or load reduction within a second of incident occurrence, targeting to serve as an alternative for amplified volume of primary response needed in the low-variable inertia power networks. The pre requirements for implementing SFC in contingency situations are as follows:

- A real-time and large-scale test system like 36-zone GB test network with appropriated dynamic types and parameters, to develop and test SFC
- Fully decentralized control of the proposed dynamic modelling of CCGTs, WTs, PVs, BESs and SIMs based on the local frequency, to optimally contribute to the inertial and primary frequency control without wide-area communication/coordination procedure.
- Fast, accurate and online estimation of disturbance size, to aid adapting the size of fast frequency regulation
- Local and wide-area SFC, to quickly initiate fast frequency service providers closer to the disturbance location with reliable communication infrastructure.

Therefore, Chapter 2 mainly dealt with investigating the dynamic performance of the reduced 36-Zone GB network topology following the loss of generation. The illustrative dynamic models of exciter system, thermal and hydroelectric units and SVCs are introduced into the network reduction for the purpose of frequency control dynamic studies. These are generically developed on the basis of literature review to make a standard real-time test system, and are not intended to be representative of specific generation connections within the GB system. Further, the dynamic impact of these devices on small signal stability and electromechanical modes in the frequency interval of 0.5-1.25 Hz is examined using the modal analysis. It is shown that the 36-Zone network developed has the similar dynamic behaviour with a single machine infinite bus system as the inertia of the whole SGs is increased. This can lead to the reduction of damping and its frequency related to the electromechanical modes. Conversely this alignment is reduced as the level of inertia and its location across the network is varied. Afterward, the mode shape concept is employed and it is observed that the first and second slowest modes of electromechanical mode group are the inter-area modes and divides the network into two major parts which swings against each other. Time domain simulation studies are also deployed to investigate the dynamic response of the network following the loss of SGs and validate the modal analysis results. Using illustrative referenced assumptions of dynamic models we therefore have been able to in the above work illustrate how both national frequency centre assessment of frequency disturbances and its regional variation may be considered within a model capturing both generator dynamic assumptions and a sufficiently extensive network reduction of transmission system topology.

In Chapter 3, the dynamic performances of four-area based KRK and 36-Zone GB network integrating CCGTs are investigated following the loss of generation and to study the influence of high penetration CCGTs on frequency control following the loss of generation. The modal analysis is selected to provide the small signal results. It is clear-cut that the change of turbine dynamic form GT to CCGT does not have considerable effect on electromechanical modes. However, converting the GT units to CCGTs can increase the damping of the electromechanical modes. In the time-domain studies, the condition of different regions from the viewpoint of frequency Nadir and maximum RoCoF for all N-1 criteria is examined. Additionally, the worst case time domain analysis is also deployed. As large scale CCGTs substitute with current conventional power plant in

future, frequency control might become more challenging. The results depict that with supplementary CCGTs on the power system, large frequency decay in Nadir and steady state conditions will be more probable while they work in full-load mode, and the system operators of GB network need to operate them in partial mode to prevent enormous load shedding. Moreover, the system operators of GB network need to prudently manage the online power plant portfolio and their loading, to prevent any potentially threatening generator interactions during operation.

In future bulk power systems with high integration of VSWTs in which they are needed to take part in primary frequency response following the considerable frequency excursions, appropriate WECS and deployment of well-designed pitch angle controller and inertial emulator is essential to ensure system operation security. While the state-of-the-art research studies have shown that wind units can provide this response, Chapter 4 identifies the issues related to the application of such controls at large scale power networks, namely huge VSWT speed changes using speed based deloaded MPPT curve, implementing one-mass drive train mechanical equations which leads to inaccurate oscillation frequency of electromechanical modes, and using measured wind speed date in their deloaded manner through blade pitching pitch angle controller. Due to measurement errors, some VSWTs might become unstable due to lack of sufficient reserve margin. With the proposed accurate VSWT mechanical power and modified functional representations of power coefficient, MPPT surface is quantified to determine the operating point of VSWT in terms of its speed and pitch angle. Then, the linear relationship between the power efficiency and pitch angle is approximated using a second-order polynomial. Using a supplementary control loop, the deloaded WECS is controlled to behave like conventional SG during depressed frequency conditions. In the proposed primary frequency control, an inertial power injection takes places followed by an active power determined by a novel pitch control when the network frequency excursion happens. This electrical power injection is defined from a control structure with a power reference adjustment obtained from rotor speed and pitch angle using the novel MPPT surface and the pitch angle reference regulation made by a governing function identical to conventional units. Additionally, the accurate double-mass mechanical system dynamics is used to characterize the drive train and oscillation frequency of electromechanical modes. The proposed frequency controller not only guarantees efficient contribution by WECSs to primary frequency regulation but also ensures their stable operation. The proposed WECS model is expected to obtain realistic and correct simulation results once utilized for the bulk power system performance studies like 36-zone GB network.

Chapter 5 introduces a control design of PV system to take part in frequency regulation by making it work away from its MPPT using delaoded based droop control and emulating inertial response without the need for BES. In the inertial emulator, the inertial power is taken from dc link capacitor by adjusting the dc link reference voltage. This approach combined with droop controller have a direct impact also over the global indicators of frequency quality such as decrease the stead-state deviation, frequency nadir and RoCoF . The main limitation of PV power plants without internal BES is their inherent incapability to obtain under-frequency response, unless reserves power is provided during the normal operation. In this study, the reserve level is selected which suffices in order for the PV system to have a positive influence on frequency regulation.

In Chapter 6, an average but accurate dynamic model of VRB is derived. One of the main functionalities of this modelling is that the boost converter and DC link are properly taken into account. Another focus of this chapter is to develop a new primary frequency control strategy that enables BESS to regulate the active power outputs and obtain 36-zone GB power system frequency regulation. In this context, two different modes are provided: i) Frequency droop control mode for BESSs to provide primary frequency support, and ii) Inertial emulator mode to synthetically inherit frequency support functions from conventional synchronous generators. Hence, the dynamic behaviour of dc link capacitor is identical to the inertia constant reverse of SG's rotors. Note, the BESSs do not contribute to the overall system inertial power as they do not have rotational parts like SGs and WTs. To this end, this inertial power is taken from dc link capacitor by adjusting the dc link reference voltage.

Chapter 7 develops a comprehensive smart induction motor variable frequency drive system for frequency regulation in large scale smart grids incorporating high penetration of power converter generating units. For

drive controlled smart induction motors, major modifications in the speed controllers are deployed to allow them to alter their power consumption in proportion to the frequency deviations and provide inertial and reserve power with no extra power electronics. This study firstly explores the dynamic formulations associated with this motor modelling and extracts its scalar speed control. Additionally, the low-speed performance of elementary volt-per-hertz speed control is improved in a compensated volt-per-hertz speed control. Moreover, the ratio of the rated frequency to arbitrary frequency term which is missed from previous literatures is added to the pertinent equations. In the model presented, the reserve rotor speed of primary controller is calculated based on the grid frequency changes to be added to the reference rotor speed. The rate of change of reserve rotor speed is also imposed by a rate limiter determined by motor active power and load inertia. This is due to the fact that amplitude of electromagnetic torque variation and motor stator's current variation would be largely underestimated neglecting motor's load inertia as done in previous studies. Furthermore, the motor inertial power is suitably emulated and the grid frequency variation is directly integrated into motor inverter reference frequency instead of rate of change of frequency. As a consequence, the amount of frequency response ancillary services required from conventional generators can be significantly mitigated. This would also permit the UK NG to accommodate larger shares of power converter based units like PVs and WECSs reducing their curtailment to maintain adequate synchronous generation and inertial and droop based primary frequency response in the grid.

One of the main goals of this research in Chapter 8 is to develop fast and accurate methodologies for estimating the size of active power disturbances using frequency data gathered by PMUs. In an online procedure, the post-event system inertia and the IR are estimated, simultaneously and independently by using the RoCoF based modified swing equation considering the discrete sampling data from PMUs. The load damping effect and its characteristic is taken into account in the proposed formulation. In this context, a simple, robust and reliable technique based on the IR is used to obtain an estimation of the LoG size. The load's power deviation after the LoG event is subtracted from the estimated IR to obtain the LoG size. Furthermore, in order to get rid of the discrete quantization, a 5th order interpolation technique applied on the estimated IR to achieve the LoG size. Considering the PMU non-ideal capability to track the frequency and RoCoF, the effectiveness of the proposed LoG size estimation approach is investigated using a real PMU implementing a commercially-available synchrophasor estimation algorithm. To this end, a 5th order interpolation technique is deployed to circumvent the frequency undershoot. Further, the PMU measurement reporting latency is also taken into account.

Chapter 9 develops a comprehensive MCS based SFC. In modernized power networks, the synchronised data gathered from PMUs in WAMS is increasingly progressing in order to become the main enabler in the real-time monitoring and control action architecture. However, despite the extraordinary implementation of the PMUs, full system observability and controllability are still unrealistic. In practice, communication infrastructure cost and its latency related to the handling large number of data sets and PMUs fuel the ambition to derive the analysis techniques in real-time power system applications. This fact further affects fast, reliable and practical local and wide-area SFC based WAMs and disturbance sizing for real-time and on-line power system applications like supporting fast frequency services. The local SFC algorithm would, based on knowing the max delta P deployment for the system prior to the disturbance and from the RoCoF (df/dt) as calculated for the centre of inertial mass in the region, deploy this scale of response in sufficient time, assuming (to make it easy) this is being achieved purely from demand reduction action. This is to target then to be delivered based on an "event trigger" according to the regional RoCoF (df/dt) and absolute frequency measured in a defined period which can be up to as long as there is a respond, the volume of response deployed by zone being dependent on the observed RoCoF (df/dt). The objective is to see that this "simple" local SFC, which would be less reliant on wide area coms and real-time calculation/coordination but which will see a regionally different RoCoF (df/dt) across the system during the event, is superior.

10.3. Contributions

The main contributions of the research presented in this thesis can be described as follows:

- Presenting a 36-Zone GB transmission system network reduction from National Grid (NG) and further data and modelling developed to support research into future power networks.
- Developing CCGT and investigating its dynamic performances in four-area based KRK and 36-Zone GB network under high penetration CCGTs.
- Creation of an appropriate WECS with well-designed pitch angle controller and inertial emulator for large scale power networks under high penetration of renewable energy sources.
- Quantifying the MPPT surface for WECS to determine the operating point of VSWT in terms of its speed and pitch angle using the proposed accurate VSWT mechanical power and modified functional representations of power coefficient.
- Providing a linear relationship between the power efficiency and pitch angle deploying a second-order polynomial.
- Defining the electrical power injection of primary frequency control of WECS from a control structure with a power reference adjustment obtained from rotor speed and pitch angle using the novel MPPT surface and the pitch angle reference regulation made by a governing function identical to conventional units.
- Deploying the accurate double-mass mechanical system dynamics to characterize the drive train and oscillation frequency of electromechanical modes in WECS.
- Developing a comprehensive smart induction motor variable frequency drive system for frequency regulation in large scale smart grids incorporating high penetration of power converter generating units.
- Applying major modifications in the speed controllers of smart motors to allow them to alter their power consumption in proportion to the frequency deviations and provide inertial and reserve power with no extra power electronics.
- Calculating the reserve rotor speed of primary controller based on the grid frequency changes to be added to the reference rotor speed.
- Imposing the rate of change of reserve rotor speed by a rate limiter determined by motor active power and load inertia.
- Emulating the motor inertial power suitably
- Introducing a control design of PV system to take part in frequency regulation by making it work away from its MPPT using delaoded based droop control and emulating inertial response without the need for BES.
- Deriving an average but accurate dynamic model of VRB.
- Developing a primary frequency control strategy that enables BESS to regulate the active power outputs and obtain 36-zone GB power system frequency regulation.
- Developing fast and accurate methodologies for estimating the size of active power disturbances using frequency data gathered by PMUs.
- Estimating the post-event system inertia and the IR simultaneously and independently by using the RoCoF based modified swing equation considering the discrete sampling data from PMUs.
- Modelling the load damping effect and its characteristic in the proposed LoG formulation.
- Creating a simple, robust and reliable technique based on the IR to obtain an estimation of the LoG size.
- Applying a 5th order interpolation technique on the estimated IR in order to get rid of the discrete quantization.
- Deploying an interpolation technique to circumvent the frequency undershoot measured by PMUs.
- Taking into account the PMU measurement reporting latency.

- Developing fast, reliable and practical local and wide-area SFC based WAMS for real-time and on-line power system applications like supporting fast frequency services.

10.4. Future Developments

The research presented in this thesis has successfully delivered on the majority of its objectives and succeeded to make several significant contributions to power system community. Nonetheless, a number of potential fields for additional development of this research are discussed hereinafter.

There is a possibility of exploring other fast service providers for local and wide-area SFC. A further option to local and wide-area SFC based WAMS is to mathematically model the expected behaviour of the system during an event in detail, in real time and by doing so anticipate and optimise the SFC requirement. The optimization will coordinate and initiate all the service providers those are armed to arrest the frequency deviation over a time scale of seconds.

The proposed framework for LoG estimation can be extended by estimating of LoG and the equivalent inertia of the system, which is highly affected by the presence of inverter-based sources. Further studies can be done to apply power variations of the CCL or CIL on the LoG size estimation. Additionally, by partitioning the network in several regions and having disturbance size estimation done with at least two generators at each region, the decentralized LoG can be derived. In this possible framework, the communication links for the incident size estimation needs to be constructed only within the PMUs of each region. This can significantly reduce the communication infrastructure cost and latency associated with data communication channels. In this approach, disturbance size estimation can be accomplished independently within each area. Moreover, the fast frequency response resources of each area can be controlled in a decentralised mode (local SFC mode) when a disturbance is characterized within each area.

The service providers modelled in this thesis can be slightly changed to take into account the virtual synchronous machine concept referring to the well-known synchronization mechanism deployed in synchronous machine, which enables WECS, BESS and etc. to synchronize with power grid. As it mentioned, they can naturally provide the desired inertial response to undertake the responsibility for the short term frequency stability especially in weak grids.

A new market mechanism and enhanced frequency based inertia market to regulate frequency or RoCoF can be created. Implementation of this ancillary service market for various technical features like fast frequency response with the aim of mitigating RoCoF can be investigated considering all fast service providers.

There is currently no commercial incentive to encourage grid users to provide very fast frequency response services; therefore, there is no business-as-usual route to justify investment. In this context, a new balancing service product, and the value of the response can be assessed and defined. The aim can be to create a new balancing service allowing immediate roll out of the EFCC, and achieving the savings envisaged on frequency response cost. A new commercial balancing service can be developed and rolled out. In this scheme, the renewables will have a new source of revenue, encouraging their growth. These new technologies such as solar PV combined with BES will have new commercial incentives to provide response to the grid. New EFCC entrants will make the frequency response market more competitive and reduce the cost and carbon impact of frequency control methods. It is envisaged in future that response services would be purchased through a commercial mechanism that reflects the value of the response provided. Faster responses that are close to the disturbance trigger are of most value to the system. A response provider could therefore choose to use only local

measurements, or to subscribe to the central control system service that would accelerate the response. The service provider would therefore balance the cost of installing communications links with the additional income from the service income.

11. Appendix

This appendix provides the list of software tools which are developed in this thesis in order to model 36-Zone GB network, all service providers (CCGT, WECS, PV, BES, SIM), LoG size estimation and SFC based MCS (See Table 11-1).

Table 11-1: List of Developed Software Tools

Developed Items	Implemented Software
36-zone GB transmission system network modeling based on NG's data	DIgSILENT (DPL/DSL)
CCGT modelling for 36-zone GB network	DIgSILENT (DPL/DSL)
WECS modelling for 36-zone GB network with well-designed pitch angle and inertial controllers	DIgSILENT (DPL/DSL)
Developing SIM variable frequency drive system for 36-zone GB network	DIgSILENT (DPL/DSL)
Deriving PV for 36-zone GB network to support SFC	DIgSILENT (DPL/DSL)
Deriving BES for 36-zone GB network to support SFC	DIgSILENT (DPL/DSL)
Developing fast and accurate LoG size estimation using frequency data gathered by PMUs	Matlab (mfile/Simulink)
Developing fast, reliable and practical local and wide-area SFC based MCS for real-time and on-line 36-zone GB power system applications like supporting fast frequency services	DIgSILENT (DPL/DSL)